

Pyrrole-based Photosensitisers for Photomedicine

*Synthesis, Photophysical and Photobiological Evaluation of Chlorins and
Dipyrrin Complexes*



Zoi Melissari M.Sc.

*A thesis submitted to Trinity College Dublin
the University of Dublin for the degree of*

Doctor of Philosophy

Under the supervision of

Prof. Dr. Mathias O. Senge (Trinity College Dublin)

and co-supervision of

Prof. Dr. Albert M. Brouwer (University of Amsterdam)

Asst. Prof. Dr. René M. Williams (University of Amsterdam)

June 2022

Pyrrole-based Photosensitisers for Photomedicine

ACADEMISCH PROEFSCHRIFT

ter verkrijging van de graad van doctor

aan de Universiteit van Amsterdam

op gezag van de Rector Magnificus

prof. dr. ir. K.I.J. Maex

ten overstaan van een door het College voor Promoties ingestelde commissie,

in het openbaar te verdedigen in Trinity College Dublin,

op maandag 30 Mei 2022, te 11.00 uur

door Zoi Melissari

geboren te Alexandroupoli

Promotiecommissie

<i>Promotores:</i>	prof. dr. A.M. Brouwer	Universiteit van Amsterdam
	prof. dr. M. O. Senge	Trinity College Dublin
<i>Copromotor:</i>	dr. R.M. Williams	Universiteit van Amsterdam
<i>Overige leden:</i>	dr. G. Gasser	Paris S & L University
	prof. dr. I. Rozas	Trinity College Dublin
	prof. dr. S. Woutersen	Universiteit van Amsterdam
	dr. H. Zhang	Universiteit van Amsterdam
	dr. ing. A. Petrignani	Universiteit van Amsterdam

Faculteit der Natuurwetenschappen, Wiskunde en Informatica

The research covered in this thesis was conducted within a Joint Doctorate in the Molecular Photonics Group at the Van 't Hoff Institute for Molecular Sciences, University of Amsterdam and in Trinity College Dublin (TCD), the University of Dublin, Ireland. The work was financially supported by the European Union's Horizon 2020 research and innovation programme under the Marie Skłodowska-Curie grant agreement no. 764837.



“Τα πάντα ρέει και ουδέν μένει”

~ Ηράκλειτος ~

“Everything flows and nothing remains”

~ Heraclitus ~

“Η ζωή μια φορά μας δίνεται, Απαξ που λένε. Σαν μια μοναδική ευκαιρία, Τουλάχιστον μ'αυτήν την αυτόνομη μορφή της δεν πρόκειται να ξαναυπάρξουμε ποτέ. Και 'μεις τι την κάνουμε, ρε? Αντί να τη ζήσουμε? Τι την κάνουμε? Την σέρνουμε από εδώ και από κει δολοφονώντας την”

~ Χρόνης Μίσσιος ~

“A self that goes on changing is a self that goes on living.”

~ Virginia Woolf ~

“Nothing in life is to be feared, it is only to be understood. Now is the time to understand more, so that we may fear less”

~ Marie Salomea Skłodowska Curie ~

Declaration

I declare that this thesis has not been submitted as an exercise for a degree at this or any other university and it is entirely my own work.

I agree to deposit this thesis in the University's open access institutional repository or allow the Library to do so on my behalf, subject to Irish Copyright Legislation and Trinity College Library conditions of use and acknowledgement.

I consent to the examiner retaining a copy of the thesis beyond the examining period, should they so wish (EU GDPR May 2018).

Furthermore, where work was carried out jointly, is duly acknowledged in the text wherever included.

A handwritten signature in blue ink, appearing to read 'Melissari', with a large loop at the end.

Signature and Date

M.Sc. Zoi Melissari

03.06.2022

The research covered in this thesis was conducted within a Joint Doctorate in the Senge Group in Trinity College Dublin (TCD), the University of Dublin, Ireland; in the Molecular Photonics Group at the Van 't Hoff Institute for Molecular Sciences, University of Amsterdam (UvA), the Netherlands; in the Photobiology Group in University of Coimbra (UC), Portugal; and in the company BIOEMTECH technologies in Athens, Greece.

This project has received funding from the European Union's Horizon 2020 research and innovation programme under the Marie Skłodowska-Curie grant agreement n°764837.

Summary

Photosensitisers (PSs) are medicinal molecules that are used as agents to induce a phototherapeutic effect upon irradiation by reacting with the molecular oxygen and producing either singlet oxygen or reactive oxygen species inside the tumorous tissue. The quest for novel molecules is prominent and ongoing in order to surmount several limitations of the commercially available PSs. In this work we aimed to develop and synthesise new molecules that are based on the pyrrole ring. Therefore, zinc(II) *gem*-dimethyl chlorins, zinc(II) chlorin-porphyrin arrays, and tris(dipyrrinato)aluminium(III) complexes were synthesised and characterised by ^1H , ^{13}C , ^{27}Al NMR spectroscopy, mass spectrometry, UV-Visible absorption, and fluorescence emission spectroscopy. A comprehensive study of the photophysical properties of the ground and excited states and the singlet oxygen determination was completed. This was aided using time-correlated single photon counting and nanosecond transient absorption spectroscopy. Furthermore, preliminary *in vitro* evaluation against a colon carcinoma cell line (CT26) was assessed to investigate their photodynamic effect. Density functional theory calculation accompanied the experimental findings, and a complementary single crystal X-ray analysis was assessed for several molecules.

Specifically, in Chapter 2, the zinc(II) *gem*-dimethyl chlorins (**Zn1** and **Zn2**) were synthesised *via* Lindsey's *de novo* synthetic procedure, with the *gem*-dimethyl group attributing resistant to their oxidation. Additionally, their free base counterparts were prepared (**FB1** and **FB2**). All the chlorins exhibited high triplet state yields ($\Phi_{\text{isc}} = 0.70 - 0.90$) with excellent singlet oxygen quantum yields in polar solvents ($\Phi_{\Delta} = 0.40 - 0.85$); with the metallochlorins displaying longer lived triplet excited states (~ 200 ns) than the free base analogues (~ 160 ns). Consequently, the free base showed higher fluorescence yields and lifetimes ($\Phi_f \sim 0.10$, $\tau_s \sim 6$ ns) than the zinc(II) chlorins ($\Phi_f \sim 0.5$, $\tau_s \sim 1$ ns). Finally, zinc complexes tend to internalise into the cells showing great phototoxicity upon irradiation at low and safe concentrations ($\text{IC}_{50} \sim 0.4 - 1$ μM).

In Chapter 3, we used the 4-bromophenyl *gem*-dimethyl chlorin for further structural alteration *via* standard palladium catalysed Suzuki reaction. Three novel porphyrin-chlorin dyads (**3.18**, **3.20**, **3.21**) and one chlorin-porphyrin-chlorin

triad (**3.19**) linked with a 1,4-phenylene bridge were synthesised. The insufficient solubility of the triad prevented further photophysical characterisation. The dyads exhibited singlet and triplet excited features similar to the chlorin subunit indicating that a fast porphyrin to chlorin energy transfer occurs upon photoexcitation. The ethylpropyl substitution of **3.21** showed an interesting, delocalised triplet excited state. All the dyads displayed moderate triplet excited lifetimes in toluene and ethanol and efficient singlet oxygen generation. Dyad **3.21** displayed the higher singlet oxygen production. Time-dependent DFT calculations predicted the electron distribution within the linker with an alteration in the conformation in comparison with the other two dyads. Lastly, However, regardless of the absence of dark toxicity, they did not exhibit any phototoxicity with light doses up to 2 J cm^{-2} , denoting that this alteration attenuates the phototoxicity that the chlorin subunit displayed.

In Chapter 4, a family of novel aluminium tris(dipyrrinato) complexes bearing different substituents in the periphery of the dipyrrin core were obtained. Their absorption spectra indicated the excitonic states formation and the co-occurrence of the $n - \pi^*$ and $^1\pi - \pi^*$ transitions. Aluminium complexes appear as weak fluorescence emitters ($\Phi_f = 0.01 - 0.07$) in toluene, whereas in ethanol the signal was negligible. A similar trend was presented in the singlet excited state lifetimes (1.5 – 5 ns). However, they showed long-lived triplet excited states in air-equilibrated conditions (250 – 350 ns) and in oxygen free conditions (50 – 200 μs). In addition, they generated moderate singlet oxygen quantum yields with **A ℓ (DIPY)₃8** (in toluene) and **A ℓ (DIPY)₃9** (in ethanol) displaying the higher. Following, the *in vitro* screening of eight of the complexes showed that four of them were able to trigger cell death upon irradiation at safe nanomolar and micromolar concentrations with the following ascending order: **A ℓ (DIPY)₃4** < **A ℓ (DIPY)₃12** < **A ℓ (DIPY)₃13** < **A ℓ (DIPY)₃8**, pointing the latter as the best PS candidate. We surmise that the polar groups can facilitate the amphiphilicity allowing for efficient cell internalisation. Ultimately, we attempted to evaluate the radiolabelling potential of **DIPY8** with indium-111. This resulted in the formation of the radiolabelled dipyrrin with indium-111 in high incorporation (95%).

samenvatting

Op pyrrool gebaseerde fotosensibilisatoren in de geneeskundige lichttherapie

*Synthese, foto-fysische en foto-biologische evaluatie van chlorine-
en dipyrriene complexen*

Zoi Melissari M.Sc.

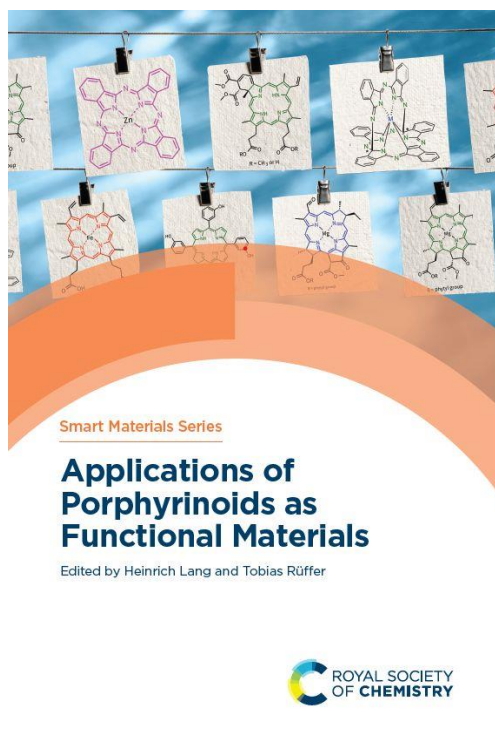
Foto-dynamische therapie (PDT) is een door licht geactiveerde therapie waarbij gebruik wordt gemaakt van een medicijn, de fotosensitizer (PS), licht en moleculaire zuurstof. Eerst wordt de PS toegediend via een systemische of plaatselijke route en vervolgens hoopt het zich op in specifiek weefsel. Het therapeutische effect hangt samen met het vermogen van de PS om zijn triplet-geëxciteerde toestandsconfiguratie te genereren bij excitatie. Deze toestand kan reageren met de aanwezige moleculaire zuurstof en de productie van zeer reactieve singlet-zuurstof ($^1\text{O}_2$) en andere reactieve zuurstofsoorten (ROS) veroorzaken. Deze soorten resulteren in een specifieke celdood van kwaadaardige cellen of een antimicrobiële werking tegen bacteriën of virussen. De huidige klinisch goedgekeurde PS's voor PDT tegen kanker zijn voornamelijk porfyrienes (bijv. Foscan, Tookad Soluble) en hebben nog steeds beperkingen (bijv. slechte oplosbaarheid in water, aggregatie, fotobleking, langzame klaring uit het lichaam, enz.); daarom is het belangrijk om alternatieve PS's te ontdekken. In dit proefschrift wordt de ontwikkeling van nieuwe op pyrrool gebaseerde PS's beschreven. Eerst werden chlorine-verbindingen met een gem-dimethylgroep gesynthetiseerd en onderzocht op hun in vitro fototoxiciteit. De resultaten toonden aan dat de chlorine-verbindingen potentiële PS-kandidaten voor PDT kunnen zijn, aangezien ze een zeer goede fototoxiciteit vertonen tegen de coloncarcinoomcellijn CT26, hoge singlet-zuurstof kwantumopbrengsten in polaire oplosmiddelen, bescheiden fluorescentie kwantumopbrengsten en matige levensduur van de triplettoestanden na foto-excitatie. Ten tweede onderging een van de zink (II) chlorine-verbindingen standaard palladium gekatalyseerde kruiskoppelingsreacties met verschillende porfyriene-eenheden, dit resulteerde in de ontwikkeling van nieuwe porfyriene-chlorine 1,4-fenyleen-gekoppelde arrays. De eigenschappen in aangeslagen toestand, de singlet-

zuurstof generatie en de in vitro-onderzoeken werpen licht op de processen die plaatsvinden bij foto-excitatie. Porphyrine-chlorine arrays resulteerden in matige fluorescentie kwantumopbrengsten en triplet-geëxciteerde levensduren. Bovendien ondergaan ze een snelle energieoverdracht van de porfyryne naar de chlorine sub-eenheid en werden hoge kwantumopbrengsten van singlet zuurstof bepaald. De voorlopige in vitro-onderzoeken waren echter niet veelbelovend omdat de moleculen vanwege hun lage permeabiliteit en hoog molecuulgewicht niet in cellen werden geïnternaliseerd. Ten derde, werd een bibliotheek van nieuwe aluminium(III)-gecoördineerde dipyrine-gebaseerde complexen ontwikkeld. De nadruk werd gelegd op de foto-fysische en foto-biologische eigenschappen om de foto-dynamische werkzaamheid te verduidelijken. De tris(dipyrinato)aluminium(III)-chelaten tonen excitonische toestanden in de absorptiespectra en zijn zwakke fluorescentie-emitters. Ze vertonen kortstondige aangeslagen singlet toestanden; ze gaan echter gepaard met langlevende triplet-aangeslagen toestanden en ze genereren matig singlet-zuurstof bij bestraling. De eigenschappen zijn afhankelijk van de polariteit van de omgeving. De in vitro fototoxiciteitsstudies tonen dat de helft van de complexen veelbelovende PDT-middelen zijn omdat ze een grote fototoxiciteit vertonen bij lage en veilige concentraties. Tijdsafhankelijke dichtheids-functionaal theorie (TD-DFT) berekeningen en mono-kristallijne röntgenanalyse worden ook beschreven.

Publications

1. **Z. Melissari**, R. M. Williams, M. O. Senge, Porphyrinoids for Photodynamic Therapy, In *Applications of Porphyrinoids as Functional Materials*, Eds. H Lang and T. Ruffer, Royal Society of Chemistry, Croydon, UK, Chapter 9, **2021**, 252–291.
2. K. J. Flanagan, M. Paradiz Dominguez, **Z. Melissari**, H.-G. Eckhardt, R. M. Williams, D. Gibbons, C. Prior, G. M. Locke, A. Meindl, A. A. Ryan, M. O. Senge, Structural effects of meso-halogenation on porphyrins, *Beilstein J. Org. Chem.* **2021**, 17, 1149–1170.
3. **Z. Melissari**, H. C. Sample, B. Twamley, R. M. Williams, M. O. Senge, Synthesis and spectral properties of *gem*-dimethyl chlorin photosensitisers, *ChemPhotoChem* **2020**, 4, 8, 601–611. An invited contribution to a Special Collection on Photopharmacology.

Cover Picture In *Applications of Porphyrinoids as Functional Materials*, Royal Society of Chemistry **2021**, Editors: Heinrich Lang, Tobias Ruffer



Notes on Publications

Chapter 1 contains details from publication 1 (book chapter) and Section 1.5 contains parts of a collaborative review project with Paula Teeuwen, manuscript in preparation.

Chapter 2 contains details from publication 3.

Chapter 3 and **Chapter 4** are in preparation for publication.

Other publication

C. Mikra, **Z. Melissari**, M. G. Kokotou, P. S. Gritzapis, K. C. Fylaktakidou, *Microwave-assisted synthesis of hydroxamic acid incorporated quinazolin-4[3H]-one derivatives*, *Sustain. Chem. Pharm.* **2022**, accepted article.

Conference Abstracts

Poster Presentations:

- ❖ Z. Melissari, H. C. Sample, R. M. Williams, M. O. Senge, “*Synthesis and spectral properties of gem-dimethyl chlorin photosensitisers*” in HighLIGHTing Science POLYTHEA meeting, 27.05.2021-28.05.2021, online, Poster no 13.

- ❖ Z. Melissari, H. C. Sample, R. M. Williams, M. O. Senge, “*Synthesis and spectral properties of gem-dimethyl chlorin photosensitisers*” in 5th Photodynamic day, in the framework of the International Day of Light 2021, 18.05.2021, online, poster P32.

- ❖ Z. Melissari, H. C. Sample, R. M. Williams, M. O. Senge, “*Synthesis and spectral properties of gem-dimethyl chlorin photosensitisers*” in ACS Spring 2021, 05.04.2021-30.04.2021, online, Poster, 3545570 (paper ID).

- ❖ Z. Melissari, H. C. Sample, R. M. Williams, M. O. Senge, “*Synthesis and spectral properties of gem-dimethyl chlorin photosensitisers*” in The Irish Association for Cancer Research (IACR) Virtual Conference, 24.03.2021-26.03.2021, online, Poster No 67.

- ❖ Z. Melissari, H. C. Sample, R. M. Williams, M. O. Senge, “*Synthesis and spectral properties of gem-dimethyl chlorin photosensitisers*” in the 27th Lecture Conference on Photochemistry, GDCh, 14.09.2020-15.09.2020, online, Abstract Poster number PP-04.

- ❖ Z. Melissari, H. C. Sample, R. M. Williams, M. O. Senge, “*Design and synthesis of optimised photosensitisers for application in photodynamic therapy*” presented to the International Advisory Board of POLYTHEA project, 16.12.2019, Amsterdam, the Netherlands.

- ❖ Z. Melissari, H. C. Sample, R. M. Williams, M. O. Senge, “*Design and synthesis of optimised photosensitisers for application in photodynamic therapy*”, NWO CHAINS 2019, The Dutch Chemistry Conference, Veldhoven, the Netherlands, 10.12.2019-11.12.2019, poster no 197.
- ❖ Z. Melissari, H. C. Sample, R. M. Williams, M. O. Senge, “*Design and synthesis of new photosensitisers with optimised photophysical properties for application in photodynamic therapy*” in the 17th Congress of the International Union of Photobiology and 18th Congress of the European Society for Photobiology (ESP), Barcelona, Spain, 25.08.2019-30.08.2019, poster no. 089.

Oral Presentations:

- ❖ Z. Melissari, R. M. Williams, M. O. Senge, “*Aluminium tris(dipyrrinato) complexes as potential photosensitisers in photodynamic therapy*”, in NWO CHAINS 2021, The Dutch Chemistry Conference, 07.12.2021-08.12.2021, ‘Molecular tools for application in life sciences’ parallel session, 08.12.2021, online.
- ❖ Z. Melissari, R. M. Williams, M. O. Senge, “*Synthesis, photochemical and photobiological evaluation of novel photosensitisers*”, 3rd year talk of Dublin Chemistry Graduate Seminars 2020/21 organised by TCD and DCU, Dublin, 02.09.2021, online.
- ❖ Z. Melissari, R. M. Williams, M. O. Senge, “*Investigation of a novel class of aluminium tris(dipyrrinato) complexes as potential photosensitisers*” in ACS fall 2021, 22.08.2021-26.08.2021, session: Coordination Chemistry: Synthesis and Characterisation, virtual zoom room 15, 22.08.2021, online.

- ❖ Z. Melissari, H. C. Sample, R. M. Williams, M. O. Senge, “*Synthesis and spectral properties of gem-dimethyl chlorin photosensitisers*”, in the 1st HighLIGHTing Science POLYTHEA meeting, 27.05.2021-28.05.2021, flash presentation, 27.05.2021, online,
- ❖ Z. Melissari, “*Development of new photosensitisers for application in Photodynamic Therapy*” in the POLYTHEA «From Academia to Industry» online Entrepreneurial Winter School, 08.12.2020-11.12.2020, flash presentation, 11.12.2020, online.
- ❖ Z. Melissari, H. C. Sample, R. M. Williams, M. O. Senge, “*Synthesis and spectral properties of gem-dimethyl chlorin photosensitisers*” in the e- Congress, Photodynamic Therapy and Photodiagnosis Update 2020, 05.11.2020-06.11.2020, poster flash presentation, 05.11.2020, online.
- ❖ Z. Melissari, “*Design of optimised photosensitisers*” in the POLYTHEA Photodynamic Therapy Intersectorial School, 15.07.2019-19.07.2019, University of Limoges, France, 16.07.2019.
- ❖ Z. Melissari, “*Design of optimised photosensitisers*” in the POLYTHEA Winter School – Fundamentals of Photodynamic Therapy, 26.11.2018-30.11.2018, University of Coimbra, Portugal, 26.11.2018.

Acknowledgements

I would like to thank my supervisors, my labmates in TCD and UvA, my friends and family and all the people involved in the POLYTHEA consortium that made this project real and offered me this great Ph.D. opportunity.

Initially, I would like to thank Prof. Dr. Mathias O. Senge for his continuous guidance and support, the fast replies, and of course the wonderful group that he opened the door for me to join. Also, I would really like to thank my co-supervisor Prof. Dr. René M. Williams for his continuous trust, help, and guidance through these years. For being always available, so I can knock his door, and with patience answering my questions, even when several photophysical aspects seemed like a mountain in front of me. I will be always grateful for the trust that they both showed me. Of course, I am thanking you also for giving me the opportunity to work in your facilities and providing all the instrumentation and the materials I needed.

Since I conducted my research within a joint degree between two universities, I would like to thank my other supervisor, Prof. Dr. A. M. Brouwer for his thorough comments and critical questions throughout the project. I thank the professors of molecular photonics group: Prof. Dr. J. Buma, Prof. Dr. S. Woutersen, Prof. Dr. H. Zhang, and Prof. Dr. A. Petrigiani for the insightful comments in our group meetings.

Many thanks to Dr. Lígia C. Gomes-da-Silva for having me in her group for a two-month training (University of Coimbra), for supporting me, and for teaching me how to conduct the *in vitro* photobiological experiments. Also, I am thankful to Dr. Fábio Schaberle for his great help and guidance. It was an unforgettable experience where I met amazing people! Then, I thank Prof. Dr. George Loudos for having me for a three-week training in 'BIOEMISSION TECHNOLOGY SOLUTIONS IKE, Athens, Greece', and Dr. Sophia Sarpaki for supervising me. It was a great experience for me to conduct radiochemical experiments and spend time to their company.

I thank all the POLYTHEA consortium people, the advisory board, Prof. Dr. Stéphanie Leroy-Lhez for making this project real and of course Aurore Berthier

for being always there to help and respond to our queries. I enjoyed so much all our meetings and schools; it was unfortunate that we could not meet in person one more time during the pandemic (I cannot leave the Covid-19 pandemic unmentioned...). I really wish we would be able to meet in person!

Next, a special thank you to Dr. John O'Brien, Dr. Brendan Twamley and Dr. Gary Hessman in TCD for their help on the characterisation of the compounds that are presented in this thesis, and also Drs. Ing. M.F. Michiel Hilbers at UvA for his help with EKSPLA laser and TCSPC equipment. Dr. Wim G. Roeterdink and Drs. Hans J. Sanders for helping in the lab.

I also want to thank my Master's supervisor Prof. Dr. Konstantina Fylaktakidou who trusted me and gave me the chance to conduct my master's thesis project in her lab under the supervision of Dr. Panagiotis Gritzapis. She supported me through a crucial period of my life, and I am glad that our work is on the way to be published.

A huge thanks goes to all my labmates. Dr. Nitika Grover, my fume hood mate for nine months, deserves my honest gratitude for her invaluable support, and her patience, while helping and teaching me during the first months of my Ph.D. in TCD. So, thank you "teacher".

I feel glad and lucky to get to know such beautiful people and colleagues. I do not know where to start. Thanks to the Senge group for sharing knowledge, helping in any possible way, and making the lab such an enjoyable place. I really miss those Friday nights and the after-work (support) pints! I am thankful to everyone for our chats, hikes, coffees, pints, mini trips, and nights out. Special thanks to Piotr, for being my buddy since the beginning, being always there for each other during our Ph.D. time, for helping me acclimatise in Coimbra, for the "irrelevant" coffee breaks, drinks, dances, laughs, and all experiences! I thank Claire, my Penela roommate, finally overlapping in Dublin and Athens for a while which was great (Agistri time was perfect)! Elisabeth, for all the help, tennis (who won at the end?), and our lovely porterhouse nights! Karolis, my fume hood neighbour the past months in TCD, for the support and chats, and... look at us finally submitting our Ph.D. thesis the exact same day, UNREAL! Asterios, for all the help with my project since he joined the group, and our weekend's coffee-

walking arounds. Jessica, thanks for the dates during the lock-down and the chit-chats. Keith, for our little breaks, and your patience with repeating yourself (whaaaat?). Susan (Kill...iney?), thanks for the yummy dinners, the hospitality in Mayo, and the fast proof-read of my book chapter. Harry, thanks for providing the other half for the chlorins. Also I thank Marie, Marc, Gemma, Gana, Alina, Adam, Deirdre and Marta. Bhavya and Begum for our little chit chats and laughs around. I really appreciate and thank Max and Hernán for helping me with my first analysis of data and the calculations at UVA. I thank Max for always be there to help and solve any issues with the measurements and I thank the chaps, Hernán and Dáire, for the laughs and for the after-work pints! Janani, thanks for showing me the “command world”, I am so glad I have you in my Amsterdam life. Jiayun, thanks for the nice Chinese dinners (so smart), Robert, Orr, Alessandra, Ivan, Chao, Federico, Giulia, Yanni, Roberto, Kefan, Jelena, Mauricio, Arno, Rinz, Katerina and the POLYTHEA candidates that were not in Dublin or Amsterdam, Nidia, João, Emma, and Manuel.

I thank, again, Asterios, Claire, and Nitika for proof-reading parts of my thesis.

Ultimately, I would like to greatly thank all my friends, my family, my grandparents Ioakim and Zoi, my godmother Fotini, for the care and love, the support of my choices, the continuous encouragement, for listening to me and be there in my ups and downs throughout my life. My family in Thiva, uncle Dimitris, aunt Tasula, cousins Eleni and Thanasis. My father would be proud of me. My friends in Greece that were always by my side to cheer me up and listen to me, Sofia, Christina, Vaso, Alikí, Tania, Nikolas, Anastasis, Dora, Theodora, Clio, Evgenia, Michalis, Savvas. My childhood friend Christina, in Australia, I owe her a great “thank you griniariko”.

I am exceptionally grateful for my friends who were constantly checking on me lately. 😊

I would like to extend my sincere thanks to my brother Nasos, who selflessly supported my choices, my mother Maria, my uncle Giorgos, my cousins Stella and Ioakim, and my aunt Lemonia, like a sister, she is always by my side and supports me. Finally, I thank myself for reaching this point after all that I have been through! 😊

List of Abbreviations

Ar	Aryl group
APCI	Atmospheric pressure chemical ionisation source
calcd.	Calculated
d	Doublet (NMR)
dec.	Decomposed
DCM	Dichloromethane
dd	Doublet of doublets (NMR)
DIPY	Dipyrrin
DIP-MS	Direct insertion probe-Mass spectrometry
DMF	N,N'-Dimethylformamide
DMEM	Dulbeccos' modified Eagle's medium
DPM	Dipyrromethane
eq.	Equivalents
Eq.	Equation
ESI	Electrospray ionisation
FCS	Fetal calf serum
HOMO	Highest occupied molecular orbital
HRMS	High resolution mass spectrometry
h	Hour
IC	Internal conversion
IC50	Half maximal inhibitory concentration
ICT	Intra-ligand charge transfer
ISC	Intersystem crossing
<i>J</i>	Coupling constant
Laser	Light amplification by stimulated emission of radiation
LED	Light-emitting diode
LUMO	Lowest unoccupied molecular orbital
L.D.	Light dose
MALDI	Matrix assisted laser desorption ionisation
Mes	Mesityl group
min	Minute
M.p.	Melting point

m	Multiplet (NMR)
<i>m/z</i>	mass/charge
NIR	Near infrared
NBS	N-Bromosuccinimide
NMR	Nuclear magnetic resonance
PDT	Photodynamic therapy
Ph	Phenyl
ppm	Parts per million
PBS	Phosphate buffer solution
PS	Photosensitiser
q	Quarter (NMR)
Q-ToF	Quad-time of flight
R_f	Retention factor
RPMI	Culture media (Roswell Park Memorial Institute)
r.t.	Room temperature
ROS	Reactive oxygen species
SEM	Standard error of mean
SBCT	Symmetry breaking charge transfer
s	Singlet (NMR)
S_0	Singlet ground state
S_1	First excited singlet state
T_1	First excited triplet state
t	Triplet (NMR)
t_{inc}	Incremental time
TMP	2,2,6,6-tetramethylpiperidine
TA	Transient absorption (spectroscopy)
TCSPC	Time-correlated single photon counting
TFA	Trifluoroacetic acid
THF	Tetrahydrofuran
TLC	Thin layer chromatography
UV	Ultraviolet
UV/Vis	Ultraviolet-visible spectroscopy
°C	Degree Celsius
δ	Chemical shift (NMR)

λ	Wavelength
Φ_{Δ}	Singlet oxygen quantum yield
Φ_f	Fluorescence quantum yield
τ_T	Triplet state lifetime (phosphorescence)
τ_s	Singlet state lifetime (fluorescence)
k_r	Rate constant of radiative (fluorescent) transition from S_1 to S_0
k_{nr}	Rate constant of non-radiative (fluorescent) transition from S_1 to S_0
k_{isc}	Rate constant of inter-system crossing
k_{ic}	Rate constant of internal conversion
k_q	Rate constant for oxygen quenching rate of triplet state

Table of Contents

Declaration	1
Summary	3
Publications	7
Conference Abstracts	9
Acknowledgements	12
List of Abbreviations	15
Table of Contents	18
Explanatory Note	23
Chapter 1: General Introduction	24
1.1 Historical Overview of Phototherapy.....	24
1.2 Mechanism of Photodynamic Therapy.....	29
1.3 Photodynamic Therapy and Cancer	31
1.4 Photosensitisers in PDT	33
1.4.1 Clinically approved photosensitisers	34
1.4.2 Photosensitisers under development	41
1.5 Dipyrrinato Metal Complexes as Potential PS and their Photophysics ...	46
1.5.1 Zn(II), Ni(II), Cu(II), Pd(II) and Pt(II) dipyrrinato complexes.....	49
1.5.2 Re(I), Ru(II), Rh(III), and Ir(III) dipyrrinato complexes	58
1.6 Photophysical Aspects of PDT.....	69
1.6.1 Ground and excited state properties	69
1.6.2 Photooxidation processes with molecular oxygen.....	76
1.6.3 Light sources.....	79
1.7 Photopharmacological Aspects of PDT	81
1.8 Strategies for Improvement of PS.....	86
1.8.1 Modulation of the photophysical properties	86

1.8.2 Photosensitiser uptake and cellular localisation	88
1.8.3 Targeted PDT and nano-approaches.....	89
Chapter 2: <i>gem</i>-Dimethyl Chlorins as Potential Photosensitisers in PDT	91
2.1 Introduction.....	91
2.2 Objectives.....	98
2.3 Results and Discussion	99
2.3.1 Synthesis of <i>gem</i> -dimethyl chlorins.....	99
2.3.2 Photophysical characterisation and DFT calculations	103
2.3.2.1 Ground state properties.....	103
2.3.2.2 Excited state properties	105
2.3.2.3 Singlet oxygen phosphorescence and quantum yield.....	111
2.3.2.4 DFT and TD-DFT calculations.....	112
2.3.3 <i>In vitro</i> phototoxicity studies of zinc(II) chlorins	114
2.4 Conclusions and Future Work	119
Chapter 3: Synthesis and Photophysical Studies of 1,4-Phenylene-linked Porphyrin-Chlorin Arrays	121
3.1 Introduction.....	121
3.2 Objectives.....	124
3.3 Results and Discussion	125
3.3.1 Synthesis of 1,4-phenylene-linked porphyrin-chlorin arrays.....	125
3.3.2 Photophysical characterisation	127
3.3.2.1 Ground state properties.....	127
3.3.2.2 Excited state properties	131
3.3.2.3 Singlet oxygen phosphorescence and quantum yield.....	139
3.3.3 <i>In vitro</i> evaluation of porphyrin-chlorin dyads.....	141
3.4 Conclusions and Future Work	143
Chapter 4: Tris(dipyrrinato)aluminium(III) Complexes as Potential Photosensitisers in Photodynamic Therapy	145

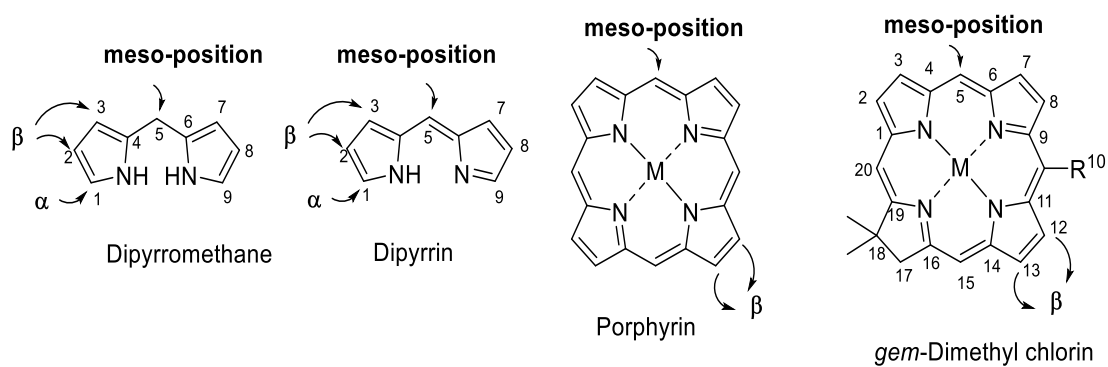
4.1 Introduction	145
4.2 Objectives	152
4.3 Results and Discussion	154
4.3.1 Synthesis of tris(dipyrrinato)aluminium(III) complexes	154
4.3.1.1 Post functionalisation of Al l (DIPY) $_3$ complexes	157
4.3.2 Single-crystal X-ray structure analysis	163
4.3.3 Photophysical characterisation.....	173
4.3.3.1 Ground state properties	173
4.3.3.2 Excited state properties	180
4.3.3.2.1 Singlet excited state	180
4.3.3.2.2 Triplet excited state	185
4.3.3.3 Singlet oxygen generation	189
4.3.4 Photobiological evaluation – <i>in vitro</i> phototoxicity studies	192
4.3.5 Radio labelling with Indium-111	199
4.4 Conclusions and Future Work.....	202
Chapter 5: Experimental Details	205
5.1 General Information and Instrumentation	205
5.2 Single-crystal X-ray Structure Determinations	208
5.2.1 X-ray crystallography details for the chlorins.....	208
5.2.2 X-ray crystallography details for the Al l (DIPY) $_3$ complexes.....	210
5.3 Procedures for the Photophysical Measurements	218
5.3.1 UV-Visible absorption spectra	218
5.3.2 Fluorescence emission and quantum yields.....	218
5.3.3 Time-correlated single photon counting – TCSPC	219
5.3.4 Nanosecond transient absorption spectroscopy.....	219
5.3.5 Singlet oxygen determination and quantum yields	220
5.3.6 Density functional theory (DFT) calculations	221
5.4 Protocols for <i>In Vitro</i> Cytotoxicity Studies	222

5.4.1 Cell culture and preparation of stock solutions.....	222
5.4.2 Dark toxicity studies using resazurin assay.....	222
5.4.3 Phototoxicity studies using resazurin assay.....	223
5.4.4 Cellular uptake studies.....	224
5.5 Synthetic Procedures and Characterisation.....	225
5.5.1 Chapter 2: <i>gem</i> -Dimethylchlorins as potential PSs in PDT.....	225
5.5.1.1 General synthetic procedures.....	225
5.5.1.2 Synthetic details and characterisation.....	227
5.5.2 Chapter 3: Synthesis and photophysical studies of 1,4-Phenylene-linked Porphyrin-Chlorin Arrays.....	235
5.5.2.1 Synthetic procedures and characterisation.....	235
5.5.3 Chapter 4: Tris(dipyrrinato)aluminium(III) complexes as potential PSs in PDT.....	241
5.5.3.1 General synthetic procedures.....	241
5.5.3.2 Starting materials.....	242
5.5.3.3 Synthetic details and characterisation.....	243
5.5.3.4 Radiochemistry procedures.....	263
References.....	265
Appendix.....	286
Chapter 2.....	286
X-Ray crystal structure.....	286
Absorption and fluorescence emission spectra.....	287
Fluorescence decays.....	288
Triplet-triplet transient absorption spectra (TA).....	289
Singlet oxygen emission spectra.....	295
Chapter 3.....	297
Absorption and fluorescence emission spectra.....	297
Fluorescence decays.....	298

Triplet-triplet transient absorption spectra at ambient conditions	299
Singlet oxygen emission spectra.....	303
Chapter 4.....	304
X-Ray crystal structures	304
Triplet-triplet transient absorption spectra (TA)	306
Singlet oxygen emission spectra.....	318

Explanatory Note

Nomenclature for the dipyrromethane, dipyrryn, porphyrin and chlorin cores:



Chapter 1: General Introduction

“Healing is a matter of time, but it is sometimes also a matter of opportunity.”

~ Hippocrates ~

“And if you can't shape your life the way you want, at least try as much as you can not to degrade it.”

~ Konstantinos P. Kavafis ~

1.1 Historical Overview of Phototherapy

Heliotherapy (*Greek etymology: ήλιο + θεραπεία = sun + therapy*) is the alleviating and therapeutic effect of natural sunlight that can be used to treat skin or muscle disorders. Phototherapy (PT) (*Greek etymology: φώτο + θεραπεία = light + therapy*), dates back thousands of years when Egyptians, Indians, Chinese, Romans, and Greeks were instinctively utilising sunlight to treat several diseases including vitiligo, tuberculosis, and psoriasis.^[1] Advances related to the clinical use and safety of PT have been made in the last 50 years, notably in the area of photodynamic therapy (PDT). PDT is an example of PT where light is used to alleviate and treat malignant diseases such as cancer and infections. In PDT, the so-called photosensitiser (PS) is the medium agent needed to convert molecular oxygen to singlet oxygen or other reactive oxygen species, following light irradiation, leading to a therapeutic response.

Delving into the past from Ancient times to the Modern era, several civilisations used light as a treatment for diseases. Egyptians used the extract of *Ammi Majus* seeds in combination with sunlight to treat leukoderma or vitiligo, whereas Indians utilised the extract of *Psoralea Corylifolia* seeds for repigmentation.^[2] Today this therapy is known as PUVA photochemotherapy (psoralen plus UVA light) and uses psoralens to treat various skin disorders *i.e.*, psoriasis and vitiligo.








Another putative benefit from the healing power of light was reported by the ancient Chinese. Interestingly, they ingested colored sheets that were first exposed to sunlight (for men) or moonlight (for women), probably influenced by their cultural background. Romans and Greeks used sunbaths for physical improvement and skin treatment (first treatment for acne). Both ancient Greeks, the historian and philosopher Herodotus (~450 BC) and the physician Herodotus (~1st century AD), recommended that light can be therapeutic. The former attributed the thicker skulls of Egyptian soldiers to the power of sun exposure since they shaved their heads from childhood; in comparison to the Persians who wore hats. The latter stated that the human body can remain healthier with exposure to sunlight '*exposure to the sun is eminently necessary for people who need to eat and take on flesh...however the head must be covered*' (in "*περί ηλιώσεως*" at "*περί τῶν ἔξωθεν προσπιπτόντων βοηθημάτων*"); and also with hot sand fomentation ("*Περί αμμοχωσίας*").^[3] Hippocrates the "father of medicine" was the first to use the term heliotherapy and introduced the healing properties of sunlight by incorporating it into his treatment methods together with a healthy diet, hydrotherapy, massages, and physical exercise.^[1,4] Table 1.1 summarises, in chronological order, important events and developments related to phototherapy and photodynamic therapy throughout the ages.^[5]

The term PDT as it is known today, was introduced by Hermann von Tappeiner, whose student, Oscar Raab (1898), accidentally discovered that the combination of a dye (acridine) and light had a fatal effect on paramecia cells (*Paramecium caudatum*).^[6-8] Following his research on the therapeutic effect of red light on smallpox, in 1903, Niels Finsen won the Nobel prize in medicine and physiology for his contribution to the treatment of *Lupus vulgaris* by ultraviolet light.^[9] The connection between tetrapyrroles and phototherapy dates back to the first biological experiments conducted by Hausmann and Pfeiffer (1908-1911), who reported the photosensitisation in white mice and guinea pigs, using hematoporphyrin (HP) and subsequently resulting in mortality. A couple of years after that, Meyer-Betz injected himself with 200 mg of hematoporphyrin and sensitised himself with sunlight (1913) (Table 1.1).^[10] Regardless of these advancements, it was only after 1970 that PDT was really developed as a medical treatment by Thomas Dougherty and co-workers^[11,12] as a follow up to

Baldes and Lipson,^[13,14] who developed a water-soluble mixture of porphyrin molecules named “hematoporphyrin derivative” (HpD), which became one of the first generation PSs, known as Photofrin (purified form: Photofrin sodium).

Table 1.1. Historical overview of events of phototherapy and photodynamic therapy.

Year	Event
3000 BC – 1800 AD	✚ Romans and Greeks utilised sunlight (sunbathing or using seeds from plants) to treat vitiligo, acne, rickets (rachitis) and psychosis. Hippocrates used exposure to sunlight as one of his treatments.
	✚ Antylos treats rachitis and muscle atonia with sunlight and states the hygienic action of the sunlight (300 AD).
	✚ Larrey (Napoleon’s physician) observed that soldiers’ traumatic ulcers healed quickly after sun exposure (Egypt 1798-1799).
	✚ Discovery of the sun’s infrared spectrum by F. W. Herschel (1800).
	✚ Discovery of ultraviolet radiation by J. W. Ritter and W. Hyde (1801).
1834	5-Methoxypsoralen (5-MOP) was isolated from bergamot oil by Kalbrunner
1841	Discovery of hematoporphyrin (HP) by removing iron from dried blood by Scherer
1855	A. Rikli opened a healthcare station in Slovenia and reintroduced the concept of phototherapy. He developed therapeutic guidelines still applicable today.
1867	Hematoporphyrin fluorescence and fluorescence spectrum by J. L. W. Thudichum.
1871	F. Hoppe-Seyler named the red-purple substance in iron-free heme as hematoporphyrin.
1874	J. H. Schultz first described errors in heme biosynthesis and a porphyria patient.
1877	A. H. Downes and T. P. Blunt first observed ultraviolet light and antimicrobial effect.
1890	T. A. Palm suggested that the sun could play a therapeutic role in rickets.
1898	O. Raab discovered phototoxicity of acridine dye against paramecia.
1899	O. Bernhard promoted heliotherapy at a private clinic in Switzerland.
1903	✚ In Leysin, Switzerland, A. Rollier established the first clinic for the treatment of tuberculosis and rachitis with sunlight.
	✚ N. R. Finsen won the Nobel Prize in Physiology and Medicine for his contribution to the treatment of diseases, especially tuberculosis (lupus vulgaris), with concentrated light radiation
1904	Reports that the presence of oxygen was essential for photosensitisation. H. von Tappeiner and A. Jodlbauer introduced the term “ <i>Photodynamic action</i> ” (“ <i>Photodynamische Wirkung</i> ”).
1905	H. von Tappeiner and A. Jesionek introduced the topical use of eosin as a photosensitiser against facial basal cell carcinoma.
1908-1911	Experiments with hematoporphyrin and light on white mice and guinea pigs by W. Hausmann and H. Pfeiffer.
1913	F. M. Betz self-sensitised himself using hematoporphyrin (HP) injection.

1923	W. H. Goeckerman used a high-pressure mercury lamp to produce artificial broadband UV-B plus topical coal tar to treat psoriasis.
1924	Localisation and fluorescence of endogenous porphyrins in tumours by A. Policard
1928	R. S. Mulliken reported the existence of singlet oxygen.
1930	H. Fischer won the Nobel Prize in Chemistry for his research into the composition of heme and chlorophyll and especially for the synthesis of haemin.
1930s	<ul style="list-style-type: none">  H. Kautsky reported oxygen quenching effect of fluorescence and phosphorescence of dye molecules and the production of metastable singlet oxygen.  H. Kautsky and H. de Bruijn suggested the excited electronic state intermediates of oxygen in chemical reactions.
1947	<p>I. R. Fahmy isolated the active ingredients of <i>Ammi majus</i>, 8-methoxypsoralen (8-MOP) and 5-methoxypsoralen (5-MOP).</p> <ul style="list-style-type: none">  In Egypt, A. M. El-Mofty carried out the first trials with 8-MOP and sun exposure in vitiligo patients.  H. Auler and G. Banzer carried out the first study of selective hematoporphyrin accumulation and photodynamic action in tumours.  Laboratory animal research by H. J. Figge <i>et al.</i> showed that porphyrins have a preferential affinity not only to malignant cells but also to rapidly dividing cells.
1948	
1955	S. Schwartz discovered and isolated the hematoporphyrin derivatives as crude mixture (HpD).
1957	In Essex, England, R. Cremer used phototherapy as a treatment for neonatal jaundice (blue light phototherapy).
1959	D. Harman proposed the free radical theory of ageing and disease.
1960	Lipson and F. J. Baldes reported the tumour localisation and detection by the fluorescence of hematoporphyrin derivative (HpD).
1961	H. G. Magnus described erythropoietic protoporphyria (EPP) as a genetic disorder resulting from decreased activity of ferrochelatase, which is responsible for adding iron to protoporphyrin to form heme.
1962	J. D. Ridgen and A. D. White developed the first helium-neon continuous operating laser which aided Dougherty <i>et al.</i> during the first clinical studies on hematoporphyrin derivative (1978).
1963	A. Wiskemann constructed a phototherapy system with Osram Ultravitalux lamps and another with fluorescent UVB tubes.
1966	Lipson <i>et al.</i> first reported the use of HpD to treat recurrent breast carcinoma.
1974	<ul style="list-style-type: none">  T. B. Fitzpatrick and J. A. Parrish developed PUVA photochemotherapy to control psoriasis vitiligo and other skin disorders.  T. J. Dougherty found that fluorescein diacetate could act as photosensitiser against tumour-bearing animals.
1975	T. J. Dougherty <i>et al.</i> used HpD and red-light irradiation to cure mice and rats bearing a variety of tumours.

1976	<ul style="list-style-type: none"> ✚ K. R. Weishaupt and T. J. Dougherty identified that singlet oxygen is the cytotoxic product of the photochemical reaction with red light. ✚ J. F. Kelly <i>et al.</i> used HpD in patients with bladder cancer.
1978	T. J. Dougherty <i>et al.</i> provide the first large series treatment where 113 cutaneous or subcutaneous malignant tumours were treated by intravenous hematoporphyrin derivative (HpD) Photofrin.
1979	Z. Malik and M. Djaldetti reported the protoporphyrin IX (PpIX) photoinduction from 5-aminolevulinic acid (ALA).
1987-1995	QLT developed and commercialised Photofrin.
1987	D. Dolphin found benzoporphyrin derivative (BPD) to be 10-70 times more cytotoxic than HpD <i>in vitro</i> .
1990	J. Kennedy and R. Pottier discovered the clinical application of ALA.
1993	First PDT drug approval was given to Photofrin for use in bladder cancer in Canada.
1999	The FDA approved 5-ALA (Levulan) for actinic keratosis.
2001	Visudyne (benzoporphyrin derivative-BPD) approved for age macular degeneration AMD (QLT).
2001	Foscan approved in Europe for head and neck squamous cell cancer (Scotia/Biolitec).
2017	The FDA approved the use of 5-ALA (5-aminolevulinic acid) as an optical imaging agent in patients affected by high-grade gliomas (Photonamic GmbH and Co. KG)

Hematoporphyrin (derived from Greek: deep red-purple pigment of blood) first isolated by Scherer in 1841, is a protoporphyrin IX derivative (PpIX) originating from heme (iron-containing porphyrin). It was the molecule that established the link between tetrapyrroles and photosensitisers (PSs) for PDT. Other naturally occurring tetrapyrrolic pigments are chlorophylls, bacteriochlorophylls, and coenzyme B12.^[15] Porphyrins are key elements of metabolic processes and life. Most of the approved drugs for PDT are porphyrin-based PSs with chemical similarity to natural pigments. These examples are clear to see; between protoporphyrin and Photofrin, between chlorophyll a and chlorin e6, between bacteriochlorophyll α and Tookad soluble, and between pheophorbide a and Photochlor (Figure 1.1, Figure 1.3 and Figure 1.4). Porphyrin-type molecules have a high affinity for cancerous tissue and thus preferential accumulation occurs in such tissue. In 1948 Figge *et al.* was the first to report this unique property with an *in vivo* study in mice with various types of cancers using hematoporphyrin injection.^[16] The missing piece of the PDT puzzle was discovery

1.6.1). In PDT, the triplet state of the PS can interact with naturally occurring molecular oxygen and produce either reactive oxygen species ROS *via* an electron transfer process (Type I reaction, electron transfer) or singlet oxygen species $^1\text{O}_2$ *via* an energy transfer process (Type II reaction) or both. PDT relies on the intracellular formation of these cytotoxic species in specific organelles such as mitochondria or lysosomes or indirect effects such as vascular PDT.

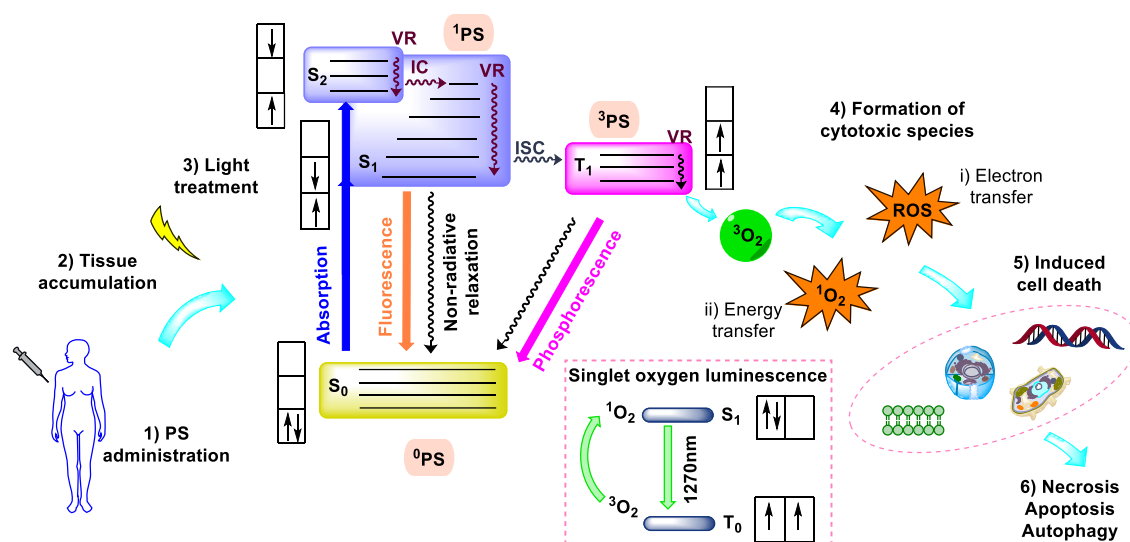


Figure 1.2. Modified Jablonski diagram displaying the photochemical pathways of PS upon excitation; IC: internal conversion; ISC: intersystem crossing; VR: vibrational relaxation.

Finally, this process will lead to a light induced cell death through apoptosis, necrosis, or autophagy with the preferable cell death pathway being apoptotic “natural” cell death, where a low inflammatory response is induced.^[21–24] The same concept is used for extensive ongoing research in the antimicrobial PDT (aPDT); a review by Wiehe *et al.* suitably discusses the antiviral applications and potentials.^[25]

The key points in PDT are the efficient generation of cytotoxic singlet oxygen, which should take place only after light radiation and the enhanced localisation of the PSs in malignant cells. Yet several drawbacks characterise many current PSs, some of which include poor water-solubility, slow body clearance, photobleaching, long-lasting phototoxicity, and shallow skin penetration. These limitations prevent the treatment of deep localised tumours. Hence, it is of great importance to introduce potential candidates with appropriate characteristics. To

summarise the physicochemical, photophysical, and pharmacological features of a PS, an ideal PS should:

- ✚ be pure and stable at room temperature
- ✚ have a low production cost and be commercially available
- ✚ display amphiphilicity and water-solubility
- ✚ show minimum dark-toxicity and high phototoxicity, while not producing toxic metabolites
- ✚ have optimal ADME properties (absorption, distribution, metabolism, excretion)
- ✚ have a strong absorption in the red or NIR region of the electromagnetic spectrum (600 – 800 nm), so that light can deeply penetrate the target tissue and activate the PS; this also depends of the targeted cancer type and the way that the PS is administered (e.g., see TLD-1433)
- ✚ have high selectivity and specific accumulation in target tumour tissues and have subcellular localisation in mitochondria, lysosomes, or the endoplasmic reticulum
- ✚ display high singlet oxygen quantum yields ($\Phi_{\Delta} > 0.50$) or ROS generation
- ✚ have a high ISC yield and thus high triplet energy state yield ($\Phi_{T} > 0.80$) and triplet state lifetimes (τ_{T} ns – μ s scale)
- ✚ have post excitation process-yields that sum to unity ($\Phi_f + \Phi_{isc} + \Phi_{ic} = 1$). However, regarding the fluorescence quantum yields (Φ_f) and singlet excited state lifetimes (τ_s), a compromise can be made. The higher the fluorescence yield the lower the PDT properties and *vice versa*.

1.3 Photodynamic Therapy and Cancer

Cancer is characterised by the uncontrolled proliferation of cells, resulting from DNA damage or mutation; and is the second-highest cause of deaths worldwide after cardiovascular diseases. According to the World Health Organisation (WHO), the latest update in December 2020 estimated 10.0 million cancer deaths resulting from the following five types of cancer: breast, lung, colorectal, prostate, and stomach. Pancreatic and cervical cancer have high fatality rates and often their symptoms are difficult to diagnose, therefore early-stage diagnosis can be crucial and lifesaving.^[26,27] Current treatments mainly rely on chemotherapy,

surgery, immunotherapy and radiotherapy; clearly, further development is needed.

PDT can serve as a treatment option for age-related macular degeneration, malignant and premalignant non-melanoma skin cancer and other cancers such as head and neck cancer, prostate cancer, cholangiocarcinoma, lung, and breast cancer.^[28,29] PDT is used therapeutically in dermatology for the treatment of non-melanoma skin cancers, inflammatory skin diseases, and virus-induced skin lesions caused by human papilloma virus.^[30] Especially for skin treatments, PDT can be beneficial with good cosmetic outcomes as it is active locally in a controlled way.^[31] Most of the PSs that are under investigation for the treatment of cancer and pre-cancerous diseases are based on the tetrapyrrole structure but not only, examples include porphyrins (HpD), chlorins (BPD, SnEt₂, *m*-THPC), bacteriochlorins (Tookad soluble), phthalocyanines (Pc4, AIPcS), texaphyrins (Lutex) and a Ru(II) polypyridyl complex (TLD-1433) (Figure 1.5).

Gene mutations after radiation or chemotherapy develop resistance to treatment. Concerning PDT, as singlet oxygen is the mode of action, cross-resistance is rare, which encourages the use of PDT against cancers that recur after conventional therapy.^[32] Additionally, PDT is cost-effective and can potentially stimulate anti-tumour immunity which contributes to a long-term control of the disease.^[33]

Another important fact to consider is that 90% of cancer deaths are due to cancer metastasis and not due to the primary tumour.^[34] The vascular system plays a pivotal role, as travel from one site to another happens through the blood and/or lymphatic vessels. It is reported that breast cancer usually develops metastases to bone, liver, brain, and lung tissue; prostate cancer frequently metastasises to the bone, and colorectal cancer metastasises in the liver.^[35,36] PDT is a potential treatment against several cancers and a possible solution for metastasis prevention especially when a PS can be used as a dual treatment and imaging agent to track and visualise tumorous lesions.^[37]

Moreover, PDT appears as an interesting therapy for acute coronary syndrome and atherosclerosis. Preclinical studies have shown that plaque progression is reduced and restenosis post coronary intervention with balloon angioplasty or

stenting is prevented. Waksman *et al.* applied intravascular PDT with MV0611-porphyrin-based PS [chloro(mesoporphyrinato IX dimethyl ester)gallium(III)] and light through a catheter-based diode laser to rabbits and pigs. The encouraging findings showed a reduction in macrophages and consequently cytokines in the plaque area reduced inflammation and attenuating atherosclerosis.^[38,39] The perspective of applying PDT with catheter-based DT in interventional cardiology is ongoing and clinical trials involving Antrin, an expanded porphyrin (motaxefin lutetium), are underway.^[40] This new feature of PDT can be of significance in the case of coronary syndromes and prevent patients recurrent atherosclerosis.

1.4 Photosensitisers in PDT

Since 1993, when the first PDT drug was approved in Canada for the treatment of bladder cancer (Photofrin), significant effort and research focused on tumour treatment have been made. Since then, several PDT drugs have been approved worldwide by health organisations and others are in clinical trials.^[41,42] However, we are still awaiting the ideal PS that will fulfil all the features listed above. PSs that have been either approved or under clinical development for PDT will be presented next.

First-generation PSs include hematoporphyrin derivatives (HpD) and porfimer sodium (Photofrin), which have been in use against various cancers (such as lung, oesophagus, and non-small cell lung cancer). Photofrin was approved in 1993 for bladder treatment in Canada; however, it has many limitations including long-lasting photosensitivity and a weak light absorption profile signal at 630 nm.^[43] Since then, second-generation PSs have been developed to overcome these limitations. Porphyrins,^[44] chlorins,^[45] bacteriochlorins,^[46] corroles,^[47,48] texaphyrins,^[49] and phthalocyanines^[50] are based on the tetrapyrrolic unit and constitute potential PDT candidates with several already having been approved by health organisations and others being currently in clinical trials (e.g., redaporfin LUZ11).^[51] Second generation PSs include either a prodrug formulation e.g., 5-aminolevulinic acid (ALA) as biosynthetic precursor for PpIX (Levulan) and ALA-ester mALA (METVIX),^[52,53] or a tetrapyrrole macrocycle structure, e.g., temoporfin (Foscan),^[54] verteporfin (Visudyne),^[55] padeliporfin (Tookad soluble).^[56] A common characteristic of these aromatic molecules is their

high conjugation and uniquely strong absorption profile, which contributes their application in biomedicine, material sciences, electronics, and catalysis.^[57,58] Today, research groups are targeting third-generation PSs, which are composed of second-generation PSs in conjugation or encapsulation with biocompatible nanomaterials or antibody conjugates, to induce cancer targeting and/or drug delivery.^[59] The majority of compounds used in PDT are porphyrinoids. The incorporated type of macrocycle determines the photophysical and photobiological features; however, as previously mentioned, they present similar drawbacks (e.g., poor water-solubility, slow body clearance resulting in long-lasting photosensitivity). To surmount these limitations, apart from the development of third-generation PS, attention has been dedicated towards other metal complexes with attractive photophysical and biological properties (e.g., strong luminescence, long excited lifetime, large Stokes shift, water-solubility, efficient cellular uptake and photostability). These potential PS scaffolds include transition polypyridine metal complexes [ruthenium(II), iridium(III), platinum(IV), rhenium(I) or osmium(II)]^[60,61] and dipyrin-based metal complexes, where boron-difluoride complex of dipyrin have been studied in-depth.^[62–64] In fact, a Ru(II) polypyridine complex (TLD-1433, Figure 2) has entered Phase II clinical trials against non-muscle invasive bladder cancer.^[60] Lastly, hypericin, an anthraquinone based PS, is demonstrating efficacy for the treatment of cutaneous T-cell lymphoma.^[65]

1.4.1 Clinically approved photosensitisers

Porfimer sodium or Photofrin is a first-generation PS, which exists as a mixture of monomeric and oligomeric derivatives of hematoporphyrin (HpD) linked by ether and ester bonds (up to eight porphyrin units). It is employed for the treatment of oesophageal cancer, endobronchial non-small-cell lung cancer, and for the ablation of high-grade dysplasia in Barrett's oesophagus.^[29] Photofrin is intravenously administered and then the treatment area is illuminated by laser light using cylindrical fibre optic diffusers to activate the drug after 40–50 h.^[66]

It selectively accumulates in malignant tissues and localises in the Golgi apparatus and plasma membrane. The primary mechanism of action is vascular damage of diseased tissue by ischemic tumour cell necrosis.^[67] The main

drawbacks are high post photosensitivity, long clearance (7 to 14 days), poor water-solubility, and a low molar absorption coefficient ($\sim 1,170 \text{ M}^{-1} \text{ cm}^{-1}$) at 630 nm, which leads to a low penetration depth (5 mm in tissue). Photosensitivity can occur up to 30 days after the injection; thus, it is advised that exposure to sunlight should be avoided. In addition to the approved indications, Photofrin has been clinically tested against bladder cancers, brain recurrent cancers, biliary tract cancer, breast metastases, skin cancers, gynaecological malignancies, cholangiocarcinoma, and head and neck cancers.^[68,69] Phase II clinical trials are ongoing for patient recruitment for a combination of interstitial PDT with chemotherapy against the locally advanced and recurrent head and neck cancer.^[70,71]

Second-generation PSs have been developed to overcome the drawbacks of the first generation. They are chemical pure compounds, display a red-shift in their absorption spectrum ca. 650–750 nm and thus deeper penetration (1–2 cm), display higher singlet oxygen quantum yields, and show higher tumour selectivity.^[72]

5-Aminolevulinic acid (ALA) is a naturally occurring precursor of PpIX and heme and it is widely used as a second-generation PSs (Levulan or Ameluz) against face and scalp actinic keratosis, and bladder cancer. Effective responses to ALA-PDT have been reported for the treatment of basal cell carcinoma (BCC) and squamous cell carcinoma (SCC).^[73,74] ALA is used as a 20% aqueous solution (Levulan), which enhances penetration from the abnormal epithelium. It is applied topically with a typical time interval of 14–18 h in the case of actinic keratosis, but only 3 h for upper extremities.^[74,75] ALA selectively accumulates in mitochondria, cytosol, and cytosolic membranes in tumour lesions increasing the production of PpIX and directly resulting in tumour cytotoxicity.^[52] PpIX as a photoactive PS absorbs light at 635 nm with a quiet low molar absorption coefficient ($5,000 \text{ M}^{-1} \text{ cm}^{-1}$) and has a reported 1 mm penetration depth.

ALA hydrochloride (ALA HCl, Gleolan) was recently approved by the U.S. Food and Drug Administration (FDA) for fluorescence-guided surgery (FGS) as an adjuvant to assist conventional glioma surgery providing real-time detection and visualisation of malignant tissues during surgery. A dose of 20 mg kg^{-1} is orally

administered three hours before the anaesthesia and consequently, blue light illumination is used to visualise PpIX with a neurosurgical microscope.^[76] Patients are advised to avoid exposure to light for 24 h post-treatment (body clearance: 1–2 days).

Table 1.2. Clinically approved photosensitizers for photodynamic therapy.

PS	Application	λ_{\max}	Drug dose Fluence rate & light dose	Approved
Photofrin	Bladder, esophageal, lung & brain cancer, Barrett's esophageal cancer, cervical dysplasia	630	2 mg kg ⁻¹ 130 to 300 J cm ⁻² 100 mW cm ⁻¹	Worldwide (Withdrawn in EU for commercial reasons)
Levulan/ Ameluz	Skin, bladder, brain & ovarian cancer, Barrett's esophageal cancer, actinic keratosis, BCC, diagnostics of brain & bladder	635	20% aqueous solution 100 J cm ⁻² 100–150 mW cm ⁻²	Worldwide In U.S. for actinic keratosis
Metvix/ Metvixia	Actinic keratosis, BCC, Bowen's disease	570–670	16.8% cream 75 J cm ⁻² 200 mW cm ⁻²	Worldwide
Hexvix	Bladder diagnosis	380–450	100 mg (HCl salt) 180–360 J cm ⁻² 0.25 mW cm ⁻²	EU, U.S.
Foscan	Head and neck, lung, brain, skin, bile duct, prostate, bronchial & pancreatic cancer	652	0.15 mg kg ⁻¹ 20 J cm ⁻² 100 mW cm ⁻²	EU
Visudyne	AMD, pancreatic adenocarcinoma, BCC	690	0.1–2.0 mg kg ⁻¹ 50 J cm ⁻² 600 mW cm ⁻²	Worldwide
Tookad Soluble	Prostate cancer	762	4 mg kg ⁻¹ 200 J cm ⁻² 150 mW cm ⁻²	EU, Mexico
Photosense	Lung, skin, breast, gastrointestinal, head and neck cancer, AMD	675	0.5–2 mg kg ⁻¹ 100 J cm ⁻² 150–250 mW cm ⁻²	Russia
Talaporfin Laserphyrin	Early stage lung cancer, liver metastases of colorectal cancer, hepatocellular carcinoma	664	0.5–3.5 mg kg ⁻¹ 100 J cm ⁻² 150 mW cm ⁻²	Japan, Russia
Redaporfin	Biliary tract cancer	749	0.75 mg kg ⁻¹ 50–100 J cm ⁻² 100–150 mW cm ⁻²	Orphan status in EU
Synthetic hypericin	Cutaneous T-cell lymphoma	570–650	0.25% ointment 5 J cm ⁻²	Orphan status in EU & U.S.

ALA-methyl ester derivative (MALA or Metvix) also is a second-generation PSs, approved for actinic keratosis and BCC.^[77] It has the same mechanism of action and localisation as Levulan; however, it displays deeper penetration into the skin (2 mm) compared to Levulan (1 mm) due to its lipophilicity.^[78] A short time interval is required (3 h) after the application of Metvix for the achievement of the high fluorescence of PpIX in the treated lesions after illumination with red light (570 to 670 nm). Currently, daylight PDT (DL-PDT) has attracted attention from clinical dermatologists who aim to reduce the use of blue or red-light irradiation. Recent reports for actinic keratosis treatment show that Metvix application under daylight has the same effect as in the combination with blue light PDT and that ALA is more effective than MALA in DL-PDT.^[79,80] In the case of DL-PDT, the quantification of light dose, which is directly dependent on the environmental conditions, is of great importance.^[81]

Other **ALA-hexyl ester derivatives** are Hexvix and Cysview. They are approved for bladder cancer diagnostics in combination with blue light fluorescence cystoscopy. The recommended dose for adults is 100 mg dissolved in 50 mL of diluent, which is administered *via* intravesical instillation into the bladder, where it selectively localises in the bladder walls.^[82,83] Illumination during the cystoscopy examination should take place within 60 min with blue light (380-450 nm).

Benzoporphyrin monoacid ring A (BPD) derivative or verteporfin (Visudyne) is a second-generation PS, too. It is a liposomal formulation of a 1:1 racemic mixture of two regioisomers (BPD-MAC and BPD-MAD). It is approved for the treatment of subfoveal choroidal neovascularisation (CNV) due to age-related macular degeneration (AMD) or pathologic myopia.^[55,84] 15 Minutes after intravenous administration, red light (689 nm) is delivered to the retina as a single circular spot *via* a fibre optic and a slit lamp. In the bloodstream, verteporfin binds to LDL and selectively accumulates within the neovasculature, resulting in apoptosis in neoplastic tissues.^[85] Verteporfin reaches the maximum concentration after 30 min and has rapid body clearance rates and subsequently minimal skin photosensitivity (3 days). It has a high molar absorption coefficient ($35,000 \text{ M}^{-1} \text{ cm}^{-1}$) at 689 nm, which allows for deeper penetration. Promising outcomes from clinical trials against BCC have been reported and currently a

Phase II clinical trial is recruiting patients for PDT treatment of advanced pancreatic adenocarcinoma.^[86,87]

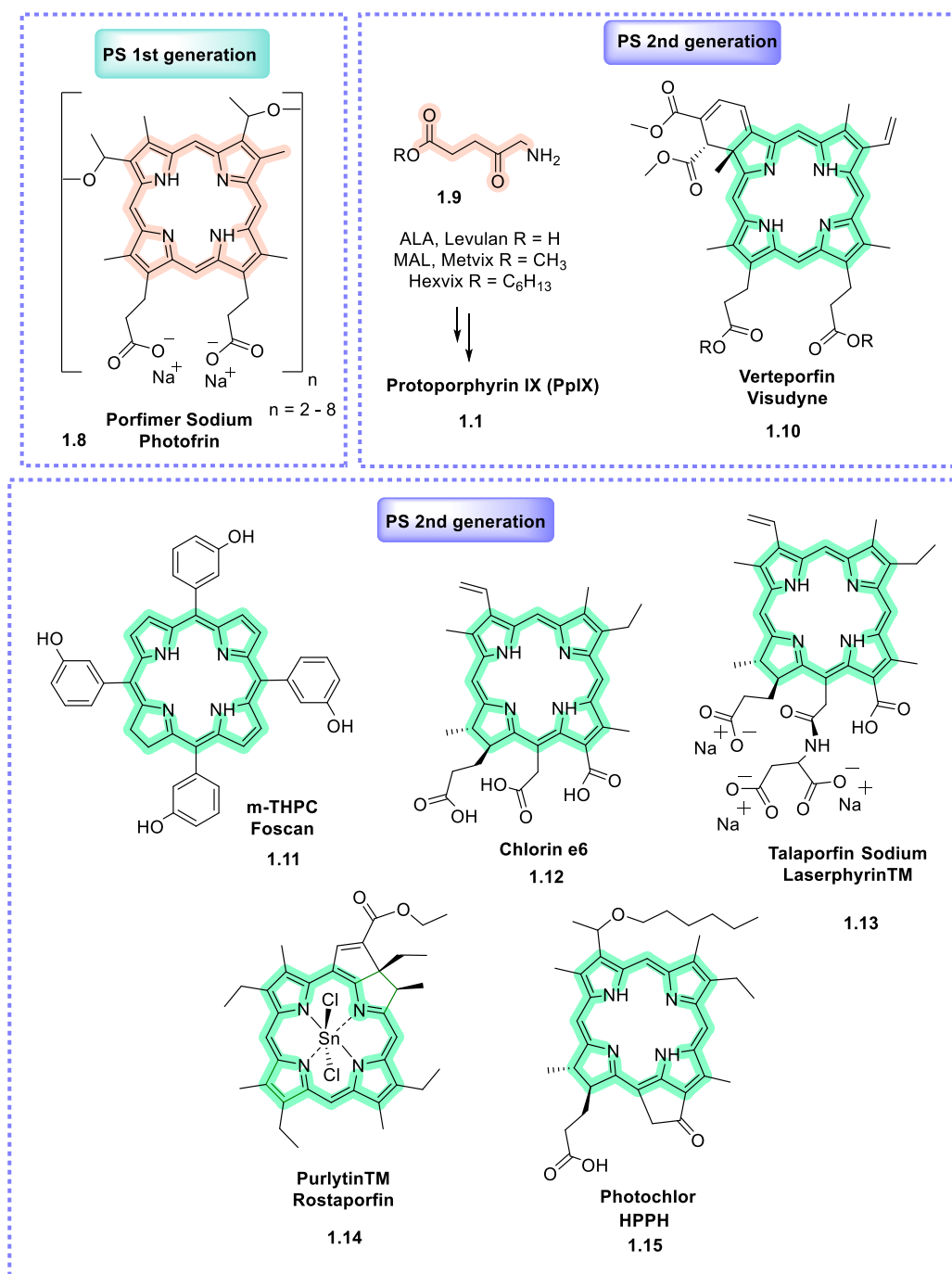


Figure 1.3. Chemical structures of photosensitisers.

Temoporfin or 5,10,15,20-tetrakis(meta-hydroxyphenyl)chlorin (*m*THPC, formulation as Foscan) is a second-generation PS from the chlorin family. It is approved for the treatment of squamous head and neck carcinoma.^[88] 96 h after intravenous administration, red-light illumination at 652 nm is delivered to the

tumorous site through a microlens optic fibre. Temoporfin accumulates in the vasculature walls of tumour brain tissue and also intracellularly, resulting in tumour cell death and vascular damage through both necrosis and apoptosis.^[88–90] *m*THPC has a relatively high molar absorption coefficient ($30,000 \text{ M}^{-1} \text{ cm}^{-1}$) at 652 nm and thus, a low dose is needed in comparison with Photofrin (100 times lower).^[91] Temoporfin is one of the most effective PSs, although its main drawback is its poor water-solubility and high post-treatment photosensitivity, where patients are advised to avoid exposure to light for 15 days. Moreover, the treatment area should not be exposed to light for up to 6 months.^[72,92] PDT with Foscan had promising results in clinical trials for the treatment of breast and pancreatic cancer.^[93,94]

Padeliporfin-dipotassium (Tookad soluble, WST-11) is a Pd(II)bacteriochlorin second-generation PS derived from the photosynthetic pigment bacteriochlorophyll α (BChl α), which is found in bacteria. It is a follow-up PS to padoporfin (WST-09) designed with increased water-solubility and is one of the more recent developments in PDT. It is approved in the European Union (EU) for the treatment of adenocarcinoma of the prostate.^[95,96] 15 min after intravenous administration, under general anaesthesia, light is delivered through interstitial optical fibres to the prostate gland area.^[56] Tookad is a vascular-targeted photodynamic therapy (VTP) and thereby localises in the tumour blood vessels where it initiates inflammation, hypoxia, necrosis, and tumour eradication through vascular damage.^[97] It has the advantage of deeper penetration (4 mm) as it absorbs in the red area of the spectrum with a high molar absorption coefficient at 762 nm ($88,500 \text{ M}^{-1} \text{ cm}^{-1}$).^[98] Tookad has a fast body clearance rate, resulting in low skin photosensitivity as patients are advised to avoid light for only 6 h post-treatment. Tookad has also been tested against established bone metastasis and orthotopic prostatic models.^[99] On February 2020, the FDA's Oncologic Drugs Advisory Committee (ODAC) refused to accept Tookad VTP; questioning the therapy's trial design, endpoints, missing follow-up data, and adverse events.^[100] A follow-up Phase IV to evaluate erectile dysfunction, urinary incontinence, and related quality of life post-treatment for low-risk prostate cancer was terminated due to difficulty to enrol patients.^[101]

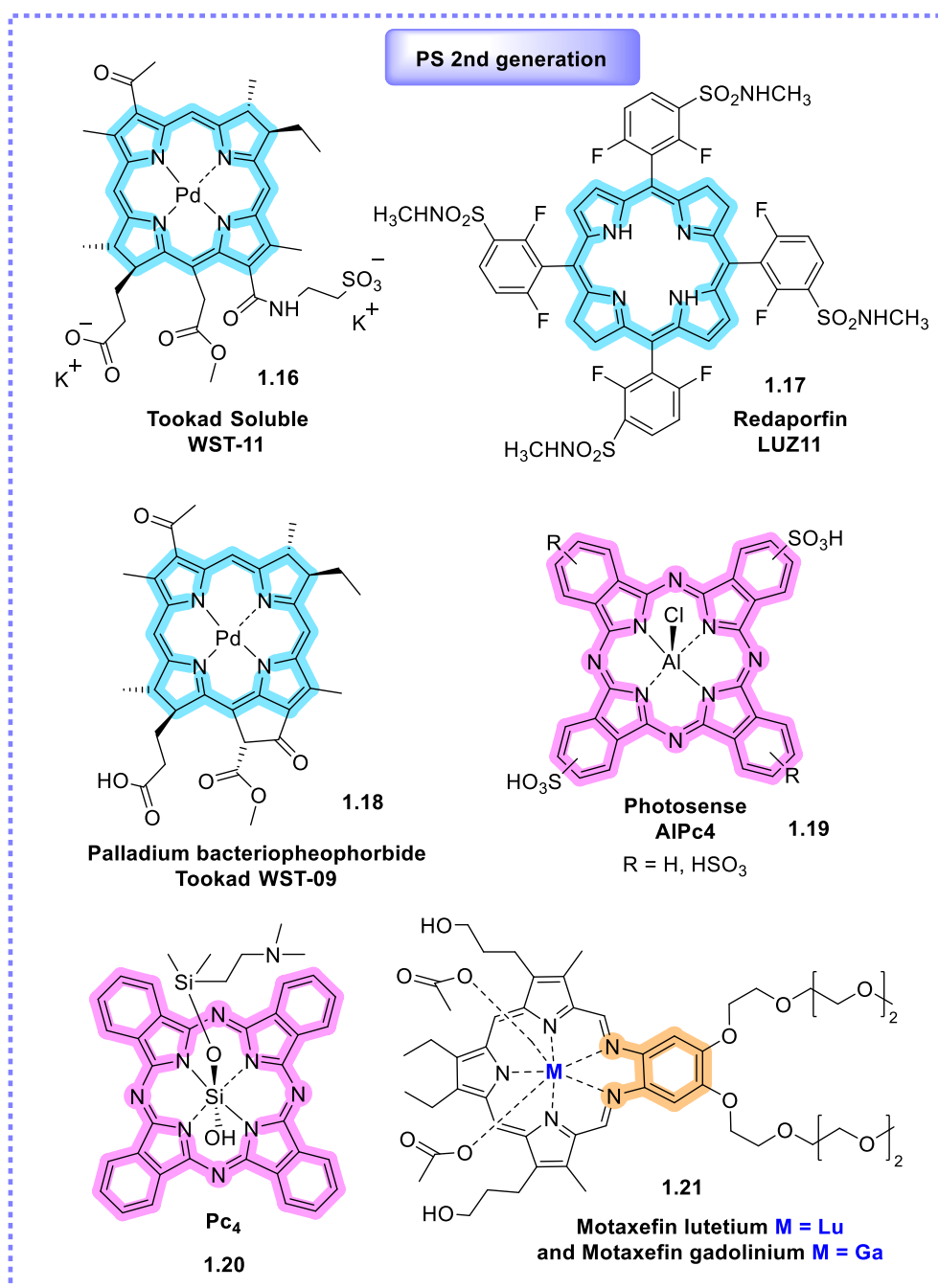


Figure 1.4. Chemical structures of photosensitisers.

Mono-L-aspartyl chlorin e6 (talaporfin sodium, Laserphyrin, NPe6) is a hydrophilic rhodochlorin derived from chlorophyll α . It has been approved by the Japanese government for the treatment of lung cancer.^[102,103] Talaporfin selectively accumulates in the malignant site and 4 h after intravenous administration laser light is endoscopically delivered through a quartz optic fibre. Post-irradiation causes vascular flow stasis and direct tumour cytotoxicity through apoptosis and necrosis.^[104,105] It has a high molar absorption coefficient at 664

nm ($40,000 \text{ M}^{-1} \text{ cm}^{-1}$) and efficient antitumour effects, as well as low skin photosensitivity (1 week) and fast body clearance rates compared to Photofrin, making this PS a promising PDT agent.^[102] Talaporfin was also employed in clinical trials for the treatment of early stage head and neck cancer, colorectal neoplasms, and liver metastasis.^[106,107]

1.4.2 Photosensitisers under development

Redaporfin or Luz11 is a second-generation PS from the bacteriochlorin family and was developed by Arnaut and co-workers.^[108] It was granted orphan designation by the EU and U.S. for the treatment of biliary tract.^[109] Gomes-da-Silva *et al.* investigated the mechanism of action of redaporfin and reported that it selectively localises in the endoplasmic reticulum (ER) and the Golgi apparatus (GA), which after light activation leads to ER and GA functional disruption. This results in tumour cell death and direct antineoplastic effects through apoptosis, as well as indirect immune-dependent destruction of malignant lesions through ROS generation.^[51] Redaporfin has a very high molar absorption coefficient at 745 nm ($140,000 \text{ M}^{-1} \text{ cm}^{-1}$), which allows for deep light penetration. Recently reported by Rocha *et al.* an *in vivo* study of the necrosis depth in liver rats showed that redaporfin benefits from deeper necrosis at a drug-light combination ca. 50 times lower than that of Photofrin.^[110] Light illumination at 750 nm was delivered 15 min following the intravenous administration of redaporfin (0.75 mg kg^{-1}), which led to a liver necrosis depth of approximately 4 mm with frontal illumination (25 J cm^{-2}) and a necrotic radius of 0.7 cm with interstitial illumination (100 J cm^{-2}). Redaporfin is currently in Phase I/II clinical trials for the treatment of head and neck cancer with promising results.^[109,111]

Texaphyrins are metal-coordinating expanded porphyrins with enhanced water-solubility and this class of compounds was pioneered by Sessler for use in medicine and biology.^[112] Texaphyrins show promising results as PDT or radiation agents and mainly two lanthanide(III) texaphyrin complexes are under investigation for PDT treatments or imaging applications. The main advantage of texaphyrins as PDT agents is their strong absorption profile at a much longer wavelength due to their extended macrocycle (700–750 nm), which allows for effective treatment at a greater depth. Other advantages include that they initiate

the apoptotic pathway without disrupting DNA; thereby they are not mutagenic and preferably localise in cancerous sites. Moreover, they are an attractive option for contrast agents in magnetic resonance imaging (MRI), which allows for non-invasive evaluation of tumorous tissues.^[49]

Clinical trials with **Motaxefin lutetium(III)** (Lu-Tex, Lutrin, Antrin, or Optrin) for the treatment of prostate and cervical dysplasia or cancer are complete; however, they have not been granted approval from FDA or European Medicines Agency (EMA). Moreover, this drug has been under preclinical investigations as a possible therapy for AMD and photo-angioplasty of peripheral arterial diseases.^[40,113,114] Young and Woodburn *et al.* reported the selective uptake and retention by cancerous lesions and atheromatous plaque after intravenous administration as well as microvasculature selectivity, resulting in selective photodamage.^[115,116] Lutrin displays deep tissue penetration (molar absorption coefficient $42,000 \text{ M}^{-1} \text{ cm}^{-1}$ at 732 nm) and quick body clearance thereby minimising retention in tissue and limiting skin and systemic post photosensitivity (24–48 h).^[112]

Motaxefin gadolinium(III) (Gd-Tex, Xcytrin) is a gadolinium texaphyrin complex that displays intense fluorescence at 750 nm and has found application in *in vivo* real-time imaging making it a potent candidate for use as a contrast agent in facilitating clinical diagnosis of atherosclerosis.^[117] Motaxefin gadolinium MRI visualisation showed that it preferably accumulates in tumours and is well-tolerated. Clinical trials for the treatment of brain metastases from lung and breast cancer under whole brain radiation showed promising results; however, further evaluation is required to elucidate the safety and efficacy.^[118,119]

Purpurins are chlorin based structures and were first synthesised by Woodward during his seminal chlorophyll synthesis.^[120] Tin ethyl etiopurpurin or **Rostaporfine** (Purlytin or SnET₂) is the most efficient purpurin and belongs to the series of second-generation PSs. It has been under clinical trials Phase II/III for the treatment of cutaneous cancer, for metastatic breast cancer, AIDs related Kaposi's sarcoma, and AMD.^[68] A follow-up study on the clinical trial (Phase II/III) for the treatment of breast cancer had a complete response for over 90% of patients.^[121] The tin atoms result in a redshift of the absorption profile

accompanied by a high molar absorption coefficient at 660 nm ($40,000 \text{ M}^{-1} \text{ cm}^{-1}$).^[122] Purlytin has drawbacks including dark toxicity and photosensitivity (1 month) and it also has poor water-solubility. The latter can be overcome by formulations with the use of lipid emulsions *i.e.* cremophor EL emulsion, liposome encapsulation, or cyclodextrins.^[123] Although promising, there is still no authorised approval for cancer treatment.

Another novel and very promising chlorin-based PS currently in clinical trials is the hexyl ether derivative of derived from pheophorbide- α from *Spirulina* algae (2-[1-hexyloxyethyl]-2-devinyl pyropheophorbide- α , **HPPH or Photochlor**).^[124] HPPH is under evaluation in Phase I for its safety and tolerability post-injection in patients with oesophageal cancer.^[125] A search of clinicaltrial.gov identifies several clinical trials involving HPPH in Phase I (treatment of oral cavity carcinoma, Barrett's oesophagus, lung cancer, head and neck cancer, BCC, and oesophageal cancer), Phase II (lung cancer, oesophageal cancer), and an active study (Phase II) for treating patients with oral cavity squamous cell carcinoma. The main advantages of HPPH are its high molar absorption coefficient at 665 nm ($47,000 \text{ M}^{-1} \text{ cm}^{-1}$) and the considerably low cutaneous phototoxicity compared to patients treated with Photofrin or Foscan.^[126]

Phthalocyanines (Pcs) are extended, artificial porphyrin systems with a unique structure where each pyrrole moiety is fused with a benzene ring resulting in a red-shifted absorption spectrum and a deeper penetration range. They are characterised by a relatively easy preparation, thus, large-scale synthesis at a relatively low cost can be performed. Lately, there has been a focus on Pcs in PDT and two recent reviews by Lo *et al.*^[127] and Li *et al.*^[128] perfectly summarise their properties and applications. Their main drawback is their very low water-solubility, which can be overcome by introducing polar groups, *e.g.*, sulfonated Pc derivatives, or using nano-formulations such as nanoparticles (liposomes or polyethylene glycol polymers).^[129,130] It was shown that metal insertion increases the triplet state yield and the singlet oxygen quantum yield of Pcs, *i.e.*, zinc, aluminium, and silicon derivatives.^[127] As such, Pc derivatives are under development and currently undergoing preclinical and clinical evaluation. One liposomal zinc Pc developed by Ciba-Geigy underwent Phase I/II clinical trials

against squamous cell carcinomas of the upper aerodigestive tract; however, no additional data have been reported yet.^[127,130]

Photosense or AIPcS is a water-soluble sulfonated mixture of di-, tri- and tetra-sulfonated aluminium phthalocyanines and it has been approved by the Russian Ministry of public health.^[68] It is indicated for patients with AMD, head and neck, lung, breast, skin, and gastrointestinal cancers. It is administered intravenously with a 24 h drug-light interval and it selectively accumulates in the cancerous sites.^[131] Laser light is delivered to tumours *via* quartz optical fibres at 675 nm, where Photosense absorbs with its characteristic high molar absorption coefficient ($42,000 \text{ M}^{-1} \text{ cm}^{-1}$). Noteworthy, a Photosense analog with two sulfonic groups in the adjacent isoindole subunits (AIPcS_{2adj}) proved to be a powerful photochemical internalisation (PCI) agent.^[132]

Pc4 is a silicon-based phthalocyanine, which has been under Phase I clinical trials for cutaneous cancers. After activation, it initiates apoptosis in cancer cells leading to photodamage. A clinical study reported by Baron *et al.* showed that Pc4-PDT is a safe and tolerable treatment for cutaneous malignancies such as mycosis fungoides.^[133,134] In another trial from the same principle investigator, Pc4-PDT was used to treat cutaneous T-cell non-Hodgkin lymphoma.^[135]

In the search for other improved PSs for PDT a non-porphyrin PS has also been granted orphan designation by the EU and US. This synthetic **hypericin** (SGX301, Figure 1.5) derivative belongs to the extended quinone family. It is used to treat early-stage cutaneous T-cell lymphoma (CTCL) and a pivotal Phase III clinical trial was recently completed achieving a statistically significant treatment response rate ($p=0.04$) in overall three cycles of the patients treatment (36 weeks).^[136] SGX301 is topically administered as a hydrophilic ointment, twice per week, and covered with a bandage for 12-24 h. Then, the area is treated with visible fluorescent light. Hypericin tends to accumulate in T-cells and localises in the ER, GA, lysosomes, and mitochondria. After light activation, singlet oxygen and ROS are formed and initiate the mitochondrial apoptotic pathway causing cellular toxicity and killing the targeted T-cells.^[65] Hypericin has a high molar absorption coefficient at 590 nm ($45,000 \text{ M}^{-1} \text{ cm}^{-1}$) and displays low toxicity and dark toxicity as it only targets the T-cells in the skin layer.^[22]

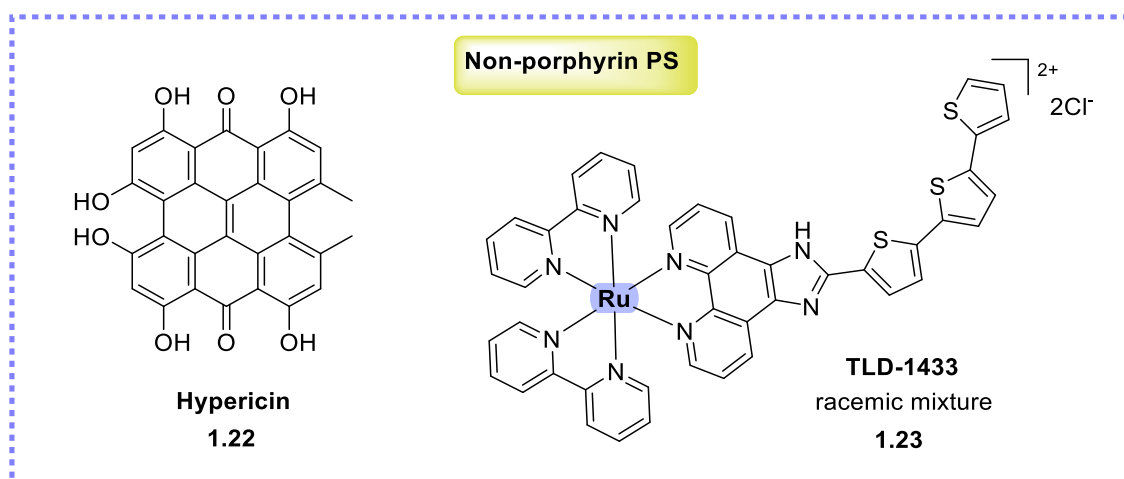


Figure 1.5. Chemical structures of non-porphyrin potential PSs.

Another non-porphyrin complex developed by Mc Farland and co-workers is the **TLD-1433** ruthenium (Figure 1.5) polypyridine complex.^[61,137] It is currently in a Phase II clinical trial in Canada for the treatment of non-muscle invasive bladder cancer. This ruthenium complex absorbs at 525 nm with a low molar absorption coefficient $2,000 \text{ M}^{-1} \text{ cm}^{-1}$; however, it displays efficient intersystem crossing, intra-ligand charge transfer post excitation, and high singlet oxygen quantum yield. TLD-1433 interacts with the biological environment by electron transfer reactions and inducement of ROS.^[42] The prevalent production of hydroxyl radicals in a hypoxic environment is an indication for its use in solid tumours.^[138] The high selectivity for cancer cells is based on a higher expression of transferrin receptors that are upregulated on the cancer cell surface.^[137,139] During a Phase I clinical trial involving TLD-1433 for the treatment of bladder cancer, an aqueous solution of the metal complex was administered into the bladder *via* a catheter (minimal dose: 0.35 mg cm^{-2} , therapeutic dose 0.70 mg cm^{-2}), following rinsing after 1 h (removal of excess of the compound) and filling with water to allow a constant light exposure of the bladder surface. An optical fibre with a diffuser was used and the bladder wall was irradiated at 520 nm (90 J cm^{-2}).^[140] The results were promising since two out of three patients had full response and no recurrence or progressing of the bladder tumour. An ongoing Phase II clinical trial is planned to treat ~ 120 patients with non-muscle invasive bladder cancer in the USA and Canada who are intolerant or unresponsive to bacillus Calmette-Guérin therapy (therapeutic dose 0.70 mg cm^{-2}).^[42,141,142]

1.5 Dipyrrinato Metal Complexes as Potential PS and their Photophysics

Metal-based complexes have found use since ancient times; for example, one of the first metal-based compound was the arsenic trioxide (ATO). ATO was used by Chinese medical practitioners as an antiseptic, and against rheumatoid diseases, syphilis, and psoriasis; by 1970 it found use in the treatment of leukaemia (1970, China). In the early 20th century its use was replaced by radiation and cytotoxic chemotherapy.^[143,144] A breakthrough in medicine for metal complexes in medicine was the discovery of the arsenic containing drug arsphenamine (a mixture of trimer and pentamer) as an antimicrobial agent and the platinum containing drug cisplatin as an anticancer agent.^[145,146] Currently, cisplatin, carboplatin, and oxaliplatin are platinum containing drugs used in chemotherapy (Figure 1.6).^[147] However, these complexes are related with acute side effects such as peripheral neuropathy and the increase of drug-resistant tumours. This has resulted in the use of combination of therapies including radiotherapy, immunotherapy and surgery in order to surmount the limitations and improve the survival rates.^[148] In addition, mercury is known as toxic, but is also used in merbromin as an antiseptic agent where it combines with carbon (carbon-mercury bond) to form an organic mercury compound.^[149]

Metal complexes display characteristic features *i.e.*, structural diversity, redox or catalytic properties, and ligand exchange propensity,^[144] but they can also display toxicity. All the above depend on the type of metal, its oxidation state, the coordination geometry, the variety of coordinated ligands *etc.*^[60] To overcome the limitations that arise, such as toxicity and cross-resistance, novel molecules are sought after and the demand for metal-based compounds is continuing for cancer treatments.

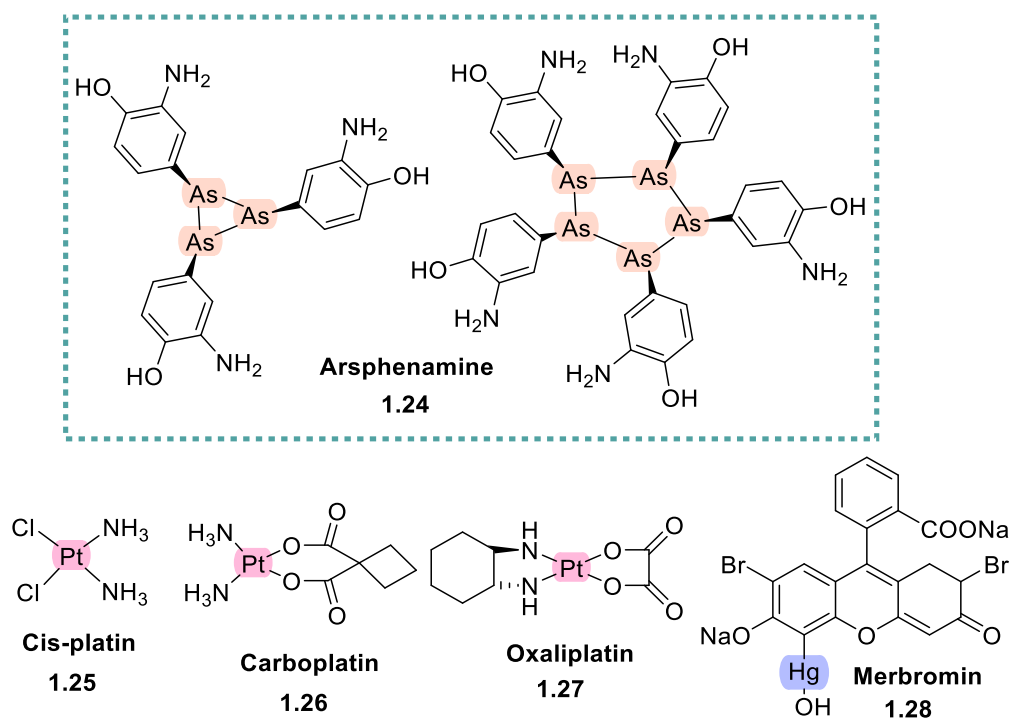


Figure 1.6. Chemical structures of metal-based complexes used in the clinics.

The quest for ideal PS in PDT has prompted substantial interest in evaluating the attributes and limitations of the natural related metal-based products, *e.g.*, porphyrinoids, or other types of molecules, *e.g.*, transition metal polypyridine complexes ruthenium(II), iridium(III), platinum(IV), rhenium(I), and osmium(II) or mono-, bis-, and tris- dipyrinato complexes.^[23,42] Transition metal complexes of ruthenium are under scrutiny, due to their attractive photophysical, biological, and anticancer properties *i.e.*, strong luminescence, long fluorescence lifetimes, large Stokes shifts, water-solubility, high cellular uptake with promising cytotoxicity, and photostability. As mentioned, the first Ru(II)-based photosensitizer (TLD-1433) is the first that has entered into clinical trials against non-muscle invasive bladder cancer.^[61]

Another family related to porphyrinoids are the dipyrrens that can serve as perfect ligands with multiple types of metal coordination. The dipyrren moiety consists of two pyrrole rings bridged with a methine group and occurs in a planar configuration. The dipyrrenato ligand, upon deprotonation, can coordinate with various cationic species and form stable complexes.^[150] It is a π -conjugated system that can absorb light (450 – 550 nm) and undergo $^1\pi - \pi^*$ transitions. In bis- and tris- dipyrrenato complexes, where the moieties are in proximity but not

in conjugation, exciton coupling of the $^1\pi - \pi^*$ transitions can take place, leading to non-degenerate excitonic states.^[151] This is observed in the UV-Visible absorption spectra of the complexes with a splitting of the absorption bands (Davydov splitting) (see 4.3.3.1). Circular dichroism (CD) spectroscopy is another means to determine if exciton coupling occurs. The post-excitation luminescence features can be tuned and are greatly dependent on the environment polarity and the structural variety upon modifications on the periphery. The latter can occur by the introduction of various 5- substituents on the dipyrin moiety or at α - or β -pyrrole rings and can alter drastically the photoluminescence properties. Cohen, Halper, Dolphin, Lindsey, Bocian, Nishihara, Holten, Telfer and their co-workers have reported their work on dipyrins, their complexes, and their ground- and excited- state properties. They also reported that the modifiability of the periphery of such systems is feasible and can alter the photophysical properties.^[150,152–161]

A variety of substituents can alter the excited states formation in metal-based systems, having great dependency on the polarity of the environment. In addition, the different type of metal coordinated centres can result in electronic configurations upon excitation that may favour the triplet state population. These configurations can be metal-centred (MC), within a single ligand (intraligand, IL), or involve a charge transfer (CT) state between them. The CT states can be metal-to-ligand (MLCT), ligand-to-metal (LMCT), within a ligand (ILCT) or between two different ligands (LLCT).^[61] The majority of dipyrinato metal-based complexes are considered as weak luminophores. The non-emissive charge separated states may occur upon excitation, specifically in polar solvents, and this usually increases with a less structural constrains in the system's periphery. Depending on the oxidation state, the electronic configuration of the metal ion and the nature of the ligands, the dipyrinato complexes have either a preference for octahedral, tetrahedral or square planar geometries.

Dipyrinato complexes with calcium, magnesium, lithium, natrium and potassium have been previously reported; however, to date they do not display any capability as PSs and limited information can be found with regards to their geometries and optical properties.^[162–164] Lithium dipyrinato salts can be used as precursors in the synthesis of other dipyrinato complexes.^[165]

Another type of dipyrrens are the N_2O_2 and aza-dipyrrens. N_2O_2 -type ligands are similar to dipyrrens but with phenol groups attached on the pyrrolic α positions. N_2O_2 -type ligands can form complexes with Zr, Ti, Mn, Co, Ni, Cu, Pt and Au, B, In, Ga, Si, Ge, Sn and Al.^[159,166–171] Aza-dipyrren ligands consist of a nitrogen atom instead of the carbon in the methine bridge and can form complexes with Cu(I), Ag(I), Au(I), Zn(II), Re(I), Co(II), Ni(II), Hg(II), Rh(I), Ir(I), Ir(III), Li, Na, K, B and P.^[172,173] For dipyrrenato complexes with Mn(II), Mn(III), Mo(VI) and Cr(III) only few photophysical data have been reported apart from the occasional UV-Visible absorption spectra.^[174–178]

In this section we will focus on dipyrrenato based metal complexes with potential applicability toward photomedicine, apart from boron dipyrrenato dyes (BODIPY) which are well-known and extensively investigated. In particular, the photophysical properties of **Zn(II)**, **Ni(II)**, **Cu(II)**, **Pd(II)**, **Pt(II)**, **Re(I)**, **Ru(II)** and **Ir(III)** dipyrrenato complexes will be described below and **Ga(III)**, **In(III)** and **Al(III)** dipyrrenato complexes are described in section 4.1.

1.5.1 Zn(II), Ni(II), Cu(II), Pd(II) and Pt(II) dipyrrenato complexes

Bis(dipyrrenato) **Zn(II)** dipyrren complexes are most studied for their luminescence efficiency and photophysical properties. (Dipyrrenato)zinc(II) complexes usually obtain a tetrahedral configuration. Figure 1.7 presents several bis(dipyrrenato)zinc(II) complexes.

Several factors can result in modulation of the emissive properties of these complexes such as modulation of substitution at α -, β -, or 5-position. Sazanovich *et al.* reported that structural modifications caused by bulky aryl groups (mesityl) at the meso position of the corresponding dipyrrens in bis(dipyrrenato)zinc(II) complex resulted in increased steric hindrance and consequently in a great improvement of the fluorescence quantum yield. Namely, the fluorescence quantum yield of the mesityl derivative **130g** was higher (0.36) than the phenyl and tert-butyl analogues **130b** and **130e** (0.006 and 0.007, respectively). Additionally, the singlet state lifetime of **1.30g** (3 ns) was longer than that of **129b** (0.09 ns).^[156,179] Furthermore, other facts that impact the luminescence are the introduction of iodine atoms or methyl groups on the dipyrren core. It was demonstrated that the presence of iodine atoms in **132g** ($R^2 = I$) resulted in a

decreased fluorescence quantum yield and increased CS state formation when compared to the derivative without iodine **132g** ($R^2 = H$). Therefore, the introduction of heavy atoms can facilitate the formation of long-lived triplet states, increase the ISC rate, and a red-shift of the electronic absorption spectrum.^[180]

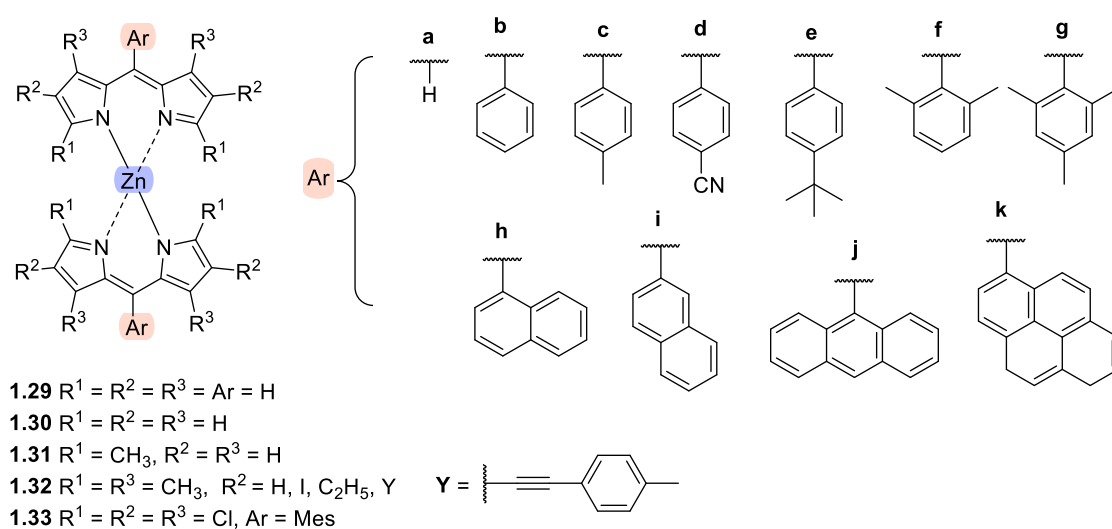


Figure 1.7. Chemical structures of homoleptic zinc(II) dipyrinato complexes.

Charge transfer (CT) between chromophores happens after photoexcitation, producing symmetry-breaking (SB) charge separation (CS) states and the emission quenching upon SBCS states in polar solvents is considerable. The SBCT and the formation of ligand-ligand charge transfer states is also called Intramolecular Charge Transfer (ICT) states (ICT energy states are governed by solvent dipolar stabilisation) (Figure 1.9).^[179–183] Nishihara and co-workers introduced another approach to enhance the luminescence of dipyrinato metal complexes. In the heteroleptic complexes the SBCT process is less important, since there is no symmetry. The heteroleptic bis(dipyrinato)zinc(II) complexes **1.34**, **1.35** and **1.36** (Figure 1.8) have different photophysical properties from the homoleptic analogues (Figure 1.7).^[160,181] The absorption spectrum of **1.34** was the sum of the absorption bands of the homoleptic analogues **1.31g** and **1.32f** ($R^2 = Y$) and the emission spectrum showed one emission band of the dipyrinato ligand D2 ($\lambda_{em} = 578 \text{ nm}$) both in the cases when exciting the D1 ligand (495 nm), and after exciting selectively the D2 ligand (553 nm). This was ascribed to the presence of energy transfer from D1 to D2, followed by emission from a [D1-Zn-D2*] state. Furthermore, the heteroleptic zinc complexes displayed higher fluorescence quantum yield than the corresponding homoleptic analogues.^[160,181]

Specifically, a higher fluorescence quantum yield was reported for **1.34** ($\Phi_f = 0.76$ in toluene and $\Phi_f = 0.52$ in DCM) compared to the homoleptic analogue **1.31g** ($\Phi_f = 0.28$ in toluene and non-emissive in DCM). The same group also observed the same effect with tris(dipyrrinato)indium(III) complexes.^[159]

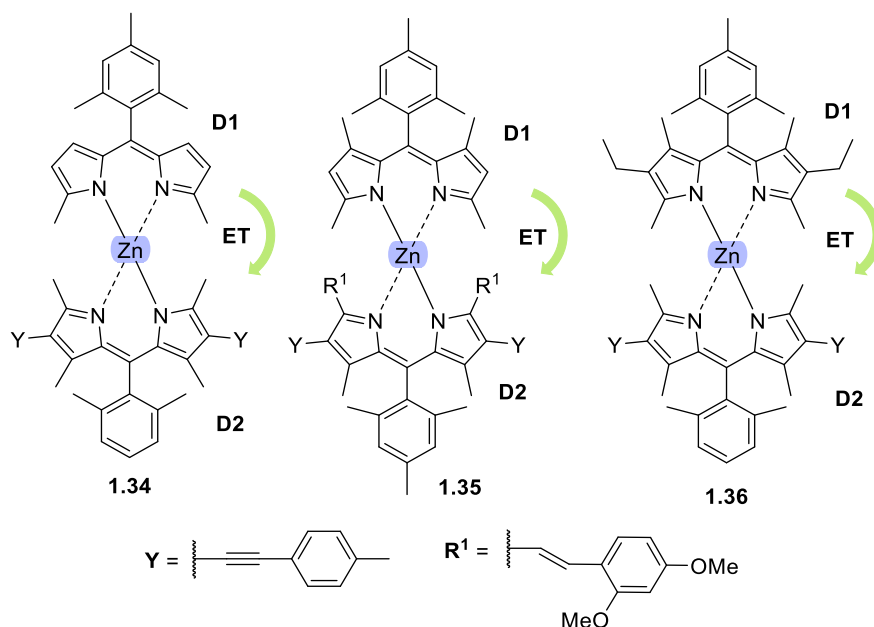


Figure 1.8. Chemical structures of heteroleptic Zn(II) dipyrinato complexes reported. The green arrow indicates energy transfer (ET) from the D1 ligand to the D2 ligand.

Consequently, the same group reported heteroleptic zinc dipyrin complexes with bulkier substituents in the pyrrolic ring. The most promising candidate in terms of fluorescence properties was **1.35** showing a high luminescence quantum yield of 0.62 – 0.72 in both polar and non-polar solvents; an absorption maxima ($\lambda_{\text{max}} = 671 \text{ nm}$ in toluene), a large ϵ of $89,000 \text{ M}^{-1} \text{ cm}^{-1}$ or $180,000 \text{ M}^{-1} \text{ cm}^{-1}$ (for each ligand) and large Stokes shifts of $\sim 5400 \text{ cm}^{-1}$. Nevertheless, an improved fluorescence quantum yield for heteroleptic complexes compared to their homoleptic analogues is not a strict rule. For instance, complex **1.36** showed a significantly lower Φ_f in non-polar and also polar solvents ($\Phi_f = 0.07 - 0.08$ in toluene and $\Phi_f = 0.01 - 0.03$ in DCM). The presence of electron donating methyl and ethyl groups raised the energy of the HOMO-1 of the D1 ligand and reversed the electronic distribution between the ligands in the HOMO and HOMO-1 (comparing with **1.34**) resulting in a favourable electron transfer process $[D1\text{-Zn-D2}^*] \rightarrow {}^1[D1^{+\cdot}\text{-Zn-D2}^{\cdot-}]$ and an efficient generation of non-emissive ${}^1[D1^{+\cdot}\text{-Zn-D2}^{\cdot-}]$ state, characterised by a decreased Φ_f .^[160,181]

In addition, it was reported that triplet excited state formation can be enhanced by ICT states in polar solvents for (dipyrrinato)zinc(II) complexes.^[179,180] Das *et al.* demonstrated that the triplet state of **1.33** was generated *via* ISC from the S₁ state in non-polar solvents, whereas in polar solvents triplets were rapidly generated *via* charge recombination from ICT states with higher triplet state yields (Figure 1.9).^[183] Similarly, Mahmood *et al.* synthesised a series of bis(dipyrrinato)zinc(II) complexes **1.32b**, **1.32i**, **1.32j**, and **1.32k** (R² = H) and demonstrated that their triplet excited state dynamics can be effectively tuned by structural modifications. This can occur by altering the energy gap between the CT and T_n states along with the geometry by introducing electron donating aryl moieties at the meso-positions of the complexes. In this way, the ISC yield and triplet excited state lifetime can be tuned and resulted effectively in the singlet oxygen production through SBCT state. Due to the bulky pyrene and anthracene groups the intramolecular rotations are hampered and their fluorescence decay is slower, leading to efficient ISC and longer triplet lifetime. The ascending order of the singlet and triplet lifetimes and the singlet oxygen quantum yield was as follows: **1.32i** < **1.32b** < **1.32k** < **1.32j** (R² = H).^[182]

The reaction can occur through a radical pair intersystem crossing (RP-ISC) which involves mixing between ¹ICT (¹[D^{•+}-Zn-D^{•-}]) and ³ICT (³[D^{•+}-Zn-D^{•-}]) states. These states can undergo ¹ICT → ³ICT transition followed by a rapid charge recombination to the lowest triplet state (³ICT → T₁). On the other hand, ISC may also happen directly from ¹ICT → T₁ state *via* spin-orbit charge-transfer intersystem crossing (SOCT-ISC). This happens in the case that the orbital symmetries are involved in the way that the spin flip is coupled with an accompanying orbital angular momentum change [dominates when a strong electronic coupling between the donor (D^{•+}) and acceptor (D^{•-}) radical pairs exists]. Usually, it is difficult to differentiate between RP-ISC and SOCT-ISC mechanisms; however, the electronic coupling and thus the distance and orientation between the donor and acceptor has a significant role in controlling the ISC mechanism.^[184–187] Theoretical calculations in radical pairs illustrated that SOCT-ISC was enhanced with orthogonality between the orbitals involved and was reduced with the longer distance between the orbitals.^[188] Finally, in non-polar solvents the preferable transition is from S₁ → T₁ state *via* ISC.

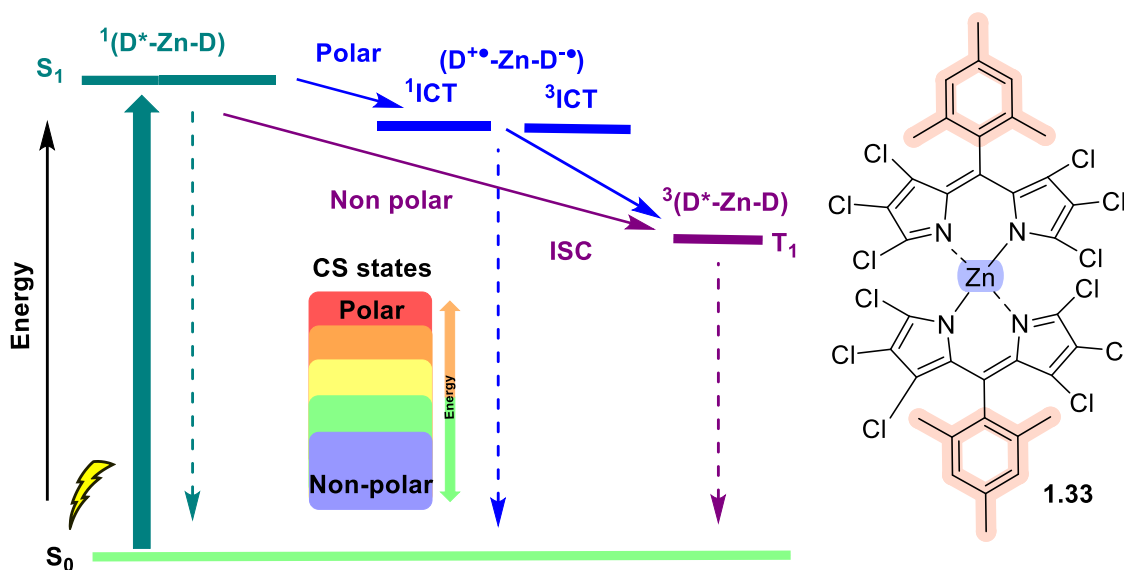


Figure 1.9. Simplified energy diagram showing the excited-state decay pathways and one example of bis(dipyrrinato)zinc(II) complex.^[183]

Karges *et al.* investigated **1.32b**, **3.32f**, **1.32g**, and **1.32j** ($R^2 = I$) for potential PDT application. These complexes absorbed at ~ 515 nm, and the iodine atoms promoted spin-orbit coupling resulting in ISC and singlet oxygen generation upon irradiation [at 510 nm (20 min, 5.0 J cm^{-2}) and at 540 nm (40 min, 9.5 J cm^{-2})], which was confirmed by EPR spectroscopy. The phototoxicity studies were performed using human retinal epithelial cells (RPE-1), human cervical carcinoma (HeLa), mouse colon carcinoma (CT-26), and human glioblastoma astrocytoma (U373) cells. They efficiently entered in cancer cells within 4 hours through passive diffusion and localised in the cytoplasm. All the four complexes showed no dark toxicity and they were phototoxic against several cancer cell lines at a low micromolar concentration. Additionally, they were found to be active in a HeLa MCTS (multicellular tumour spheroids) 3D tumour model. The anthracene derivative **1.32j** ($R^2 = I$) displayed the higher cell uptake efficiency. Since their excited states were quenched in polar environment due to the formation of a SBCT state, the mesityl derivative **1.32g** ($R^2 = I$, with the best photophysical and phototoxic properties) was encapsulated in a polymer matrix (1,2-distearoyl-sn-glycero-3-phosphoethanolamine-N-[methoxy(polyethylene glycol)-2000] ammonium salt (DSPE-PEG2000-OCH₃). The nanoparticles improved the water solubility, enhanced the photophysical properties and the selective localisation in lysosomes, contrary to the complex alone that

accumulated in the cytoplasm. Upon light exposure, the particles lead to cell death at low micromolar concentrations in the monolayer cancer cells and HeLa MCTS 3D tumour model, presenting potential as PSs.^[189]

The same group reported that the heavy atom-free bis(dipyrrinato)zinc(II) analogues **1.32b**, **3.32f**, **1.32g**, and **1.32j** ($R^2 = H$) showed potential as imaging probes. These complexes had intense fluorescence in non-polar solvents, the emission was quenched in polar environment, and were localised in HeLa cells cytoplasm by passive diffusion. In order to overcome the quenching and increase the water-solubility, complex **1.32g** ($R^2 = H$) was encapsulated in a polymer matrix with biotin group. The nanoparticles maintained their bright fluorescence and similarly with the iodinated analogues they selectively localised in the HeLa cancer cells lysosomes and fully penetrated 3D MCTS. All the zinc components did not show any dark toxicity, either phototoxicity upon irradiation [at 510 nm (20 min, 5.0 J cm⁻²) and 540 nm (40 min, 9.5 J cm⁻²)] toward non-cancerous retinal pigment epithelium (RPE-1) and human cervical carcinoma (HeLa) cells ($IC_{50} > 100 \mu M$).^[190]

Ni(II) and **Cu(II)** dipyrinato complexes favour square planar or tetrahedral configurations depending on the nature of the ligands (Figure 1.10).^[150] The steric repulsion from α -substituents can be adapted by creating intermediate geometries between square planar and tetrahedral.^[150,191,192] A distorted square planar geometry (α -substituent = H) or a distorted tetrahedral geometry (α -substituent = CH₃ or Ph) were observed for bis(dipyrrinato)Ni(II) complexes.^[150,155,193] The CH₃ and Ph groups are larger and can introduce steric hindrance, thereby increasing the inter-ligand dihedral angle. Similar distorted geometries were observed for bis(dipyrrinato) Cu(II) and Zn(II) complexes.^[150,174,189,191] The order of deviation from the tetrahedral angle caused by α -substitution is: Zn(II) < Ni(II) < Cu(II).^[174]

Usually the Ni(II) and Cu(II) dipyrinato complexes are non-luminescent. However, Cu(II) dipyrinato complexes **1.39** and **1.42** displayed weak fluorescence. For example, the dipyrinato complex **1.39** weakly emits at ~ 500 nm and **1.42** at 570 – 630 nm in several solvents. The fluorescence quantum yield of the later was estimated 0.001 in butyronitrile.^[194]

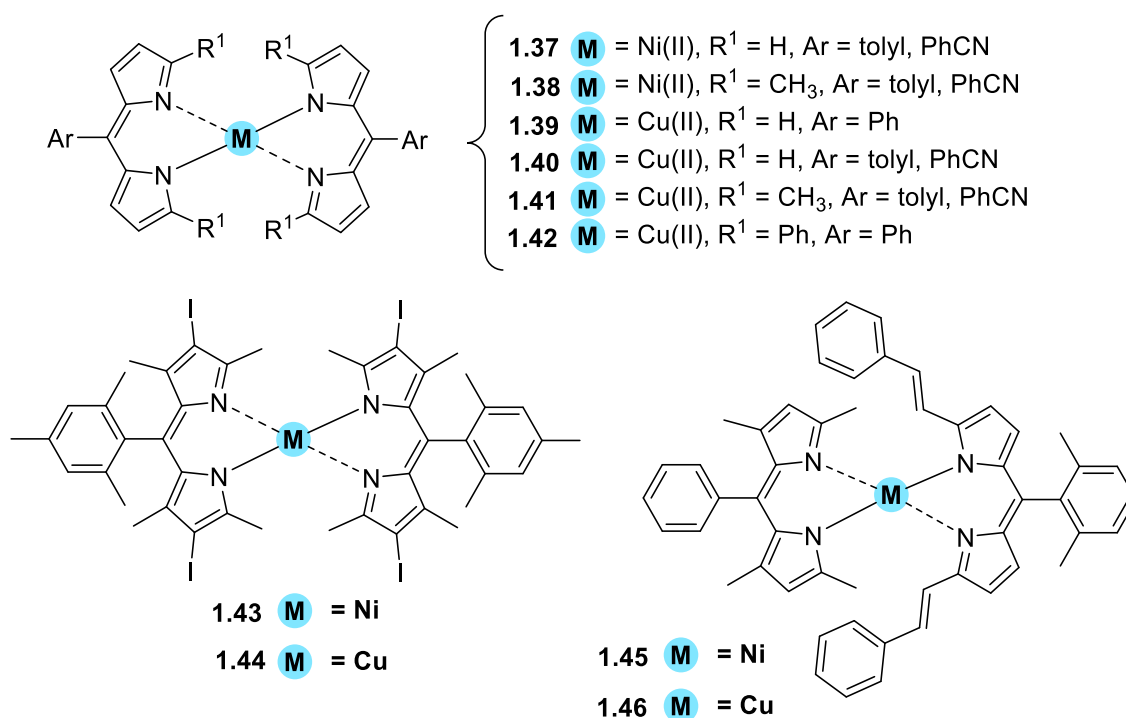


Figure 1.10. Chemical structures of Ni(II) and Cu(II) bis(dipyrrinato) complexes.

Karges *et al.* investigated two iodo-substituted Ni(II) and Cu(II) homoleptic dipyrrinato complexes **1.43** and **1.44** as PSs for PDT (Figure 1.10). These are direct analogues of the zinc complex **1.32g** ($R^2 = \text{I}$) which has exhibited potential for PDT. Both complexes displayed distorted geometries in between square planar and tetrahedral. The complexes had strong absorption in the green area of the electromagnetic spectrum $\sim 525 \text{ nm}$ but they were poorly emissive and scarcely generated singlet oxygen upon irradiation. Ni(II) complex **1.43** had no fluorescence signal and Cu(II) analogue **1.44** displayed a low emission signal with a fluorescence quantum yield of 0.1%. The biological evaluation revealed that they had low dark cytotoxicity in non-cancerous retinal pigment epithelium and human cervical carcinoma (HeLa) cells ($\text{IC}_{50} = 157.1 - 185.3 \mu\text{M}$); however, a negligible effect was observed on the cell viability upon irradiation (at 510 nm , 20 min , 5.0 J cm^{-2}).^[191]

Nishihara and co-workers synthesised heteroleptic Ni(II) and Cu(II) complexes **1.45** and **1.46** which adopted tetrahedral geometries, due to the bulky α -substituents on one of the dipyrrin ligands. Both complexes were non-emissive, while the heteroleptic and tetrahedral Zn(II) complexes were emissive. The structures were analysed by X-ray single crystal, and investigated by using cyclic

voltammetry, chronocoulometry, and UV/vis absorption spectroscopy. No data with regards to PDT have been reported [195]

Pd(II) and **Pt(II)** dipyrinato complexes are mainly investigated in context of their geometry and their luminescence properties. Most palladium and platinum bis(dipyrinato) complexes form 4-coordinated complexes and the ligands can either bind in a tetrahedral or a square planar configuration and in this case the preferred configuration is square planar.

Mathew *et al.* recently reported four homoleptic bis(dipyrinato)palladium(II) complexes *via* a one-pot reaction and a preliminary investigation on their antitumor activity (**1.47** – **1.50**, Figure 1.11). The absorption spectra of these chelates displayed one intense band for $^1\pi - \pi^*$ transitions at $\sim 470 - 490$ nm ($\epsilon = 55,000 \text{ M}^{-1} \text{ cm}^{-1}$) and a broad band ca. $350 - 400$ nm ($\epsilon = 10,000 \text{ M}^{-1} \text{ cm}^{-1}$), that the authors ascribed to an MLCT transition. The respective complexes displayed weak luminescence and overall fluorescence quantum yields lower than 0.03 in acetonitrile, chloroform, and toluene. Their singlet state lifetimes were in the range of $2.5 - 3.8$ ns representing this weak fluorescence feature. In addition, the average singlet oxygen quantum yield in all the solvents was relatively low (Φ_{Δ} ca. ~ 0.08), with the phenyl derivative **1.47** displaying the higher value in acetonitrile ($\Phi_{\Delta} = 0.17$) whereas their triplet excited state lifetimes were also short ($30 - 70$ ns). Finally, *in vitro* cytotoxicity against DLA cancer cell lines was assessed and the selectivity of action of the complexes was validated with respect to non-cancerous rat spleen cell lines. Interestingly, all the complexes **1.47** – **1.50** exhibited cytotoxicity against cancerous DLA cells and had no effect on the non-cancerous cells. The cyanophenyl derivative **1.49** was the more cytotoxic with a low IC_{50} value of $50.73 \mu\text{g mL}^{-1}$.^[196] Pd(II) complexes have not yet investigated toward a PDT application; however, with further development they could reveal a potential as anticancer agent. Lastly, the respective palladium complexes adopt a slightly distorted square planar geometry where a loss of coplanarity between the dipyrin ligands and a curvature of the bis-pyrrolic core were observed.

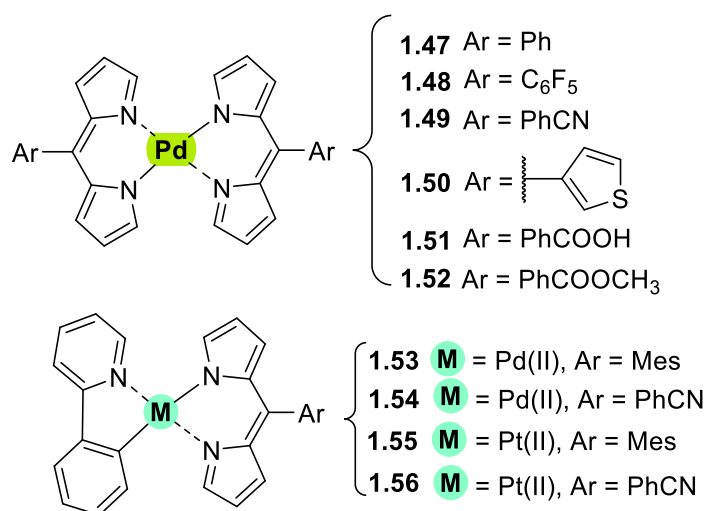


Figure 1.11. Chemical structures of Pd(II) and Pt(II) bis(dipyrrinato) complexes

Another report for complex **1.47**, showed that it undergoes a key structural reorganisation in its excited state and yields a triplet state from a square planar configuration. Fluorescence decay studies along with DFT calculations showed the involvement of ¹LC₂ and ¹LC₁ (ligand-centred) excited states where population of ¹LC₂ upon excitation results in a short-lived singlet state that is quickly relaxed to ¹LC₁. By this state they observed that due to a probable structural flexibility of **1.47** the symmetry was disturbed and resulted in a partially allowed fluorescence. The triplet state adopts a geometry which was supported by DFT calculations and is dominated by a fast ISC process from LC states to triplet states with an ISC rate constants of ca. (13 –16 ps)⁻¹. Lastly, the absence of any phosphorescence emission of bis(dipyrrinato)Pd(II) complex was validated by the structural reorganisation leading to a non-emissive triplet metal centred state (³MC).^[197]

Bronner *et al.* synthesised and photophysically evaluated four new Pt(II) and Pd(II) complexes that combine a mesityl dipyrrin or benzonitrile dipyrrin ligands with a cyclometallated Pd(II) and Pt(II) moieties of 2-phenylpyridine (ppy) (**1.53** – **1.56**, Figure 1.11). The geometry of the Pd(II) centre deviated slightly from the square planar with a deviation from planarity orientating either above or below the plane defined by the Pd(II) and the 2-phenylpyridine (ppy) ligand and each pyrrolic ring. The geometry around the Pt(II) metal centre is square planar; however, the two pyrrolic rings were not coplanar and showed a distortion. Interestingly, palladium complex **1.54** was not isostructural to its platinum

analogue **1.56**. These complexes displayed an intense absorption band at ~500 nm, corresponding to the $^1\pi - \pi^*$ transition of the dipyrin ligand, whereas a band at ~430 nm was only evident on the Pt(II) complexes which can be ascribed to MLCT state. Nevertheless, their luminescence was rather weak, even at lower temperatures. Amongst the complexes, the Pt(II) derivatives exhibit the stronger fluorescence emission, and particularly the mesityl derivative **1.55**. This indicates that the singlet state of Pt(II) chelates undergo faster radiative processes and slower non-radiative processes. This is related, as previously described, to the restriction of rotational freedom which increases the emission intensity and fluorescence quantum yield, e.g., by mesityl group.^[198] For Pd(II) complexes, the out-of-plane distortion can result in a low-lying MC state which favours the deactivation pathways.^[198]

In general, α -substituents in the pyrrolic rings of the dipyrin can cause strain between them which can be released when the structure can reorient and distort away from the square planar configuration providing room for the α -substituents and deviating from the square planar geometry.^[199] However, Pd(II) dipyrin complexes were observed to maintain a strictly square planar configuration upon coordination environment with Pd(II). Telfer *et al.* showed that the repulsion could be accommodated by forcing the ligands to lean away from the Pd-N₄ plane, and a non-planar distortion of the bis-pyrrolic core was observed due to close interligand contacts of their α hydrogen atoms (**1.51**, **1.52**, Figure 1.11).^[200] These complexes displayed intense bands in their UV-Vis spectra at ~ 480 nm, which can be ascribed to $^1\pi - \pi^*$ transitions of the dipyrin moieties; however they were non-emissive upon excitation.

1.5.2 Re(I), Ru(II), Rh(III), and Ir(III) dipyrinato complexes

Re(I) complexes with ligands other than dipyrins, e.g., pyridine, polypyridyl, tricarbonyl, pyridocarbazole or phenanthroline ligands, are well studied complexes in the context of triplet state population and photosensitised generation of singlet oxygen and PDT application.^[201–209] Most of the complexes involve a long $^3\text{MLCT}$ state lifetime which enhances the possibility of energy transfer process, followed by high values of singlet oxygen quantum yields. Their potential mechanism of action include i) phototoxicity; ii) DNA binding; iii) enzyme

inhibition; iv) mitochondrial effects or v) oxidative stress regulation. Many ligands have been described that can modulate the lipophilicity, the luminescent properties, the cellular uptake, the biodistribution, the cytotoxicity, the pharmacological and toxicological profile. Nevertheless, concerning Re(I) dipyrinato complexes only few photophysical properties have been published to date (Figure 1.12).^[210–214]

Telfer and co-workers synthesised Re(I) complexes coordinated with dipyrin ligands and different number of CO- or phosphine ligands (**1.57** and **1.58**, Figure 1.12). These complexes showed intense absorption in the visible region (470 – 480 nm); however, they displayed weak or no emission from the $^1\pi - \pi^*$ transition ($\Phi_f < 0.01$, at ~ 700 nm) and large Stokes shifts ($6,000\text{ cm}^{-1}$). Exciton coupling is not observed since they are mono dipyrinato type of complexes. Exchanging the PPh₃ phosphine ligands with PBu₃ ligands caused a blue-shift in the UV-Vis absorption spectra of the $\pi - \pi^*$ band. Additionally, by increasing the number of phosphine ligands from one to two resulted in a blue-shift with a decrease in the absorption intensity. Formation of a $^3\text{MLCT}$ state and phosphorescence from a dipyrin-centred triplet excited state was proposed by DFT calculations.^[210] Following, the same group, synthesised Re(I) dipyrins with various meso substituents were the complexes **1.59** presented negligible luminescence. Since **1.57** and **1.58** were emissive, this difference could occur due to the complexation with the pyridine moiety in **1.59**.^[213]

Manav *et al.* investigated the singlet oxygen efficiency and photostability of Re(I) complexes **1.60** (Figure 1.12). These complexes had strong absorption in the UV-Visible spectra but very weak fluorescence with a large Stokes shifts values ($5600 - 6960\text{ cm}^{-1}$) and they displayed high singlet oxygen yields ($\Phi_\Delta = 0.75 - 0.99$) with the highest value for **1.60b** ($\Phi_\Delta = 0.99$), followed by *N*-butylcarbazole **1.60g** in the second place (0.98). The substitution at the meso position did not impact the absorption maxima of the absorption band; however, the substituents had an impact on the phosphorescence wavelengths.^[211] The different substituents from electron donating (*e.g.*, carbazole) to electron withdrawing (*e.g.*, pentafluorophenyl) altered the structural, electrochemical, and spectroscopic properties of these complexes. Thus, the bulky electron rich aromatic groups (**1.60f,g,h**, Figure 1.12) showed phosphorescence between 681 – 692 nm with

relatively smaller Stokes shifts. Conversely, the electron withdrawing halobenzene groups showed maxima at higher wavelengths ca. 698 – 736 nm. The complex with the strongest electron withdrawing group, pentafluorophenyl **160a**, and the thienyl **160e** exhibited the most red-shifted absorption profile. Finally, these complexes displayed long triplet excited state lifetimes ($\tau_T = 9 - 29 \mu\text{s}$) resulting in efficient singlet oxygen generation ($\Phi_\Delta \sim 0.75 - 0.98$) along with their distinct photo-stability showing potential for use as PSs.^[211]

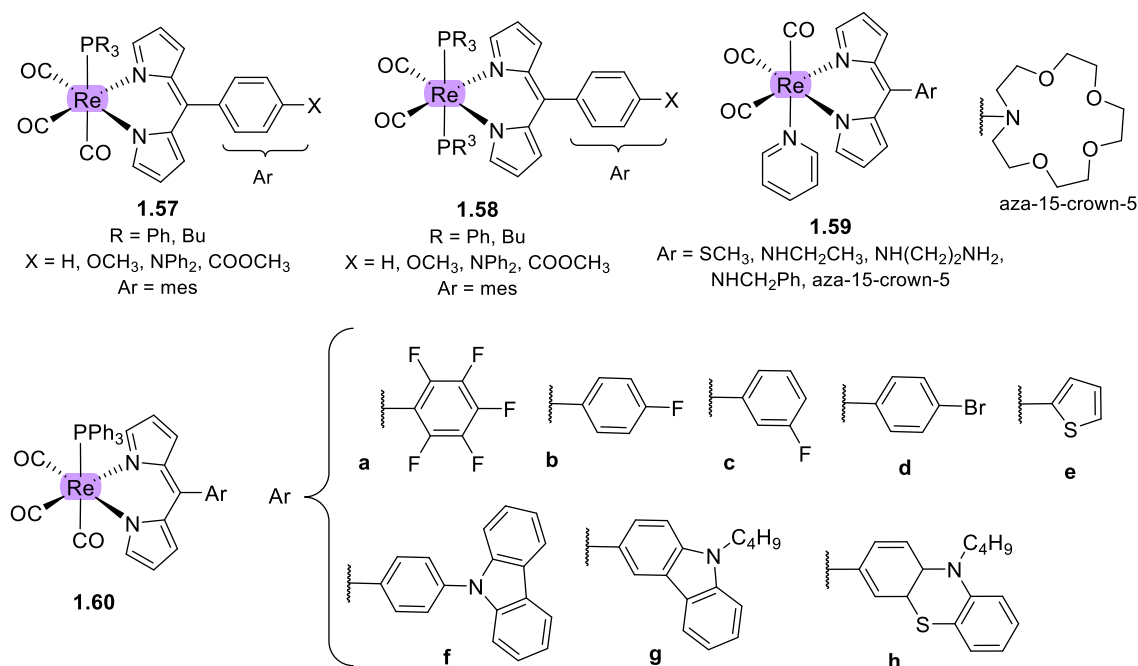


Figure 1.12. Chemical structures of Re(I) dipyrrinato complexes.

The **Ru(II)** complexes have been extensively studied for different applications due to their relative stability and their unique photophysical properties. As previously stated TLD-1433 is a ruthenium based PS. The majority of these chelates have good water-solubility, long luminescence decays, high singlet oxygen production, and chemical and photophysical stability.^[61]

Yin *et al.* reported blue-green absorbing Ru(II) complexes with π -conjugated ligands which exhibit long-lived triplet lifetimes and can be activated with red/NIR light to yield PSs for multiwavelength PDT. Remarkably, these ruthenium complexes had photodynamic efficacy when they were excited at longer wavelength (625 nm, L.D. of 100 J cm^{-2}) even with low absorptivity at this region ($\epsilon < 100 \text{ M}^{-1} \text{ cm}^{-1}$). Although these complexes absorb outside the photo therapeutic window ($< 500 \text{ nm}$), they displayed promising potential as PSs for

PDT, with light EC₅₀ values of 0.4 – 1.9 μM against HL60 human promyelocytic leukaemia cells.^[209] Another article described a red-shift in the absorption of Ru(II) polypyridyl complexes towards the therapeutic window. This was achieved *via* the introduction of suitable π-conjugated moieties on the [Ru(bipy)₃]²⁺ core, such as extension with methyl groups or vinyl dimethylamino groups, presenting phototoxicity against cervical cancerous HeLa cells.^[215]

With regards to Ru(II) complexes with dipyrin ligands there are reports on heteroleptic complexes, which focus on their synthesis, photophysical properties, antitumor activity, and applications in dye-sensitised solar cells.^[216–220] The heteroleptic Ru(II) dipyrin and bipyridine complexes with carboxyl, carboxylate, or ester as functional groups **1.62** – **1.67** (Figure 1.13)^[200,217] displayed an intense absorption band and **1.65** displayed two distinct bands in the visible region and prominent exciton coupling features. One strong band at 483 nm was assigned to the ¹π - π* transition and a broader at 512 nm to a Ru(II) bipy MLCT transition. This second one is slightly red-shifted compared to the corresponding MLCT transition of [Ru(bipy)₃]²⁺. For **1.67** the most interesting feature is a broad, intense band at 638 nm that was ascribed to a Ru → bipy (MLCT) transition while the band at 480 nm is due to intraligand dipyrin ¹π - π* transition. Complexes **1.62-1.67** had weak or negligible luminescence and Raman spectroscopy indicated that only weak electronic interactions were present between the MLCT and ¹π - π* transitions (even though they were both coordinated to the Ru(II) metal ion). In addition, **1.68** Ru(II) complexes have been developed without further characterisation apart from X-ray analysis.^[221]

Swavey *et al.* reported heteroleptic monometallic **1.69** and trimetallic **1.70** Ru(II) complexes with π-extended dipyrinato ligands. They have been characterised and evaluated as possible PSs using the human lung cancer cell line A549. Both complexes showed absorption at ~ 290 nm that belong to π - π* transition of bipyridine moieties, and the trimetallic complex showing higher intensity due to the increased number of bipyridines. Complex **1.69** displayed a band at 570 nm with a shoulder at 540 nm due to an overlap of transitions by the dipyrins and a transition overlap of the ruthenium and bipyridines metal to ligand charge transfer (MLCT) transitions, respectively. Complex **1.70** had two distinct bands at 502 and

578 nm that presumably belong to the ruthenium to bipyridine MLCT transition and the dipyrin intra-ligand charge transfer transition, respectively. The latter can also include an overlap of dipyrin ILCT and Ru(II) dipyrin MLCT transitions. In addition **1.70** had another absorption band at 350 nm, most likely connected with a higher energy MLCT transition originating from the peripheral Ru(II) centres.

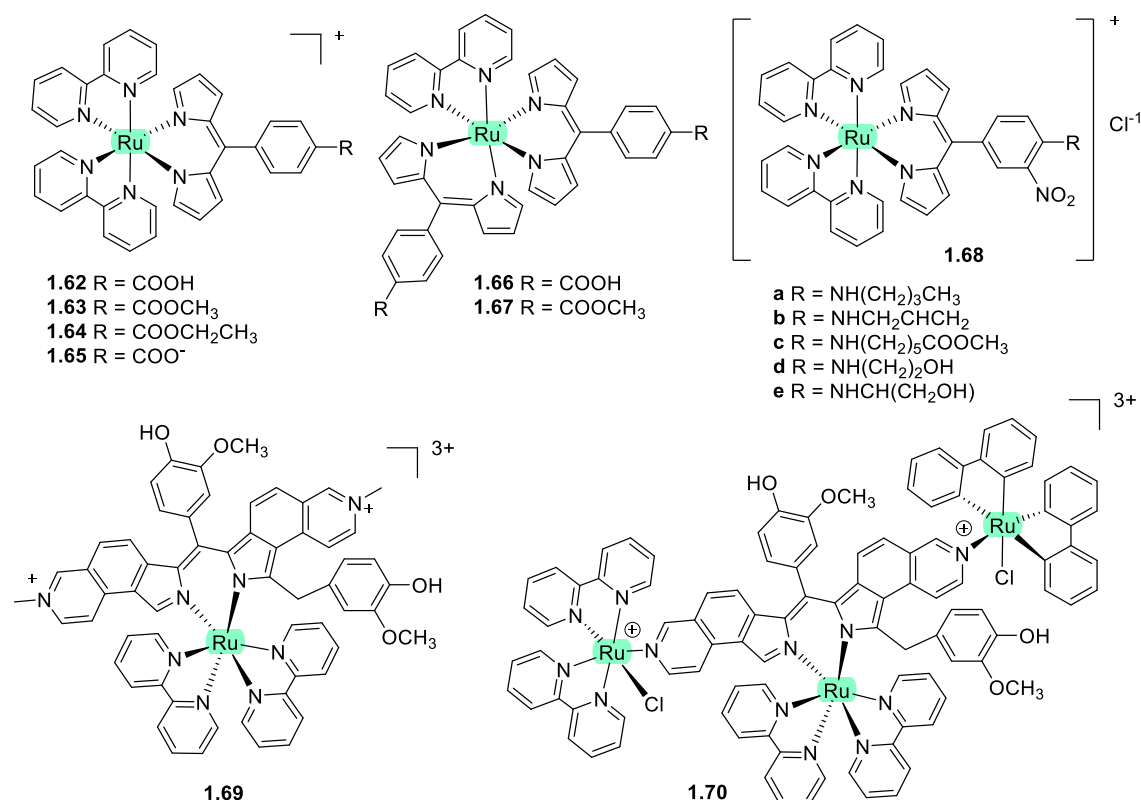


Figure 1.13. Chemical structures of Ru(II) dipyrinato based complexes.

The complexes generate singlet oxygen sufficiently to operate efficiently *via* type II mechanism irradiating within the PDT window or at high energy (420 nm). The *in vitro* (photo)cytotoxicity was evaluated and both complexes did not exhibit any dark toxicity against lung cancer cells (A549 cell line) up to 50 μ M. Upon irradiation of the cells (\sim 420 nm, 2.3 μ W cm⁻²) **1.69** did not show any phototoxicity; however, the trimetallic Ru(II) complex **1.70** displayed significant phototoxicity at 50 μ M concentration. This was explained by the fact that **1.70** generated 50% higher light-induced ROS compared to the control. Interestingly, photocleavage studies with supercoiled plasmid DNA (pUC18) demonstrated that the complexes initiated the DNA photodegradation (irradiation > 550 nm). It was reported that **1.70** photo reacted with DNA under hypoxic conditions causing

DNA photodamage, which is crucial in PDT since in cancer cells and tumorous sites oxygen concentrations are low.^[216]

Furthermore, heteroleptic Ru(II) complexes with (methoxypyridyl)phenyl, methylthiophenyl, pyrimidyl-piperazine, *p*-cymene and ferrocene substitution have been reported to demonstrate binding affinity to DNA or proteins and act as anticancer agents.^[214,218–220,222,223] Some of the Rh(III) and Ir(III) based heteroleptic dipyrin analogues were also reported. Research relevant to PDT is not yet well investigated.

Paitandi *et al.* synthesised and investigated a series of **Ru(II)**, **Rh(III)** and **Ir(III)** complexes with a ferrocenyl dipyrin for use as anticancer agents. At the UV-Visible spectra the ligand itself displays two weak absorption bands at 480 nm (Fe-Cp) and at 395 nm due to $\pi - \pi^*$ charge transfer transitions, respectively. The complexes had intense band $\sim 500 - 510$ nm which were assigned to $\pi - \pi^*$ charge transfer transitions due to dipyrin moiety, whereas the weaker ones $\sim 418 - 450$ nm to the MLCT transitions. Intense high energy transitions $\sim 340 - 350$ nm were assigned to intra-ligand $\pi - \pi^*$ transitions. Interactions of the complexes with calf thymus DNA (CT-DNA) and BSA (bovine serum albumin) have been assessed *via* UV-Visible absorption, ethidium bromide displacement fluorescence studies, synchronous, and 3D fluorescence spectroscopy. In addition, molecular docking studies proposed that the complexes bind with the minor groove of DNA, and are located within the subdomain IIA cavity of the protein. *In vitro* anticancer studies showed that **1.71 – 1.75** (Figure 1.14) induced cytotoxicity and apoptosis against Dalton's lymphoma (DL) cell line. The ruthenium complexes exhibited cytotoxicity and rhenium was the most toxic, effectively inducing apoptosis at low concentrations. The toxicity was according to the following descending order: **1.74** ($IC_{50} = 20-30 \mu\text{g mL}^{-1}$) > **1.73** ($IC_{50} = 80-90 \mu\text{g mL}^{-1}$) > **1.72** ($IC_{50} = 100-110 \mu\text{g mL}^{-1}$) > **1.71** ($IC_{50} = 110 \mu\text{g mL}^{-1}$) > **1.75** ($IC_{50} 110 \mu\text{g mL}^{-1}$).^[219]

The same group worked on a new set of Ru(II) organometallic complexes **1.76 – 1.79** (Figure 1.14). Absorption spectra displayed three bands: a strong band at low energy $\sim 490 - 510$ nm corresponding to $^1\pi - \pi^*$ charge transfer from the conjugated dipyrin core; another band at higher energy $\sim 420 - 460$ nm assigned

to MLCT transitions; and a third band in UV region at ~ 305 – 340 nm that was ascribed to dipyririn based intra-ligand $\pi - \pi^*$ transitions. Following, the DNA binding affinity of the demonstrated the interaction of the complexes with CT-DNA through intercalation in the DNA and molecular docking studies suggested that they bind with the minor groove of the DNA same as the previous work. Finally, a significant cytotoxicity against A549 cell line was present for all the complexes (**1.76 – 1.79**) inducing apoptosis efficiently and the most prominent, with the lowest IC₅₀ value (20 μ M), was the pentafluorophenyl derivative **1.77**.^[220]

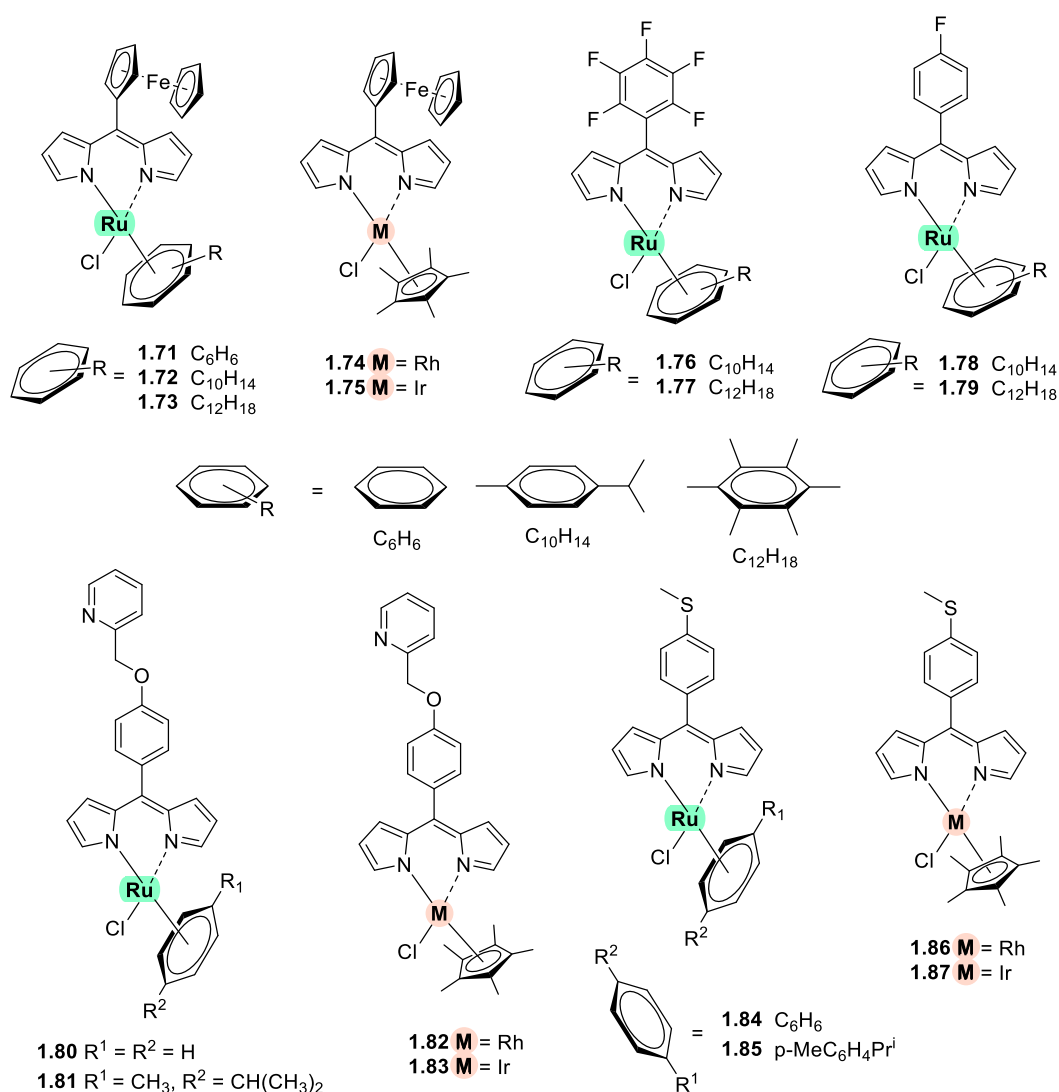


Figure 1.14. Chemical structures of heteroleptic Ru(II), Rh(II) and Ir(III) dipyrinato complexes.

Gupta *et al.* developed four new heteroleptic complexes with $(\eta^6\text{-arene})\text{Ru-}$, $(\eta^5\text{-C}_5\text{Me}_5)\text{Rh-}$, and $(\eta^5\text{-C}_5\text{Me}_5)\text{Ir-}$ moieties and 4-(2-methoxypyridyl)phenyldipyririn **1.80 – 1.83** (Figure 1.14). Their absorption spectra displayed an intense low

energy band ~ 485 – 500 nm that was assigned to conjugated dipyrin $^1\pi - \pi^*$ transition and MLCT transitions, whereas the high energy bands at ~ 260 nm and at ~ 350 to dipyrin based intra-ligand $\pi - \pi^*$ transitions. Their DNA binding activity was evident even at very low concentrations. The cytotoxic efficacy against DL cells of these complexes based on binding constant and antitumor activity was as follows: **1.81** ($IC_{50} = 5-10 \mu\text{g mL}^{-1}$) > **1.80** ($IC_{50} = 8-10 \mu\text{g mL}^{-1}$) > **1.83** ($IC_{50} = 30-40 \mu\text{g mL}^{-1}$) > **1.82** ($IC_{50} = 75-100 \mu\text{g mL}^{-1}$).^[214]

The same group evaluated a new class of heteroleptic dipyrinato complexes based on Ru(II), Rh(III), and Ir(III) **1.84** – **1.87** containing 5-(4-methylthiophenyl)dipyrin (Figure 1.14). They exhibited strong low energy absorptions at ~ 490 – 500 nm; weak bands at ~ 385 – 430 nm in the absorption spectra; and high energy intense bands at ~ 250 nm which have been ascribed to the intraligand $^1\pi - \pi^*$ transitions. Similarly with the previous reports these complexes appeared to act as intercalators in the DNA (through the minor DNA groove) as they bind efficiently through intercalative or electrostatic interactions. *In vitro* anticancer activity of the complexes was remarkably improved since they had better cytotoxicity, and higher activation of the endonuclease for DNA cleavage. The descending order was: **1.85** ($IC_{50} = 5-10 \mu\text{g mL}^{-1}$) > **1.84** ($IC_{50} = 8-10 \mu\text{g mL}^{-1}$) > **1.87** ($IC_{50} = 30-40 \mu\text{g mL}^{-1}$) > **1.86** ($IC_{50} = 75-100 \mu\text{g mL}^{-1}$).^[222]

Similar observations were made by this group with arene Ru(II) heteroleptic dipyrinato complexes containing 5-(2-pyrimidylpiperazine)phenyldipyrin and 5-(2-pyridylpiperazine)phenyldipyrin, that displayed *in vitro* cytotoxicity against kidney cancer cell line (ACHN) and suggested an apoptotic mode of cell death.^[218]

Iridium metal complexes are widely investigated for applications in catalysis, materials in electronic devices such as photoelectronic sensors, photochemistry and luminescent chemosensors or LEDs. The application toward biomedicine is still in its infancy; however, there is an increasing effort in developing Ir(III) based chelates with biomedical purposes. Most of the Ir(III) complexes related to PDT research are based on polypyridyl ligands. Looking in Ir(III) and dipyrin ligands only a limited number of complexes is investigated in the context of PDT.^[224]

Particularly, Hohlfeld *et al.* investigated the application of a wide range of heteroleptic (dipyrrinato)iridium(III) complexes for application in PDT with four tumour cell lines and antibacterial PDT with two bacterial strains known to pose one major problem in hospital infections (Gram-positive germ *S. aureus* and Gram-negative germ *P. aeruginosa*).

A number of heteroleptic (dipyrrinato)Ir(III) complexes with several functional groups were synthesised. These could be grouped into the chlorido(dipyrrinato)(pentamethyl- η^5 -cyclopentadienyl)iridium(III) type **1.70** – **1.71** or (dipyrrinato)bis(2-phenylpyridyl)iridium(III) type **1.72** – **1.73** (Figure 1.15). Both the groups were sub grouped by two types of aromatic substituents, one with 4R-tetrafluorophenyl (substituent X) and second with 3-nitrophenyl-4R (substituent Y). To investigate the scope of the reaction the complexes were functionalised *via* nucleophilic substitution, glycosylation, and BODIPY conjugation.^[225]

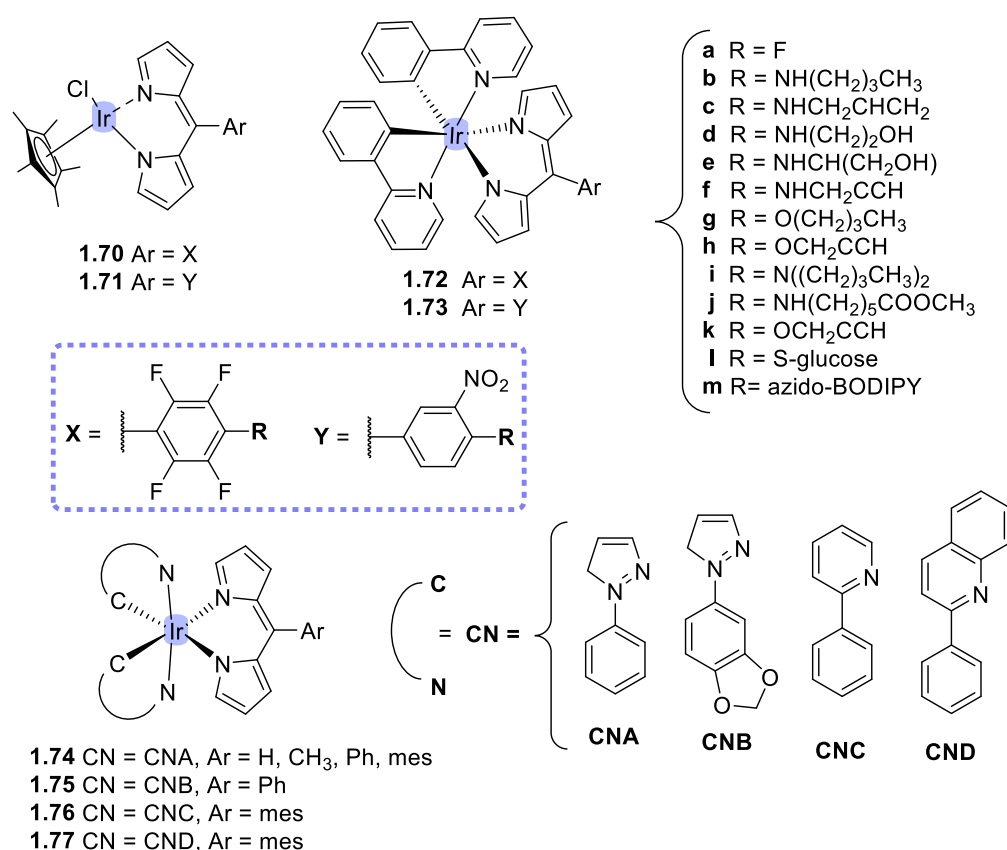


Figure 1.15. Chemical structures of heteroleptic Ir(III) based dipyrrinato complexes.

The (cyclopentadienyl)(dipyrrinato)iridium(III) complexes **1.70** – **1.71** displayed two absorption maxima at ~ 450 – 465 nm and ~ 500 nm, whereas for the corresponding (dipyrrinato)bis(2-phenylpyridyl)iridium(III) complexes **1.72** – **1.73** only one absorption maximum at ~ 485 nm was observed. In general, the tetrafluorophenyl substituted dipyrrinato complexes exhibit a red-shift absorption (~ 10 nm) compared to the nitrophenyl substituted. Their suitability for PDT was assessed in cellular and bacterial assays with and without light with the **1.70** – **1.71** complexes and the glyco-substituted iridium(III) complexes showing prominence as photomedicine candidates. There was a tendency for the X-substituted complexes to show higher phototoxic activity than the Y-substituted complexes. Within the **1.72** – **1.73** complexes the ones with alkenyl, alkynyl, and polar substituents exhibited the higher phototoxicity, with glycosylated complexes being most effective. This study illustrated the potential for Ir(III) complexes as PSs for PDT. In the evaluation against bacteria **1.70** – **1.71** group displayed high toxicity with but also in the absence of light, regardless of the substitution.

Apart from this comprehensive report on Ir(III) complexes for PDT, there is no published research related to Ir(III) dipyrrin complexes and PDT. One work focused on the phosphorescence of bis-cyclometalated Ir(III) dipyrrin complexes with application in OLEDs. A variety of co-ligands (CN) and substituents on the meso-position of the dipyrrin ligand were introduced **1.74** – **1.77** (Figure 1.15).^[226] The electrochemical and photophysical properties of the complexes were governed by the dipyrrin ligand acted as the chromophore and showed strong absorption of visible light (~ 470 – 485 nm, $\epsilon = 38,000 \text{ M}^{-1} \text{ cm}^{-1}$) with large Stokes shifts. The complexes showed phosphorescence at room temperature from a dipyrrin-centred triplet state with quantum yields up to 11.5% and triplet state lifetimes ~ 12.9 – 23.1 μs with emission maxima ranging from 658 – 685 nm. Additionally, it was suggested that the efficient triplet state formation upon photoexcitation is caused by the formation of the ^3IL state.^[227] These features and the efficient triplet state formation may facilitate possible applications as PSs.

Ultimately, another study associated with dipyrrinato ligands was based on homoleptic tris(dipyrrinato) **Ga(III)**, **In(III)** and **Fe(III)** complexes (Figure 1.16). The absorption spectra of Ga(III) and In(III) tris(dipyrrinato) complexes showed two distinct absorption bands at ~ 450 and ~ 515 nm whereas in the spectrum of

Fe(III) complex these bands are evidently broader. The cytotoxicity of selected complexes **1.84** – **1.87** in the absence and presence of light was evaluated in human epidermoid carcinoma (A253), human epithelial carcinoma (A431), human oral adenosquamous carcinoma (CAL27), and colorectal adenocarcinoma (HT29) cell lines whilst the mouse fibroblast cell line L929 was tested as a non-tumorous cell line. Lastly, the bacteria photoinactivation was evaluated with **1.84** – **1.87** against the Gram-positive bacterium *S. aureus*. Overall, the phototoxic effect against tumor cells and against *S. aureus* was predominantly observed with the glycosylated gallium(III) complexes (**1.85** and **1.87**) and the activity was dependent on the metal and the presence of carbohydrate unit.^[228]

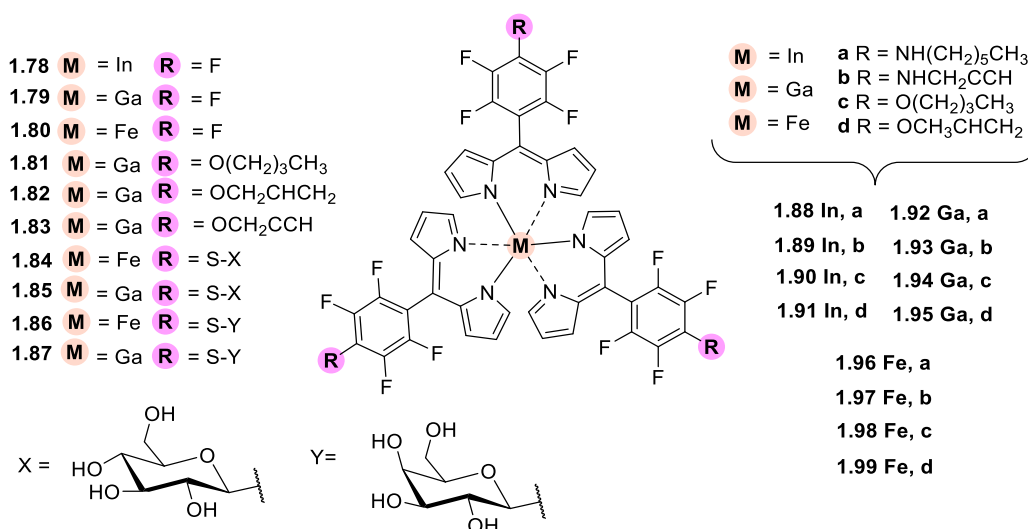


Figure 1.16. Chemical structures of homoleptic tris(dipyrrinato) Ga(III), In(III) and Fe(III) complexes.

Metal coordination complexes are promising material for metal organic frameworks (MOFs) preparation through the self-assemblies of organic ligands and metal ions (or clusters) and coordination bonds that lead to a crystalline network structure formation. Bis- and tris- dipyrrinato complexes are excellent materials towards the formation of supramolecular structures. The advantage over BODIPY, that consists of one dipyrrin ligand, is their spontaneous coordination bonds that allow the development of self-assembled supramolecular and polymeric architectures.^[161,229] Additionally, metal organic frameworks (MOFs) have been investigated as drug delivery systems in PDT due to its porous network that can be used to encapsulate molecules minimising the aggregation

and enhancing the singlet oxygen yields. Another advantage is that the physicochemical properties of MOFs are modifiable, they can present good biocompatibility and can be degraded in the organisms. Finally, loaded MOFs can enhance the solubility of PSs and increase the cellular uptake.^[230]

1.6 Photophysical Aspects of PDT

An efficient PS can be developed by modifying the core structure of the macrocycle or the periphery of the ligands and modulating the photophysical and photopharmacological properties. Candidates that absorb intensively at the red or NIR region (590 – 850) are more likely to find use in PDT since the penetration of light into tissue proportionally increases with wavelength. The identity of the metal in the coordination centre can influence the relative energies, together with the substitution on the core structure. This has a consequent effect in the emissive properties such as fluorescence and triplet efficiency. PDT and PS activation depend directly on the light source and dose. Interactions between light and tissue such as refraction, reflection, and scattering can be overcome by applying the beam of light perpendicular to the tissue. However, the “optical therapeutic window” for PDT treatment is defined by two factors. The first limitation, between 650 – 1200 nm, arises from the absorption of tissue chromophores *i.e.*, water, melanin, oxyhemoglobin, deoxyhemoglobin, and cytochromes. The second limitation between 650 – 850 nm comes from the desired triplet state energy level of the PS which should be sufficient to generate efficiently singlet oxygen, thus $\geq 94.3 \text{ kJ mol}^{-1}$ (0.97 eV).^[231] Finally, the desired outcome is the singlet oxygen or ROS production and the efficient cell uptake in order for the photodynamic effect to take place.

1.6.1 Ground and excited state properties

The fundamental photophysical processes of molecules associated with photon ($h\nu$) absorption are listed below:

- ✚ Excitation, when a molecule in the singlet ground state is excited and promoted to singlet excited states: $S_0 + h\nu \rightarrow S_{1/n}$.

- ✚ Two-photon singlet-singlet absorption, when a molecule in the ground state absorbs simultaneously two photons and elevates to the S_1 state: $S_0 + 2 h\nu \rightarrow S_1$.
- ✚ Singlet-triplet absorption, when the absorbed energy is insufficient to excite the molecule to S_1 but can excite it to the triplet excited state: $S_0 + h\nu \rightarrow T_1$.
- ✚ Singlet-singlet absorption, when a molecule in the lowest singlet excited state absorbs energy leading to a transition to higher singlet states: $S_1 + h\nu \rightarrow S_n$.
- ✚ Triplet-triplet absorption, when a molecule in the lowest triplet excited state absorbs energy leading to a transition to higher triplet states: $T_1 + h\nu \rightarrow T_n$.
- ✚ Fluorescence emission, when a molecule from the lower excited singlet state decays to the ground state radiatively: $S_1 \rightarrow S_0 + h\nu$.
- ✚ Phosphorescence, is a phenomenon of long-lived luminescence where a molecule in the excited triplet state emits a photon and returns to the singlet ground state radiatively: $T_1 \rightarrow S_0 + h\nu$.
- ✚ Internal conversion (IC) is a non-radiative isoenergetic transition between two electronic states of the same multiplicity; a strong overlap of vibrational wave functions is required: e.g., $S_1 \rightarrow S_0$ and $T_2 \rightarrow T_1$.
- ✚ Vibrational relaxation (VR), occurs within the vibrational levels of the same excited state.
- ✚ Intersystem crossing (ISC), is a special case where a molecule in an excited state undergoes a non-radiative iso-energetic transition to another electronic state with a different spin multiplicity: $S_1 \rightarrow T_1$ and $T_1 \rightarrow S_0$.

Porphyrin-based molecules display a unique UV-Visible absorption profile with a strong absorption band at 400 – 450 nm (Soret or B band) and less intense band(s) between 500 – 800 nm (Q bands), which are the basis of their application in PDT. This unique profile is the result of splitting of the frontier molecular orbitals (FMO), as described by Gouterman's four orbital model (HOMO-1, HOMO, LUMO, and LUMO+1 orbitals) (Figure 1.17).^[232–234] As mentioned above, a series of competitive photochemical processes commence post irradiation. These

processes depend on the structural pattern of the PS. Generally, in porphyrinoids the Soret band stems from the strong electronic transition from the ground state to the second excited singlet state $S_0 \rightarrow S_{2/n}$ and the Q bands arise from the transition to the first excited singlet state $S_0 \rightarrow S_1$. The loss of energy (*via* heat) from the S_2 state by internal conversion (IC) is very fast and fluorescence is observed because of the depopulation of the first excited singlet state to the ground state $S_1 \rightarrow S_0$. There are important differences in the absorption profile in regard to the Q bands (red-shifted) and the absorption intensity (different molar absorption coefficient) of porphyrins, chlorins (one reduced pyrrole), and bacteriochlorins (two reduced pyrroles) due to the destabilisation of the HOMOs (and stabilisation of the LUMOs) of the latter molecules.^[235] The multiplicities of the Q bands are related to the transition dipole which is orientated on x or y axes resulting to the named Q_x and Q_y excitations. When the symmetry is reduced *e.g.*, free base porphyrin or chlorin, the two axes are no longer equivalent and the transitions between the MO are no longer degenerate causing the splitting of the MO and therefore the Q band transitions.

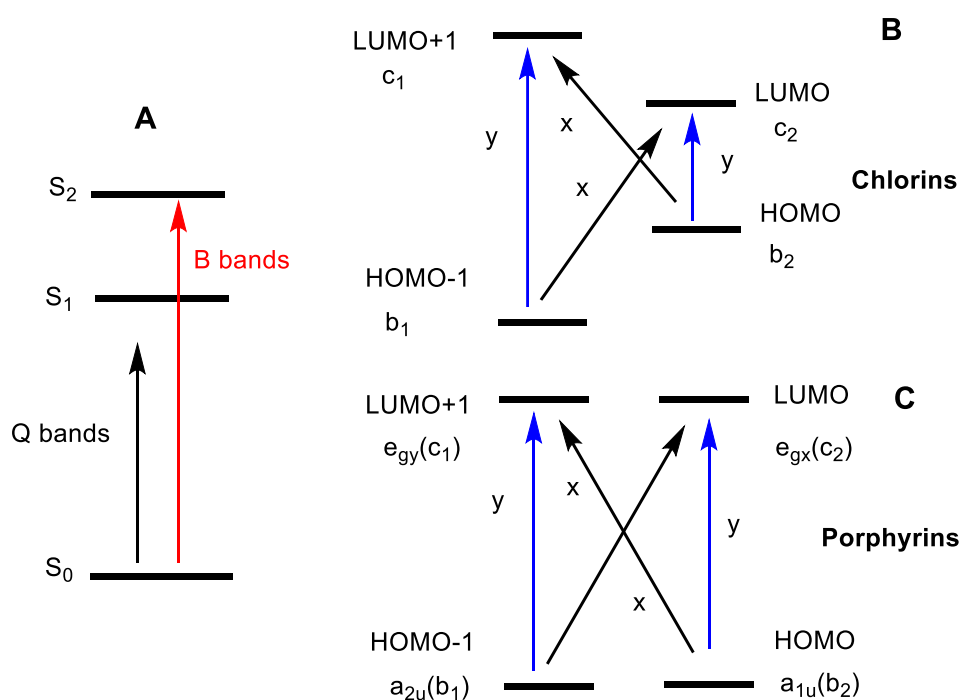


Figure 1.17. Simplified one electron transitions of porphyrinoids (A); Gouterman's four orbital model representing the HOMOs and LUMOs of chlorins (B) and porphyrins (C).

Changes to the absorption profile can be achieved by reducing the energy gap between the HOMOs and LUMOs, leading to red-shifted absorption spectra, which is of major importance in PDT. Modifications can occur inside the macrocycle either by reducing the pyrroles or by exchanging them with other rings or modifications on the periphery with functional moieties. Altering the symmetry of the macrocycle results in a red-shifted absorption profile and thus enables deeper skin penetration. It is known that substitution of the periphery with meso- or β - substituents can cause a bathochromic shift (red-shift) of both the B and Q_y bands and a hypochromic shift (decrease of the absorptivity) of the Q_y band, which is of great importance for photochemical applications.^[236] The reduction in the pyrrole rings does not change the 18 π -conjugation of the macrocycle but results in a difference in the UV-Visible spectrum due to the change of the symmetry and the reduced energy gap allowing for longer wavelength transitions. Figure 1.18 shows examples of magnesium 2,3,7,8,12,13,17,18-octaethylporphyrin, chlorophyll α and bacteriochlorophyll α together with their electronic absorption spectra.

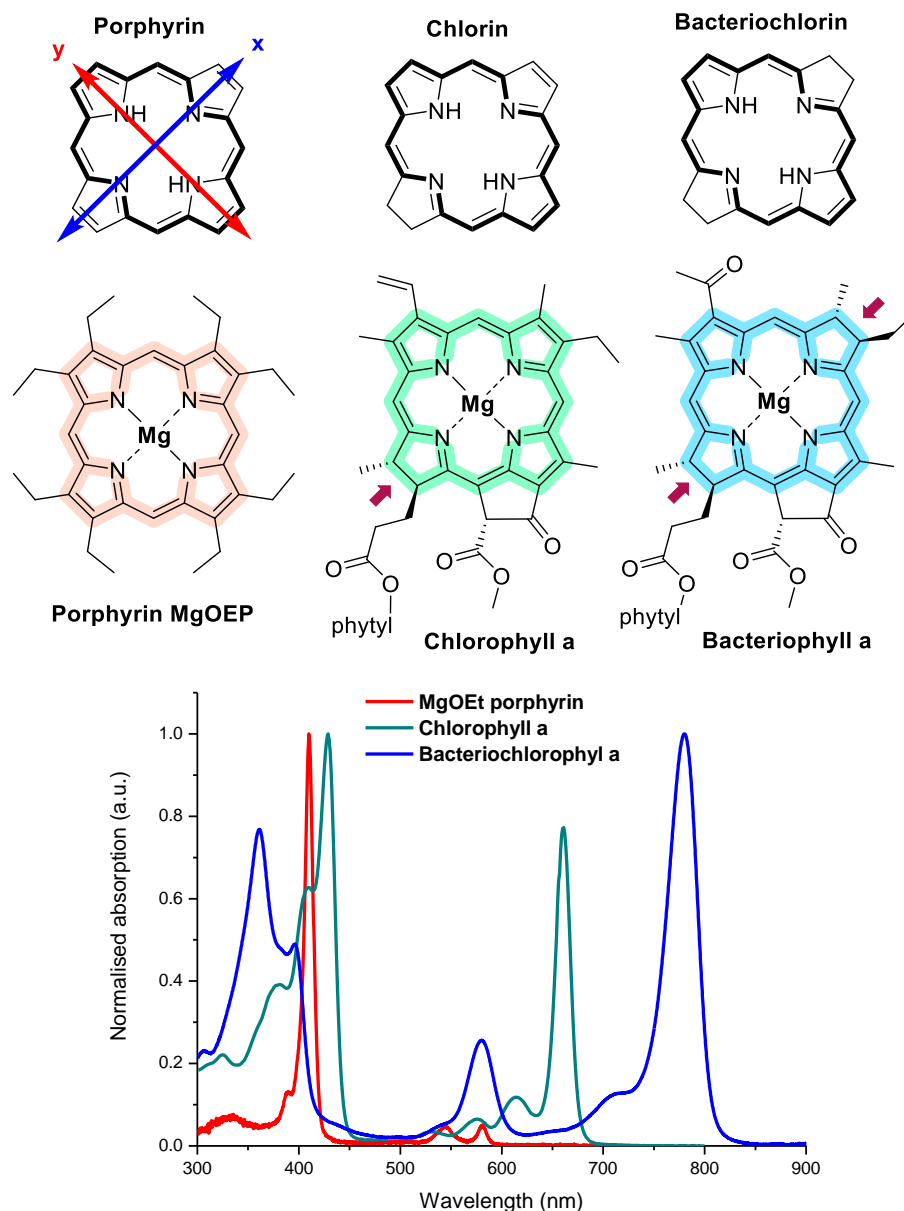


Figure 1.18. Chemical structures of porphyrinoids along with their electronic absorption spectra; data obtained from PhotochemCAD database.^[237,238]

To achieve a high triplet state energy efficient ISC from the singlet excited state to the triplet excited state ($S_1 \rightarrow T_1$) must occur. ISC depends on the energy of the triplet state and the presence of heavy atom (structurally). Heavy atoms such as transition metals or halogens enhance ISC *via* spin-orbit coupling (SOC)^[227,239,240] and when introduced to a porphyrin type molecule they increase the triplet state quantum yield. Increase of ISC lowers the fluorescence lifetime and yield. A consequence of the introduction of heavy atoms is often an increase in the dark toxicity of the PS;^[227] hence, new methods to increase the ISC pathway with heavy atom free molecules are under development. Equation 1.1

displays the relationship between the singlet-triplet energy gap ($\Delta E_{S_1-T_1}$) and the ISC rate constant (k_{isc}), indicating that ISC occurs with a small energy gap (H_{SO} : the Hamiltonian for the spin-orbit coupling):^[227]

$$k_{isc} \propto \frac{\langle T_1 | H_{SO} | S_1 \rangle^2}{(\Delta E_{S_1-T_1})^2} \quad \text{Eq. 1.1}$$

Moreover, the triplet excited state lifetime should be sufficiently long-lived, and the triplet energy state should be higher than that of singlet oxygen, so it can efficiently produce moderate singlet oxygen yields through energy transfer (Type II). Except for high triplet state yields, a sufficient triplet energy level is needed to activate molecular oxygen in its triplet state condition to form the excited configuration – singlet oxygen (94 kJ mol⁻¹, 0.97 eV).

As previously mentioned, another excited state that may occur is the formation of the charge transfer states which is directly dependent to the solvent polarity and consequently form triplets. The solvent dependency of PSs post excitation can lead to charge-separated states (CSS) and triplet formation by charge transfer (CT) or charge recombination (CR), thus establishing alternative ways to access the desired triplet state (see section 1.5).^[187] BODIPY dimers or dyads [e.g., BODIPY-fullerene C₆₀ or BODIPY-anthracene dyads (BADs)], display CSS and donor-acceptor properties, which opens doors for medical and optoelectronic applications.^[44,241,241–243]

The identity of the metal in the core of the macrocycle can influence the relative HOMO-LUMO energies and the triplet quantum yields. On one hand paramagnetic metals appear to shorten triplet lifetimes, while on the other hand diamagnetic metals appear to promote ISC with longer triplet lifetimes; however, this is not a fixed rule.^[242] Generally, zinc chelates show low fluorescence quantum yields and higher ISC yields, whereas magnesium results in higher fluorescence yield and longer singlet lifetime. Palladium complexes display marginal fluorescence and high triplet state yields. Furthermore, in porphyrinoids, axial metal coordination is possible for some metal ions which can further introduce new substituents and therefore new photophysical features. Dąbrowski *et al.* described the resulting modifications of metallo-tetrapyrrolic PSs.^[244]

The free base porphyrins show the intense Soret band and four Q bands in the visible region stemming from vibrational coupling effects [HOMO–LUMO, (HOMO–1)–(LUMO+1) transitions]. Metal insertion alters the symmetry of the molecule (from D_{2h} to D_{4h}) significantly and this leads to a reduction of the Q bands from four to two. In addition, the absorption wavelength maxima differ, with the free base absorbing in longer wavelengths. On the other hand, metal insertion into chlorins and bacteriochlorins does not alter the symmetry as it is already changed by the pyrrole reduction, but can still effect the position and the shape of the absorption spectra.^[234,235,245]

PSs can undergo several cycles of photoactivation and absorption of photons of energy until they lose the ability to induce further photooxidation reactions. This effect is called photobleaching and is the irreversible photo destruction of the PS linked with its photostability.^[246] The final photodynamic effect depends on the nature of the generated reactive oxygen species. For instance, palladium porphyrin derivatives result in ROS production and a faster photobleaching is observed. This happens due to the hydroxyl radicals that are formed upon irradiation and thus the PS is more susceptible to photodegradation and less photostable. On the other hand, in zinc porphyrins singlet oxygen production is more favourable after excitation and therefore they are more photostable.^[244]

Dimeric aggregates or higher order aggregates can form in porphyrin solutions as a result of their hydrophobic skeleton, resulting in “sandwich” (H-aggregates) or linear (J-aggregates) self-assemblies. This should be minimised as it can significantly reduce the absorption intensity, mislead clinical results, and negatively affect the efficiency of the PS. Depending on the solvent, especially in aqueous media, the ISC capability of molecules can be reduced and energy can be dissipated through radiative (fluorescence) or non-radiative decay (IC). However, H-aggregates aid the photostability of the micellar assemblies of Photosan.^[247–249] The absorption profile of the aggregated PS usually differs from the monomeric form. To address this issue, amphiphilic PSs can be employed to lower aggregation and this is an active research area. Another solution lies on nanotechnology-based drug delivery systems such as liposomes or protein binding systems, which can assist with de-aggregation and lead to a red-shift in the absorption spectrum whilst increasing the triplet state lifetime.^[250]

1.6.2 Photooxidation processes with molecular oxygen

Singlet oxygen is the major cytotoxic agent that allows for the PDT therapeutic effect. Molecular oxygen or dioxygen is in the ground state and it has two unpaired electrons with parallel spins in two degenerate antibonding orbitals, which gives a spin multiplicity of three (Figure 1.19). Thus, without activation, molecular oxygen is in the triplet state. It very seldom reacts with other molecules in the singlet state; however, it can react with radicals.^[251–253] Triplet excited configurations of a PSs induce chemical reactions, including Type I and II reactions, with neighbouring molecular oxygen O_2 ($^3\Sigma_g^-$) (Figure 1.2).

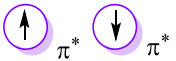
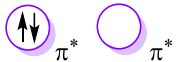
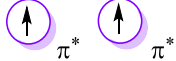
States of oxygen	Occupancy of highest orbital	Energy above the ground state
Second excited state	$^1\Sigma_g^+$ 	157 kJ mol ⁻¹
First excited state	$^1\Delta_g$ 	94 kJ mol ⁻¹
Ground state	$^3\Sigma_g^-$ 	

Figure 1.19. Electronic configurations of the different states of molecular oxygen.

Type I involves electron or proton transfer to yield radical cations or anions (reactive oxygen species, ROS). The latter can react with oxygen to form superoxide anions ($O_2^{\cdot-}$), which are not very reactive but can undergo dismutation or electron reduction to form hydrogen peroxide (H_2O_2), which is cytotoxic. Hydrogen peroxide can further react with superoxide anions to produce hydroxyl radicals (OH^{\cdot}), which can oxidise cellular components. Furthermore, iron or copper from the micro-environment promote hydroxyl radical formation. Both hydrogen peroxide and hydroxyl radicals have high diffusion properties and can pass through biological membranes causing cellular damage to several cellular compartments (plasma, mitochondria, lysosomes, proteins, nuclear, and cell membranes). **Type II** involves energy transfer from the triplet PS directly to oxygen resulting in singlet oxygen 1O_2 ($^1\Delta_g$). Singlet oxygen is an uncharged molecule and can diffuse through the cytoplasm and biological membranes.^[23,217,231,240,241] Singlet oxygen in its singlet excited state is characterised by paired electrons (with opposite spins) in the outer orbital.

Although it is common to refer to the first excited state as singlet oxygen, there are two excited electronic states of oxygen and the second excited state ($^1\Sigma_g^+$) ($157.0 \text{ kJ mol}^{-1}$, 1.63 eV) decays efficiently to the first excited state (94.3 kJ mol^{-1} , 0.98 eV).^[254] There is no evidence that the latter is an intermediate in solution-phase photo-oxygenations.^[255,256] Type II reactions dominate the action of porphyrin PSs while Type I reactions are dominant for other PS structures.^[23,231] Hamblin and Abrahamse outlined a non-oxygen photoinactivation pathway for aPDT (Type III reaction process), which opened a new PDT perspective.^[257]

Singlet oxygen generation is dependent on various parameters: the triplet state yield of the PS, the triplet excited state lifetime, the sensitisation efficiency of the PS, oxygen concentration, photosensitiser photostability under those conditions, and the reactivity of singlet oxygen in a particular environment. First, singlet oxygen production is a second-order effect that depends on the triplet PS concentration and the triplet lifetime. Second, the concentration of ground state oxygen (triplet state configuration) also plays a role in singlet oxygen generation. The fact that the quantum yield of singlet oxygen upon purging with oxygen gas is higher than it is under ambient conditions indicates that the emission of singlet oxygen is due to a second-order process. As such, the oxygen quenching constant is a universal expression for the potential of singlet oxygen generation.^[258,259]

The quantum yield of singlet oxygen emission is defined as the number of photons emitted by singlet oxygen divided by the number of photons absorbed by the photosensitiser. The detection of singlet oxygen and the determination of its quantum yield are challenging. The majority of methods rely on relative indirect chemical methods such as using singlet oxygen scavengers and probes with high selectivity for singlet oxygen. The use of 9,10-diphenylanthracene (DPA) or 1,3-diphenylisobenzofuran (DPBF) where a stable endoperoxide is formed is most frequent and the singlet oxygen quantum yield can be calculated from the absorption decay of the probe. Alternatively, fluorescent probes such as 9-[2-(3-carboxy-9,10-dimethyl)anthryl]-6-hydroxy-3*H*-xanthen-3-one (DMAX), DPBF or Singlet Oxygen Sensor Green (SOSG) are non-fluorescent but their endoperoxides fluoresce, allowing for singlet oxygen detection and yield calculation.^[260] The same techniques can be applied to ROS detection but

quantification is limited by the specificity of the reaction towards singlet oxygen.^[261] Fluorescence microscopy is also used for the spatial detection of singlet oxygen and thus helps to reveal the intracellular localisation pattern. Electron paramagnetic resonance (EPR) detects unpaired electrons in molecules and thus it consists of an indirect method to detect singlet oxygen in combination with spin traps (e.g., 2,2,6,6-tetramethylpyridine (TEMP), 4-hydroxy-TEMP) to form spin-active stable radicals; however, short lifetimes and side products from microenvironment interactions can influence the results and lead to significant errors.^[262]

Direct determination of singlet oxygen *via* its phosphorescence emission at ~1275 nm can be challenging because the emission is usually weak. Therefore, highly sensitive NIR detectors are required, such as cryogenic germanium diodes, semiconductor detectors, and photomultipliers.^[259] Appropriate reference materials for calibrating the NIR detector are needed. For instance, a Nd:YAG laser rod is suitable for solid state lasers. Time-resolved spectroscopy is used to determine the lifetime and provide insight into the kinetics and the decay profiles.^[263] The singlet oxygen lifetime is sensitive towards its environment and it has been calculated in solvents on the μs scale from time-resolved phosphorescence experiments by Ogilby and co-workers.^[264] However, singlet oxygen has a shorter lifetime in biological media and can only react with biomolecules in its proximity, which limits the possible applications.^[23,265] Singlet oxygen's intracellular lifetime is $\sim 3 \mu\text{s}$ (τ_{Δ}) and is longer than what was reported initially ($0.04 \mu\text{s}$).^[265-267] This new estimate also changed the singlet oxygen diffusion distance, which is calculated from equation 1.2, defining its sphere of activity approximately at $\sim 100 \text{ nm}$ (previously reported: 20 nm).^[268]

$$d = \sqrt{6tD} \quad \text{Eq. 1.2}$$

where d is the diffusion distance that singlet oxygen would move in a period time t (i.e., a period equal to its intracellular lifetime) and D is the diffusion coefficient (a value of $\sim 2 - 4 \times 10^{-6} \text{ cm}^2 \text{ s}^{-1}$ for intracellular D).

Elucidating the fundamentals of the mechanism of action and kinetics of singlet oxygen can help the design of PS by regulating the long-lived triplet states of the PS, leading to high concentrations of singlet oxygen in biological media and

resulting in cell death.^[20,269,270] Singlet oxygen has a longer lifetime in deuterated water ($D_2O \sim 67 \mu s$) than in water ($H_2O \sim 3.5 \mu s$). Surprisingly, replacing H_2O with D_2O has no major effect on cells with the exception of neuron cases where membrane ion channels respond to this difference.^[259,263] Nierde *et al.* used a NIR photomultiplier to first report the lifetime of singlet oxygen *in vitro* and *in vivo* in the skin and liver of rats during PDT.^[267] High-level computational methods are now shedding light on the electronic states of oxygen, its properties in solution and biological media, and its cellular mechanisms.^[271]

1.6.3 Light sources

A suitable combination of PS, light source, and treatment parameters is critical for successful PDT and is directly connected to the size of the treatment area. Brancalion and Moseley reported the available laser and non-laser options for PDT.^[272] The optimal light source should match the absorption maxima of the PS and the delivery of an appropriate light dose (L.D.) is important for generating a therapeutic response in the target tissue. There are several types of light sources that are effectively used: arc and xenon lamps, light-emitting diodes (LEDs), laser beams, and increasingly daylight sun. Low-cost conventional lamps have a broad spectral output, which can be limited with filters to match the PS and therefore, they have found application in dermatology for the treatment for larger skin lesions. Advancements in light sources led to the development and use of high energy monochromatic laser beams, which are highly efficient and provide precise light delivery to the target, particularly in cases of non-superficial tumours where a combination of laser and fibres is beneficial, *e.g.*, endoscopic or interstitial light delivery.^[273,274] The development of optical fibres has enabled the precise delivery of light through a specially designed illuminator tip such as microlens, cylindrical, or spherical diffusers where light can pass through and reach the target.^[275] Lasers used for PDT are: i) argon dye lasers (primary choice for PDT); ii) metal-vapor lasers (Cu- and Au- vapor lasers); iii) solid-state lasers (Nd:YAG, Ho:YAG, KTP:YAG/dye laser), and iv) semiconductor diode lasers.^[276] Diode lasers are employed in PDT especially because they are small and cost-effective, easy to install and operate, and can be operated with either a pumped or continuous wave beam light (picosecond to millisecond).^[272] The main limitation of a diode laser is that it operates at a single-wavelength and a separate

unit is required for each photosensitiser. A breakthrough will open the road to new multi-wavelength laser diode systems where the wavelength can be adjusted. Light-emitting diodes (LEDs) are an alternative low-cost and highly efficiency technology used to irradiate tissue surfaces. Their versatility enables a flexible arrangement (different irradiation geometries) and the potential to cover and irradiate larger areas for treatment.^[274] Femtosecond lasers are presently used for two-photon excitation in several advanced research areas such as microscopy and spectroscopy. Due to the suitability of the fs-pulsed lasers for two-photon absorption, they have been proposed for two-photon PDT as discussed extensively in reviews by Kobuke *et al.* and Sun *et al.*^[277,278]

Kercher *et al.* developed a cost-effective LED technology capable of switching between wavelengths to facilitate the next generation of PDT systems. Using two well-known PSs, aminolevulinic acid (ALA) and verteporfin, 90% cell death was observed in a primary ovarian cancer cell line after treatment with L.D. of 50 J cm⁻².^[279] Another tunable light source of interest is the organic light-emitting diodes (OLEDs). Attili *et al.* reported an open pilot study of ambulatory ALA-PDT and suggested that the use of a low-irradiance device can be painless, effective, and convenient. The use of a wearable low-irradiance OLED light source after ALA application exhibited positive outcomes for patients with non-melanoma skin cancer (Bowen's disease and superficial basal cell carcinoma).^[280] These discoveries enable OLEDs to be the ideal candidate for ambulatory PDT light sources. Clinically applied PDT treatment regimens use various light dose approaches. ALA, in the case of the treatment of actinic keratosis, is topically administered and activated by a blue fluorescent lamp with a L.D. of 10 J cm⁻² (BLU-U Blue Light Photodynamic Therapy Illuminator) at 417 ± 5 nm. Visudyne, which is used for the treatment of age-related macular degeneration (AMD), is activated by a laser (689 ± 3 nm with a light dose of 50 J cm⁻²).^[279] Tookad Soluble (WST11), a recently approved drug, is used as an alternative treatment for prostate cancer, delivers light to the target tumour through fibre optic tubes; although invasive, this approach benefits from deeper tissue penetration. The Tookad regime is a focal vascular targeted PDT (VTP) that focuses particularly on the prostate and delivers a laser light energy of 200 J cm⁻² at 753 nm.^[281,282]

1.7 Photopharmacological Aspects of PDT

“What is there that is not poison? All things are poison and nothing is without poison. Solely the dose determines that a thing is not a poison”

Paracelsus defined the concept of the balance between the benefits (therapeutic effects) and the risks (adverse effects) of a drug in correlation to the dosage.^[283] Generally, a combination of several factors influences the photodynamic effect of a potential PS. Not only should it generate singlet oxygen but it should also localise effectively in the cellular compartments with minimal dark toxicity in order to induce significant phototoxicity.

Depending on the mechanism of action, a potential light-activated drug candidate, after its photo-activation, can cause cell death through different mechanisms. It can be a non-specific damage to the cells by producing ROS which is the basis of PDT; or by a selective binding of the drug to a molecular target that is connected to a specific disease. This can lead to a photopharmacological effect *via* a light-induced isomerisation of the agent that goes from an inactive to an active state (a photo-switchable unit into the molecular structure of the bioactive compound itself) resulting in a precisely targeted biological effect.^[284] Focusing on PDT treatment, the efficacy depends on the PS dose, the time of exposure, and intensity of the light, considering that the overall protocol is not life-threatening and does not result in serious complications. Important factors influencing the properties of the PS and light activation aspects were discussed above. However, how a drug affects the body and *vice versa* determines the pharmacological response. The pharmacodynamics (PD) and pharmacokinetics (PK) explain the relationship between drug dose and response. Usually, the administration route of PDT is intravenous, which circumvents the first-pass effect and metabolism, allowing direct absorption from systemic circulation and a higher drug availability with a minimum delay. Although in the case of a pro-drug formulation, such as ALA-mediated PDT, metabolic activation is required to form the photosensitising protoporphyrin IX.

Since 1924 and the first report of porphyrin localisation, it has been established that porphyrins display a greater affinity for cancer cells and malignant tissues compared to normal ones.^[1] The higher accumulation of PSs in malignant tissues/cells can be influenced by several factors: enhanced vascular permeability in tumour vessels; lymph drainage, which decreases excretion; protein binding; the upregulation of LDL-receptors, which increases the mediated endocytosis; the acidic pH of the tumour (average pH: 6.5), which can increase the distribution of the weak acid PS; the large number of macrophages which can excessively accumulate porphyrin-type molecules; and larger interstitial space.^[285–288]

Protein binding followed by distribution to the targeted tissue (*via* diffusion or receptor-mediated endocytosis) and consequent cellular localisation is directly dependent on the hydrophilicity, molecular weight, and charge of the PS.^[20] Hydrophobic and small drugs passively diffuse through the cell membranes equilibrating between the inside and outside of the cell. The blood flow strongly determines the rate of absorption as it constantly maintains the concentration gradient, which is necessary for passive diffusion. The affinity of the PS to bind proteins in plasma can significantly influence its half-life, define the time interval of the treatment, and affect photosensitivity. Larger particles with incorporated PSs can be absorbed by phagocytosis or micropinocytosis.^[289] Carrier-mediated diffusion occurs for less hydrophobic molecules and for those that resemble endogenous compounds for which specific membrane receptors and carrier systems already exist. It is worth noting that heme biosynthesis takes place partly in mitochondria and cytosol, starting from mitochondria where 5-aminolevulinic acid (ALA) is formed, then in the cytosol where several enzymatic reactions form coproporphyrinogen III, which transports the compound to the mitochondria to form heme.^[290] Porphyrins, including Photofrin, display an affinity for binding to mitochondrial benzodiazepine receptors, which can explain, to some extent, the internalisation and accumulation in this vital organelle.^[291–293] The mechanism of action is also dependent on the cell genotype, the adenosine triphosphate levels (ATP), and the PS localisation.^[294,295] There are three mechanisms of tumour destruction: direct cytotoxic effect against malignant cells; indirect vascular damage of the tumour, and macrophage-mediated immune system activation.

The latter is a result of a pharmacological response and is described in the referenced reviews.^[33,296] Figure 1.20 summarises the signal pathways activated after PDT. Events occur at receptors located at the plasma membrane and lead to changes in cellular metabolism. These may tend towards increasing apoptosis or increasing cell survival.

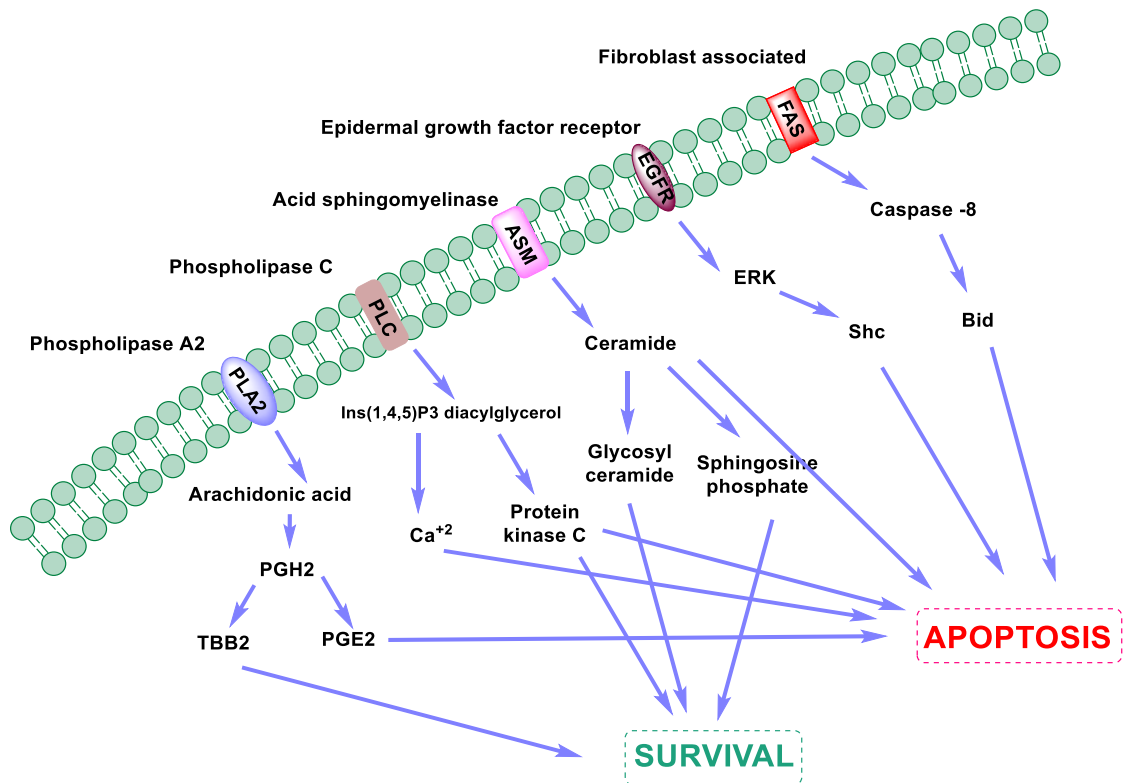


Figure 1.20. Signal transduction pathways activated after PDT.^[21]

In the bloodstream, a hydrophobic PS (e.g., unsubstituted phthalocyanines, tin-etiopurpurin) usually binds to low-density lipoproteins (LDL, HDL, and VLDL). Amphiphilic PSs (e.g., disulfonated derivatives of tetraphenylporphyrin, lutetium texaphyrin, and benzoporphyrin derivate monoacid) bind with both HDL and albumin; whereas the more hydrophilic [e.g., tri- and tetrasulfonated tetraphenylporphyrins, chloro(phthalocyaninato)aluminium(III)] bind to serum proteins such as albumin. Following this, the PS should bind and penetrate through the vessel walls and thus diffuse throughout the target. The hydrophobic PS usually diffuses faster into the diseased cells and preferentially localises in intracellular compartments such as mitochondria and nuclear membranes. The hydrophilic PS is absorbed by pinocytosis or endocytosis and localises mostly in lysosomes. Upon photoactivation, a chain of photoreactions together with

enzymatic reactions and alterations are triggered and result in cancer treatment through necrosis, apoptosis, or autophagy.^[297–299] Firstly, necrosis is unprogrammed cell death that involves degradation, cytoplasm swelling, and cell membrane disruption and leads to inflammation. Secondly, apoptosis is a programmed cell death that involves cell shrinkage. The intracellular organelles are being removed by phagocytes through membrane-enclosed spherical vesicles. Apoptosis usually does not involve inflammation. Finally, autophagy is a process that involves the transportation of cellular organelles through lysosomal degradation pathways; usually it does not involve inflammation. Cellular targets of PSs include the plasma membrane, mitochondria, lysosomes, the Golgi apparatus, the endoplasmic reticulum (ER), and components of the cytosol. Vascular targets include the vascular wall of normal and tumour vessels, which can destruct blood supply to the tumour by depriving the tissue of oxygen and nutrients causing starvation of the diseased tissue.^[250,300] A review by Almeida *et al.* regarding intracellular signalling mechanisms thoroughly describes the molecular pathways of PDT and the role of each enzyme, factor, and receptor. Briefly, there are two apoptotic pathways both leading to pro-caspase -3, -6, and -7 activation that play a pivotal role in apoptosis.^[21,23,24,295,301] The first is the extrinsic pathway which is death receptor-mediated through activation of the cell surface death receptors (Fas, TNF-RI, TRAIL), leading to the formation of death-inducing signal complexes (DISCs) and activating pro-caspase-8 and pro-caspase-10. The second is the intrinsic pathway which is mitochondria-mediated through disruption of the mitochondrial function, resulting in the cytochrome c release to cytosol, which in the presence of ATP or dATP activates pro-caspase-9 and -3 (Figure 1.21).

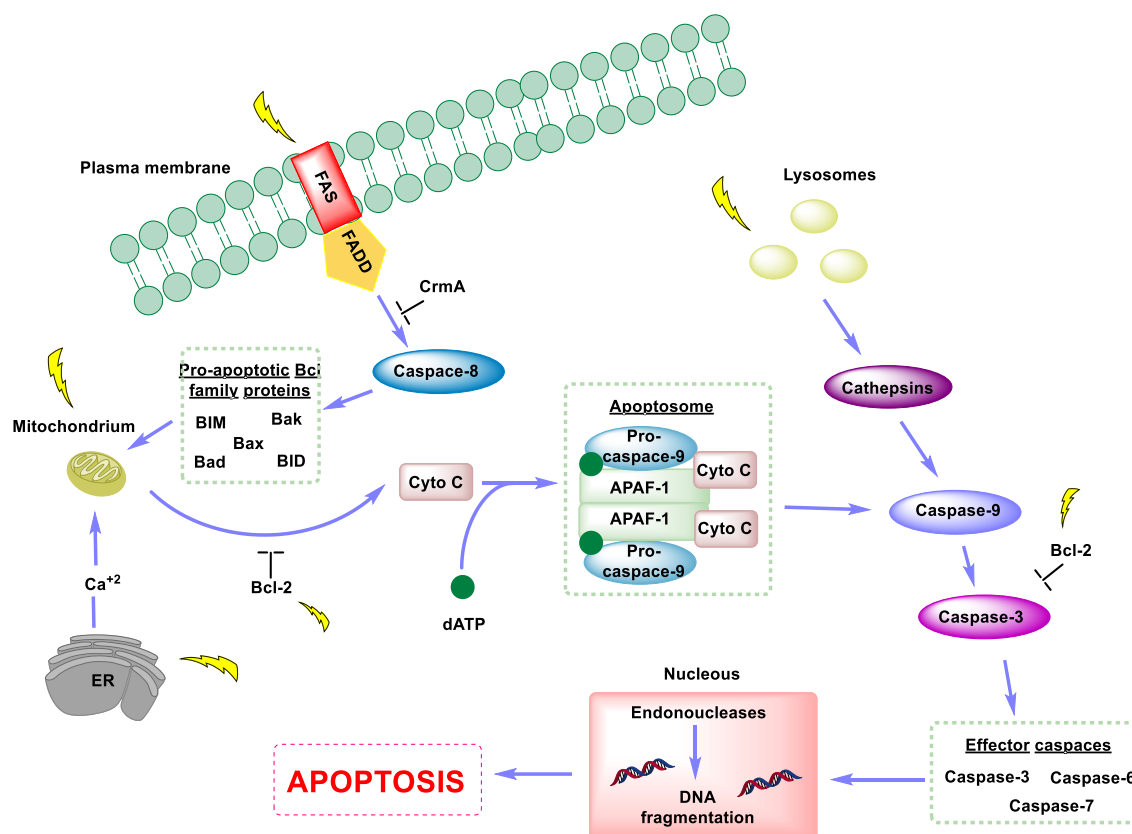


Figure 1.21. Signalling pathways in cells post PDT resulting in apoptosis. The targets of PDT depend on PS localisation in mitochondria, lysosomes, endoplasmic reticulum (ER), plasma membrane, and PS binding to Bcl-2.^[21]

Hydrophilic sulfonated aluminium phthalocyanines (AlPcS_n) with three or four sulfonated groups tend to localise in lysosomes while more hydrophobic PSs with one or two sulfonated groups target the mitochondria or membranes.^[302] However, hydrophobic molecules and molecules that localise predominantly in the mitochondria are more effective PSs, probably because they initiate cell death *via* the apoptotic pathway as compared to those that localise in lysosomes, although this is not a hard-and-fast rule.^[303,304] Lysosomal photodamage resulting in mitochondrial-mediated apoptosis has been reported by Kessel and co-workers. Murine hepatoma cells (1c1c7) were treated with N-aspartyl-chlorin e6 (NPe6) and upon irradiation, the mitochondrial pathway was triggered by cytochrome c, Bid, and caspase -3 and -9 activation.^[305] Lutetium texaphyrin (Lu-Tex) was found to localise in lysosomes in murine mammary sarcoma cells (EMT6). Post irradiation there was a loss of lysosomal fluorescence resulting in cell death, which was found to follow the apoptotic pathway by DNA ladder fragmentation analysis.^[306]

Finally, the PS will be eliminated from the tissue by lymphatic or blood vessels and excreted through the liver or kidney to the bile. From there, it can either circulate for a second time or be eliminated permanently through intestines *via* faecal or urine elimination.^[307] For example, the pharmacokinetic profile of Tookad soluble (see section 1.4.1) indicates fast body clearance rates (alpha and beta half-lives: 2 min and 1.3 h, respectively) and less post-treatment photosensitivity; whereas Photofrin stays in the body longer (alpha, beta and gamma half-lives: 16 h, 7.5 days and 155.5 days respectively) and patients have persistent photosensitivity, in some cases, for more than a month.^[308–310]

Another fact that should be considered is that light irradiation can induce drug relocalisation. Sulfonated meso-tetraphenylporphyrins relocalise from lysosomes to cytoplasmic and nucleus areas.^[311] Kessel *et al.* reported that monocationic porphyrins relocalise from the plasma membrane to cytosol, which then leads to procaspase-3 and -9 photodamage.^[312]

1.8 Strategies for Improvement of PS

There are several ways to control the selectivity of cancerous cells and modulate singlet oxygen production. Below, some of the strategies under investigation to achieve advanced PSs are briefly discussed. Third generation PSs aim to advance the photophysical properties and improve the drug delivery properties. Expanding the π -conjugation to refine the absorption profile, introducing functional groups to enhance singlet oxygen generation, utilising antibody bioconjugation or encapsulation of PSs in nanoparticles to control cancer targeting methods and drug delivery are some of the ways to manage the therapeutic outcome.

1.8.1 Modulation of the photophysical properties

As mentioned, triplet state formation (through ISC or ICT) and singlet oxygen generation directly influence the overall PDT effect. Slight changes in the molecular structure of a compound may modulate its photosensitising properties. The photophysical properties of a PS are influenced by the presence and nature of a metal atom in the core or at the periphery. Enhancing the triplet state quantum yield and consequently the singlet oxygen quantum yield can primarily

occur by heavy atom insertion (e.g., Br, I), the so called “heavy atom effect”, particularly when it is attached directly to either porphyrinoids or dipyrinato systems.^[239,313] In addition, a variety of second-generation PSs contain a central metal atom (e.g., Zn, SnEt₂, and AlPcSn); however, this does not directly define the photoactivity of a PS.^[314] The development of PSs with an absorption profile in the red-visible or near infrared (NIR) region along with an enhanced molar absorption coefficient specifically at the Q bands (500–750 nm) in porphyrin based molecules is a challenge. The position of the Soret band can be influenced by the structural variation of the macrocycle. The position and the relative intensities of the Q bands can vary according to the nature and the position of the substituents. Expanding the π -conjugation of the macrocycle can result in a bathochromic shift due to the delocalisation of the frontier MO, as discussed earlier. This can be achieved by modulating the periphery with either β - or meso-substituents, which can promote a bathochromic shift and at the same time endorse a hyperchromic effect on the peak intensity (molar absorption coefficient).^[232,236,315] Additionally, an increased absorption coefficient in the NIR wavelength region can be obtained by reducing one or two of the double bonds in the conjugated ring structure (i.e., ϵ bacteriochlorins > ϵ chlorins > ϵ porphyrins). Another way to alter the intensity of the visible bands is the replacement of methine bridge with aza-nitrogen atom, as such in phthalocyanines. Also, substitution with electron-rich donor groups, in particular amino groups, induces a bathochromic shift in the absorption spectra, and therefore, can enhance the penetration of light in human tissue. Similar strategies apply in BODIPY dyes.^[232,316] Considering other metal complexes, a way to enhance their photophysical properties is the introduction of a variety of substituents, preferably π -conjugated ones, attached to the respective ligands. For instance, heteroleptic bis(dipyrinato)zinc(II) complexes and their homoleptic counterparts displayed distinctive photophysical properties, such as photoillumination in the red region (~671 nm), with higher fluorescence efficiencies for the heteroleptic complexes compared to their homoleptic analogues. However, the non-emissive SBCT state in polar solvents reduced the fluorescence emissive properties of the zinc complexes.^[160,317] These strategies can be considered as useful tools for altering the electronic configuration of

potential PSs; however, sometimes they are accompanied by decreased singlet oxygen quantum yields.

1.8.2 Photosensitiser uptake and cellular localisation

Among the PSs there is a preferable selectivity towards the tumorous sites, as previously discussed, which can be modulated with targeting approaches.^[16,318] The hydrophobic character of the PSs usually increases the cellular uptake; however, it also causes poor solubility and hydrophobic molecules have a tendency to form aggregates in biological aqueous media, therefore, preventing their biological application. Additionally, such molecules have shorter triplet lifetimes and singlet oxygen quantum yields. On the other hand, hydrophilic PSs are unable to cross amphiphilic cellular membranes, resulting in poor cellular uptake. Hence, there should be a balance between the hydrophilicity and hydrophobicity of the PS to achieve the desired localisation.^[72,314,319] Another approach that has been described is the insertion of metal complexes as macrocycle substituents. Poon *et al.* reported that the use of a polypyridyl Ru(II) complex, as substituent attached to the hydroxylphenyl group (meso-position) of the porphyrin macrocycle, improved the photodynamic efficiency of the conjugate. The amphiphilic system with a Ru(II) complex as the hydrophilic head and a porphyrin unit as the hydrophobic tail, resulted in the enhancement of the system's two-photon absorption, high singlet oxygen quantum yield, rapid cellular uptake, and high phototoxicity.^[320] The water-solubility can be enhanced by functionalisation of the porphyrin ring with cationic or anionic substituents *i.e.*, amine, pyridyl, pyridinium, imidazolyl, carboxylate sulfonyl and phosphate groups.^[321] Third-generation PSs are envisaged to surmount this limitation by designing amphiphilic PSs through the introduction of hydrophilic groups like peptides, PEGs, and carbohydrates at their peripheral or axial positions.^[322,323] Also, the introduction of bioconjugates that are either covalently bound to the PS or incorporated into a drug delivery system (DDS) aims to improve the tumour specificity of the PS.

1.8.3 Targeted PDT and nano-approaches

Targeted PDT is a far-reaching field and there are extensive article reviews where this is widely discussed. In 1891, Ehrlich, the pioneer of chemotherapy, coined the term “magic bullet”, which represents the first description of the drug targeting concept.^[324,325] Nanomedicine refers to the use of so-called nanoparticles (NPs) designed for specific drug delivery with an accurate concentration over a specific period of time. Nanoparticles are stable, solid colloidal particles consisting of biodegradable polymer or lipid materials and range in size from 10 to 1,000 nm. It should be noted that the EMA has a limit of 100 nm for nanoparticle containing drug systems.^[326,327] NPs can improve water-solubility and the biocompatibility of a drug, can mitigate the degradation of a drug after administration, and can potentially decrease side effects. The clinical use of targeted PDT is still limited. The best example of targeted PDT involving porphyrins is Visudyne, which is a liposomal formulation of verteporfin approved for treatment of AMD and polypoidal choroidal vasculopathy.^[55] In addition to liposomes, DDS utilise various NPs, including polymeric nanoparticles, niosomes, solid lipid nanoparticles, nanoemulsions, nanocrystals, cubosomes, hexosomes, dendrimers, micelles, microcapsules, quantum dots, silica and gold NPs, superparamagnetic iron oxide nanoparticles, carbon nano-platforms, and different nanoassemblies.^[328–330] Lastly, other approaches include the use of ligands/conjugates such as vitamins, folates, glycoproteins, peptides, oligonucleotide aptamers, growth factors, lipoproteins, and other useful tools to target nanoparticles to cancer cells.^[326,331–333]

Additionally, to enhance the selectivity and specificity of a PSs towards tumour tissue, it is possible to utilise active targeting where PS conjugates are fashioned with receptor targeting moieties.^[334] Some examples include monoclonal antibodies such as herceptin (antibody to the HER2 receptor), folate-modified nanocarriers, antibodies against transferrin receptors (TfR), which are over-expressed on the surface of many solid tumours, as well as Tf itself.^[335,336]

An interesting study by Sitti and co-workers involved the use of microrobots, the “micro-rollers”, which consist of gold and nickel layers that allow for the control of blood flow circulation by applying a weak magnetic field. After reaching the

tumour target, they bind to cancer cell proteins (anti-HER2) *via* the antibody. Following UV irradiation, they release the anticancer drug (doxorubicin). This opens new approaches to drug delivery that can be applied in PDT.^[337,338] One of the most important advances in nanomedicine is the improvement of targeted DDS that can maximise the therapeutic efficacy.

Chapter 2: *gem*-Dimethyl Chlorins as Potential Photosensitisers in PDT

“However bad life may seem, there is always something you can do and succeed at. Where there's life, there's hope”

~ Stephen Hawking ~

2.1 Introduction

Chlorins are frequently encountered in nature as chlorophylls (derived from the Greek word: *χλωροφύλλη* = green natural pigment); which exist in all photosynthetic organisms, including plants, bacteria, and algae. Functionally, chlorophyll serves as photoreceptor molecule, absorbing light energy to perform the biological processes of photosynthesis. Besides their natural function in photosynthesis, chlorins are used as diagnostic or therapeutic agents and also have found application in the food industry, in materials chemistry, and in photovoltaic solar energy applications.^[339–341] Considering that the penetration of light into tissue proportionally increases with wavelength, candidates with strong absorptivity in the red region (600 – 850 nm) such as chlorins or bacteriochlorins are more likely to become appropriate photosensitisers (PSs), with the former being chemically more stable. As mentioned in Chapter 1, chlorins are popular for their photodynamic activity and they hold a keystone position in PDT (see 1.4) since they tend to access high triplet state yields and lifetimes and generate singlet oxygen. Additionally, they can maintain moderately high fluorescence quantum yields and lifetimes and find use in bioimaging.^[342]

This chapter focuses particularly on the so-called *geminal* (*gem*) dialkyl chlorins and specifically the *gem*-dimethyl type. Two naturally occurring chlorins (Figure 2.1), which both bear a *gem*-dialkyl group, Faktor I (derived from vitamin B12 biosynthetic pathway), and Bonellin (green pigment of marine worm, *Bonellia viridis*), intrigued the development of new synthetic routes towards such systems.^[343–345]

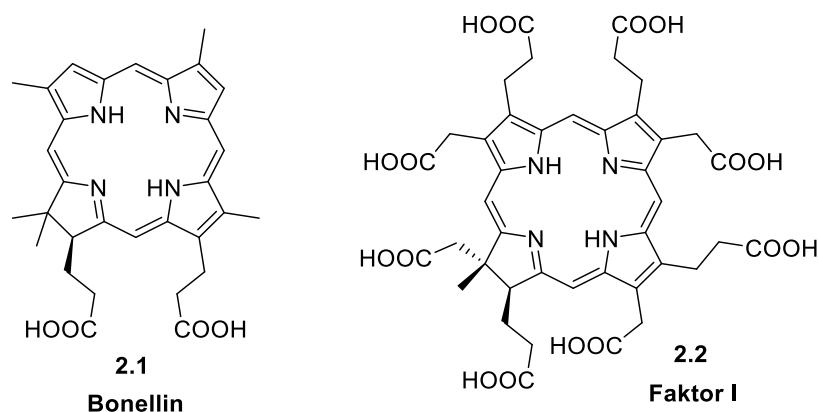
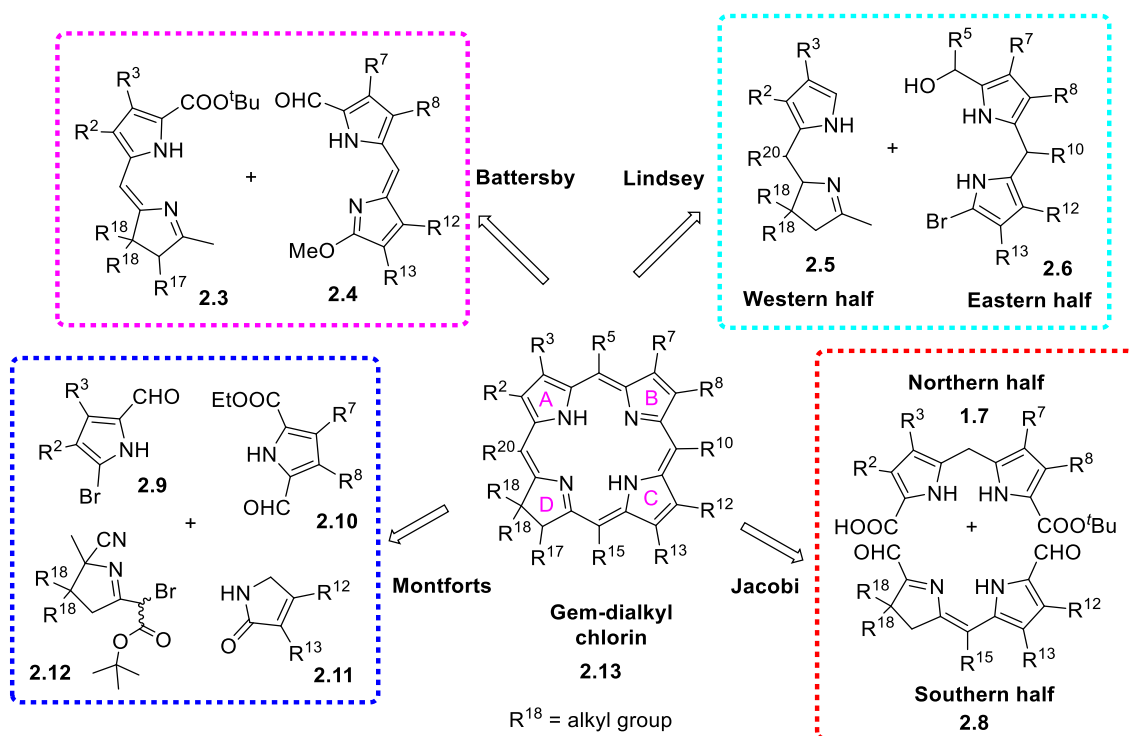


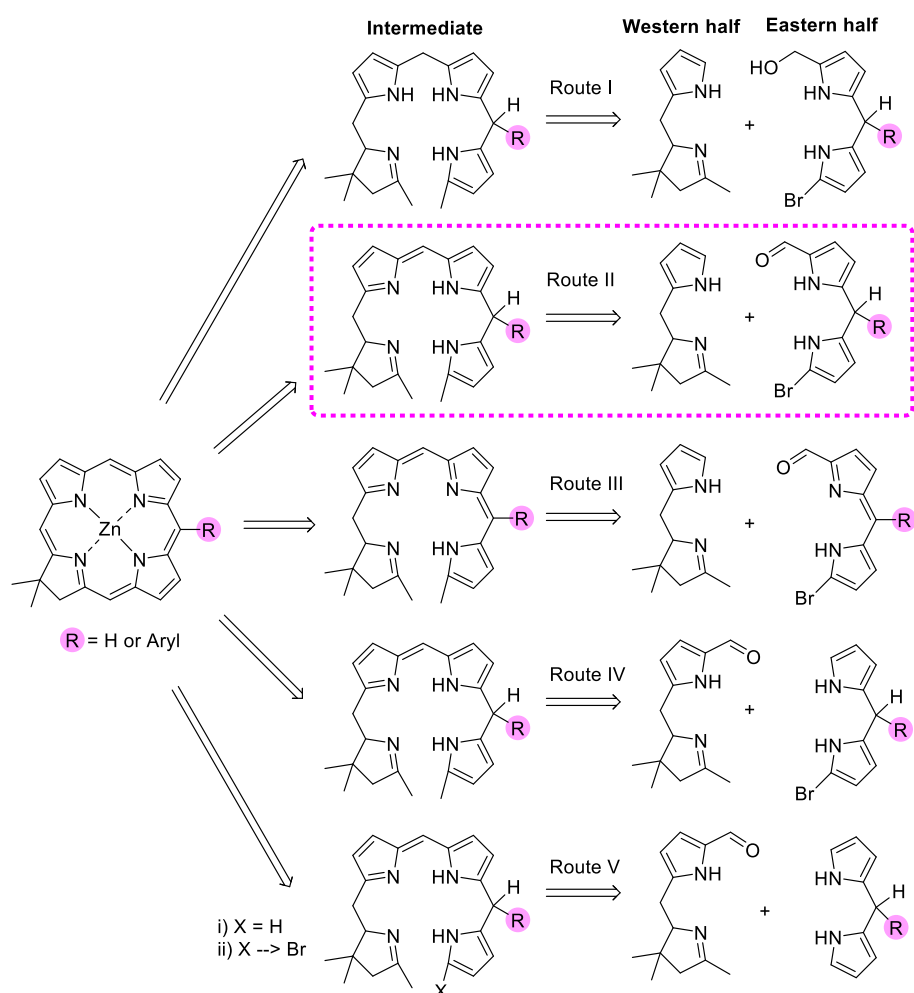
Figure 2.1. Chemical structures of the natural chlorins Bonellin and Faktor I.

The *gem*-dialkylchlorins are more stable and less susceptible to oxidation due to the disubstitution on the 18-position, yet they maintain their physicochemical properties.^[346] Originating from 1980, research on *gem*-dialkyl chlorins is a recent field in chlorin chemistry; however, synthetic advances already present great versatility. Comprehensive reviews by Lindsey cover the *de novo* synthesis of such chlorins and compare approaches from works reported by Battersby, Jacobi, Lindsey, and Montforts. Scheme 2.1 displays examples of simplified general routes developed by the aforementioned researchers.^[347,348]



Scheme 2.1. Simplified *de novo* routes to *gem*-dialkylchlorins.

Extensive investigation of the synthetic routes towards the synthesis of *gem*-dimethyl chlorins have been conducted through the last three decades. Lindsey and co-workers have greatly contributed to the improvement of the chlorin preparation pathways. To summarise, Ptaszek *et al.* exploited five routes towards the synthesis of 10-substituted chlorins depending on the sites of the electrophilic-nucleophilic complementary groups on the pyrrole and pyrroline rings (Scheme 2.2). They concluded that Route II was the most beneficial route in terms of quantity and stability of the products. Route II entails the use of the Eastern (9-bromo-1-formyl-dipyrromethane) and Western half (tetrahydrodipyririn) under an acidic condensation.

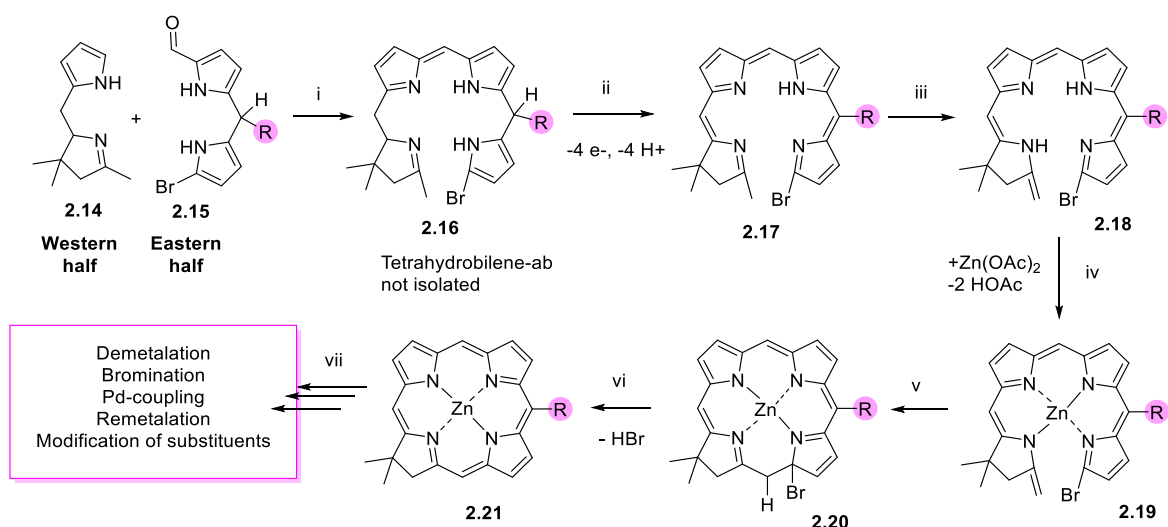


Scheme 2.2. Routes to 10-substituted chlorins.

The 5-substituted dipyrromethane (DPM) scalable synthesis (Eastern half) has been refined *via* reducing the oligomer production (by-products) in a one-flask synthesis, optimising the acidic condensation, and purification which yields 9-

bromo-1-formyl-DPMs.^[349–351] Moreover, the synthetic pathway of the Western half towards a more stable tetrahydrodipyrin derivative, 2,3,4,5-tetrahydro-1,3,3-trimethyldipyrin has been achieved. This dipyrin shows an increased reactivity to acid-catalysed condensations in the pyrrolic α -position, thereby facilitating the formation of the intermediate **2.16**.^[352]

The exact intermediates on the synthetic pathway of the chlorins are not yet fully determined. Several aspects can affect the outcome of the reaction *i.e.*, choice of the solvent, the metal coordination, choice of the oxidant, the base selection, and the temperature. Taniguchi *et al.* and Strachan *et al.*, with the guidance and propositions of Battersby and Montfort's works, simplified and proposed possible steps; however, the sequence may vary. First, the two halves form the 2,3,4,5-tetrahydrobiladiene-*ab* **2.16** under acidic condensation; then four electrons and four protons are removed *via* oxidation **2.17**; subsequent imine to enamine tautomerisation **2.18** is followed by zinc complexation **2.19**, and lastly carbon-carbon bond formation **2.20** and HBr elimination **2.21** (Scheme 2.3).



Scheme 2.3. Processes and possible intermediates in 10-substituted *gem*-dimethyl chlorin formation (Route II); i) acidic condensation; ii) oxidation; iii) tautomerisation; iv) complexation; v) C-C bond formation; vi) HBr elimination; vii) post modifications.

The use of base is to neutralise the acetic acid (formed upon zinc insertion) and the hydrobromic acid (formed upon aromatisation) and possibly to ease the imine-enamine tautomerisation. The metal complex is used to direct electrocyclisation and the silver salt to ease dehydrobromination.^[353,354]

Following these studies, each position of the chlorin (either meso or β/β' position) can now be modified *via de novo* synthetic approaches. The red-shifted absorption spectrum stems from the transitions along the polarised axis bisecting A and C rings, hence the substitution on 2, 3, 12 or 13 position significantly alters the absorption features. Namely, β -substitution causes a red-shift in absorption spectra accompanied by a relative increase in the intensity (hyperchromic shift) of the Q_y band coupled with an increase in the fluorescence quantum yield. Moreover, it is known that the increasing number of meso-substituents (0-4 substituents at the 5, 10, 15 or 20 position) causes a bathochromic shift (red-shift) of both B and Q_y bands and a hypochromic shift (decrease of the absorptivity) of the Q_y band, which is of great importance for photochemical applications. The above observations apply primarily to zinc or magnesium metallated chlorins and also to their free base counterparts. Regarding the latter, they tend to have longer singlet lifetimes and higher fluorescence quantum yields than the zinc chelates since their absorption features appear in longer wavelengths. Data of the quantum yields of the excited states by metallated or free base porphyrins, chlorins or bacteriochlorins can be summarised as average ranges in Table 2.1. The trend for the fluorescence quantum yield follows an ascending order: porphyrins < chlorins < bacteriochlorins, and the triplet state quantum yield follows as expected an inversely proportional order. Internal conversion (IC) appears to be at the same range for chlorins and porphyrins, however for bacteriochlorins is higher due to the fact that they have lower excited singlet states and thus an increased vibrational overlap explained by Franck-Condon factor and the definition of the energy gap law for the non-radiative decays.^[355–358]

Table 2.1. General range of the quantum yields in porphyrins, chlorins or bacteriochlorins.

	Φ_f	Φ_{isc}	Φ_{ic}
Porphyrins	0.10 (0.03–0.16)	0.80 (0.7–0.9)	0.10 (0.05–0.2)
Chlorins	0.20 (0.1–0.3)	0.70 (0.6–0.8)	0.10 (0.1–0.2)
Bacteriochlorins	0.15 (0.1–0.3)	0.50 (0.3–0.8)	0.35 (0.3–0.4)

The non-radiative rate constant ($k_{nr} = k_{ic} + k_{isc}$) in zinc derivatives is greater relative to the free base and is consistent with the more facile ISC anticipated from the heavy atom effect on spin-orbit coupling in the metallochlorins. An enhanced non-radiative decay is associated with enhanced ISC since the higher energy state Q_y is expected to decrease the IC contribution. However, regarding the free base chlorins, the involvement of N-H vibrations of the inner core might enhance the Franck-Condon factor for the IC decay process. The relation between the rate constants, singlet excited state lifetime, and quantum yields can be summarised by equations 2.2 and 2.3.^[359,360]

$$\tau = \frac{1}{k_f + k_{ic} + k_{isc}} \quad \text{Eq. 2.2}$$

$$\Phi_f = \frac{k_f}{k_f + k_{ic} + k_{isc}} \quad \text{Eq. 2.3}$$

An efficient PS should possess a long-lived triplet excited state and a higher triplet energy state than that of the singlet oxygen ($\geq 94.3 \text{ kJ mol}^{-1}$), so it can efficiently undergo Type I/II electron or energy transfers reacting with ground state molecular oxygen. Chlorins usually satisfy these conditions and they generate singlet oxygen efficiently.^[346]

Surprisingly, *gem*-dimethyl chlorins have not gained much attention relating to their photoactivity *in vitro* or *in vivo*. To our knowledge only Ogilby *et al.* have investigated the localisation of the lipophilic unsubstituted free base *gem*-dimethyl chlorin (**2.22**) using HeLa cells in comparison to the hydrophilic cationic porphyrin 5,10,15,20-tetrakis(*N*-methyl-4-pyridyl)-21*H*,23*H*-porphyrin (**2.23**) (Figure 2.2). The goal of the study was to determine the intracellular generation of singlet oxygen *via* time-resolved singlet oxygen phosphorescence measurements at the level of a single cell using molecules that localise in different subcellular areas. The hydrophilic porphyrin molecules **2.23** tended to accumulate in the nucleus and cytoplasm of the cell yielding an intracellular singlet oxygen lifetime of ca. 30 – 40 μs . Chlorin **2.22** was accumulated non homogeneously outside the nucleus in the cell cytoplasm; however, the exact organelle localisation of **2.22** in the cytoplasm has not been yet determined.^[361] Worth mentioning, Hamblin and co-workers have investigated the *in vitro* PDT

potential of similar *gem*-dimethyl bacteriochlorins against HeLa human cancer cells.^[362,363]

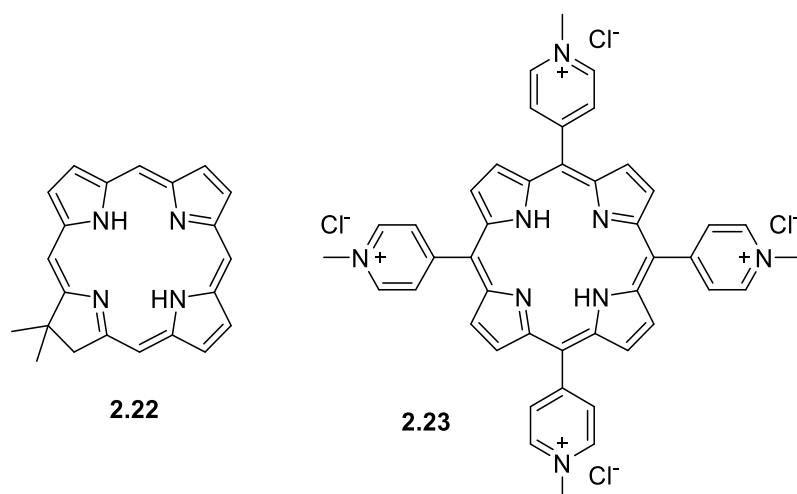


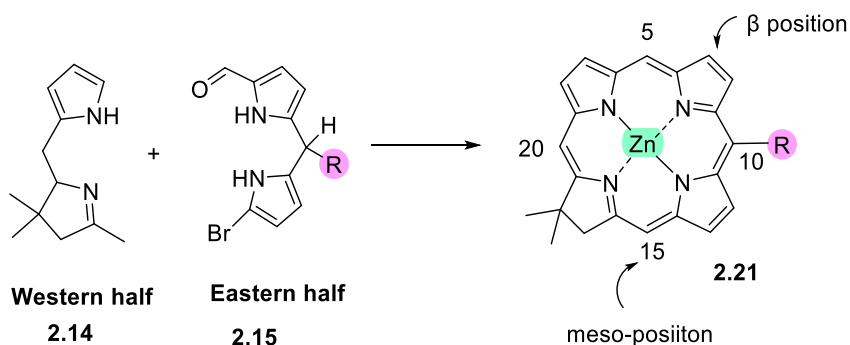
Figure 2.2. Chemical structures of the free base *gem*-dimethyl chlorin (**2.22**) and 5,10,15,20-tetrakis(*N*-methyl-4-pyridyl)-21*H*,23*H*-porphyrin (**2.23**).

Overall, depending on the final application that each researcher is seeking, different tailoring on the macrocycle periphery should be taken; thus there is no rule we need to follow in the exploitation of the *gem*-dimethyl functionality for the production of new molecules.

2.2 Objectives

This study aimed to develop new derivatives of oxidation resistant chlorins for maximum singlet oxygen generation that can be used as potential PSs for PDT, either individually or as building blocks for new materials. These chlorins bear a *gem*-dimethyl group in the reduced pyrrole ring that prevents oxidation and thus attributes advantageous stability to the chlorins. Numerous similar complexes have been synthesised; however, little advances have been made to investigate their potential of singlet oxygen generation and the photodynamic effect. Hence, this work focuses on the development of such systems through the introduction of different substituents in the macrocycle periphery.

We aimed to synthesise and characterise zinc *gem*-dimethyl chlorins and their free base counterparts, following Lindsey's procedures by using a [2+2] condensation of 9-bromo-1-formyl-5-substituted dipyrromethane (Eastern half) and 2,3,4,5-tetrahydro-1,3,3-trimethyldipyrin (Western half) which yields chlorins with functional moieties in the meso-position (Scheme 2.4). A 4-bromophenyl or naphthyl meso-substitution was introduced with the aim to investigate the scope of the reaction, as well as to prepare a series of analogues with handles for further periphery modifications. Additionally, we aimed to characterise photophysically the target compounds regarding their ground and excited states properties. Specifically, singlet and triplet state lifetimes and the respective quantum yields have been experimentally determined along with their singlet oxygen quantum yield. These studies were accompanied by density functional theory (DFT) calculations to assess the features of the frontier molecular orbitals and the theoretical excited states properties. Ultimately, we aimed to investigate the *in vitro* phototoxic activity against a mouse colon carcinoma cell line (CT26).

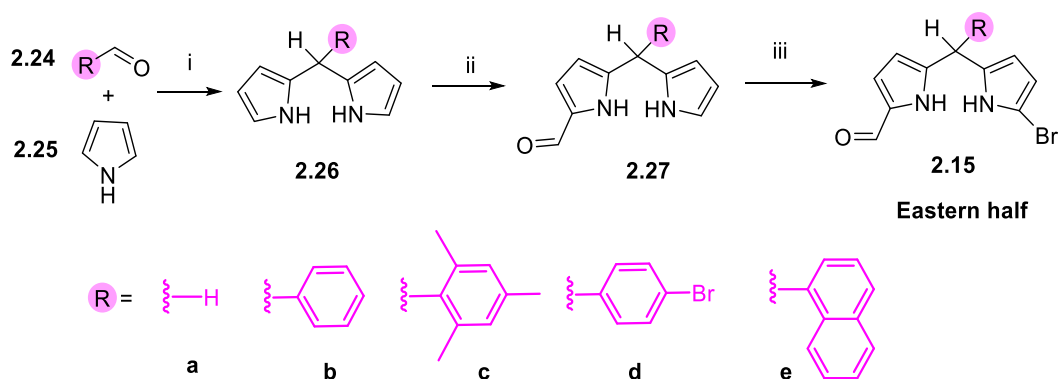


Scheme 2.4. Structure and general scheme of *gem*-dimethyl chlorin synthesis.

2.3 Results and Discussion

2.3.1 Synthesis of *gem*-dimethyl chlorins

Zinc chlorins and their free base counterparts have been investigated as potential PDT agents. The [2+2]-type synthesis is the most suitable way to synthesise these molecules on realistic scales involving a tetrahydrodipyrin and a brominated-formylated-dipyrromethane. Starting with the synthesis of the Eastern half of the targeted chlorins, 9-bromo-1-formyl-5-substituted DPMs (**2.15a-e**) were synthesised according to literature procedures (Scheme 2.5).^[349–351] A variety of meso-substituents were introduced to investigate the scope of the reaction and to prepare a series of analogues with handles for further periphery modifications.



Scheme 2.5. Synthesis of 9-bromo-1-formyl-5-substituted dipyrromethanes (Eastern half) over three steps; (i) 0.1 eq. TFA for **2.26a,b,d,e** and MgBr₂ in case of **2.26c**, rt, 1 – 1.5 h; (ii) DMF/POCl₃, 0 °C, 2 h, EtOAc/NaOAc; (iii) 1 eq. NBS, THF, -78 °C, 1 h.

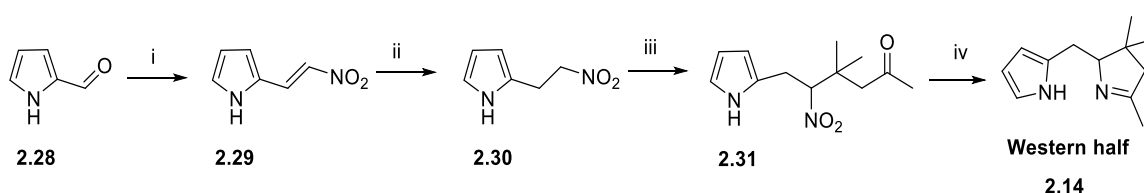
The first step towards the synthesis of Eastern half involves the corresponding aldehyde and pyrrole condensation forming the meso-free and 5-substituted DPMs. For compounds **2.26b**, **2.26d**, and **2.26e** dichloromethane was used together with pyrrole as solvent, reducing the final usage of pyrrole equivalents. Thus, using 10 eq. of pyrrole and 0.1 eq. of trifluoroacetic acid (TFA) or MgBr₂ in case of **2.26c**, DPMs were obtained in 42 – 62% yield. Subsequent Vilsmeier-Haack formylation of the DPMs utilising POCl₃/DMF yielded the 1-formyl-5-substituted-DPMs **2.27a-e** in 39 – 65% yield.^[364] The diformylated products were observed by TLC; however, these were not isolated or characterised. Lastly, electrophilic aromatic substitution using 1 eq. of NBS in anhydrous THF yielded

the desired 9-bromo-1-formyl-dipyrromethanes **2.15a-e** in 45 – 85% yield.^[355,356] In some cases, bromination of 1-formyl-DPMs yielded multiple products, and likewise these were not isolated. Yields for each step of the DPM synthesis are shown in Table 2.2. DPMs are light- and heat-sensitive compounds, therefore protection from light during the reaction, purification, and storage was of paramount importance to ensure these compounds do not degrade. Regarding compounds **2.15a-e**, in most of the cases, the solvent was removed at 25 °C.

Table 2.2. Reaction yields for every step of the synthesis of DPMs.

R	2.26	2.27	2.15
H (a)	43 %	42 %	85 %
Phenyl (b)	42 %	42 %	67 %
Mesityl (c)	62 %	65 %	45 %
4-Bromophenyl (d)	48 %	39 %	70 %
1-Naphthyl (e)	56 %	42 %	55 %

Western half **2.14** was synthesised in accordance with literature procedures.^[352,353] Starting from pyrrole-2-carboxaldehyde and following the sequence: Henry addition, reduction, Michael addition, and reductive cyclisation resulted in the desired dipyrin in 30% yield over four steps (Scheme 2.6).^{1[349,365]}



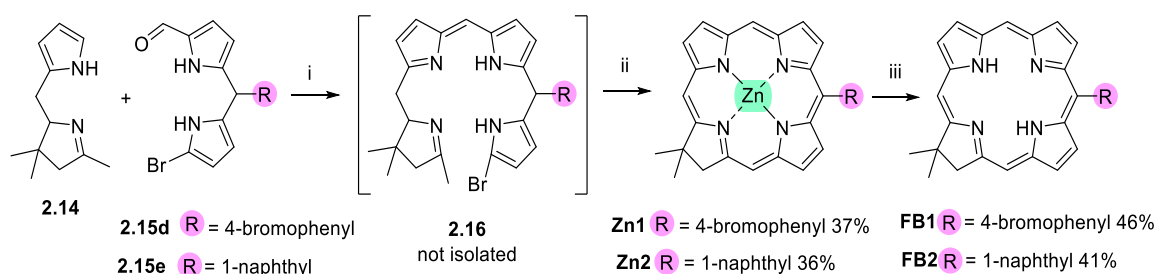
Scheme 2.6. Synthesis of the Western half over four steps in 30% yield; (i)

MeNH₂·HCl, KOAc, MeNO₂, EtOH, rt, 2 h; (ii) LiBH₄, THF, -10 °C, 0.25 h; (iii) mesityl oxide, DBU, rt, 24 h; (iv) Zn/HCOONH₄, THF, 40 °C, 26 h.

The present flexibility in the syntheses of the 17,18-dihydro-18,18-dimethylchlorins stems from the far-reaching and ground-breaking studies of the Lindsey group.^[24] Synthesis of the targeted chlorins, bearing a

¹ Compound **2.14** was synthesised by Harry C. Sample, Polythea Ph.D. student, TCD.

gem-dimethyl group was performed using a one-pot reaction according to Lindsey's [2+2] chlorin synthesis following the Route II reported by Ptaszek *et al.* (Scheme 2.7).^[353,366] Two of the 5-substituted DPMs were utilised for the chlorin condensation as they can provide interesting features in the chlorin derivatives. In particular, the 4-bromophenyl group on the periphery was introduced to enhance the ISC (heavy atom effect),^[227,239] and to allow further functionalisation through standard palladium-catalysed cross-coupling reactions. The choice of the naphthyl group stemmed from the interest for a possible attempt to perform an intramolecular ring fusion with the β -carbon of the macrocycle, in the hope of accessing a π -extended *gem*-dimethyl chlorin framework and enhancing the π -conjugation.



Scheme 2.7. Synthesis of *gem*-dimethyl chlorins displaying the non-isolated 2,3,4,5-tetrahydrobiladiene-*ab*, and the final products **Zn1**, **Zn2**, **FB1** and **FB2**; (i) *p*-TsOH·H₂O, CH₂Cl₂/CH₃OH, 20 °C, 0.5 h; (ii) 2,2,6,6-tetramethylpiperidine, Zn(OAc)₂, AgOTf, 90 °C, 18 – 20 h, CH₃CN; (iii) TFA/CH₂Cl₂, 20 °C, 1 h.²

This synthetic pathway consists of an acid catalysed pyrrole-aldehyde condensation, thus forming the linkage between the *A* and *B* rings, yielding the non-isolated 2,3,4,5-tetrahydrobiladiene-*ab* **2.16**, which is then subjected to basic conditions, metallation, and an oxidant. Hence, **2.14** was reacted with **2.15d** or **2.15e** and 5 eq. of *p*-TsOH·H₂O in CH₂Cl₂/CH₃OH for 30 min and the subsequent removal of the solvent resulted in the yielding of the non-isolated intermediate (**2.16**). This was immediately treated with CH₃CN, 2,2,6,6-tetramethylpiperidine, anhydrous Zn(OAc)₂, AgOTf and was allowed to stir at 90 °C for 18 – 20 h. The products formed were either the desired chlorin or degraded products (which stay on the baseline on the TLC). Therefore, the desired chlorin

² Compounds **FB1** and **FB2** were synthesised by Harry C. Sample – step iii Scheme 2.7.

products were isolated after column chromatography as blue-purple solids in good yields (37% for **Zn1** and 36% for **Zn2**).

With the aim to evaluate and compare the photophysical properties between zinc and free base complexes, demetallation of both zinc-chlorins was carried out to yield the free base counterparts **FB1** and **FB2** (46% and 41% yields, respectively) (Scheme 2.7).^[354]

During the preparation of the present work Borbas *et al.* published the synthesis of 10-substitued zinc *gem*-dimethyl chlorins focusing on the kinetics of the acidic demetallation.^[367] One of the differences that can be drawn between our syntheses is that purification of the final brominated-formylated-dipyrromethane has a significant effect on the final yield of the chlorin: *i.e.*, when **2.15d** is not isolated the yield of the respective chlorin drops drastically to half. Additionally, the demetallation of the chlorins can be done quicker with a lower concentration of TFA and quenching with triethylamine is more fruitful than the use of sodium bicarbonate presented herein.

Next, compounds **Zn1** and **FB1** were further characterised by single-crystal X-ray diffraction analysis and crystal structures obtained (Figure 2.3- Figure A 1).³

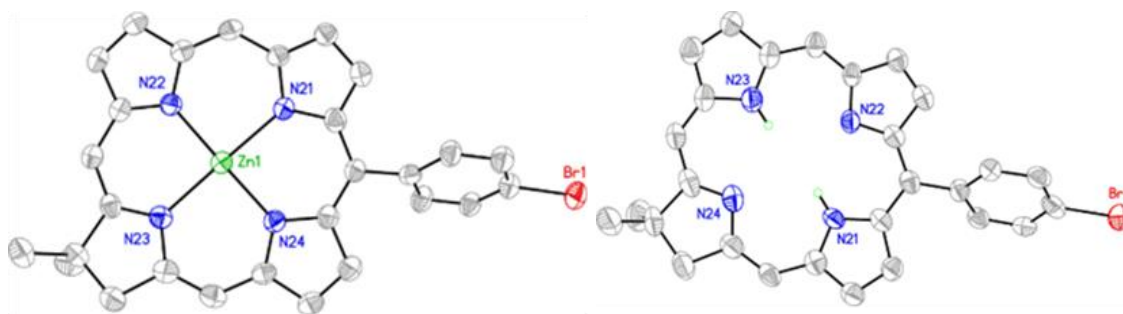


Figure 2.3. View of the molecular structures of **Zn1** (left) and **FB1** (right) in the crystal, shown with displacement at 50% probability and heteroatoms labelled. Inner chlorin hydrogen atoms shown in **FB1**, all others omitted for clarity.

³ Crystal structures were determined by Dr. Brendan Twamley, TCD

2.3.2 Photophysical characterisation and DFT calculations

The chlorins synthesised herein were investigated regarding their ground and excited state properties. Together with the singlet oxygen generation, we illustrate that they possess desirable photophysical and -chemical characteristics deeming them suitable for use as PSs. Yields and rate constants of the decay pathways of the singlet excited state (S_1) were experimentally determined whilst the triplet state energy for each chlorin (T_1) was estimated using DFT (Density Functional Theory) calculations.

2.3.2.1 Ground state properties

UV-Visible absorption spectra of all compounds were recorded in ethanol, and DCM and they are displayed in Figure 2.4 and Figure A 2. The free base and Zn(II)chlorins display absorption spectra that differ from each other due to the metal effect and the variation in the respective molecular orbitals. The absorption spectra of chlorins show a strong B-band in blue-violet region at ~400 nm, with minor difference between Zn(II)chlorins and their free base analogues. The last Q-band (~ 640 nm) of the free base chlorins exhibits a significant red shift (ca. 30 nm) as compared to Zn(II) complexes, which is likely due to a reduction in the energy gap between the MOs. From DFT calculations we have assumed that this is due to the (HOMO-1) – LUMO and (HOMO-1) – (LUMO+1) energy gap reductions.

Coordination with Zn(II), which acts as a Lewis acid by accepting electron density from the macrocycle, results in stabilisation of the chlorin core and thus lowers the energies of the MOs.^[245,368] Furthermore, the ratio of the intensity of the $Q_y(0,0)$ and B bands (Table 2.3) provides a relative measure of the hyperchromic effect on the $Q_y(0,0)$ band showing the following descending order **FB2 > FB1 > Zn2 > Zn1**.

Comparison of these compounds with regards to meso-substituents indicates that there is no dramatic difference between the 4-bromophenyl and 1-naphthyl group; only a slight bathochromic shift for the Q_y band, in favour of the naphthalene substituent. A broader Q_x band for **FB1** and **FB2** is displayed at ~500 nm, which is indicative of different electronic transitions occurring, in

comparison with **Zn1** and **Zn2**, due to the vibronic borrowing from the strong B transitions.^[359,369,370]

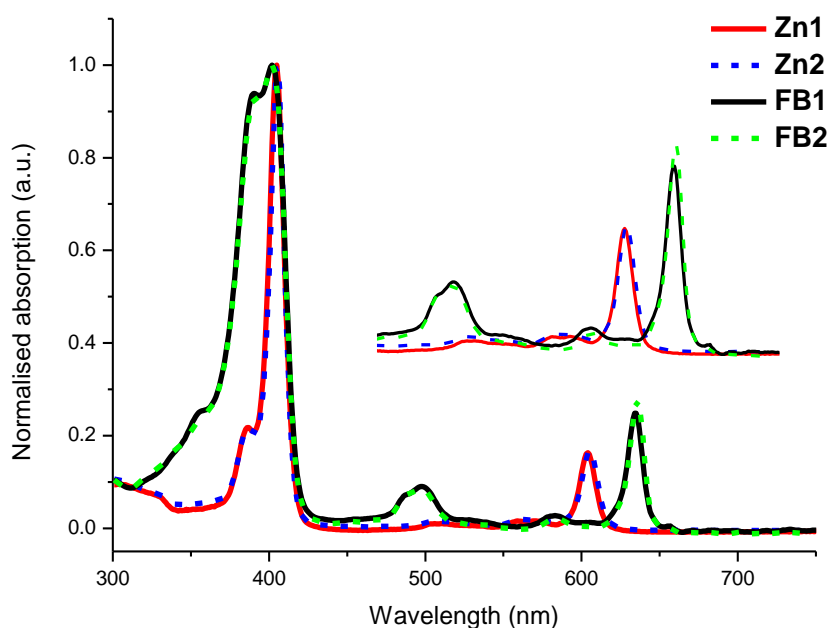


Figure 2.4. Normalised UV-Visible absorption spectra of the chlorins in ethanol. Spectra are normalized at the maximum of the B bands with an inset showing the Q-bands between ca. 450 – 700 nm (**Zn1** red, **Zn2** dashed blue, **FB1** black, **FB2** dashed green).

Table 2.3. UV-Visible absorption data of the chlorins in ethanol or dichloromethane.

Chlorin	λ_{max} (nm) ^a				Q_y/B ^b
	B band	$Q_x(1,0)$	$Q_y(1,0)$	$Q_y(0,0)$	
Zn1 *	405 (5.40)	506 (3.40)	559 (3.59)	604 (4.61)	0.16
Zn2 *	405 (5.54)	506 (3.73)	561 (3.83)	605 (4.76)	0.17
FB1 **	407 (5.08)	503 (4.00)	586 (3.56)	638 (4.43)	0.22
FB2 **	407 (5.24)	501 (4.17)	587 (3.70)	639 (4.64)	0.25

^a Values in parentheses refer to $\log \epsilon$; ^b ratio of the intensities of the $Q_y(0,0)$ and Soret (B) bands; *ethanol; **dichloromethane.

2.3.2.2 Excited state properties

The excited state properties of all the chlorins were determined in polar solvents (ethanol or methanol). Fluorescence emission spectra were recorded, and the quantum yields were calculated by using cresyl violet as reference compound. Additionally, singlet and triplet state lifetimes were determined experimentally by time-correlated single photon counting (TCSPC) and nanosecond transient absorption spectroscopy. Their respective quantum yields, and radiative and non-radiative rates were calculated.

Fluorescence emission is determined by the $S_1 \rightarrow S_0$ transition as the IC from $S_2/S_n \rightarrow S_1$ is very fast and undetectable. Therefore, fluorescence spectra of the chlorins are dominated by the $Q_y(0,0)$ band with a shoulder of the $Q_y(1,0)$ band, the vibronic satellite, clearly displaying the mirror image of the absorption spectrum. Compounds **Zn1** and **Zn2** display a fluorescence peak maximum (λ_{max}) at ca. 610 nm with a vibronic satellite at ~ 660 nm, while compounds **FB1** and **FB2** display their peak maximum at ca. 638 nm with two vibronic satellites at 667 and 700 nm (Figure 2.5 and Figure A 3).

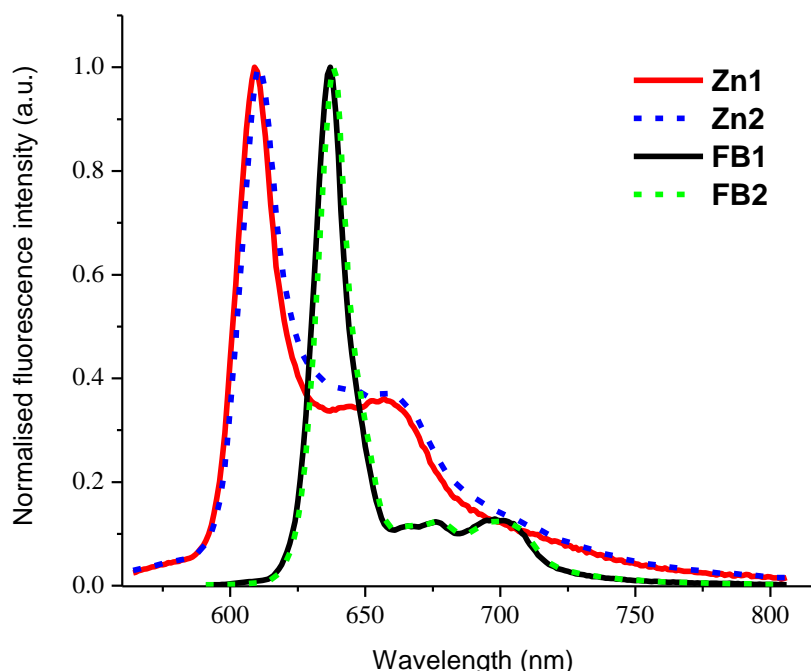


Figure 2.5. Normalised fluorescence emission spectra of the chlorins in ethanol (**Zn1** red, **Zn2** dashed blue, **FB1** black, **FB2** dashed green); $\lambda_{exc} = 560$ nm for **Zn1/Zn2** and 500 nm for **FB1/FB2**.

Stokes shift ($\Delta\nu$) is the difference between the position of the absorption and fluorescence emission peak,^[371] and it was calculated from the corresponding UV-Vis and emission spectra in EtOH or MeOH. A minor Stokes shift from 50 to 160 cm^{-1} (2 to 6 nm) occurs between $Q_y(0,0)$ absorption and Q_y emission peak with the free base chlorins displaying a smaller shift (50 – 70 cm^{-1}). This profile is the same in both ethanol and methanol solution indicating a significant overlap of the corresponding absorption and emission spectra.^[372] Fluorescence quantum yields (Φ_f) of **Zn1** and **Zn2** range from 0.03 to 0.08, respectively and from 0.08 to 0.14 for **FB1** and **FB2**, respectively. The Φ_f of the free base chlorins is around two times higher than the Φ_f of the Zn(II) chelates following the trend of reported values in literature of similar compounds.^[358]

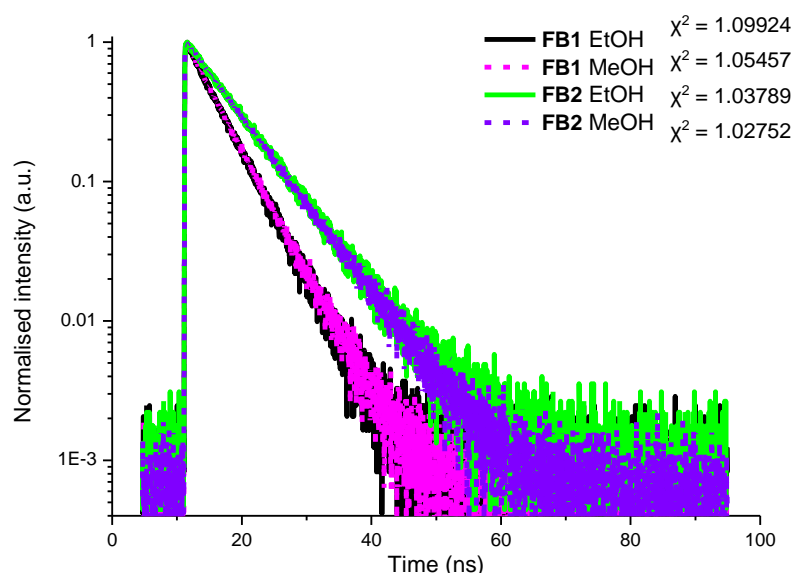


Figure 2.6. Fluorescence lifetime decays of **FB1** and **FB2** in ethanol and methanol. Reduced χ^2 value is presented (black: **FB1** in EtOH; magenta dotted: **FB1** in MeOH; green: **FB2** in EtOH, purple dotted: **FB2** in MeOH); $\lambda_{\text{exc}} = 400 \text{ nm}$; $\lambda_{\text{det}} = 637 \text{ nm}$.

There is a general correlation between the fluorescence quantum yield (Φ_f) and the Q_y/B absorption ratio and the fluorescence lifetime: the free base chlorins with the lowest excited singlet states (the most red-shifted Q_y bands) have the largest relative Q_y/B ratio along with the higher fluorescence lifetimes and yields (Table 2.3 and Table 2.4).

Time-correlated single photon counting (TCSPC) was performed and the fluorescence decay profiles of each chlorin in ethanol and methanol are shown in Figure 2.6 and Figure A 4. Lifetime values of the singlet excited state (τ_s)

remain the same between ethanolic and methanolic solutions. The radiative ($k_r = k_f$ = fluorescence rate constant) and non-radiative ($k_{nr} = k_{ic} + k_{isc}$) rate constants, were calculated by using equations 2.4 and 2.5, following reported methods and are summarised in Table 2.5 and Table 2.5.^[373,374]

$$k_x = \frac{\Phi_x}{\tau_s} \quad \text{Eq. 2.4}$$

where x is f, ISC or IC.

$$\Phi_{ic} = 1 - \Phi_{isc} - \Phi_f \quad \text{Eq. 2.5}$$

Table 2.4. Photophysical properties of the chlorins in polar solvents.

Chlorin	λ_{em} (nm)	$\Delta\nu$ (cm ⁻¹)	τ_s (ns)	Φ_f	k_f ×10 ⁷ s ⁻¹
Zn1*	609	163	0.9	0.03	3.3
Zn1**	609	136	0.9	0.04	4.4
Zn2*	611	162	1.5	0.05	3.3
Zn2**	611	162	1.5	0.08	5.3
FB1*	637	74	5	0.07	1.4
FB1**	637	74	5	0.08	1.6
FB2*	637	50	7	0.10	1.4
FB2**	638	50	7	0.14	2.0

* MeOH; ** EtOH; $\Delta\nu$ Stokes shift; standard errors (percentage of value) are $\tau_s \pm 5\%$, $\Phi_f \pm 10\%$, $k_f \pm 10\%$.

Furthermore, as expected, the fluorescence lifetime of **Zn1** and **Zn2** is lower than the free base analogues and ranges between 1 – 1.5 ns whilst that of **FB1** and **FB2** ranges between 5 – 7 ns (Figure 2.6 and Figure A 4). Thus, Zn(II) derivatives have an almost five times shorter fluorescence lifetime as compared to the free base, which indicates that Zn(II) chelates undergo faster ISC to the triplet excited state in comparison to the free base counterparts due to the heavy atom effect.^[227,239,375] Additionally, the lowest Φ_f is displayed by chlorins **Zn1** and **FB1** with the 4-bromophenyl substituent. The results are comparable with similar compounds in the literature (Table 2.5).^[376,377] In addition, k_f values of **Zn1** and

Zn2 are typical for Zn(II) chlorins as are the k_{nr} values of the free base analogues.^[358,359]

Since ISC feature is dominant in the photochemical pathway for the chlorins, nanosecond transient absorption (TA) spectroscopy was performed and the triplet state lifetimes (τ_T) and quantum yields (Φ_T or Φ_{isc}) were calculated from the triplet-triplet absorption spectra, and these are shown in Figure A 5 - Figure A 12 (ambient conditions) and Figure A 13 - Figure A 20 (oxygen-free conditions).

Table 2.5. Photophysical properties of the chlorins in polar solvents.

Chlorin	τ_T^a (ns)	τ_T^b (μ s)	Φ_{isc}	Φ_{ic}	Φ_Δ	k_{isc} $\times 10^8 \text{ s}^{-1}$	k_{ic} $\times 10^7 \text{ s}^{-1}$	k_q^c $\times 10^9 \text{ M}^{-1} \text{ s}^{-1}$
Zn1*	200	27	0.82	0.15	0.60	9.1	16	2.36
Zn1**	202	26	0.90	0.06	0.90	10	6.6	2.34
Zn2*	210	28	0.78	0.17	0.55	5.2	11	2.25
Zn2**	210	30	0.88	0.03	0.85	5.9	2.0	2.25
FB1*	160	47	0.78	0.15	0.40	1.6	3.0	2.97
FB1**	170	70	0.80	0.12	0.70	1.6	2.4	2.79
FB2*	150	50	0.70	0.20	0.38	1.0	2.9	3.17
FB2**	166	64	0.75	0.11	0.60	1.1	1.6	2.86

^a Triplet state lifetime in air (equilibrated); ^b triplet state lifetime in oxygen free solution; ^c oxygen quenching rate; * MeOH; ** EtOH; standard errors (percentage of value) are $\tau_T \pm 10\%$, $\Phi_{isc} \pm 10\%$, $\Phi_{ic} \pm 15\%$, $\Phi_\Delta \pm 10\%$, $k_{ic} \pm 10\%$, $k_{isc} \pm 10\%$, $k_q \pm 15\%$.

Triplet state lifetimes (τ_T) at ambient and oxygen-free conditions (through degassing with argon) in methanol or ethanol are shown in Table 2.5. The triplet absorption profile of the TA spectra of metallochlorins (**Zn1**, **Zn2**) and the free base chlorins (**FB1**, **FB2**) display very similar shapes, both in ethanol and methanol. Figure 2.7 displays representative TA spectra of **Zn1** (left) and **FB1** (right). They show an absorption maximum at 420 – 460 nm and negative absorbance signals that are caused by bleaching of the ground-state, which is characteristic of the significant electronic transitions at 400 – 500 nm (B band, $S_0 \rightarrow S_n$) and 600 – 650 nm (Q_y band, $S_0 \rightarrow S_1$). The lifetime of the Zn(II) chelates under ambient conditions is longer (200 – 210 ns) than that of the free base chlorins (150 – 170 ns). In contrast, the Zn(II) complexes display shorter lifetimes

in oxygen free conditions (26 – 30 μ s) than the free base analogues (47 – 70 μ s), which shows that free base compounds have intrinsically longer triplet lifetimes. There is a large difference from the ns to the μ s time scale at ambient and in oxygen free conditions.

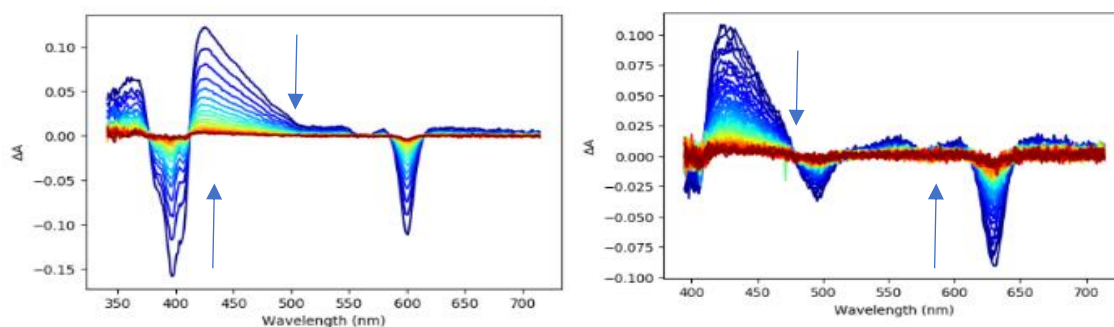


Figure 2.7. TA spectra of **Zn1** in methanol (ambient conditions; incremental time 40 ns; 604 nm λ_{exc}) on the left; TA spectra of **FB1** in methanol (oxygen free conditions; incremental time 3 μ s; 637 nm λ_{exc}) on the right. Arrows pointing from blue to red colour show the decay from the maximum intensity in the successive steps respectively.

Stimulated emission spectra which appeared at early delay times were not taken into consideration for the triplet lifetime calculation. Nevertheless, these features allowed us to estimate the triplet state quantum yield as they contain the singlet state features. Hence, the triplet state quantum yields (Φ_T or Φ_{isc}) were determined from the triplet-triplet absorption spectra as the average of individual experiments, by comparing the bleaching magnitudes at long times (due to the triplet formation) versus the ones from the immediate excitation flash (due to the singlet formation). Triplet state yields are higher in the zinc chelates ($\Phi_T \sim 0.75 - 0.90$) than the free base analogues ($\Phi_T \sim 0.70 - 0.80$) with a descending order **Zn1** > **Zn2** > **FB1** > **FB2** following the anticipated trend $(1 - \Phi_f) < \Phi_T < \Phi_\Delta$ and also illustrated the more dominant pathway of IC and ISC of the zinc chelates.

Moreover, the IC quantum yield along with the corresponding rate constants (k_{ic} , k_{isc}) were calculated (equation 2.5) and presented in Table 2.5. The IC quantum yield of the free base chlorins is higher than those of the zinc complexes, due to the Franck-Condon factor. However, the IC rate constants for $S_1 \rightarrow S_0$ of **Zn1** and **Zn2** are greater than those for the free base **FB1** and **FB2**. This is probably due to structural or vibrational effects of the possible axial coordination of the central zinc ion with the hydroxyl- groups of the solvent. In general, the

methanolic solution displays a rise for the IC quantum yields and rates, in comparison with the ethanolic solutions, which is more apparent in the zinc complexes (Table 2.5).

Last, another feature of the triplet excited states is the triplet-triplet molar absorption coefficient (ϵ_{τ}). An estimate calculation of the ϵ_{τ} for **Zn1** in ethanol was found as $18,750 \text{ M}^{-1} \text{ cm}^{-1}$ at 446 nm and this value is comparable with the ϵ_{τ} of *m*THPC (temoporfin) known as $19,300 \text{ M}^{-1} \text{ cm}^{-1}$ in methanol.^[45] This value was derived by determining the iso-absorptive points among a TA trace spectrum and the TA+A sum spectrum (TA spectrum + UV-Vis absorption spectrum expressed in ϵ) scaling the latter in a positive range in order to eliminate the ground state photobleaching features (Figure 2.8).^[378]

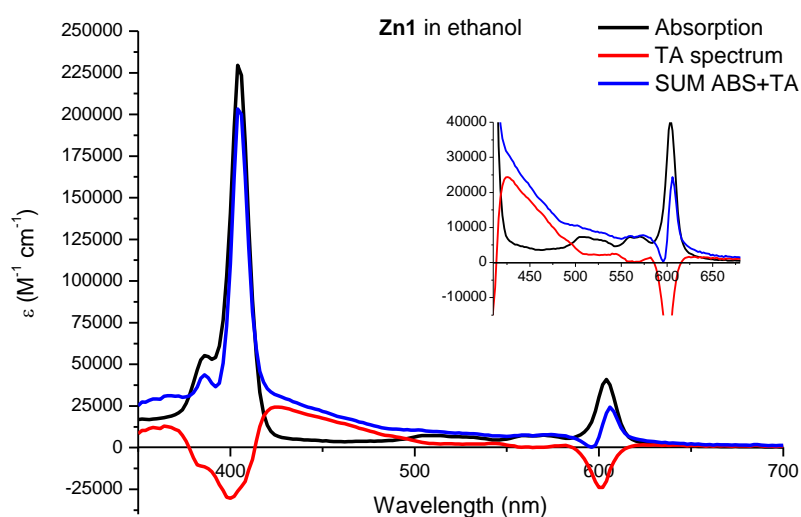


Figure 2.8. Representation of the spectra used for ϵ_{τ} determination of **Zn1** in ethanol (black: absorption; red: TA trace; blue: sum of TA and absorption values).

As previously mentioned, there is a large difference between the triplet excited state lifetimes in presence and absence of oxygen. This denotes that oxygen plays a significant role in chemical processes upon photoirradiation and, energy transfer from the triplet state of the molecules to molecular oxygen in the microenvironment takes place efficiently. Indeed, the singlet oxygen quantum yield is relatively high for both **Zn1** and **Zn2** in methanol and ethanol. In the latter, it reaches 90% while **FB1** and **FB2** show lower singlet oxygen quantum yields as expected due to their lifetimes and rates. The Stern–Volmer equation was applied to calculate the energy transfer of the compounds from the triplet state to molecular oxygen (k_q) (equation 2.6).^[379–381]

$$k_q = \frac{\left[\left(\frac{1}{\tau}\right) - \left(\frac{1}{\tau^0}\right)\right]}{[O_2]} \quad \text{Eq. 2.6}$$

where; k_q is the rate constant for quenching of the triplet state by oxygen, τ^0 the triplet lifetime in oxygen free conditions, τ the triplet lifetime in the presence of oxygen and, $[O_2]$ is the concentration of oxygen which is 2.1×10^{-3} M in methanol and ethanol at 20 °C.^[382] Values are shown in Table 2.5 and they are consistent with other chlorin molecules in the literature.^[377,383]

2.3.2.3 Singlet oxygen phosphorescence and quantum yield

Singlet oxygen determination was achieved by the direct detection of its luminescence emission at 1275 nm using an InGaAs NIR detector. Singlet oxygen quantum yields (Φ_Δ) in polar solvents were calculated by using Rose Bengal as reference. Representative emission spectra of the singlet oxygen luminescence are presented in Figure 2.9 (methanol) and the corresponding values are shown in Table 2.5.

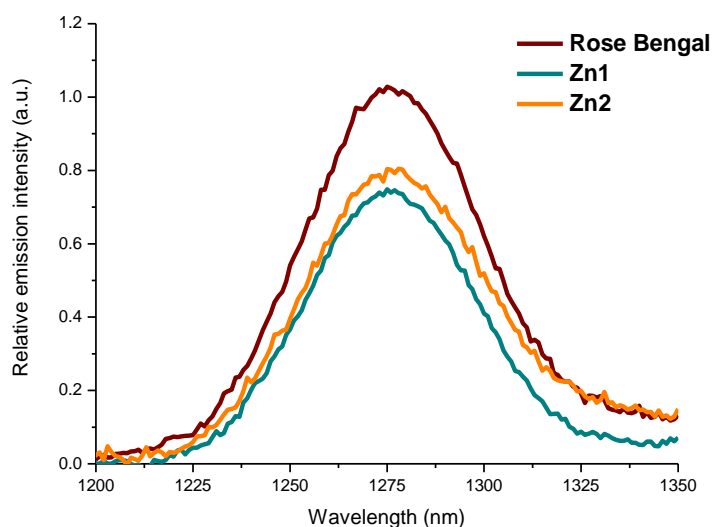


Figure 2.9. Singlet oxygen emission spectra of **Zn1**, **Zn2** and Rose Bengal in MeOH, $\lambda_{exc} = 512$ nm; 15 s integration time; Φ_Δ **Zn1** = 0.61; Φ_Δ **Zn2** = 0.64.

As previously mentioned, when chlorins undergo ISC as the dominant decay pathway ($S_1 \rightarrow T_1$), this triplet excited state reacts with molecular oxygen and produces singlet oxygen (1O_2). The triplet energy of an ideal PS should be higher than the lowest excited singlet state of molecular oxygen ($94.3 \text{ kJ}\cdot\text{mol}^{-1}$ or 0.977 eV) to be able to generate singlet oxygen. It is reported that in chlorinated

solvents such as CH_2Cl_2 ,^[384] the singlet oxygen quantum yield can be overestimated; thus, ethanol and methanol were used with regards to their future compatibility for *in vitro* evaluation.

All chlorins exhibit high singlet oxygen quantum yields both in methanol and ethanol. Noteworthy, the Φ_Δ values, as well as the Φ_f values, in methanol are clearly lower for all compounds (and the Φ_{ic} values are slightly higher in methanol). The triplet excited state lifetimes, akin to the Φ_{isc} are reasonably similar for all four compounds in both solvents (Table 2.5). This discrepancy is puzzling, and we tentatively attribute this to a different chemical reactivity of the two solvents with singlet oxygen, somehow influenced by the presence of the chlorins. This reactivity may be correlated to the different singlet oxygen lifetime values in different solvents (15 μs in ethanol; 9 μs in methanol), but perhaps trace water content may also play a role. The molecular oxygen concentration [$^3\text{O}_2$] does not differ between the two solvents. These are the factors that can attribute to the Φ_Δ difference between methanol and ethanol reported in this work.^[385] It should be noted that temoporfin also displays lower singlet oxygen quantum yields in methanol in comparison with ethanol.^[45,386] Additionally, as the luminescence of singlet oxygen is difficult to detect, longer time integrals were used for the Φ_Δ measurements. As a result of the short fluorescence lifetimes, high ISC quantum yields, and longer triplet state lifetimes, **Zn1** and **Zn2** display higher values on average in both solvents (0.55 – 0.90) when compared with the free base counterparts (0.40 – 0.70) while **Zn1** and **FB1** display slightly higher values, as a result of the 4-bromophenyl substituent (Figure A 21 - Figure A 23).

2.3.2.4 DFT and TD-DFT calculations

Density functional theory (DFT) and time-dependent DFT (TD-DFT) calculations were performed to investigate the ground-state and the excited-state properties of the chlorins. Hybrid B3LYP functional,^[387,388] and a 6-31G* basis set were used for the ground state (S_0) geometry optimisation. For zinc complexes the axial coordination with an alcohol molecule (ethanol) was included in the optimised structure and for the free base chlorins, calculations were performed taking into account the presence of ethanol [with the respective keyword for ethanol `scrf=(cpcm,solvent=ethanol)`]. The same methods were applied and TD-DFT

calculations were performed to calculate the excited singlet (S_1) and triplet (T_1) states and the respective molecular orbitals (MOs).

The goal was to determine the theoretical singlet and triplet excited level of the chlorins, compute the singlet-triplet gap and visualise the electron-density distribution in HOMOs and LUMOs (Figure 2.10). The S_1 ($^1E_{00}$) and T_1 ($^3E_{00}$) energies and the difference between the first singlet excited and triplet energy state (ΔE_{S-T}) are shown in Table 2.6, along with the oscillator strengths (f) and the energy difference between [HOMO – LUMO], [(HOMO-1) – LUMO] and [(HOMO-1) – (LUMO+1)]. The S_1 singlet state level of all chlorins was determined experimentally from the intersection of the normalised absorption and emission spectra ($^1E_{00}$).

Table 2.6. Molecular orbital energies (eV) and differences between HOMO/LUMO and singlet and triplet excited states from TD-DFT calculations.

Chlorin	LUMO – HOMO	LUMO – (HOMO-1)	(LUMO+1) – (HOMO-1)	f^a	$^1E_{00}$	$^3E_{00}$	ΔE_{S-T}	$^1E_{00}^b$
Zn1	2.519	2.772	3.460	0.370	2.14	1.15	0.82	2.05
Zn2	2.523	2.803	3.500	0.396	2.14	1.16	0.82	2.04
FB1	2.610	2.517	3.325	0.266	2.16	1.00	0.93	1.95
FB2	2.609	2.795	3.366	0.299	2.16	0.98	0.93	1.94

^aOscillator strength of transition $S_0 \rightarrow S_1$; ^b experimental value for S_1 .

In all optimised structures, the HOMO-1 displays an electron density localised on the four meso-positions. Specifically, in the free base chlorins, electron density is localised on the core N-atoms, whereas, in the Zn(II) analogues, it is also localised on the core metal atom. In accordance with a previous report by Aravindu and co-workers, HOMOs do not show electron density at meso-positions; hence, the substitution at meso-position/s can significantly alter the HOMO-1 energy level which is visible in the UV-Vis spectra of the complexes. The same group applied the four-orbital model to assign the electronic transitions from the calculations to the experimental spectra.^[359] This proved that the HOMO-1 \rightarrow LUMO and HOMO \rightarrow LUMO+1 correspond to B_x and Q_x bands and HOMO-1 \rightarrow LUMO+1 and HOMO \rightarrow LUMO correspond to Q_y bands. This can

be applied to the corresponding chlorins, as they have similar properties, energies, and electron-density of MOs.^[356,389]

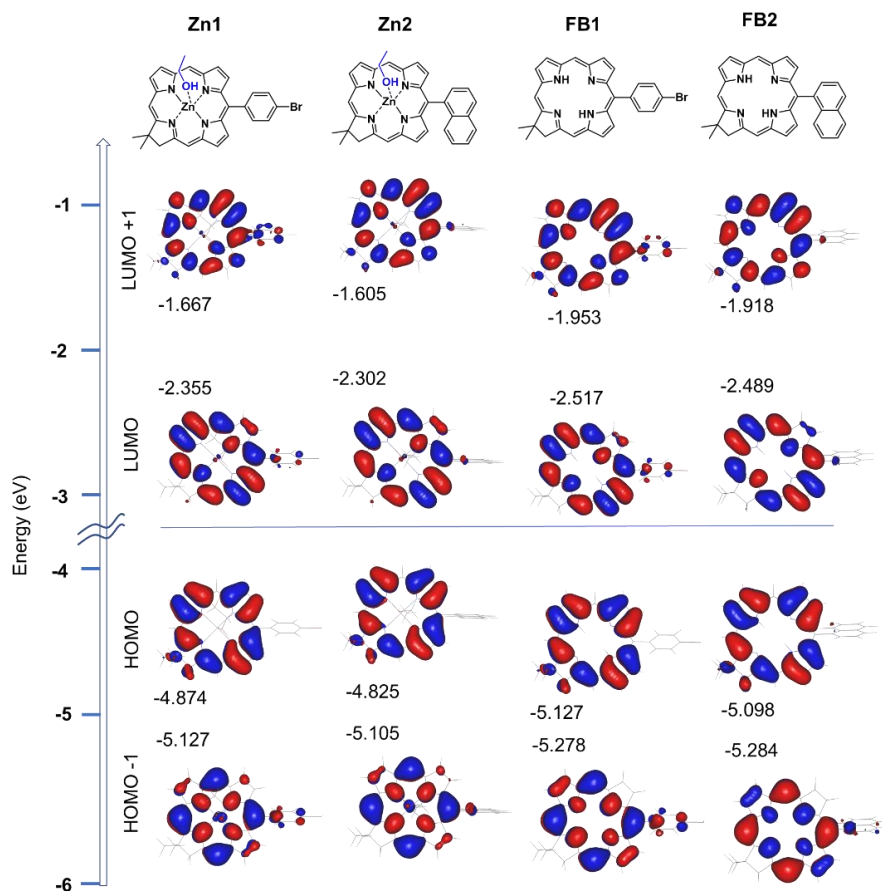


Figure 2.10. Molecular orbital energies and electron-density distribution of the chlorins obtained from TD-DFT calculations; B3LYP/6-31G*.

The results of the theoretical calculations agree with the ones from the ground state absorption experiments. This is exemplified by looking at the HOMO-1 of the corresponding chlorins; free base chlorins undergo destabilisation resulting in smaller energy gaps [(HOMO-1) – LUMO] and [(HOMO-1) – (LUMO+1)] as shown in Table 2.6.

2.3.3 *In vitro* phototoxicity studies of zinc(II) chlorins⁴

Zinc chlorins which displayed high singlet oxygen quantum yields were tested for *in vitro* phototoxicity against the mouse colon carcinoma cell line (CT26). Colorectal cancer is considered as one of the most common cause of cancer

⁴ The experiments were conducted during a training secondment in the photobiology group at the University of Coimbra, under the supervision of Dr. Lígia C. Gomes-da-Silva and with the help of Dr. Fábio Schaberle.

death worldwide. There are treatment plans to restrain the disease and shrink tumours. These usually include a combination of surgery, radiation therapy, immunotherapy, targeted therapy, and chemotherapy.^[390] However, there is still space of improvement. Namely, PDT allows for a selective treatment irradiating only the target tissues and can stimulate an anti-tumour immunity contributing to the long-term control of the disease.^[33]

Cell viability was accessed by using resazurin assay where viable cell metabolise the blue non-fluorescent dye resazurin (Alamar blue) to the highly pink fluorescence compound resorufin by reduction.^[391,392] Cell survival may be determined as the fluorescence from the non-treated control sample which is considered as 100% of viability. Additionally, since these compounds displayed fluorescence properties, cell uptake studies were conducted by flow cytometry. In order to determine the toxicity in the absence of light (dark toxicity), CT26 cells were first incubated with **Zn1** and **Zn2** for 24 h with concentrations ranging from 0.62 to 20 μM . Both chlorins showed considerable dark toxicity above 5 μM with a statistically high significant level ($P \leq 0.001$) (Figure 2.11). Consequently, *in vitro* evaluation for their cellular uptake and phototoxicity was conducted with concentrations lower than 5 μM .

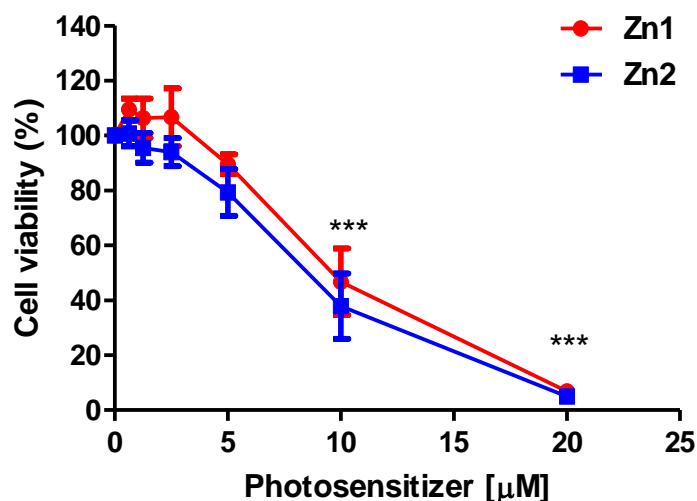


Figure 2.11. Cell viability of CT26 cells post incubation (24 h) with **Zn1** (red) and **Zn2** (blue) in the absence of light; results are expressed as the mean values of three independent experiments \pm SEM ($n = 3$); one-way ANOVA in comparison with untreated cells, $p < 0.001$ for ***.

Phototoxicity was determined under two different light doses (L.D.) 0.5 J cm⁻² or 1 J cm⁻². The final concentration of the chlorin derivatives was in the range of 0.04 to 5 μM when a L.D. of 0.5 J cm⁻² was delivered, whereas concentrations ranging from 0.01 to 1.25 μM were used for L.D. of 1 J cm⁻². Colon carcinoma cells were incubated with chlorin derivatives for 24 h followed by a washing step and irradiation at the indicated L.D. Cell irradiation was performed by using a visible broadband light (LED, 400-700 nm, light potency 10 mW cm⁻²). Accurate light doses were estimated considering the overlap between the LED and the complex spectrum.^[393] Cellular viability was evaluated 24 h post irradiation using the resazurin reduction assay. The results of merged independent experiments are displayed in Figure 2.12 and Figure 2.13. Both chlorins showed significant phototoxicity at low concentrations with IC₅₀ ca. 0.30 – 0.40 μM in the case of 1 J cm⁻² light dose, which is a relatively low energy treatment. As an example, a comparative study showed that temoporfin has an IC₅₀ of 0.9 μM (with light dose of 15 J cm⁻²) against human ovarian cancer cell line (SK-OV3).^[394] These results are promising and along with the high singlet oxygen production denote a potential photodynamic effect.

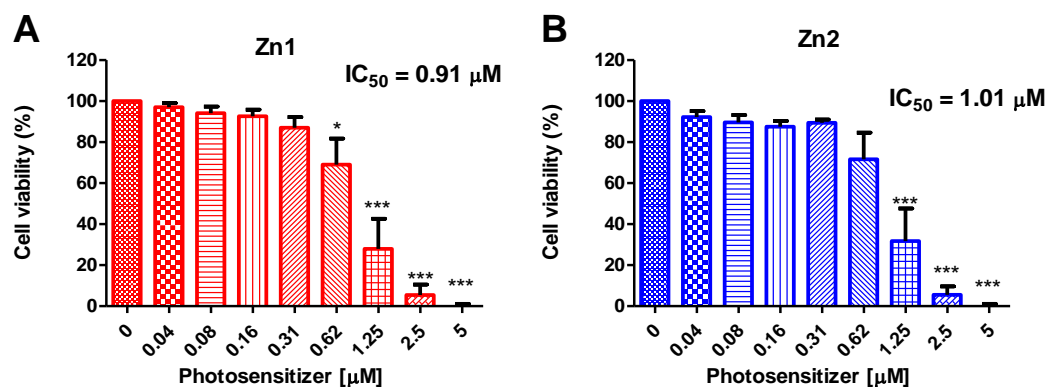


Figure 2.12. Cell viability of CT26 cells incubated with **Zn1** (A) and **Zn2** (B) for 24 h followed by irradiation with L.D. of 0.5 J cm⁻²; results are expressed as the mean values of four individual experiments ± SEM (n = 4); one-way ANOVA in comparison with untreated cells, p < 0.05 for *, p < 0.001 for ***.

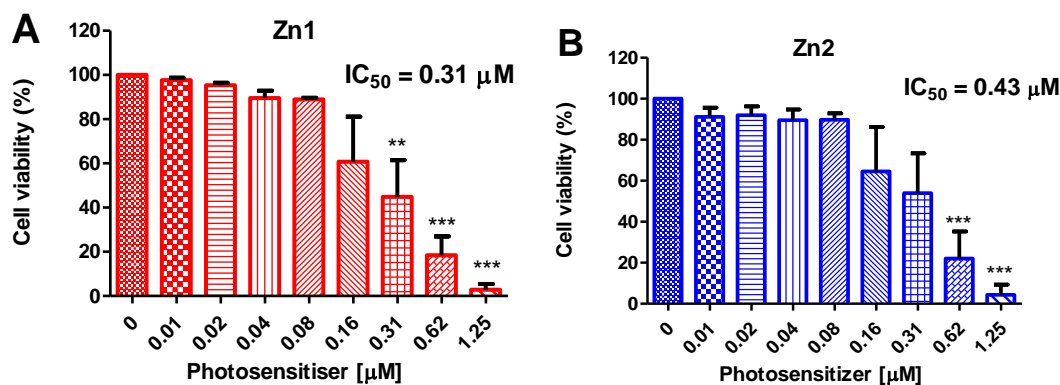


Figure 2.13. Cell viability of CT26 cells incubated with **Zn1** (A) and **Zn2** (B) for 24 h followed by irradiation with L.D. of $1 J cm^{-2}$; results are expressed as the mean values of four individual experiments \pm SEM ($n=4$); one-way ANOVA in comparison with untreated cells, $p < 0.01$ for **, $p < 0.001$ for ***.

To evaluate the ability of **Zn1** and **Zn2** to be internalised by cancer cells, cell uptake studies were conducted by taking advantage of the intrinsic fluorescence of these compounds. CT26 cells were incubated with the indicated PSs at 1.25 and $2.5 \mu M$, for 24 h (Figure 2.14). Cells were then washed to remove the non-internalised compound and their associated fluorescence was measured by flow cytometry. PSs fluorescence was measured upon excitation with the 405 nm laser and detection was performed using the 615/24 nm filter (Figure 2.15). The obtained data showed that both chlorins are efficiently internalised by cells. The display of higher cell uptake of **Zn2** is probably due to the fact that the fluorescence quantum yield is relatively higher than that of **Zn1** (Table 2.4). Possibly their relative uptake is the same since the phototoxicity is similar with **Zn1** even showing a slight increased phototoxicity in comparison to **Zn2** due to higher singlet oxygen generation. The fact that **Zn1** is more phototoxic than **Zn2** is also indicated by the phototoxicity index ($PI = IC_{50} \text{ in the dark} / IC_{50} \text{ with light irradiation}$). PI was calculated for **Zn1** and was found to be 11 at $0.5 J cm^{-2}$ and 31 at $1 J cm^{-2}$ whereas for **Zn2** was lower: 9 at $0.5 J cm^{-2}$ and 21 at $1 J cm^{-2}$. Overall, these results demonstrated that **Zn1** and **Zn2** combine efficient cell internalisation with high singlet oxygen production which results in high phototoxicity at low and safe concentrations.

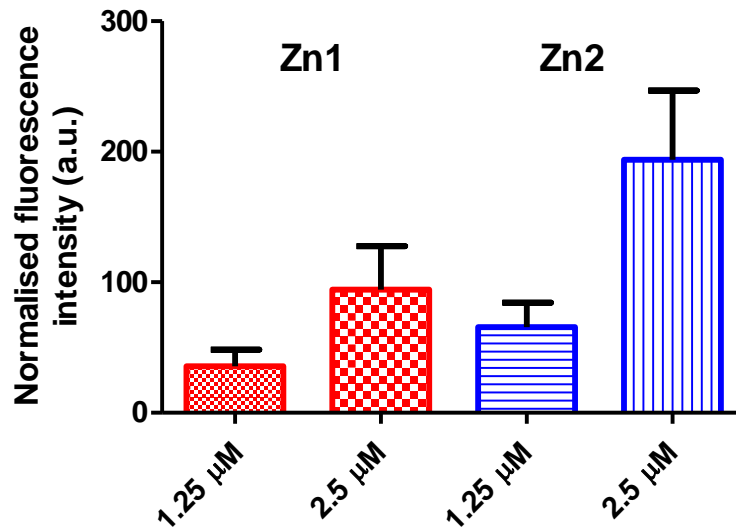


Figure 2.14. Cellular uptake of the chlorins **Zn1** (red) and **Zn2** (blue) evaluated by flow cytometry. Values are normalised against the signal of the untreated cells and results are expressed as the mean values of two individual experiments \pm SEM (n = 2).

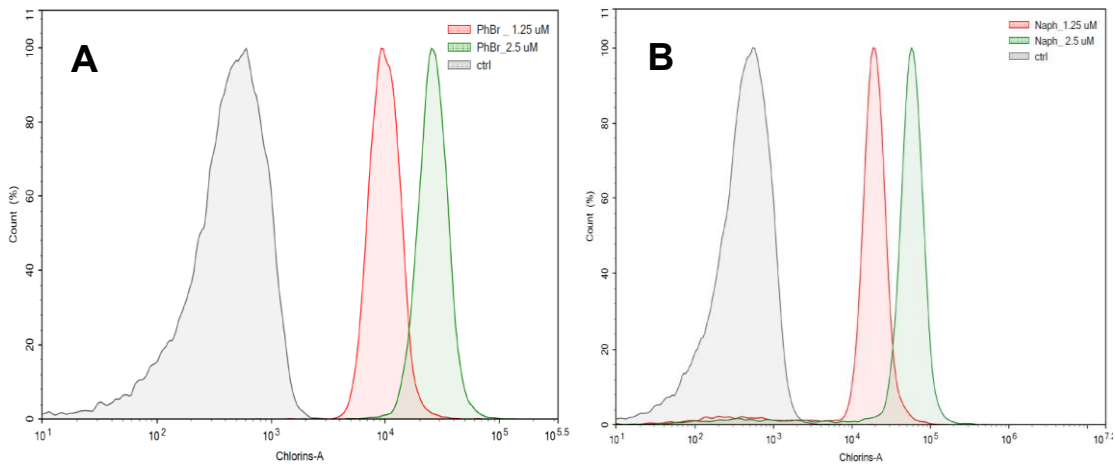


Figure 2.15. Flow cytometry histograms showing the signal detected of the control cells (grey); **Zn1** at 1.25 μ M (red), **Zn1** at 2.5 μ M (green) (**A**); **Zn2** at 1.25 μ M (red) and **Zn2** at 2.5 μ M (green) (**B**) detected with 615/24 nm filter.

2.4 Conclusions and Future Work

To conclude, a series of DPMs and two zinc(II) *gem*-dimethyl chlorins (**Zn1** and **Zn2**) were successfully synthesised together with their free base counterparts (**FB1** and **FB2**). Photophysical characterisations, including steady state- and time resolved-spectroscopy, were performed to evaluate the ground and excited state properties (singlet and triplet) of all chlorins. DFT calculations were performed to compute the energy of the excited states of the chlorins, visualise the HOMOs and LUMOs, and determine the triplet state energy. Moreover, they were evaluated for their capability to generate singlet oxygen and the best candidates were tested for their dark and phototoxicity against a cancer cell line (colon carcinoma cell line, CT26). Along with this, crystal X-ray structures of **Zn1** and **FB1** have been successfully obtained.

Prior to this work, such complexes had not been investigated regarding their singlet oxygen generation and we have found that both **Zn1** and **Zn2** exhibit high triplet state yields ($\Phi_{isc} = 0.70 - 0.90$) and excellent singlet oxygen quantum yields in methanol and ethanol ($\Phi_{\Delta} = 0.60 - 0.85$); in comparison the free base analogues also exhibited suitable singlet oxygen quantum yields ($\Phi_{\Delta} = 0.40 - 0.70$). Additionally, zinc complexes tend to internalise into the cells displaying great phototoxicity upon irradiation with a broadband light source at low concentrations where they do not show any dark toxicity. Specifically, they displayed an IC_{50} value of $\sim 1 \mu M$ with L.D. $0.5 J cm^{-2}$ and an IC_{50} value of $\sim 0.4 \mu M$ with L.D. $1 J cm^{-2}$.

The results show that the chlorins can be efficient PS candidates for use in photomedicine, given that they display *in vitro* phototoxicity, high singlet oxygen quantum yields in polar solvents, modest fluorescence quantum yields and moderate triplet state lifetimes and yields upon photoexcitation.

Future work includes the modification of the chlorin periphery in the meso and/or β -positions in order to fine-tune their electronic properties, *i.e.*, red-shifting of the Q_y band in the absorption spectra towards the NIR region; longer singlet and triplet lifetimes, whilst maintaining the singlet oxygen quantum yield, to allow the photobiological effect. This can be employed by introducing halogens in desirable positions and subsequently extending the π -conjugation *via* palladium-mediated

coupling reactions. The challenge is the development of chlorins with enhanced hydrophilicity and tumour tissue selectivity (amphiphilicity and biocompatibility) that will allow further *in vitro* and possibly *in vivo* evaluation studies. Amide and amine linkers, aniline and phenol groups, carboxylic acids, and alkoxy groups are sought after to enhance the water solubility.^[395] Attaching bioconjugatable groups, such as polyethylene glycol or polysaccharides, may enhance the amphiphilicity. A further evaluation of the mechanism of the photocytotoxicity is envisioned.

Chapter 3: Synthesis and Photophysical Studies of 1,4-Phenylene-linked Porphyrin-Chlorin Arrays

*“Like a bird with broken wing that has traveled through wind for years . . .
I sleep and my heart stays awake . . .”*

~ Giorgos Seferis ~

3.1 Introduction

The development of tetrapyrrolic systems with tunable photophysical properties and absorption that reaches the red region is essential for diverse applications. Nature’s photosynthetic chromophores engage light-harvesting antenna systems that absorb light and funnel the energy to the photochemical reaction centres.^[396] Since photosynthetic processes can only happen within assemblies the design and synthesis of conjugated or non-conjugated tetrapyrrolic scaffolds have prompted interest. Exploiting the photochemical reactions not only gives answers to the fundamental mechanism of photoexcitation in natural systems, but also provides opportunities for applications in material and biological sciences.^[397]

Functionalisation of the tetrapyrrolic structures towards light-harvesting systems or biological tools intends to cover several photophysical criteria. Some of those include an intense and red-shift absorption and efficient emission, long-lived excited state lifetimes, and photostability. Other chemical and biological characteristics include a facile synthesis, chemical stability, tailorable solubility, introduction of handles for bioconjugation.^[398] Expanding the system’s π -conjugation is one of the main strategies for shifting the absorption wavelength.^[399,400] In porphyrinoids, this can be achieved *via* designing assemblies which include (i) the introduction of a nitrogen or oxygen or sulfur atom instead of a methine carbon bridge (aza-, oxa-, and thia- porphyrins), (ii) a fused benzene (benzoporphyrin) or naphthalene (naphthoporphyrin) ring

attached to the pyrrole, (iii) a combination of the above, e.g., in phthalocyanines, (iv) introduction of suitable functional groups at meso- and/or β - positions of the macrocycle, or (v) connecting two or more porphyrinoids directly or *via* a linker, or (vi) by reducing one or more pyrrole rings in the porphyrin macrocycle (forming chlorins or bacteriochlorins).^[401–405] In the case where a linker is used, the electronic and steric nature of a linker molecule dictates the photophysical properties of an array.^[406]

In 1982 the first porphyrin dimer bearing a phenylene linker was reported.^[407] Since then dimer systems have been designed towards optoelectronic and light-harvesting applications, biomedical applications or the lately popular two-photon absorption (TPA) spectroscopy.^[399] The latter concerns also applications involving the treatment of deep tumours by PDT, with porphyrin dimers reported with enhanced potential for TPA and moderate singlet oxygen generation.^[408] In a review article, Kim *et al.* stated various strategies to increase the efficiency of the two-photon absorption process of porphyrin related systems. While monomers exhibit relatively small two-photon absorption cross-section values, dimers may increase the TPA efficiency.^[409]

Focusing on the case of linker mediated conjugation, when an aryl substituent is placed at the meso position to form a dimer, it can result in a twisted conformation and the molecule may lose the planarity with attenuation in its π -conjugation. On the other hand, aryl-ethynyl linkers may increase the co-planarity and thus the π -conjugation.^[403,404] A recent review by Jing *et al.* comprehensively summarises the phenylene linked tetrapyrrole arrays covering systems that predominantly contain porphyrins with very few chlorins and bacteriochlorins.^[410] Porphyrin arrays having a π -conjugated linker exhibit electron delocalisation, resulting in the mixing of the frontier molecular orbitals (MOs) of the subparts. This leads to a small(er) LUMO – HOMO gap and a bathochromic shift in the UV-Vis spectrum. However, in some cases, the desired bathochromic shift is associated with an unfavourable reduction in the excited state lifetimes.^[411] Additionally, the possible torsional rotations, observed in chlorin and bacteriochlorin dyads, depending on the linker identity and attachment site, are keen on accelerating internal conversion processes.^[412]

Tetrapyrrolic arrays constructed by conjugating linkers such as ethynyl and butadiynyl groups have been extensively investigated by Therien and co-workers and Anderson and co-workers.^[413–419] Moreover, they have exploited the excited states of such molecules and their potential in optoelectronics or as nanotechnological materials. The expanded π -conjugation through bridges at the meso position had led to Soret band splitting and a red-shift into the near-IR regions, therefore this strategy can be employed as another means in deeper absorption into the NIR region.^[420]

With regards to chlorins, various dyads have been reported, such as chlorin-porphyrin or chlorin-bacteriochlorin dyads for energy-transfer studies^[421,422] or chlorin-chlorin dyads.^[420,423] Additionally, introducing groups, such as polyethylene glycol (PEG), cyclodextrin or glucose units, that enhance biocompatibility and amphiphilicity is of significant importance for potential applications in photomedicine.^[374,377] Figure 3.1 shows some of the reported dyads.

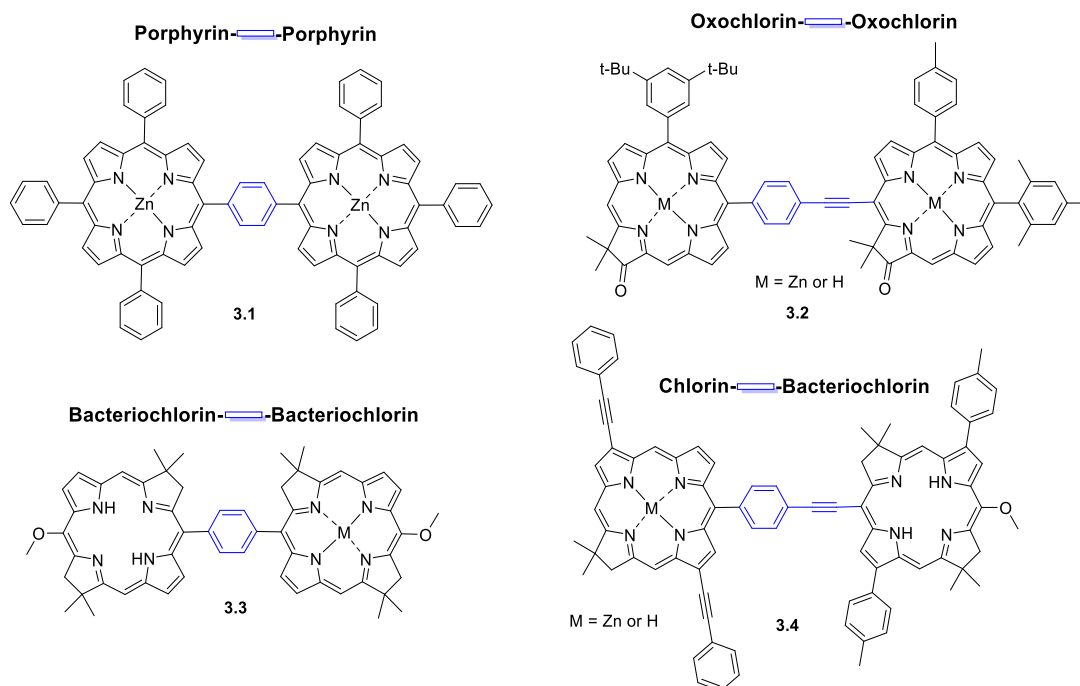


Figure 3.1. Examples of reported dyads with a phenylethyne or 1,4-phenylene linker.

3.2 Objectives

Chlorins bearing a 4-bromophenyl substituent at the 10-position allow for subsequent chemical modulation of their periphery. They can act as primary building block, which can undergo structural alteration *via* palladium catalysed cross-coupling reactions resulting in the development of new products (*e.g.*, π -extended chlorins), having different photophysical properties as compared to their parent molecule.

Herein, to develop novel dyads with a 1,4-phenylene linker we included the *gem*-dimethyl chlorin (**Zn1**, Chapter 2) as a benchmark and consequently aimed to introduce various moieties on the periphery. Modifications have been achieved through the synthesis of three new porphyrin-chlorin dyads and one triad which bear different substituents at the meso-positions (Figure 3.2). Despite the tractable porphyrin dimers, such systems with a phenylene bridge between the chlorin and porphyrin moiety are not investigated. They are expected to undergo energy transfer upon photoexcitation, *via* through-bond or through-space interactions.

The complete characterisation of these complexes was achieved through NMR spectroscopy, UV-Vis spectroscopy and mass spectrometry. In order to shed light on their photophysical properties and excited state features, steady state and time resolved spectroscopy were employed. In addition, singlet oxygen determination was planned together with their evaluation for a potential photodynamic effect.

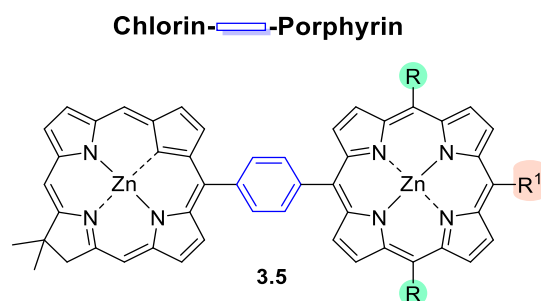


Figure 3.2. General chemical structure of the chlorin-porphyrin arrays.

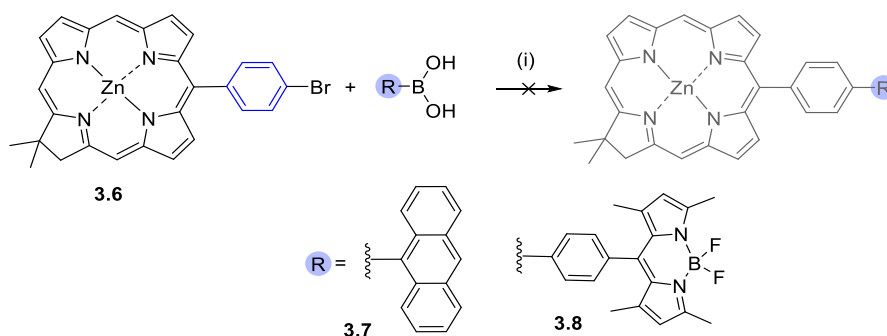
3.3 Results and Discussion

3.3.1 Synthesis of 1,4-phenylene-linked porphyrin-chlorin arrays

The chlorin core can be modified *via* several approaches with the most common one being the bromination and subsequent palladium catalysed cross-coupling reactions.^[347] Bromine atoms at the chlorin periphery can be introduced either by direct bromination of the intact chlorin or a condensation reaction between bromo-substituted Eastern and Western halves in total synthesis approaches.^[424] Then, palladium-catalysed cross-coupling reactions such as Suzuki,^[425] or Sonogashira,^[426–428] can be used to access the desired substituents at the chlorin periphery.

The zinc chelates of *gem*-dimethyl chlorins (**Zn1** and **Zn2**, Chapter 2) showed excellent singlet oxygen generation, moderate fluorescence quantum yields and high phototoxicity against CT26 cells which displayed a potential application as PS.^[372] The zinc chlorin with the 4-bromophenyl substituent **3.6**, can provide a synthetic handle for further modification, and hence, was subjected to palladium catalysed reactions.

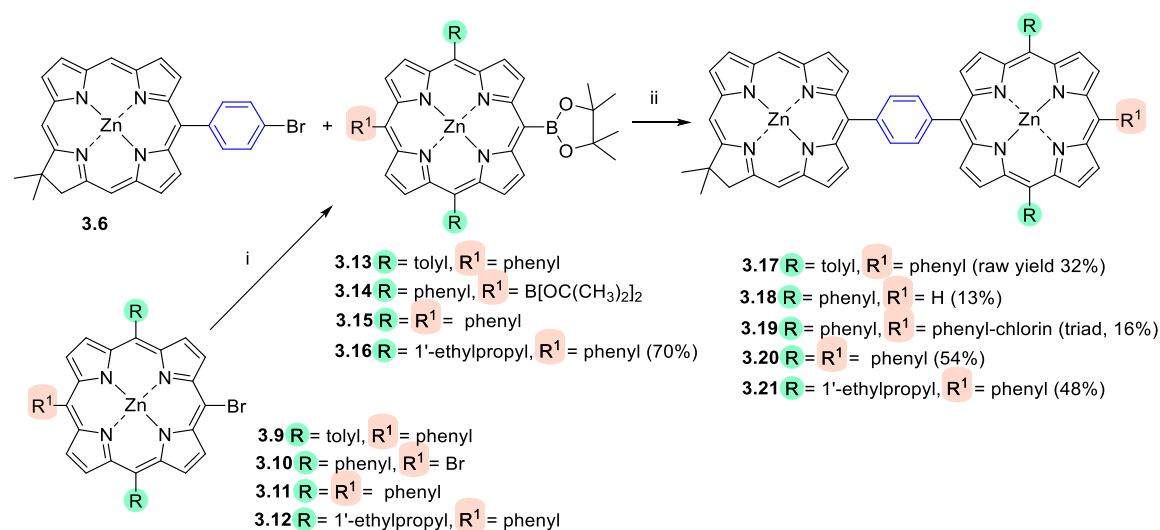
First, efforts to introduce an anthracene **3.7** or BODIPY⁵ **3.8** moiety to yield chlorin-anthracene and chlorin-BODIPY dyads bearing a 1,4-phenylene bridge, were not fruitful (Scheme 3.1). In particular a reaction of anthracene or BODIPY boronic acid with chlorin **3.6** under Suzuki coupling conditions did not yield the desired product.



Scheme 3.1. Attempts of Suzuki cross-coupling reactions to obtain dyads of compound **3.6**; (i) 10 eq. Cs₂CO₃, 0.2 eq. Pd(PPh₃)₄, toluene:DMF (2:1).

⁵ Compound **3.8** was provided by Elisabeth Sitte, Ph.D. student, TCD.

Furthermore, directing the functionalisation of the bromophenyl chlorin towards bulkier systems; the introduction of porphyrin moieties was carried out successfully. Following the same Suzuki cross-coupling conditions, the meso-monoborylated/diborylated porphyrins **3.13** – **3.16** reacted smoothly to yield porphyrin-chlorin dyads (**3.17**, **3.18**, **3.20** and **3.21**) and a chlorin-porphyrin-chlorin triad **3.19**, respectively (Scheme 3.2). Borylated porphyrins **3.13** – **3.16** were synthesised by bromoporphyrin analogues **3.9**–**3.12** according to literature procedures and **3.16** was fully characterised as a new compound.^[429,430]



Scheme 3.2. Suzuki cross-coupling reactions between chlorin and porphyrins; (i) 0.1 eq. PdCl₂(PPh₃)₂, 1,2-dichloroethane, 10 eq. TEA, 10 eq. pinacol boran, 80 °C, 30 min; (ii) 10 eq. Cs₂CO₃, 0.2 eq. Pd(PPh₃)₄, toluene:DMF (2:1), 85 °C, 1-2 h.⁶

As a consequence, the introduction of porphyrins with a variety of substituents in the periphery such as phenyl, tolyl or ethylpropyl groups was achieved. Namely, dyad **3.17** was synthesised from **3.6** and **3.13** and identified by mass spectrometry: HRMS (MALDI) *m/z* calcd. for C₆₈H₄₈N₈Zn₂ [M]⁺: 1104.2585, found: 1104.2581. However, purification was cumbersome and it has thus far been proven difficult to remove traces of the deborylated porphyrin. As such, the purification issues set a drawback and a final effort to purify *via* alumina column chromatography (Al₂O₃) resulted in degradation and partial oxidation of the chlorin to the oxochlorin (carbonyl group at 17 position).^[431]

⁶ Compounds **3.9**, **3.10**, **3.11**, **3.13**, **3.14**, **3.15** were provided by Dr. Nitika Grover; compound **3.12** was provided by Dr. Gemma M. Locke, TCD.

On the other hand, dyads with phenyl or 1-ethylpropyl substituents at meso positions of porphyrin, were easier to purify. The diborylated porphyrin **3.14** resulted in the formation of two products, the dyad **3.18** and the triad **3.19**. The tedious purification of the chlorin-porphyrin-chlorin triad **3.19** along with the insufficient solubility, precluded further photophysical characterisation. Nevertheless, it was characterised by NMR and UV-Vis spectroscopy and mass spectrometry. The corresponding reaction yields were low with 13% for the dyad and 16% for the triad. Lastly, dyads **3.20** and **3.21** were synthesised under the same conditions with relatively high reaction yields: 54% and 48% respectively. Partial deborylation of the porphyrin moiety during the coupling reactions was identified as a potential cause for the low reaction yields.

To best of our knowledge systems that contain a *gem*-dimethyl chlorin and porphyrin connected *via* 1,4-phenylene spacer at meso-position have not yet been reported or investigated. However, it is previously reported that similar frameworks can participate in excited state energy- and electron- transfer processes^[432,433] and can be useful material for two-photon absorption (TPA) spectroscopy.^[408,409]

3.3.2 Photophysical characterisation

3.3.2.1 Ground state properties

UV-Visible absorption spectra of the three dyads **3.18**, **3.20**, **3.21** and triad **3.19** were recorded and are displayed in Figure 3.3. Their absorption features did not show a significant red-shift in the UV-Visible spectra when comparing with the parent compound **3.6**; however, there is an apparent overlapping of the electronic absorption spectra in the region of the Soret band. All arrays displayed an intense Soret band at 418 – 426 nm stemming from the porphyrin benchmark and a less intense band at ~ 402 nm arising from the chlorin.^[372,434,435]

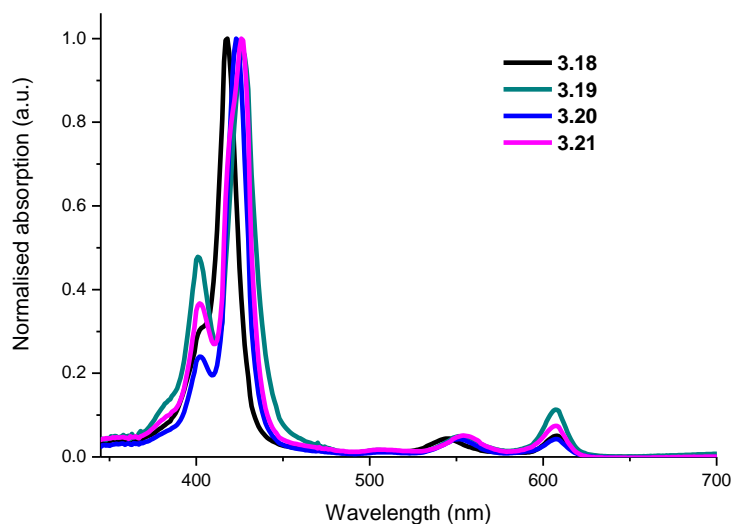


Figure 3.3. Normalised (at the maximum of the Soret band) UV-Visible spectra of dyads and triad in DCM.

Array **3.18** showed a weaker Soret band with a shoulder rather than a separate peak and had the more blue-shifted absorption spectrum compared to the other arrays. This indicates that the meso-substitution may influence the absorption characteristics and thus when one substituent is missing, the Soret band is slightly distinct and blue-shifted compared to the fully meso-substituted porphyrin arrays. Nevertheless, looking into the solvent dependency on the absorption profiles, it is indicative that non-polar toluene has an apparent attenuation on the chlorin-related Soret band intensity (~ 400 nm); whereas in ethanol or DCM the two peaks are separated. This is less clear for **3.18** (Figure 3.4 A) and more evident for dyads **3.20** and **3.21** (Figure 3.4 B, C) and can be attributed to the presence of exciton coupling of the two excited states of the subunits due to the polar solvent.^[436,437]

The respective Q bands of the arrays in the visible region were found between 500 – 610 nm with the last Q_y band being the more intense particularly for the triad system **3.19** due to the two chlorin macrocycles. The metallated porphyrin benchmarks display two Q bands at ~ 540 nm and ~ 580 nm with the latter being weaker,^[434,435] whereas the chlorin displays three Q bands between 510 – 600 nm with higher absorptivity.

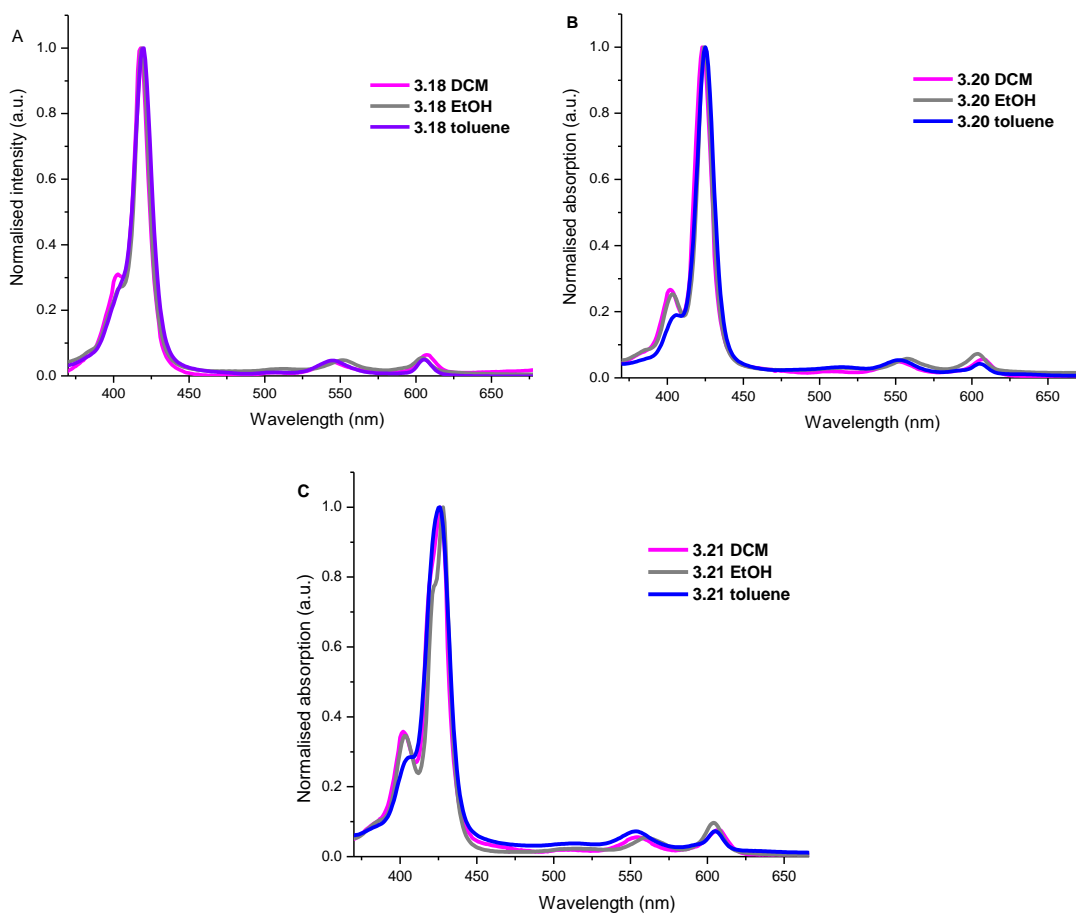


Figure 3.4. Normalised UV-Visible spectra (at the maximum of the Soret band) of dyads in DCM, ethanol and toluene.

Representative spectra of benchmarks and final arrays are collectively presented in Figure 3.5 and Figure A 24. The Q band of the arrays at ~ 540 nm is related to porphyrin and the low-energy transition band at ~ 600 nm is exclusively related to the chlorin $Q_y(0,0)$ peak. However, the absorptivity of the $Q_y(0,0)$ peak of the dyads ($\sim 20,000 \text{ M}^{-1} \text{ cm}^{-1}$) is reduced compared to the chlorin ($\sim 40,000 \text{ M}^{-1} \text{ cm}^{-1}$), reflecting a weak electronic coupling. The respective arrays display a minimal red-shift of 3 – 4 nm of the Q_y band compared to the chlorin benchmark (604 nm), indicating a minimal effect from the porphyrin system. Furthermore, the ratio of the intensity of the Q_y and B bands (Table 3.1) provides a relative measure of the hyperchromic effect on the $Q_y(0,0)$ band showing the following descending order **3.19 > 3.21 > 3.18 > 3.20**.

Therefore, the spectrum of the dyads and triad is essentially the sum of the spectra of the benchmark monomers. Similar observations have been reported in *gem*-dimethyl chlorin-bacteriochlorin phenylethyne-linked arrays. The latter,

similarly to the case herein, displayed a weak electronic coupling between the two moieties, in comparison with the case where a direct ethynyl linker joined the macrocycles and resulted in profound spectral alterations due to the more intense electronic coupling.^[438]

Table 3.1. UV-Visible absorption data of the dyads in dichloromethane.

Compound	λ_{max} (nm) ^a		Q/B ^b
	B bands	Q bands	
3.18	403 (4.89), 418 (5.40)	544 (3.87), 607 (4.06)	0.05
3.19	401 (5.35), 427 (5.64)	504 (4.26), 552 (4.49), 607 (4.76)	0.11
3.20	402 (5.04), 423 (5.67)	551 (4.31), 608 (4.29)	0.04
3.21	402 (5.00), 426 (5.44)	554 (4.15), 607 (4.31)	0.07

^a Values in parentheses: $\log \epsilon$; ^b ratio of the intensities of $Q_y(0,0)$ and Soret bands

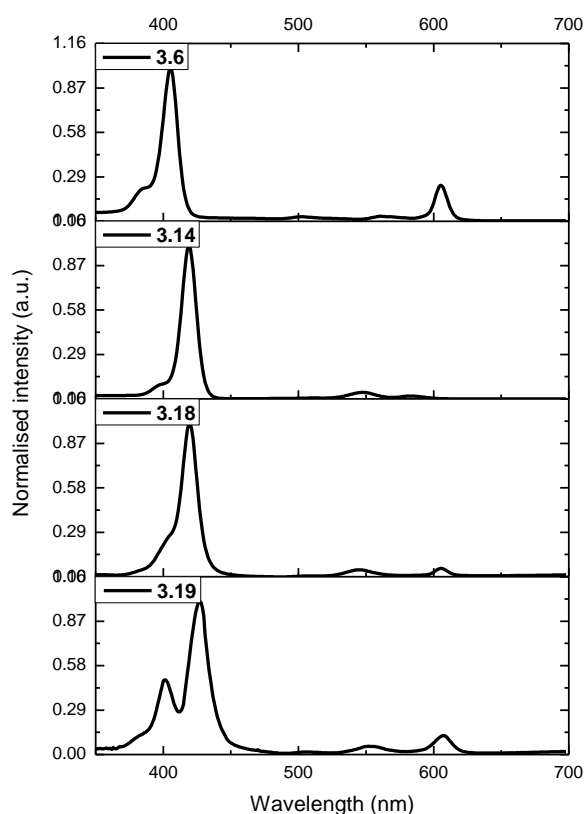


Figure 3.5. Normalised UV-Visible spectra of the chlorin **3.6**, porphyrin **3.14** and the corresponding dyad **3.18** in toluene and triad **3.19** (DCM).

3.3.2.2 Excited state properties

The excited state properties of dyads **3.18**, **3.20** and **3.21** were determined in ethanol and toluene. Fluorescence emission spectra were recorded for all the dyads and the triad, and quantum yields were calculated by using cresyl violet as a reference compound. Additionally, singlet and triplet state lifetimes were determined experimentally for dyads by using time-correlated single photon counting (TCSPC) and nanosecond transient absorption (TA) spectroscopy, respectively.

Fluorescence spectra of the benchmark chlorin and porphyrins along with the dyads in ethanol and toluene are displayed in Figure 3.6 (A, B, C). For triad **3.19** fluorescence was recorded in DCM with a weak signal (Figure 3.6 A). The key photophysical characteristics are summarised in Table 3.2.

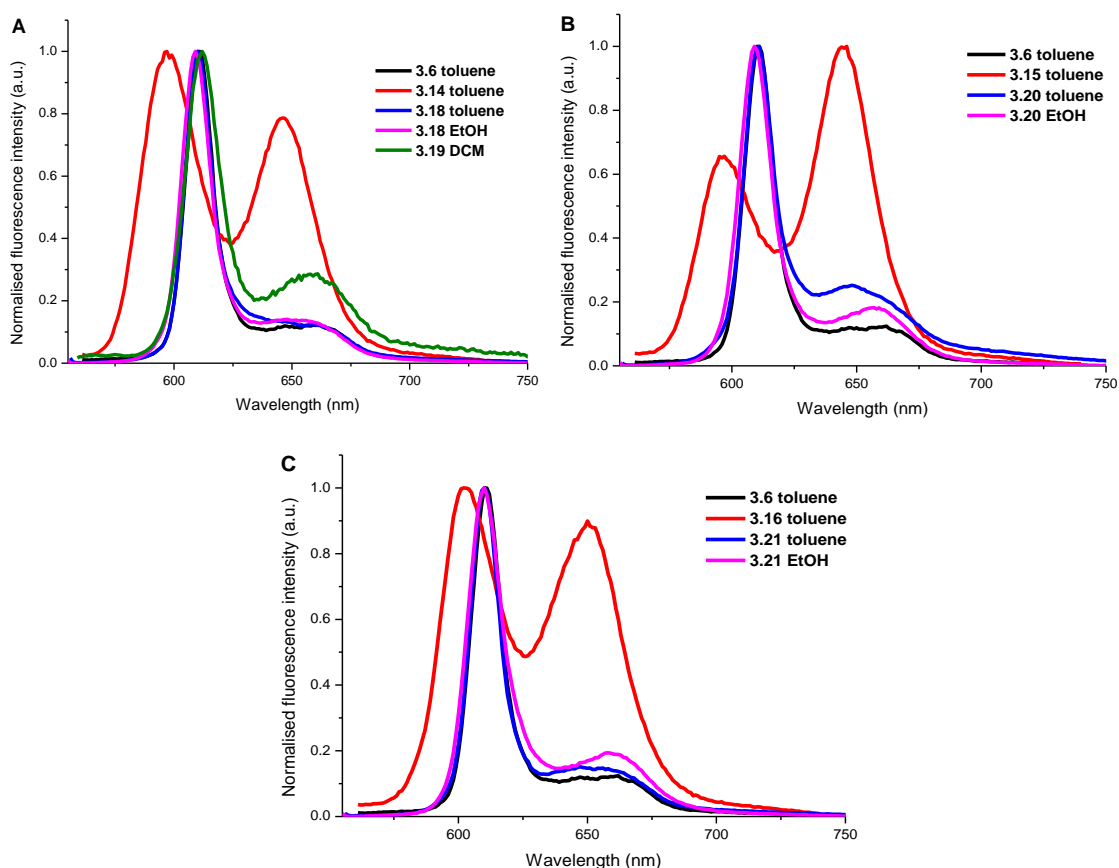


Figure 3.6. Normalised fluorescence emission spectra of the chlorin, porphyrins and the corresponding dyad arrays in toluene, ethanol or DCM ($\lambda_{\text{exc}} = 550 - 560 \text{ nm}$).

Compared to the fluorescence spectra of chlorin and porphyrins benchmarks, the arrays show an identical spectrum to that of the chlorin precursor **3.6**, reflecting the relatively weak electronic coupling between the chromophores in the dyad (in both ground and excited electronic states).^[439] The spectrum is dominated by the $Q_y(0,0)$ band of the chlorin with a shoulder of a vibronic component displaying the mirror image of the absorption spectra. Namely, they displayed a fluorescence peak maximum at ca. 610 nm with the vibronic satellite at ~ 660 nm. Consequently, the fluorescence from the dyads and the triad occurs mainly from the chlorin subunit regardless of whether the porphyrin subunit is preferentially (but not exclusively) excited. In addition, taking into consideration the absorptivity of the dyads at 550 nm *via* the molar absorption coefficients of each subunit (at 550 nm) we determined that ca. 93% of the absorption stems from the porphyrin; hence, the absence of porphyrin emission feature upon excitation at 550 nm characterises the insignificant emission contributed from the porphyrin. These findings indicate the anticipated fast energy transfer from the porphyrin to chlorin subunit in the early times (ps scale) after excitation, which could be further investigated in the future by femtosecond transient absorption spectroscopy.^[440]

Additionally, the Stokes shifts ($\Delta\nu$) between the fluorescence and corresponding absorption maximum were calculated to be in the range of 100 – 170 cm^{-1} (Table 3.2).^[371] The relatively low values suggest a minimal rearrangement of molecular structures in the excited versus the ground states.^[412] Lastly, the singlet state level (S_1) was calculated from the intersection of the normalised absorption (last Q band) and emission spectra. The S_1 value of the borolated porphyrins in toluene was found: 2.10 eV for **3.14** and **3.15**, and 2.08 eV for **3.16**; whereas S_1 of chlorin **3.6** was found 2.05 eV. The experimental values of the dyads in ethanol or toluene were slightly lower: 2.03 – 2.04 eV (Table 3.2); supporting the marginal red-shift (3 – 4 nm) of the electronic absorption spectra (compared to the chlorin benchmark).

Fluorescence quantum yields of the dyads were calculated in ethanol and toluene with cresyl violet as reference compound (Table 3.2). The differences between the solvents were minimal between the range of 0.03 – 0.05. For **3.18** the yield was also determined in methanol and was found 0.02 (Figure A 25 displays the

fluorescence emission spectrum) and for triad **3.19** the corresponding yield in dichloromethane was negligible (<0.01).

Table 3.2. Photophysical properties of porphyrin-chlorin arrays.

	λ_{em} (nm)	$\Delta\nu^a$ (cm ⁻¹)	τ_s (ns)	Φ_f	k_f x10 ⁷ s ⁻¹	k_{nr} x10 ⁸ s ⁻¹	S_1	τ_T (ns)	Φ_Δ^b
3.18*	609	136	1.3	0.03	2.3	7.5	2.04	190 ± 12	0.47*
3.18†	610	108	1.4	0.04	2.9	6.9	2.04	230 ± 13	3.43 [§]
3.19‡	612	135	-	<0.01	-	-	2.03	-	-
3.20*	609	163	1.3	0.03	2.3	7.5	2.04	210 ± 7	0.59*
3.20†	611	176	1.6	0.03	1.9	6.1	2.04	220 ± 10	3.56 [§]
3.21*	610	163	1.6	0.05	3.1	5.9	2.04	220 ± 10	0.76*
3.21†	610	149	1.5	0.04	2.7	6.4	2.04	240 ± 20	3.65 [§]

* Ethanol; † toluene; ‡ DCM; ^a Stokes shift; ^b singlet oxygen quantum yield calculated in ethanol (with Rose Bengal as reference compound) and [§] ratio of Φ_Δ of dyads (in toluene) to Φ_Δ of reference compound (Rose Bengal in ethanol); standard errors (percentage of value) are $\tau_s \pm 5\%$, $\Phi_f \pm 10\%$, $k_f \pm 10\%$, $k_{nr} \pm 10\%$.

In addition, the respective yields of the subunits were determined in toluene. Borylated porphyrin fluorescence quantum yields have not been yet reported elsewhere. Likewise, the chlorin subunit has been investigated; however, the yield in toluene has not been reported. The fluorescence quantum yields of the precursors in toluene were determined as follows: 0.06 for chlorin **3.6**; 0.04 for porphyrin **3.14**; 0.04 for porphyrin **3.15**, and 0.03 for porphyrin **3.16**. Therefore, the emission profile of the dyads is mainly related to the emission of the chlorin subunit but their yield decreases ca. 1.5-fold. Note, that there can be a slight discrepancy when using different reference compounds for calculating the yields. Herein, when 5,10,15,20-tetraphenylporphyrin (H₂TPP) was used as reference in toluene to determine the fluorescence quantum yield of the dyads, these were found as follows: 0.07 for **3.18**; 0.09 for **3.20**, and 0.08 for **3.21**; being slightly higher than the values obtained by using cresyl violet as standard reference (in ethanol). A recent review by Taniguchi *et al.* has listed the different values reported of H₂TPP and the zinc analogue (ZnTPP) denoting the discrepancies due to variation of the experimental conditions across articles from different

groups and different eras (e.g., deaerated or air saturated solutions, diversity of fluorescence reference compounds).^[441]

Singlet excited state lifetimes of the respective dyads were determined in ethanol and toluene by TCSPC and are presented in Figure 3.7 and Figure A 26, respectively. The fluorescence lifetimes of the dyads in both solvents were similar to equal and ranged between 1.3 – 1.6 ns with **3.20** displaying a difference in the lifetime values between ethanol (1.3 ns) and toluene (1.6 ns) (Table 3.2). The dyads exhibit singlet excited state lifetimes similar to those of related chlorin subunits in toluene (e.g., phenyl *gem*-dimethyl chlorin derivative: 1.5 ns),^[358] whilst in ethanol they have slightly longer lifetime than that of the chlorin subunit (0.9 ns in ethanol, see Table 2.4). Conversely, comparing with values of similar porphyrin subunits such as (5,15-diphenylporphyrinato)zinc(II) ($S_1 = 2.16$ eV, $\tau_s = 2.3$ ns, $\Phi_f = 0.03$), or (5,10,15-triphenylporphyrinato)zinc(II) ($S_1 = 2.12$ eV, $\tau_s = 2.3$ ns, $\Phi_f = 0.03$) in toluene;^[442] the dyads display slightly shorter singlet lifetimes and lower S_1 . Thus, upon excitation of the porphyrin, energy flows in high yield to the chlorin and then the resulting excited chlorin can behave as an isolated unit, with almost 99% quenching of the porphyrin constituent emission. Consequently, the radiative and non-radiative rate constants were determined (equations: $k_f = \Phi_f / \tau_s$, $k_{nr} = (1 - \Phi_f) / \tau_s$). The radiative rate (fluorescence) and non-radiative decay rates (IC, ISC) are of the order of 10^7 s⁻¹ and 10^8 s⁻¹, respectively.^[440]

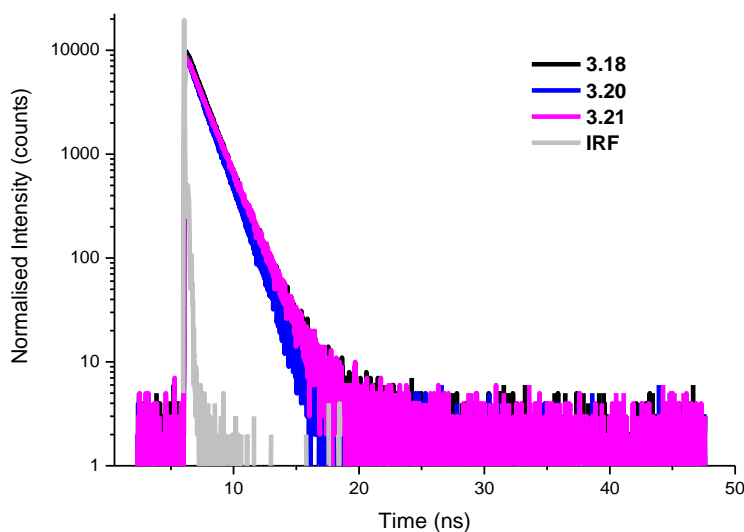


Figure 3.7. Fluorescence lifetime decays of the dyads in ethanol; $\lambda_{exc} = 425$ nm; $\lambda_{det} = 610$ nm.

Since the formation of triplet excited states is crucial in PDT, nanosecond transient absorption (TA) spectroscopy was employed to determine whether a triplet excited state forms upon photoexcitation in ethanol or toluene. All porphyrin-chlorin dyads displayed triplet excited state lifetimes on the order of ~ 200 ns. Representative spectra of each dyad are shown in Figure 3.8 and all spectra obtained are displayed in Figure A 27 – Figure A 33. The relevant triplet excited state lifetimes are summarised in Table 3.2. Similarly to the ethanolic solution, the triplet lifetime of **3.18** in methanol was 200 ± 20 ns (Figure A 28). It can be noted that porphyrin-chlorin dyads have a slightly longer triplet lifetime in toluene than in ethanol; hence, the polarity can marginally alter their triplet photophysical properties.

The most important feature deduced from TA spectra is that the ground state bleaching of the arrays **3.18** and **3.20** is mainly ascribed to the chlorin moiety at ~ 400 and 600 nm with a weak contribution of a neighbouring ground state bleaching at ~ 430 nm. Surprisingly, the TA spectra of **3.21** showed a second intense band at ~ 430 nm that can be ascribed on the porphyrin constituent along with an appearance of a weak feature at ~ 580 nm. This indicates that in the triplet excited state both the porphyrin and chlorin subunits in **3.21** are ground state bleached and they are interacting with each other; whereas in **3.18** and **3.20** chlorin is the dominant triplet excited species. Therefore, we can denote that the porphyrin substitution can alter the profile and looking jointly at the LUMO (Figure 3.10) it is evident that there is a higher electron delocalisation over the molecule, which can occur likewise on the triplet excited state. The bulky ethylpropyl group of array **3.21** influences the outcome of the photoexcitation in a way that the singlet absorptivity at the porphyrin subunit is higher, therefore changes the triplet state profile resulting in a more intense ground state bleaching (Figure 3.8 C).

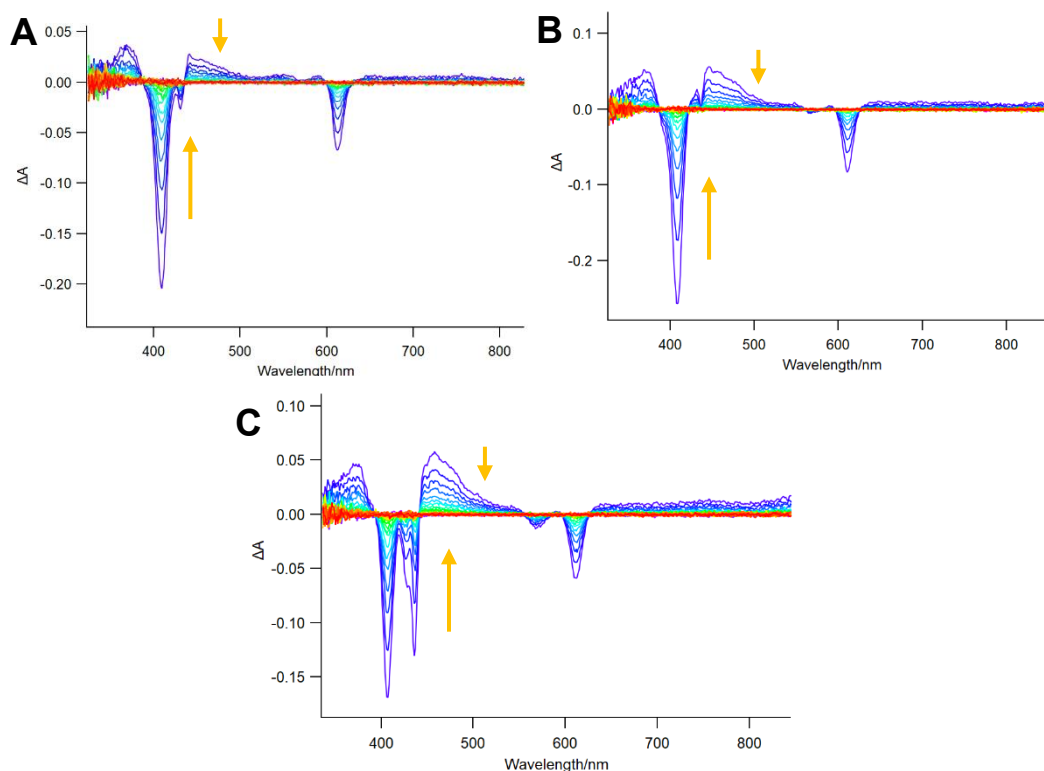


Figure 3.8. TA spectra of **3.18** in toluene (**A**); **3.20** in ethanol (**B**), and **3.21** in ethanol (**C**) after excitation at 604 nm; ambient conditions; $t_{inc} = 80$ ns; arrows pointing from blue to red colour show the decay from the maximum intensity in the successive steps respectively.

Additionally, looking at the TA features of the dyads in different solvents (toluene or ethanol) there is no significant alteration on the obtained spectra for **3.18** and **3.20** regardless exciting at 550/560 nm (excitation of both subunits) or at 604 nm, which can be of chlorin mainly, denoting that the chlorin triplet state is dominant. However, in the case of **3.21**, there is a distinct difference in the ground state bleaching between 400 – 450 nm in toluene and different excitation wavelengths. Exciting both chlorin and porphyrin subunits at 560 nm results in ground state bleaching (Figure 3.9, A) stemming from both chlorin and porphyrin; however, the porphyrin triplet feature is attenuated when the dyad is selectively excited in the chlorin subunit at 604 nm (Figure 3.9, B). This finding supports that in **3.21** apart for a fast energy transfer in the singlet state, a triplet energy transfer can occur and is more apparent in toluene as solvent. To unveil how the lowest electronic excited state evolves to the nanosecond timescale, ultrafast femtosecond TA (fs-TA) spectroscopy should be employed in the future.

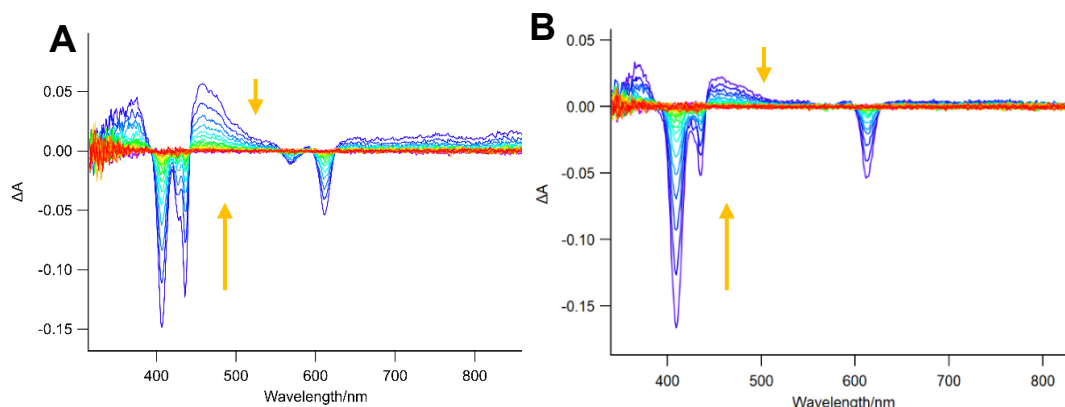


Figure 3.9. TA spectra of **3.21** in toluene after excitation at 560 nm (**A**) or 604 nm (**B**); ambient conditions; $t_{inc} = 80$ ns; arrows pointing from blue to red colour show the decay from the maximum intensity in the successive steps, respectively.

Complementary TD-DFT calculations were performed for the porphyrin-chlorin dyads (**3.18**, **3.20** and **3.21**). Hybrid B3LYP functional,^[387,388] and a 6-31G* basis set in the gas phase were used for the ground state (S_0) geometry optimisation, the calculation of the excited singlet (S_1) and triplet (T_1) states, and visualisation of the respective molecular orbitals (MOs). The respective MOs and the predicted electronic distribution showed that the electron localisation is ambiguous with an important overlap between porphyrin and chlorin (Figure 3.10). Looking at the changes within the energies of the frontier MO between the arrays there are alterations related to the introduction of two or three substituents. The ethylpropyl groups and the phenyl group of dyad **3.21** cause a substantial destabilisation of the HOMO-1, a small stabilisation of the HOMO and a lesser destabilisation of the LUMO and the LUMO+1 when compared to array **3.18**. A similar trend in the HOMOs appears between **3.20** and **3.18** whereas LUMO has no difference and LUMO+1 displays a small stabilisation. Moreover, at the HOMO-1 and LUMO+1 the electron distribution localises also in the meso phenyl moieties whilst in the ethylpropyl electron distribution is marginal.

Hence, the energy gap between the S_1 of the porphyrins and the S_1 of the chlorin benchmark is small (difference of 0.05 eV); thus, along with the MOs representation we can presume that energy can flow fairly within the constituents and their HOMO/(-1) and LUMO/(+1). Additionally, all the arrays have considerable electron density in HOMO-1 and LUMO within the phenylene linker which can indicate the energy flow between the two units upon excitation. As

mentioned before, a possible energy transfer from porphyrin to chlorin should be considered and this can occur from HOMO-1 to LUMO/LUMO+1 transitions. As derived from the optimised geometries, the dihedral angle between the chlorin and porphyrin subunit was found to be 1.8° and 1.3° in **3.18** and **3.20** arrays, respectively, whilst for **3.21** it was 44.1°. In the optimised singlet excited state (S_1) there was an increase of this angle with **3.21** showing a dihedral angle 57.9° (+13.8°) while **3.18** and **3.20** showed a marginal increase 3.4° (+1.6) and 5.1° (+3.8°), respectively. Presumably, there is an increased steric hindrance induced by the ethylpropyl groups in the porphyrin subunit, which leads to a ruffled conformation of the macrocycle as it was previously reported by Senge *et al.*^[443] Lastly, the triplet excited energy level was predicted as 1.53 eV which is above the singlet oxygen (0.98 eV); sought-after for singlet oxygen generation.

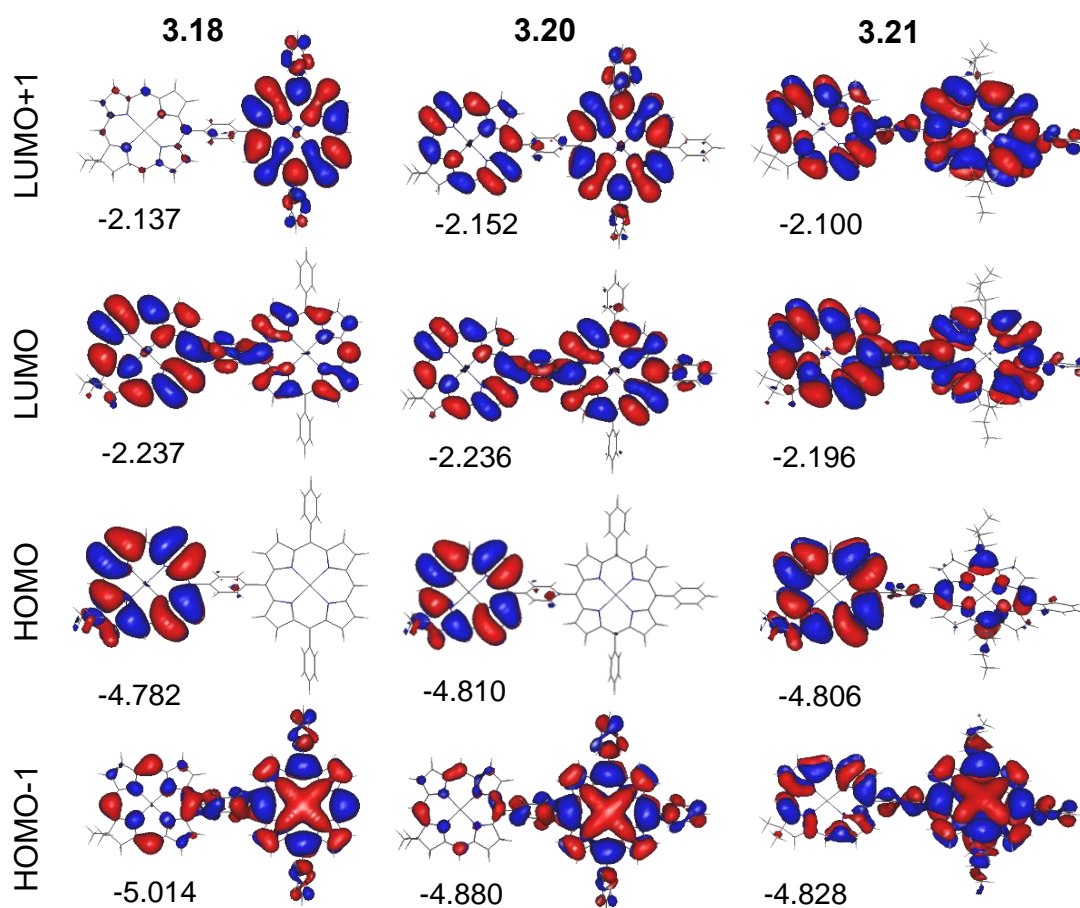


Figure 3.10. Molecular orbital energies and electron-density distribution of the dyads obtained from TD-DFT calculations; B3LYP/6-31G*.

3.3.2.3 Singlet oxygen phosphorescence and quantum yield

Singlet oxygen was determined by its luminescence emission at 1275 nm with the use of an InGaAs NIR detector. The singlet oxygen quantum yield (Φ_{Δ}) in ethanol was calculated by using Rose Bengal as reference. Representative emission spectra of the singlet oxygen luminescence are given in Figure 3.11 and the corresponding values are shown in Table 3.2.

The capability of a system to generate singlet oxygen relies on the triplet excited energy level, which should be higher than the lowest singlet state of molecular oxygen (0.977 eV). The calculated desired triplet energy level (1.54 eV) and moderate triplet lifetimes for the dyads **3.18**, **3.20** and **3.21** indicated towards moderate singlet oxygen quantum yields. As expected, the arrays exhibit singlet oxygen quantum yields in ethanol ranging between 0.5 and 0.7 and the ascending order is as follows: 0.47 for **3.18** < 0.59 for **3.20** < 0.76 for **3.21**. Trying to find a suitable reference compound in toluene was challenging and therefore the ratio was calculated as a relative measurement confirming the same trend as above (Figure A 34). Compared to the chlorin subunit (~ 0.90 in ethanol, Table 2.5) there is a reduction in the singlet oxygen efficiency.

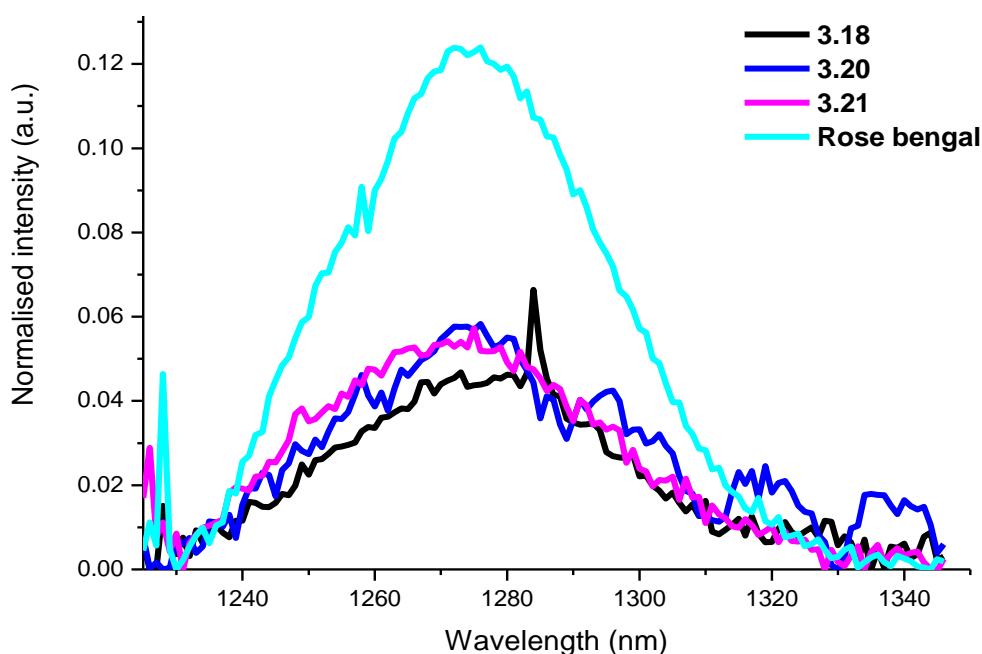


Figure 3.11. Singlet oxygen emission spectra of dyads and Rose Bengal in ethanol; $\lambda_{\text{exc}} = 550 \text{ nm}$; 10 s integration time.

Lastly, looking collectively at the values in Table 3.2 we can summarise, as expected, that the meso-substituents can affect the photophysical outcome. Array **3.18** with two phenyl moieties exhibits shorter singlet and triplet state lifetimes and lower singlet oxygen quantum yield in comparison to arrays **3.20** and **3.21**. Arrays that bear three substituents in the porphyrin periphery, exhibit slightly longer lifetimes and higher singlet oxygen quantum yield.

3.3.3 *In vitro* evaluation of porphyrin-chlorin dyads

As shown in Chapter 2, zinc chlorins are capable of singlet oxygen generation and exhibit high phototoxicity as they efficiently internalise into cells. The 4-bromophenyl *gem*-dimethyl chlorin **Zn1 (3.6)** showed high phototoxicity at safe and low concentrations ($IC_{50} = 0.31 \mu\text{M}$, 1 J cm^{-2}). The aim of this study was to screen the potential phototoxic effect of the porphyrin-chlorin dyads, since they generated singlet oxygen as well. Therefore, **3.18**, **3.20** and **3.21** were used for the *in vitro* studies with the aim to elucidate their phototoxicity against CT26 mouse colon carcinoma cell line.⁷

In order to determine the dark toxicity, CT26 cells were incubated with the indicated dyads for 24 h with final concentrations from 1.25 to 40 μM . Cell survival was accessed by resazurin assay (Alamar blue).^[391] Neither of the dyads showed any dark toxicity at the corresponding range of concentrations (Figure 3.12, A). Consequently, keeping the same concentrations, phototoxicity studies were conducted. CT26 were incubated with the dyads for 24 h, followed by a washing step and irradiation. Cells illumination was performed by using a visible broadband lamp (LED, 400 – 700 nm) and a correction factor was applied in order to deliver accurate light doses (L.D.) of 0.5 J cm^{-2} , 1 J cm^{-2} and 2 J cm^{-2} .^[393] Cellular viability was evaluated 24 h post-irradiation using resazurin reduction assay. Results are shown in Figure 3.12 (B, C and D). In comparison to the chlorin benchmark which displayed great phototoxic effect at $0.5 - 1 \text{ J cm}^{-2}$, herein it is apparent that the dyads do not exhibit any phototoxicity upon irradiation with L.D. in the range of $0.5 - 2 \text{ J cm}^{-2}$. Presumably, the dyads do not penetrate the cell membranes due to the large molecular weight of the systems and the reduced amphiphilicity. An effort to assess their cellular uptake, CT26 mouse colon carcinoma cancer cells were incubated with the indicated dyads at 5 and 10 μM , for 24 h. After a washing step, fluorescence was measured by flow cytometry. The fluorescence was determined upon excitation with 405 nm laser and detection was performed by using 615/24 nm filter. The obtained signal was weak (Figure 3.13), and along with the relatively low fluorescence quantum yield

⁷ The experiments were conducted during a training secondment in the photobiology group at the University of Coimbra, under the supervision of Dr. Lígia C. Gomes-da-Silva and the assistance of Dr. Fábio Schaberle.

of the respective dyads, it is clearly difficult to draw any conclusions on the cellular uptake result.

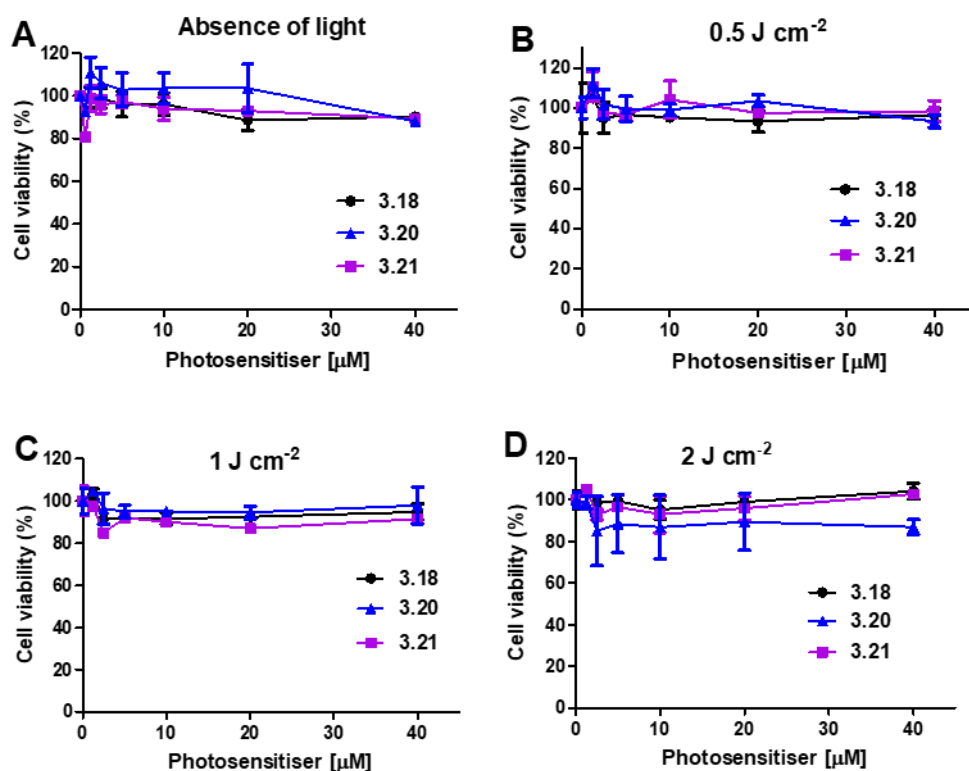


Figure 3.12. Cell viability of CT26 cells post incubation (24 h) with **3.18** (black), **3.20** (blue) and **3.21** (purple) in the absence of light (**A**); followed by irradiation with L.D. of 0.5 J cm^{-2} (**B**); 1 J cm^{-2} (**C**); 2 J cm^{-2} (**D**); results presented are a single representative experiment.

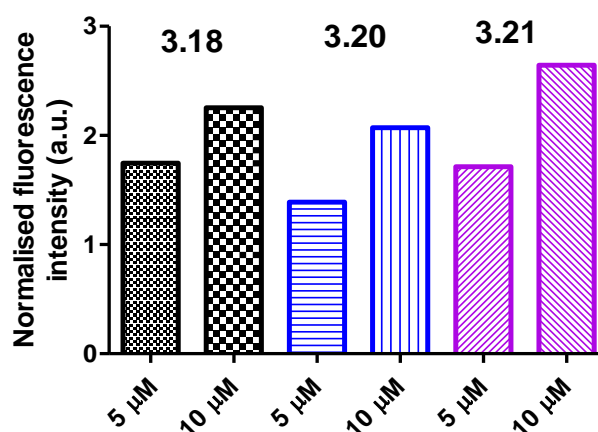


Figure 3.13. Cellular uptake of the dyads **3.18** (black), **3.20** (blue), and **3.21** (purple) evaluated by flow cytometry. Values are normalised against the signal of the untreated cells; results presented are a single representative experiment..

3.4 Conclusions and Future Work

In this study we utilised a potential photosensitiser chlorin (**3.6**) which displayed excellent phototoxicity in low concentrations and high singlet oxygen yield as a building block for dyads. We assessed the modifications *via* standard palladium catalysed Suzuki reaction to create arrays linked with a 1,4-phenylene unit. As a result, three new dyads (**3.18**, **3.20**, **3.21**) and one triad (**3.19**) were obtained and fully characterised by NMR spectroscopy, mass spectrometry, UV-Vis absorption and fluorescence emission spectroscopy. Additionally, the excited states were evaluated by TCSPC and transient absorption spectroscopy and the yield of singlet oxygen generation was determined. The insolubility of chlorin-porphyrin-chlorin triad prevented further photophysical characterisation. Ultimately, *in vitro* evaluation was employed to elucidate whether the phototoxic effect of the constituent chlorin moiety is retained.

The excited state features resembled the chlorin constituent indicating that a fast porphyrin to chlorin energy transfer occurs upon photoexcitation. Additionally, the ethylpropyl substitutions in array **3.21** led to an interesting delocalised triplet excited state. TD-DFT calculations provided a supplementary study of the excited states for the arrays, predicting the electron distribution within the linker and the alteration in the conformation due to the different substitution. The dyads maintained moderate triplet excited lifetimes both in toluene and ethanol which resulted in efficient singlet oxygen generation with dyad **3.21** displaying the higher singlet oxygen production. However, the *in vitro* evaluation was not as expected, regardless of the absence of dark toxicity; dyads did not exhibit any phototoxicity with light doses up to 2 J cm^{-2} , possibly due to their high molecular weight and a low permeability into the cells.

For future reference, the biological properties could be improved by incorporation in nanosystems since the arrays are not phototoxic but have moderate singlet oxygen quantum yield and they are triplet generators. These factors probably render the porphyrin-chlorin systems interesting towards other directions, such as potential light-harvesting materials or application in a two-photon absorption spectroscopy. For further investigation about how the lowest electronic excited

state evolves on an ultrafast to nanosecond timescale, femtosecond transient absorption (fs-TA) measurements should be employed in the future.

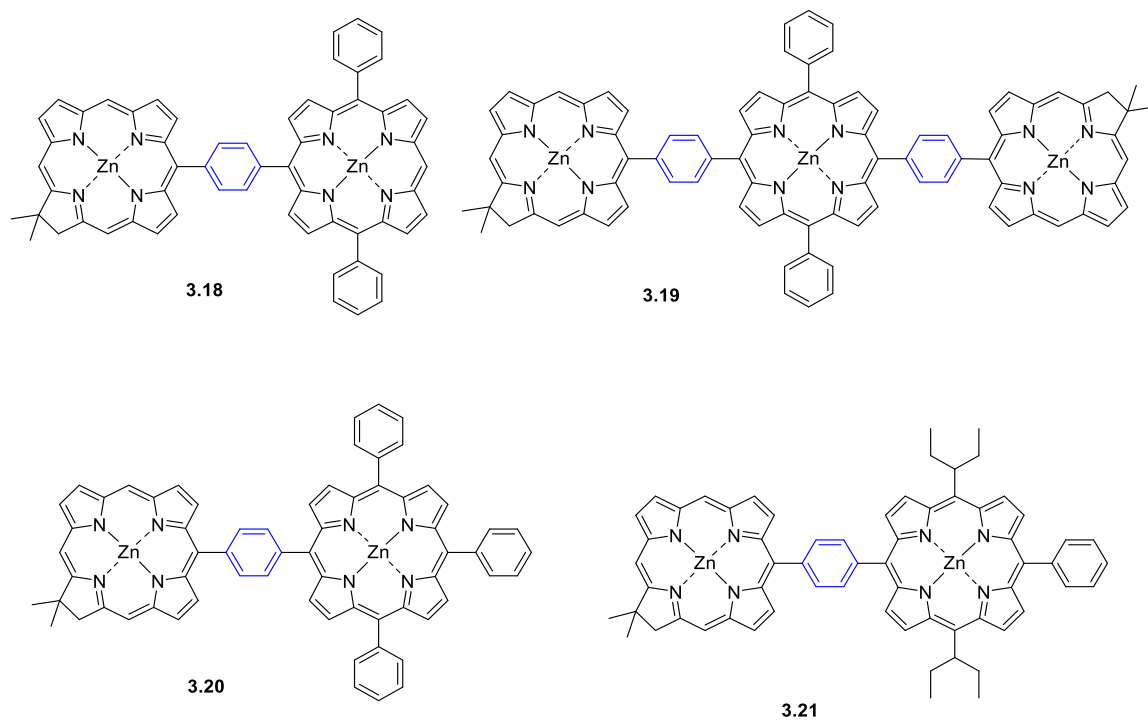


Figure 3.14. Chemical structures of the porphyrin-chlorin dyads and chlorin-porphyrin-chlorin triad obtained.

Chapter 4: Tris(dipyrrinato)aluminium(III) Complexes as Potential Photosensitisers in Photodynamic Therapy

“You must wish to consume yourself in your own flame: how could you wish to become new unless you had first become ashes”

~ Friedrich Nietzsche ~

4.1 Introduction

Aluminium belongs to Group 13 elements of the periodic table together with boron, gallium, indium, and thallium. Aluminium is the third most abundant element found in the earth's crust (8.3% by weight) and is exceeded only by oxygen (45.5%) and silicon (25.7%).^[444] It was first observed by the father of modern chemistry A. Lavoisier in 1782, named by H. Davy in 1808, and isolated by H. C. Ørsted in 1825.^[444,445] Commonly, it has a high affinity to oxygen atoms and is usually found in the form of oxides or hydroxides, with bauxite being the main source. Importantly, metallic aluminium, its oxides, and aluminium salts are not presenting either genotoxicity or carcinogenicity and the biological tolerance value for occupational exposure is: 50 µg of aluminium/gram of creatinine (urine).^[446,447]

Aluminium finds a wide range of uses in material, pharmaceutical sciences, and food industry. Organometallic complexes containing aluminium are used as catalysts in reactions and aluminium plays an important role in the vaccine production as an adjuvant.^[448] Moreover, it is a main ingredient in antacid drugs that contain aluminium hydroxide along with the magnesium hydroxide neutralising the acid in gastric secretions; resulting in relief of indigestion, gastro-oesophageal reflux disease (heartburn) and healing peptic ulcer diseases. Also, it is widely used as construction material in electrical devices, conductor in cables and for food preservation (canning and packaging).^[447,448] An example of

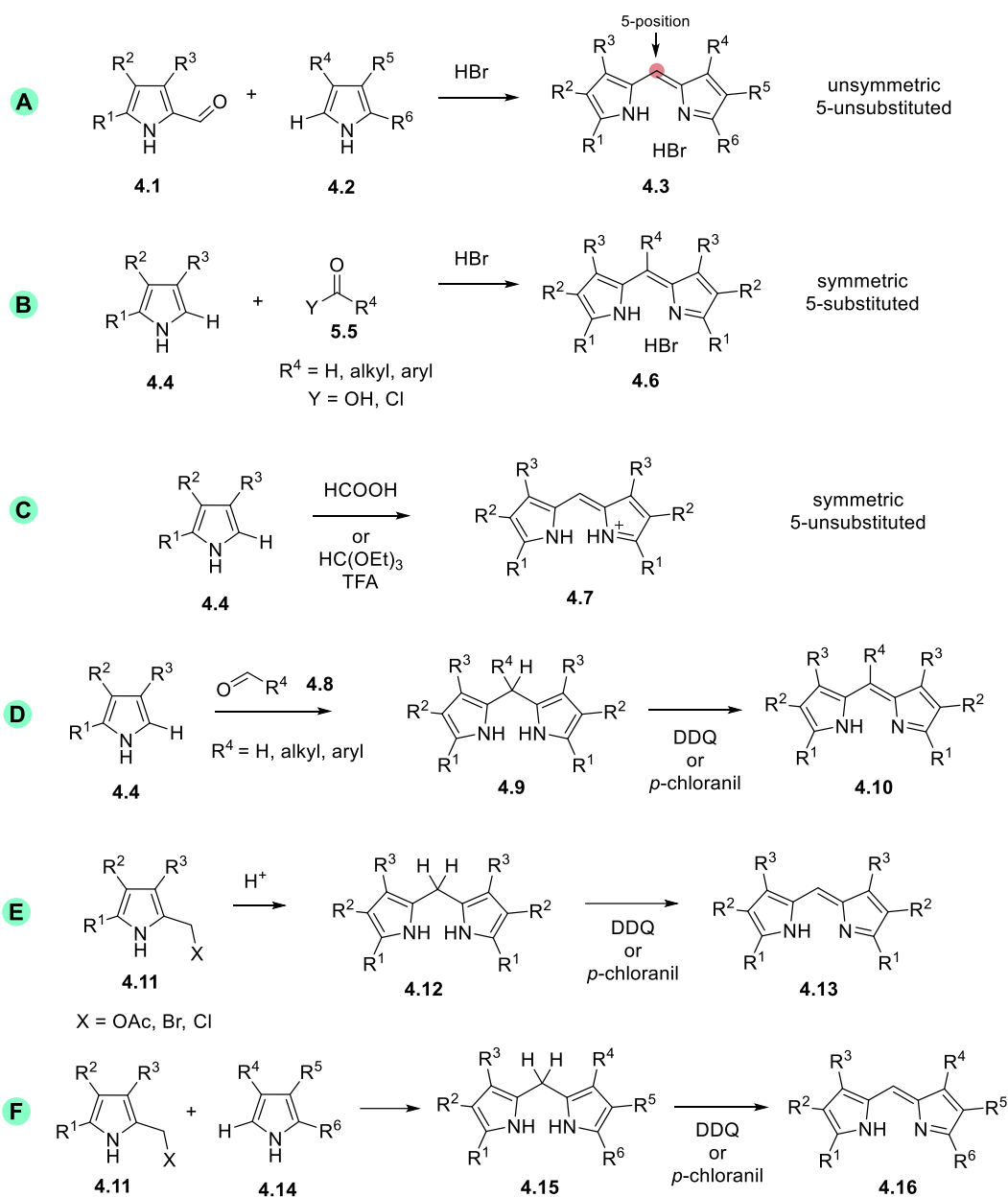
aluminium drugs in PDT is a sulfonated aluminium phthalocyanine (Photosens[®]), which has been clinically approved in Russia for the treatment of lung, liver, breast, skin and gastrointestinal cancer.^[68]

Dipyrins have been studied widely since the beginning of 20th century and H. Fischer is considered a pioneer in dipyrin complexes chemistry.^[449] Selecting a suitable synthetic method for dipyrins varies according to the desired product, while the number and nature of substituents can be critical. The presence of substituents on the skeleton of the dipyrin prevents possible oligomerisation and lowers the susceptibility to attack by electrophiles or nucleophiles enhancing the stability of the product.^[192,450] The synthesis of dipyrins can be achieved mainly *via* pyrrole condensation (Scheme 4.1, A, B, C) or *via* dipyrromethane (DPM) oxidation (Scheme 4.1, D, E, F).^[451,452] Specifically, the synthesis of unsymmetric 5-unsubstituted dipyrins involves the acid-catalysed condensation of two different pyrrolic components (2-formylpyrrole and 2-unsubstituted pyrrole), the so-called MacDonald coupling (Scheme 4.1, A).^[453] Symmetric 5-substituted dipyrins have been prepared by condensation of carboxylic acid or acid halide and two equivalents of 2-unsubstituted pyrrole (Scheme 4.1, B).^[454,455] Next, synthesis of symmetric 5-unsubstituted dipyrins can be performed by using two equivalents of 2-unsubstituted pyrrole in a strong acidic environment (mixture of acids) (Scheme 4.1, C).^[456]

Alternatively, DPM oxidation can yield the corresponding dipyrin by using oxidising agents such as DDQ or *p*-chloranil. Three different pathways are outlined in Scheme 4.1 (D, E and F).^[150,457] Generally, the reaction of two equivalents of 2-unsubstituted pyrrole with an aldehyde yields symmetric dipyrins (Scheme 4.1, D) and the acidic self-condensation of an 2-acyl substituted pyrrole yields 5-unsubstituted symmetric dipyrins (Scheme 4.1, E).^[458] In addition, reaction of a 2-acyl substituted pyrrole with a 2-unsubstituted pyrrole yields unsymmetric 5-unsubstituted dipyrins (Scheme 4.1, F).^[451]

Dipyrins are well-known for their ability as ligands in coordination chemistry, as they form isolable complexes with a range of metal ions.^[451] Upon deprotonation, the anionic dipyrinato moiety coordinates with a metal centre and forms metal chelates in the presence of metal salts. Depending on the metal employed,

dipyrinato complexes can bear one or more ligands and are classified as homoleptic when the ligands are identical or as heteroleptic when ligands are different.^[163,451,452]



Scheme 4.1. Synthetic procedures for dipyrins.

Dipyrinato complexes with elements from Group 13 have been widely investigated in photomedicine, with boron complexes being the most famous chelates. Particularly, the so-called BODIPY dyes, which consist of one dipyrin ligand with a boron centre, have received considerable attention due to their relatively facile preparation and functionalisation.^[62,459] Their advantageous emissive features direct the focus towards their application as fluorescence

probes and sensors finding use in optoelectrical devices and bioimaging.^[62,460] Likewise, gallium and indium complexes can be coordinated with dipyrin ligands forming homoleptic or heteroleptic tris(dipyrinato) complexes.^[152,159,228,461] Frequently, dipyrin complexes, in comparison with the boron common alternatives, are considered as poor emissive chelates; however, this is not a hard-and-fast rule.^[451] Recently, Wan *et al.* reported the synthesis of the stable monomeric gallium chelate **4.17**, a direct analogue of BODIPYs, by using an intermediate lithium-dipyrin salt. The gallium complex resembled the highly fluorescence profile and the photophysical properties of the BODIPY dyes along with a similar tetrahedral geometry.^[462] Note that the tris(dipyrinato)gallium(III) complex **4.18** showed poor fluorescence emission ($\Phi_f = 0.024$ in hexane),^[152] whilst the monomeric complex **4.17** had highly luminescent properties ($\Phi_f = 0.82$ in DCM, 0.91 in toluene).^[462]

Factors that play a key role and affect the absorption and emission properties include the metal centre but also the number and nature of the coordinated ligands. Sazanovich *et al.* showed that by altering the 5-substitution and by increasing the size of the aryl group in zinc bis(dipyrins), the non-radiative decay could be diminished, with a considerable increase in the fluorescence quantum yield.^[156] Similarly, the homoleptic tris(dipyrinato)indium(III) complexes **4.19** and **4.22** were emitting less ($\Phi_f = 0.074$ in hexane and $\Phi_f = 0.028$ in toluene, respectively) than the heteroleptic analogues **4.20** and **4.21** (Figure 4.1), which exhibit stronger fluorescence features ($\Phi_f = 0.41$ and $\Phi_f = 0.34$ in toluene, respectively).^[152,159] The UV-Vis absorption spectra of complexes **4.20**, **4.21** and the **4.22** had similarities which evidence the exciton coupling between the ligands, resulting in a band splitting of the $^1\pi - \pi^*$ transitions. Namely, heteroleptic **4.20** and **4.21** displayed two distinct bands at ~ 480 and ~ 580 nm corresponding to $^1\pi - \pi^*$ transitions; whereas the absorption of the homoleptic **4.22** was broader at $\sim 520 - 590$ nm.

With reference to dipyrins and aluminium as a coordination centre only little advances and few reports have been made to date. The introduction of bulky aryl groups at the α -position of the pyrrole ring results in a steric hindrance which stabilise the reactive $Al(III)$ centre towards the formation of the mono dipyrin aluminium complexes. Giannopoulos *et al.* described the synthesis of monomeric

dipyrinato aluminium (AlDIPY) complexes bearing mesityl substituents at the α -pyrrolic positions **4.23** – **4.33** (Figure 4.2).^[463,464]

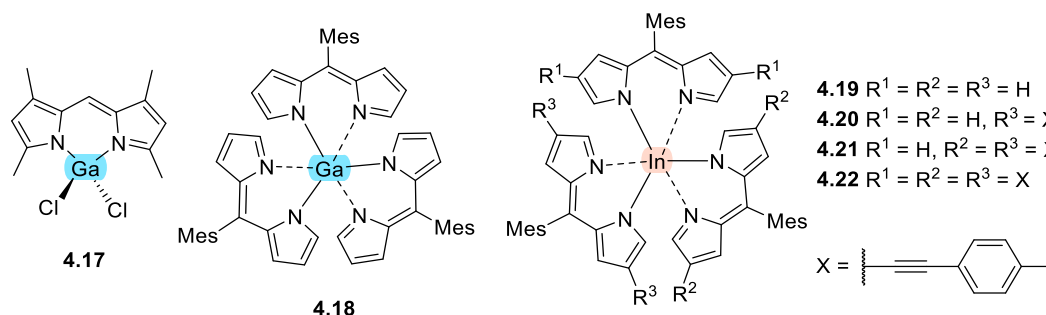


Figure 4.1. Gallium and indium dipyrinato complexes reported in the literature.

Whilst the photophysical properties were beyond the aim of the work, it was noted that compound **4.23** was fluorescent (green) whilst complexes **4.24** – **4.26** were non-emissive. Complexes **4.24** – **4.26** were stable to air or moisture while **4.23**, **4.27** and **4.28** were moisture sensitive, with dihydride **4.23** resulting in the formation of oxo-bridged aluminoxane **4.33** upon reaction with water. Ikeda *et al.* reported N_2O_2 -type aluminium dipyrins which displayed an absorption maximum at ca. 600 nm and exhibited moderate to high fluorescence quantum yields. Specifically, the mesityl derivative showed higher fluorescence quantum yield than the phenyl derivative due to the restricted rotation of the mesityl group (Φ_f of **4.34** = 0.23 and Φ_f of **4.35** = 0.72 in toluene:methanol, 99:1).^[156] The aluminium coordination in N_2O_2 -type AlDIPY complexes adopted a square planar geometry, which allowed for extra octahedral coordination. Their fluorescence intensity and wavelength significantly changed upon the addition of zinc salts and the consequent formation of heterometallic Al(III)-dipyrinato-Zn(II) adducts **4.36** – **4.38** (Φ_f of **4.36** = 0.55, Φ_f of **4.37** = 0.56, Φ_f of **4.38** = 0.83 in toluene:methanol, 99:1) (Figure 4.2).^[170] This was probably caused by the enhanced rigidity of the dipyrin framework after chelation, reducing the energy loss *via* radiationless decay. Lastly, another report of aluminium dipyrin complexes investigated the binding ability of AlDIPY complexes with alkaline earth ions (Ca^{+2} , Mg^{+2} , Ba^{+2} , Sr^{+2}). Both monomer [**4.39**·(CH₃OH)·(H₂O)] and dimer [**4.40**·(CH₃OH)₄] aluminium complexes worked as selective receptors for alkaline earth metal ions *via* selective binding in aqueous media.^[465]

It has been demonstrated that lacking of a pyrrolic substitution at α -positions allows for the formation of 1:3 metal to ligand complexes of trivalent metals.^[175,466] The common oxidation state of aluminium is +3; hence, in the absence of α -substitution the complex can adopt an octahedral coordination geometry. A Japanese patent by Toguchi *et al.*, 20 years ago, reported the structures of tris(dipyrinato)aluminium(III) complexes **4.41** – **4.44** (Figure 4.2). Apart from this patent, which was directed for an application towards optoelectronics, there is no chemical neither photophysical characterisation of such complexes.^[467]

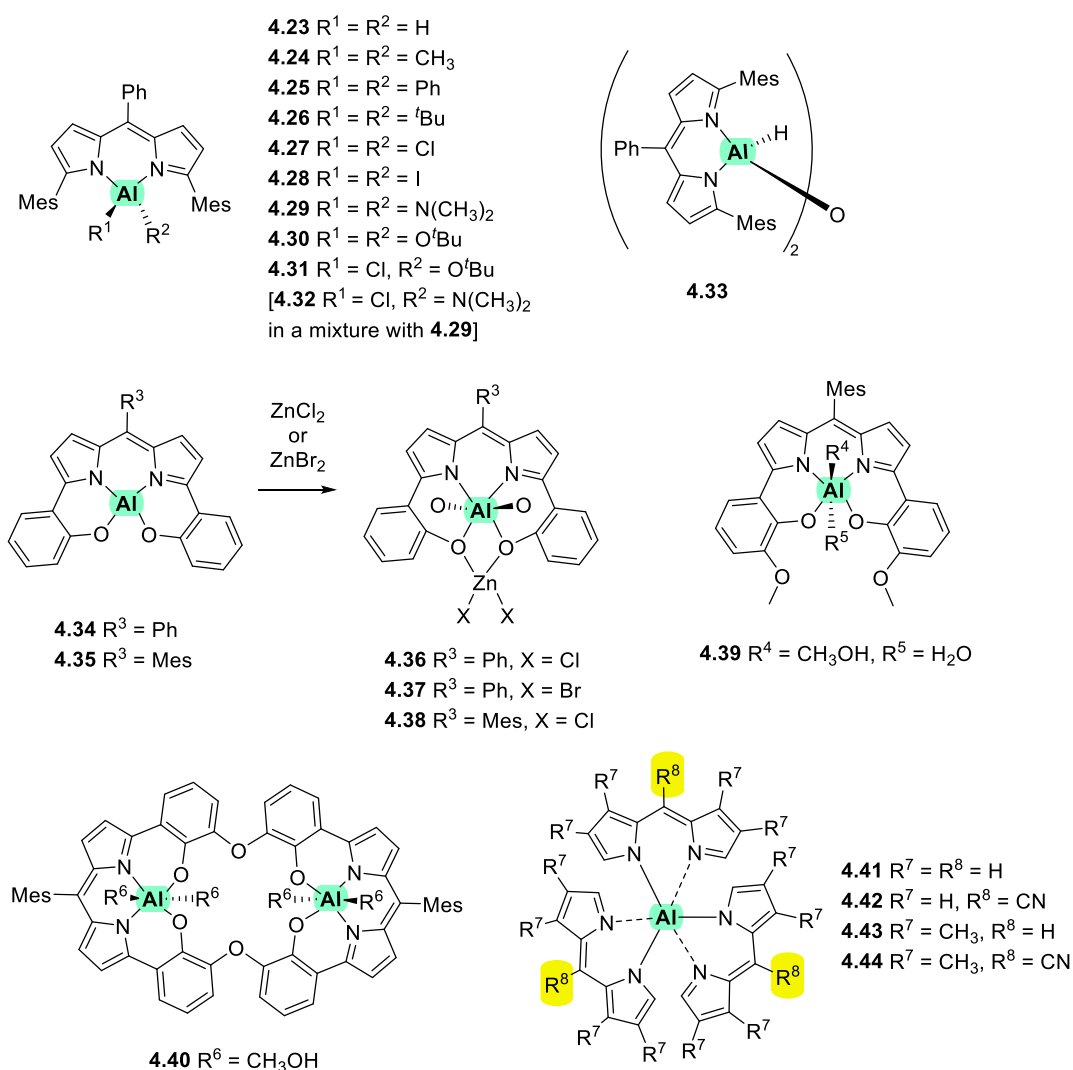


Figure 4.2. Dipyrin and aluminium coordinated complexes reported in the literature.

As mentioned, the metal centre, the substitution, and bulkiness of the ligand(s) can influence the optical properties. Another factor that contributes and alters the emissive features of the complexes is the solvent. Upon photoexcitation, and after the population of the singlet excited state (S_1), certain systems can undergo

charge transfer (CT) processes and form charge-separated (CS) states. This CT state is a long-lived state, originates from a intramolecular charge separation process, and is highly dependent on the polarity of the medium (solvent effect). From there, the photogenerated states can recombine back to singlet ground state (S_0), repopulate the singlet excited state (S_1), or populate the triplet excited state (T_1) *via* charge recombination of the intramolecular charge transfer (ICT) state or otherwise called symmetry breaking charge transfer (SBCT) process.^[187] This characteristic can be advantageous with regards to a photobiological and photodynamic application.

In the dipyrin complexes the electronic configurations after excitation can be located on the metal, within a single ligand (intra-ligand) or involve a charge transfer (CT) state between the ligands. It has been shown for zinc dipyrinato complexes that in non-polar solvents the total energy of the ICT state lies above that of the first excited state (local excited state), thus the S_1 state will undergo ordinary ISC to the triplet state (competing with IC). By increasing the polarity of the environment, the ICT state is stabilised through dipole-dipole interactions with the solvent molecules. Therefore, it is preferably populated, giving access to a new T_1 state *via* ICT state recombination. Consequently, instead of undergoing regular ISC, the complex forms the charge separated states and reverts to the triplet state *via* the ICT states. Conversely, moving to greater polarity, the ICT state stabilisation can be such that the ICT state behaves as an energetic trap and can reduce the triplet yield.^[179,183] Similar solvent effects have been described in heavy atom-free BODIPYs where in polar solvents they form CT states *via* photoinduced electron transfer (PeT) process.^[242,468,469] Since in PDT one of the expectations is the singlet oxygen or ROS production *via* triplet formation, such systems could be applied as triplet sensitisers.^[470]

Lastly, as described in section 1.5.2, Gütsche *et al.* evaluated the phototoxicity of indium(III), iron(III), and gallium(III) tris(dipyrinato) complexes bearing pentafluorophenyl moieties with alcohols and thiocarbohydrates. They tested the phototoxicity against various tumour cell lines and against the bacterium *S. aureus*. Most promising phototoxic results were exhibited by the glycosylated analogues of tris(dipyrinato)gallium(III) complexes ^[228]

4.2 Objectives

Metal coordinated complexes play a pivotal role in medicinal chemistry, as well as in photodynamic therapy (PDT), and they have gained a lot of attention over the past years (e.g., ruthenium, boron, gallium, or iridium complexes). The current clinically approved photosensitisers (PSs), mainly porphyrinoids (e.g. Foscan, Tookad Soluble), for anti-cancer PDT still encounter drawbacks (e.g., poor water solubility, aggregation, photobleaching, slow clearance from the body, etc.); therefore, it is important to discover alternative PSs. Metals from group 13 of the periodic table coordinated with dipyrins have been reported. Nevertheless, aluminium complexes have not yet been investigated in terms of their photophysical or photobiological properties.

In this study, we sought to develop a library of novel homoleptic tris(dipyrinato)aluminium(III) complexes with the aim of a photodynamic effect (Figure 4.3). We intended to expand and optimise the library of $Al(DIPY)_3$ complexes through a simple and rational synthesis and stepwise functionalisation. X-ray single crystal analysis was set to accompany the majority of the corresponding structures. This type of complexes may form charge transfer (CT) excited states; hence, it is important to investigate the influence of the dipyrin substitution and the metal coordination centre in order to shed light on the excited states. As a consequence, we aimed to elucidate their photophysical properties upon photoexcitation and their tendency to react with the molecular oxygen of the microenvironment and generate singlet oxygen. Therefore, fluorescence quantum yields, singlet and triplet excited state lifetimes and singlet oxygen quantum yields should be determined in polar and non-polar environment. These studies are complemented by density functional theory (DFT) calculations to assess the possible electronic distribution on the frontier molecular orbitals within the complex. We also planned to investigate their phototoxicity potential to prove our state-of-the-art concept towards applications in photodynamic therapy. An initial screening of the $Al(DIPY)_3$ complexes was assessed *via in vitro* phototoxicity studies against a mouse colon carcinoma cell line (CT26). Last, we aimed to evaluate the radio labelling potential of a dipyrin molecule with indium-111.

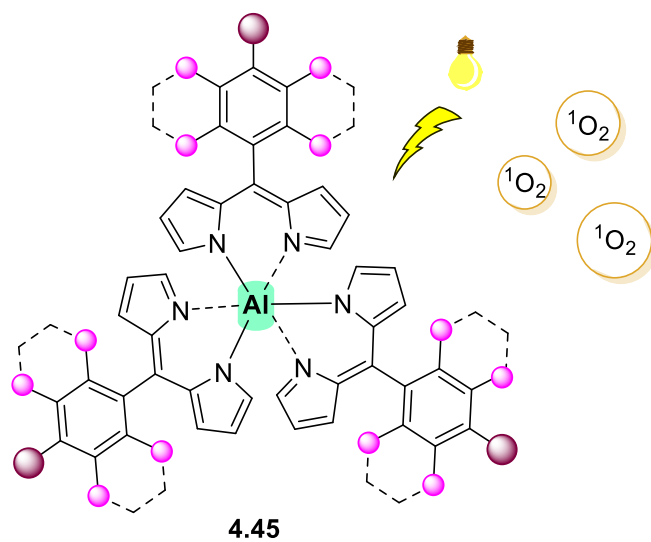


Figure 4.3. General chemical structure of homoleptic tris(dipyrinato)aluminum(III) complexes.

4.3 Results and Discussion

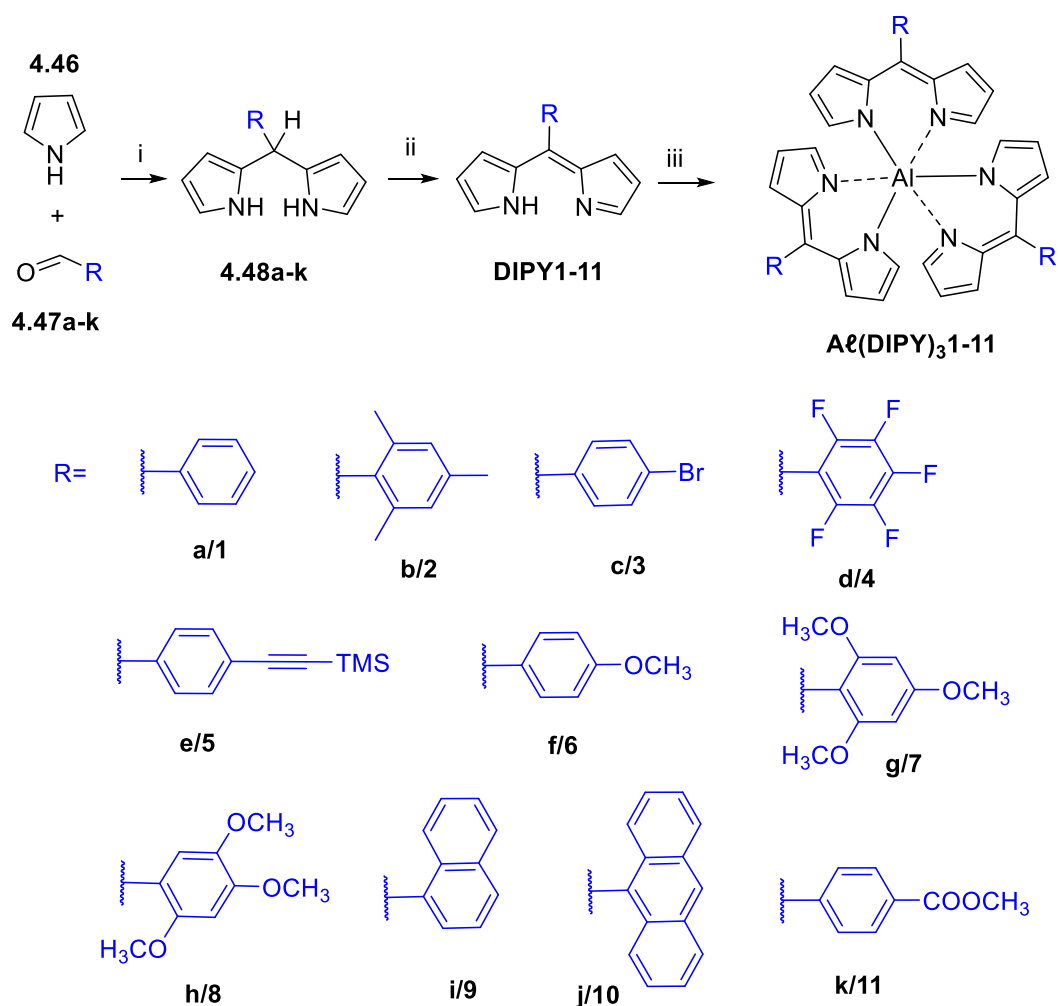
4.3.1 Synthesis of tris(dipyrrinato)aluminium(III) complexes

A new class of tris(dipyrrinato)aluminium(III) complexes $Al(DIPY)_3$ was synthesised and fully characterised with the aim to evaluate their applicability to PDT. To our knowledge such compounds have only been reported in a Japanese patent in 2000 by Toguchi *et al.* under the concept of organic electroluminescent components and devices.^[467] Considering the elements from Group 13, aluminium is the least investigated as the emissive properties, such as fluorescence emission, are meant to be diminished.^[152,156]

Tris(dipyrrinato)aluminium(III) complexes were synthesised *via* a three step synthetic process adapting literature procedures.^[150,157,228] A library of homoleptic dipyrrinato complexes was developed bearing different substituents at the 5-position (meso), whilst lacking α - or β - substitution. The simple meso-free dipyrrin was not included in the library due to its instability.^[150] The synthetic process, where various substituents were introduced, involved the acidic condensation of pyrrole **4.46** and the appropriate aldehyde **4.47a-k** to yield the respective DPMs **4.48a-k**. Then, DPM oxidation with DDQ yielded the corresponding dipyrrins **DIPY1-11**; and finally use of aluminium chloride ($AlCl_3$) salt under basic conditions yielded the corresponding tris(dipyrrinato)aluminium(III) complexes **$Al(DIPY)_3$ 1-11** (Scheme 4.2).

5-Substituted dipyrrins were synthesised in accordance with literature procedures^[150,471,472] and four of the derivatives were fully characterised since their characterisation has not been reported. Reaction yields were relatively good in the range of 30 – 90 % and they are presented in Table 4.1 for all dipyrrins. N-H protons of the dipyrrin moiety show a broad and weak resonance (sometimes not easy to detect) in the range of 11 – 13 ppm in their 1H NMR spectra, as their arrangement results in a planar conformation with a fast tautomeric exchange of the N-H proton between the nitrogens of the pyrrolic units. The aromatic properties of these compounds are demonstrated by the 1H NMR shifts where β -

protons appear in the range of 6.30 – 6.70 ppm and α protons appear in the range of 7.50 – 7.70 ppm.



Scheme 4.2. Synthesis of dipyrins and aluminium complexes; (i) acidic condensation reaction between an aromatic aldehyde and pyrrole yielding DPMs **4.48 a-k**; (ii) oxidation yielding dipyrins **DIPY1-11**, 1.1 eq. DDQ, DCM, r.t. 1 h; (iii) aluminium complexation to yield tris(dipyrinato)aluminium(III) complexes **Al(DIPY)₃1-11**, 3 eq. dipyrin, CHCl₃, 1.4 eq. AlCl₃, 3 eq. DIPEA, 70 °C, overnight.

Aluminium salt AlCl₃ in mild basic conditions was utilised for the N-H deprotonation and complex formation. The lack of α - or β - pyrrole substitution resulted in a less sterically hindered environment which, along with the presence of the aluminium trivalent metal ion, resulted in the formation of the tris(dipyrinato) complexes. Attempts for *in situ* complexation, of the respective dipyrins without purification, as it is common in the case of BODIPY complexes,^[459] were unsuccessful. This has been already reported for other trivalent Group 13 metal ion complexes. Moreover, it has been reported that

dipyrrin isolation was eased through copper(II) complexation prior to the desired product formation.^[473] In our case, TLC reaction monitoring showed predominately the dipyrrin spot and by-product formation with a less intense orange spot of the desired $Al(DIPY)_3$ compound. Therefore dipyrrin purification prior to complexation is essential in order to assess the corresponding $Al(DIPY)_3$ complexes in good yields (Table 4.1). The majority of the aluminium complexes were obtained in moderate to high yields of 50 – 90 % with the lowest yield being calculated for the mesityl derivative (18%).

Table 4.1. Reaction yields of the synthesis of dipyrrins and aluminium complexes.

Entry	Aryl group	Dipyrrin moiety		Aluminium complex	
		Product	Yield	Product	Yield
a	Phenyl-	DIPY1	55%	$Al(DIPY)_3$1	96%
b	Mesityl-	DIPY2	80%	$Al(DIPY)_3$2	18%
c	4-Bromophenyl-	DIPY3	82%	$Al(DIPY)_3$3	75%
d	2,3,4,5,6-Pentafluorophenyl-	DIPY4	75%	$Al(DIPY)_3$4	58%
e	4-TMS-phenyl-	DIPY5	85%	$Al(DIPY)_3$5	75%
f	4-Methoxyphenyl-	DIPY6	60%	$Al(DIPY)_3$6	74%
g	2,4,6-Trimethoxyphenyl-	DIPY7	31%	$Al(DIPY)_3$7	35%
h	2,4,5-Trimethoxyphenyl-	DIPY8	70%	$Al(DIPY)_3$8	80%
i	Naphthyl-	DIPY9	95%	$Al(DIPY)_3$9	65%
j	Anthracenyl-	DIPY10	34%	$Al(DIPY)_3$10	40%
k	Ester-	DIPY11	70%	$Al(DIPY)_3$11	76%

Irrespective of increasing the number of $AlCl_3$ equivalents unreacted dipyrrin remained after complexation, but could be recovered *via* column chromatography. The majority of these complexes adopt a symmetrical octahedral geometry with clear signals in the proton and carbon NMR spectra testifying the expected symmetry. As mentioned, α -pyrrole protons of the dipyrrin precursors appear at a lower field ~ 7.50 – 7.60 ppm, whilst in the octahedral complex configuration they appear at higher field ~ 6.70 – 7.00 ppm. This stems from the increasing shielding effect (double) by the two adjacent dipyrrinato

moieties.^[150,472] Moreover, mass spectrometry was employed and exact mass was confirmed by APCI method. Additionally, the octahedral aluminium coordination centre was confirmed *via* ²⁷Al NMR with a signal/resonance in the range of 6.50 – 7.15 ppm which is characteristic of the octahedral coordination (between – 46 and 40 ppm).^[445]

The insufficient solubility of **Al(DIPY)₃7** resulted in technical issues, thereby it was difficult to proceed with the complete photophysical characterisation, yet it was characterised by UV-Vis, NMR and M.S.

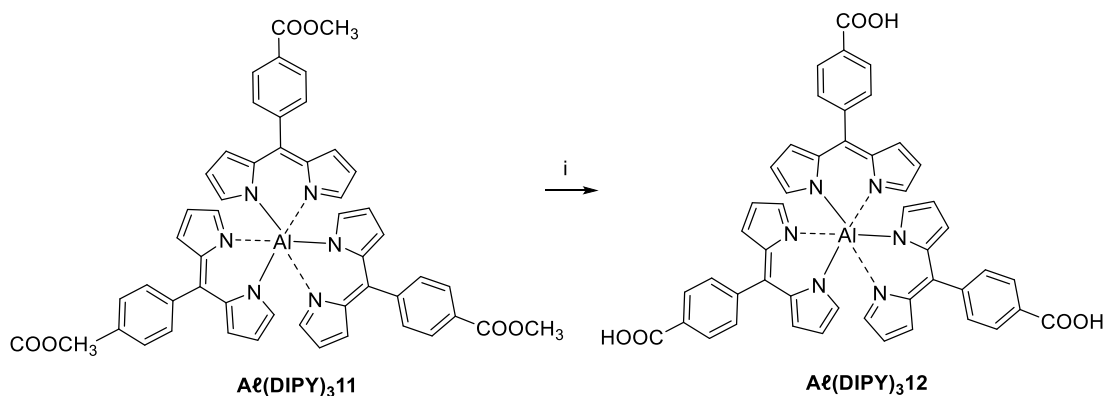
An alternative effort to obtain the monomeric aluminium dipyrin complex (ML1), involved the reaction of **DIPY1** or **DIPY6** with *n*-BuLi and AlCl₃, analogous to how AlDIPYs **4.27** and **4.28** were prepared.^[464] As expected due to the lack of α -substitution in the pyrrole and the possible instability of the products, the desired complex was not isolated. The reaction gave a mixture of products likely due to the high reactivity of *n*-BuLi. However, monitoring the reaction mixture with UV-Vis spectroscopy showed a red-shifted absorption band in comparison with the UV-Vis of the respective dipyrin precursor. This approach requires the usage of α substituted dipyrins as precursors and further optimisation in order to achieve the monomeric AlDIPY complex.

4.3.1.1 Post functionalisation of Al(DIPY)₃ complexes

To investigate the potential of post functionalisation on the periphery of Al(DIPY)₃ complexes, derivatisation was attempted and some trial reactions were performed on the aluminium complexes. Hence, attempts to introduce polar groups, which increase the water solubility, and palladium-catalysed coupling reactions were carried out.

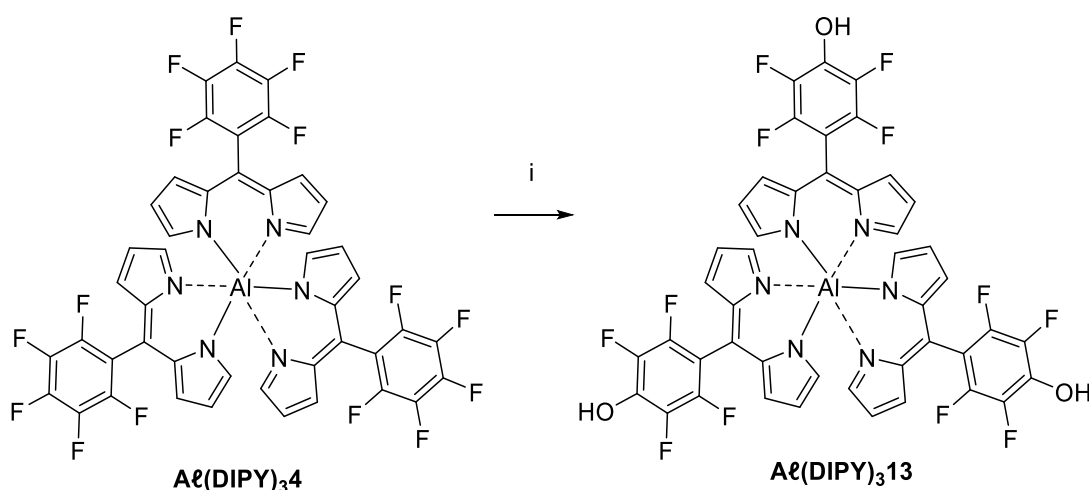
First, ester hydrolysis of the 4-methoxycarbonylphenyl derivative **Al(DIPY)₃11** was conducted straightforward yielding the corresponding carboxylic acid derivative **Al(DIPY)₃12** in 95% yield (Scheme 4.3). A typical hydrolysis procedure was followed by dissolving **Al(DIPY)₃11** in polar media under basic conditions. The presence of carboxylic acid groups can facilitate the biological applicability since they increase the solubility in more polar solvents. Moreover,

the introduction of carboxylic acid group can act as an anchor side for further modification; such as formation of amide groups.



Scheme 4.3. Ester hydrolysis (i) 1 eq. **Al(DIPY)₃11**, 60 eq. KOH, water/THF/MeOH, overnight, 80 °C.

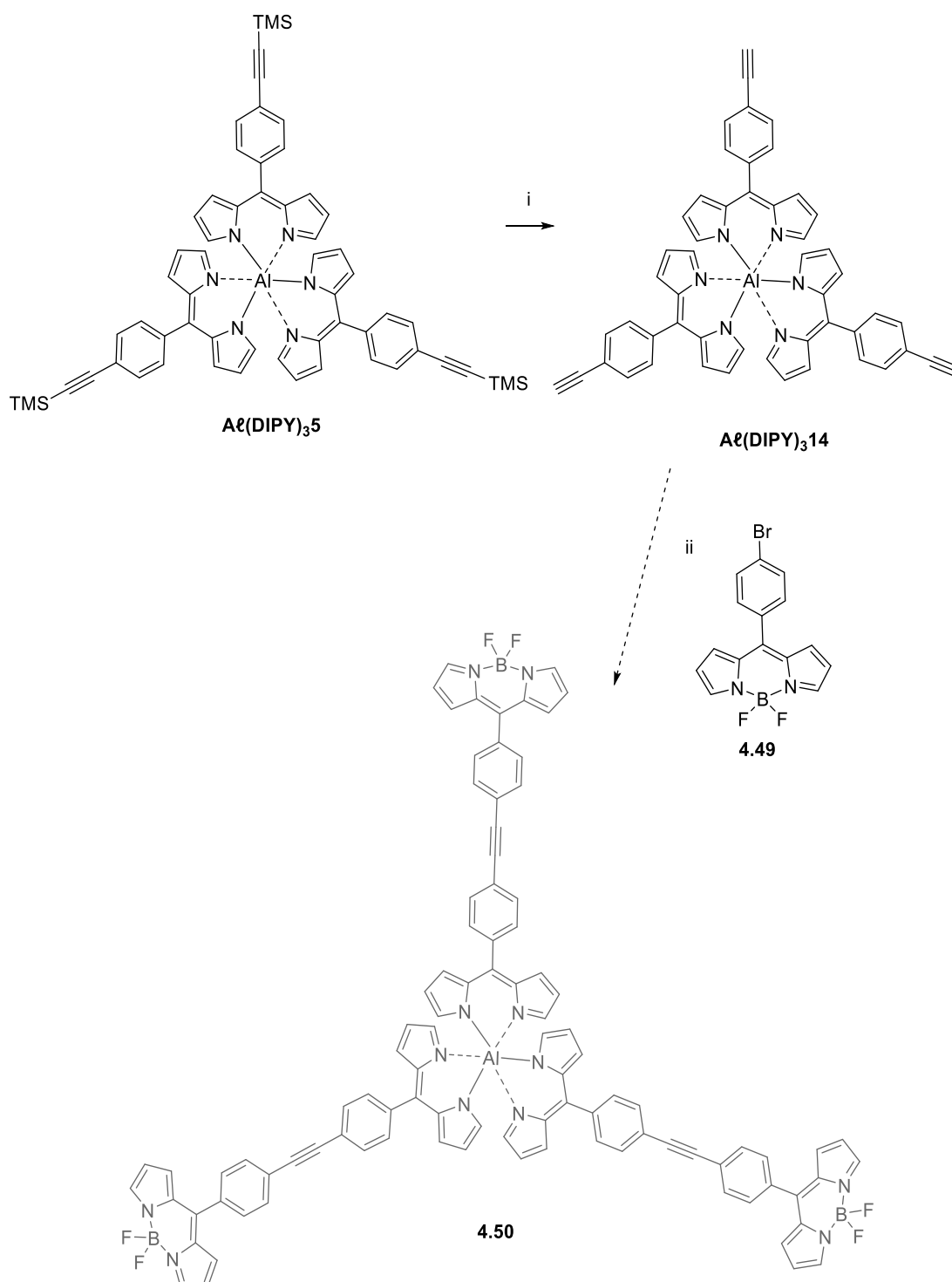
Next, the pentafluorophenyl substituents of **Al(DIPY)₃4** enabled the nucleophilic substitution on the respective *para*-fluorine position under basic conditions. First attempt was to introduce the propargyl group as recently published by Gutsche *et al.*; however, the reaction yielded the 4-hydroxy-2,3,5,6-tetrafluorophenyl derivative **Al(DIPY)₃13** in good yield 85% (Scheme 4.4), therefore optimisation of the reaction is required.^[228] Purification of complex **Al(DIPY)₃13** was tedious and different solvent systems were required with increasing polarity.



Scheme 4.4. Fluorine nucleophilic substitution (i) 1 eq. **Al(DIPY)₃4**, 15 eq. KOH, 20 eq. propargyl alcohol, THF, overnight, r.t.

Finally, palladium-catalysed cross-coupling reactions were performed by using BODIPY moieties for the respective couplings. First, **Al(DIPY)₃5** underwent TMS

deprotection prior to Sonogashira cross-coupling conditions (Scheme 4.5).^[474] The deprotected chelate **Aℓ(DIPY)₃14** was purified, characterised, and subsequently used for reaction with BODIPY **4.49** (Scheme 4.5).^[474] Several by-products were formed and purification was tedious. The monosubstituted product **4.51** (Figure 4.4) was isolated in traces *via* column chromatography and was confirmed by mass spectrometry *via* APCI method. Optimisation is needed for this reaction in order to increase the yield and direct the product formation; however, it proves that Aℓ(DIPY)₃ complexes is stable and the formation of supramolecular complexes is feasible.



Scheme 4.5. TMS deprotection of **Al(DIPY)₃5** and subsequent attempt of Sonogashira cross-coupling reaction; (i) 1 eq. **Al(DIPY)₃5**, 3 eq. TBAF (1M THF), 40 min, r.t.; (ii) 1 eq. **Al(DIPY)₃14**, 4.5 eq. **4.49**, 0.3 eq. CuI, 0.2 eq. PdCl₂(PPh₃)₂, NEt₃:THF (1:3), 2.5 h, 40 °C.

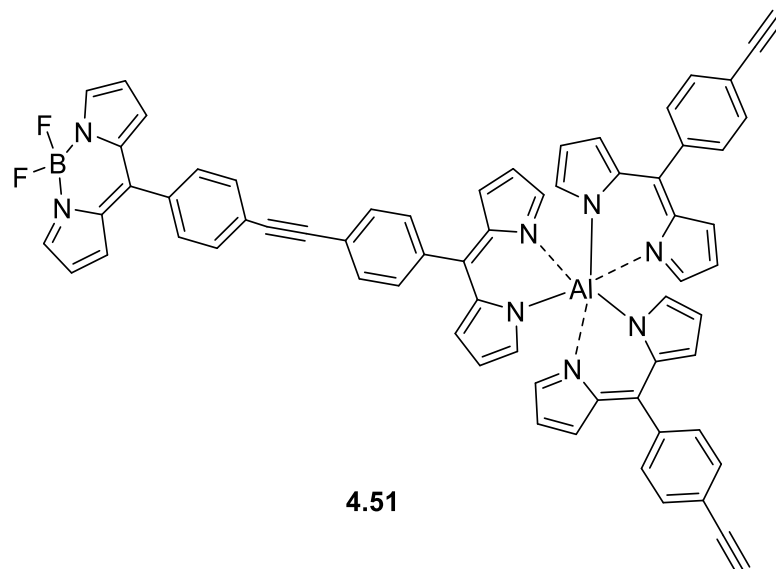
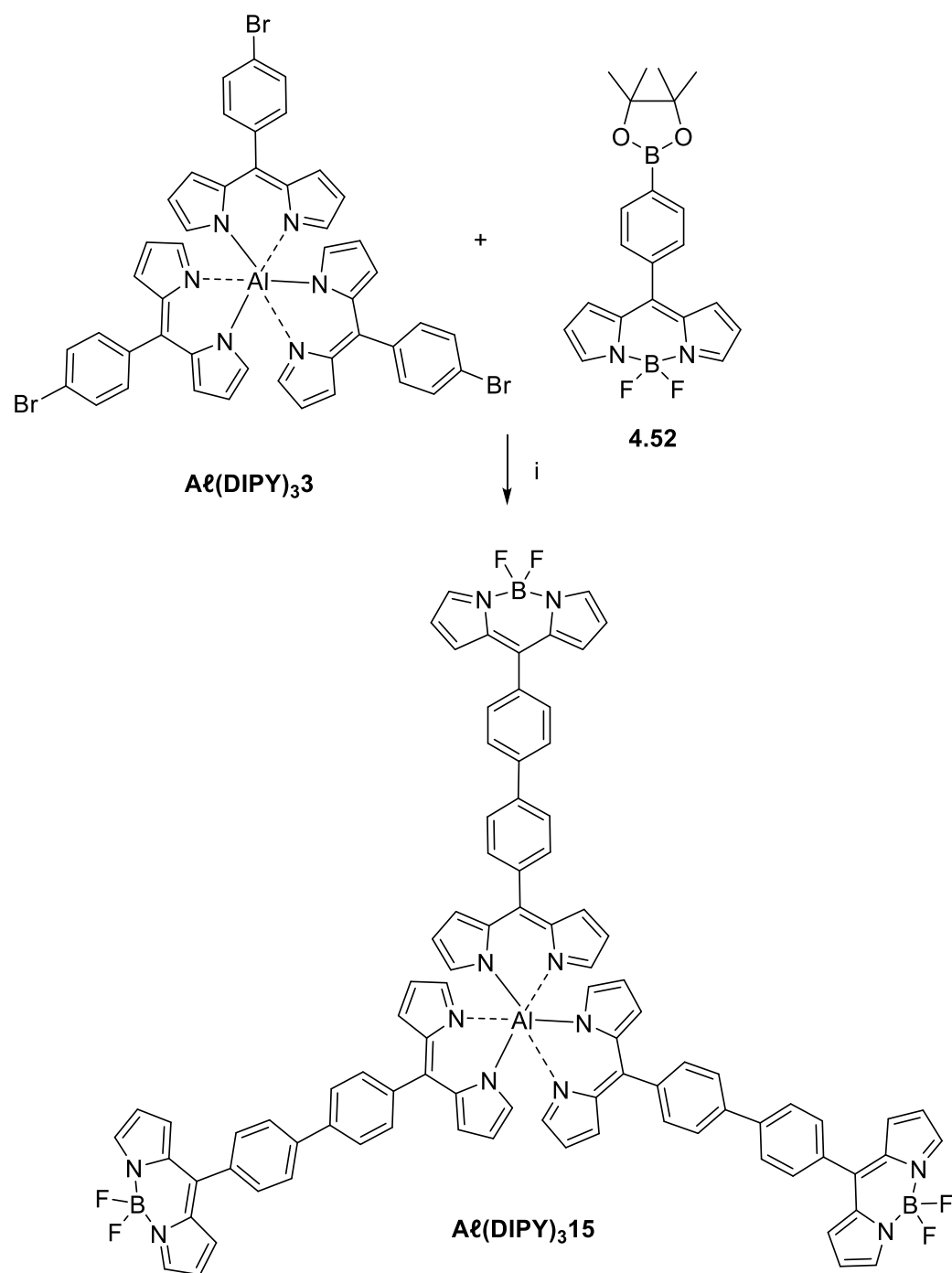


Figure 4.4. Chemical structure of the product **4.51** from a Sonogashira reaction identified *via* mass spectrometry.

On the other hand, palladium-catalysed Suzuki reaction with **Al(DIPY)₃** and the borylated BODIPY **4.52** was successful, yielding the desired product in high yield (72%) (Scheme 4.6). The respective product was purified, characterised, and its structure was confirmed by single crystal analysis (see section 4.3.2).



Scheme 4.6. Synthesis of $\text{Al}(\text{DIPY})_315$ via Suzuki coupling reaction; (i) 1 eq. $\text{Al}(\text{DIPY})_33$, 4 eq. **4.52**, 10 eq. Cs_2CO_3 , 0.2 eq. $\text{Pd}(\text{PPh}_3)_4$, toluene/DMF, 2.5 h, 40 °C.

4.3.2 Single-crystal X-ray structure analysis

Single crystal X-ray diffraction analysis was performed to determine the molecular geometry of four dipyrins **DIPY1**, **DIPY6**, **DIPY7** and **DIPY8** (Figure 4.5, Figure A 35 – Figure A 38) and the majority of homoleptic tris(dipyrinato)aluminium(III) complexes. Crystal structures of such aluminium complexes have not been reported to date. The experimental details and the crystallographic data are presented in section 5.2.2.

The dipyrin core mainly adopts a planar conformation assisted by intramolecular hydrogen bonds (N···H) with an average distance ~ 2.06 Å. There are two independent molecules in the asymmetric unit of **DIPY8** (Figure 4.5, D). Molecule **1** of **DIPY8** shows an intramolecular hydrogen bond, enabling a planar conformation, whereas molecule **2** is not planar and no intramolecular hydrogen bond occurs (larger distance, N – H = 2.227 Å). The dihedral angle between the plane and the substituent is locked between 55 – 90 degrees with an ascending order: **DIPY6** with $52.57(3)^\circ$ < **DIPY1** with $67.52(4)^\circ$ < **DIPY7** with $83.45(2)^\circ$ < **DIPY8** with $93.20(19)^\circ$.

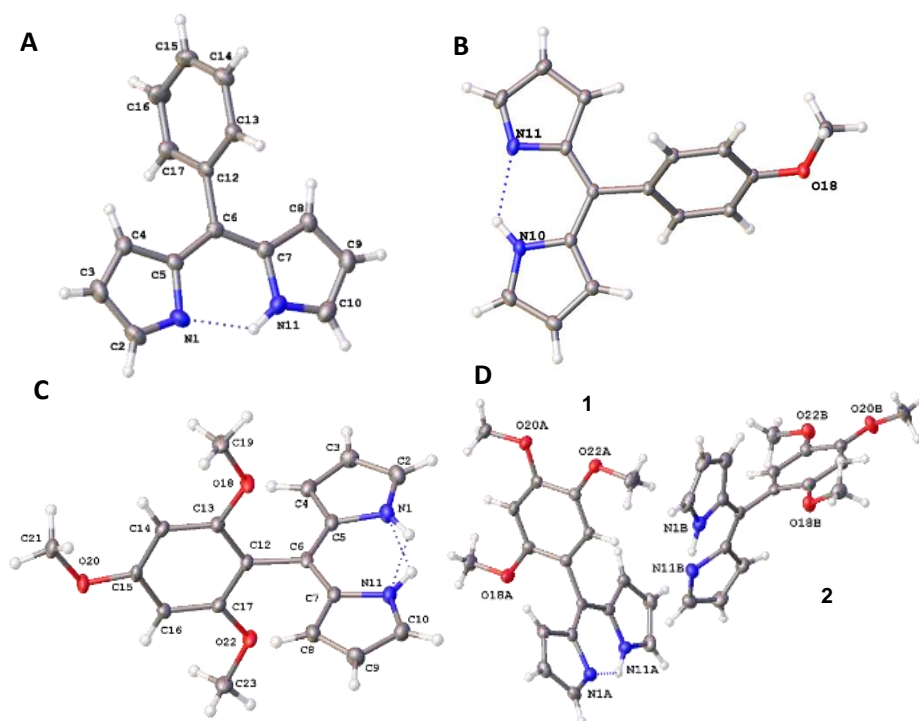


Figure 4.5. Molecular structure of **DIPY1** (A) **DIPY6** (B) **DIPY7** (C) and **DIPY8** (D) (thermal ellipsoid plot), shown with atomic displacement at 50% probability.

The trimeric octahedral configuration of the tris(dipyrrinato)aluminium(III) complexes was confirmed by single-crystal X-ray crystallography. The crystal structure of the phenyl tris(dipyrrinato) derivative **Al(DIPY)₃1** (Figure 4.6) was found to be isostructural to the iron(III) analogue.^[153] There is a half molecule in the asymmetric unit, with the rest symmetry generated. The dihedral angle between the dipyrrin and the substituent for the two moieties is between 65 – 76 ° and the structure is tightly packed without any solvent.

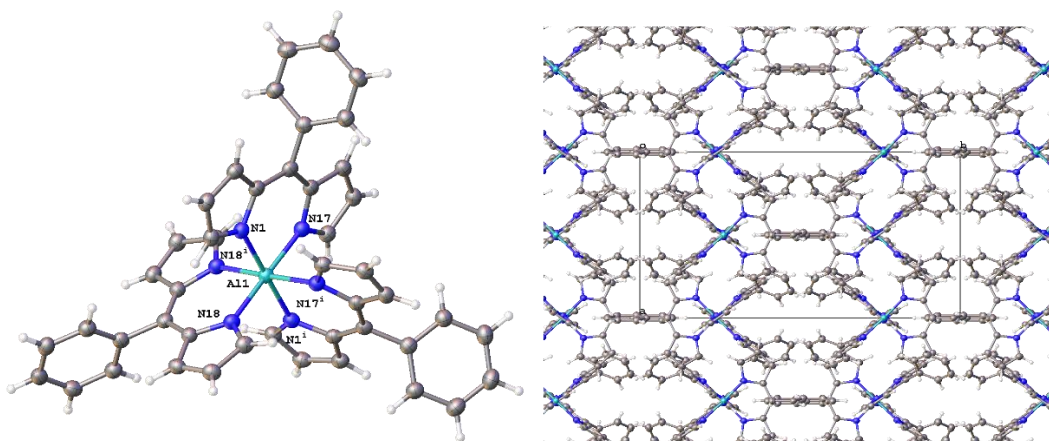


Figure 4.6. Molecular structure (left) and packing diagram viewed normal to the c-axis (right) of **Al(DIPY)₃1** (thermal ellipsoid plot), shown with atomic displacement at 50% probability.

The asymmetric unit of **Al(DIPY)₃2** is comprised of 1/3 of the disordered molecule at the mesityl group and 1/6 of the next molecule. Mesityl groups are disordered (see section 5.2.2) and the voids are occupied by DCM molecules. **Al(DIPY)₃2** is tightly packed with encapsulated solvent (Figure 4.7) and a dihedral angle of 83.44° between the dipyrrin plane and the mesityl group. Indium and gallium analogues have been reported by Thoi *et al.* with equal asymmetric units, similar metal-nitrogen distances and degrees of dihedral angles of mesityl group and dipyrrin moieties.^[152]

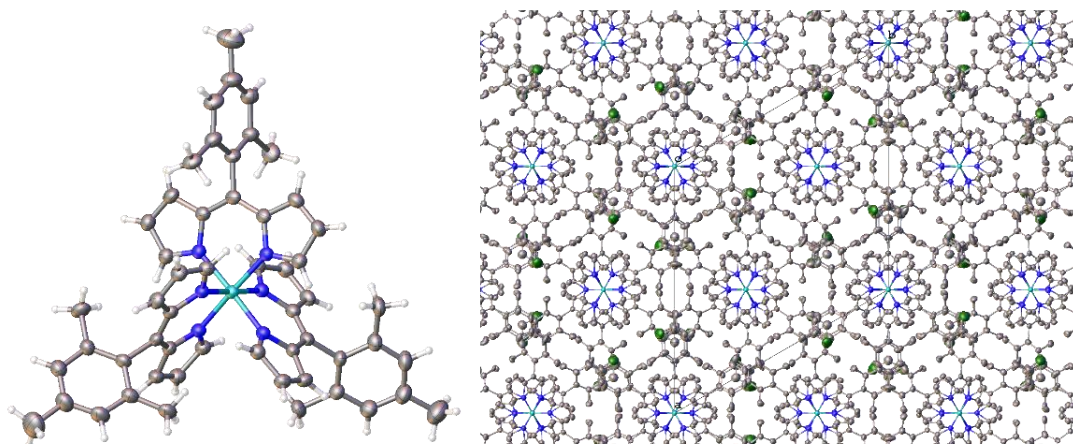


Figure 4.7. Molecular structure (left) and packing diagram viewed normal to the *c*-axis (right) of **Al(DIPY)₃2** (thermal ellipsoid plot), shown with atomic displacement at 50% probability.

Al(DIPY)₃3 crystallised with one complete molecule in the asymmetric unit with partially occupied hexane (Figure 4.8). The partially occupied hexane molecule occupy a channel parallel to the *a*-axis. The bromophenyl group/dipyrin plane normal is ca. 120.2°. Similarly with the Co(III) analogue halogen–halogen interactions do not appear to be significant in this structure. Intermolecular contacts involving Br atoms are possible with Br...Br distances of ca. 3.57 Å.^[475]

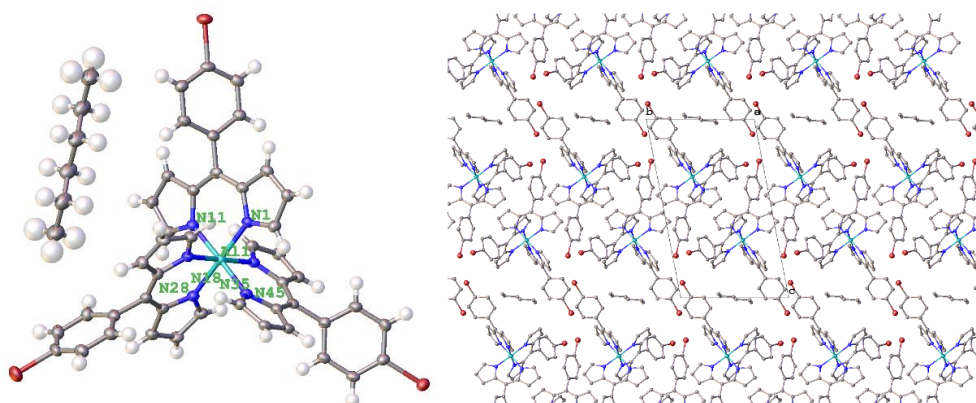


Figure 4.8. Molecular structure (left) and packing diagram viewed normal to the *a*-axis (right) of **Al(DIPY)₃3** (thermal ellipsoid plot), shown with atomic displacement at 50% probability (partially occupied hexane incorporated into the structure).

Al(DIPY)₃4 was solved with a 1/2 of the molecule in the asymmetric unit partially occupied by hexane (Figure 4.9). There is a dihedral angle of 74 – 84° between the dipyrins and the pentafluorophenyl groups. The solvent is incorporated in the

void channel that runs parallel to the c-axis. Analogous structures of gallium and indium have been previously reported by our group.^[228]

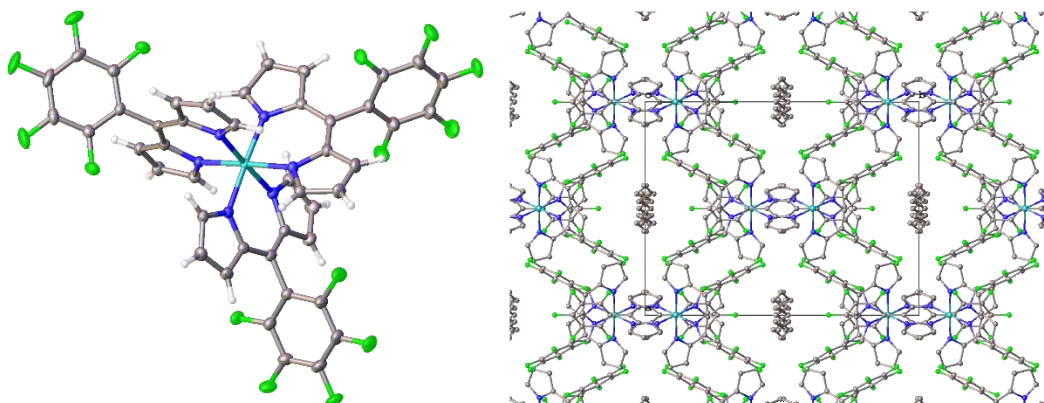


Figure 4.9. Molecular structure (left) and packing diagram viewed normal to the c-axis (right) of **Al(DIPY)₃4** (thermal ellipsoid plot), shown with atomic displacement at 50% probability (disordered hexane incorporated into the structure).

Al(DIPY)₃6 formed a complete molecule in the asymmetric unit (Figure 4.10). In this molecule there are intermolecular interactions between oxygen and hydrogen (C-H \cdots O) with a distance of 2.61 Å. The structure shows a tight packing in ‘stacks’ parallel to the a-axis with weak H-bonding and no solvent, and a dihedral angle between the dipyrin plane and the substituent between 32 – 66°.

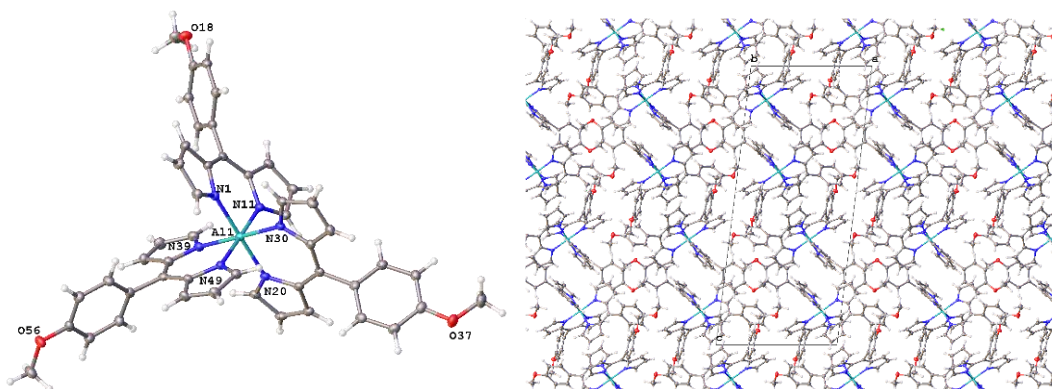


Figure 4.10. Molecular structure (left) and packing diagram viewed normal to the b-axis (right) of **Al(DIPY)₃6** (thermal ellipsoid plot), shown with atomic displacement at 50% probability.

Regarding complexes **Al(DIPY)₃8** and **Al(DIPY)₃9** an atropisomeric formation was displayed. This was proven by single crystal X-ray analysis and both molecules were crystallised with one complete molecule highly disordered both

on the phenyl methoxy and naphthyl substitution (Figure 4.11 and Figure 4.12). In **A ℓ (DIPY)₃8** there is a partial occupation of disordered hexane and a dihedral angle between the dipyrin plane and the substituents in the range of 64 – 99°. In addition, intermolecular hydrogen bonds are formed between the methoxy groups [C(42)-H(42C)⋯O(66A), C(67A)-H(67D)⋯O(41), C(6S)-H(6SB)⋯O(45A)] with a distance of 2.14 – 2.47 Å. The disordered structure of **A ℓ (DIPY)₃9** is tightly packed without solvent and the naphthyl group was twisted by 74 – 98° from the dipyrin core.

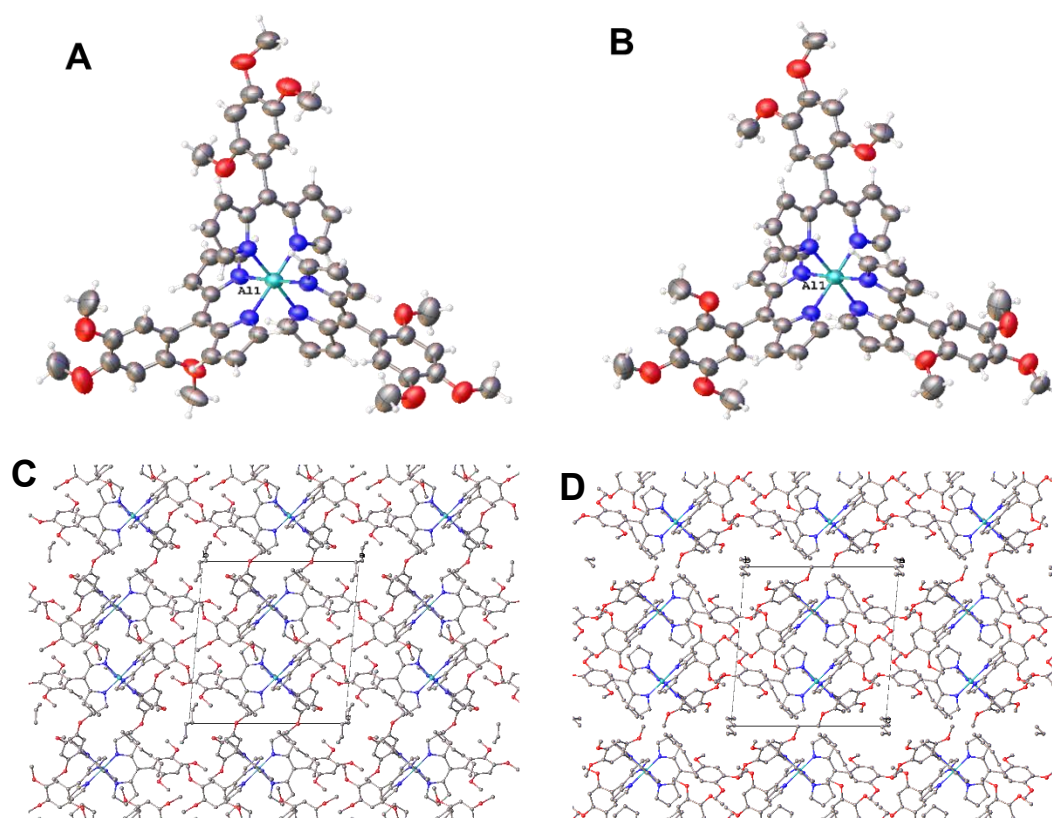


Figure 4.11. Individual representations of each disordered moiety of **A ℓ (DIPY)₃8** with atomic displacement shown at 50% occupancy (**A** and **B**); packing diagrams of each disordered moiety of **A ℓ (DIPY)₃8** with the major moiety (**C**) and minor moiety (**D**) both viewed normal to the a-axis.

A ℓ (DIPY)₃10 has one complete molecule in the asymmetric unit (Figure 4.13). The dihedral angle between the dipyrin plane and the anthracene unit is between 88 – 92°. The structures are highly occupied with solvent molecules of hexane and DCM with three solvent sites per asymmetric unit.

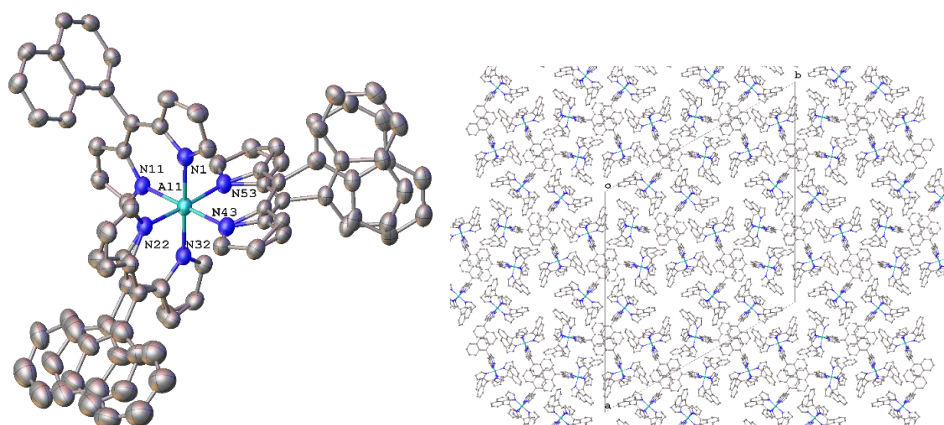


Figure 4.12. Disordered molecular structure with two ligands disordered (left) and packing diagram viewed normal to c-axis (right) of **Al(DIPY)₃9** (thermal ellipsoid plot), shown with atomic displacement at 50% probability.

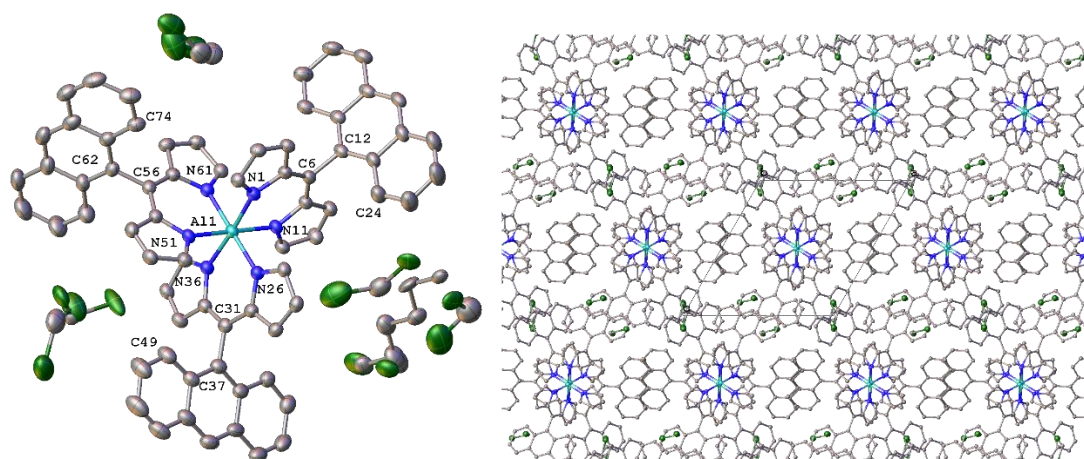


Figure 4.13. Molecular structure (left) and packing diagram viewed normal to the b-axis (right) of **Al(DIPY)₃10** (thermal ellipsoid plot), shown with atomic displacement at 50% probability.

Al(DIPY)₃11 crystallised with one complete molecule in the asymmetric unit (Figure 4.14). The crystals were tightly packed with no solvent and formed intermolecular hydrogen bonds between the ester groups [C(56)-H(56)⋯O(40), C(63)-H(63B)⋯O(20)] with a distance of 2.42 – 2.47 Å between hydrogen and oxygen atoms. Additionally, the dihedral angles between the dipyrin plane and the substituents were found to be 58° and 77°.

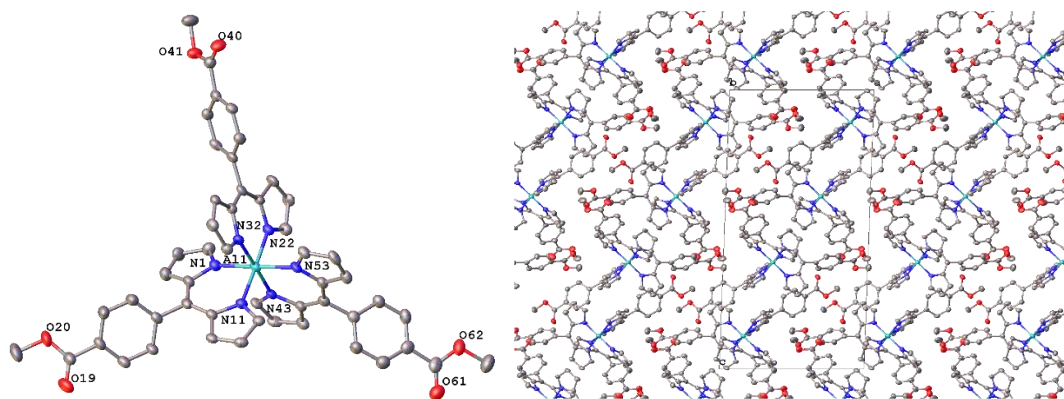


Figure 4.14. Molecular structure (left) and packing diagram (right) of **Al(DIPY)₃11** (thermal ellipsoid plot), shown with atomic displacement at 50% probability.

Al(DIPY)₃12 was solved with 1/2 of the molecule present in the asymmetric unit (Figure 4.15) which displayed a disordered benzoic acid moiety. The crystals are partially occupied with solvent molecules of hexane and water and formed intermolecular hydrogen bonds between the carboxylic acid moiety and water molecules [O(19)-H(19)⋯O(20), O(35)-H(35)⋯O(1S), C(6S)-H(6SC)⋯O(19), C(6S)-H(6SC)⋯O(20)] with a distance of 1.73 – 2.49 Å. Additionally, they form voids where the solvent is encapsulated. The phenyl rings are orientated out of the plane of the dipyrin by 70° – 80°, but the -COOH groups remain nearly coplanar with the phenyl ring. The acid dimer formation is well known for the organisation of frameworks, and similar tris(dipyrinato) octahedral chelates have been reported with a rhodium and cobalt metal centre.^[200,475]

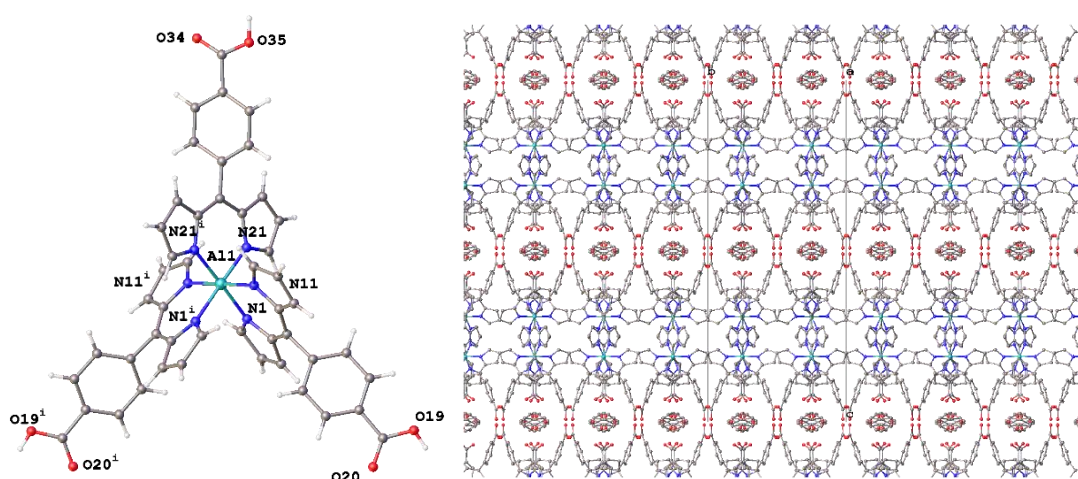


Figure 4.15. Molecular structure of **Al(DIPY)₃12** (left), and packing diagram with solvent channels viewed normal to a-axis (right), shown with atomic displacement at 50% probability.

Al(DIPY)₃15 was crystallised in the asymmetric unit with one complete molecule which displayed two disordered ligands. The respective dihedral angles between the dipyrin plane (of aluminium dipyrin) and the phenyl substituent were found to be between 69° and 70°. The distance between the aluminium and boron atoms was 16.35 – 16.50 Å. The X-ray analysis showed that the conjugate had potential of metal organic framework (MOF) structures. This represents a promising route towards nanomaterials that can be useful for encapsulating PSs as drug delivery platforms, enhancing the biocompatibility or finding use in different fields.^[476]

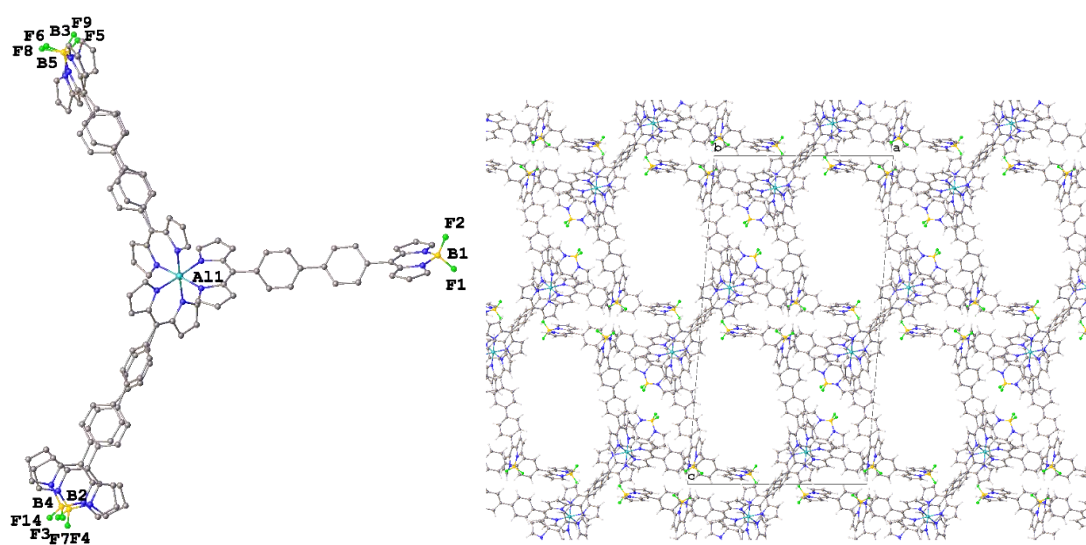


Figure 4.16. Disordered molecular structure of **Al(DIPY)₃15** (left) and packing diagram viewed normal to b-axis with major moiety showing the large voids with solvent contribution removed (right); atomic displacement shown at 50% probability.

Table 4.2 presents the dihedral angle of the dipyrin plane and the aryl substituent at the meso position of the tris(dipyrinato)aluminium(III) complexes, the N-Al distance, and the sigma parameter which represents the sum of the deviation from 90° of the angles in the coordination sphere (of the metal atom) reflecting the deformation of the octahedron.

Sigma values determine the distortion of the complexes, the larger the value the higher distortion from the ideal octahedral conformation. Therefore, we can conclude that **Al(DIPY)₃2**, **Al(DIPY)₃4**, **Al(DIPY)₃10** and **Al(DIPY)₃15** showed the higher distortion (sigma = 15 – 21), presumably due to their bulkier substitution that induces stronger strains within the molecules. The lower values

were found for **Al(DIPY)₃1**, **Al(DIPY)₃3**, and **Al(DIPY)₃9** (sigma = 8 – 11); however, all the structures are very close to the ideal octahedral configuration.

Table 4.2. Data obtained from the crystal structures of the **Al(DIPY)₃** chelates.

Entry	Dihedral angle(°) ^a	Al-N (Å) ^b	Sigma ^c
Al(DIPY)₃1	64.59(2)/75.59(19)	2.011	11.3074
Al(DIPY)₃2	83.44(4)	2.00	21.9086/18.9962
Al(DIPY)₃3	59.93(18)/60.97(2)/67.87(18)	2.01	11.8779
Al(DIPY)₃4	74.43(3)/84.27(2)	2.006	15.3841
Al(DIPY)₃6	31.36(8)/65.25(14)/66.56(2)	2.005	14.0017
Al(DIPY)₃8	63.74(3)/95.02(4)/98.79(3)	2.009	13.4427
Al(DIPY)₃9	74.31(15)/78.86(3)/98.82(14)	2.010	8.2846
Al(DIPY)₃10	88.81(3)/91.45(3)/91.77(2)	2.007	15.985
Al(DIPY)₃11	57.59(11)/59.07(3)/76.58(3)	1.999	10.8695
Al(DIPY)₃12	69.70(18)/79.80(7)	2.011	12.2155
Al(DIPY)₃15	68.81(3)/71.20(4)/72.18(4)	1.999	18.439

^a Angle between the dipyrin plane and the 5-substituent; ^b average of Al-N distance;

^c parameter which presents the sum of the deviation from 90° of the octahedron configuration.

To conclude, all the complexes presented herein were characterised by an octahedral configuration of the aluminium centre. The dipyrin core was relatively planar and the substituents were twisted out of its plane between 30 – 98° indicating that the attached groups on the phenyl ring play a significant role in the final configuration. Chelates **Al(DIPY)₃2**, **Al(DIPY)₃8**, **Al(DIPY)₃9** and **Al(DIPY)₃10** displayed the higher tilt distortion of the aryl ring attached at the meso position of the dipyrin. In addition, the bigger range on the degrees of this angle was exhibited by **Al(DIPY)₃8** which the two 2,4,5-trimethoxyphenyl moieties were almost perpendicular to the dipyrin, but also one had 63°. We assume that there is a higher repulsion related to the methoxy groups when compared to the above. In addition, **Al(DIPY)₃9** and **Al(DIPY)₃10** had almost orthogonal configuration between the dipyrin and the substituent. On the other hand, **Al(DIPY)₃6** showed the smaller distortion of the substitution. The same trend in the degrees of the dihedral angles was followed by their precursors: **DIPY6** (53°) < **DIPY1** (68°) < **DIPY7** (83°) < **DIPY8** (93°).

Regardless the similarities on the single crystal conformation of **Al(DIPY)₃12** and its rhodium analogue, their absorption spectra differ significantly denoting the key role of the metal centre in the photophysical properties. Moreover, the distances of aluminium metal centre and nitrogen (Al-N) atoms were in the range of 1.97 – 2.02 Å (ca. 2 Å), which is similar with the rhodium and gallium analogues whereas is slightly longer than the cobalt analogues and shorter than the indium analogues.^[152,228,475] Finally, looking at the packing and specifically of the **Al(DIPY)₃4**, **Al(DIPY)₃12** and **Al(DIPY)₃15** crystal structures, we can observe that the carboxylic acid and the fluorine groups play a role in the structure giving a packing with voids and prominent porous networks.

4.3.3 Photophysical characterisation

Steady state and transient absorption spectroscopy were employed in order to investigate the ground and excited state properties of the homoleptic tris(dipyrrinato)aluminium(III) complexes. The photophysical results and data of those complexes may resemble other trivalent metal complexes (ML_3) of Co(III), Ga(III), In(III), Rh(III).^[152,200,228] Fluorescence studies have been reported but singlet oxygen determination and triplet state properties are yet to be explored. Specifically, the triplet excited states properties of the aforementioned complexes have remained unexplored until now. In this study, we discuss and aim to explore the photochemistry of $Al(DIPY)_3$ chelates and evaluate their capability towards exerting photodynamic effect. Insufficient solubility of some complexes resulted in the exclusion of measurements and thus certain values have not been determined yet. Ground state analysis and (TD)-DFT calculations predicted the absorption profile of the $Al(DIPY)_3$ complexes. Quantum yields and rate constants of the decay pathways of the singlet excited state (S_1) along with the singlet and triplet excited state lifetimes were experimentally calculated. Furthermore, singlet oxygen luminescence and singlet oxygen quantum yields upon sensitisation were determined.

4.3.3.1 Ground state properties

The absorption spectra of the $Al(DIPY)_3$ complexes were recorded and they are displayed in Figure 4.17 (A, B, C). For clarity the spectra were grouped and distributed in three graphs as their features are overlapping.

All the aluminium coordinated complexes display two pronounced characteristic bands at ca. 450 and 500 nm with moderate molar absorption coefficients with the band at 450 nm showing the stronger absorption (Table 4.3). The lower values of molar absorption coefficient (ϵ), at the 450 nm, range from $\sim 40,000$ to $\sim 60,000 \text{ cm}^{-1} \text{ M}^{-1}$ for **$Al(DIPY)_3$ 1**, **$Al(DIPY)_3$ 10**, **$Al(DIPY)_3$ 12**, **$Al(DIPY)_3$ 13**, and **$Al(DIPY)_3$ 14**; whilst for **$Al(DIPY)_3$ 3**, **$Al(DIPY)_3$ 6**, **$Al(DIPY)_3$ 8**, and **$Al(DIPY)_3$ 9** ϵ is two times higher (range of $\sim 90,000$ to $\sim 140,000 \text{ cm}^{-1} \text{ M}^{-1}$). As expected, the conjugate of BODIPY **4.52** with **$Al(DIPY)_3$ 3**, **$Al(DIPY)_3$ 15** displayed the highest absorptivity $\sim 250,000 \text{ cm}^{-1} \text{ M}^{-1}$ at 500 nm due to the strong absorbance of the

BODIPY moiety. The difference between the absorption spectra of the single dipyrroin chromophore and the $\text{Al}(\text{DIPY})_3$ complexes is apparent, with the former displaying a broader single band at ~ 430 nm (Figure 4.18) with lower molar absorption coefficient and the latter displaying a double, red-shifted band.

Table 4.3. UV-Visible absorption data of $\text{Al}(\text{DIPY})_3$ complexes.

$\text{Al}(\text{DIPY})_3$ complexes	λ_{max} (nm) (log ϵ)
$\text{Al}(\text{DIPY})_{31}$	320 (4.21), 450 (4.80), 500 (4.74)
$\text{Al}(\text{DIPY})_{32}$	350 (4.01), 454 (4.85), 500 (4.80)
$\text{Al}(\text{DIPY})_{33}$	329 (4.48), 451 (4.98), 501 (4.92)
$\text{Al}(\text{DIPY})_{34}$	461 (4.90), 512 (4.87)
$\text{Al}(\text{DIPY})_{35}$	342 (4.50), 452 (4.88), 502 (4.82)
$\text{Al}(\text{DIPY})_{36}$	357 (4.71), 450 (5.15), 499 (5.01)
$\text{Al}(\text{DIPY})_{37}$	357 (4.13), 457 (4.93), 502 (4.88)
$\text{Al}(\text{DIPY})_{38}$	362 (4.18), 454 (4.97), 502 (4.91)
$\text{Al}(\text{DIPY})_{39}$	351 (4.24), 456 (4.94), 504 (4.90)
$\text{Al}(\text{DIPY})_{310}$	351 (4.32), 369 (4.47), 390 (4.45), 460 (4.74), 508 (4.69)
$\text{Al}(\text{DIPY})_{311}$	452 (4.93), 502 (4.87)
$\text{Al}(\text{DIPY})_{312}^*$	451 (4.79), 502 (4.71)
$\text{Al}(\text{DIPY})_{313}^{**}$	455 (4.62), 506 (4.59)
$\text{Al}(\text{DIPY})_{314}$	333 (4.36), 452 (4.80), 502 (4.74)
$\text{Al}(\text{DIPY})_{315}$	384 (4.95), 454 (5.07), 503 (5.41)

UV-Vis spectra were recorded in DCM, THF(*) and MeOH(**)

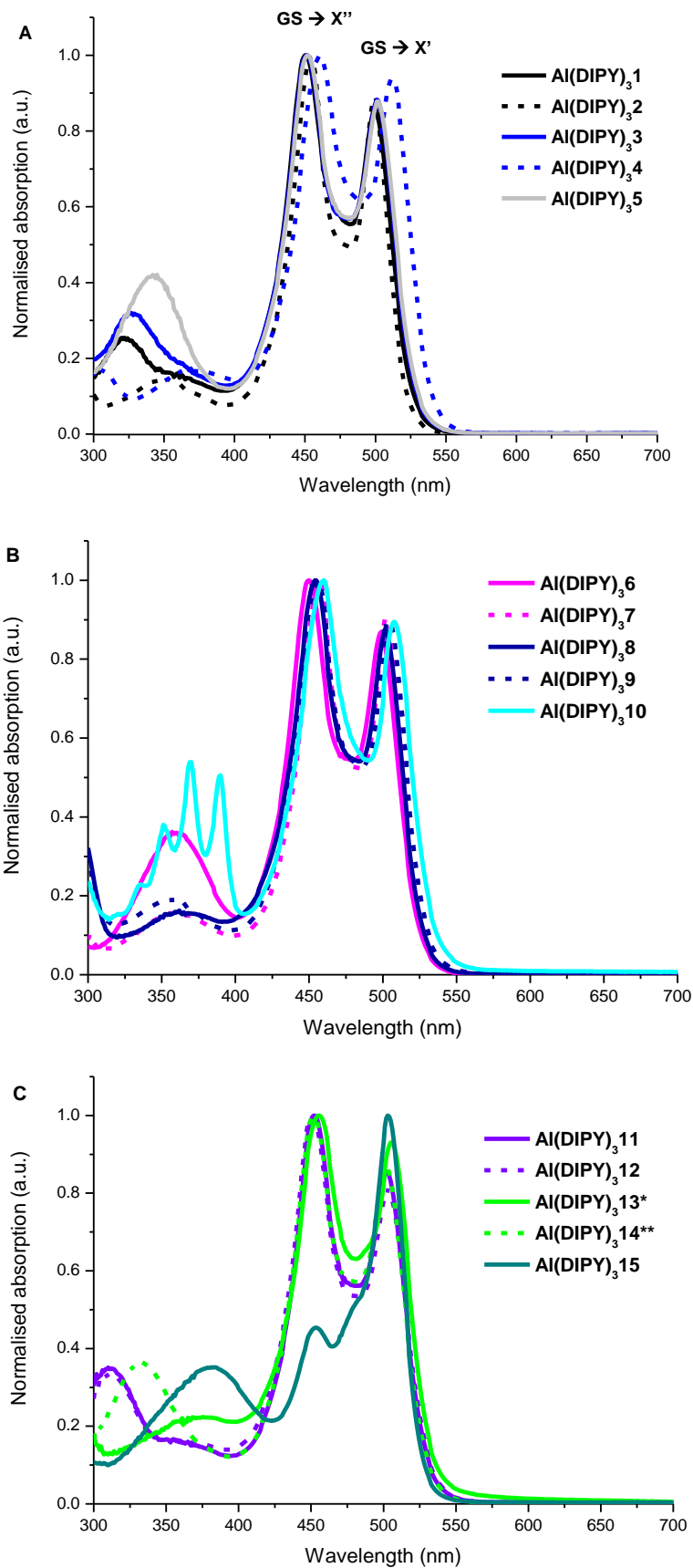


Figure 4.17. Normalised UV-Visible spectra of the Al(DIPY)₃ complexes in DCM (*in THF; ** in MeOH).

This can be explained by the phenomenon of exciton coupling, well defined by Kasha *et al.*, which can be observed in the absorption spectra as the apparent splitting of the absorption bands (Davydov splitting).^[477] Bosnich summarised the analysis of the exciton coupling effect in a coherent way for octahedral configurations of metal complexes and this justification can be applied in the case of the tris(dipyrrinato)aluminium(III) complexes (ML_3 , see below).^[151,478] Additionally, the octahedral configuration was confirmed by the single crystal analysis for the majority of the chelates.

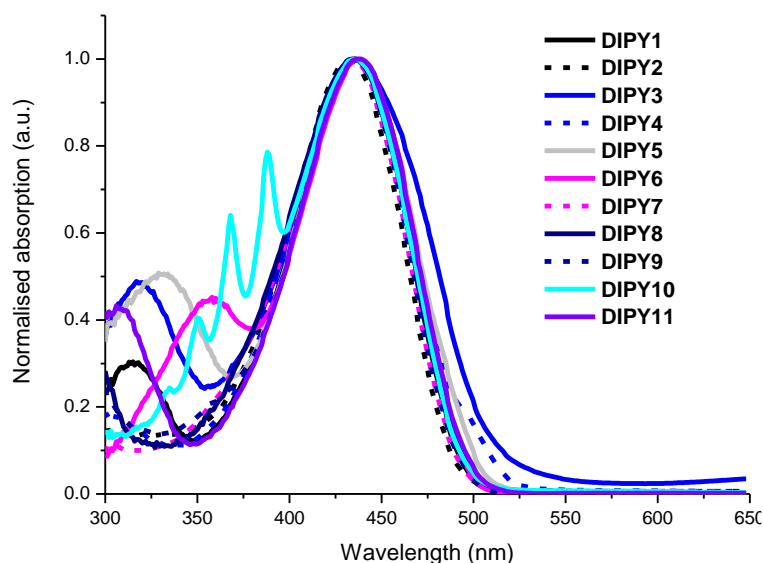


Figure 4.18. Normalised UV-Visible spectra of the dipyrrin precursors (DCM).

When various chromophores are localised in proximity, transition dipole moments can interact and the electronic excitation is delocalised across the molecule; therefore the original excited states of each chromophore are coupled with each other resulting in excitonic states that are pairs of nondegenerate states (in comparison with the parent). The energy shared between the chromophores produces the X' and X'' excitonic states where transitions are allowed. The X'' higher excitonic energy stems from the coupling of the dipole moments ($\mu_1 + \mu_2 + \mu_3$), and the X' lower state from two dipole coupling configurations ($2\mu_1 - \mu_2 - \mu_3$) and ($\mu_2 - \mu_3$) (Figure 4.19). Excitonic splitting of the respective energy state is leading to the case where the lowest exciton state is closer to the triplet excited state and therefore can efficiently result in higher intersystem crossing yields, efficiently producing triplet excited states, which is the aim of PDT.^[479,480]

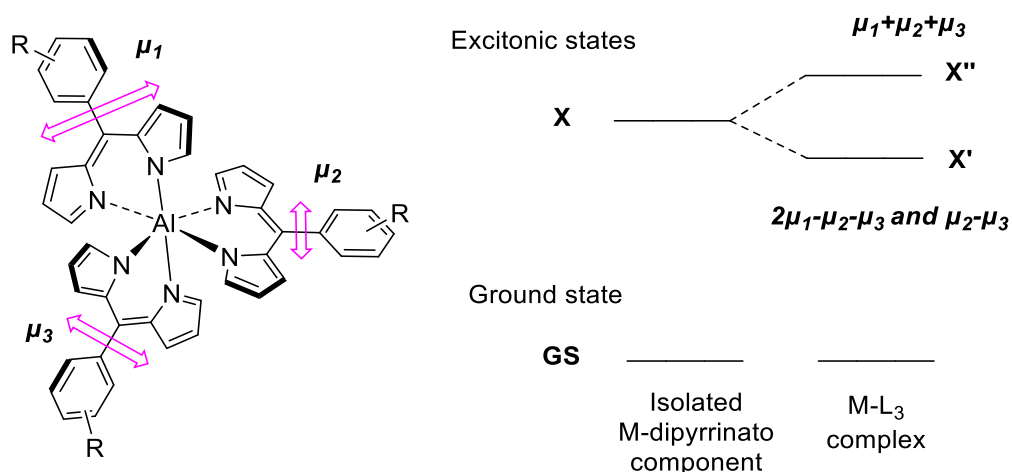


Figure 4.19. Three transition dipole moments of the dipyrin moieties are coupled to produce two excitonic states (X' and X'') that can be observed in the UV-Vis spectra of the $Al(DIPY)_3$ complexes; adapted from the literature.^[151]

The two bands in the absorption profile of the $Al(DIPY)_3$ complexes in the region of 450 – 500 nm correspond to the excitonic states. The absorption data match other reported UV-Vis features of similar coordination complexes. Co(III), Rh(III), and Fe(III) tris(dipyrinato) complexes have a broader band splitting compared with the In(III) or Ga(III) counterparts, which have a more profound double peak, and the same characteristic appears in the aluminium complexes with two bands at 450 – 500 nm.^[200,228,475] Hence, metal coordination can affect the absorption profile as it presumably can alter the excited state properties. Another effect that impacts the features of the absorption spectra is the atomic radius of the elements. The excitonic energy gap splitting is inversely proportional to the distance between the component molecules.^[477]

Moreover, comparing the UV-Vis of the parent dipyrins (Figure 4.18) and the $Al(DIPY)_3$ complexes (Figure 4.17) it is evident that not all the dipyrins display a band in the range of 300 – 400 nm; however, all the $Al(DIPY)_3$ chelates display a band in this range, with some of them exhibiting higher molar absorption coefficient than others. For example, the anthracene moiety absorbs in this region, displaying four peaks as a characteristic feature of both **DIPY10** and **$Al(DIPY)_3$ 10**. Consequently, bands that appear at the region 300 – 400 nm are related to dipyrin based charge transfer transitions (intramolecular charge transfer ICT) along with the co-occurrence of the $n - \pi^*$ and $^1\pi - \pi^*$ transitions by the various meso-substituents (-R).^[481] Additionally, a possible metal to ligand

charge transfer transition has been previously assigned for both low- and high-energy bands in relevant complexes, and may be expected to co-occur with the associated charge transfer within the dipyrrens and the $^1\pi-\pi^*$ transitions.^[154,472,481] Presumably, in this case the metal to ligand charge transfer is not possible.

Lastly, regarding the influence of meso-substitution there was only a marginal difference in the absorption spectra of the $\text{Al}(\text{DIPY})_3$ complexes and thus different substituents do not greatly affecting the absorption profile. This outcome is in accordance with the reports of similar compounds and it is mostly related to the conformation in space between the substituent and the plane of the dipyrren.^[156,228,460] The electron-withdrawing substituent in **$\text{Al}(\text{DIPY})_3\mathbf{4}$** results in a slight, bathochromic (red-shifted) absorption spectrum compared with the other complexes (~ 10 nm), and the electron donating **$\text{Al}(\text{DIPY})_3\mathbf{6}$** appears to have the more blue-shifted absorption peaks. The post-functionalised complex **$\text{Al}(\text{DIPY})_3\mathbf{13}$** displays a 6 nm blue-shift compared to its precursor **$\text{Al}(\text{DIPY})_3\mathbf{4}$** and both profiles of the electronic spectra are similar. The carboxylic acid **$\text{Al}(\text{DIPY})_3\mathbf{12}$** derivative exhibits the same absorption profile as its precursor **$\text{Al}(\text{DIPY})_3\mathbf{11}$** . Also, **$\text{Al}(\text{DIPY})_3\mathbf{5}$** and **$\text{Al}(\text{DIPY})_3\mathbf{14}$** display the same profile with only a slight difference in the shoulder (~ 330 nm). The conjugate **$\text{Al}(\text{DIPY})_3\mathbf{15}$** shows a strong absorption band at 500 nm attributed to the $\text{Al}(\text{DIPY})_3$ and the three BODIPY moieties with a high molar absorption coefficient. There is a shoulder at 454 nm due to the $\text{Al}(\text{DIPY})_3$ moiety **$\text{Al}(\text{DIPY})_3\mathbf{3}$** and it is noted that there is no BODIPY related exciton splitting due to the long distance between the $\text{Al}(\text{DIPY})_3$ and BODIPY moieties. The corresponding high-energy band of **$\text{Al}(\text{DIPY})_3\mathbf{3}$** appears at 320 nm; thus, the red-shifted shoulder at ~ 370 nm of **$\text{Al}(\text{DIPY})_3\mathbf{15}$** stems from the precursors **$\text{Al}(\text{DIPY})_3\mathbf{3}$** and **BODIPY2** that now are in conjugation.

DFT and TD-DFT calculations were conducted for representative complexes **$\text{Al}(\text{DIPY})_3\mathbf{1}$** , **$\text{Al}(\text{DIPY})_3\mathbf{4}$** , **$\text{Al}(\text{DIPY})_3\mathbf{8}$** , **$\text{Al}(\text{DIPY})_3\mathbf{9}$** and **$\text{Al}(\text{DIPY})_3\mathbf{13}$** by using a hybrid B3LYP functional^[387,388] and a LANL2DZ basis set.^[473] The aim was to visualise the frontier molecular orbitals (FMOs) and the electron-density distribution within the complexes. Additionally, the theoretical singlet S_1 ($^1E_{00}$) and triplet T_1 ($^3E_{00}$) excited levels of the $\text{Al}(\text{DIPY})_3$ complexes were determined along with the singlet-triplet gap (ΔE_{S-T}). As shown in Figure 4.20 there is no

apparent electronic distribution in the metal centre and indeed it was localised within the dipyrin moieties confirming the inter-ligand excitation profile and the charge transfer between the ligands. This result is in accordance with the literature.^[152,159] DFT calculations of Ga(III) and In(III) analogues attributed the electronic distribution mainly as ligand centred in the intra-ligand charge transfer. Kusaka *et al.* investigated the heteroleptic tris(dipyrinato) indium(III) coordinated complexes and showed that there is no significant influence of the metal centre in the FMOs; the HOMO and LUMO are localised on the dipyrin ligands. Ultimately, the computed triplet excited energy was found between 1.60 – 1.75 eV following the trend: **$\text{Al}(\text{DIPY})_3\mathbf{4} < \text{Al}(\text{DIPY})_3\mathbf{13} < \text{Al}(\text{DIPY})_3\mathbf{9} < \text{Al}(\text{DIPY})_3\mathbf{8} < \text{Al}(\text{DIPY})_3\mathbf{1}$** , and prerequisite that a PS should be able to generate singlet oxygen ($T_1 > 0.98$ eV, the lowest excited singlet state of oxygen).

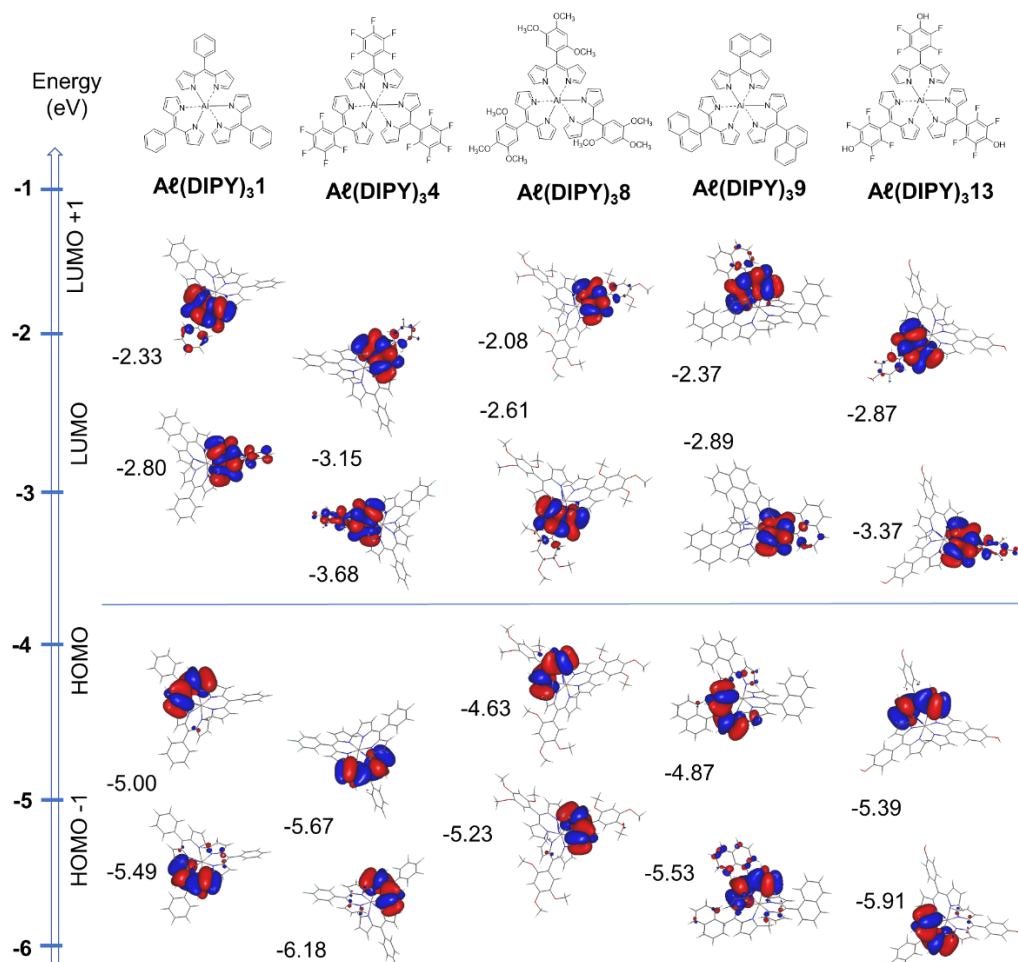


Figure 4.20. Molecular orbital energies and electron-density distribution of representative $\text{Al}(\text{DIPY})_3$ complexes obtained from TD-DFT calculations; B3LYP/LANL2DZ.

4.3.3.2 Excited state properties

Steady-state and nanosecond transient spectroscopy experiments were undertaken to elucidate the singlet and triplet excited state properties of the $\text{Al}(\text{DIPY})_3$ chelates. Toluene or ethanol was mainly used as solvent depending on the solubility of the respective molecules. For clarity they are displayed in two separate figures (Figure 4.21, A and B).

4.3.3.2.1 Singlet excited state

Fluorescence emission spectra of $\text{Al}(\text{DIPY})_3$ complexes were recorded, and the fluorescence quantum yield was calculated by using rhodamine 6G or coumarine 153 as reference compounds. The emission profile of the fluorescence spectra of the $\text{Al}(\text{DIPY})_3$ complexes is rather similar displaying one broad band which is relatively weak. The emission band of the $\text{Al}(\text{DIPY})_3$ occurs between 530 – 590 nm, and spans across a range of more than 100 nm (Figure 4.21), being a mirror image of the absorption band at ~ 500 nm. Conjugate **$\text{Al}(\text{DIPY})_3\mathbf{15}$** displayed one broad peak ~ 570 nm indicating its origin from the emission of precursor **$\text{Al}(\text{DIPY})_3\mathbf{3}$** , rather than that of the BODIPY. Excitation either at 450 or 500 nm had no influence on the emission profile of **$\text{Al}(\text{DIPY})_3\mathbf{15}$** , which means the typical strong BODIPY emission at $\lambda_{\text{max}} \sim 520$ nm is attenuated, since no emissive BODIPY feature is observed.^[482]

Fluorescence quantum yields for the majority of the compounds were calculated in the range of 0.01 – 0.07 (Φ_f) following an ascending order: **$\text{Al}(\text{DIPY})_3\mathbf{12}$** , **$\text{Al}(\text{DIPY})_3\mathbf{13}$** < **$\text{Al}(\text{DIPY})_3\mathbf{4}$** , **$\text{Al}(\text{DIPY})_3\mathbf{5}$** , **$\text{Al}(\text{DIPY})_3\mathbf{11}$** , **$\text{Al}(\text{DIPY})_3\mathbf{15}$** < **$\text{Al}(\text{DIPY})_3\mathbf{1}$** , **$\text{Al}(\text{DIPY})_3\mathbf{3}$** , **$\text{Al}(\text{DIPY})_3\mathbf{6}$** < **$\text{Al}(\text{DIPY})_3\mathbf{8}$** < **$\text{Al}(\text{DIPY})_3\mathbf{9}$** < **$\text{Al}(\text{DIPY})_3\mathbf{10}$** < **$\text{Al}(\text{DIPY})_3\mathbf{2}$** (Table 4.4). The highest yields were displayed by **$\text{Al}(\text{DIPY})_3\mathbf{2}$** , **$\text{Al}(\text{DIPY})_3\mathbf{9}$** , and **$\text{Al}(\text{DIPY})_3\mathbf{10}$** probably due to the bulky 5-substitution and the steric hindrance. It has been previously reported that mesityl substitution on the meso position and restriction of the internal rotation can drastically increase the fluorescence quantum yields of dipyrinato metal complexes.^[156,483] This shows the potential for enhancing the fluorescence, which can also be influenced by the introduction of β -substituents.^[159] The trends observed in In(III) and Ga(III) homoleptic complexes asserts that Group 13 complexes are less luminescent than the zinc or boron complexes.^[152]

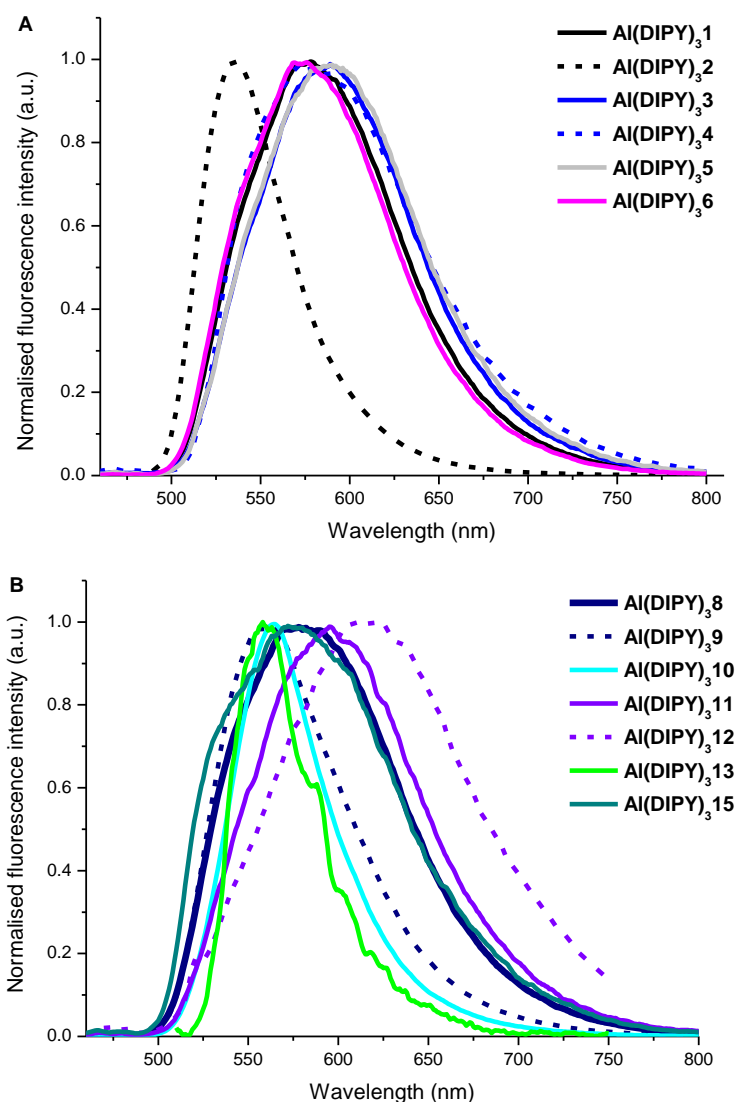


Figure 4.21. Normalised fluorescence emission spectra of $\text{Al}(\text{DIPY})_3$ chelates in toluene ($\lambda_{\text{exc}} = 450 \text{ nm}$), $\text{Al}(\text{DIPY})_3\mathbf{12}$ in THF ($\lambda_{\text{exc}} = 445 \text{ nm}$), $\text{Al}(\text{DIPY})_3\mathbf{13}$ in DMF ($\lambda_{\text{exc}} = 500 \text{ nm}$).

Most of the complexes were soluble in toluene and thus it was used for the measurements. Trials to determine the fluorescence yield in ethanol (for example for $\text{Al}(\text{DIPY})_3\mathbf{8}$ and $\text{Al}(\text{DIPY})_3\mathbf{5}$) were not successful. The emission band appeared quite noisy and weak. Additionally, the fluorescence quantum yield of $\text{Al}(\text{DIPY})_3\mathbf{12}$ and $\text{Al}(\text{DIPY})_3\mathbf{13}$ was difficult to calculate due to a very feeble fluorescence intensity. For $\text{Al}(\text{DIPY})_3\mathbf{12}$ the use of THF or ethanol were the appropriate solvents in terms of solubility; however, the fluorescence yield was calculated to be less than 0.01 in both solvents with a broad emission band at $\sim 610 \text{ nm}$ (Figure 4.21, B). Similarly, a low yield was reported for the homoleptic 4-

carboxyphenyl rhodium(III) complex derivative whilst counterparts of Co(III) ML₃ are completely non-emissive.^[200]

Table 4.4. Photophysical data of singlet excited states of the Al(DIPY)₃ complexes.

Compound	λ_{em} (nm)	$\Delta\nu$ (cm ⁻¹)	τ_s (ns)	Φ_f	k_f ×10 ⁶ s ⁻¹	k_{nr} ×10 ⁸ s ⁻¹	S ₁ (eV)
Al(DIPY)₃1	576	2639	2.2	0.02	9.1	4.5	2.38
Al(DIPY)₃2	535	1308	4.7	0.07	14.9	2.0	2.42
Al(DIPY)₃3	587	2924	1.9	0.02	10.5	5.2	2.36
Al(DIPY)₃4	580	2290	3.6	0.01	2.8	2.8	2.35
Al(DIPY)₃5	596	2971	1.3	0.01	7.7	7.6	2.36
Al(DIPY)₃6	571	2527	2.1	0.02	9.5	4.7	2.38
Al(DIPY)₃8	580	2679	3.7	0.03	8.1	2.6	2.38
Al(DIPY)₃9	560	1984	4.0	0.04	10.0	2.4	2.38
Al(DIPY)₃10	564	1955	4.3	0.05	11.6	2.2	2.35
Al(DIPY)₃11	595	3114	1.4	0.01	7.1	7.1	2.35
Al(DIPY)₃12*	615	3700	1.3	<0.01	0.8	7.7	2.31
Al(DIPY)₃13**	559	1952	-	<0.01	-	-	2.33
Al(DIPY)₃15	576	2520	1.4	0.01	7.1	7.1	2.41

Respective data and spectra were obtained in toluene; * THF; ** DMF; $\Delta\nu$ Stokes shift; S₁ determined experimentally by intersection; standard errors (percentage of value) are

$$\tau_s \pm 5\%, \Phi_f \pm 10\%, k_f \pm 10\%, k_{nr} \pm 10\%.$$

For **Al(DIPY)₃13** attempts to use DMSO, THF, or 2-propanol were unsuccessful, whilst in ethanol or DMF a weak band appeared with negligible yield (< 0.001). Presumably, in polar media there is a prominent possibility of either solvent fluorescence quenching or formation of non-emissive ICT states which lead to a more efficient triplet formation *via* charge recombination and non-radiative decay as the dominant pathway. On the other hand, in non-polar solvents the ICT state will not stabilise and therefore, the excited state S₁ will undergo ordinary ISC (in competition with the IC).^[179,183,189,484] Indeed, all the aluminium complexes display moderate triplet state lifetimes in air equilibrated solutions (see section 4.3.3.2.2).

The emission peaks are equating to Stokes shifts between a minimum 1308 cm⁻¹ for **Al(DIPY)₃2** and a maximum 3114 cm⁻¹ for **Al(DIPY)₃11** (Table 4.4). Complexes **Al(DIPY)₃2**, **Al(DIPY)₃9**, **Al(DIPY)₃10** have smaller Stokes shifts pointing to a reduced amount of molecular rearrangements reflecting less conformational freedom in the ground and/or excited states due to the steric hindrance by the substituents.^[156] The considerable Stokes shifts and the moderately low fluorescence quantum yields support that non-radiative decay pathways are the most dominant processes (ISC and IC).

TCSPC was performed and fluorescence lifetimes were determined to assess the singlet photophysical properties of the complexes (Table 4.4). The singlet state lifetimes of the Al(DIPY)₃ complexes in toluene (**Al(DIPY)₃12** in THF) ranged from 1.3 to 4.7 ns with the ascending order: **Al(DIPY)₃5**, **Al(DIPY)₃12** < **Al(DIPY)₃11**, **Al(DIPY)₃15** < **Al(DIPY)₃3** < **Al(DIPY)₃6** < **Al(DIPY)₃1** < **Al(DIPY)₃4** < **Al(DIPY)₃8** < **Al(DIPY)₃9** < **Al(DIPY)₃10** < **Al(DIPY)₃2**. Figure 4.22 displays all the fluorescence decays. Comparing **Al(DIPY)₃2** with the respective mesityl-dipyrrinato Ga(III) and In(III) complexes, aluminium complex appears to have slightly increased Stokes shifts and longer singlet excited lifetime (+1 – 2 ns) whilst maintaining a moderately high fluorescence quantum yield equal to the In(III) counterpart: Ga(III) complex: $\Phi_f = 0.02$, $\tau_s = 3.75$ ns, $\Delta\nu = 1220$ cm⁻¹ and In(III) complex: $\Phi_f = 0.07$, $\tau_s = 1.93$ ns, $\Delta\nu = 1113$ cm⁻¹ (in hexane).^[152] As expected, the singlet state lifetime of **Al(DIPY)₃13** was not detected neither in DMSO nor ethanol or THF (< 1 ns).

Consequently, the radiative and non-radiative rate constants were determined ($n: k_f = \Phi_f / \tau_s$, $k_{nr} = (1 - \Phi_f) / \tau_s$) and are consistent with the fluorescence profile of the Al(DIPY)₃ complexes. The radiative rate (fluorescence) and non-radiative decay rates (IC, ISC, ICT) are of the order of 10⁶ s⁻¹ and 10⁸ s⁻¹, respectively, supporting the prevalence of the non-radiative decays (Table 4.4). Similar values have been reported of dipyrin complexes showing that increasing the number of dipyrin moieties in proximity influences the emissive properties and enhances the triplet state or internal conversion processes to the ground state.^[480] Lastly, the singlet excited energy state was determined experimentally *via* the intersection of the normalised absorption and emission spectra and was found to be in the range of 2.3 – 2.4 eV (Table 4.4).

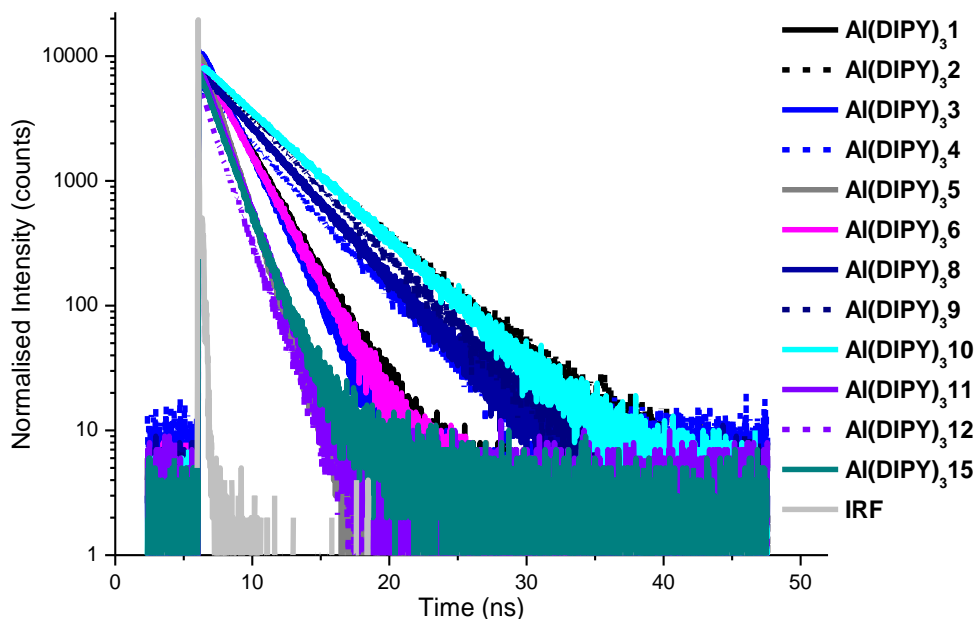


Figure 4.22. Fluorescence lifetime decays of the $\text{Al}(\text{DIPY})_3$ complexes in toluene, $\text{Al}(\text{DIPY})_3\text{12}$ in THF; $\lambda_{\text{exc}} = 450 \text{ nm}$; $\lambda_{\text{det}} = 580 \text{ nm}$.

The possible charge separated states result in non-emissive charge separated states which can undergo IC ($S_1 \rightarrow S_0$) and ICT or ISC ($S_1 \rightarrow T_{n/1}$) as the most probable decay pathways. Additionally, the non-radiative relaxation from a higher to lower excitonic state and the weak emission profile suggest that the prominent electronic transitions are ligand centred. These observations indicate that the chromophores undergo excited-state non-radiative relaxations (conformational, vibrational, electronic) prior to the observed steady-state emission spectrum with the radiationless ISC process (with rate constants of the order of 10^8 s^{-1}) expected to lead to an efficient triplet formation.^[468] Any possible metal-to-ligand charge transfer that might co-occur could be merged with the broad peak of the emission spectrum since it is already red shifted (500 – 700 nm) where CT emission can be expected.^[186]

Kusaka *et al.* considered an equilibrium between the emissive $^1\pi\text{-}\pi^*$ transition of the ligand and the non-emissive charge separated states of tris(dipyrrinato) In(III) complexes.^[159] They surmised that in homoleptic complexes (with β substitution) there was a bigger contribution of the charge separated states among the ligands leading to low fluorescence quantum yields, whilst in heteroleptic complexes a smaller contribution of the charge-separated states resulted to the highest fluorescence quantum yield.

Thus far, we sought to shed light on the singlet excited states and the processes after photoexcitation. As stated, the possible formation of intramolecular charge transfer (ICT) between the ligands of the complex might reduce the fluorescence emission, but on the other hand, enhance the triplet generation yield.^[183]

4.3.3.2 Triplet excited state

Nanosecond transient absorption (TA) spectroscopy was employed to explore the triplet excited states and the proposed non-radiative pathways of the $\text{Al}(\text{DIPY})_3$ chelates. A relative estimation of the triplet state quantum yield between the complexes was made. The desired long-lived triplet excited states were observed, and the triplet excited lifetimes (τ_T) were defined in air equilibrated solutions by simple monoexponential fitting. TA spectra were recorded in non-polar toluene solution and polar ethanolic solution. For **$\text{Al}(\text{DIPY})_3\mathbf{12}$** and **$\text{Al}(\text{DIPY})_3\mathbf{13}$** the same issue with solvent compatibility was encountered, concluding that ethanol was the appropriate option for the measurements. Although the corresponding signal most of the times was noisy, we were able to extract the triplet state lifetimes. DMSO, DMF and DCM were also used as solvents, but the spectra obtained were noisier with negligible peaks. For the latter solvent, decomposition was observed by monitoring the UV-Vis before and after the experiment. For **$\text{Al}(\text{DIPY})_3\mathbf{15}$** the respective TA spectra resembled each other post excitation at 450 or 500 nm with no major difference.

The triplet absorption profiles of the $\text{Al}(\text{DIPY})_3$ complexes have similar shapes and the excited state absorption bands appear between 380 – 700 nm. Representative spectra of **$\text{Al}(\text{DIPY})_3\mathbf{1}$** , **$\text{Al}(\text{DIPY})_3\mathbf{4}$** , **$\text{Al}(\text{DIPY})_3\mathbf{8}$** and **$\text{Al}(\text{DIPY})_3\mathbf{9}$** are shown in Figure 4.23 and in Figure A 39 – Figure A 59 all the TA spectra along with the time trace fittings are depicted. It is apparent that TA spectra are superimposed by the ground state bleaching resulting in an absorption maximum at ~ 400 nm with two prominent negative absorbance signals at ~ 450 and ~ 500 nm reproducing the exciton split bands of the ground state. These are the characteristic peaks of the ground state electronic transitions of the complexes and provide information that the triplet-triplet absorptivity is weaker than the singlet absorptivity, although occurring in decent yields. TA spectra of **$\text{Al}(\text{DIPY})_3\mathbf{2}$** , **$\text{Al}(\text{DIPY})_3\mathbf{4}$** , **$\text{Al}(\text{DIPY})_3\mathbf{5}$** , **$\text{Al}(\text{DIPY})_3\mathbf{6}$** , **$\text{Al}(\text{DIPY})_3\mathbf{8}$** , **$\text{Al}(\text{DIPY})_3\mathbf{9}$** ,

Al(DIPY)₃**10**, and **A**l(DIPY)₃**11** display a broad band between 550 – 700 nm. Complex **A**l(DIPY)₃**4** displays nearly the same intensity of the two ground-state bleaching bands indicating a weaker triplet-triplet absorption at 500 nm. Conjugate **A**l(DIPY)₃**15** is maintaining moderate triplet state lifetime displaying one ground state bleaching band at ~ 500 nm (Figure A 59), repeating the absorption pattern typical of the BODIPY moiety in nanosecond TA experiments.^[185]

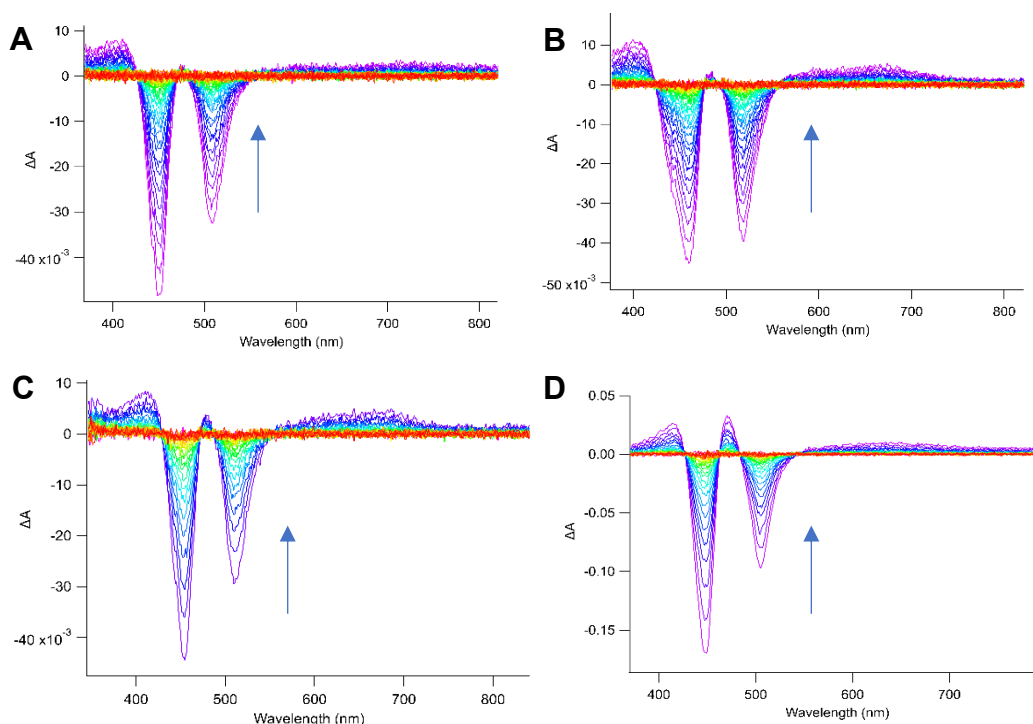


Figure 4.23. TA spectra at ambient conditions of **A**l(DIPY)₃**1** in ethanol (40 ns t_{inc} ; 450 nm λ_{exc}) (A); **A**l(DIPY)₃**4** in toluene (40 ns t_{inc} ; 450 nm λ_{exc}) (B); **A**l(DIPY)₃**8** in toluene (80 ns t_{inc} ; 450 nm λ_{exc}) (C); **A**l(DIPY)₃**9** in ethanol (60 ns t_{inc} ; 450 nm λ_{exc}) (D); arrows pointing from blue to red colour show the decay from the maximum intensity in the successive steps, respectively

The corresponding triplet state lifetimes of the Al(DIPY)₃ complexes in toluene were in the range of 290 – 400 ns with the longer triplet lifetime displayed by **A**l(DIPY)₃**2** and **A**l(DIPY)₃**8** showing the following descending order: **A**l(DIPY)₃**2**, **A**l(DIPY)₃**8** > **A**l(DIPY)₃**9** > **A**l(DIPY)₃**3**, **A**l(DIPY)₃**10** > **A**l(DIPY)₃**11** > **A**l(DIPY)₃**4**, **A**l(DIPY)₃**5**, **A**l(DIPY)₃**6**, **A**l(DIPY)₃**15** > **A**l(DIPY)₃**1** (Table 4.5). The results are similar to previously reported triplet excited state lifetimes of In(III) and Ga(III) chelates.^[152] However, to date only few

studies focussed on the photoexcitation processes of this class of tris(dipyrrinato) complexes. A comparable trend occurs in ethanolic solutions where the triplet state lifetime underwent a significant decrease (where comparison is possible) of the order of ~ 90 ns, except for **A ℓ (DIPY)₃5** which shows a minor difference. The latter, together with **A ℓ (DIPY)₃8** and **A ℓ (DIPY)₃9**, display the higher triplet state lifetime in ethanol ~ 290 ns. **A ℓ (DIPY)₃3**, **A ℓ (DIPY)₃4**, **A ℓ (DIPY)₃12**, and **A ℓ (DIPY)₃13** display a triplet state lifetime of around 250 ns with an overall lower value than in toluene solutions. Lastly, we can observe that the respective errors of the fitting curves are smaller in toluene than in ethanol and along with the higher triplet state lifetime values (in toluene) this is indicative that solvent significantly affects the results.

Table 4.5. Triplet excited state lifetimes of the A ℓ (DIPY)₃ complexes at ambient (τ_T) and oxygen free conditions (τ_T^0) in toluene and ethanol.

Compound	τ_T (ns)		τ_T^0 (μ s)	
	Ethanol	Toluene	Ethanol	Toluene
Aℓ(DIPY)₃1	-	290 \pm 6	-	89 \pm 4
Aℓ(DIPY)₃2	-	390 \pm 12	-	202 \pm 22*
Aℓ(DIPY)₃3	250 \pm 17	340 \pm 6	-	66 \pm 5
Aℓ(DIPY)₃4	230 \pm 14	310 \pm 8	34 \pm 3	67 \pm 4
Aℓ(DIPY)₃5	280 \pm 25	300 \pm 12	-	150 \pm 12
Aℓ(DIPY)₃6	-	300 \pm 11	-	87 \pm 6
Aℓ(DIPY)₃8	300 \pm 25	390 \pm 8	170 \pm 4	190 \pm 20
Aℓ(DIPY)₃9	280 \pm 8	360 \pm 7	-	74 \pm 4
Aℓ(DIPY)₃10	-	330 \pm 9	-	86 \pm 5
Aℓ(DIPY)₃11	-	320 \pm 7	-	88 \pm 6
Aℓ(DIPY)₃12	240 \pm 30	-	100 \pm 16	-
Aℓ(DIPY)₃13	250 \pm 30	-	170 \pm 20	-
Aℓ(DIPY)₃15	-	300 \pm 10	-	110 \pm 6

*calculated by biexponential fitting

Another complementary feature that can be estimated from TA spectra, and the intensity of the ground state bleaching, is the triplet state relative efficiency (Φ_{isc}).

Since the UV-Vis absorption at the excitation wavelength was set to the same range (0.4 – 0.5), the relative triplet state yield can be estimated comparing the intensity of the TA spectra of each of the $\text{Al}(\text{DIPY})_3$ complexes (preferably by experiments on the same day). The ascending order of the relative triplet state yields in toluene is: $\text{Al}(\text{DIPY})_{313} < \text{Al}(\text{DIPY})_{312} < \text{Al}(\text{DIPY})_{35} < \text{Al}(\text{DIPY})_{31}$, $\text{Al}(\text{DIPY})_{36}$, $\text{Al}(\text{DIPY})_{311} < \text{Al}(\text{DIPY})_{32}$, $\text{Al}(\text{DIPY})_{313}$, $\text{Al}(\text{DIPY})_{315} < \text{Al}(\text{DIPY})_{34} < \text{Al}(\text{DIPY})_{39} < \text{Al}(\text{DIPY})_{38} < \text{Al}(\text{DIPY})_{310}$; while the order in ethanol is: $\text{Al}(\text{DIPY})_{34} < \text{Al}(\text{DIPY})_{35}$, $\text{Al}(\text{DIPY})_{312}$, $\text{Al}(\text{DIPY})_{313} < \text{Al}(\text{DIPY})_{33} < \text{Al}(\text{DIPY})_{38} < \text{Al}(\text{DIPY})_{39}$. Therefore, we can postulate that $\text{Al}(\text{DIPY})_{38}$ and $\text{Al}(\text{DIPY})_{39}$ are more likely for efficient triplet sensitisation since they persistently exhibit higher triplet state yields in both solvents; however, $\text{Al}(\text{DIPY})_{32}$ and $\text{Al}(\text{DIPY})_{310}$ may have the same potential since they display relatively high triplet state lifetimes in toluene whilst they both have moderate fluorescent characteristics. In comparison to toluene, complexes $\text{Al}(\text{DIPY})_{312}$ and $\text{Al}(\text{DIPY})_{313}$ illustrated a greater triplet absorptivity in ethanol and $\text{Al}(\text{DIPY})_{34}$ absorb less. TA spectra in DCM exhibited intense peaks with longer triplet lifetimes, but as there is degradation we did not proceed with other experiments. The obtained triplet excited state lifetimes were calculated as follows: $\text{Al}(\text{DIPY})_{38}$: 650 ± 40 ns, $\text{Al}(\text{DIPY})_{39}$: 870 ± 38 ns, $\text{Al}(\text{DIPY})_{310}$: 760 ± 34 ns (Figure A 50, Figure A 53 and Figure A 55). The depicted differences of the triplet state lifetimes among the solvents support the fact that photoexcitation processes are affected by the nature of the solvent both in the triplet and singlet excited states and imply that non-radiative decay $T_1 \rightarrow S_0$ is also significant.

Additionally, to testify whether oxygen is a keystone element upon photoexcitation, the triplet state lifetimes under oxygen-free conditions of the $\text{Al}(\text{DIPY})_3$ complexes were calculated by simple monoexponential fitting (unless stated otherwise). TA spectra and time trace fittings are shown in Figure A 60 – Figure A 73. Solutions were subjected to five freeze-pump-thaw cycles prior to photoexcitation. TA features of the $\text{Al}(\text{DIPY})_3$ complexes were similar, with triplet excited state lifetimes being extremely longer, in the range of $\sim 80 - 200$ μs , giving testimony that oxygen significantly alters the outcome of the excitation. Noteworthy, this condition is consistently observed for all the $\text{Al}(\text{DIPY})_3$ chelates (Table 4.5).^[185,480] Lastly, the rate constant for quenching of the triplet state by

oxygen was also determined to be in the range of $1.60 - 1.90 \times 10^{-9} \text{ M}^{-1} \text{ s}^{-1}$ ($[\text{O}_2]$ in ethanol: $2.1 \times 10^{-3} \text{ M}$; $[\text{O}_2]$ in toluene: $1.8 \times 10^{-3} \text{ M}$, at $20 \text{ }^\circ\text{C}$).^[382]

4.3.3.3 Singlet oxygen generation

Singlet oxygen phosphorescence was determined at 1270 nm and the singlet oxygen quantum yields were calculated relative to 5,10,15,20-tetraphenylporphyrin (H₂TPP) in toluene^[485] or erythrocin B in ethanol^[486] as standard reference compounds (Figure 4.24, Figure A 74 and Figure A 75). Table 4.6 summarises the singlet oxygen quantum yields in ethanol and toluene. Additionally, a ratio of the Φ_Δ of **Aℓ(DIPY)₃** chelates and Φ_Δ of the reference (erythrocin B) was defined in another attempt to demonstrate the relative singlet oxygen generation. Singlet oxygen determination can be affected by the oxygen concentration and its lifetime in different solvents.^[258] There is a significant variation in the determined singlet oxygen quantum yield of **Aℓ(DIPY)₃8** between ethanol ($\Phi_\Delta = 0.15$) and toluene ($\Phi_\Delta = 0.70$) solutions, while for **Aℓ(DIPY)₃9** the opposite trend occurs: $\Phi_\Delta = 0.35$ in ethanol; $\Phi_\Delta = 0.07$ in toluene. Since singlet oxygen phosphorescence is a sensitive method, and taking into consideration that oxygen concentration in air equilibrated solutions is mainly the same in both solvents, the discrepancies between the two solvents can be ascribed to the difference in the singlet oxygen lifetimes: singlet oxygen lifetime in toluene (27 μs) is almost two times greater than that in ethanol (15 μs).^[382,487]

The combination of the absolute values and the calculated ratios leads to the conclusion that chelates **Aℓ(DIPY)₃4**, **Aℓ(DIPY)₃6**, **Aℓ(DIPY)₃8**, **Aℓ(DIPY)₃9** and **Aℓ(DIPY)₃10** can be efficient singlet oxygen generators. Therefore, their respective triplet state energy level should be higher than the lowest energy of molecular oxygen (0.98 eV) to generate singlet oxygen. To conclude, since exciton coupling splits the singlet excited state into two excitonic states with higher (X'') and lower energy level (X'), it is expected that the X' state is closer to the triplet excited state. Therefore, a decrease of this energy gap can enhance the ISC efficiency and result in higher singlet oxygen generation. The occurrence of a high IC yield from non-radiative decay to the ground state ($S_1/T_1 \rightarrow S_0$) cannot be eliminated and it can be higher than the ISC in some of the complexes, therefore further investigation is needed.^[152,156,157]

Table 4.6. Singlet oxygen quantum yields of Al(DIPY)₃ complexes in toluene and ethanol.

Compound	$\Phi_{\Delta \text{ toluene}}^a$	$\Phi_{\Delta \text{ ethanol}}^b$	$\Phi_{\Delta x} / \Phi_{\Delta r}^c$
Al(DIPY)₃1	0.03	-	0.98
Al(DIPY)₃2	0.07	-	2.03
Al(DIPY)₃3	0.03	0.13	1.00
Al(DIPY)₃4	0.59	0.13	1.89
Al(DIPY)₃5	0.02	0.18	0.54
Al(DIPY)₃6	0.38	-	0.93
Al(DIPY)₃8	0.70	0.15	1.98
Al(DIPY)₃9	0.07	0.35	2.25
Al(DIPY)₃10	0.76	-	2.41
Al(DIPY)₃11	0.02	-	0.55
Al(DIPY)₃12	-	0.10	0.65*
Al(DIPY)₃13	-	0.10	-
Al(DIPY)₃15	0.20	-	0.51

^a Absolute value of singlet oxygen quantum yield in toluene calculated with H₂TPP as reference compound; ^b absolute value of singlet oxygen quantum yield in ethanol calculated with erythrocyanin B as reference compound; ^c ration of Φ_{Δ} of Al(DIPY)₃ complexes (in toluene) to Φ_{Δ} of reference compound (erythrocyanin B in ethanol);

***Al(DIPY)₃12** in THF and erythrocyanin B in ethanol.

The quantum yield of ISC (or ICT) and IC should be following the general trend: $\Phi_{\Delta} < \Phi_{isc} + \Phi_{ic} < 1 - \Phi_f$. An approximation of the radiationless processes could be given by the singlet oxygen quantum yields and the triplet state information indicating that **Al(DIPY)₃4**, **Al(DIPY)₃6**, **Al(DIPY)₃8**, **Al(DIPY)₃9** and **Al(DIPY)₃10** may possess an enhanced intersystem crossing yield which is in agreement with the increased k_{nr} . Moreover these chelates display moderate singlet excited state lifetimes. Additionally, the large Stokes shifts, the low radiative rates and the long triplet lifetimes confirmed the emission through the excited triplet state of the aluminium complexes. These findings can lead to the inter-ligand based triplet excited state $^3\pi-\pi^*$ (long-lived 3IL) originating from the initial $^1\pi-\pi^*$ states. All the above are extremely dependent on the polarity of the

environment, which influences the processes and the competing pathways. The reduction of singlet oxygen efficiency has been observed in polar solvents (aqueous media) and is related to the low solubility of oxygen in water in comparison to other organic solvents as well to the lower singlet oxygen lifetime in water.^[488] Moreover, excited state quenching or aggregation in polar environments can occur resulting in singlet oxygen attenuation. For instance, encapsulation in a polymer matrix to generate nanoparticles or addition of poly(ethylene) glycol (PEG) substituents can enhance the water solubility and biocompatibility of the potential therapeutic agents.^[189,489]

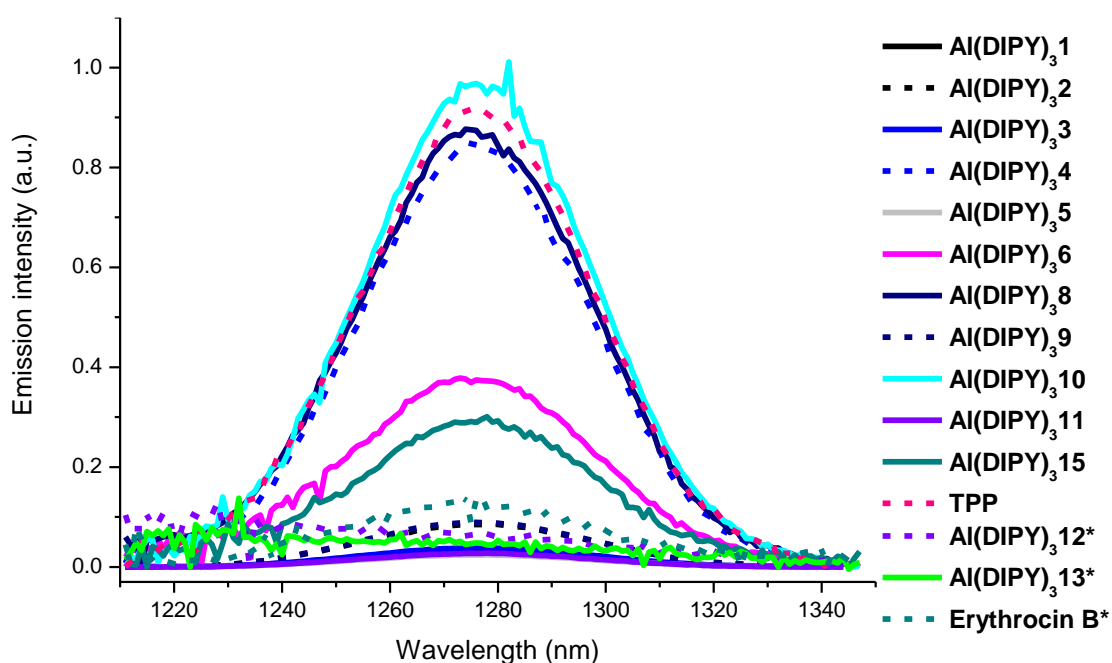


Figure 4.24. Singlet oxygen emission spectra of $Al(DIPY)_3$ complexes after excitation at 500 nm in toluene or ethanol (*) with erythrocin B as reference compound.

4.3.4 Photobiological evaluation – *in vitro* phototoxicity studies⁸

Following the chemical and photophysical characterisation of the $Al(DIPY)_3$ complexes, their photobiological evaluation was assessed in view of their application as PSs in PDT.

The $Al(DIPY)_3$ chelates used for the *in vitro* studies were chosen in terms of their solubility in DMSO in order to obtain stock solutions with concentrations of 1 – 2 mM. Therefore, eight of the complexes were investigated with regards to their phototoxic effect against the CT26 mouse colon carcinoma cell line (Figure 4.25). Cell viability was assessed by using resazurin assay where the cell survival is determined in comparison with the non-treated control sample which corresponds to 100% cell viability.^[391,392]

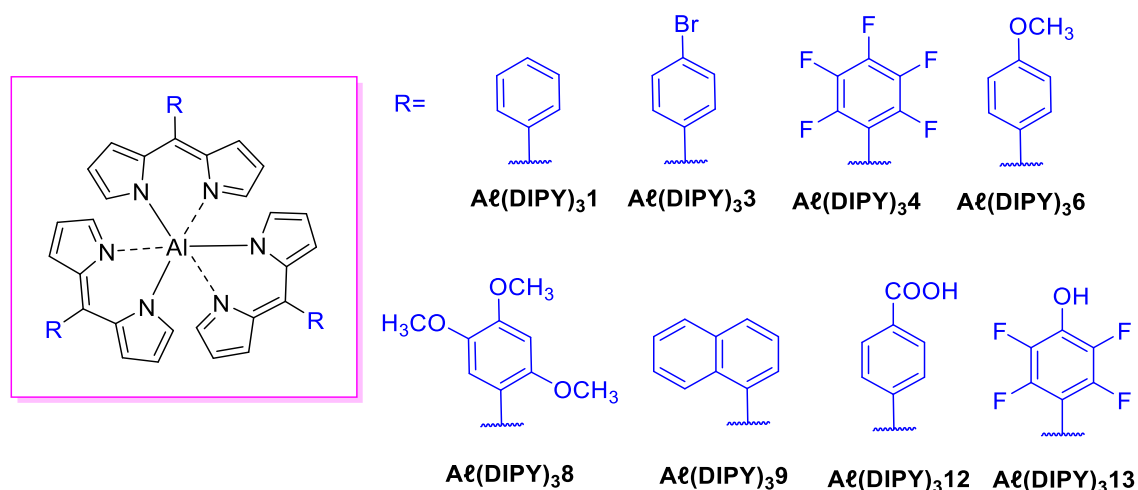


Figure 4.25. Chemical structures of the $Al(DIPY)_3$ complexes used for the photobiological evaluation.

In a first set of studies, the toxicity of the selected $Al(DIPY)_3$ compounds was evaluated in the absence of light using the CT26 cell line (Figure 4.26). For this, cells were incubated during 24 h with the respective $Al(DIPY)_3$ complexes using concentrations from 0.62 to 20 μ M. Then, after a washing step, cell viability was assessed by resazurin assay.^[391] The majority of the complexes showed no toxicity up to 20 μ M except for **$Al(DIPY)_313$** which displayed 40 – 50% of cell

⁸ *In vitro* studies were conducted during a two month internship in the photobiology group at the University of Coimbra in Portugal, under the supervision of Dr. Lúcia Catarina Gomes-da-Silva and with the support of Dr. Fábio A. Schaberle.

death at 20 μM (Figure 4.26). As a consequence, in the following phototoxicity studies, the highest concentration of **$\text{Al}(\text{DIPY})_3\mathbf{13}$** that was tested was 10 μM .

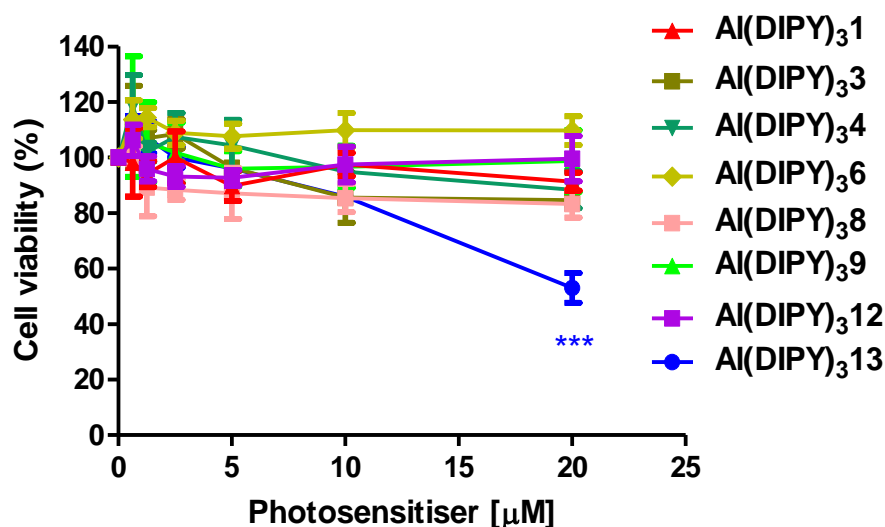


Figure 4.26. Cell viability of CT26 cells post incubation (24 h) with $\text{Al}(\text{DIPY})_3$ complexes in the absence of light; results are expressed as the mean values of three individual experiments \pm SEM ($n = 3$); one-way ANOVA in comparison with untreated cells, $p < 0.001$ for ***.

The phototoxicity effect of the $\text{Al}(\text{DIPY})_3$ chelates in CT26 cell line was assessed as previously described (see 2.3.3), by using a broadband lamp (LED) with a light dose (L.D.) of 2.6 J cm^{-2} . Accurate light doses were estimated considering the overlap between the LED and the photosensitiser spectrum.^[393] Final concentration of **$\text{Al}(\text{DIPY})_3\mathbf{1}$** – **$\text{Al}(\text{DIPY})_3\mathbf{12}$** was in the range from 0.62 to 20 μM , whereas concentrations from 0.31 to 10 μM of **$\text{Al}(\text{DIPY})_3\mathbf{13}$** were used. CT26 cells were incubated with the aluminium complexes for 24 h followed by their replacement by fresh medium. Then, cells were irradiated at 2.6 J cm^{-2} (LED, 400 – 700 nm, light potency 10 mW cm^{-2}) and 24 h later, cell viability was assessed (Figure 4.27).

Our results show that complexes **$\text{Al}(\text{DIPY})_3\mathbf{1}$** , **$\text{Al}(\text{DIPY})_3\mathbf{6}$** and **$\text{Al}(\text{DIPY})_3\mathbf{9}$** (Figure 4.27 A, D and F) are not phototoxic at the indicated light dose, while **$\text{Al}(\text{DIPY})_3\mathbf{3}$** (Figure 4.27 B) showed a marginal phototoxicity at 20 μM . Complex **$\text{Al}(\text{DIPY})_3\mathbf{4}$** displayed a higher phototoxic effect, since it reduced cell viability by 50 – 60 % at 20 μM (Figure 4.27, C).

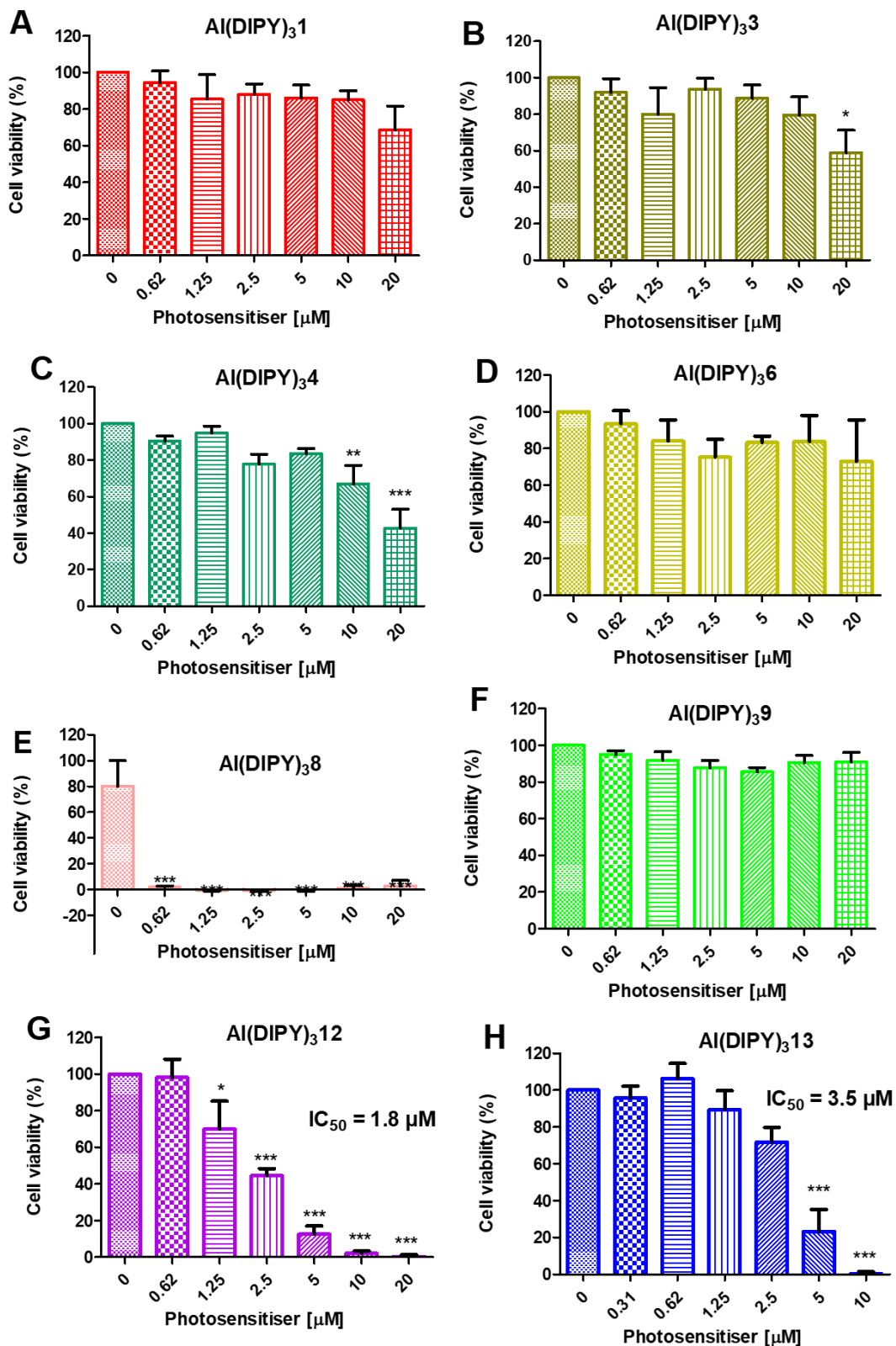


Figure 4.27. Cell viability of CT26 cells post incubation with $Al(DIPY)_3$ complexes and irradiation with L.D. of $2.6 J cm^{-2}$; results are expressed as the mean values of the individual experiments \pm SEM ($n = 3 - 4$); one-way ANOVA in comparison with untreated cells, $p < 0.05$ for *, $p < 0.01$ for **, $p < 0.001$ for ***.

Interestingly, **Aℓ(DIPY)₃12** and **Aℓ(DIPY)₃13** had a very good phototoxic effect on the colon carcinoma cell line, whilst they were the most difficult to handle during the photophysical characterisation studies. Their non-emissive singlet state properties led to an efficient triplet excited state formation and a low singlet oxygen generation ($\Phi_{\Delta} = 0.10$ in ethanol), yet suitable to develop the desired photodynamic effect. It seems that the polar hydroxyl and carboxyl groups can enhance the phototoxicity effect since the post-functionalised **Aℓ(DIPY)₃13** exhibits greater phototoxicity in comparison with its precursor **Aℓ(DIPY)₃4**. The IC₅₀ values of **Aℓ(DIPY)₃12** and **Aℓ(DIPY)₃13** are fairly low with the former being slightly more phototoxic: 1.8 μM and 3.5 μM for **Aℓ(DIPY)₃12** and **Aℓ(DIPY)₃13**, respectively.

Lastly, **Aℓ(DIPY)₃8** that contains three methoxy groups in the phenyl rings showed great phototoxic potential with approximately 100% of cell death at all the tested concentrations (0.62 to 20 μM). In contrast, **Aℓ(DIPY)₃6**, bearing only one methoxy group on each phenyl ring, did not exhibit any phototoxic effect (Figure 4.27, E). This can be attributed to the fact that **Aℓ(DIPY)₃8** exhibited higher singlet oxygen quantum yield ($\Phi_{\Delta} = 0.70$ in toluene) in comparison to **Aℓ(DIPY)₃6** ($\Phi_{\Delta} = 0.38$ in toluene). In order to calculate the IC₅₀ value for **Aℓ(DIPY)₃8**; a new set of phototoxicity studies was carried out using lower concentrations of **Aℓ(DIPY)₃8** and/or lower L.D.

An IC₅₀ value in the nanomolar range (80 nM) was determined when **Aℓ(DIPY)₃8** was used in the range of 0.04 – 5 μM with a L.D. of 2.6 J cm⁻² (Figure 4.28, A). A slightly higher IC₅₀ (0.18 μM) was calculated when **Aℓ(DIPY)₃8** was examined under a lower L.D. of 1 J cm⁻² (0.08 – 10 μM) (Figure 4.28, B). The low IC₅₀ value is of great importance as it gives room for less exposure to the PSs, which can contribute in reducing unwanted side effects while maintaining the phototoxicity.

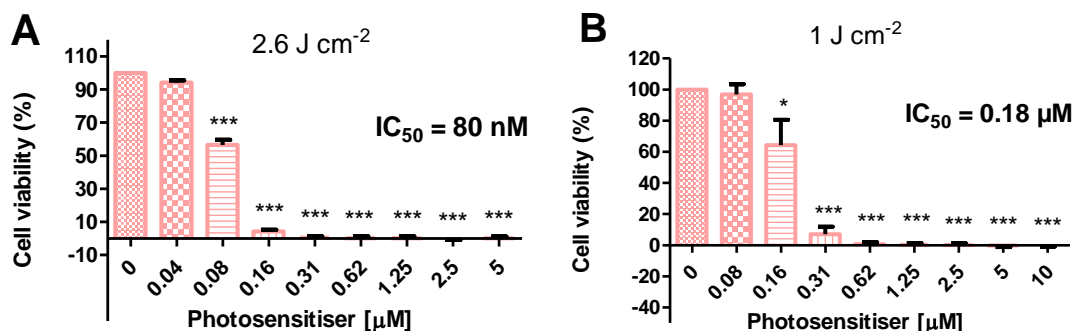


Figure 4.28. Cell viability of CT26 cells post incubation with **Aℓ(DIPY)₃8** and irradiation with L.D. of 2.6 J cm⁻² (**A**) and 1 J cm⁻² (**B**); results are expressed as the mean values of the individual experiments ± SEM (n = 2); one-way ANOVA in comparison with untreated cells, p < 0.05 for *, p < 0.001 for ***.

Note, that **Aℓ(DIPY)₃8** exists as an isomeric mixture; however, this is not a new concept for PS in PDT; Ru(III) complex TLD-1433 is a chloride salt of a racemic mixture of two isomers and can be effectively utilised as long as the toxicity profile is acceptable.^[61] The high phototoxicity mediated by **Aℓ(DIPY)₃8** is consistent with its photophysical properties. Both in toluene and ethanol **Aℓ(DIPY)₃8** can effectively generate singlet oxygen, particularly in toluene ($\Phi_{\Delta} = 0.70$). **Aℓ(DIPY)₃8** has a moderate fluorescence quantum yield ($\Phi_f = 0.03$) taking into consideration that such molecules are normally poor emitters. Moreover, triplet excited state lifetimes were long and greatly affected by oxygen. Overall, the optimal photophysical properties of **Aℓ(DIPY)₃8** are correlated with the significant phototoxicity and the lack of dark toxicity in CT26 cancer cells. The observed morphology under the microscope of the CT26 cells is depicted in Figure 4.29. Viable cells (control) are adhesive in the substrate and show a regular morphology (left); whilst cell death is observed post incubation with **Aℓ(DIPY)₃8** and irradiation (right).

Surprisingly, **Aℓ(DIPY)₃9** which had improved singlet and triplet state properties, and singlet oxygen formation in polar solvent ($\Phi_{\Delta} = 0.34$), did not induce any phototoxicity at 2.6 J cm⁻². It is hypothesised that the lack of activity might be explained by its poor internalisation or possible aggregation. However, it should

be noted that the applied L.D. was relatively low in comparison with other reports, which leaves room for exploration.^[209,228,490]

Ultimately, we can surmise that the $A\ell(\text{DIPY})_3$ complexes with -OH, -COOH, -OCH₃ groups in the phenyl moieties exhibit better biological compatibility and probably cell permeability. These polar groups may increase the amphiphilicity of the compounds which at the end can facilitate their cellular uptake. Another factor that can be crucial is the varied solubility in the medium; if aggregation takes place, they might lose their activity. This can be overcome by attaching polymer moieties or encapsulate the complexes in polymer matrixes.

Although these complexes absorb outside the photo therapeutic window; they display promising potential as new homoleptic complexes for photodynamic therapy or antimicrobial inactivation. Additionally, another aspect that should be taken into account is the possibility of DNA intercalation, as in the case of other metal complexes, e.g., Ru(II) bipyridine derivatives, upon photoirradiation. These classes of molecules are non-emissive in aqueous solutions and by interference with DNA they act as “*molecular light switches*”. Specifically, upon intercalation of the complex in the hydrophobic cavity of DNA and with the prevention of water access by the duplex DNA surroundings, the emissive properties of the complex are revealed. This occurs through the local region that acts like an organic solvent and allows the luminescence properties to be unveiled enabling singlet oxygen generation upon irradiation. Another action can be through the minor or/and major groove binding. One similarity between the metallo-intercalators and the $A\ell(\text{DIPY})_3$ chelates is the octahedral configuration.^[491–494] Early reports on the DNA-binding of octahedral metal centres (e.g., tris-phenanthroline complexes of ruthenium, chromium, zinc, nickel, cobalt) showed that the complexes could bind to DNA *via* a hydrophobic interaction in the minor groove or by a partial intercalation of the ligand into the helix in the major groove or these can happen simultaneously.^[495–497]

Overall, our preliminary results demonstrated that **$A\ell(\text{DIPY})_3\mathbf{8}$** , **$A\ell(\text{DIPY})_3\mathbf{12}$** and **$A\ell(\text{DIPY})_3\mathbf{13}$** are promising photosensitisers as they exhibit high phototoxicity at low concentrations. Further studies are crucial to unveil the underlying mechanism of action of the $A\ell(\text{DIPY})_3$ complexes.

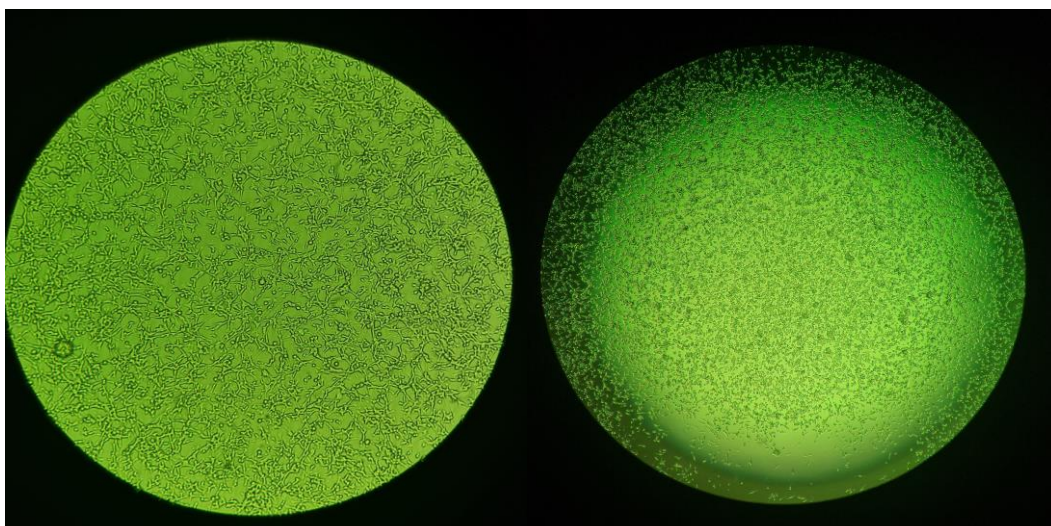


Figure 4.29. Cell morphology of CT26 cells under inverted microscope (Motic AE2000); left: viable cancer cells (control); right: cell death is observed after the treatment with **Aℓ(DIPY)₃8** upon irradiation.

4.3.5 Radio labelling with Indium-111⁹

The aim of this study was to investigate the potential and the capability of one dipyrin molecule to form the corresponding indium-111 radiolabelled chelate. Upon successful radiolabelling *in vivo* biodistribution is envisioned.

Regardless of the previously reported trivalent indium complexes and the common use of indium-111 as a radioisotope in the pharmaceutical drug industry, there are no reports on the radiolabelling potential of tris(dipyrinato)indium(III) complexes.^[152,159,228] Indium-111 is considered an excellent imaging radioisotope as it has a moderate radiation dose, facile labelling procedures and most importantly, appropriate half-life. A burden is the cost, a slow clearance of the body and the short self-life that requires a weekly order.^[498,499] Herein, we attempted to evaluate the radiolabelling potential of 5-(2',4',5'-trimethoxyphenyl)dipyrin (**DIPY8**) to form the corresponding tris(dipyrinato) complex with the indium-111 isotope as metal centre. Since **Al(DIPY)₃8** showed the highest *in vitro* phototoxicity among the tris(dipyrinato)aluminium(III) complexes against the CT26 cell line, **DIPY8** was handpicked for the radiolabel attempt.

Several attempts were made to generate the corresponding tris(dipyrinato) indium-111 complex. The reaction was monitored by using HPLC equipped with UV-Vis absorption and gamma detector. Efforts to radiolabel **DIPY8** by using indium-111 chloride [¹¹¹In]InCl₃ with solvent or buffer - such as sodium acetate, ammonium acetate, methanol, HEPES (4-(2-hydroxyethyl)-1-piperazineethanesulfonic acid), or triethylammonium acetate - did not result in the formation of any radiolabelled compound. Conversely, upon addition of aq. NaOH, a new product was formed and detected by HPLC, indicating that the use of base is essential for successful radiolabelling (Figure 4.30). Therefore, a solution of ammonium acetate with indium-111 chloride was left to react in order to increase the binding activity of indium-111 while Cl⁻ dissociates. Then **DIPY8**

⁹ This piece of work was conducted during a three week training in our POLYTHEA industrial partner 'BIOEMISSION TECHNOLOGY SOLUTIONS IKE, Athens, Greece'. The work was carried out under the supervision and guidance of Dr. Sophia Sarpaki and Asst. Dr. George Loudos. The general objective of the secondment was to follow a radiolabelling protocol and get an insight of the company's performance and activities.

and aq. NaOH were added and after 40 min the reaction was monitored by radio HPLC in order to assess the binding efficiency of Indium-111 labelled dipyririn. The product **4.53** was formed after binding in 95% incorporation (Reg#2, Figure 4.31).

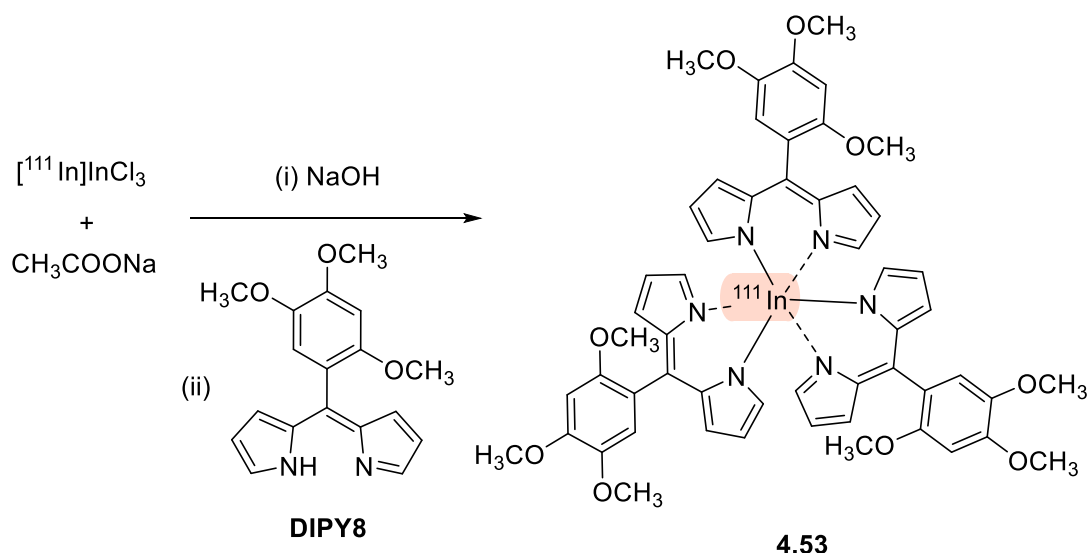


Figure 4.30. Radiolabelling of **DIPY8** by using $[^{111}\text{In}]\text{InCl}_3$ in ammonium acetate and sodium hydroxide solution.

In the UV-Vis HPLC the peak at ~ 8.30 min corresponds to the ligand precursor **DIPY8** (Figure 4.31, top). Looking at the radio HPLC, the peak at ~ 2.5 min (Reg#1) corresponds to the unbound $[^{111}\text{In}]\text{In(III)}$ and the broad peak at ~ 7.5 min (Reg#2) corresponds to the radiolabelled compound (Figure 4.31, bottom).

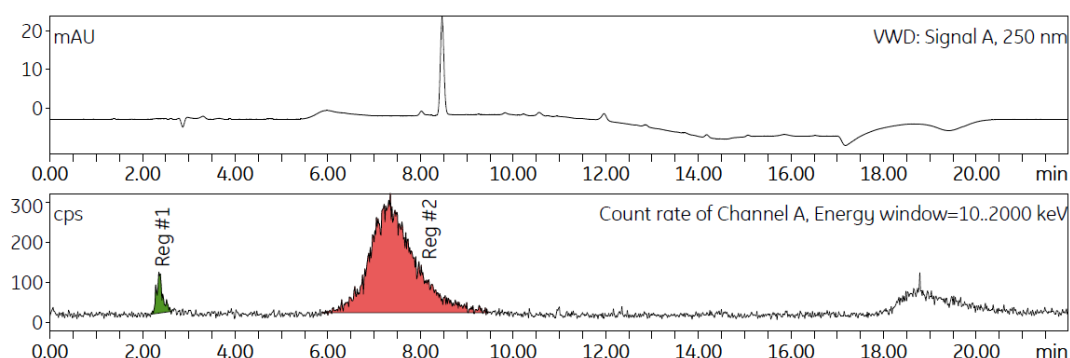


Figure 4.31. UV-Vis HPLC (top) and radio HPLC (bottom) of the reaction, 95.26% incorporation after the peak integration./HPLC chromatogram of ^{111}In -labelled complex.

Furthermore, kinetic stability studies of the radiolabelled indium-111 chelate were conducted. This was assessed by monitoring the percentage of indium-111

incorporation at various temperatures (4, 24, and 37 °C) and in saline as medium (37 °C) for 24 h, post preparation. No significant changes in the incorporation were observed after 24 h (Figure 4.32). These studies suggest that the respective complex is stable with respect to loss of the metal ion at different temperatures and in saline solution. This can be advantageous for future *in vitro* or *in vivo* imaging studies, enabling control over the localisation and minimise the non-target accumulation of the isotope. Preliminary non-invasive imaging experiments in a healthy mouse are sought after to investigate the biodistribution of the indium-111 chelate.

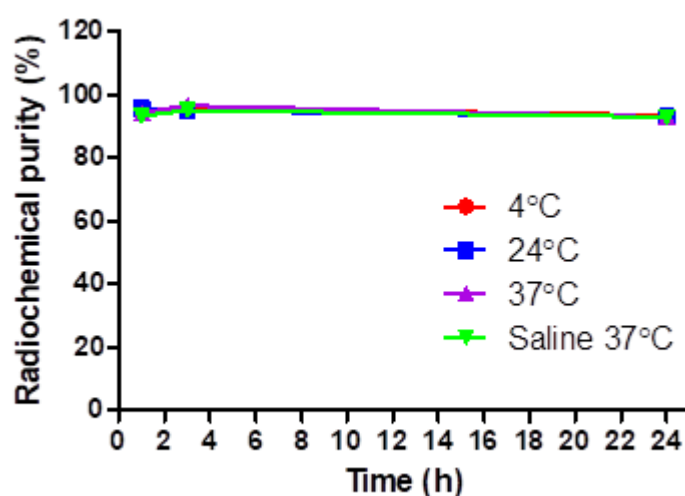


Figure 4.32. Radiochemical purity of tris(dipyrrinato) ¹¹¹Indium complex at different temperatures and in saline, at different time points.

4.4 Conclusions and Future Work

In this study we successfully synthesised a library of novel tris(dipyrrinato)aluminium(III) complexes in a three step synthesis **Al(DIPY)₃1** – **Al(DIPY)₃11**. We exploited the stability of the complexes by introducing polar anchor groups in the periphery [**Al(DIPY)₃12**, **Al(DIPY)₃13**] and by performing palladium catalysed cross-coupling reactions. Overall, neither the strong basic condition of the ester cleavage nor the palladium catalysed reaction conditions affected aluminium complexes, proving their stability upon functionalisation. Lastly, X-ray single crystal analysis was performed for most of the corresponding structures with **Al(DIPY)₃2**, **Al(DIPY)₃8**, **Al(DIPY)₃9** and **Al(DIPY)₃10** displaying the higher distortion of the aryl ring attached at the meso position of the dipyrin. Noteworthy, conjugate **Al(DIPY)₃15** has the potential to form metal organic frameworks (MOFs).

With the aim to elucidate their photophysical features and excited state properties, steady state absorption and fluorescence along with transient absorption spectroscopy were employed in polar and non-polar solvents. Generally, **Al(DIPY)₃** complexes resulted in excitonic and ICT states leading to non-radiative decays upon excitation. DFT calculations supported the inter- and intra- ligand electronic transitions that may occur and the marginal metal contribution on the transitions. However, long-lived triplet excited states were formed and allowed for singlet oxygen generation. In PDT, long triplet excited state lifetimes are envisioned and this could be advantageous for aluminium dipyrinato complexes launching a new ground in research towards photomedicine.

Namely, **Al(DIPY)₃** chelates displayed fluorescence emissive properties with fluorescence quantum yields in the range of 0.01 – 0.07 in toluene; whereas in ethanol the signal was negligible. Chelates **Al(DIPY)₃2**, **Al(DIPY)₃8**, **Al(DIPY)₃9** and **Al(DIPY)₃10** displayed the higher yields in toluene. A similar trend was observed in the singlet excited state lifetimes ranging from 1.5 – 5 ns. Consequently, as a result of the CT states, **Al(DIPY)₃** complexes efficiently populate triplet excited states with long-lived triplet state lifetimes in air-equilibrated conditions (250 – 350 ns). Complexes **Al(DIPY)₃4**, **Al(DIPY)₃8**,

Al(DIPY)₃9 and **Al(DIPY)₃10** displayed the higher triplet state lifetimes in toluene and **Al(DIPY)₃3**, **Al(DIPY)₃8** and **Al(DIPY)₃9** in ethanol. Additionally, in the absence of oxygen the triplet state lifetimes ascend up to the range of 50 – 200 μ s, confirming that the complexes' reactivity with oxygen is of paramount importance after photoexcitation. Next, comparing the singlet oxygen formation in ethanol and toluene, we can conclude that in the polar solvent, luminescence is apparent but not significantly detected, while toluene proved more suitable for the measurements. Complexes **Al(DIPY)₃4**, **Al(DIPY)₃6**, **Al(DIPY)₃8**, **Al(DIPY)₃9** and **Al(DIPY)₃10** showed high singlet oxygen generation in both solvents.

Moreover, we performed an *in vitro* screening of eight **Al(DIPY)₃** against CT26 cells in order to evaluate their applicability in photodynamic therapy. Preliminary results are promising as these complexes were able to trigger cell death upon irradiation at safe nanomolar and micromolar concentrations. Specifically, we identified possible PS candidates since four of the complexes induced phototoxicity with the following ascending order: **Al(DIPY)₃4** < **Al(DIPY)₃12** < **Al(DIPY)₃13** < **Al(DIPY)₃8**, pointing the latter as the best PS candidate. We presume that complexes with polar groups attached might express improved amphiphilicity, allowing for a better cell internalisation and permeability.

Finally, an interesting approach to evaluate the radiolabelling potential of **DIPY8** with indium-111 was achieved, resulting in radiolabelling of dipyrin 5-(2',4',5'-trimethoxyphenyl)dipyrin (**DIPY8**) with indium-111 in high incorporation (95%). The isotope incorporation remains stable over 24 h post preparation which can facilitate the outcome on a future biodistribution study.

To summarise, we conducted a comprehensive study on the development of novel homoleptic tris(dipyrrinato)aluminium(III) complexes (Figure 4.33) along with the investigation of their photocytotoxicity and their photophysical properties. Preliminary results show that they can be considered as triplet photosensitisers since they illustrated photodynamic potential.

The future direction of this project will entail broadening the scope of the aluminium complexes *via* introducing various anchor groups in the periphery with the aim to optimise their emissive profile and improve the photophysical

properties. Additional work on these systems will require their solvent compatibility and biocompatibility to assist the excited states analysis and the understanding of the photochemical and photobiological processes. Finally, the development of monomeric or heteroleptic aluminium complexes is envisioned in order to alter, fine-tune, and compare the spectral and physical characteristics.

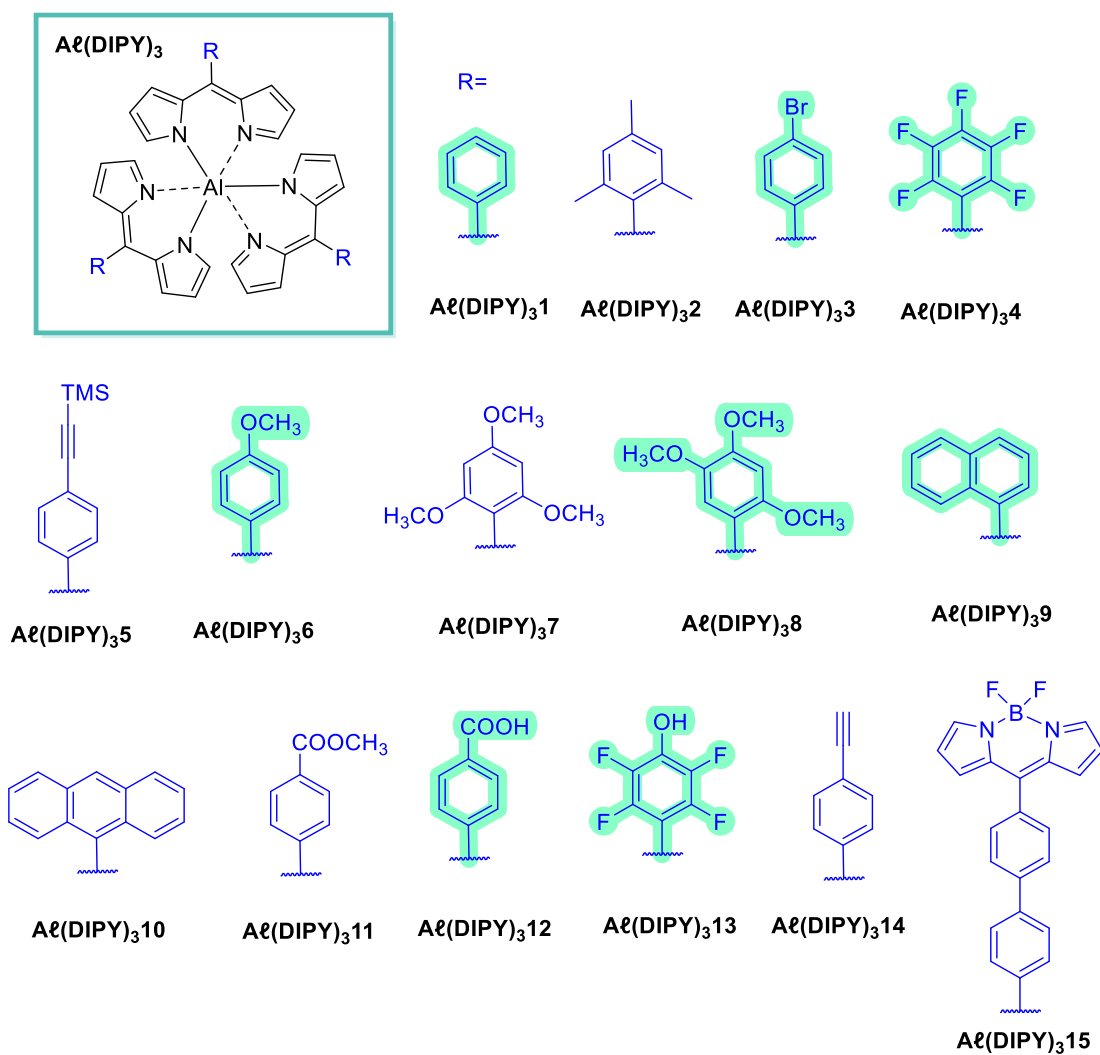


Figure 4.33. Library of the obtained tris(dipyrrinato)aluminium(III) complexes; the highlighted complexes were used for the phototoxicity studies.

Chapter 5: Experimental Details

“The beginning is perhaps more difficult than anything else, but keep heart, it will turn out all right”

~ Vincent van Gogh ~

5.1 General Information and Instrumentation

Reagents and solvents were of analytical grade and commercially acquired and used without further purification unless stated otherwise. All air and/or water-sensitive materials were handled using standard high vacuum techniques. Dry CH₃CN was obtained by passing through alumina under N₂ in a solvent purification system and then dried over activated molecular sieves. Dry DMF, THF and MeOH were purchased from Sigma-Aldrich. EtOH and MeOH of spectroscopy grade were purchased from Merck KGaA.

Analytical thin-layer chromatography (TLC) was performed using silica gel 60 (fluorescence indicator F254, pre-coated sheets, 0.2 mm thick, 20 cm × 20 cm; Merck) plates and visualised by UV irradiation ($\lambda = 254$ nm). Column chromatography was carried out using Fluka Silica Gel 60 (230–400 mesh; Merck). Mobile phases are given as (v/v).

Melting points are uncorrected and were measured using a Stuart SMP10 melting point apparatus. NMR spectra were recorded at room temperature on a Bruker AV 600, Bruker Advance III 400 MH or a Bruker DPX400 400 MHz or an Agilent 400 spectrometer. Mass spectrometry analysis (HRMS) was performed with a Q-ToF Premier Waters MALDI quadrupole time-of-flight (Q-TOF) mass spectrometer equipped with Z-spray electrospray ionisation (ESI) and matrix assisted laser desorption ionisation (MALDI) sources in positive mode with *trans*-2-[3-(4-*tert*-butylphenyl)-2-methyl-2-propenylidene]malononitrile as the matrix. ESI mass spectra were acquired in positive modes as required, using a Micromass TOF mass spectrometer interfaced to a Waters 2960 HPLC or a

Bruker microTOF-Q III spectrometer interfaced to a Dionex UltiMate 3000 LC. Atmospheric pressure chemical ionisation (APCI) experiments were performed on a Bruker microTOF-Q III spectrometer interfaced to a Dionex UltiMate 3000 LC.

Photophysical measurements were carried out with the respective solvents of spectroscopy grade. All solutions were filtered with Fisherbrand PTFE syringe filters with pore size 0.45 μm to prevent aggregation. UV/Visible spectra were recorded in solution at room temperature using a Specord 250 spectrophotometer from Analytic Jena (1 cm path length quartz cell) or a Hewlett-Packard/Agilent 8453 diode array UV-Vis or Shimadzu UV2700 spectrophotometer.

Fluorescence emission spectra were recorded on a SPEX Fluorolog 3 fluorometer with double grating monochromators in the excitation and emission channels. Excitation light source was a Xenon lamp (450 W, Osram) and the detector was a Peltier cooled photomultiplier tube (Hamamatsu, R636-10). The fluorescence emission signal is collected in a right-angle geometry, and the fluorescence spectra are corrected for fluctuations of the excitation source flux.

For the singlet oxygen emission at 1275 nm, a highly sensitive liquid nitrogen cooled InGaAs detector (Electro-Optical Systems DSS series cryogenic receiver, 2 mm InGaAs photodiode) was coupled to a Horiba Jobin Yvon Spex Fluorolog 3 spectrofluorometer. Maximum slits (excitation and emission) and long integration times (10 – 15 s) were used. A 850 nm cut-off filter was used in the emission path, to prevent second order effects of the fluorescence compounds.

Triplet state lifetimes were determined by nanosecond time-resolved absorption spectroscopy using an EKSPLA NT342B laser system in which the third harmonic of a Nd:YAG laser system was used to pump an optical parametric oscillator (OPO) at the corresponding excitation wavelengths for each experiment. The typical power was 1 – 2 mJ per pulse and the laser system was operated at 5 Hz. Probe light, running at 10 Hz, was generated using a high-stability short arc xenon flash lamp (FX-1160, Excelitas Technologies) with a PS302 controller (EG&G). The probe light was split in a signal and a reference beam with a 50/50 beam splitter and focused on the entrance slit of a

spectrograph (SpectraPro150, Princeton Instruments). The signal beam ($A = 1 \text{ mm}^2$) was passed through a sample cell and overlapped with the excitation light on a $1 \text{ mm} \times 1 \text{ cm}$ area, perpendicular to the excitation beam. A reference beam was used to normalise the signal for fluctuations in the flash lamp intensity. Both beams were recorded with an intensified CCD camera (PI-MAX3, Princeton Instruments) using 5 – 20 ns gate depending on the time steps of the measurements. The timing was achieved with a delay generator 6 (DG535, Stanford Research Systems, Inc.) and the setup was controlled with an in-house written program (LabView).

Time-resolved fluorescence decays were measured using a TCSPC technique. The relevant excitation wavelengths were generated by frequency doubling of the output of a tunable Titanium:Sapphire laser (Chameleon Ultra, Coherent). The repetition rate is decreased from the fundamental 80 MHz to a lower value (usually 8 MHz) using a pulse picker (Pulse Select, APE). The fluorescence was detected with a multichannel plate photomultiplier tube (R3809U-50, Hamamatsu) through a single-grating monochromator (Newport Cornerstone 260, $f = 250 \text{ mm}$, grating 300 ln/mm blaze 422 or grating 300 ln/m blaze 750 nm M20, Carl Zeiss, 600 lines/mm). The overall instrument response is usually 20 – 25 ps (FWHM) measured from a dilute scattering solution (Ludox) at the excitation wavelength. TCSPC histograms were recorded using $\sim 10^4$ counts in the peak channel using the SPCM program (Becker & Hinkle).

Data analysis and spectra fitting were done in Microsoft excel, Igor-Pro 7,^[500] OriginPro^[501] and Spectragryph.^[502]

HPLC was carried out using an Agilent HPLC system, 1260 Infinity II analytical series with quaternary pump linked to a (i) Elysia Flow-Count radioactivity detector and (ii) variable wavelength UV detector; using a Agilent Zorbax Eclipse Plus C18 column ($4.6 \times 250 \text{ mm}$), $5 \mu\text{m}$ (Agilent) at a flow rate of 1.0 min mL^{-1} . A Capintec™ CRCR-55tR dose calibrator was used to determine the intensity of the radioactive source expressed in μCi .

5.2 Single-crystal X-ray Structure Determinations¹⁰

5.2.1 X-ray crystallography details for the chlorins

Single-crystal X-ray diffraction data were collected on a Bruker APEX KAPPA DUO using Cu K α ($\lambda = 1.54178 \text{ \AA}$) radiation. The sample was mounted on a MiteGen microloop and data collected at 100(2) K. Bruker APEX^[503] software was used to collect and reduce data and determine the space group. The structure was solved using direct methods (XT)^[504] and refined with least squares minimisation in Olex2.^[505] Absorption corrections were applied using SADABS.^[506]

Crystals suitable for single crystal X-ray diffraction analysis were grown by slow layer diffusion. For **Zn1**, the chlorin was dissolved in DCM, and layered with hexane. For **FB1**, a DCM/hexane mixture evaporated slowly at rt. Crystals of poor quality were obtained for **Zn1** in a DCM/hexane solvate and **FB1** was also poorly diffracting. The free base and metallated chlorins are shown in Figure 2.3 (see Table 5.1 for crystal data). The macrocycle of **FB1** is notably planar. Partial bromination substitution of the C ring occurred during synthesis with approx. 3% present in the structure (Br3 = 3% and Br4 = 3% occupied) (Figure A 1). Hydrogen atoms inside the chlorin were located. The Zn is displaced from the plane of the chlorin by ca. 0.315 \AA . In both the **FB1** and **Zn1** structures the phenyl ring is twisted to the chlorin plane (64.7° in **FB1** and 63.03(19)° in **Zn1**).

¹⁰ The structural analysis was performed by Dr. Brendan Twamley, TCD unless stated otherwise.

Table 5.1. Crystal data and structure refinement for **FB1** and **Zn1**.

Identification code	FB1	Zn1
CCDC deposition no.	1990004	1990003
Empirical formula	C ₂₈ H _{22.95} Br _{1.03} N ₄	C _{29.08} H _{23.51} BrCl _{0.1} N ₄ Zn
Formula weight g/mol	497.96	577.77
Temperature (K)	100(2)	100(2)
Crystal system	monoclinic	triclinic
Space group	P2 ₁ /n	P $\bar{1}$
a (Å)	15.2041(9)	16.5765(9)
b (Å)	9.8625(5)	16.9003(10)
c (Å)	31.7167(18)	16.9698(10)
α (°)	90	119.694(3)
β (°)	97.607(4)	102.715(3)
γ (°)	90	93.421(3)
Volume (Å ³)	4714.1(5)	3947.8(4)
Z	8	6
ρ_{calc} (g/cm ³)	1.403	1.458
μ (mm ⁻¹)	2.615	3.349
F(000)	2041	1756
Crystal size (mm ³)	0.14 × 0.04 × 0.02	0.12 × 0.05 × 0.04
Radiation	CuK α (λ = 1.54178)	CuK α (λ = 1.54178)
2 θ range for data collection (°)	5.622 to 118.526	5.576 to 137.21
Reflections collected	33238	48448
	6800	14460
Independent reflections	R _{int} = 0.1542 R _{sigma} = 0.1132]	R _{int} = 0.0794 R _{sigma} = 0.0738
Data/restraints/parameters	6800/16/612	14460/113/1049
Goodness-of-fit on F ²	1.024	1.004
Final R indexes [$I \geq 2\sigma(I)$]	R ₁ = 0.0729 wR ₂ = 0.1685	R ₁ = 0.0692 wR ₂ = 0.1863
Final R indexes [all data]	R ₁ = 0.1568 wR ₂ = 0.2115	R ₁ = 0.0966 wR ₂ = 0.2044
Largest diff. peak/hole (e Å ⁻³)	1.01/-0.62	1.26/-0.97

5.2.2 X-ray crystallography details for the $\text{Al}(\text{DIPY})_3$ complexes

Data for the ligand samples **DIPY1**, **6**,¹¹ **7** and **8** were collected on a Bruker D8 Quest ECO or DUO using Mo $K\alpha$ radiation ($\lambda = 0.71073 \text{ \AA}$). Each sample was mounted on a MiTeGen cryoloop and data collected at 100(2) K using an Oxford Cryostream.

Data for the aluminium complexes $\text{Al}(\text{DIPY})_3$ **1**, **3**, **4**, **8**, **9**, **10**, **12**, **15** were collected on a Bruker APEX DUO using Cu $K\alpha$ radiation ($\lambda = 1.54178 \text{ \AA}$) and also $\text{Al}(\text{DIPY})_3$ **2**, **6** and **11** on a Bruker D8 Quest ECO using Mo $K\alpha$ ($\lambda = 0.71073 \text{ \AA}$). Each sample was mounted on a MiTeGen cryoloop and data collected at 100(2) K using an Oxford Cobra cryosystem and Cryostream respectively.

Data were collected by using omega and phi scans and were corrected for Lorentz and polarisation effects using APEX.^[503] Absorption corrections were applied using SADABS.^[507] The structure was solved with the XT structure solution program,^[504] using the intrinsic phasing solution method and refined against $|F^2|$ with XL using least squares minimisation^[508] within OLEX2.^[505] Hydrogen atoms, unless specified, were placed in geometrically calculated positions and refined using a riding model. Details of data refinements are mentioned in Table 5.2 – Table 5.6. Molecular graphics were generated using OLEX2.

For dipyrin crystal structures: in **DIPY7**, the nitrogen donor atoms were located and refined semi-free with distance restraints (DFIX) with the displacement riding on the carrier atom. Occupancy set at 50% for H1 and H11. In **DIPY8**, the N-H hydrogen atoms were located and refined. Data refined as a racemic twin.

Regarding the tris(dipyrinato)aluminium(III) chelates: it is noted that $\text{Al}(\text{DIPY})_3$ **1** is isostructural to tris(phenyldipyrin-N,N')-iron(iii).^[153] In $\text{Al}(\text{DIPY})_3$ **2**, the crystals were rotationally twinned. The twin law was obtained using TWINROT^[509] in PLATON^[510] giving a 2-axis rotation around reciprocal (1 0 0), Angle = 0.00°, (1.000, 1.000, 0.000, 0.000, -1.000, 0.000, 0.000, 0.000, -1.000) with a refined BASF of 0.0606(14). The mesityl groups were disordered and C12-C20 modelled

¹¹ Crystal structure DIPY6 was determined by Dr. Christopher J. Kingsbury, TCD.

in two positions (61:39% occupancy) using geometric and displacement restraints (SADI, SIMU, ISOR); C27-C35 lies along the 2-fold axis and was modelled as a complete rigid group, half occupied, using restraints (SIMU). A partially occupied CH₂Cl₂, also on the 2-fold axis, was modelled 10% occupied with restraints (SIMU, ISOR).

Aℓ(DIPY)₃3 has partially occupied hexane solvate in the voids (37.5%) and **Aℓ(DIPY)₃4** has disordered partially occupied (65% total, 2×17.5 and 2×15% for all positions) hexane solvate modelled with a rigid group over the inversion centre in two positions with restraints (SIMU). In **Aℓ(DIPY)₃8**, each trimethoxy phenyl group is disordered. The disorder in each substituent was different with the group at C12/C12a 58:42%, C35, C35a, 63:37% and C58/C58a 80:20%. The disorder was modelled with restraints (SADI, SIMU, and DFIX). There are two partially occupied disordered hexane solvate molecules in the lattice (75% occupancy and modelled with restraints SIMU, SADI, ISOR, and constraint EADP for C9s, C9sa). Similarly, **Aℓ(DIPY)₃9** is also disordered - two of the ligands (2,2'-(naphthalen-1-ylmethylene)bis(3H-pyrrole)) are modelled in two locations, with occupancies N22/N32 72:27 %, N43/N53 76:24%, and refined using restraints (FLAT, SADI, SIMU, ISOR) and constraints (EXYZ, EADP for C28/C28B).

Aℓ(DIPY)₃10 is highly solvated with disorder. Solvents included are DCM and hexane, all modelled with rigid groups and restraints (SIMU, ISOR) and constraints (RIGU - C19 C110 C86 C13 C14 C83). There are three solvent sites in the ASU and in the first DCM, C76, C11, C12 is disordered over two locations, 65:35% occupied. The second has partially occupied, DCM C83 C13, C14, 25% occupied and C86, C19, C110, 5% occupied. The last site is more complex and consists of hexane 33%, and 3 partial DCM molecules - C84, C15, C16 5%, C85, C17, C18 20% and C87 C111, C112 3% occupied.

Aℓ(DIPY)₃11 has weak diffraction at higher angle, leading to a high R(int) and **Aℓ(DIPY)₃12** also displays disorder in one dipyrromethenebenzoic acid group over a 2-fold axis. The benzoic acid moiety is modelled as a complete unit with half occupancy using restraints (ISOR, SIMU, SADI). There are partially occupied water molecules (2×25% occupancy in the ASU) as well as hexane (15%

occupied in ASU) and all modelled with restraints (SIMU, DFIX, ISOR and DANG).

Lastly, **A₂(DIPY)₃15** was more challenging with a diffraction limit = 0.97 Å due to weak diffraction. The diffuse contribution of solvent in the voids was accounted for by using the SQUEEZE^[511] routine in PLATON, with two voids of 2688 and 2689 Å³ with 729 electrons each removed. Two arms (biphenyl-dipyrromethane) were disordered over two locations and modelled with a combination of rigid groups (AFIX 66 and AFIX 176) using restraints (SADI, SIMU, ISOR) with occupancies of 70:30% (C50:C50B) and 65:35% (C84:C84a).

Table 5.2. Crystal data and structure refinement for **DIPY1**, **DIPY6** and **DIPY7**.

Identification code	DIPY1	DIPY6	DIPY7
Empirical formula	C ₁₅ H ₁₂ N ₂	C ₁₆ H ₁₄ N ₂ O	C ₁₈ H ₁₈ N ₂ O ₃
Formula weight g/mol	220.27	250.29	310.34
Temperature (K)	100(2)	100(2)	100(2)
Crystal system	triclinic	orthorhombic	monoclinic
Space group	P $\bar{1}$	P b c a	P2 ₁ /c
a (Å)	6.8079(6)	15.3607(4)	12.5511(7)
b (Å)	9.2020(8)	7.2185(2)	13.7153(8)
c (Å)	9.7551(9)	22.7229(5)	8.9474(5)
α (°)	79.313(4)	90	90
β (°)	76.202(3)	90	99.8086(14)
γ (°)	80.019(3)	90	90
Volume (Å ³)	577.83(9)	2519.54(11)	1517.71(15)
Z	2	8	4
ρ_{calc} (g/cm ³)	1.266	1.320	1.358
μ (mm ⁻¹)	0.076	0.084	0.094
F(000)	232.0	1056	656.0
Crystal size (mm ³)	0.33 × 0.14 × 0.06	0.106 × 0.142 × 0.428	0.37 × 0.23 × 0.11
Radiation (Å)	Mo K α (λ = 0.71073)	Mo K α (λ = 0.71073)	Mo K α (λ = 0.71073)
Reflections collected	10110	116487	28565
	2536	6080	3553
Independent reflections	R _{int} = 0.0578, R _{sigma} = 0.0508	R _{int} = 0.1109 R _{sigma} = 0.0399	R _{int} = 0.0427, R _{sigma} = 0.0227
Data/restraints/parameters	2536/1/159	6080/0/177	3553/2/218
Goodness-of-fit on F ²	1.029	1.085	1.027
Final R* indexes [$I \geq 2\sigma(I)$]	R ₁ = 0.0489, wR ₂ = 0.0988	R ₁ = 0.0581 wR ₂ = 0.1164	R ₁ = 0.0386, wR ₂ = 0.0934
Final R indexes [all data]	R ₁ = 0.0855, wR ₂ = 0.1134	R ₁ = 0.0972 wR ₂ = 0.1337	R ₁ = 0.0527, wR ₂ = 0.1027
Largest diff. peak/hole (e Å ⁻³)	0.27/-0.20	0.540/-0.264	0.26/-0.25
Flack parameter	-		-

$$^* R_1 = \frac{\sum ||F_o| - |F_c||}{\sum |F_o|}, wR_2 = \left[\frac{\sum w(F_o^2 - F_c^2)^2}{\sum w(F_o^2)^2} \right]^{1/2}.$$

Table 5.3. Crystal data and structure refinement for **DIPY8**, **Aℓ(DIPY)₃1** and **Aℓ(DIPY)₃2**.

Identification code	DIPY8	Aℓ(DIPY) ₃ 1	Aℓ(DIPY) ₃ 2
Empirical formula	C ₁₈ H ₁₈ N ₂ O ₃	C ₄₅ H ₃₃ AlN ₆	C _{54.1} H _{51.4} AlCl _{0.2} N ₆
Formula weight	310.34	684.75	819.68
Temperature (K)	100(2)	100(2)	110(2)
Crystal system	monoclinic	monoclinic	trigonal
Space group	Pn	C2/c	P-3c1
a (Å)	13.5936(6)	12.1938(4)	23.2826(10)
b (Å)	8.9845(3)	22.7452(8)	23.2826(10)
c (Å)	14.2796(5)	13.4258(5)	14.6760(9)
α (°)	90	90	90
β (°)	115.2191(15)	105.6156(18)	90
γ (°)	90	90	120
Volume (Å ³)	1577.76(10)	3586.2(2)	6889.7(7)
Z	4	4	6
ρ _{calc} (g/cm ³)	1.307	1.268	1.185
μ (mm ⁻¹)	0.090	0.817	0.099
F(000)	656.0	1432.0	2606.0
Crystal size (mm ³)	0.43 × 0.15 × 0.11	0.23 × 0.1 × 0.09	0.444 × 0.102 × 0.091
Radiation (Å)	Mo Kα (λ = 0.71073)	Cu Kα (λ = 1.54178)	Mo Kα (λ = 0.71073)
Reflections collected	31398	22286	4774
	8178	3381	4774
Independent reflections	R _{int} = 0.0838, R _{sigma} = 0.0689	R _{int} = 0.0622, R _{sigma} = 0.0393	R _{int} = 0.0768 R _{sigma} = 0.0519
Data/restraints/parameters	8178/4/431	3381/0/237	4774/451/390
Goodness-of-fit on F ²	1.026	1.033	1.078
Final R* indexes [<i>I</i> ≥ 2σ (<i>I</i>)]	R ₁ = 0.0484, wR ₂ = 0.0866	R ₁ = 0.0570, wR ₂ = 0.1584	R ₁ = 0.0700 wR ₂ = 0.1607
Final R indexes [all data]	R ₁ = 0.0812, wR ₂ = 0.0979	R ₁ = 0.0643, wR ₂ = 0.1645	R ₁ = 0.1280 wR ₂ = 0.2012
Largest diff. peak/hole (e Å ⁻³)	0.24/-0.22	0.57/-0.36	0.34/-0.31
Flack parameter	-1.1(12)		

$$*R_1 = \frac{\sum ||F_o| - |F_c||}{\sum |F_o|}, wR_2 = \left[\frac{\sum w(F_o^2 - F_c^2)^2}{\sum w(F_o^2)^2} \right]^{1/2}.$$

Table 5.4. Crystal data and structure refinement for **Al(DIPY)₃3**, **Al(DIPY)₃4** and **Al(DIPY)₃6**.

Identification code	Al(DIPY) ₃ 3	Al(DIPY) ₃ 4	Al(DIPY) ₃ 6
Empirical formula	C _{47.25} H _{35.25} AlBr ₃ N ₆	C _{48.9} H _{27.1} AlF ₁₅ N ₆	C ₄₈ H ₃₉ AlN ₆ O ₃
Formula weight	953.77	1010.64	774.83
Temperature (K)	100(2)	100(2)	100(2)
Crystal system	triclinic	monoclinic	monoclinic
Space group	P- $\bar{1}$	C2/c	P2 ₁ /n
a (Å)	9.5017(3)	18.5194(7)	12.8307(5)
b (Å)	11.8656(4)	20.4712(7)	9.9624(4)
c (Å)	19.5844(7)	14.1052(5)	29.7795(10)
α (°)	100.3242(18)	90	90
β (°)	91.6719(17)	120.6321(13)	97.1375(12)
γ (°)	102.4851(17)	90	90
Volume (Å ³)	2115.58(12)	4601.3(3)	3777.1(2)
Z	2	4	4
ρ_{calc} (g/cm ³)	1.497	1.459	1.363
μ (mm ⁻¹)	4.058	1.316	0.108
F(000)	958.0	2042.0	1624.0
Crystal size (mm ³)	0.37 × 0.05 × 0.04	0.24 × 0.11 × 0.06	0.278 × 0.221 × 0.184
Radiation (Å)	Cu K α (λ = 1.54178)	Cu K α (λ = 1.54178)	Mo K α (λ = 0.71073)
Reflections collected	33339 7924	39351 4331	66464 8395
Independent reflections	R _{int} = 0.0632 R _{sigma} = 0.0566	R _{int} = 0.0685 R _{sigma} = 0.0348	R _{int} = 0.0626 R _{sigma} = 0.0322]
Data/restraints/parameters	7924/0/524	4331/156/391	8395/0/527
Goodness-of-fit on F ²	1.032	1.056	1.025
Final R* indexes [$ I \geq 2\sigma(I)$]	R ₁ = 0.0474 wR ₂ = 0.1255	R ₁ = 0.0502 wR ₂ = 0.1476	R ₁ = 0.0394, wR ₂ = 0.0867
Final R indexes [all data]	R ₁ = 0.0556 wR ₂ = 0.1321	R ₁ = 0.0543 wR ₂ = 0.1525	R ₁ = 0.0619 wR ₂ = 0.0983
Largest diff. peak/hole (e Å ⁻³)	1.14/-1.48	0.59/-0.35	0.28/-0.28
Flack parameter			

$$^*R_1 = \frac{\sum ||F_o| - |F_c||}{\sum |F_o|}, wR_2 = \left[\frac{\sum w(F_o^2 - F_c^2)^2}{\sum w(F_o^2)^2} \right]^{1/2}.$$

Table 5.5. Crystal data and structure refinement for **Aℓ(DIPY)₃8**, **Aℓ(DIPY)₃9** and **Aℓ(DIPY)₃10**.

Identification code	Aℓ(DIPY) ₃ 8	Aℓ(DIPY) ₃ 9	Aℓ(DIPY) ₃ 10
Empirical formula	C _{60.75} H _{66.75} AlN ₆ O ₉	C ₅₇ H ₃₉ AlN ₆	C _{72.58} H _{52.83} AlCl _{3.16} N ₆
Formula weight	1051.93	834.92	1147.99
Temperature (K)	100(2)	100(2)	100(2)
Crystal system	triclinic	trigonal	triclinic
Space group	P- $\bar{1}$	R-3	P- $\bar{1}$
a (Å)	12.1521(5)	47.0719(11)	14.8501(4)
b (Å)	15.1353(7)	47.0719(11)	15.1267(5)
c (Å)	15.6212(7)	10.2208(3)	15.3138(4)
α (°)	84.640(3)	90	97.488(2)
β (°)	85.663(3)	90	117.4200(10)
γ (°)	82.793(3)	120	99.915(2)
Volume (Å ³)	2832.0(2)	19612.8(11)	2920.20(15)
Z	2	18	2
ρ_{calc} (g/cm ³)	1.234	1.272	1.306
μ (mm ⁻¹)	0.812	0.772	2.023
F(000)	1116.0	7848.0	1194.0
Crystal size (mm ³)	0.11 × 0.1 × 0.08	0.313 × 0.067 × 0.038	0.32 × 0.05 × 0.04
Radiation (Å)	Cu K α (λ = 1.54178)	Cu K α (λ = 1.54178)	Cu K α (λ = 1.54178)
Reflections collected	48784 10708	80794 8133	54629 10956
Independent reflections	R _{int} = 0.0754 R _{sigma} = 0.1011	R _{int} = 0.1080, R _{sigma} = 0.0658	R _{int} = 0.0569, R _{sigma} = 0.0412
Data/restraints/parameters	10708/1291/1066	8133/971/745	10956/330/901
Goodness-of-fit on F ²	1.046	1.031	1.040
Final R* indexes [$\geq 2\sigma$ (I)]	R ₁ = 0.1011 wR ₂ = 0.2820	R ₁ = 0.0792, wR ₂ = 0.2187	R ₁ = 0.0715, wR ₂ = 0.2045
Final R indexes [all data]	R ₁ = 0.1411 wR ₂ = 0.3294	R ₁ = 0.1105, wR ₂ = 0.2445	R ₁ = 0.0809, wR ₂ = 0.2127
Largest diff. peak/hole (e Å ⁻³)	0.66/-0.47	0.72/-0.44	0.65/-0.49
Flack parameter			

$$^*R_1 = \frac{\sum ||F_o| - |F_c||}{\sum |F_o|}, wR_2 = \left[\frac{\sum w(F_o^2 - F_c^2)^2}{\sum w(F_o^2)^2} \right]^{1/2}.$$

Table 5.6. Crystal data and structure refinement for **Al(DIPY)₃11**, **Al(DIPY)₃12** and **Al(DIPY)₃15**.

Identification code	Al(DIPY) ₃ 11	Al(DIPY) ₃ 12	Al(DIPY) ₃ 15
Empirical formula	C ₅₁ H ₃₉ AlN ₆ O ₆	C _{49.8} H _{39.2} AlN ₆ O ₇	C ₉₀ H ₆₅ AlB ₃ F ₆ N ₁₂
Formula weight	858.86	860.65	1482.91
Temperature (K)	100(2)	100(2)	100(2)
Crystal system	monoclinic	orthorhombic	monoclinic
Space group	P2 ₁ /n	lbca	P2/n
a (Å)	14.7975(9)	13.4554(3)	23.2627(16)
b (Å)	9.7051(6)	16.2673(4)	11.8862(8)
c (Å)	28.6373(18)	40.1809(10)	42.842(3)
α (°)	90	90	90
β (°)	92.1360(16)	90	94.584(4)
γ (°)	90	90	90
Volume (Å ³)	4109.8(4)	8794.9(4)	11808.0(13)
Z	4	8	4
ρ _{calc} (g/cm ³)	1.388	1.300	0.834
μ (mm ⁻¹)	0.112	0.899	0.526
F(000)	1792.0	3592.0	3064.0
Crystal size (mm ³)	0.24 × 0.16 × 0.05	0.311 × 0.224 × 0.042	0.16 × 0.08 × 0.08
Radiation (Å)	Mo Kα (λ = 0.71073)	Cu Kα (λ = 1.54178)	CuKα (λ = 1.54178)
Reflections collected	54340	38465	72031
	7857	4139	13222
Independent reflections	R _{int} = 0.1595, R _{sigma} = 0.0900	R _{int} = 0.0602, R _{sigma} = 0.0324	R _{int} = 0.1815, R _{sigma} = 0.1285
Data/restraints/parameters	7857/0/580	4139/165/392	13222/2125/1287
Goodness-of-fit on F ²	1.018	0.990	1.145
Final R* indexes [I ≥ 2σ (I)]	R ₁ = 0.0694, wR ₂ = 0.1635	R ₁ = 0.0590, wR ₂ = 0.1760	R ₁ = 0.1290, wR ₂ = 0.3533
Final R indexes [all data]	R ₁ = 0.1412, wR ₂ = 0.2094	R ₁ = 0.0699, wR ₂ = 0.1897	R ₁ = 0.2124, wR ₂ = 0.4079
Largest diff. peak/hole (e Å ⁻³)	0.30/-0.31	0.72/-0.39	0.34/-0.30
Flack parameter			

$$*R_1 = \frac{\sum ||F_o| - |F_c||}{\sum |F_o|}, wR_2 = \left[\frac{\sum w(F_o^2 - F_c^2)^2}{\sum w(F_o^2)^2} \right]^{1/2}.$$

5.3 Procedures for the Photophysical Measurements

5.3.1 UV-Visible absorption spectra

The absorption spectra were recorded in DCM, EtOH, MeOH, toluene or THF at room temperature and molecular absorption coefficients were calculated from Beer Lambert's law $A = \epsilon c x l$, where A the absorbance of the molecule at specific wavelength; ϵ the molar extinction coefficient; c the concentration of the sample in the cuvette; l the length of the light path (the width of the cuvette was 1 cm).

5.3.2 Fluorescence emission and quantum yields

The respective compounds were dissolved in methanol, ethanol, toluene, DCM, THF, or DMF and their absorbance in the UV-Vis spectrum was adjusted to ca. 0.10 at the wavelength of excitation. Steady-state fluorescence emission spectra were obtained upon excitation at the indicated wavelength:

- ✚ at 558/561 nm for **Zn1** and **Zn2**.
- ✚ at 500/640 nm for **FB1** and **FB2**.
- ✚ at 550 – 560 nm for **3.6**, **3.14 – 3.16** and **3.18 – 3.21**.
- ✚ at 445 – 500 nm for **Aℓ(DIPY)₃** complexes.

Depending on the absorption profile, different standard references were selected for the determination of the fluorescence quantum yield (Φ_f). For the **chlorins**, **dyads** and **porphyrins**, cresyl violet^[512,513] ($\Phi_f = 0.54$ in MeOH, $\Phi_f = 0.56$ in EtOH) or H₂TPP^[514] ($\Phi_f = 0.11$ in toluene) were used as reference compounds. For the **Aℓ(DIPY)₃** chelates the fluorescence quantum yields (Φ_f) were calculated with rhodamine 6G ($\Phi_f = 0.94$ in EtOH), or coumarine 153 ($\Phi_f = 0.38$ in EtOH) as standard references.^[513] The fluorescence quantum yield was determined by equation 5.1^[515] (1 s integration time; 3 nm excitation slit; 3 nm emission slit).

$$\Phi_x = \Phi_r \times \left(\frac{A_r(\lambda_r)}{A_x(\lambda_x)} \right) \times \left(\frac{I(\lambda_r)}{I(\lambda_x)} \right) \times \left(\frac{n_x^2}{n_r^2} \right) \times \left(\frac{D_x}{D_r} \right) \quad \text{Eq. 5.1}$$

where Φ is the quantum yield; $A_{(\lambda)}$ is the absorbance of the solution at the excitation wavelength λ ; I is the relative intensity of the exciting light at wavelength λ ; n is the refractive index of the solvent and D is the integrated area

under the corrected emission spectrum. Subscripts x and r refer to the unknown and reference solutions, respectively.

5.3.3 Time-correlated single photon counting – TCSPC

The respective chlorins, dyads and $Al(DIPY)_3$ complexes were dissolved in methanol, ethanol, toluene or THF and their absorbance in the UV-Vis spectrum was adjusted to ca. 0.10 at the wavelength of excitation. TCSPC was performed and the spectra were obtained upon excitation:

- ✚ at 400 nm for the chlorins both in MeOH and EtOH of spectroscopy grade. The detection wavelength for **Zn1** and **Zn2** was set to 610 nm whilst for **FB1** and **FB2** was 637 nm.
- ✚ at 425 nm for all **dyads** both in ethanol and toluene. The detection wavelength was set to 610 nm.
- ✚ at 450 nm for all **$Al(DIPY)_3$** complexes in toluene and THF. The detection wavelength was set to 580 nm.

Fluorescence lifetimes for all the compounds were calculated at picosecond scale.

5.3.4 Nanosecond transient absorption spectroscopy

The respective compounds were dissolved in ethanol, methanol, toluene or DCM and their absorbance in the UV-Vis spectrum was adjusted to ca. 0.50 at the wavelength of excitation. Transient absorption (TA) spectroscopy on nanosecond time scale was recorded upon excitation at the indicated wavelength and they were probed from 400 to 800 nm.

- ✚ at 604 nm for **Zn1** and **Zn2**.
- ✚ at 635/637 nm for **FB1** and **FB2**.

Triplet state transient absorption decays $\Delta A(t)$ were analysed and triplet state lifetimes were calculated by monoexponential fitting. Stimulated emission spectra which appeared at early delay times were not taken into consideration for the triplet lifetime calculation. Nevertheless, the latter spectra supported the calculation of the triplet state quantum yields by comparing the first TA spectrum, which consists of singlet state features in early delay times (20 ns), with the TA

at long time (40 ns) which refers to the T_1 excited state (triplet-triplet absorption features). The measurement was performed both at ambient conditions (gate width 5 ns) and in oxygen-free conditions by purging with argon for 1 – 2 h (gate width 10 ns) in MeOH and EtOH of spectroscopy grade.

✚ at 604 or 550/560 nm for **dyads**.

The measurement was performed at ambient conditions (gate width 20 ns). Triplet state transient absorption decays $\Delta A(t)$ were analysed and triplet state lifetimes were calculated by monoexponential fitting.

✚ at 450 nm for **A ℓ (DIPY) $_3$** complexes.

The measurement was performed both at ambient conditions (gate width 20 ns) and in oxygen-free conditions after five pump-freeze-thaw cycles (gate width 50 ns) in toluene, or EtOH of spectroscopy grade. Triplet state transient absorption decays $\Delta A(t)$ were analysed and triplet state lifetimes were calculated by monoexponential fitting (unless stated otherwise).

5.3.5 Singlet oxygen determination and quantum yields

The respective compounds were dissolved in methanol, ethanol, toluene or THF and their absorbance in the UV-Vis spectrum was adjusted to ca. 0.10 – 0.20 at the wavelength of excitation. Direct detection of the luminescence emission of 1O_2 at 1275 nm was achieved upon excitation:

✚ at 558/561 nm for **Zn1** and **Zn2**.

✚ at 500/640 nm for **FB1** and **FB2**.

✚ at 500 or 550 nm for **dyads**.

✚ at 500 or 508 nm for **A ℓ (DIPY) $_3$** complexes.

Singlet oxygen quantum yields (Φ_Δ) were calculated by equation 5.1,^[515] with Rose Bengal ($\Phi_\Delta = 0.80$ in MeOH, $\Phi_\Delta = 0.86$ in EtOH) as standard for **Zn1** and **Zn2**,^[516,517] and temoporfin ($\Phi_\Delta = 0.43$ in MeOH, $\Phi_\Delta = 0.65$ in EtOH) for **FB1** and **FB2**.^[45,386] For the **dyads** Rose Bengal in ethanol ($\Phi_\Delta = 0.86$ in EtOH) or H₂TPP in toluene with $\Phi_\Delta = 0.68$ (for the ratio) were used. For the **A ℓ (DIPY) $_3$** complexes erythrocyanin B in ethanol with $\Phi_\Delta = 0.69$,^[486] or 5,10,15,20-tetraphenylporphyrin (H₂TPP) in toluene with $\Phi_\Delta = 0.68$ were used as reference compounds.^[485] The

wavelength range of the emission was recorded from 1150 nm to 1350 nm; 10 or 15 s integration time; 14 nm excitation slit; 40 nm emission slit. D was calculated from the area under the curve between 1220 – 1340 nm. Note, that for singlet oxygen quantum yield calculations, the reference and unknown compound should be diluted and measured in the same solvent.

5.3.6 Density functional theory (DFT) calculations

DFT calculations were performed in Gaussian 16;^[518] on the Dutch national e-infrastructure with the support of SURF Cooperative (lisa.surfsara.nl). Avogadro^[519] and Gabedit^[520] were used for the molecular editing and the MOs visualisation. Density functional theory (DFT) and time-dependent DFT (TD-DFT) calculations were performed to investigate the ground-state and the excited-state properties of the respective dyads and five representative $Al(DIPY)_3$ complexes. Details for the chlorins can be found in section 2.3.2.4.

Hybrid B3LYP functional was used for all the compounds,^[387,388] and 6-31G* basis set for the dyads whereas a LANL2DZ basis set for $Al(DIPY)_3$ complexes to optimise the ground state (S_0) geometry in the gas phase.^[152] The same methods were applied and TD-DFT calculations were performed to calculate the excited singlet (S_1) and triplet (T_1) states and visualise the respective molecular orbitals (MOs). The S_1 ($^1E_{00}$) and T_1 ($^3E_{00}$) energies, the difference between the first singlet excited and triplet energy state (ΔE_{S-T}) are shown in Table 5.7 – Table 5.8 along with the energy difference between [HOMO – LUMO], [(HOMO-1) – LUMO], [(HOMO-1) – (LUMO+1)] and [HOMO – (LUMO+1)].

Table 5.7. Energy differences between HOMO/LUMO molecular orbitals of the dyads and singlet and triplet excited states from TD-DFT calculations.

Dyad	LUMO	LUMO	(LUMO+1)	(LUMO+1)	$^1E_{00}$	$^3E_{00}$	ΔE_{S-T}
	– HOMO	– (HOMO-1)	– (HOMO-1)	– HOMO			
3.18	2.54	2.78	2.88	2.64	2.31	1.53	0.79
3.20	2.57	2.64	2.73	2.66	2.27	1.53	0.74
3.21	2.61	2.63	2.73	2.71	2.26	1.53	0.73

Table 5.8. Energy differences between HOMO/LUMO molecular orbitals and singlet of the $A\ell(\text{DIPY})_3$ complexes and triplet excited states from TD-DFT calculations.

$A\ell(\text{DIPY})_3$ complexes	LUMO – HOMO	LUMO – (HOMO-1)	(LUMO+1) – (HOMO-1)	(LUMO+1) – HOMO	$^1E_{00}$	$^3E_{00}$	ΔE_{S-T}
$A\ell(\text{DIPY})_3\mathbf{1}$	2.20	2.69	3.16	2.67	2.15	1.76	0.39
$A\ell(\text{DIPY})_3\mathbf{4}$	1.98	2.50	3.03	2.52	1.97	1.60	0.38
$A\ell(\text{DIPY})_3\mathbf{8}$	2.02	2.62	3.15	2.54	1.98	1.72	0.26
$A\ell(\text{DIPY})_3\mathbf{9}$	1.97	2.64	3.16	2.50	1.91	1.68	0.23
$A\ell(\text{DIPY})_3\mathbf{13}$	2.02	2.54	3.04	2.52	1.99	1.61	0.38

5.4 Protocols for *In Vitro* Cytotoxicity Studies

5.4.1 Cell culture and preparation of stock solutions

The CT26 cell line (mouse colon carcinoma) was obtained from American Type Culture Collection Cells. Cells were kept in DMEM (Dulbeccos' modified Eagle's medium, Sigma) with 10% heat inactivated fetal bovine serum (Gibco, Life Technologies) and 1% penicillin streptomycin (Sigma) in a humidified incubator with 5% CO₂ at 37 °C. Cells were detached using trypsin-EDTA solution (Sigma), counted, and seeded at the necessary concentration in plates of the appropriate size. A stock solution of the respective compounds (ca. 1 mM) was prepared with DMSO Hybri-Max™ (Sigma) and stored at - 20 °C. Before each experiment, the stock solutions were diluted with the cell culture medium at the desired concentration and then added to the cells. Owing to the inherent toxicity of DMSO, the final concentration of DMSO never exceeded 1 – 2% after the dilution in DMEM.

5.4.2 Dark toxicity studies using resazurin assay

CT26 (7000 cells/well) were seeded in 96-well plates to achieve a monolayer configuration. After 24 hours of incubation, a volume of 200 μL of the indicated concentration of the respective compounds was added into the appropriate triplicate wells with the final concentrations of: 0.625, 1.25, 2.5, 5, 10, 20 μM for the **chlorins**; 1.25, 2.5, 5, 10, 20 and 40 μM for the **dyads**; 0.625, 1.25, 2.5, 5,

10, 20 μM for the **$\text{Al}(\text{DIPY})_3$** complexes. CT26 cells were incubated with the compounds for 24 h, followed by cell washing with medium. To assess cell viability, resazurin blue (Sigma, diluted in PBS, phosphate buffer solution) was used (150 μL in each well, 0.1 mg mL^{-1}). After ca. 1.5 h, the fluorescence of resorufin, the metabolic product that results from resazurin reduction, was recorded with a microplate reader (Biotek Synergy HT) using 528/20 nm excitation and 590/35 nm emission filters. The experiment was repeated three times and the final cell viability was accessed after merging the mean values of all the independent experiments. The statistical significance analysis was applied by using Graphpad software. Significance was evaluated with one-way ANOVA in comparison to the untreated cells with the Dunnett's Multiple Comparison Test and it is displayed with stars in the respective figures; for the p-value: $p < 0.001$ for ***.

5.4.3 Phototoxicity studies using resazurin assay

CT26 (6000 cells/well) were plated in 96-well plates to achieve a monolayer configuration. After 24 hours of incubation, a volume of 200 μL of the indicated concentration of the compounds was added into the appropriate triplicate wells. CT26 cells were incubated with the complexes with the indicated final concentrations for 24 h:

- ✚ For **chlorins** final concentrations from 0.04 to 5 μM were used when a L.D. of 0.5 J cm^{-2} was delivered; whereas concentrations from 0.01 to 1.25 μM were used for L.D. of 1 J cm^{-2} .
- ✚ For **dyads** final concentrations from 1.25 to 40 μM were used for all phototoxicity experiments.
- ✚ For **$\text{Al}(\text{DIPY})_3$** complexes final concentrations from 0.625 to 20 μM when a L.D. of 2.6 J cm^{-2} was delivered except for **$\text{Al}(\text{DIPY})_3\text{13}$** (which exhibited dark toxicity at 20 μM), where the final concentrations were: from 0.31 to 10 μM . The addition experiments with **$\text{Al}(\text{DIPY})_3\text{8}$** included concentrations from 0.04 to 5 μM (2.6 J cm^{-2}) and 0.08 to 10 μM (1 J cm^{-2}).

After a washing step with medium to remove any non-internalised compound, 200 μL of a medium without red phenol were added (RPMI, culture media: Roswell Park Memorial Institute) and the cells were irradiated with a LED

broadband lamp (400 – 700 nm). The correction factor from the overlap of the absorption spectra between the LED and each group of compounds was calculated and applied in order to achieve accurate light doses.^[393] The cells were irradiated with a light dose of 0.5 J cm⁻² (10 mW cm⁻² broadband lamp, 4 min), 1 J cm⁻² (10 mW cm⁻² broadband lamp, 8 min), 2 J cm⁻² (10 mW cm⁻² broadband lamp, 17 min), or 2.6 J cm⁻² (10 mW cm⁻² broadband lamp, 48 min). After an additional incubation of 24 h, resazurin assay was applied to determine the cell viability (150 µL in each well, 0.1 mg mL⁻¹). In the case of chlorins and Al(DIPY)₃ the experiment was repeated two to four times and the final cell viability was accessed after merging the mean values of the individual experiments. In the case of dyads the experiment was performed one time for each L.D. A statistical significance analysis was applied by using Graphpad software. Significance was evaluated with one-way ANOVA in comparison to the untreated cells with the Dunnett's Multiple Comparison Test and it is displayed with stars in the respective figures; for the p-value: p < 0.05 for *, p < 0.01 for **, p < 0.001 for ***.

5.4.4 Cellular uptake studies

CT26 (40000 cells/well) were seeded in 24-well plates and led to adapt for 24 h. A volume of 500 µL of the compound solutions in DMEM was added in duplicates at final concentration: 1.25 and 2.5 µM for the chlorins; 5 and 10 µM for the dyads. After 24 h of incubation, cells were washed three times with DMEM prior addition of trypsin (200 µL). Next, cells were washed with PBS and analysed by flow cytometry using a Novocyte[®] TM 2000 (ACEA). Fluorescence measurement was carried out upon excitation with 405 nm laser followed by detection with 615/24 nm emission filter. For the chlorins two independent experiments were conducted and the data were normalised against the signal of the untreated cells (mean values); whereas for dyads only one experiment was performed.

5.5 Synthetic Procedures and Characterisation

5.5.1 Chapter 2: *gem*-Dimethylchlorins as potential PSs in PDT

5.5.1.1 General synthetic procedures

General procedure A – dipyrromethane synthesis

Following literature procedures,^[349–351] a mixture of the appropriate aldehyde (1 eq.), pyrrole (10 – 25 eq.), and DCM (15 – 20 mL) (in case of **2.26a**, **2.26b**, **2.26d** and **2.26e**), were added to a dry round-bottomed flask and the solution was degassed with argon for 20 min. TFA (0.1 eq.) or MgBr₂ (2 eq.) for **2.26c** was added and the reaction mixture was protected from light and stirred for 1 – 1.5 h at rt. The reaction was quenched by the addition of aqueous NaOH (100 – 200 mL, 0.1 M), stirred for 30 min, followed by extraction with DCM (3 × 100 mL). The combined organic phase was washed with brine (3 × 50 mL), H₂O (3 × 50 mL) and dried over Na₂SO₄. The resulting solvent and unreacted pyrrole were removed under reduced pressure and the resultant crude mixture was adsorbed onto silica and purified by column chromatography.

General procedure B – DPM formylation

The Vilsmeier reagent was prepared following a literature procedure.^[353,364] DMF (7 eq.) was added to a dry round-bottom flask and cooled to 0 °C, then POCl₃ (0.9 eq.) was added dropwise and stirred for 30 minutes under argon. In a separate dry round-bottom flask the appropriate DPM (1 eq.) was dissolved in DMF (10 – 20 mL) under argon and cooled to 0 °C. The Vilsmeier reagent was added dropwise to the reaction mixture and stirred at 0 °C for 1 – 2 h whilst shielded from light. A solution of EtOAc (100 mL) and saturated aq. NaOAc (100 mL) was added and stirred at room temperature for 2 – 4 h. The mixture was extracted with EtOAc (3 × 50 mL). The combined organic extracts were washed with brine (3 × 50 mL), NaHCO₃ (3 × 50 mL), H₂O (3 × 50 mL), dried over Na₂SO₄ and evaporated *in vacuo*. The product was adsorbed onto silica and purified by column chromatography.

General procedure C – 1-formyl-DPM bromination

Following literature procedures^[355,356] 1 eq. of NBS was dried *in vacuo*, dissolved in dry THF (5 – 10 mL) and degassed with argon. In a dry Schlenk tube the appropriate 1-formyl-DPM (1 eq.) was added and dissolved in dry THF (5 – 10 mL). The mixture was protected from light and cooled to -78 °C under argon. NBS was added dropwise to this solution and stirred for 1 h. A mixture of hexane and H₂O (1:1) were added, the cooling bath was removed. After the reaction mixture reached r.t., extractions with EtOAc (3 × 50 mL) were carried out. The combined organic layers were collected, dried over Na₂SO₄, filtered, and evaporated *in vacuo*. (Caution: The water bath temperature should not exceed 25 °C). The product was adsorbed onto silica and purified by column chromatography.

General procedure D – zinc chlorin synthesis

Following literature procedures,^[353,366] 2,3,4,5-tetrahydro-1,3,3-trimethyldipyrrin (**2.14**) (1 eq.) and the appropriate 9-bromo-1-formyl-DPM **2.15d,e** (1 eq.) were dissolved in dry DCM (dried prior to use). The mixture was treated with a solution of *p*-TsOH·H₂O (5 eq.) in anhydrous MeOH and the resulting dark red solution was stirred at rt for 30 min. Then 2,2,6,6-tetramethylpiperidine (7.4 eq.) was added and the mixture was concentrated. The resulting solid was dissolved in dry CH₃CN and 2,2,6,6-tetramethylpiperidine (25 eq.), anhydrous Zn(OAc)₂ (15 eq.) and AgOTf (3 eq.) were added. The mixture was refluxed in the presence of air for 20 h and then the excess of solvent was removed under reduced pressure, followed by purification *via* column chromatography (SiO₂, DCM:hexane, 1:1, v/v).

General procedure E – zinc chlorin demetallation

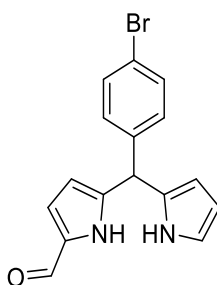
Following literature procedures,^[354] the appropriate zinc chlorin was dissolved in DCM and TFA was added. The mixture was stirred at 20 °C for 1 h and then it was quenched with the addition of sat. NaHCO₃ solution. The layers were separated, and the organic phase was washed with sat. NaHCO₃ solution (1 × 25 mL), water (1 × 25 mL), brine (1 × 25 mL) and dried (MgSO₄). The resulting solution was passed through a pad of silica (DCM) and excess solvent was removed under reduced pressure to yield the desired product.

5.5.1.2 Synthetic details and characterisation

Dipyrromethane synthesis

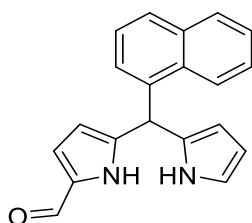
Dipyrromethane (**2.26a**), 5-phenyl-dipyrromethane (**2.26b**), 5-mesityl-dipyrromethane (**2.26c**), 5-(4'-bromophenyl)dipyrromethane (**2.26d**), 5-(1'-naphthyl)dipyrromethane (**2.26e**), 1-formyl-dipyrromethane (**2.27a**), 1-formyl-5-phenyl-dipyrromethane (**2.27b**), 1-formyl-5-mesityl-dipyrromethane (**2.27c**), 9-bromo-1-formyl-dipyrromethane (**2.15a**), 9-bromo-1-formyl-5-phenyl-dipyrromethane (**2.15b**), 9-bromo-1-formyl-5-mesityl-dipyrromethane (**2.15c**), were synthesised and characterised in accordance with the literature and the general procedures A, B and C.

1-Formyl-5-(4'-bromophenyl)dipyrromethane (**2.27d**)



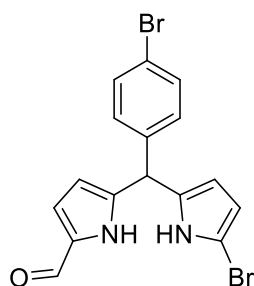
General procedure B was followed by using DMF (11.5 mL, 151 mmol) and POCl₃ (1.8 mL, 19.3 mmol) for the preparation of the Vilsmeier reagent and 5-(4'-bromophenyl)dipyrromethane **2.26d** (6.5 g, 21.5 mmol) was dissolved in DMF (20 mL). The product was purified *via* column chromatography (SiO₂, hexane:EtOAc, 85:15, *v/v*) and collected as the second fraction. Removal of the solvents under reduced pressure resulted in a light brown solid (2.75 g, 8.5 mmol, 39%); M.p.: dec. >150 °C; R_f = 0.57 (SiO₂, hexane:EtOAc, 3:2, *v/v*); ¹H NMR (400 MHz, CDCl₃): δ = 5.46 (s, 1H, meso-*H*), 5.92 – 5.94 (m, 1H, β-*H*), 6.05 – 6.06 (m, 1H, β-*H*), 6.16 (q, *J* = 2.8 Hz, 1H, β-*H*), 6.72 – 6.74 (m, 1H, β-*H*), 6.88 – 6.90 (m, 1H, β-*H*), 7.05 (d, *J* = 8 Hz, 2H, Ar-*H*), 7.44 (d, *J* = 8 Hz, 2H, Ar-*H*), 7.98 (br s, 1H, -NH), 9.17 (br s, 1H, -NH), 9.37 ppm (s, 1H, -CHO); ¹³C NMR (101 MHz, CDCl₃): δ = 43.5, 108.1, 108.8, 110.8, 118.2, 121.4, 122.0, 129.7, 129.9, 131.9, 132.4, 139.4, 141.6, 178.7 ppm; DIP-MS *m/z* calcd. for C₁₆H₁₃BrN₂O [M]⁺: 329.1970, found: 329.0401.

1-Formyl-5-(1'-naphthyl)dipyrromethane (2.27e)



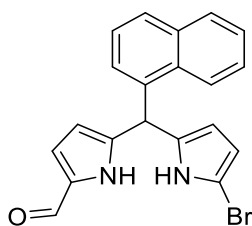
General procedure B was followed by using DMF (6 mL, 77.4 mmol) and POCl₃ (0.9 mL, 7.2 mmol) for the preparation of the Vilsmeier reagent and 5-(1'-naphthyl)dipyrromethane **2.26e** (3 g, 11 mmol) was dissolved in DMF (14 mL). The product was purified *via* column chromatography (SiO₂, hexane:EtOAc, 85:15, *v/v*) and collected as the second fraction. Removal of the solvents under reduced pressure resulted in a beige solid (1.40 g, 4.6 mmol, 42%); M.p.: dec. >100 °C; R_f = 0.63 (SiO₂, hexane:EtOAc, 3:2, *v/v*); ¹H NMR (400 MHz, CDCl₃): δ = 5.99 (br, 1H, β-*H*), 6.10 – 6.11 (m, 1H, β-*H*), 6.18 (q, *J* = 2.7 Hz, 1H, β-*H*), 6.28 (s, 1H, meso-*H*), 6.69 – 6.70 (m, 1H, β-*H*), 6.90 – 6.92 (m, 1H, β-*H*), 7.11 (d, *J* = 7.1 Hz, 1H, Ar-*H*), 7.40 (t, *J* = 7.6 Hz, 1H, Ar-*H*), 7.43 – 7.50 (m, 2H, Ar-*H*), 7.81 (d, *J* = 8.3 Hz, 1H, Ar-*H*), 7.85 – 7.89 (m, 2H, Ar-*H*, -*NH*), 7.95 (d, *J* = 9.2 Hz, 1H, Ar-*H*), 9.00 (br s, 1H, -*NH*), 9.39 ppm (s, 1H, -*CHO*); ¹³C NMR (101 MHz, CDCl₃): δ = 40.4, 108.2, 108.8, 110.9, 117.8, 121.9, 123.1, 125.5, 125.9, 126.2, 126.7, 128.5, 128.9, 129.9, 131.2, 132.2, 134.0, 136.1, 141.9, 178.5 ppm; DIP-MS *m/z* calcd. for C₂₀H₁₆N₂O [M]⁺: 300.1263, found: 300.1386.

9-Bromo-5-(4'-bromophenyl)-1-formyl-dipyrromethane (2.15d)



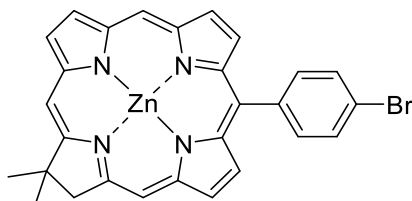
General procedure B was followed by dissolving NBS (216 mg, 1.2 mmol, 1 eq.) in anhydrous THF (5 mL) and 1-formyl-5-(4'-bromophenyl)dipyrromethane **2.27d** (400 mg, 1.2 mmol, 1 eq.) in THF (10 mL). The product was purified *via* column chromatography (SiO₂, hexane:EtOAc, 85:15, *v/v*) and collected as the first fraction. The solvents were removed *in vacuo* to yield a light brown solid (350 mg, 0.85 mmol, 70%); M.p.: dec. >100 °C; R_f = 0.65 (SiO₂, hexane:EtOAc, 3:2, *v/v*); ¹H NMR (400 MHz, THF-d₈): δ = 5.44 (s, 1H, meso-*H*), 5.63 – 5.64 (m, 1H, β-*H*), 5.90 – 5.91 (m, 1H, β-*H*), 5.97 (dd, *J* = 3.4, 2.4 Hz, 1H, β-*H*), 6.84 (dd, *J* = 3.7, 2.4 Hz, 1H, β-*H*), 7.13 – 7.16 (m, 2H, Ar-*H*), 7.46 – 7.50 (m, 2H, Ar-*H*), 9.44 (s, 1H, -CHO), 10.55 (br s, 1H, -NH), 11.26 ppm (br s, 1H, -NH); ¹³C NMR (101 MHz, THF-d₈): δ = 43.5, 97.2, 109.1, 109.3, 109.9, 120.4, 130.3, 131.2, 133.0, 133.5, 140.7, 141.2, 177.6 ppm; DIP-MS *m/z* calcd. for C₁₆H₁₂Br₂N₂O [M]⁺: 408.0930, found: 408.9592.

9-Bromo-5-(1'-naphthyl)-1-formyl dipyrromethane (**2.15e**)



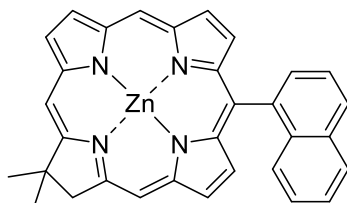
General procedure C was followed by dissolving NBS (622 mg, 3.5 mmol, 1 eq.) in THF (12 mL) and 1-formyl-5-(1'-naphthyl)dipyrromethane **2.27e** (1.050 g, 3.5 mmol, 1 eq) in THF (12 mL). The product was purified *via* column chromatography (SiO₂, hexane:EtOAc, 9:1 → 4:1, *v/v*) and collected as the first fraction. Removal of the solvents under reduced pressure resulted in a light brown solid (730 mg, 1.92 mmol, 55%); M.p.: dec. >100 °C; R_f = 0.68 (SiO₂, hexane : EtOAc, 3:2, *v/v*); ¹H NMR (400 MHz, THF-d₈): δ = 5.55 (t, *J* = 3.0 Hz, 1H, β-*H*), 5.79 – 5.8 (m, 1H, β-*H*), 5.93 (t, *J* = 2.9 Hz, 1H, β-*H*), 6.20 (s, 1H, meso-*H*), 6.77 – 6.79 (m, 1H, β-*H*), 7.09 (d, *J* = 7.1 Hz, 1H, Ar-*H*), 7.40 (t, *J* = 7.7 Hz, 1H, Ar-*H*), 7.42 – 7.44 (m, 2H, Ar-*H*), 7.78 (d, *J* = 8.2 Hz, 1H, Ar-*H*), 7.85 – 7.87 (m, 1H, Ar-*H*), 8.01 – 8.03 (m, 1H, Ar-*H*), 9.41 (s, 1H, -CHO), 10.56 (br s, 1H, -NH), 11.28 ppm (br s, 1H, -NH); ¹³C NMR (101 MHz, THF-d₈): δ = 41.1, 97.7, 110.2, 110.4, 111.5, 124.1, 126.0, 126.1, 126.7, 128.3, 129.3, 132.5, 134.1, 134.3, 134.8, 138.1, 142.4, 178.4 ppm; DIP-MS *m/z* calcd. for C₂₀H₁₅BrN₂O [M]⁺: 379.2570, found: 379.0666.

[10-(4'-Bromophenyl)-17,18-dihydro-18,18-dimethylporphyrinato]zinc(II)
(Zn1)



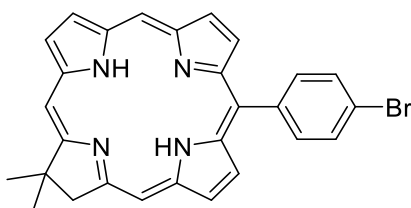
General procedure D was followed by using **2.14** (90 mg, 0.473 mmol), **2.15d** (206 mg, 0.505 mmol), anhydrous DCM (10.8 mL), *p*-TsOH·H₂O (472 mg, 2.48 mmol, 5 eq.), anhydrous MeOH (6.25 mL), 2,2,6,6-tetramethylpiperidine (0.63 mL, 3.71 mmol, 7.5 eq.), anhydrous MeCN (50 mL), further 2,2,6,6-tetramethylpiperidine (2.10 mL, 12.40 mmol, 25 eq.), anhydrous Zn(OAc)₂ (1.370 g, 7.50 mmol, 25 eq.), and AgOTf (0.387 g, 1.508 mmol, 3 eq.). The product was purified *via* column chromatography (SiO₂, DCM:hexane, 1:1, *v/v*) and collected as the second fraction. The solvents were removed *in vacuo* to yield a blue solid (97 mg, 173.6 μmol, 37%). M.p.: >220 °C; *R*_f = 0.78 (SiO₂, DCM:hexane, 1:1, *v/v*); ¹H NMR (400 MHz, CDCl₃): δ = 2.04 (s, 6 H, C(CH₃)₂), 4.54 (s, 2H, -CH₂-), 7.83 (d, *J* = 8.4 Hz, 2H, Ar-*H*), 7.95 (d, *J* = 8.4 Hz, 2H, Ar-*H*), 8.50 (d, *J* = 4.4 Hz, 1H, β-*H*), 8.64 (s, 1H, meso-*H*), 8.66 (s, 2H, β-*H*), 8.73 (s, 1H, meso-*H*), 8.80 (d, *J* = 4.4 Hz, 1H, β-*H*), 8.89 (d, *J* = 4.4 Hz, 1H, β-*H*), 9.12 (d, *J* = 4.4 Hz, 1H, β-*H*), 9.65 ppm (s, 1H, meso-*H*); ¹³C NMR (101 MHz, CDCl₃): δ = 31.6, 45.4, 50.3, 94.4, 97.1, 109.5, 121.9, 127.0, 127.5, 128.3, 128.8, 129.8, 132.8, 133.1, 135.0, 141.4, 145.6, 146.1, 146.6, 146.8, 153.2, 154.2, 159.5, 171.2 ppm; UV-Vis (EtOH): λ_{abs} (log ε) = 405 (5.40), 506 (3.40), 559 (3.59), 604 (4.61) nm; HRMS (MALDI) *m/z* calcd. for C₂₈H₂₁BrN₄Zn [M]⁺: 556.0241, found: 556.0256.

[17,18-Dihydro-18,18-dimethyl-10-(naphthalen-1'-yl)porphyrinato]zinc(II)
(Zn2)



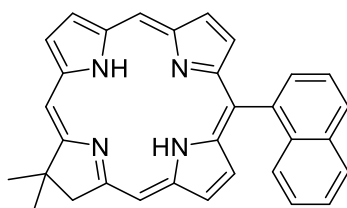
General procedure D was followed by using **2.14** (33.6 mg, 176.6 μmol), **2.15e** (57.8 mg, 152.4 μmol), anhydrous DCM (4 mL), *p*-TsOH·H₂O (111 mg, 0.583 mmol), anhydrous MeOH (1 mL), 2,2,6,6-tetramethylpiperidine (0.16 mL, 0.948 mmol), anhydrous MeCN (20 mL), further 2,2,6,6-tetramethylpiperidine (0.55 mL, 3.26 mmol), anhydrous Zn(OAc)₂ (358 mg, 1.95 mmol) and AgOTf (100 mg, 0.390 mmol). The product was purified *via* column chromatography (SiO₂, DCM:hexane, 1:1, *v/v*) and collected as the second fraction. The solvents were removed *in vacuo* to yield a dark green-blue solid (29.0 mg, 54.7 μmol , 36%). M.p.: >250 °C; R_f = 0.46 (SiO₂, DCM:hexane, 1:1, *v/v*); ¹H NMR (400 MHz, CDCl₃): δ = 2.08 (s, 3H, -CH₃), 2.09 (s, 3H, -CH₃), 4.58 (s, 2H, -CH₂-), 7.06 – 7.10 (m, 1H, Ar-H), 7.19 – 7.21 (m, 1H, Ar-H), 7.46 – 7.50 (m, 1H, Ar-H), 7.82 – 7.86 (m, 1H, Ar-H), 8.10 (d, *J* = 8 Hz, 1H, Ar-H), 8.18 – 8.19 (m, 1H, β -H), 8.20 – 8.28 (m, 2H, Ar-H), 8.48 (d, *J* = 4.4 Hz, 1H, β -H), 8.59 (d, 1H, *J* = 4.4 Hz, β -H), 8.69 (s, 1H, meso-H), 8.74 (s, 1H, meso-H), 8.81 (d, *J* = 4.4 Hz, 1H, β -H), 8.84 (d, *J* = 4.4 Hz, 1H, β -H), 9.15 (d, *J* = 4 Hz, 1H, β -H), 9.67 ppm (s, 1H, meso-H); ¹³C NMR (101 MHz, CDCl₃): δ = 31.0, 45.3, 50.3, 94.4, 97.0, 109.5, 124.2, 125.5, 125.8, 127.0, 127.3, 127.8, 128.2, 128.4, 129.0, 131.5, 132.9, 132.9, 133.1, 136.3, 139.7, 146.0, 146.4, 147.9, 146.6, 153.2, 154.0, 159.4, 171.0 ppm; UV-Vis (EtOH): λ_{abs} (log ϵ) = 405 (5.54), 506 (3.73), 561 (3.83), 605 nm (4.76); HRMS (MALDI) *m/z* calcd. for C₃₂H₂₄N₄Zn [M]⁺: 528.1292, found: 528.1301.

10-(4'-Bromophenyl)-17,18-dihydro-18,18-dimethylporphyrin (FB1)



General procedure E was followed by using **Zn1** (54.0 mg, 96.6 μmol), DCM (10 mL) and TFA (0.50 mL, 6.54 mmol) to yield a dark green solid (22.0 mg, 44.4 μmol , 46%). M.p.: dec. > 250 $^{\circ}\text{C}$, R_f = 0.71 (SiO₂, DCM:hexane, 1:1, v/v); ¹H NMR (600 MHz, CDCl₃): δ = -2.32 (s, 1H, *N*²¹-H), -1.94 (br, 1H, *N*²³-H), 2.08 (s, 6H, C(CH₃)₂), 4.62 (s, 2H, -CH₂-), 7.90 (d, J = 7.8 Hz, 2H, Ar-*H*), 8.05 (d, J = 8.4 Hz, 2H, Ar-*H*), 8.66 (d, J = 4.2 Hz, 1H, β -*H*), 8.80 (d, J = 4.2 Hz, 1H, β -*H*), 8.84 (d, J = 4.8 Hz, 1H, β -*H*), 8.96 (s, 1H, meso-*H*), 8.98 (d, J = 4.2 Hz, 1H, β -*H*), 9.01 (d, J = 4.2 Hz, 1H, β -*H*), 9.03 (s, 1H, meso-*H*), 9.24 (d, J = 4.2 Hz, 1H, β -*H*), 9.88 ppm (s, 1H, meso-*H*); ¹³C NMR (151 MHz, CDCl₃): δ = 31.3, 46.6, 52.1, 94.5, 97.1, 107.4, 119.9, 122.4, 123.9, 128.0, 128.5, 130.1, 131.9, 132.7, 134.4, 135.0, 135.6, 139.6, 140.9, 141.1, 151.1, 152.2, 163.1, 175.6 ppm; ¹⁵N/¹H-HSQC (CDCl₃): 134.06 (*N*²¹), 134.12 (*N*²³) ppm. UV-Vis (DCM): λ_{abs} (log ϵ) = 395 (5.00), 407 (5.08), 491 (3.90), 503 (4.00), 586 (3.56), 638 (4.43) nm; APCI *m/z* calcd. for [M+H]⁺: 495.1179, found: 495.1181.

17,18-Dihydro-18,18-dimethyl-10-(naphthalen-1'-yl)porphyrin (FB2)



General procedure E was followed by using **Zn2** (36.0 mg, 67.9 μmol), DCM (7 mL) and TFA (0.20 mL, 2.62 mmol) to yield a dark green solid (13.0 mg, 27.9 μmol , 41%). M.p.: $>300\text{ }^\circ\text{C}$, $R_f = 0.66$ (SiO_2 , DCM:hexane, 1:1, v/v); $^1\text{H NMR}$ (600 MHz, CDCl_3): $\delta = -2.19$ (s, 1H, $N^{21}\text{-H}$), -1.81 (s, 1H, $N^{23}\text{-H}$), 2.09 (s, 3H, $-\text{CH}_3$), 2.10 (s, 3H, $-\text{CH}_3$), 4.66 (s, 2H, $-\text{CH}_2-$), $7.08 - 7.10$ (m, 1H, Ar-H), 7.24 (d, $J = 8.4$ Hz, 1H, Ar-H), $7.48 - 7.51$ (m, 1H, Ar-H), $7.84 - 7.87$ (m, 1H, Ar-H), 8.14 (d, $J = 9$ Hz, 1H, Ar-H), 8.24 (d, $J = 6.6$ Hz, 1H, Ar-H), 8.27 (d, $J = 8.4$ Hz, 1H, Ar-H), 8.38 (d, $J = 4.2$ Hz, 1H, $\beta\text{-H}$), 8.58 (d, $J = 4.8$ Hz, 1H, $\beta\text{-H}$), 8.75 (d, $J = 4.8$ Hz, 1H, $\beta\text{-H}$), 8.89 (d, $J = 4.2$ Hz, 1H, $\beta\text{-H}$), 8.96 (s, 1H, meso-H), 8.98 (d, $J = 4.2$ Hz, 1H, $\beta\text{-H}$), 9.03 (s, 1H, meso-H), 9.25 (d, $J = 4.2$ Hz, 1H, $\beta\text{-H}$), 9.87 (s, 1H, meso-H) ppm. $^{13}\text{C NMR}$ (151 MHz, CDCl_3): $\delta = 31.3, 31.3, 46.6, 52.2, 94.6, 97.0, 107.4, 107.4, 118.9, 123.3, 123.8, 124.4, 125.8, 126.1, 128.0, 128.3, 128.4, 128.5, 128.6, 132.1, 132.2, 132.7, 133.1, 134.4, 136.0, 136.6, 139.1, 139.7, 140.9, 151.1, 153.5, 163.2, 175.3$ ppm. $^{15}\text{N}/^1\text{H}$ -HSQC (CDCl_3): 134.5 (N^{21}), 133.5 (N^{23}) ppm; UV-Vis (DCM): λ_{abs} ($\log \epsilon$) = 394 (5.15), 407 (5.24), 494 (4.11), 501 (4.17), 587 (3.70), 639 nm (4.64); APCI m/z calcd. for $[\text{M}+\text{H}]^+$: 467.2230, found: 467.2235.

5.5.2 Chapter 3: Synthesis and photophysical studies of 1,4-Phenylene-linked Porphyrin-Chlorin Arrays

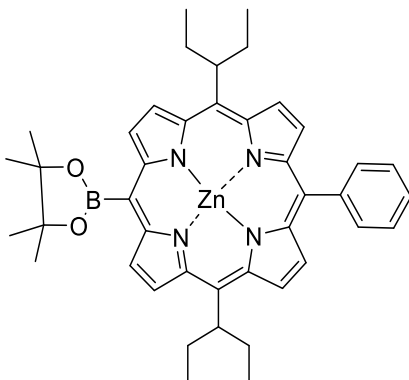
5.5.2.1 Synthetic procedures and characterisation

General procedure A

Suzuki coupling for the synthesis of 1,4-phenylene linked dyads and triad. Following literature procedures,^[427,428] an oven dried Schlenk tube was charged with chlorin **3.6** (1 eq.), appropriate porphyrin (1 eq.), Cs₂CO₃ (10 eq.) and Pd(PPh₃)₄ (0.2 eq.) and dried under high vacuum for 1 h. Then dry solvents toluene:DMF (2:1) were added and the mixture was subjected to three freeze-pump-thaw cycles before releasing to argon. The reaction mixture was covered with foil and stirred at 85 °C. The reaction was followed by TLC. Once the reaction was completed, DCM was added and the mixture was washed with NaHCO₃ (3 × 50 mL), brine (3 × 50 mL), H₂O (3 × 50 mL) and dried over Na₂SO₄. The organic extracts were evaporated under reduced pressure and the resulting product was purified by silica gel column chromatography or preparative TLC.

Chlorin **3.6** and bromo- and borylated- porphyrins **3.9-3.15** were prepared following literature procedures.^[372,435,521,522]

[5,15-Bis(1'-ethylpropyl)-10-phenyl-20-(4',4',5',5'-tetramethyl-1',3',2'-dioxaborolan-2'-yl)porphyrinato]zinc(II) (3.16)

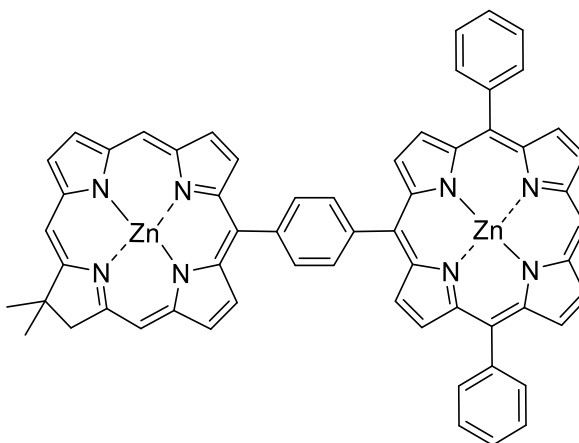


The borylated porphyrin was synthesised following literature procedure.^[521] Porphyrin [5-bromo-10,20-bis(1'-ethylpropyl)-15-phenylporphyrinato]zinc(II) **3.12** (40 mg, 0.06 mmol, 1 eq.) and PdCl₂(PPh₃)₂ (4.20 mg, 6 μmol, 0.1 eq.) were placed in an oven-dried Schlenk tube and dried under high vacuum. Dry 1,2-dichloroethane (5 mL) was added and the solution was subjected to three freeze-pump-thaw cycles before releasing to argon. TEA (0.08 mL, 0.6 mmol, 10 eq.) and pinacol boran (4,4,5,5-tetramethyl-1,3,2-dioxaborolane, 0.09 mL, 0.6 mmol, 10 eq.) were added *via* syringe under argon atmosphere. The reaction mixture was allowed to stir for 30 min at 80 °C. DCM was added and the organic phase was washed with brine (x2) and water (x2), dried over Na₂SO₄, and the resulting solvent was removed *in vacuo*. The product was purified *via* column chromatography (SiO₂, hexane:CH₂Cl₂, 3:2, *v/v*) and the desired compound was collected as the fourth fraction. Removal of the solvents *in vacuo* afforded the title compound as a pink solid (30 mg, 0.04 mmol, 70%); M.p.: > 300 °C; R_f = 0.32 (SiO₂, DCM:hexane, 3:2, *v/v*); ¹H NMR (400 MHz, CDCl₃): δ = 0.6 (t, *J* = 7.4 Hz, 12H, -CH₃), 1.93 (s, 12H, C(CH₃)₂), 2.85 (s, 4H, -CH₂-), 3.02 (s, 4H, -CH₂-), 5.18 (s, 2H, -CH-), 7.75 – 7.84 (m, 3H, Ar-*H*), 8.24 (d, *J* = 6.7 Hz, 2H, Ar-*H*), 8.98 (d, *J* = 8.1 Hz, 2H, β-*H*), 9.73 (d, *J* = 12.8 Hz, 2H, β-*H*), 9.87 – 9.95 ppm (m, 4H, β-*H*); ¹³C NMR (151 MHz, CDCl₃): δ = 14.1, 14.2, 25.4, 34.8, 50.5, 85.2, 123.6, 126.3, 127.4, 128.4, 128.5, 128.8, 130.9, 131.7, 132.0, 132.2, 132.3, 132.6, 134.2, 143.3, 149.1, 149.6, 151.9 ppm; UV-Vis (DCM): λ_{max} (log ε) = 419 (5.66), 550 (4.26), 593 nm (3.64); APCI *m/z* calcd. for C₄₂H₄₇BN₄O₂Zn [M]⁺: 714.3084; found 714.3107.

Porphyrin–chlorin dyad (3.18) and chlorin-porphyrin-chlorin triad (3.19).

General procedure A was adapted as follows: In a dry Schenk tube porphyrin [5, 15-diphenyl-10,20-bis(4',4',5',5'-tetramethyl-1',3',2'-dioxaborolan-2'-yl)-porphinato zinc(II)] **3.14** (100 mg, 129 μmol , 1.5 eq.), chlorin **3.6** (96 mg, 171 μmol , 2 eq.) and Cs_2CO_3 (280 mg, 857 μmol) were added and dried under high vacuum. Then dry toluene (8 mL) and DMF (4 mL) were added and the mixture was degassed with argon for 30 min followed by the addition of $\text{Pd}(\text{PPh}_3)_4$ (20 mg, 17 μmol , 0.2 eq.) while degassing the solution. The reaction mixture was protected from light and stirred at 85 °C for 3 h. Once the reaction was completed, DCM was added and the mixture was washed with NaHCO_3 (3 \times 50 mL), brine (3 \times 50 mL), H_2O (3 \times 50 mL) and dried over Na_2SO_4 . The organic extracts were evaporated under reduced pressure and the resulting products **3.18** and **3.19** were purified by two consecutive preparative TLC (SiO_2 , DCM) and recrystallised from DCM/hexane.

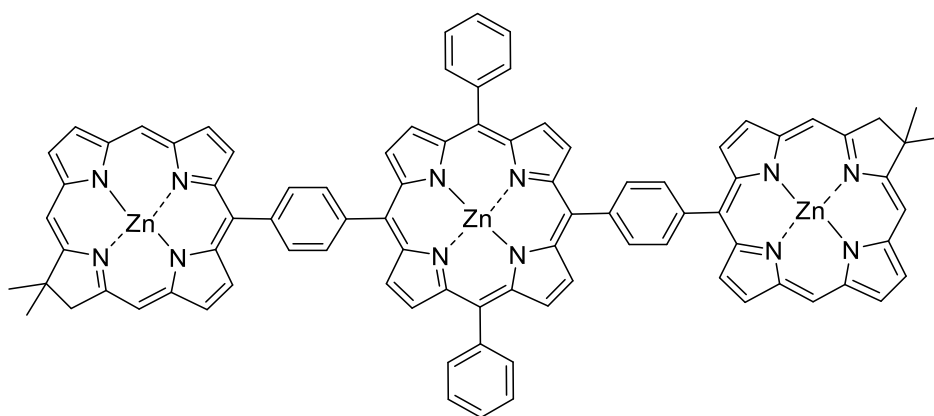
(5'-{4-[(17,18-Dihydro-18,18-dimethylporphyrinato)zinc(II)-10-yl]phenyl}-10', 20'-diphenylporphyrinato)zinc(II) (3.18)



The desired compound was isolated as a dark purple solid (17 mg, 17 μmol , 13%). M.p.: >250 °C; R_f = 0.64 (SiO_2 , DCM, v/v); ^1H NMR (600 MHz, CDCl_3): δ = 2.11 (s, 6 H, $\text{C}(\text{CH}_3)_2$), 4.63 (s, 2H, $-\text{CH}_2-$), 7.86 – 7.87 (m, 6 H, Ar- H), 8.35 – 8.36 (m, 4H, Ar- H), 8.50 (d, J = 7.4 Hz, 2H, Ar- H_{linker}), 8.60 (d, J = 7.5 Hz, 2H, Ar- H_{linker}), 8.71 (s, 1H, meso- H), 8.85 (s, 1H, meso- H), 8.86 (m, 2H, β - H), 9.02 (d, J = 4.0 Hz, 1H, β - H), 9.08 (d, J = 4.0 Hz, 1H, β - H), 9.19 (m, 4H, β - H), 9.22 (m, 2H, β - H), 9.45 – 9.47 (m, 4H, β - H), 9.76 (s, 1H, meso- H), 10.33 ppm (s, 1H, meso- $H_{\text{porphyrin}}$); ^{13}C NMR (151 MHz, CDCl_3): δ = 31.0, 45.45, 50.4, 94.4, 97.2, 106.0,

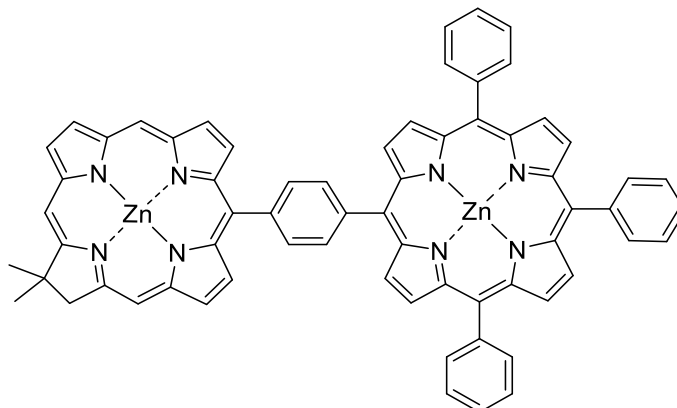
106.1, 109.6, 120.8, 120.8, 121.5, 123.5, 126.6, 127.0, 127.5, 127.6, 128.4, 129.3, 131.8, 131.8, 132.1, 132.1, 132.2, 132.2, 132.7, 132.8, 133.1, 133.3, 134.6, 141.7, 142.0, 142.7, 146.1, 146.1, 146.7, 147.5, 150.0, 150.1, 150.3, 150.3, 150.3, 153.3, 154.2, 159.4, 171.2 ppm; UV-Vis (DCM): λ_{\max} (log ϵ) = 403 (4.89), 418 (5.40), 544 (3.87), 607 nm (4.06); HRMS (MALDI) m/z calcd. for $C_{60}H_{40}N_8Zn_2$ $[M]^+$: 1000.1959, found: 1000.1971.

(5',15'-di{4-[(17,18-Dihydro-18,18-dimethylporphyrinato)zinc(II)-10-yl]phenyl}-10', 20'-diphenylporphyrinato)zinc(II) (3.19)



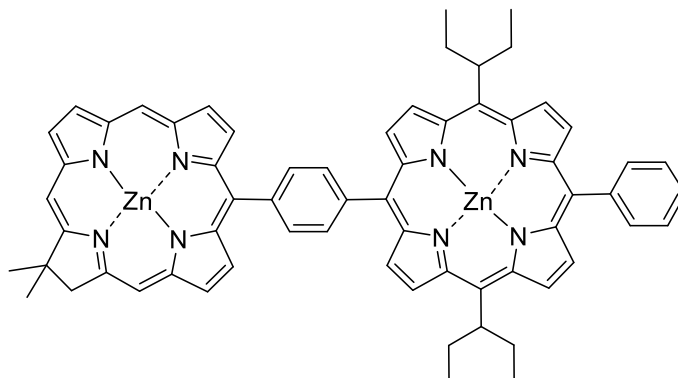
The desired compound was isolated as a dark green-purple solid (30 mg, 20 μ mol, 16%). M.p.: >250 $^{\circ}C$; R_f = 0.8 (SiO₂, DCM:EtOAc, 10:0.1, v/v); ¹H NMR (600 MHz, CDCl₃): δ = 2.12 (s, 12H, C(CH₃)₂), 4.64 (s, 4H, -CH₂-), 7.90 (s, 6H, Ar-H), 8.42 (m, 4H, Ar-H), 8.54 – 8.56 (m, 4H, Ar-H_{linker}), 8.64 – 8.65 (m, 4H, Ar-H_{linker}), 8.72 (s, 2H, meso-H), 8.87 – 8.89 (m, 6H, 2 \times meso-H, 4 \times β -H), 9.05 (br s, 2H, β -H), 9.12 (br s, 3H, β -H), 9.20 (br s, 3H, β -H), 9.24 (m, 5H, β -H), 9.48 (m, 3H, β -H), 9.78 ppm (s, 2H, meso-H); ¹³C NMR (151 MHz, CDCl₃): δ = 31.0, 45.4, 50.4, 94.4, 97.2, 109.6, 121.2, 121.5, 123.6, 126.7, 127.1, 127.5, 127.6, 128.4, 129.3, 131.9, 132.3, 132.3, 132.3, 132.4, 132.8, 133.1, 133.4, 134.6, 141.7, 142.0, 142.9, 146.1, 146.2, 146.7, 147.5, 150.5, 150.5, 153.3, 154.2, 159.4, 171.2 ppm; UV/Vis (DCM): λ_{\max} (log ϵ) = 401 (5.35), 4.27 (5.64), 504 (4.26), 552 (4.49), 607 nm (4.76); HRMS (MALDI) m/z calcd. for $C_{88}H_{60}N_{12}Zn_3$ $[M]^+$: 1476.2938, found: 1476.2936.

(5'-{4-[(17,18-Dihydro-18,18-dimethylporphyrinato)zinc(II)-10-yl]phenyl}-10',15',20'-triphenylporphyrinato)zinc(II) (3.20)



Compound **3.20** was synthesised according to general procedure A using porphyrin [5,10,15-triphenyl-20-(4',4',5',5'-tetramethyl-1',3',2'-dioxaborolan-2'-yl)porphyrinato]zinc(II) **3.15** (33 mg, 45 μmol , 1 eq.), chlorin **3.6** (25 mg, 45 μmol , 1 eq.), $\text{Pd}(\text{PPh}_3)_4$ (10 mg, 9 μmol , 0.2 eq.), Cs_2CO_3 (146 mg, 447 μmol , 10 eq.), dry toluene (3 mL) and DMF (1.5 mL). The product was purified *via* column chromatography (SiO_2 , DCM:hexane 3:7 \rightarrow 7:3, *v/v*) and the desired compound was collected as the third fraction. The solvents were removed *in vacuo* to yield a dark purple/green powder (26 mg, 24 μmol , 54%). M.p.: >300 $^\circ\text{C}$; $R_f = 0.38$ (SiO_2 , DCM:hexane, 4:1, *v/v*); ^1H NMR (400 MHz, CDCl_3): $\delta = 2.11$ (s, 6H, $\text{C}(\text{CH}_3)_2$), 4.62 (s, 2H, $-\text{CH}_2-$), 7.82 – 7.85 (m, 9H, Ar-*H*), 8.29 – 8.31 (m, 2H, Ar-*H*), 8.32 – 8.35 (m, 4H, Ar-*H*), 8.52 (d, $J = 7.7$ Hz, 2H, Ar- H_{linker}), 8.61 (d, $J = 7.7$ Hz, 2H, Ar- H_{linker}), 8.71 (s, 1H, meso-*H*), 8.83 – 8.88 (m, 3H, 1 \times meso-*H*, 2 \times β -*H*), 9.02 – 9.09 (m, 6H, β -*H*), 9.16 – 9.22 (m, 4H, β -*H*), 9.45 (d, $J = 4.6$ Hz, 2H, β -*H*), 9.74 ppm (s, 1H, meso-*H*); ^{13}C NMR (151 MHz, CDCl_3): $\delta = 31.0, 45.4, 50.3, 94.3, 97.8, 109.6, 121.1, 121.2, 121.3, 123.5, 126.6, 126.6, 127.0, 127.5, 127.5, 128.4, 129.3, 131.9, 132.1, 132.2, 132.2, 132.2, 132.3, 132.8, 133.1, 133.3, 134.4, 134.5, 141.7, 141.9, 142.8, 146.1, 146.1, 146.7, 147.5, 150.3, 150.4, 153.3, 154.2, 159.4, 171.2$ ppm; UV-Vis (DCM): λ_{max} ($\log \epsilon$) = 402 (5.04), 423 (5.67), 551 (4.31), 608 nm (4.29); HRMS (MALDI) m/z calcd. for $\text{C}_{66}\text{H}_{44}\text{N}_8\text{Zn}_2$ $[\text{M}]^+$: 1076.2272, 1076.2290 found.

(5'-{4-[(17,18-Dihydro-18,18-dimethylporphyrinato)zinc(II)-10-yl]phenyl}-10', 20'-bis(1'-ethylpropyl)-15'-phenylporphyrinato)zinc(II) (3.21)



Compound **3.21** was synthesised according to general procedure A using porphyrin [5,15-bis(1'-ethylpropyl)-10-(4',4',5',5'-tetramethyl-1',3',2'-dioxaborolan-2'-yl)-20-phenyl-porphyrinato]zinc(II) **3.16** (32 mg, 45 μmol , 1 eq.), chlorin **3.6** (25 mg, 45 μmol , 1 eq.), $\text{Pd}(\text{PPh}_3)_4$ (10 mg, 9 μmol , 0.2 eq.), Cs_2CO_3 (146 mg, 447 μmol , 10 eq.), dry toluene (3 mL) and DMF (1.5 mL). The product was purified by preparative TLC (SiO_2 , THF:hexane, 1:4, v/v) to yield a deep purple/blue solid (23 mg, 22 μmol , 48%). M.p.: >300 $^\circ\text{C}$; $R_f = 0.4$ (SiO_2 , DCM:hexane, 4:1, v/v); ^1H NMR (400 MHz, CDCl_3): $\delta = 1.02$ (t, $J = 7.3$ Hz, 12H, $-\text{CH}_3$), 2.10 (s, 6H, $\text{C}(\text{CH}_3)_2$), 2.98 (d, $J = 81.8$ Hz, 8H, $-\text{CH}_2\text{-porphyrin}$), 4.61 (s, 2H, $-\text{CH}_2\text{-chlorin}$), 5.23 (br s, 2H, $-\text{CH}-$), 7.77 – 7.83 (m, 3H, Ar- H), 8.27 (d, $J = 7.6$ Hz, 2H, Ar- H), 8.52 (d, $J = 7.8$ Hz, 2H, Ar- H_{linker}), 8.59 (d, $J = 7.8$ Hz, 2H, Ar- H_{linker}), 8.68 (s, 1H, meso- H), 8.82 (s, 1H, meso- H), 8.84 (d, $J = 4.3$ Hz, 1H, β - H), 8.88 (d, $J = 4.4$ Hz, 1H, β - H), 9.00 (br s, 2H, β - H), 9.06 (d, $J = 4.1$ Hz, 1H, β - H), 9.10 (d, $J = 4.2$ Hz, 1H, β - H), 9.16 (d, $J = 4.3$ Hz, 1H, β - H), 9.23 (d, $J = 4.3$ Hz, 1H, β - H), 9.43 (br s, 2H, β - H), 9.74 (s, 2H, 1 \times meso- H , 1 \times β - H), 9.80 (br s, 1H, β - H), 9.93 ppm (d, $J = 22.9$ Hz, 2H, β - H); ^{13}C NMR (101 MHz, CDCl_3): $\delta = 14.4$, 29.7, 31.0, 34.9, 50.4, 50.6, 94.1, 96.9, 109.4, 123.5, 124.0, 126.4, 127.0, 127.4, 128.3, 129.2, 131.8, 132.6, 133.0, 133.3, 134.3, 141.7, 142.5, 143.5, 146.1, 146.6, 147.5, 153.2, 154.1, 159.2, 171.1 ppm; UV-Vis (DCM): λ_{max} (log ϵ) = 402 (5.00), 426 (5.44), 554 (4.15), 607 nm (4.31); APCI m/z calcd. for $\text{C}_{64}\text{H}_{56}\text{N}_8\text{Zn}_2$ [$\text{M}+\text{H}$] $^+$: 1065.3211; found 1065.327463.

5.5.3 Chapter 4: Tris(dipyrrinato)aluminium(III) complexes as potential PSs in PDT

5.5.3.1 General synthetic procedures

General procedure A – dipyrromethane synthesis

The corresponding DPM synthesis has been described in section 5.5.1.1. DPMs were synthesised following literature procedures by using the appropriate aldehyde (1 eq.), pyrrole (10 – 25 eq.), TFA (0.1 eq.) or MgBr_2 (2 eq.), and DCM (15 – 20 mL).^[349–351] ¹²

General procedure B – dipyrin synthesis

Dipyrins were synthesised in accordance with literature procedures.^[150,471,472] The corresponding 5-substituted DPM (1 eq.) was dried under vacuum and dissolved in DCM (HPLC grade). Then, DDQ (1.1 eq.) was added to the solution and the reaction mixture was stirred for 1 h at r.t. The mixture was washed with aq. solution of NaOH (x2), NaHCO_3 (x2), water (x2), and brine (x2), dried over Na_2SO_4 and filtered. The resulting DCM was evaporated to give a dark crude mixture or an oily product in some cases. The product was adsorbed onto silica and purified by column chromatography.

General procedure C – tris(dipyrrinato)Al(III) complex synthesis

Synthesis of the tris(dipyrrinato)aluminium(III) complexes followed adapted literature procedures by using aluminium salt for the complexation.^[228,472] In a dry Schlenk tube the corresponding 5-substituted dipyrin (3 eq.) and AlCl_3 (1.2 – 1.4 eq.) were added and dried under vacuum for 1 h. Then, chloroform was added under argon atmosphere and the resulting slur/solution was degassed with argon for 30 min. DIPEA (3 eq.) was added dropwise and the reaction mixture was stirred overnight at 70 °C under reflux. Colour changed from dark yellow/brown to dark red. Then the reaction mixture was allowed to reach r.t. and DCM was added. Organic phase was washed with brine (x2), NaHCO_3 (x2) and water (x2),

¹² Compound **4.48d** was provided by Dr. Nitika Grover, compound **4.48e** by Jessica O. Brien, compounds **4.48g** and **4.48h** by Dr. Asterios Charisiadis, compound **4.58k** by Harry C. Sample; Senge group members, TCD.

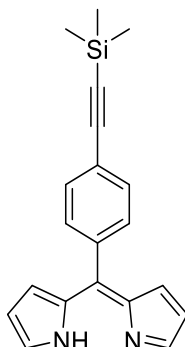
dried over Na₂SO₄, filtered, and the resulting solution was evaporated *in vacuo* to give a dark brown/red crude mixture. The product was purified *via* column chromatography.

5.5.3.2 Starting materials

5-Phenyl-dipyrromethane (**4.48a**), 5-mesityldipyrromethane (**4.48b**), 5-(4'-bromophenyl)dipyrromethane (**4.48c**), 5-(pentafluorophenyl)dipyrromethane (**4.48d**), 5-(4'-trimethylsilylethynylphenyl)dipyrromethane (**4.48e**), 5-(4'-methoxycarbonylphenyl)dipyrromethane (**4.48f**), 5-(2',4',6'-trimethoxyphenyl)dipyrromethane (**4.48g**), 5-(2',4',5'-trimethoxyphenyl)dipyrromethane (**4.48h**), 5-(1'-naphthyl)dipyrromethane (**4.48i**), 5-(anthracene-9'-yl)dipyrromethane (**4.48j**), 5-(4'-methoxyphenyl)dipyrromethane (**4.48k**), 5-phenyldipyrrin (**DIPY1**), 5-mesityldipyrrin (**DIPY2**), 5-(4'-bromophenyl)dipyrrin (**DIPY3**), 5-(pentafluorophenyl)dipyrrin (**DIPY4**), 5-(4'-methoxyphenyl)dipyrrin (**DIPY6**), 5-(anthracene-9'-yl)dipyrrin (**DIPY10**), 5-(4'-methoxycarbonylphenyl)dipyrrin (**DIPY11**), were synthesised and characterised in accordance with literature procedures and general procedures A and B. BODIPY compounds **4.49** and **4.52** were synthesised following literature procedures.^[522,523]

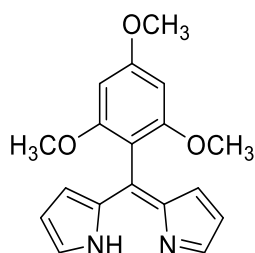
5.5.3.3 Synthetic details and characterisation

5-(4'-Trimethylsilylethynylphenyl)dipyrrin (DIPY5)



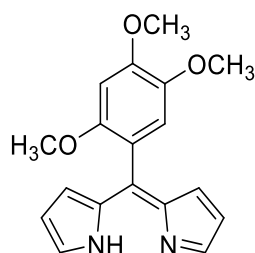
General procedure B was followed by using 5-(4'-trimethylsilylethynylphenyl)dipyrromethane (500 mg, 0.57 mmol) **4.48e**, DCM (150 mL), and DDQ (392 mg, 1.73 mmol) to give a dark brown oily mixture. The product was purified *via* column chromatography (SiO₂, EtOAc:hexane, 1.5:8.5, *v/v*) and collected as the second fraction. Removal of the solvents under reduced pressure resulted in a green/brown solid (420 mg, 1.33 mmol, 85%); M.p.: dec. >100 °C; *R_f* = 0.46 (SiO₂, DCM, *v/v*); ¹H NMR (400 MHz, CDCl₃): δ = 7.66 (s, 2H, α-*H*), 7.55 (d, *J* = 8.2 Hz, 2H, Ar-*H*), 7.44 (d, *J* = 8.1 Hz, 2H, Ar-*H*), 6.57 (d, *J* = 4.1 Hz, 2H, β-*H*), 6.41 (dd, *J* = 4.2, 1.2 Hz, 2H, β-*H*), 0.28 ppm (s, 9H, -CH₃); ¹³C NMR (101 MHz, CDCl₃): δ = 143.9, 140.5, 137.5, 131.3, 130.8, 128.9, 124.0, 117.9, 104.5, 96.9, 0.08 ppm; UV-Vis (DCM): λ_{abs} (log ε) = 330 (4.06), 436 nm (4.35); APCI *m/z* calcd. for C₂₀H₂₀N₂Si [M+H]⁺: 317.1396; found 317.1467.

5-(2',4',6'-Trimethoxyphenyl)dipyrrin (DIPY7)



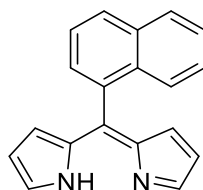
General procedure B was followed by using 5-(2',4',6'-trimethoxyphenyl)dipyrromethane (450 mg, 1.44 mmol) **4.48g**, DCM (150 mL), and DDQ (350 mg, 1.58 mmol) to give a dark brown oily mixture. The product was purified *via* column chromatography (SiO₂, DCM → 1% EA in DCM, *v/v*) and collected as the third fraction. Removal of the solvents under reduced pressure resulted in a dark orange solid (140 mg, 0.45 mmol, 31%); M.p.: dec. >110 °C; *R_f* = 0.42 (SiO₂, hexane:EtOAc, 3:2, *v/v*); ¹H NMR (600 MHz, CDCl₃): δ = 7.57 (d, *J* = 0.9 Hz, 2H, *α*-H), 6.52 (d, *J* = 4.1 Hz, 2H, *β*-H), 6.32 (dd, *J* = 4.1, 1.3 Hz, 2H, *β*-H), 6.22 (s, 2H, Ar-H), 3.89 (s, 3H, *p*-OCH₃), 3.66 ppm (s, 6H, *o*-OCH₃); ¹³C NMR (151 MHz, CDCl₃): δ = 161.8, 159.5, 143.1, 141.8, 135.7, 127.6, 117.3, 107.9, 90.8, 56.2, 55.5 ppm; UV-Vis (DCM): λ_{abs} (log ε) = 434 nm (4.37); APCI *m/z* calcd. for C₁₈H₁₈N₂O₃ [M+H]⁺: 311.1317; found 311.1383.

5-(2',4',5'-Trimethoxyphenyl)dipyrrin (DIPY8)



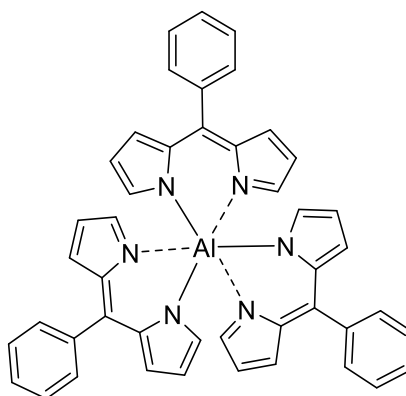
Compound **DIPY8** was synthesised by following general procedure B with minor modifications. Using 5-(2',4',5'-trimethoxyphenyl)dipyrromethane (600 mg, 1.92 mmol) **4.48h**, DCM (150 mL), and DDQ (480 mg, 2.11 mmol) gave a dark brown viscous oil which was dissolved in toluene (3 – 4 mL). This solution was added dropwise into a stirring solution of hexane (80 mL) resulting in a brown precipitate which was removed by filtration. The solvent was removed *in vacuo* to yield a viscous yellow oil, which after the addition of hexane (3 mL) and consequent storage at $-10\text{ }^{\circ}\text{C}$ for 24 h yielded orange crystals (420 mg, 1.35 mmol, 70%); M.p.: $110 - 120\text{ }^{\circ}\text{C}$; $R_f = 0.4$ (SiO_2 , DCM:MeOH, 9.5:0.5, v/v); $^1\text{H NMR}$ (400 MHz, CDCl_3): $\delta = 12.75$ (br s, NH), 7.62 (d, $J = 1.1$ Hz, 2H, $\alpha\text{-H}$), 6.84 (s, 1H, Ar-H), 6.63 (s, 1H, Ar-H), 6.57 – 6.55 (dd, $J = 4.2, 0.9$ Hz, 2H, $\beta\text{-H}$), 6.37 – 6.35 (dd, $J = 4.2, 1.5$ Hz, 2H, $\beta\text{-H}$), 3.97 (s, 3H, $p\text{-OCH}_3$), 3.82 (s, 3H, $m\text{-OCH}_3$), 3.69 ppm (s, 3H, $o\text{-OCH}_3$); $^{13}\text{C NMR}$ (151 MHz, CDCl_3): $\delta = 152.1, 150.2, 143.4, 142.5, 141.1, 128.6, 117.7, 117.5, 115.5, 98.1, 57.2, 56.6, 56.2$ ppm; UV-Vis (DCM): λ_{abs} (log ϵ) = 435 nm (4.31); APCI m/z calcd. for $\text{C}_{18}\text{H}_{18}\text{N}_2\text{O}_3$ $[\text{M}+\text{H}]^+$: 311.1317; found 311.1392.

5-(1'-Naphthyl)dipyrrin (DIPY9)



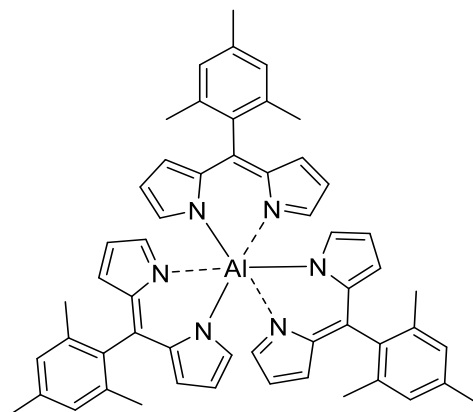
General procedure B was followed by using 5-(1'-naphthyl)dipyrromethane (400 mg, 1.47 mmol) **4.48i**, DCM (200 mL), and DDQ (366 mg, 1.62 mmol) to give a dark red crude mixture. The product was purified as the third fraction *via* column chromatography (SiO₂, DCM:hexane, 1:1, *v/v*) resulting in a viscous dark yellow oil which solidified overnight in fridge to yield a dark yellow solid (380 mg, 1.41 mmol, 95%); M.p.: 75 – 85 °C; R_f = 0.53 (SiO₂, hexane:EtOAc, 5:1, *v/v*); ¹H NMR (400 MHz, CDCl₃): δ = 12.5 (br s, 1H, N-H), 7.96 – 7.94 (m, 1H, Ar-H), 7.90 (d, J = 8.2 Hz, 1H, Ar-H), 7.81 (d, J = 8.4 Hz, 1H, Ar-H), 7.67 (t, J = 1.2 Hz, 2H, α-H), 7.56 – 7.52 (m, 2H, Ar-H), 7.47 (ddd, J = 8.1, 6.8, 1.2 Hz, 1H, Ar-H), 7.37 (ddd, J = 8.2, 6.8, 1.3 Hz, 1H, Ar-H), 6.32 – 6.29 ppm (m, 4H, β-H); ¹³C NMR (101 MHz, CDCl₃): δ = 143.7, 141.5, 140.0, 134.5, 133.1, 128.8, 128.6, 128.0, 127.9, 126.6, 126.3, 126.0, 124.6, 117.7 ppm; UV-Vis (DCM): λ_{abs} (log ε) = 435 nm (4.41); APCI *m/z* calcd. for [M+H]⁺: 271.1157; found 271.1227.

Tris(5-phenyldipyrinato)aluminium(III) ($\text{Al}(\text{DIPY})_3\text{1}$)



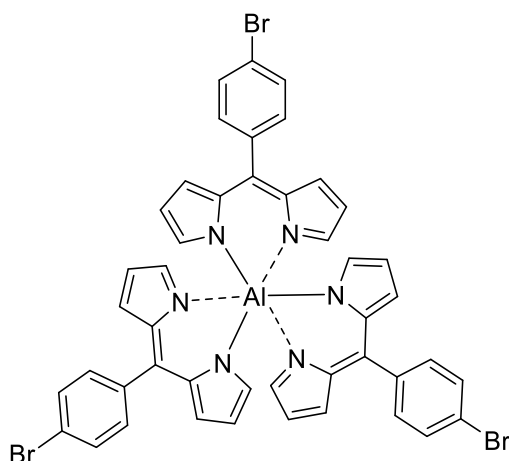
Compound **$\text{Al}(\text{DIPY})_3\text{1}$** was synthesised in accordance with general procedure C using 5-phenyldipyrin (50 mg, 0.23 mmol) **DIPY1**, AlCl_3 (10 mg, 0.076 mmol), CHCl_3 (8 mL), and DIPEA (0.04 mL, 0.23 mmol). The product was purified *via* column chromatography (SiO_2 , DCM:hexane,1:1, *v/v*) and eluted as the first fraction. The solvents were removed *in vacuo* yielding an orange solid (50mg, 0.07 mmol, 96%); M.p.: dec. >250 °C; R_f = 0.40 (SiO_2 , DCM:hexane, 1:2, *v/v*); ^1H NMR (400 MHz, CDCl_3): δ = 7.48 – 7.43 (m, 15H, Ar-*H*), 6.79 (s, 6H, α -*H*), 6.64 (d, J = 3.6 Hz, 6H, β -*H*), 6.26 ppm (dd, J = 4.0, 1.2 Hz, 6H, β -*H*); ^{13}C NMR (101 MHz, CDCl_3): δ = 149.2, 147.4, 139.1, 138.4, 132.4, 130.2, 128.1, 126.9, 116.5 ppm; ^{27}Al NMR (104 MHz, CDCl_3): δ = 6.64 ppm; UV-Vis (DCM): λ_{abs} (log ϵ) = 320 (4.21), 450 (4.80), 500 nm (4.74); APCI m/z calcd. for $\text{C}_{45}\text{H}_{33}\text{AlN}_6$ $[\text{M}+\text{H}]^+$: 685.2582; found 685.2657.

Tris(5-mesityldipyrrinato)aluminium(III) ($\text{Al}(\text{DIPY})_3\mathbf{2}$)



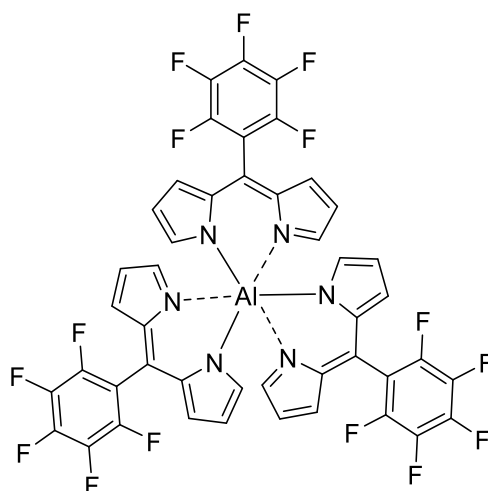
Compound $\text{Al}(\text{DIPY})_3\mathbf{2}$ was synthesised in accordance with general procedure C using 5-mesityldipyrrin (380 mg, 1.45 mmol) **DIPY2**, AlCl_3 (90 mg, 0.68 mmol), CHCl_3 (10 mL), and DIPEA (0.25 mL, 1.45 mmol). The product was purified *via* column chromatography (dry loaded, SiO_2 , DCM:hexane, 1:4, *v/v*) and collected as the first fraction. Removal of the solvents *in vacuo* resulted in an orange solid (70 mg, 0.09 mmol, 18%); M.p.: > 300 °C; $R_f = 0.53$ (SiO_2 , DCM:hexane, 1:2, *v/v*); ^1H NMR (400 MHz, CDCl_3): $\delta = 6.90$ (s, 6H), 6.81 (s, 6H, $\alpha\text{-H}$), 6.50 (d, $J = 3.3$ Hz, 6H, $\beta\text{-H}$), 6.15 (d, $J = 2.9$ Hz, 6H, $\beta\text{-H}$), 2.35 (s, 9H, $p\text{-CH}_3$), 2.07 ppm (s, 18H, $o\text{-CH}_3$); ^{13}C NMR (101 MHz, CDCl_3): $\delta = 148.6, 138.4, 136.9, 136.3, 134.8, 130.7, 127.4, 116.5, 20.9, 19.9$ ppm; ^{27}Al NMR (104 MHz, CDCl_3): $\delta = 6.74$ ppm; UV-Vis (DCM): λ_{abs} ($\log \epsilon$) = 350 (4.01), 454 (4.85), 500 nm (4.80); APCI *m/z* calcd. for $\text{C}_{54}\text{H}_{51}\text{AlN}_6$ $[\text{M}+\text{H}]^+$: 811.3991; found 811.406662.

Tris[5-(4'-bromophenyl)dipyrinato]aluminium(III) ($\text{Al}(\text{DIPY})_3$)



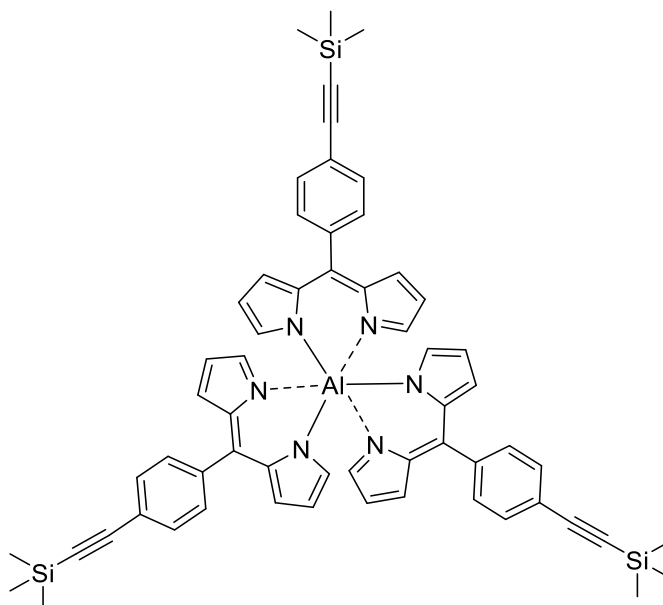
Compound $\text{Al}(\text{DIPY})_3$ was synthesised in accordance with general procedure C using 5-(4'-bromophenyl)dipyrin (400 mg, 1.34 mmol) **DIPY3**, AlCl_3 (89 mg, 0.67 mmol), CHCl_3 (40 mL), and DIPEA (0.23 mL, 1.34 mmol). The product was purified *via* column chromatography (dry loaded, SiO_2 , DCM:hexane, 1:1, v/v) and collected as the first fraction. Removal of the solvents under reduced pressure resulted in an orange powder (310 mg, 0.34 mmol, 75%); M.p.: dec. $>270^\circ\text{C}$; $R_f = 0.48$ (SiO_2 , DCM:hexane, 1:2, v/v); ^1H NMR (600 MHz, CDCl_3): $\delta = 7.56$ (d, $J = 8.3$ Hz, 6H, Ar-*H*), 7.31 (d, $J = 8.3$ Hz, 6H, Ar-*H*), 6.73 (s, 6H, α -*H*), 6.59 (dd, $J = 4.1, 1.1$ Hz, 6H, β -*H*), 6.25 ppm (dd, $J = 4.1, 1.5$ Hz, 6H, β -*H*); ^{13}C NMR (151 MHz, CDCl_3): $\delta = 149.7, 146.1, 138.9, 137.3, 132.5, 131.9, 130.4, 122.7, 117.1$ ppm; ^{27}Al NMR (104 MHz, CDCl_3): $\delta = 6.53$ ppm; UV-Vis (DCM): λ_{abs} (log ϵ) = 329 (4.48), 451 (4.98), 501 nm (4.92); APCI m/z calcd. for $\text{C}_{45}\text{H}_{30}\text{AlBr}_3\text{N}_6$ $[\text{M}+\text{H}]^+$: 918.9897; found 918.9978.

Tris[5-(pentafluorophenyl)dipyrrinato]aluminium(III) ($\text{Al}(\text{DIPY})_3$)



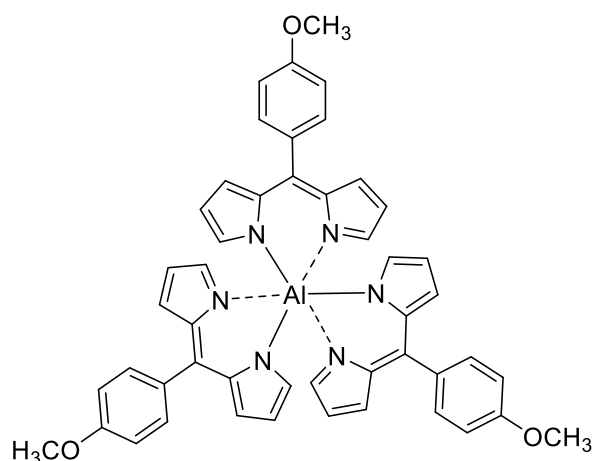
Compound $\text{Al}(\text{DIPY})_3$ was synthesised in accordance with general procedure C using 5-(pentafluorophenyl)dipyrrin (200 mg, 0.64 mmol) **DIPY4**, AlCl_3 (40 mg, 0.30 mmol), CHCl_3 (8 mL), and DIPEA (0.1 mL, 0.64 mmol). The product was purified *via* column chromatography (SiO_2 , DCM:hexane, 1:4, *v/v*) and eluted as the first fraction. The solvents were removed under reduced pressure yielding a dark orange/red powder (120 mg, 0.13 mmol, 58%); M.p.: dec. $>280^\circ\text{C}$; $R_f = 0.45$ (SiO_2 , DCM:hexane, 1:2, *v/v*); ^1H NMR (400 MHz, CDCl_3): $\delta = 6.89$ (s, 6H, α -H), 6.60 (d, $J = 3.8$ Hz, 6H, β -H), 6.32 ppm (d, $J = 3.9$ Hz, 6H, β -H); ^{13}C NMR (101 MHz, CDCl_3): $\delta = 151.5, 145.7, 144.1, 140.9, 138.4, 131.4, 129.8, 118.9, 113.0$ ppm; ^{27}Al NMR (104 MHz, CDCl_3): $\delta = 6.69$ ppm; ^{19}F NMR (377 MHz, CDCl_3): $\delta = -161.18$ (dt, $J = 21.8, 10.9$ Hz), -152.60 (t, $J = 20.8$ Hz), -139.06 ppm (dd, $J = 22.3, 6.9$ Hz); UV-Vis (DCM): λ_{abs} ($\log \epsilon$) = 461 (4.90), 512 nm (4.87); APCI *m/z* calcd. for $\text{C}_{45}\text{H}_{18}\text{AlF}_{15}\text{N}_6$ $[\text{M}+\text{H}]^+$: 955.1169; found 955.1233.

Tris[5-(4'-trimethylsilylethynylphenyl)dipyrrinato]aluminium(III)
(Al(DIPY)₃5)



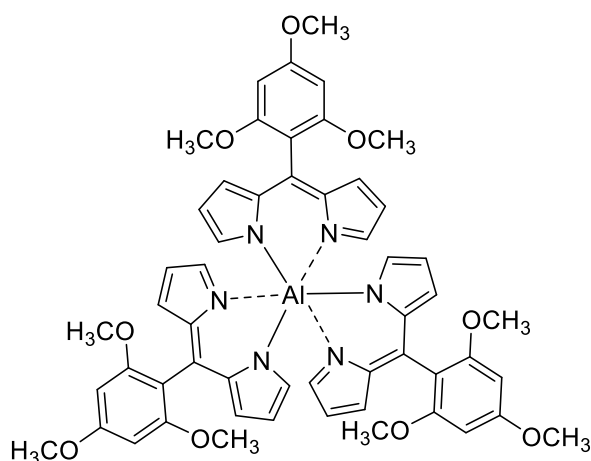
Compound **Al(DIPY)₃5** was synthesised in accordance with general procedure C using 5-(4'-trimethylsilylethynylphenyl)dipyrrin (300 mg, 0.95 mmol) **DIPY5**, AlCl₃ (59 mg, 0.44 mmol), CHCl₃ (10 mL), and DIPEA (0.17 mL, 0.97 mmol). The product was purified *via* column chromatography (SiO₂, DCM:hexane, 1:1, v/v) and eluted as the first fraction. The solvents were removed under reduced pressure yielding an orange powder (230 mg, 0.24 mmol, 75%); M.p.: >300 °C; R_f = 0.5 (SiO₂, DCM:hexane, 1:2, v/v); ¹H NMR (400 MHz, CDCl₃): δ = 7.52 (d, *J* = 8.1 Hz, 6H, Ar-*H*), 7.38 (d, *J* = 8.1 Hz, 6H, Ar-*H*), 6.73 (s, 6H, α-*H*), 6.58 (d, *J* = 3.6 Hz, 6H, β-*H*), 6.24 (dd, *J* = 4.0, 1.3 Hz, 6H, β-*H*), 0.28 ppm (s, 27H, -CH₃); ¹³C NMR (101 MHz, CDCl₃): δ = 150.0, 139.3, 139.1, 132.9, 131.2, 130.8, 123.7, 117.5, 105.0, 95.9, 0.4 ppm; ²⁷Al NMR (104 MHz, CDCl₃): δ = 6.58 ppm; UV-Vis (DCM): λ_{abs} (log ε) = 342 (4.50), 452 (4.88), 502 nm (4.82); APCI *m/z* calcd. for C₆₀H₅₇AlN₆Si₃ [M+H]⁺: 973.3768; found 973.3839.

Tris[5-(4'-methoxyphenyl)dipyrrinato]aluminium(III) (**Al(DIPY)₃6**)



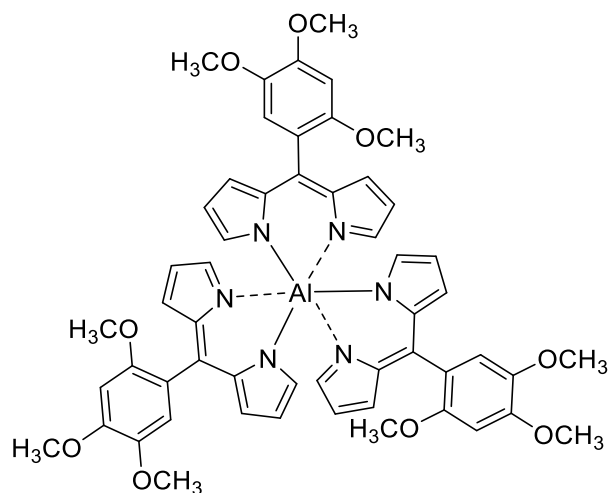
Compound **Al(DIPY)₃6** was synthesised in accordance with general procedure C using 5-(4'-methoxyphenyl)dipyrrin (300 mg, 1.2 mmol) **DIPY6**, AlCl₃ (80 mg, 0.6 mmol), CHCl₃ (10 mL), and DIPEA (0.20 mL, 1.2 mmol). The product was purified *via* column chromatography (SiO₂, DCM) and collected as the first fraction. Removal of the solvents under reduced pressure resulted in an orange powder (230 mg, 0.30 mmol, 74%); M.p.: dec. >250 °C; R_f = 0.32 (SiO₂, DCM:hexane, 1:1, v/v); ¹H NMR (400 MHz, CDCl₃): δ = 7.38 (d, *J* = 8.7 Hz, 6H, Ar-*H*), 6.93 (d, *J* = 8.7 Hz, 6H, Ar-*H*), 6.73 (s, 6H, α-*H*), 6.66 (dd, *J* = 4.0, 1.1 Hz, 6H, β-*H*), 6.22 (dd, *J* = 4.1, 1.5 Hz, 6H, β-*H*), 3.88 ppm (s, 9H, *p*-OCH₃); ¹³C NMR (151 MHz, CDCl₃): δ = 159.8, 149.1, 147.6, 139.5, 132.5, 131.9, 131.1, 116.5, 112.5, 55.3 ppm; ²⁷Al NMR (104 MHz, CDCl₃): δ = 6.51 ppm; UV-Vis (DCM): λ_{abs} (log ε) = 357 (4.71), 450 (5.15), 499 nm (5.01); APCI *m/z* calcd. for C₄₈H₃₉AlN₆O₃ [M+H]⁺: 775.2899, found 775.2971.

Tris[5-(2',4',6'-trimethoxyphenyl)dipyrinato]aluminium(III) ($\text{Al}(\text{DIPY})_3$)**7**)



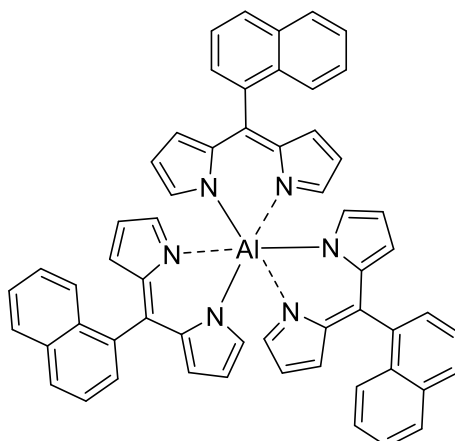
Compound **Al(DIPY)₃7** was synthesised in accordance with general procedure C using 5-(2',4',6'-trimethoxyphenyl)dipyrin (100 mg, 0.32 mmol) **DIPY7**, AlCl_3 (21 mg, 0.16 mmol), CHCl_3 (10 mL), and DIPEA (0.06 mL, 0.32 mmol). The crude mixture was dry loaded in silica and purified *via* column chromatography [note: this compound was difficult to solubilise and two columns were needed for its purification, SiO_2 , CHCl_3 (1st) and DCM:hexane 1:1 (2nd), *v/v*]. The first fraction was collected (from both columns) yielding in an orange solid after removal of the solvents *in vacuo* (36 mg, 0.04 mmol, 35%); M.p.: >300 °C; R_f = 0.49 (SiO_2 , DCM, *v/v*); ^1H NMR (600 MHz, CD_3CN): δ = 6.65 (br s, 6H, α -H), 6.59 (d, J = 3.6 Hz, 6H, β -H), 6.35 (s, 6H, Ar-H), 6.23 (d, J = 2.9 Hz, 6H, β -H), 3.90 (s, 9H, p - OCH_3), 3.67 ppm (s, 18H, o - OCH_3); ^{13}C NMR (151 MHz, CD_3CN): δ = 161.8, 158.9, 148.3, 139.9, 131.0, 108.8, 90.6, 55.7, 55.2 ppm; ^{27}Al NMR (104 MHz, DCM): δ = 6.21 ppm; UV-Vis (DCM): λ_{abs} (log ϵ) = 357 (4.13), 457 (4.93), 502 nm (4.88); APCI m/z calcd. for $\text{C}_{54}\text{H}_{51}\text{AlN}_6\text{O}_9$ $[\text{M}+\text{H}]^+$: 955.3611; found 955.3602.

Tris[5-(2',4',5'-trimethoxyphenyl)dipyrinato]aluminium(III) (**Al(DIPY)₃8**)



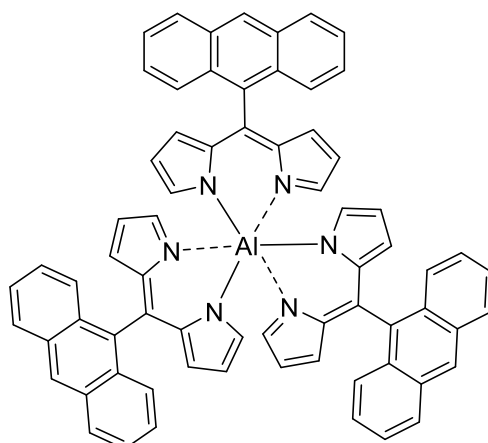
Compound **Al(DIPY)₃8** was synthesised in accordance with general procedure C using 5-(2',4',5'-trimethoxyphenyl)dipyrin (300 mg, 0.97 mmol) **DIPY8**, AlCl₃ (60 mg, 0.45 mmol), CHCl₃ (10 mL), and DIPEA (0.17 mL, 0.97 mmol). The product was purified *via* column chromatography (SiO₂, DCM) and collected as the first fraction. Removal of the solvents under reduced pressure resulted in an orange solid (250 mg, 0.26 mmol, 80%); M.p.: dec. >270 °C; R_f = 0.29 (SiO₂, EtOAc:hexane, 1:1, v/v); ¹H NMR (400 MHz, CDCl₃): δ = 6.89 – 6.79 (m, 9H, -H), 6.66 – 6.60 (m, 9H, -H), 6.22 (dd, J = 4.0, 1.3 Hz, 3H, Ar-H), 6.19 (dd, J = 4.0, 1.4 Hz, 3H, Ar-H), 3.96 (m, 9H, *p*-OCH₃), 3.84 – 3.83 (m, 9H, *m*-OCH₃), 3.63 – 3.59 ppm (m, 9H, *o*-OCH₃); ¹³C NMR (101 MHz, CDCl₃): δ = 152.1, 142.5, 142.53, 120.0, 115.2, 98.8, 58.0, 56.7, 56.7, 56.2 ppm; ²⁷Al NMR (104 MHz, CDCl₃): δ = 6.62 ppm; UV-Vis (DCM): λ_{abs} (log ε) = 362 (4.18), 454 (4.97), 502 nm (4.91); APCI *m/z* calcd. for C₅₄H₅₁AlN₆O₉ [M+H]⁺: 955.3533; found 955.360873.

Tris[5-(1'-naphthyl)dipyrrinato]aluminium(III) (**Al(DIPY)₃9**)



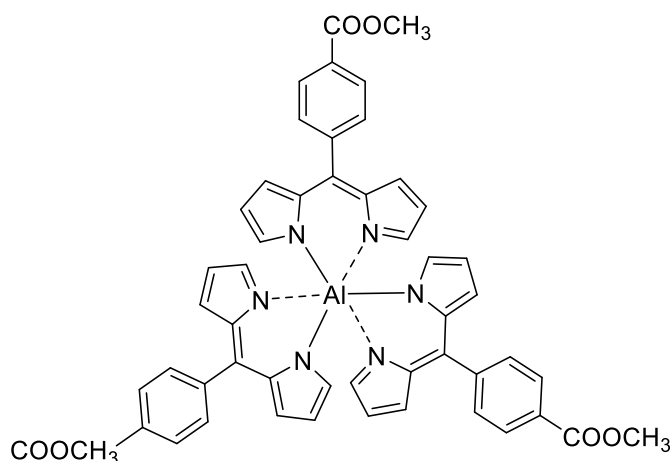
Compound **Al(DIPY)₃9** was synthesised in accordance with general procedure C using 5-(1'-naphthyl)dipyrrin (300 mg, 1.10 mmol) **DIPY9**, AlCl₃ (69 mg, 0.51 mmol), CHCl₃ (15 mL), and DIPEA (0.19 mL, 1.10 mmol). The product was dry loaded in silica and purified *via* column chromatography (SiO₂, DCM:hexane, 3:7, *v/v*). The first fraction was collected yielding a dark orange powder after removal of the solvents *in vacuo* (200 mg, 0.24 mmol, 65%); M.p.: dec. >290 °C; R_f = 0.31 (SiO₂, DCM:hexane, 1:2, *v/v*); ¹H NMR (400 MHz, CDCl₃): δ = 7.96 – 7.93 (m, 3H, Ar-*H*), 7.89 (d, *J* = 8.2 Hz, 3H, Ar-*H*), 7.74 – 7.68 (m, 3H, Ar-*H*), 7.56 – 7.54 (m, 6H), 7.47 – 7.43 (m, 3H, Ar-*H*), 7.35 – 7.27 (m, 3H, Ar-*H*), 7.01 – 6.91 (m, 6H, α-*H*), 6.50 – 6.43 (m, 6H, β-*H*), 6.31 – 6.28 (m, 3H, β-*H*), 6.23 – 6.21 ppm (m, 3H, β-*H*); ¹³C NMR (101 MHz, CDCl₃): δ = 149.7, 149.5, 149.4, 146.0, 140.2, 140.1, 139.9, 139.9, 135.9, 133.4, 132.9, 132.5, 128.5, 127.9, 127.8, 127.8, 127.7, 127.1, 127.0, 126.4, 125.8, 124.4, 117.0 ppm; ²⁷Al NMR (104 MHz, CDCl₃): δ = 6.91 ppm; UV-Vis (DCM): λ_{abs} (log ε) = 351 (4.24), 456 (4.94), 504 nm (4.90); APCI *m/z* calcd. for C₅₇H₃₉AlN₆ [M+H]⁺: 835.3130; found 835.3123.

Tris[5-(anthracene-9'-yl)dipyrinato]aluminium(III) ($\text{Al}(\text{DIPY})_3\text{10}$)



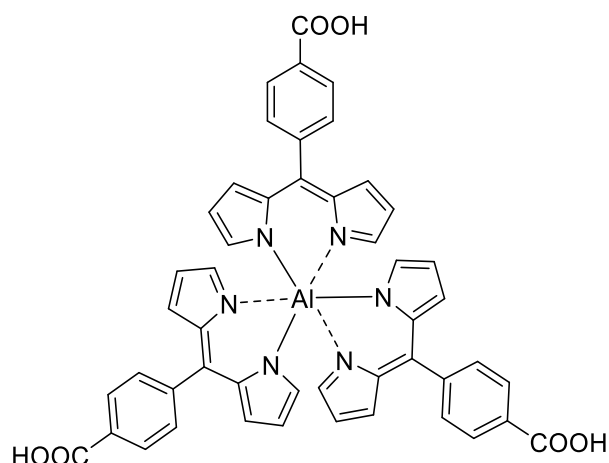
Compound $\text{Al}(\text{DIPY})_3\text{10}$ was synthesised in accordance with general procedure C using 5-(9'-anthracenyl)dipyrin (100 mg, 0.31 mmol) **DIPY10**, AlCl_3 (19 mg, 0.15 mmol), CHCl_3 (10 mL), and DIPEA (0.05 mL, 0.31 mmol). The product was purified *via* column chromatography (SiO_2 , CHCl_3 :hexane, 2:1, *v/v*) and collected as the first fraction. Removal of the solvents under reduced pressure resulted in a dark orange powder (41 mg, 0.04 mmol, 40%); M.p.: dec. >290 °C; $R_f = 0.37$ (SiO_2 , DCM:hexane, 1:1, *v/v*); ^1H NMR (400 MHz, CDCl_3): $\delta = 8.60$ (s, 3H, Ar-*H*), 8.07 (d, $J = 8.5$ Hz, 6H, Ar-*H*), 7.93 – 7.91 (m, 6H, Ar-*H*), 7.47 – 7.44 (m, 6H, Ar-*H*), 7.35 – 7.31 (m, 6H, Ar-*H*), 7.21 (br s, 6H, α -*H*), 6.32 – 6.31 (m, 6H, β -*H*), 6.28 – 6.27 ppm (m, 6H, β -*H*); ^{13}C NMR (101 MHz, CDCl_3): $\delta = 149.3, 145.0, 140.5, 132.4, 132.0, 130.9, 130.6, 127.9, 127.4, 127.0, 126.0, 125.0, 117.3$ ppm; ^{27}Al NMR (104 MHz, CDCl_3): $\delta = 7.15$ ppm; UV-Vis (DCM): λ_{abs} ($\log \epsilon$) = 351 (4.32), 369 (4.47), 390 (4.45), 460 (4.74), 508 nm (4.69); APCI m/z calcd. for $\text{C}_{69}\text{H}_{45}\text{AlN}_6$ $[\text{M}+\text{H}]^+$: 985.3521; found 985.3596.

Tris[5-(4'-methoxycarbonylphenyl)dipyrrinato]aluminium(III) ($\text{Al}(\text{DIPY})_3\mathbf{11}$)



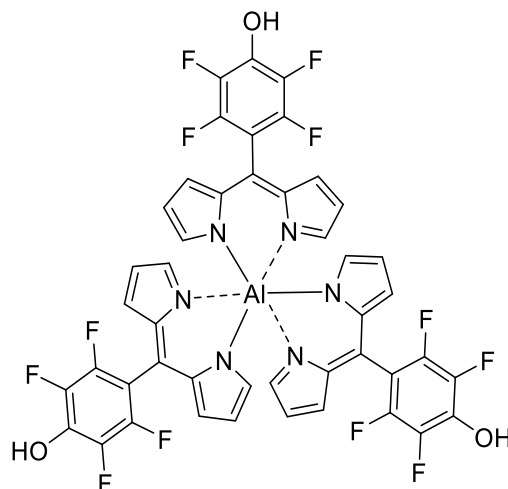
Compound $\text{Al}(\text{DIPY})_3\mathbf{11}$ was synthesised in accordance with general procedure C using 5-(4'-methoxycarbonylphenyl)dipyrrin (450 mg, 1.62 mmol) **DIPY11**, AlCl_3 (100 mg, 0.75 mmol), CHCl_3 (12 mL), and DIPEA (0.28 mL, 1.62 mmol). The product was dry loaded in silica and purified *via* column chromatography (SiO_2 , DCM:hexane, 2:1, *v/v*). The first fraction was collected yielding an orange solid after removal of the solvent *in vacuo* (350 mg, 0.41 mmol, 76%); M.p.: dec. >280 °C; $R_f = 0.30$ (SiO_2 , CHCl_3 , *v/v*); ^1H NMR (400 MHz, CDCl_3): $\delta = 8.10$ (d, $J = 8.2$ Hz, 6H, Ar-*H*), 7.52 (d, $J = 8.1$ Hz, 6H, Ar-*H*), 6.77 (s, 6H, α -*H*), 6.56 – 6.55 (m, 6H, β -*H*), 6.26 – 6.25 (m, 6H, β -*H*), 3.99 ppm (s, 9H, - CH_3); ^{13}C NMR (101 MHz, CDCl_3): $\delta = 166.9, 149.9, 146.3, 143.2, 138.9, 132.6, 130.6, 130.3, 128.6, 117.4, 52.4$ ppm; ^{27}Al NMR (104 MHz, CDCl_3): $\delta = 6.62$ ppm; UV-Vis (DCM): λ_{abs} (log ϵ) = 452 (4.93), 502 nm (4.87); APCI *m/z* calcd. for $\text{C}_{51}\text{H}_{39}\text{AlN}_6\text{O}_6$ $[\text{M}+\text{H}]^+$: 859.2825; found 859.2791.

Tris[5-(4'-carboxyphenyl)dipyrinato]aluminium(III) ($\text{Al}(\text{DIPY})_3\mathbf{12}$)



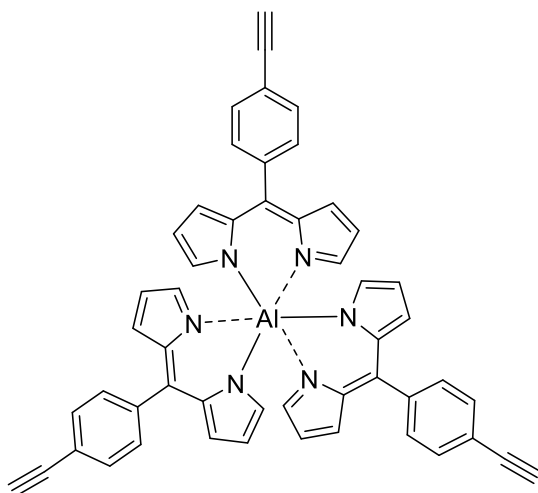
In a round bottom flask tris[5-(4'-methoxycarbonylphenyl)dipyrinato]aluminium(III) (100 mg, 0.12 mmol, 1 eq) $\text{Al}(\text{DIPY})_3\mathbf{11}$ was dissolved in THF (20 mL) and MeOH (20 mL). An aq. solution (water 8 mL) of KOH (392 mg, 6.99 mmol, 60 eq) was added to the solution and the reaction mixture was stirred overnight at 80 °C under reflux. Then solvent was removed under reduced pressure and water was added. 1M HCl solution was added dropwise to reach acidic pH 4-5 where the desired compound precipitated. The precipitate was filtered and washed with water until dryness to yield a dark red powder (90 mg, 0.11 mmol, 95%); M.p.: dec. >250 °C; $R_f = 0.15$ (SiO_2 , DCM:MeOH, 3:1, v/v); ^1H NMR (400 MHz, $d\text{THF}$): $\delta = 8.10$ (d, $J = 8.2$ Hz, 6H, Ar- H), 7.53 (d, $J = 8.3$ Hz, 6H, Ar- H), 6.81 (s, 6H, α - H), 6.57 – 6.56 (m, 6H, β - H), 6.26 – 6.25 ppm (m, 6H, β - H); ^{13}C NMR (101 MHz, $d\text{THF}$): $\delta = 167.3, 150.5, 147.5, 143.6, 139.8, 133.3, 132.1, 131.2, 129.4, 117.9$ ppm; ^{27}Al NMR (104 MHz, $d\text{THF}$): $\delta = 6.64$ ppm; UV-Vis (THF): λ_{abs} ($\log \epsilon$) = 451 (4.79), 502 nm (4.71); APCI m/z calcd. for $\text{C}_{48}\text{H}_{33}\text{AlN}_6\text{O}_6$ $[\text{M}+\text{H}]^+$: 817.2355; found 817.2352.

Tris[5-(4'-hydroxy-2',3',5',6'-tetrafluorophenyl)dipyrrinato]aluminium(III)
(Al(DIPY)₃13)



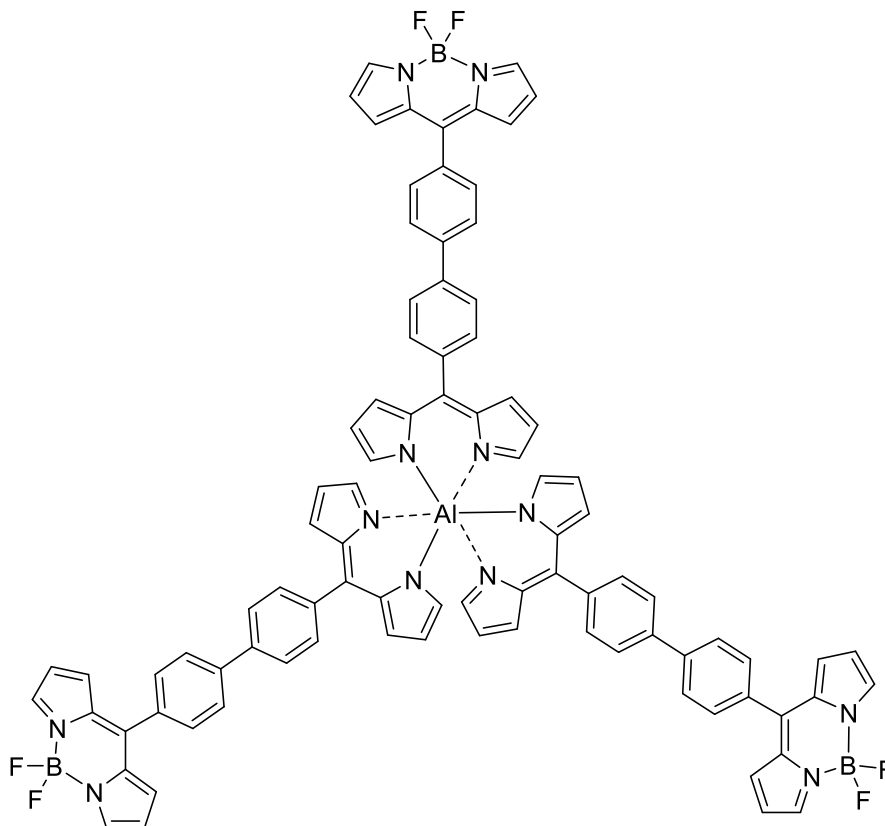
Compound **Al(DIPY)₃13** was prepared following literature procedure.^[228] In a Schlenk tube under argon atmosphere tris[5-(pentafluorophenyl)dipyrrinato]aluminium(III) (30 mg, 0.03 mmol, 1 eq.) **Al(DIPY)₃4** was added together with freshly powdered KOH (26 mg, 0.47 mmol, 15 eq.), propargyl alcohol (0.04 mL, 0.6 mmol, 20 eq.), and dry THF (10 mL) and were stirred at r.t. overnight. The mixture was washed with brine (×2) and water (×2), extracted with DCM, dried over Na₂SO₄, filtered, and solvent was evaporated under vacuum to give a dark red crude mixture. The product was purified *via* column chromatography (SiO₂, EtOAc 10% in DCM → EtOAc 100% → 2% MeOH in EA → 40% MeOH in EtOAc, *v/v*) and collected as the third fraction. Removal of the solvents under reduced pressure resulted in a dark red solid (25 mg, 0.026 mmol, 84%); M.p.: >300 °C; R_f = 0.46 (SiO₂, DCM:MeOH, 9:1, *v/v*); ¹H NMR (400 MHz, MeOD): δ = 6.85 (s, 6H, α-*H*), 6.71 (d, *J* = 4.0 Hz, 6H, β-*H*), 6.31 ppm (dd, *J* = 4.1, 1.3 Hz, 6H, β-*H*); ¹³C NMR (101 MHz, MeOD): δ = 149.6, 146.1, 143.8, 140.5, 139.2, 138.3, 133.1, 131.2, 117.0, 101.4, 101.2, 101.0 ppm; ²⁷Al NMR (104 MHz, CDCl₃): δ = 6.79 ppm; UV-Vis (MeOH): λ_{abs} (log ε) = 455 (4.62), 506 nm (4.59); APCI *m/z* calcd. for C₄₅H₂₁AlF₁₂N₆O₃ [M+H]⁺: 949.1377; found 949.1372.

Tris[5-(4'-phenylethynyl)dipyrinato]aluminium(III) (**Al(DIPY)₃14**)



Literature procedure was followed for TMS deprotection.^[474] In a round bottom flask tris[5-(4'-trimethylsilylethynylphenyl)dipyrinato]aluminium(III) (90 mg, 0.09 mmol, 1 eq) **Al(DIPY)₃5** was added and dried for 30 min. Then dry DCM (15 mL) and TBAF in THF (1M, 0.08 mL, 0.28 mmol, 3 eq) were added under argon atmosphere and the reaction stirred at r.t. until TLC analyses indicated complete consumption of starting material (40 min). Water was added and the compound was extracted with DCM (x2), dried over Na₂SO₄, filtered, and the remaining solvent was removed *in vacuo* to yield an orange solid (65 mg, 0.09 mmol, 92%); M.p.: dec >130 °C; R_f = 0.33 (SiO₂, DCM:hexane, 1:2, v/v); ¹H NMR (400 MHz, CDCl₃): δ = 7.57 (d, J = 8.1 Hz, 6H, Ar-H), 7.43 (d, J = 8.2 Hz, 6H, Ar-H), 6.77 (s, 6H, α-H), 6.62 (d, J = 3.2 Hz, 6H, β-H), 6.27 (dd, J = 4.1, 1.4 Hz, 6H, β-H), 3.19 ppm (s, 3H, -CH); ¹³C NMR (101 MHz, CDCl₃): δ = 149.6, 146.5, 139.0, 138.9, 132.5, 130.9, 130.4, 122.2, 117.0, 83.2, 78.1 ppm; ²⁷Al NMR (104 MHz, CDCl₃): δ = 6.65 ppm; UV-Vis (DCM): λ_{abs} (log ε) = 333 (4.36), 452 (4.80), 502 nm (4.74); APCI *m/z* calcd. for C₅₁H₃₃AlN₆ [M+H]⁺: 757.2660; found 757.2668.

Tris{5-[4'-(1,1'-biphenyl)-4-yl-(4,4-difluoro-4-bora-3a,4a,diaza-s-indacene-yl)]dipyrrinato}aluminium(III) ($\text{Al}(\text{DIPY})_3\text{15}$)



Using a Suzuki coupling reaction, tris[5-(4'-bromophenyl)dipyrrinato]aluminium(III) (25 mg, 0.027 mmol, 1 eq.) $\text{Al}(\text{DIPY})_3\text{3}$, borylated BODIPY **5.52** (42 mg, 0.11 mmol, 4 eq.), Cs_2CO_3 (52 mg, 0.27 mmol, 10 eq.), and $\text{Pd}(\text{PPh}_3)_4$ (7 mg, 0.005 mmol, 0.2 eq.) were added in a dry Schlenk tube and dried for 2 h. Dry toluene and DMF (3mL:1.5mL) were added under argon atmosphere and the solution was subjected to three freeze/pump-thaw cycles and stirred for 1 h at 85 °C. TLC reaction monitoring showed that aluminium complex was consumed. The reaction mixture was washed with brine ($\times 2$) and water ($\times 2$), extracted with DCM, dried over MgSO_4 , filtered, and the resulting solvent was evaporated under vacuum. The desired compound was purified *via* column chromatography (SiO_2 , DCM:hexane, 4:1 \rightarrow DCM, *v/v*) and was eluted as the forth fraction. The solvents were removed under reduced pressure to yield a dark red solid (12 mg, 8 μmol , 72%); M.p.: >300 °C; $R_f = 0.37$ (SiO_2 , DCM, *v/v*); $^1\text{H NMR}$ (400 MHz, CDCl_3): $\delta = 8.01$ (s, 6H, $\alpha\text{-H}_{\text{BODIPY}}$), 7.88 (d, $J = 8.3$ Hz, 6H, Ar-H), 7.76 (dd, $J = 13.5, 8.3$ Hz, 12H, Ar-H), 7.65 (d, $J = 8.2$

Hz, 6H, Ar-*H*), 7.07 (d, $J = 4.1$ Hz, 6H, β - H_{BODIPY}), 6.88 (s, 6H, α - H_{AlDIPY}), 6.77 (dd, $J = 4.1, 1.0$ Hz, 6H, β - H_{AlDIPY}), 6.62 (dd, $J = 4.1, 1.5$ Hz, 6H, β - H_{BODIPY}), 6.35 ppm (dd, $J = 4.1, 1.5$ Hz, 6H, β - H_{AlDIPY}); ^{13}C NMR (101 MHz, CDCl_3): $\delta = 149.6, 147.0, 146.9, 144.1, 143.0, 139.8, 139.2, 138.5, 134.9, 133.1, 132.6, 131.5, 131.2, 127.1, 125.9, 118.6, 117.0$ ppm; ^{27}Al NMR (104 MHz, CDCl_3): $\delta = 6.80$ ppm; ^{19}F NMR (377 MHz, CDCl_3): $\delta = -145.06$ ppm (dd, $J = 57.6, 29.0$ Hz); ^{11}B NMR (128 MHz, CDCl_3): $\delta = 0.32$ ppm (t, $J = 28.8$ Hz); UV-Vis (DCM): λ_{abs} (log ϵ) = 384 (4.95), 454 (5.07), 503 nm (5.41); HRMS MALDI m/z calcd. for $\text{C}_{90}\text{H}_{60}\text{AlB}_3\text{F}_6\text{N}_{12} [\text{M}]^+$: 1482.5063; found 1482.5099.

5.5.3.4 Radiochemistry procedures

A stock solution of the ligand **DIPY8** was prepared in DMSO with the concentration of 1 mg mL⁻¹. For radiolabelling 14 µL of indium-111 chloride (210 µCi) and 14 µL of ammonium acetate (0.5 M, 5-6 pH) were added in an Eppendorf tube and left to react at 37 °C for 30 min in order to increase the binding activity of indium-111 while Cl⁻ dissociates. Then 7 µL of **DIPY8** and 2 µL of NaOH 2N were added and the solution was heated at 70 °C for 40 min. There was a change of colour from dark orange to yellow after addition of NaOH. On completion of the reaction, 3 µL were removed *via* syringe, diluted with 30 – 40 µL of deuterated water and analysed by HPLC (radio and UV detection). HPLC method was performed with a gradient elution 0.1% formic acid in water as solvent A and methanol as solvent B. A reverse gradient was applied starting with A at 95% for 2 min going up to 5% A at 12 minutes, isocratic level until 14 min and gradient until 95% A at 16 min, then hold to 20 min. The reaction was repeated twice.

For the kinetic stability study, the stability of the complex was monitored at different temperatures (4 °C, 24 °C and 37 °C) and with medium saline (pH 7.4), at different time points post preparation (1 h, 3 h, and 24 h) and was assessed through HPLC with a radio-gamma-detector. Specifically:

- 10 µL of aliquots of the [¹¹¹In]In-labelled compound were incubated at 4 °C, 24 °C and 37 °C. After 1 h, 3 h and 24 h post preparation, 3 µL from each vial were removed, diluted with 40 µL of deuterated water and injected in order to perform the HPLC measurement.
- 10 µL of aliquots of the [¹¹¹In]In-labelled compound were incubated with 100 µL saline (1:10) at 37 °C. After 1 h, 3 h and 24 h post preparation, 30 µL were injected directly for the HPLC experiment.

For the kinetic stability study, HPLC method was modified to a shorter time. A gradient elution 0.1% formic acid in water as solvent A and methanol as solvent B. A reverse gradient was applied starting with A at 95% for 2 min going up to 5% A at 10 minutes, isocratic level until 12 min and gradient until 95% A at 15 min.

Note: another effort to conduct a kinetic stability study using human plasma (Sigma Aldrich) as medium was not successful: 10 μL of aliquots of the ^{111}In -labelled compound were incubated with 100 μL human plasma (1:10). After 1 h, 3 h and 24 h post preparation, 60 μL of acetonitrile were added to 30 μL of the incubated solution and centrifuged at 10000 rpm for 10 min. Then the supernatant was removed and injected for the HPLC measurement. In this case only the peak of indium-111 (radio. \sim 2.3 min) and dipyrin (UV-Vis, \sim 8 min) appeared. However, the indium-111 peak was very weak, indicating that the extraction with acetonitrile was not successful to extract the radiolabelled complex for detection.

References

- [1] M. H. Abdel-kader, in *Photodynamic Medicine: from Bench to Clinic* (Eds.: H. Kostron, T. Hasan), Royal Society of Chemistry, London, **2016**, pp. 1–21.
- [2] H. Hönigsmann, *Photochem. Photobiol. Sci.* **2013**, *12*, 16–21.
- [3] Oribasius, *Oeuvres d'Oribase: texte grec, en grande partie inédit, collationné sur les manuscrits*, A L'Imprimerie Nationale, **1854**.
- [4] C. Yapijakis, *In Vivo* **2009**, *23*, 507–514.
- [5] A. Grzybowski, J. Sak, J. Pawlikowski, *Clin. Dermatol.* **2016**, *34*, 532–537.
- [6] J. D. Spikes, *J. Photochem. Photobiol. B: Biol.* **1991**, *9*, 369–371.
- [7] J. D. Spikes, *Ann. N. Y. Acad. Sci.* **1975**, *244*, 496–508.
- [8] J. Moan, Q. Peng, in *Photodynamic Therapy* (Ed.: T. Patrice), Royal Society of Chemistry, Cambridge, **2003**, pp. 1–18.
- [9] A. Grzybowski, K. Pietrzak, *Clin. Dermatol.* **2012**, *30*, 451–455.
- [10] M. D. Daniell, J. S. Hill, *Aust. N. Z. J. Surg.* **1991**, *61*, 340–348.
- [11] T. J. Dougherty, *Photochem. Photobiol.* **1987**, *45*, 879–889.
- [12] T. J. Dougherty, J. E. Kaufman, A. Goldfarb, K. R. Weishaupt, D. Boyle, A. Mittleman, *Cancer Res.* **1978**, *38*, 2628–2635.
- [13] R. L. Lipson, *Arch. Dermatol.* **1960**, *82*, 508.
- [14] R. Ackroyd, C. Kelty, N. Brown, M. Reed, *Photochem. Photobiol.* **2007**, *74*, 656–669.
- [15] A. R. Battersby, *Nat. Prod. Rep.* **2000**, *17*, 507–526.
- [16] F. H. J. Figge, G. S. Weiland, L. O. J. Manganiello, *Proc. Soc. Exp. Biol. Med.* **1948**, *68*, 640–641.
- [17] K. R. Weishaupt, C. J. Gomer, T. J. Dougherty, *Cancer Res.* **1976**, *36*, 2326–2329.
- [18] M. L. Agarwal, M. E. Clay, E. J. Harvey, H. H. Evans, A. R. Antunez, N. L. Oleinick, *Cancer Res.* **1991**, *51*, 5993–5996.
- [19] L. E. Gerlowski, R. K. Jain, *Microvasc. Res.* **1986**, *31*, 288–305.
- [20] A. P. Castano, T. N. Demidova, M. R. Hamblin, *Photodiagn. Photodyn. Ther.* **2004**, *1*, 279–293.
- [21] A. P. Castano, T. N. Demidova, M. R. Hamblin, *Photodiagn. Photodyn. Ther.* **2005**, *2*, 1–23.
- [22] A. E. O'Connor, W. M. Gallagher, A. T. Byrne, *Photochem. Photobiol.* **2009**, *85*, 1053–1074.
- [23] H. Abrahamse, M. R. Hamblin, *Biochem. J.* **2016**, *473*, 347–364.
- [24] R. R. Allison, G. H. Downie, R. Cuenca, X.-H. Hu, C. J. Childs, C. H. Sibata, *Photodiagn. Photodyn. Ther.* **2004**, *1*, 27–42.
- [25] A. Wiehe, J. M. O'Brien, M. O. Senge, *Photochem. Photobiol. Sci.* **2019**, *18*, 2565–2612.
- [26] World Health Organisation, https://www.iarc.who.int/wp-content/uploads/2020/12/pr292_E.pdf, accessed February 2022.
- [27] World Health Organisation, <https://www.who.int/news-room/fact-sheets/detail/cancer>, accessed February 2022.
- [28] D. E. J. G. J. Dolmans, D. Fukumura, R. K. Jain, *Nat. Rev. Cancer* **2003**, *3*, 380–387.
- [29] M. Triesscheijn, P. Baas, J. H. M. Schellens, F. A. Stewart, *The Oncologist* **2006**, *11*, 1034–1044.

- [30] C. A. Kendall, C. A. Morton, *Technol. Cancer Res. Treat.* **2003**, *2*, 283–288.
- [31] R. R. Allison, C. H. Sibata, *Photodiagn. Photodyn. Ther.* **2010**, *7*, 61–75.
- [32] B. C. Wilson, M. Olivo, G. Singh, *Photochem. Photobiol.* **1997**, *65*, 166–176.
- [33] C. Donohoe, M. O. Senge, L. G. Arnaut, L. C. Gomes-da-Silva, *Biochim. Biophys. Acta BBA - Rev. Cancer* **2019**, *1872*, 188308.
- [34] S. A. Eccles, D. R. Welch, *The Lancet* **2007**, *369*, 1742–1757.
- [35] G. P. Gupta, J. Massagué, *Cell* **2006**, *127*, 679–695.
- [36] A. F. Chambers, A. C. Groom, I. C. MacDonald, *Nat. Rev. Cancer* **2002**, *2*, 563–572.
- [37] J. P. Celli, B. Q. Spring, I. Rizvi, C. L. Evans, K. S. Samkoe, S. Verma, B. W. Pogue, T. Hasan, *Chem. Rev.* **2010**, *110*, 2795–2838.
- [38] R. Waksman, I. M. Leitch, J. Roessler, H. Yazdi, R. Seabron, F. Tio, R. W. Scott, R. I. Grove, S. Rychnovsky, B. Robinson, R. Pakala, E. Cheneau, *Heart* **2006**, *92*, 1138–1144.
- [39] R. Waksman, P. E. McEwan, T. I. Moore, R. Pakala, F. D. Kolodgie, D. G. Hellings, R. C. Seabron, S. J. Rychnovsky, J. Vasek, R. W. Scott, R. Virmani, *J. Am. Coll. Cardiol.* **2008**, *52*, 1024–1032.
- [40] Kereiakes Dean J., Szyniszewski Arthur M., Wahr Dennis, Herrmann Howard C., Simon Daniel I., Rogers Campbell, Kramer Paul, Shear Wendy, Yeung Alan C., Shunk Kendrick A., Chou Tony M., Popma Jeffrey, Fitzgerald Peter, Carroll Tanya E., Forer David, Adelman Daniel C., *Circulation* **2003**, *108*, 1310–1315.
- [41] M. R. Hamblin, *Photochem. Photobiol.* **2020**, *96*, 506–516.
- [42] J. Karges, *Angew. Chem. Int. Ed.* **2022**, *61*, e202112236.
- [43] P. Agostinis, K. Berg, K. A. Cengel, T. H. Foster, A. W. Girotti, S. O. Gollnick, S. M. Hahn, M. R. Hamblin, A. Juzeniene, D. Kessel, M. Korbelik, J. Moan, P. Mroz, D. Nowis, J. Piette, B. C. Wilson, J. Golab, *CA. Cancer J. Clin.* **2011**, *61*, 250–281.
- [44] M. Vicente, *Curr. Med. Chem.-Anti-Cancer Agents* **2001**, *1*, 175–194.
- [45] R. Bonnett, P. Charlesworth, B. D. Djelal, S. Foley, D. J. McGarvey, T. G. Truscott, *J. Chem. Soc., Perkin Trans. 2* **1999**, 325–328.
- [46] Y. Chen, G. Li, R. K. Pandey, *Curr. Org. Chem.* **2004**, *8*, 1105–1134.
- [47] D. Samaroo, E. Perez, A. Aggarwal, A. Wills, N. O'Connor, *Ther. Deliv.* **2014**, *5*, 859–872.
- [48] R. D. Teo, J. Y. Hwang, J. Termini, Z. Gross, H. B. Gray, *Chem. Rev.* **2017**, *117*, 2711–2729.
- [49] J. L. Sessler, R. A. Miller, *Biochem. Pharmacol.* **2000**, *59*, 733–739.
- [50] D. Lafont, Y. Zorlu, H. Savoie, F. Albrieux, V. Ahsen, R. W. Boyle, F. Dumoulin, *Photodiagn. Photodyn. Ther.* **2013**, *10*, 252–259.
- [51] L. C. Gomes-da-Silva, L. Zhao, L. Bezu, H. Zhou, A. Sauvat, P. Liu, S. Durand, M. Leduc, S. Souquere, F. Loos, L. Mondragón, B. Sveinbjörnsson, Ø. Rekdal, G. Boncompain, F. Perez, L. G. Arnaut, O. Kepp, G. Kroemer, *EMBO J.* **2018**, *37*, e98354.
- [52] B. Krammer, K. Plaetzer, *Photochem. Photobiol. Sci.* **2008**, *7*, 283–289.
- [53] E. Christensen, T. Warloe, S. Kroon, J. Funk, P. Helsing, A. M. Soler, H. J. Stang, Ø. Vatne, C. Mørk, *J. Eur. Acad. Dermatol. Venereol.* **2010**, *24*, 505–512.

- [54] A. Wagner, U. W. Denzer, D. Neureiter, T. Kiesslich, A. Puespoeck, E. A. J. Rauws, K. Emmanuel, N. Degenhardt, U. Frick, U. Beuers, A. W. Lohse, F. Berr, G. W. Wolkersdörfer, *Hepatology* **2015**, *62*, 1456–1465.
- [55] W. M. Chan, T.-H. Lim, A. Pece, R. Silva, N. Yoshimura, *Graefes Arch. Clin. Exp. Ophthalmol.* **2010**, *248*, 613–626.
- [56] A.-R. Azzouzi, E. Barret, C. M. Moore, A. Villers, C. Allen, A. Scherz, G. Muir, M. de Wildt, N. J. Barber, S. Lebdai, M. Emberton, *BJU Int.* **2013**, *112*, 766–774.
- [57] M. Ethirajan, Y. Chen, P. Joshi, R. K. Pandey, *Chem Soc Rev* **2011**, *40*, 340–362.
- [58] M. Kielmann, C. Prior, M. O. Senge, *New J. Chem.* **2018**, *42*, 7529–7550.
- [59] M. O. Senge, *Photodiagn. Photodyn. Ther.* **2012**, *9*, 170–179.
- [60] J. Karges, *ChemBioChem* **2020**, *21*, 3044–3046.
- [61] S. Monro, K. L. Colón, H. Yin, J. Roque, P. Konda, S. Gujar, R. P. Thummel, L. Lilge, C. G. Cameron, S. A. McFarland, *Chem. Rev.* **2019**, *119*, 797–828.
- [62] A. Kamkaew, S. H. Lim, H. B. Lee, L. V. Kiew, L. Y. Chung, K. Burgess, *Chem Soc Rev* **2013**, *42*, 77–88.
- [63] M. L. Agazzi, M. B. Ballatore, A. M. Durantini, E. N. Durantini, A. C. Tomé, *J. Photochem. Photobiol. C Photochem. Rev.* **2019**, *40*, 21–48.
- [64] J. Zhao, K. Xu, W. Yang, Z. Wang, F. Zhong, *Chem. Soc. Rev.* **2015**, *44*, 8904–8939.
- [65] Z. Jendželovská, R. Jendželovský, B. Kuchárová, P. Fedoročko, *Front. Plant Sci.* **2016**, *7*, 560.
- [66] U.S. Food and Drug Administration, https://www.accessdata.fda.gov/drugsatfda_docs/label/2011/020451s0201bl.pdf, accessed February 2022.
- [67] Y.-J. Hsieh, C.-C. Wu, C.-J. Chang, J.-S. Yu, *J. Cell. Physiol.* **2003**, *194*, 363–375.
- [68] N. V. Kudinova, T. T. Berezov, *Biochem. Mosc. Suppl. Ser. B Biomed. Chem.* **2010**, *4*, 95–103.
- [69] S. K. Pushpan, S. Venkatraman, V. G. Anand, J. Sankar, D. Parmeswaran, S. G. and T. K. Chandrashekar, *Curr. Med. Chem.: Anti-Cancer Agents* **2002**, *2*, 187–207.
- [70] NIH, U.S. National Library of Medicine, ClinicalTrials.gov, <https://clinicaltrials.gov/ct2/show/NCT03727061>, accessed February 2022.
- [71] C. Mimikos, G. Shafirstein, H. Arshad, *World J. Otorhinolaryngol. - Head Neck Surg.* **2016**, *2*, 126–129.
- [72] M. J. Garland, C. M. Cassidy, D. Woolfson, R. F. Donnelly, *Future Med. Chem.* **2009**, *1*, 667–691.
- [73] K. Inoue, *Int. J. Urol. Off. J. Jpn. Urol. Assoc.* **2017**, *24*, 97–101.
- [74] J. C. Kennedy, S. L. Marcus, R. H. Pottier, *J. Clin. Laser Med. Surg.* **1996**, *14*, 289–304.
- [75] K. Kalka, H. Merk, H. Mukhtar, *J. Am. Acad. Dermatol.* **2000**, *42*, 389–413.
- [76] C. G. Hadjipanayis, W. Stummer, *J. Neurooncol.* **2019**, *141*, 479–486.
- [77] P. Lehmann, *Br. J. Dermatol.* **2007**, *156*, 793–801.
- [78] Q. Peng, A. M. Soler, T. Warloe, J. M. Nesland, K.-E. Giercksky, *J. Photochem. Photobiol. B: Biol.* **2001**, *62*, 140–145.

- [79] J. E. Räsänen, N. Neittaanmäki, L. Ylitalo, J. Hagman, P. Rissanen, L. Ylianttila, M. Salmivuori, E. Snellman, M. Grönroos, *Br. J. Dermatol.* **2019**, *181*, 265–274.
- [80] S. Assikar, A. Labrunie, D. Kerob, A. Couraud, C. Bédane, *J. Eur. Acad. Dermatol. Venereol.* **2020**, *34*, 1730–1735.
- [81] E. P. M. LaRochelle, M. S. Chapman, E. V. Maytin, T. Hasan, B. W. Pogue, *Photochem. Photobiol.* **2020**, *96*, 320–326.
- [82] A. Lapini, A. Minervini, A. Masala, L. Schips, A. Pycha, L. Cindolo, R. Giannella, T. Martini, G. Vittori, D. Zani, F. Bellomo, S. Cosciani Cunico, *Surg. Endosc.* **2012**, *26*, 3634–3641.
- [83] A. Ferré, C. Cordonnier, M. Demailly, F. Hakami, H. Sevestre, F. Saint, *Progres En Urol. J. Assoc. Francaise Urol. Soc. Francaise Urol.* **2013**, *23*, 195–202.
- [84] M. B. Parodi, C. L. Spina, L. Berchicci, G. Petruzzi, F. Bandello, *Retin. Pharmacother.* **2016**, *55*, 330–336.
- [85] K. Petermeier, O. Tatar, W. Inhoffen, M. Völker, B. A. Lafaut, S. Henke-Fahle, F. Gelisken, F. Ziemssen, S. Bopp, K. U. Bartz-Schmidt, S. Grisanti, *Br. J. Ophthalmol.* **2006**, *90*, 1034–1039.
- [86] NIH, U.S. National Library of Medicine, ClinicalTrials.gov, <https://clinicaltrials.gov/ct2/show/NCT03033225>, accessed February 2022.
- [87] M. T. Huggett, M. Jermyn, A. Gillams, R. Illing, S. Mosse, M. Novelli, E. Kent, S. G. Bown, T. Hasan, B. W. Pogue, S. P. Pereira, *Br. J. Cancer* **2014**, *110*, 1698–1704.
- [88] M. O. Senge, J. C. Brandt, *Photochem. Photobiol.* **2011**, *87*, 1240–1296.
- [89] Q. Peng, J. Moan, L.-W. Ma, J. M. Nesland, *Cancer Res.* **1995**, *55*, 2620–2626.
- [90] H. J. Jones, D. I. Vernon, S. B. Brown, *Br. J. Cancer* **2003**, *89*, 398–404.
- [91] S. Mitra, T. H. Foster, *Photochem. Photobiol.* **2005**, *81*, 849–859.
- [92] European medicines Agency, https://www.ema.europa.eu/en/documents/product-information/foscan-epar-product-information_en.pdf, accessed February 2022.
- [93] P. Wyss, V. Schwarz, D. Dobler-Girdziunaite, R. Hornung, H. Walt, A. Degen, M. Fehr, *Int. J. Cancer* **2001**, *93*, 720–724.
- [94] S. G. Bown, A. Z. Rogowska, D. E. Whitelaw, W. R. Lees, L. B. Lovat, P. Ripley, L. Jones, P. Wyld, A. Gillams, A. W. R. Hatfield, *Gut* **2002**, *50*, 549–557.
- [95] A. Noweski, A. Roosen, S. Lebdai, E. Barret, M. Emberton, F. Benzaghrou, M. Apfelbeck, B. Gaillac, C. Gratzke, C. Stief, A. R. Azzouzi, *Eur. Urol. Focus* **2019**, *5*, 1022–1028.
- [96] A. M. Bugaj, *World J. Methodol.* **2016**, *6*, 65–76.
- [97] A. R. Azzouzi, E. Barret, J. Bennet, C. Moore, S. Taneja, G. Muir, A. Villers, J. Coleman, C. Allen, A. Scherz, M. Emberton, *World J. Urol.* **2015**, *33*, 945–953.
- [98] Q. Chen, Z. Huang, D. Luck, J. Beckers, P.-H. Brun, B. C. Wilson, A. Scherz, Y. Salomon, F. W. Hetzel, *Photochem. Photobiol.* **2002**, *76*, 438–445.
- [99] N. V. Koudinova, J. H. Pinthus, A. Brandis, O. Brenner, P. Bendel, J. Ramon, Z. Eshhar, A. Scherz, Y. Salomon, *Int. J. Cancer* **2003**, *104*, 782–789.

- [100] U.S. Food and Drug Administration, <https://sperlingprostatecenter.com/fda-vetoes-photodynamic-tookad-focal-therapy-for-prostate-cancer/>, assessed February 2022.
- [101] NIH, U.S. National Library of Medicine, *ClinicalTrials.Gov*, <https://Clinicaltrials.Gov/Ct2/Show/NCT03849365>, accessed February 2022.
- [102] J. Usuda, H. Kato, T. Okunaka, K. Furukawa, H. Tsutsui, K. Yamada, Y. Suga, H. Honda, Y. Nagatsuka, T. Ohira, M. Tsuboi, T. Hirano, *J. Thorac. Oncol.* **2006**, *1*, 489–493.
- [103] J. Usuda, S. Ichinose, T. Ishizumi, H. Hayashi, K. Ohtani, S. Maehara, S. Ono, N. Kajiwara, O. Uchida, H. Tsutsui, T. Ohira, H. Kato, N. Ikeda, *J. Thorac. Oncol.* **2010**, *5*, 62–68.
- [104] K. S. McMahon, T. J. Wieman, P. H. Moore, V. H. Finger, *Cancer Res.* **1994**, *54*, 5374–5379.
- [105] H. Kato, K. Furukawa, M. Sato, T. Okunaka, Y. Kusunoki, M. Kawahara, M. Fukuoka, T. Miyazawa, T. Yana, K. Matsui, T. Shiraishi, H. Horinouchi, *Lung Cancer* **2003**, *42*, 103–111.
- [106] Y. Muragaki, J. Akimoto, T. Maruyama, H. Iseki, S. Ikuta, M. Nitta, K. Maebayashi, T. Saito, Y. Okada, S. Kaneko, A. Matsumura, T. Kuroiwa, K. Karasawa, Y. Nakazato, T. Kayama, *J. Neurosurg.* **2013**, *119*, 845–852.
- [107] M. J. Winship, S.-S. Wang, J. C. Chen, L. Keltner, J. S. Christophersen, *J. Clin. Oncol.* **2005**, *23*, 3663–3663.
- [108] J. M. Dąbrowski, L. G. Arnaut, M. M. Pereira, C. J. P. Monteiro, K. Urbańska, S. Simões, G. Stochel, *ChemMedChem* **2010**, *5*, 1770–1780.
- [109] L. L. Santos, J. Oliveira, E. Monteiro, J. Santos, C. Sarmiento, *Case Rep. Oncol.* **2018**, *11*, 769–776.
- [110] L. B. Rocha, H. T. Soares, M. I. P. Mendes, A. Cabrita, F. A. Schaberle, L. G. Arnaut, *Photochem. Photobiol.* **2020**, *96*, 692–698.
- [111] NIH, U.S. National Library of Medicine, *ClinicalTrials.Gov*, <https://Clinicaltrials.Gov/Ct2/Show/NCT02070432>, assessed February 2022.
- [112] T. D. Mody, L. Fu, J. L. Sessler, in *Progress in Inorganic Chemistry* (Ed.: K.D. Karlin), John Wiley & Sons, Ltd, New York, **2001**, pp. 551–598.
- [113] K. Verigos, D. C. H. Stripp, R. Mick, T. C. Zhu, R. Whittington, D. Smith, A. Dimofte, J. Finlay, T. M. Busch, Z. A. Tochner, S. B. Malkowicz, E. Glatstein, S. M. Hahn, *J. Environ. Pathol. Toxicol. Oncol.* **2006**, *25*, 373–387.
- [114] M. Hayase, K. W. Woodburn, J. Perloth, R. A. Miller, W. Baumgardner, P. G. Yock, A. Yeung, *Cardiovasc. Res.* **2001**, *49*, 449–455.
- [115] K. W. Woodburn, C. J. Engelman, M. S. Blumenkranz, *RETINA* **2002**, *22*, 391–405.
- [116] S. W. Young, K. W. Woodburn, M. Wright, T. D. Mody, Q. Fan, J. L. Sessler, W. C. Dow, R. A. Miller, *Photochem. Photobiol.* **1996**, *63*, 892–897.
- [117] K. W. Woodburn, S. W. Young, Q. Fan, D. Kessel, R. A. Miller, *Proc. SPIE*, **1996**, pp. 62–71.
- [118] P. Carde, R. Timmerman, M. P. Mehta, C. D. Koprowski, J. Ford, R. B. Tishler, D. Miles, R. A. Miller, M. F. Renschler, *J. Clin. Oncol.* **2001**, *19*, 2074–2083.
- [119] M. P. Mehta, W. R. Shapiro, M. J. Glantz, R. A. Patchell, M. A. Weitzner, C. A. Meyers, C. J. Schultz, W. H. Roa, M. Leibenhaut, J. Ford, W. Curran,

- S. Phan, J. A. Smith, R. A. Miller, M. F. Renschler, *J. Clin. Oncol.* **2002**, *20*, 3445–3453.
- [120] R. B. Woodward, W. A. Ayer, J. M. Beaton, F. Bickelhaupt, R. Bonnett, P. Buchschacher, G. L. Closs, H. Dutler, J. Hannah, F. P. Hauck, S. Itô, A. Langemann, E. Le Goff, W. Leimgruber, W. Lwowski, J. Sauer, Z. Valenta, H. Volz, *J. Am. Chem. Soc.* **1960**, *82*, 3800–3802.
- [121] T. S. Mang, R. Allison, G. Hewson, W. Snider, R. Moskowitz, *Cancer J. Sci. Am.* **1998**, *4*, 378–384.
- [122] P. Sekher, G. M. Garbo, *J. Photochem. Photobiol. B: Biol.* **1993**, *20*, 117–125.
- [123] R. Baskaran, J. Lee, S.-G. Yang, *Biomater. Res.* **2018**, *22*, 25.
- [124] R. K. Pandey, D. A. Bellnier, K. M. Smith, T. J. Dougherty, *Photochem. Photobiol.* **1991**, *53*, 65–72.
- [125] NIH, U.S. National Library of Medicine, *ClinicalTrials.Gov*, <https://Clinicaltrials.gov/Ct2/Show/NCT03757754>, assessed February 2022.
- [126] D. A. Bellnier, W. R. Greco, H. Nava, G. M. Loewen, A. R. Oseroff, T. J. Dougherty, *Cancer Chemother. Pharmacol.* **2006**, *57*, 40–45.
- [127] P.-C. Lo, M. S. Rodríguez-Morgade, R. K. Pandey, D. K. P. Ng, T. Torres, F. Dumoulin, *Chem. Soc. Rev.* **2020**, *49*, 1041–1056.
- [128] X. Li, B.-D. Zheng, X.-H. Peng, S.-Z. Li, J.-W. Ying, Y. Zhao, J.-D. Huang, J. Yoon, *Coord. Chem. Rev.* **2019**, *379*, 147–160.
- [129] M. V. Soares, C. M. Lanzarini, D. S. Oliveira, P. R. S. Ramos-Júnior, E. P. Santos, E. Ricci-Júnior, *Lat. Am. J. Pharm.* **2010**, *8*.
- [130] U. Isele, P. Van Hoogevest, R. Hilfiker, H. Capraro, K. Schieweck, H. Leuenberger, *J. Pharm. Sci.* **1994**, *83*, 1608–1616.
- [131] V. V. Sokolov, V. I. Chissov, R. I. Yakubovskaya, E. I. Aristarkhova, E. V. Filonenko, T. A. Belous, G. N. Vorozhtsov, N. N. Zharkova, V. V. Smirnov, M. B. Zhitkova, *Proc. SPIE* **1996**, *2625*, 281–287.
- [132] C. M. Allen, W. M. Sharman, J. E. Van Lier, *J. Porphyrins Phthalocyanines* **2001**, *5*, 161–169.
- [133] E. D. Baron, C. L. Malbasa, D. Santo-Domingo, P. Fu, J. D. Miller, K. K. Hanneman, A. H. Hsia, N. L. Oleinick, V. C. Colussi, K. D. Cooper, *Lasers Surg. Med.* **2010**, *42*, 888–895.
- [134] J. D. Miller, E. D. Baron, H. Scull, A. Hsia, J. C. Berlin, T. McCormick, V. Colussi, M. E. Kenney, K. D. Cooper, N. L. Oleinick, *Toxicol. Appl. Pharmacol.* **2007**, *224*, 290–299.
- [135] NIH, U.S. National Library of Medicine, *ClinicalTrials.gov*, <https://clinicaltrials.gov/ct2/show/results/NCT01800838>, accessed February 2022.
- [136] NIH, U.S. National Library of Medicine, *ClinicalTrials.Gov*, <https://Clinicaltrials.Gov/Ct2/Show/NCT02448381>, accessed February 2022.
- [137] G. Shi, S. Monro, R. Hennigar, J. Colpitts, J. Fong, K. Kasimova, H. Yin, R. DeCoste, C. Spencer, L. Chamberlain, A. Mandel, L. Lilge, S. A. McFarland, *Coord. Chem. Rev.* **2015**, *282–283*, 127–138.
- [138] J. Fong, K. Kasimova, Y. Arenas, P. Kaspler, S. Lazic, A. Mandel, L. Lilge, *Photochem. Photobiol. Sci.* **2015**, *14*, 2014–2023.
- [139] P. Kaspler, S. Lazic, S. Forward, Y. Arenas, A. Mandel, L. Lilge, *Photochem. Photobiol. Sci.* **2016**, *15*, 481–495.

- [140] NIH, U.S. National Library of Medicine, *ClinicalTrials.Gov*, <https://Clinicaltrials.Gov/Ct2/Show/NCT03053635>, assessed February 2022.
- [141] NIH, U.S. National Library of Medicine, *ClinicalTrials.Gov*, <https://Clinicaltrials.Gov/Ct2/Show/NCT03945162>, assessed February 2022.
- [142] S. A. McFarland, A. Mandel, R. Dumoulin-White, G. Gasser, *Curr. Opin. Chem. Biol.* **2020**, *56*, 23–27.
- [143] S. Waxman, K. C. Anderson, *The Oncologist* **2001**, *6*, 3–10.
- [144] U. Ndagi, N. Mhlongo, M. E. Soliman, *Drug Des. Devel. Ther.* **2017**, *11*, 599–616.
- [145] N. C. Lloyd, H. W. Morgan, B. K. Nicholson, R. S. Ronimus, *Angew. Chem. Int. Ed.* **2005**, *44*, 941–944.
- [146] B. Rosenberg, L. Van Camp, T. Krigas, *Nature* **1965**, *205*, 698–699.
- [147] R. K. Mehmood, *Oncol. Rev.* **2014**, *8*, 256.
- [148] M. M. Gottesman, *Annu. Rev. Med.* **2002**, *53*, 615–627.
- [149] K. A. Graeme, C. V. Pollack, *J. Emerg. Med.* **1998**, *16*, 45–56.
- [150] C. Brückner, V. Karunaratne, S. J. Rettig, D. Dolphin, *Can. J. Chem.* **1996**, *74*, 2182–2193.
- [151] S. G. Telfer, T. M. McLean, M. R. Waterland, *Dalton Trans.* **2011**, *40*, 3097–3108.
- [152] V. S. Thoi, J. R. Stork, D. Magde, S. M. Cohen, *Inorg. Chem.* **2006**, *45*, 10688–10697.
- [153] S. M. Cohen, S. R. Halper, *Inorg. Chim. Acta* **2002**, *341*, 12–16.
- [154] S. R. Halper, M. R. Malachowski, H. M. Delaney, S. M. Cohen, *Inorg. Chem.* **2004**, *43*, 1242–1249.
- [155] Q. Miao, J.-Y. Shin, B. O. Patrick, D. Dolphin, *Chem. Commun.* **2009**, *0*, 2541–2543.
- [156] I. V. Sazanovich, C. Kirmaier, E. Hindin, L. Yu, D. F. Bocian, J. S. Lindsey, D. Holten, *J. Am. Chem. Soc.* **2004**, *126*, 2664–2665.
- [157] L. Yu, K. Muthukumar, I. V. Sazanovich, C. Kirmaier, E. Hindin, J. R. Diers, P. D. Boyle, D. F. Bocian, D. Holten, J. S. Lindsey, *Inorg. Chem.* **2003**, *42*, 6629–6647.
- [158] H. L. Kee, C. Kirmaier, L. Yu, P. Thamyongkit, W. J. Youngblood, M. E. Calder, L. Ramos, B. C. Noll, D. F. Bocian, W. R. Scheidt, R. R. Birge, J. S. Lindsey, D. Holten, *J. Phys. Chem. B* **2005**, *109*, 20433–20443.
- [159] S. Kusaka, R. Sakamoto, H. Nishihara, *Inorg. Chem.* **2014**, *53*, 3275–3277.
- [160] R. Sakamoto, T. Iwashima, J. F. Kögel, S. Kusaka, M. Tsuchiya, Y. Kitagawa, H. Nishihara, *J. Am. Chem. Soc.* **2016**, *138*, 5666–5677.
- [161] R. Sakamoto, T. Iwashima, M. Tsuchiya, R. Toyoda, R. Matsuoka, J. F. Kögel, S. Kusaka, K. Hoshiko, T. Yagi, T. Nagayama, H. Nishihara, *J. Mater. Chem. A* **2015**, *3*, 15357–15371.
- [162] E. T. Clarke, P. J. Squattrito, P. R. Rudolf, R. Z. Motekaitis, A. E. Martell, A. Clearfield, *Inorg. Chim. Acta* **1989**, *166*, 221–231.
- [163] S. A. Baudron, *Dalton Trans.* **2013**, *42*, 7498–7509.
- [164] A. A.-S. Ali, J. Cipot-Wechsler, S. M. Crawford, O. Selim, R. L. Stoddard, T. S. Cameron, A. Thompson, *Can. J. Chem.* **2010**, *88*, 725–735.
- [165] W. Wan, M. S. Silva, C. D. McMillen, S. E. Creager, R. C. Smith, *J. Am. Chem. Soc.* **2019**, *141*, 8703–8707.

- [166] K. E. Thomas, N. Desbois, J. Conradie, S. J. Teat, C. P. Gros, A. Ghosh, *RSC Adv.* **2020**, *10*, 533–540.
- [167] R. Shikha Singh, R. Prasad Paitandi, R. Kumar Gupta, D. Shankar Pandey, *Coord. Chem. Rev.* **2020**, *414*, 213269.
- [168] K. Nakano, K. Kobayashi, K. Nozaki, *J. Am. Chem. Soc.* **2011**, *133*, 10720–10723.
- [169] A. Sumiyoshi, Y. Chiba, R. Matsuoka, T. Noda, Tatsuya. Nabeshima, *Dalton Trans.* **2019**, *48*, 13169–13175.
- [170] C. Ikeda, S. Ueda, Tatsuya. Nabeshima, *Chem. Commun.* **2009**, 2544–2546.
- [171] M. Yamamura, M. Albrecht, M. Albrecht, Y. Nishimura, T. Arai, T. Nabeshima, *Inorg. Chem.* **2014**, *53*, 1355–1360.
- [172] X.-D. Jiang, J. Zhao, D. Xi, H. Yu, J. Guan, S. Li, C.-L. Sun, L.-J. Xiao, *Chem. Eur. J.* **2015**, *21*, 6079–6082.
- [173] Y. Ge, D. F. O’Shea, *Chem. Soc. Rev.* **2016**, *45*, 3846–3864.
- [174] R. J. Motekaitis, A. E. Martell, *Inorg. Chem.* **1970**, *9*, 1832–1839.
- [175] Y. Murakami, Y. Matsuda, K. Sakata, K. Harada, *Bull. Chem. Soc. Jpn.* **1974**, *47*, 458–462.
- [176] Y. Matsuda, Y. Murakami, *Bull. Chem. Soc. Jpn.* **1977**, *50*, 2321–2324.
- [177] Y. Murakami, Y. Matsuda, K. Iiyama, *Chem. Lett.* **1972**, *1*, 1069–1072.
- [178] J. Locher, F. A. Watt, A. G. Neuba, R. Schoch, D. Munz, S. Hohloch, *Inorg. Chem.* **2020**, *59*, 9847–9856.
- [179] C. Trinh, K. Kirlikovali, S. Das, M. E. Ener, H. B. Gray, P. Djurovich, S. E. Bradforth, M. E. Thompson, *J. Phys. Chem. C* **2014**, *118*, 21834–21845.
- [180] N. Z. Alqahtani, T. G. Blevins, C. E. McCusker, *J. Phys. Chem. A* **2019**, *123*, 10011–10018.
- [181] S. Kusaka, R. Sakamoto, Y. Kitagawa, M. Okumura, H. Nishihara, *Chem. Asian J.* **2012**, *7*, 907–910.
- [182] Z. Mahmood, N. Rehmat, S. Ji, J. Zhao, S. Sun, M. Di Donato, M. Li, M. Teddei, Y. Huo, *Chem. Eur. J.* **2020**, *26*, 14912–14918.
- [183] S. Das, W. G. Thornbury, A. N. Bartynski, M. E. Thompson, S. E. Bradforth, *J. Phys. Chem. Lett.* **2018**, *9*, 3264–3270.
- [184] I. V. Khudyakov, Y. A. Serebrennikov, N. J. Turro, *Chem. Rev.* **1993**, *93*, 537–570.
- [185] Y. Dong, A. A. Sukhanov, J. Zhao, A. Elmali, X. Li, B. Dick, A. Karatay, V. K. Voronkova, *J. Phys. Chem. C* **2019**, *123*, 22793–22811.
- [186] Y. Hou, I. Kurganskii, A. Elmali, H. Zhang, Y. Gao, L. Lv, J. Zhao, A. Karatay, L. Luo, M. Fedin, *J. Chem. Phys.* **2020**, *152*, 114701.
- [187] D. J. Gibbons, A. Farawar, P. Mazzella, S. Leroy-Lhez, R. M. Williams, *Photochem. Photobiol. Sci.* **2020**, *19*, 136–158.
- [188] L. Carlacci, C. Doubleday, T. R. Furlani, H. F. King, J. W. McIver, *J. Am. Chem. Soc.* **1987**, *109*, 5323–5329.
- [189] J. Karges, U. Basu, O. Blacque, H. Chao, G. Gasser, *Angew. Chem. Int. Ed.* **2019**, *58*, 14334–14340.
- [190] J. Karges, O. Blacque, H. Chao, G. Gasser, *Inorg. Chem.* **2019**, *58*, 12422–12432.
- [191] J. Karges, O. Blacque, G. Gasser, *Inorg. Chim. Acta* **2020**, *505*, 119482.
- [192] K. J. Brunings, A. H. Corwin, *J. Am. Chem. Soc.* **1942**, *64*, 593–600.
- [193] H. S. Gill, I. Finger, I. Božidarević, F. Szydło, M. J. Scott, *New J. Chem.* **2005**, *29*, 68–71.

- [194] K. Servaty, E. Cauët, F. Thomas, J. Lambermont, P. Gerbaux, J. D. Winter, M. Ovaere, L. Volker, N. Vaeck, L. V. Meervelt, W. Dehaen, C. Moucheron, A. K.-D. Mesmaeker, *Dalton Trans.* **2013**, *42*, 14188–14199.
- [195] R. Toyoda, M. Tsuchiya, R. Sakamoto, R. Matsuoka, K.-H. Wu, Y. Hattori, H. Nishihara, *Dalton Trans.* **2015**, *44*, 15103–15106.
- [196] D. Mathew, Y. Hu, J. Zhao, C. Arunkumar, S. Sujatha, *Polyhedron* **2020**, *190*, 114794.
- [197] S. Riese, M. Holzapfel, A. Schmiedel, I. Gert, D. Schmidt, F. Würthner, C. Lambert, *Inorg. Chem.* **2018**, *57*, 12480–12488.
- [198] C. Bronner, S. A. Baudron, M. W. Hosseini, C. A. Strassert, A. Guenet, L. D. Cola, *Dalton Trans.* **2009**, *39*, 180–184.
- [199] F. C. March, D. A. Couch, K. Emerson, J. E. Fergusson, W. T. Robinson, *J. Chem. Soc., Inorg. Phys. Theor.* **1971**, 440–448.
- [200] J. D. Hall, T. M. McLean, S. J. Smalley, M. R. Waterland, S. G. Telfer, *Dalton Trans.* **2010**, *39*, 437–445.
- [201] A. N. Burchinov, V. M. Kiselev, A. A. Penni, V. V. Khistyayeva, *Opt. Spectrosc.* **2015**, *119*, 932–937.
- [202] R. M. Spada, M. Cepeda-Plaza, M. L. Gómez, G. Günther, P. Jaque, N. Pizarro, R. E. Palacios, A. Vega, *J. Phys. Chem. C* **2015**, *119*, 10148–10159.
- [203] F. Ragone, H. H. M. Saavedra, P. M. D. Gara, G. T. Ruiz, E. Wolcan, *J. Phys. Chem. A* **2013**, *117*, 4428–4435.
- [204] L. D. Ramos, H. M. da Cruz, K. P. M. Frin, *Photochem. Photobiol. Sci.* **2017**, *16*, 459–466.
- [205] A. A. Abdel-Shafi, J. L. Bourdelande, S. S. Ali, *Dalton Trans.* **2007**, *0*, 2510–2516.
- [206] S. C. Marker, S. N. MacMillan, W. R. Zipfel, Z. Li, P. C. Ford, J. J. Wilson, *Inorg. Chem.* **2018**, *57*, 1311–1331.
- [207] K. Wähler, A. Ludewig, P. Szabo, K. Harms, E. Meggers, *Eur. J. Inorg. Chem.* **2014**, *2014*, 807–811.
- [208] P. Collery, D. Desmaele, V. Vijaykumar, *Curr. Pharm. Des.* **2019**, *25*, 3306–3322.
- [209] H. Yin, M. Stephenson, J. Gibson, E. Sampson, G. Shi, T. Sainuddin, S. Monro, S. A. McFarland, *Inorg. Chem.* **2014**, *53*, 4548–4559.
- [210] T. M. McLean, J. L. Moody, M. R. Waterland, S. G. Telfer, *Inorg. Chem.* **2012**, *51*, 446–455.
- [211] N. Manav, P. E. Kesavan, M. Ishida, S. Mori, Y. Yasutake, S. Fukatsu, H. Furuta, I. Gupta, *Dalton Trans.* **2019**, *48*, 2467–2478.
- [212] Y. Zhang, M. R. Crawley, C. E. Hauke, A. E. Friedman, T. S. Janik, T. R. Cook, *Eur. J. Inorg. Chem.* **2017**, *2017*, 4055–4060.
- [213] D. Perl, S. W. Bisset, S. G. Telfer, *Dalton Trans.* **2016**, *45*, 2440–2443.
- [214] R. K. Gupta, R. Pandey, G. Sharma, R. Prasad, B. Koch, S. Srikrishna, P.-Z. Li, Q. Xu, D. S. Pandey, *Inorg. Chem.* **2013**, *52*, 3687–3698.
- [215] J. Karges, O. Blacque, P. Goldner, H. Chao, G. Gasser, *Eur. J. Inorg. Chem.* **2019**, *2019*, 3704–3712.
- [216] S. Swavey, K. Morford, M. Tsao, K. Comfort, M. K. Kilroy, *J. Inorg. Biochem.* **2017**, *175*, 101–109.
- [217] S. J. Smalley, M. R. Waterland, S. G. Telfer, *Inorg. Chem.* **2009**, *48*, 13–15.

- [218] R. Kumar Gupta, A. Kumar, R. Prasad Paitandi, R. Shikha Singh, S. Mukhopadhyay, S. Prakash Verma, P. Das, D. Shankar Pandey, *Dalton Trans.* **2016**, *45*, 7163–7177.
- [219] R. P. Paitandi, R. K. Gupta, R. S. Singh, G. Sharma, B. Koch, D. S. Pandey, *Eur. J. Med. Chem.* **2014**, *84*, 17–29.
- [220] R. P. Paitandi, R. S. Singh, S. Mukhopadhyay, G. Sharma, B. Koch, P. Vishnoi, D. S. Pandey, *Inorg. Chim. Acta* **2017**, *454*, 117–127.
- [221] B. F. Hohlfeld, K. J. Flanagan, N. Kulak, M. O. Senge, M. Christmann, A. Wiehe, *Eur. J. Org. Chem.* **2019**, *2019*, 4020–4033.
- [222] R. K. Gupta, G. Sharma, R. Pandey, A. Kumar, B. Koch, P.-Z. Li, Q. Xu, D. S. Pandey, *Inorg. Chem.* **2013**, *52*, 13984–13996.
- [223] C. Imberti, P. Zhang, H. Huang, P. J. Sadler, *Angew. Chem. Int. Ed.* **2020**, *59*, 61–73.
- [224] A. Zamora, G. Viguera, V. Rodríguez, M. D. Santana, J. Ruiz, *Coord. Chem. Rev.* **2018**, *360*, 34–76.
- [225] B. F. Hohlfeld, B. Gitter, C. J. Kingsbury, K. J. Flanagan, D. Steen, G. D. Wieland, N. Kulak, M. O. Senge, A. Wiehe, *Chem. Eur. J.* **2021**, *27*, 6440–6459.
- [226] K. Hanson, A. Tamayo, V. V. Diev, M. T. Whited, P. I. Djurovich, M. E. Thompson, *Inorg. Chem.* **2010**, *49*, 6077–6084.
- [227] J. Zhao, W. Wu, J. Sun, S. Guo, *Chem. Soc. Rev.* **2013**, *42*, 5323–5351.
- [228] C. S. Gutsche, S. Gräfe, B. Gitter, K. J. Flanagan, M. O. Senge, N. Kulak, A. Wiehe, *Dalton Trans.* **2018**, *47*, 12373–12384.
- [229] R. Matsuoka, T. Nabeshima, *Front. Chem.* **2018**, *6*.
- [230] S. R. Alves, I. R. Calori, A. C. Tedesco, *Mater. Sci. Eng. C* **2021**, *131*, 112514.
- [231] K. Plaetzer, B. Krammer, J. Berlanda, F. Berr, T. Kiesslich, *Lasers Med. Sci.* **2009**, *24*, 259–268.
- [232] M. Gouterman, *J. Mol. Spectrosc.* **1961**, *6*, 138–163.
- [233] M. Gouterman, G. H. Wagnière, L. C. Snyder, *J. Mol. Spectrosc.* **1963**, *11*, 108–127.
- [234] P. J. Spellane, M. Gouterman, A. Antipas, S. Kim, Y. C. Liu, *Inorg. Chem.* **1980**, *19*, 386–391.
- [235] M. O. Senge, A. A. Ryan, K. A. Letchford, S. A. MacGowan, T. Mielke, *Symmetry* **2014**, *6*, 781–843.
- [236] A. K. Mandal, M. Taniguchi, J. R. Diers, D. M. Niedzwiedzki, C. Kirmaier, J. S. Lindsey, D. F. Bocian, D. Holten, *J. Phys. Chem. A* **2016**, *120*, 9719–9731.
- [237] M. Taniguchi, J. S. Lindsey, *Photochem. Photobiol.* **2018**, *94*, 290–327.
- [238] M. Taniguchi, J. S. Lindsey, *Photochem. Photobiol.* **2021**, *97*, 136–165.
- [239] E. G. Azenha, A. C. Serra, M. Pineiro, M. M. Pereira, J. Seixas de Melo, L. G. Arnaut, S. J. Formosinho, A. M. d'A. Rocha Gonsalves, *Chem. Phys.* **2002**, *280*, 177–190.
- [240] N. J. Turro, V. Ramamurthy, V. Ramamurthy, J. C. Scaiano, in *Principles of Molecular Photochemistry: An Introduction*, University Science Books, **2009**.
- [241] A. K. Manna, B. D. Dunietz, *J. Chem. Phys.* **2014**, *141*, 121102.
- [242] M. A. Filatov, S. Karuthedath, P. M. Polestshuk, H. Savoie, K. J. Flanagan, C. Sy, E. Sitte, M. Telitchko, F. Laquai, R. W. Boyle, M. O. Senge, *J. Am. Chem. Soc.* **2017**, *139*, 6282–6285.

- [243] J. Zhao, K. Chen, Y. Hou, Y. Che, L. Liu, D. Jia, *Org. Biomol. Chem.* **2018**, *16*, 3692–3701.
- [244] J. M. Dąbrowski, B. Pucelik, A. Regiel-Futyra, M. Brindell, O. Mazuryk, A. Kyzioł, G. Stochel, W. Macyk, L. G. Arnaut, *Coord. Chem. Rev.* **2016**, *325*, 67–101.
- [245] R. Giovannetti, in *Macro Nano Spectroscopy* (Ed.: J. Uddin), InTech, Vol.1, Rijeka, Croatia, **2012**, pp. 87–108.
- [246] R. Bonnett, G. Martínez, *Tetrahedron* **2001**, *57*, 9513–9547.
- [247] P. F. C. Menezes, H. Imasato, J. Ferreira, V. S. Bagnato, C. H. Sibata, J. R. Perussi, *Laser Phys. Lett.* **2007**, *5*, 227.
- [248] G. Streckyte, R. Rotomskis, *J. Photochem. Photobiol. B: Biol.* **1993**, *18*, 259–263.
- [249] S. M. Andrade, R. Teixeira, S. M. B. Costa, A. J. F. N. Sobral, *Biophys. Chem.* **2008**, *133*, 1–10.
- [250] Y. N. Konan, R. Gurny, E. Allémann, *J. Photochem. Photobiol. B: Biol.* **2002**, *66*, 89–106.
- [251] W. T. Borden, R. Hoffmann, T. Stuyver, B. Chen, *J. Am. Chem. Soc.* **2017**, *139*, 9010–9018.
- [252] F. Wilkinson, D. J. McGarvey, A. F. Olea, *J. Phys. Chem.* **1994**, *98*, 3762–3769.
- [253] M. S. Baptista, J. Cadet, P. D. Mascio, A. A. Ghogare, A. Greer, M. R. Hamblin, C. Lorente, S. C. Nunez, M. S. Ribeiro, A. H. Thomas, M. Vignoni, T. M. Yoshimura, *Photochem. Photobiol.* **2017**, *93*, 912–919.
- [254] M. J. Paterson, O. Christiansen, F. Jensen, P. R. Ogilby, *Photochem. Photobiol.* **2006**, *82*, 1136–1160.
- [255] R. D. Scurlock, B. Wang, P. R. Ogilby, *J. Am. Chem. Soc.* **1996**, *118*, 388–392.
- [256] A. Blázquez-Castro, M. Westberg, M. Bregnhøj, T. Breitenbach, D. J. Mogensen, M. Etzerodt, P. R. Ogilby, in *Oxidative Stress* (Ed.: H. Sies), Academic Press, London, **2020**, pp. 363–388.
- [257] M. R. Hamblin, H. Abrahamse, *Antibiotics* **2020**, *9*, 53.
- [258] P. R. Ogilby, *Chem. Soc. Rev.* **2010**, *39*, 3181.
- [259] C. Schweitzer, R. Schmidt, *Chem. Rev.* **2003**, *103*, 1685–1758.
- [260] H. Wu, Q. Song, G. Ran, X. Lu, B. Xu, *TrAC Trends Anal. Chem.* **2011**, *30*, 133–141.
- [261] A. Gomes, E. Fernandes, J. L. F. C. Lima, *J. Biochem. Biophys. Methods* **2005**, *65*, 45–80.
- [262] E. Koh, R. Fluhr, *Plant Signal. Behav.* **2016**, *11*, e1192742.
- [263] P. R. Ogilby, *Photochem. Photobiol. Sci.* **2010**, *9*, 1543–1560.
- [264] M. Bregnhøj, M. Westberg, F. Jensen, P. R. Ogilby, *Phys. Chem. Chem. Phys.* **2016**, *18*, 22946–22961.
- [265] S. Hatz, J. D. C. Lambert, P. R. Ogilby, *Photochem. Photobiol. Sci.* **2007**, *6*, 1106–1116.
- [266] J. Moan, *J. Photochem. Photobiol. B: Biol.* **1990**, *6*, 343–344.
- [267] M. Niedre, M. S. Patterson, B. C. Wilson, *Photochem. Photobiol.* **2002**, *75*, 382–391.
- [268] S. Hatz, L. Poulsen, P. R. Ogilby, *Photochem. Photobiol.* **2008**, *84*, 1284–1290.
- [269] J. M. Dąbrowski, L. G. Arnaut, *Photochem. Photobiol. Sci.* **2015**, *14*, 1765–1780.

- [270] S. Callaghan, M. O. Senge, *Photochem. Photobiol. Sci.* **2018**, *17*, 1490–1514.
- [271] T. Keszthelyi, D. Weldon, T. N. Andersen, T. D. Poulsen, K. V. Mikkelsen, P. R. Ogilby, *Photochem. Photobiol.* **1999**, *70*, 531–539.
- [272] L. Brancaleon, H. Moseley, *Lasers Med. Sci.* **2002**, *17*, 173–186.
- [273] S. Pervaiz, M. Olivo, *Clin. Exp. Pharmacol. Physiol.* **2006**, *33*, 551–556.
- [274] B. C. Wilson, M. S. Patterson, *Phys. Med. Biol.* **2008**, *53*, R61–R109.
- [275] T. C. Zhu, J. C. Finlay, *Med. Phys.* **2008**, *35*, 3127–3136.
- [276] M. Yang, T. Yang, C. Mao, *Angew. Chem. Int. Ed Engl.* **2019**, *58*, 14066–14080.
- [277] K. Okawa and Y. Kobuke, *Anticancer Agents Med. Chem.* **2008**, *8*, 269–279.
- [278] Z. Sun, L.-P. Zhang, F. Wu, Y. Zhao, *Adv. Funct. Mater.* **2017**, *27*, 1704079.
- [279] E. M. Kercher, K. Zhang, M. Waguespack, R. T. Lang, A. Olmos, B. Q. Spring, *J. Biomed. Opt.* **2020**, *25*, 063811.
- [280] S. K. Attili, A. Lesar, A. McNeill, M. Camacho-Lopez, H. Moseley, S. Ibbotson, I. D. W. Samuel, J. Ferguson, *Br. J. Dermatol.* **2009**, *161*, 170–173.
- [281] A.-R. Azzouzi, S. Lebdai, F. Benzaghrou, C. Stief, *World J. Urol.* **2015**, *33*, 937–944.
- [282] N. Betrouni, S. Boukris, F. Benzaghrou, *Lasers Med. Sci.* **2017**, *32*, 1301–1307.
- [283] J. F. Borzelleca, *Toxicol. Sci.* **2000**, *53*, 2–4.
- [284] W. A. Velema, W. Szymanski, B. L. Feringa, *J. Am. Chem. Soc.* **2014**, *136*, 2178–2191.
- [285] M. R. Hamblin, E. Luke Newman, *J. Photochem. Photobiol. B: Biol.* **1994**, *23*, 3–8.
- [286] J. C. Mazière, P. Morlière, R. Santus, *J. Photochem. Photobiol. B: Biol.* **1991**, *8*, 351–360.
- [287] R. W. Boyle, D. Dolphin, *Photochem. Photobiol.* **1996**, *64*, 469–485.
- [288] P. M. Gullino, F. H. Grantham, S. H. Smith, A. C. Haggerty, *JNCI J. Natl. Cancer Inst.* **1965**, *34*, 857–869.
- [289] S. Zhang, H. Gao, G. Bao, *ACS Nano* **2015**, *9*, 8655–8671.
- [290] T. Brody, in *Nutritional Biochemistry Second Edition* (Ed.: T. Brody), Academic Press, San Diego, **1999**, pp. 693–878.
- [291] D. Kessel, *Cancer Lett.* **1988**, *39*, 193–198.
- [292] J. Morgan, A. R. Oseroff, *Adv. Drug Deliv. Rev.* **2001**, *49*, 71–86.
- [293] L. Rogers, M. O. Senge, *Future Med. Chem.* **2014**, *6*, 775–792.
- [294] L. Wyld, M. W. R. Reed, N. J. Brown, *Br. J. Cancer* **2001**, *84*, 1384–1386.
- [295] R. D. Almeida, B. J. Manadas, A. P. Carvalho, C. B. Duarte, *Biochim. Biophys. Acta* **2004**, *1704*, 59–86.
- [296] A. P. Castano, P. Mroz, M. R. Hamblin, *Nat. Rev. Cancer* **2006**, *6*, 535–545.
- [297] D. Kessel, *Photochem. Photobiol.* **2019**, *95*, 119–125.
- [298] T. Kiesslich, N. Tortik, M. Pichler, D. Neureiter, K. Plaetzer, *J. Porphyrins Phthalocyanines* **2013**, *17*, 197–209.
- [299] D. Kessel, M. G. H. Vicente, J. J. Reiners, *Lasers Surg. Med.* **2006**, *38*, 482–488.
- [300] M. O. Senge, M. W. Radomski, *Photodiagn. Photodyn. Ther.* **2013**, *10*, 1–16.

- [301] P. Agostinis, E. Buytaert, H. Breyskens, N. Hendrickx, *Photochem. Photobiol. Sci.* **2004**, *3*, 721–729.
- [302] Q. Peng, G. W. Farrants, K. Madslie, J. C. Bommer, J. Moan, H. E. Danielsen, J. M. Nesland, *Int. J. Cancer* **1991**, *49*, 290–295.
- [303] M. Korbelik, *J. Photochem. Photobiol. B: Biol.* **1992**, *12*, 107–109.
- [304] G. Jori, E. Reddi, *Int. J. Biochem.* **1993**, *25*, 1369–1375.
- [305] J. J. Reiners Jr, J. A. Caruso, P. Mathieu, B. Chelladurai, X.-M. Yin, D. Kessel, *Cell Death Differ.* **2002**, *9*, 934–944.
- [306] K. W. Woodburn, Q. Fan, D. R. Miles, D. Kessel, Y. Luo, S. W. Young, *Photochem. Photobiol.* **1997**, *65*, 410–415.
- [307] A. P. Castano, T. N. Demidova, M. R. Hamblin, *Photodiagn. Photodyn. Ther.* **2005**, *2*, 91–106.
- [308] T. Gheewala, T. Skwor, G. Munirathinam, *Oncotarget* **2017**, *8*, 30524–30538.
- [309] S.-I. Moriwaki, J. Misawa, Y. Yoshinari, I. Yamada, M. Takigawa, Y. Tokura, *Photodermatol. Photoimmunol. Photomed.* **2001**, *17*, 241–243.
- [310] D. A. Bellnier, T. J. Dougherty, *J. Clin. Laser Med. Surg.* **1996**, *14*, 311–314.
- [311] K. Berg, K. Madslie, J. C. Bommer, R. Oftebro, J. W. Winkelman, J. Moan, *Photochem. Photobiol.* **1991**, *53*, 203–210.
- [312] D. Kessel, *Photochem. Photobiol. Sci.* **2002**, *1*, 837–840.
- [313] X.-F. Zhang, *J. Photochem. Photobiol. Chem.* **2018**, *355*, 431–443.
- [314] L. B. Josefsen, R. W. Boyle, *Met.-Based Drugs* **2008**, *2008*, 1–23.
- [315] B. Ventura, L. Flamigni, G. Marconi, F. Lodato, D. L. Officer, *New J. Chem.* **2008**, *32*, 166–178.
- [316] Y. Ni, J. Wu, *Org. Biomol. Chem.* **2014**, *12*, 3774–3791.
- [317] R. Tabone, D. Feser, E. D. Lemma, U. Schepers, C. Bizzarri, *Front. Chem.* **2021**, *9*.
- [318] J. Moan, S. Sommer, *Cancer Lett.* **1983**, *21*, 167–174.
- [319] A. Wiehe, E. J. Simonenko, M. O. Senge, B. RÖder, *J. Porphyrins Phthalocyanines* **2001**, *5*, 758–761.
- [320] C.-T. Poon, P.-S. Chan, C. Man, F.-L. Jiang, R. N. S. Wong, N.-K. Mak, D. W. J. Kwong, S.-W. Tsao, W.-K. Wong, *J. Inorg. Biochem.* **2010**, *104*, 62–70.
- [321] Michael Luciano, Christian Brückner, *Molecules* **2017**, *22*, 980.
- [322] N. Mehraban, H. S. Freeman, *Materials* **2015**, *8*, 4421–4456.
- [323] C. Moylan, E. M. Scanlan, M. O. Senge, *Curr. Med. Chem.* **2015**, *22*, 2238–2348.
- [324] G. F. Gensini, A. A. Conti, D. Lippi, *J. Infect.* **2007**, *54*, 221–224.
- [325] F. Himmelweit, in *Collected papers of Paul Ehrlich*, Pergamon, London, **1960**, p. 555.
- [326] J. D. Kingsley, H. Dou, J. Morehead, B. Rabinow, H. E. Gendelman, C. J. Destache, *J. Neuroimmune Pharmacol.* **2006**, *1*, 340–350.
- [327] B. Flühmann, I. Ntai, G. Borchard, S. Simoens, S. Mühlebach, *Eur. J. Pharm. Sci.* **2019**, *128*, 73–80.
- [328] M. F. Attia, N. Anton, J. Wallyn, Z. Omran, T. F. Vandamme, *J. Pharm. Pharmacol.* **2019**, *71*, 1185–1198.
- [329] V. P. Torchilin, *AAPS J.* **2007**, *9*, E128–E147.
- [330] P. Gierlich, A. I. Mata, C. Donohoe, R. M. M. Brito, M. O. Senge, L. C. Gomes-da-Silva, *Molecules* **2020**, *25*, 5317.

- [331] C. Moylan, A. M. K. Sweed, Y. M. Shaker, E. M. Scanlan, M. O. Senge, *Tetrahedron* **2015**, *71*, 4145–4153.
- [332] M. Sibrian-Vazquez, T. J. Jensen, M. G. H. Vicente, *Bioconjug. Chem.* **2007**, *18*, 1185–1193.
- [333] C. Staneloudi, K. A. Smith, R. Hudson, N. Malatesti, H. Savoie, R. W. Boyle, J. Greenman, *Immunology* **2007**, *120*, 512–517.
- [334] L. Zhang, F. X. Gu, J. M. Chan, A. Z. Wang, R. S. Langer, O. C. Farokhzad, *Clin. Pharmacol. Ther.* **2008**, *83*, 761–769.
- [335] E. Paszko, C. Ehrhardt, M. O. Senge, D. P. Kelleher, J. V. Reynolds, *Photodiagn. Photodyn. Ther.* **2011**, *8*, 14–29.
- [336] J. E. Roberts, *Photochem. Photobiol.* **2020**, *96*, 524–528.
- [337] Y. Alapan, U. Bozuyuk, P. Erkoc, A. C. Karacakol, M. Sitti, *Sci. Robot.* **2020**, *5*, eaba5726.
- [338] A. J. Marko, N. J. Patel, P. Joshi, J. R. Missert, R. K. Pandey, in *Handbook of Photodynamic Therapy* (Eds.: R. K. Pandey, D. Kessel, T. J. Dougherty), World Scientific, Singapore, **2016**, pp. 3–43.
- [339] A. G. Maher, G. Passard, D. K. Dogutan, R. L. Halbach, B. L. Anderson, C. J. Gagliardi, M. Taniguchi, J. S. Lindsey, D. G. Nocera, *ACS Catal.* **2017**, *7*, 3597–3606.
- [340] W. W. L. Chin, P. W. S. Heng, P. S. P. Thong, R. Bhuvanewari, W. Hirt, S. Kuenzel, K. C. Soo, M. Olivo, *Eur. J. Pharm. Biopharm.* **2008**, *69*, 1083–1093.
- [341] J. R. Stromberg, A. Marton, H. L. Kee, C. Kirmaier, J. R. Diers, C. Muthiah, M. Taniguchi, J. S. Lindsey, D. F. Bocian, G. J. Meyer, D. Holten, *J. Phys. Chem. C* **2007**, *111*, 15464–15478.
- [342] A. Srivatsan, Y. Wang, P. Joshi, M. Sajjad, Y. Chen, C. Liu, K. Thankppan, J. R. Missert, E. Tracy, J. Morgan, N. Rigual, H. Baumann, R. K. Pandey, *J. Med. Chem.* **2011**, *54*, 6859–6873.
- [343] A. Pelter, J. A. Ballantine, V. Ferrito, V. Jaccarini, A. F. Psaila, P. J. Schembri, *J. Chem. Soc., Chem. Commun.* **1976**, 999.
- [344] L. Agius, J. A. Ballantine, V. Ferrito, V. Jaccarini, P. Murray-Rust, A. Pelter, A. F. Psaila, P. J. Schembri, *Pure Appl. Chem.* **1979**, *51*, 1847–1864.
- [345] M. Imfeld, D. Arigoni, R. Deeg, G. Müller, in *Vitamine B12* (Eds.: B. Zagalak, W. Friedrich), Zurich, Switzerland, De Gruyter, **2019**, pp. 315–316.
- [346] K. E. Borbas, in *Handbook of Porphyrin Science* (Eds.: K. M. Kadish, K. M. Smith, R. Guilard), World Scientific Publishing Company, Vol. 36, Singapore, **2016**, pp. 1–149.
- [347] J. S. Lindsey, *Chem. Rev.* **2015**, *115*, 6534–6620.
- [348] M. Taniguchi, J. S. Lindsey, *Chem. Rev.* **2017**, *117*, 344–535.
- [349] C.-H. Lee, J. S. Lindsey, *Tetrahedron* **1994**, *50*, 11427–11440.
- [350] B. J. Littler, M. A. Miller, C.-H. Hung, R. W. Wagner, D. F. O’Shea, P. D. Boyle, J. S. Lindsey, *J. Org. Chem.* **1999**, *64*, 1391–1396.
- [351] J. K. Laha, S. Dhanalekshmi, M. Taniguchi, A. Ambroise, J. S. Lindsey, *Org. Process Res. Dev.* **2003**, *7*, 799–812.
- [352] M. Ptaszek, J. Bhaumik, H.-J. Kim, M. Taniguchi, J. S. Lindsey, *Org. Process Res. Dev.* **2005**, *9*, 651–659.
- [353] M. Taniguchi, D. Ra, G. Mo, T. Balasubramanian, J. S. Lindsey, *J. Org. Chem.* **2001**, *66*, 7342–7354.

- [354] J.-P. Strachan, D. F. O'Shea, T. Balasubramanian, J. S. Lindsey, *J. Org. Chem.* **2000**, *65*, 3160–3172.
- [355] O. Mass, M. Ptaszek, M. Taniguchi, J. R. Diers, H. L. Kee, D. F. Bocian, D. Holten, J. S. Lindsey, *J. Org. Chem.* **2009**, *74*, 5276–5289.
- [356] J. K. Laha, C. Muthiah, M. Taniguchi, B. E. McDowell, M. Ptaszek, J. S. Lindsey, *J. Org. Chem.* **2006**, *71*, 4092–4102.
- [357] M. Taniguchi, M. Ptaszek, B. E. McDowell, P. D. Boyle, J. S. Lindsey, *Tetrahedron* **2007**, *63*, 3850–3863.
- [358] H. L. Kee, C. Kirmaier, Q. Tang, J. R. Diers, C. Muthiah, M. Taniguchi, J. K. Laha, M. Ptaszek, J. S. Lindsey, D. F. Bocian, D. Holten, *Photochem. Photobiol.* **2007**, *83*, 1110–1124.
- [359] K. Aravindu, H.-J. Kim, M. Taniguchi, P. L. Dilbeck, J. R. Diers, D. F. Bocian, D. Holten, J. S. Lindsey, *Photochem. Photobiol. Sci.* **2013**, *12*, 2089–2109.
- [360] M. Liu, C.-Y. Chen, A. K. Mandal, V. Chandrashaker, R. B. Evans-Storms, J. B. Pitner, D. F. Bocian, D. Holten, J. S. Lindsey, *New J. Chem.* **2016**, *40*, 7721–7740.
- [361] M. K. Kuimova, G. Yahiolglu, P. R. Ogilby, *J. Am. Chem. Soc.* **2009**, *131*, 332–340.
- [362] S. K. Sharma, M. Krayner, F. F. Sperandio, L. Huang, Y.-Y. Huang, D. Holten, J. S. Lindsey, M. R. Hamblin, *J. Porphyrins Phthalocyanines* **2013**, *17*, 73–85.
- [363] Y.-Y. Huang, P. Mroz, T. Zhiyentayev, S. K. Sharma, T. Balasubramanian, C. Ruzié, M. Krayner, D. Fan, K. E. Borbas, E. Yang, H. L. Kee, C. Kirmaier, J. R. Diers, D. F. Bocian, D. Holten, J. S. Lindsey, M. R. Hamblin, *J. Med. Chem.* **2010**, *53*, 4018–4027.
- [364] M. Ptaszek, B. E. McDowell, J. S. Lindsey, *J. Org. Chem.* **2006**, *71*, 4328–4331.
- [365] M. Krayner, M. Ptaszek, H.-J. Kim, K. R. Meneely, D. Fan, K. Secor, J. S. Lindsey, *J. Org. Chem.* **2010**, *75*, 1016–1039.
- [366] M. Ptaszek, B. E. McDowell, M. Taniguchi, H.-J. Kim, J. S. Lindsey, *Tetrahedron* **2007**, *63*, 3826–3839.
- [367] A. I. Arkhypchuk, R. Xiong, K. E. Borbas, *J. Inorg. Biochem.* **2020**, *205*, 110979.
- [368] D. Marsh, L. Mink, *J. Chem. Educ.* **1996**, *73*, 1188.
- [369] M. Gouterman, in *The Porphyrins* (Ed.: D. Dolphin), Academic Press, New York, **1978**, *3*, pp. 1–165.
- [370] K. E. Borbas, V. Chandrashaker, C. Muthiah, H. L. Kee, D. Holten, J. S. Lindsey, *J. Org. Chem.* **2008**, *73*, 3145–3158.
- [371] J. R. Lakowicz, in *Principles of Fluorescence Spectroscopy* (Ed.: J.R. Lakowicz), Springer US, Boston, MA, **2006**, pp. 1–26.
- [372] Z. Melissari, H. C. Sample, B. Twamley, R. M. Williams, M. O. Senge, *ChemPhotoChem* **2020**, *4*, 601–611.
- [373] R. Liu, M. Liu, D. Hood, C.-Y. Chen, C. J. MacNevin, D. Holten, J. S. Lindsey, *Molecules* **2018**, *23*, 130.
- [374] A. K. Mandal, T. Sahin, M. Liu, J. S. Lindsey, D. F. Bocian, D. Holten, *New J. Chem.* **2016**, *40*, 9648–9656.
- [375] E. F. F. Silva, F. A. Schaberle, C. J. P. Monteiro, J. M. Dąbrowski, L. G. Arnaut, *Photochem. Photobiol. Sci.* **2013**, *12*, 1187.
- [376] N. Chaudhri, N. Grover, M. Sankar, *Inorg. Chem.* **2017**, *56*, 11532–11545.

- [377] A. Bautista-Sanchez, A. Kasselouri, M.-C. Desroches, J. Blais, P. Maillard, D. M. de Oliveira, A. C. Tedesco, P. Prognon, J. Delaire, *J. Photochem. Photobiol. B: Biol.* **2005**, *81*, 154–162.
- [378] J. Baffreau, S. Leroy-Lhez, N. Vãn Anh, R. M. Williams, P. Hudhomme, *Chem. Eur. J.* **2008**, *14*, 4974–4992.
- [379] F. Wilkinson, A. A. Abdel-Shafi, *J. Phys. Chem. A* **1997**, *101*, 5509–5516.
- [380] A. Beeby, A. E. Jones, *Photochem. Photobiol.* **2000**, *72*, 10–15.
- [381] E. Zenkevich, E. Sagun, V. Knyukshto, A. Shulga, A. Mironov, O. Efremova, R. Bonnett, S. P. Songca, M. Kassem, *J. Photochem. Photobiol. B: Biol.* **1996**, *33*, 171–180.
- [382] M. Montalti, A. Credi, L. Prodi, M. T. Gandolfi, in *Handbook of Photochemistry*, CRC/Taylor & Francis, Boca Raton, **2006**.
- [383] J. M. Dąbrowski, L. G. Arnaut, M. M. Pereira, K. Urbańska, S. Simões, G. Stochel, L. Cortes, *Free Radic. Biol. Med.* **2012**, *52*, 1188–1200.
- [384] N. Epelde-Elezcano, V. Martínez-Martínez, E. Peña-Cabrera, C. F. A. Gómez-Durán, I. L. Arbeloa, S. Lacombe, *RSC Adv.* **2016**, *6*, 41991–41998.
- [385] F. Wilkinson, W. P. Helman, A. B. Ross, *J. Phys. Chem. Ref. Data* **1995**, *24*, 663–677.
- [386] M. Wacker, K. Chen, A. Preuss, K. Possemeyer, B. Roeder, K. Langer, *Int. J. Pharm.* **2010**, *393*, 254–263.
- [387] C. Lee, W. Yang, R. G. Parr, *Phys. Rev. B* **1988**, *37*, 785–789.
- [388] A. D. Becke, *J. Chem. Phys.* **1993**, *98*, 5648–5652.
- [389] H. L. Kee, C. Kirmaier, Q. Tang, J. R. Diers, C. Muthiah, M. Taniguchi, J. K. Laha, M. Ptaszek, J. S. Lindsey, D. F. Bocian, D. Holten, *Photochem. Photobiol.* **2007**, *83*, 1125–1143.
- [390] H. Sung, J. Ferlay, R. L. Siegel, M. Laversanne, I. Soerjomataram, A. Jemal, F. Bray, *CA. Cancer J. Clin.* **2021**, *71*, 209–249.
- [391] J. O'Brien, I. Wilson, T. Orton, F. Pognan, *Eur. J. Biochem.* **2000**, *267*, 5421–5426.
- [392] E. M. Czekanska, in *Mammalian Cell Viability: Methods and Protocols* (Ed.: M.J. Stoddart), Humana Press, Totowa, NJ, **2011**, pp. 27–32.
- [393] F. A. Schaberle, *Photodiagn. Photodyn. Ther.* **2018**, *23*, 75–77.
- [394] K. Gharehbaghi, A. Kubin, M. Grusch, E. Gharehbaghi-Schnell, F. Wierrani, H. N. Jayaram, W. Grunberger, T. Szekeres, *Anticancer Res.* **2000**, *20*, 2647–2652.
- [395] S. Hiroto, Y. Miyake, H. Shinokubo, *Chem. Rev.* **2017**, *117*, 2910–3043.
- [396] R. E. Blankenship, D. M. Tiede, J. Barber, G. W. Brudvig, G. Fleming, M. Ghirardi, M. R. Gunner, W. Junge, D. M. Kramer, A. Melis, T. A. Moore, C. C. Moser, D. G. Nocera, A. J. Nozik, D. R. Ort, W. W. Parson, R. C. Prince, R. T. Sayre, *Science* **2011**, *332*, 805–809.
- [397] G. de la Torre, G. Bottari, M. Sekita, A. Hausmann, D. M. Guldi, T. Torres, *Chem. Soc. Rev.* **2013**, *42*, 8049–8105.
- [398] H. Kobayashi, M. Ogawa, R. Alford, P. L. Choyke, Y. Urano, *Chem. Rev.* **2010**, *110*, 2620–2640.
- [399] T. Tanaka, A. Osuka, *Chem. Soc. Rev.* **2015**, *44*, 943–969.
- [400] B. Pucelik, A. Sufek, J. M. Dąbrowski, *Coord. Chem. Rev.* **2020**, *416*, 213340.
- [401] A. Tsuda, A. Osuka, *Science* **2001**, *293*, 79–82.

- [402] O. S. Finikova, S. E. Aleshchenkov, R. P. Briñas, A. V. Cheprakov, P. J. Carroll, S. A. Vinogradov, *J. Org. Chem.* **2005**, *70*, 4617–4628.
- [403] S. M. LeCours, H.-W. Guan, S. G. DiMagno, C. H. Wang, M. J. Therien, *J. Am. Chem. Soc.* **1996**, *118*, 1497–1503.
- [404] T. V. Duncan, K. Susumu, L. E. Sinks, M. J. Therien, *J. Am. Chem. Soc.* **2006**, *128*, 9000–9001.
- [405] P. K. Goldberg, T. J. Pundsack, K. E. Splan, *J. Phys. Chem. A* **2011**, *115*, 10452–10460.
- [406] H. S. Cho, D. H. Jeong, M.-C. Yoon, Y. H. Kim, Y.-R. Kim, D. Kim, S. C. Jeoung, S. K. Kim, N. Aratani, H. Shinmori, A. Osuka, *J. Phys. Chem. A* **2001**, *105*, 4200–4210.
- [407] I. Tabushi, T. Sasaki, *Tetrahedron Lett.* **1982**, *23*, 1913–1916.
- [408] L. M. Mazur, T. Roland, S. Leroy-Lhez, V. Sol, M. Samoc, I. D. W. Samuel, K. Matczyszyn, *J. Phys. Chem. B* **2019**, *123*, 4271–4277.
- [409] K. S. Kim, J. M. Lim, A. Osuka, D. Kim, *J. Photochem. Photobiol. C Photochem. Rev.* **2008**, *9*, 13–28.
- [410] H. Jing, J. Rong, M. Taniguchi, J. S. Lindsey, *Coord. Chem. Rev.* **2022**, 214278.
- [411] R. Shediach, M. H. B. Gray, H. T. Uyeda, R. C. Johnson, J. T. Hupp, P. J. Angiolillo, M. J. Therien, *J. Am. Chem. Soc.* **2000**, *122*, 7017–7033.
- [412] H. S. Kang, N. N. Esemoto, J. R. Diers, D. M. Niedzwiedzki, J. A. Greco, J. Akhigbe, Z. Yu, C. Pancholi, G. Viswanathan Bhagavathy, J. K. Nguyen, C. Kirmaier, R. R. Birge, M. Ptaszek, D. Holten, D. F. Bocian, *J. Phys. Chem. A* **2016**, *120*, 379–395.
- [413] V. S.-Y. Lin, S. G. DiMagno, M. J. Therien, *Science* **1994**, *264*, 1105–1111.
- [414] R. Kumble, S. Palese, V. S.-Y. Lin, M. J. Therien, R. M. Hochstrasser, *J. Am. Chem. Soc.* **1998**, *120*, 11489–11498.
- [415] J. J. Piet, P. N. Taylor, H. L. Anderson, A. Osuka, J. M. Warman, *J. Am. Chem. Soc.* **2000**, *122*, 1749–1757.
- [416] J. J. Piet, J. M. Warman, H. L. Anderson, *Chem. Phys. Lett.* **1997**, *266*, 70–74.
- [417] P. N. Taylor, A. P. Wylie, J. Huuskonen, H. L. Anderson, *Angew. Chem. Int. Ed.* **1998**, *37*, 986–989.
- [418] H. L. Anderson, S. J. Martin, D. D. C. Bradley, *Angew. Chem. Int. Ed. Engl.* **1994**, *33*, 655–657.
- [419] H. L. Anderson, *Chem. Commun.* **1999**, 2323–2330.
- [420] D. P. Arnold, R. D. Hartnell, *Tetrahedron* **2001**, *57*, 1335–1345.
- [421] H. L. Kee, R. Nothdurft, C. Muthiah, J. R. Diers, D. Fan, M. Ptaszek, D. F. Bocian, J. S. Lindsey, J. P. Culver, D. Holten, *Photochem. Photobiol.* **2008**, *84*, 1061–1072.
- [422] M. A. F. Faustino, M. G. P. M. S. Neves, J. A. S. Cavaleiro, M. Neumann, H.-D. Brauer, G. Jori, *Photochem. Photobiol.* **2000**, *72*, 217–225.
- [423] L. Jaquinod, D. J. Nurco, C. J. Medforth, R. K. Pandey, T. P. Forsyth, M. M. Olmstead, K. M. Smith, *Angew. Chem. Int. Ed. Engl.* **1996**, *35*, 1013–1016.
- [424] C. Muthiah, D. Lahaye, M. Taniguchi, M. Ptaszek, J. S. Lindsey, *J. Org. Chem.* **2009**, *74*, 3237–3247.
- [425] Norio. Miyaura, Akira. Suzuki, *Chem. Rev.* **1995**, *95*, 2457–2483.
- [426] K. Sonogashira, *J. Organomet. Chem.* **2002**, *653*, 46–49.

- [427] M. Taniguchi, M. N. Kim, D. Ra, J. S. Lindsey, *J. Org. Chem.* **2005**, *70*, 275–285.
- [428] M. O. Senge, Y. M. Shaker, M. Pinteá, C. Ryppa, S. S. Hatscher, A. Ryan, Y. Sergeeva, *Eur. J. Org. Chem.* **2010**, *2010*, 237–258.
- [429] A. G. Hyslop, M. A. Kellett, P. M. Iovine, M. J. Therien, *J. Am. Chem. Soc.* **1998**, *120*, 12676–12677.
- [430] S. G. DiMagno, V. S. Y. Lin, M. J. Therien, *J. Org. Chem.* **1993**, *58*, 5983–5993.
- [431] M. Taniguchi, H.-J. Kim, D. Ra, J. K. Schwartz, C. Kirmaier, E. Hindin, J. R. Diers, S. Prathapan, D. F. Bocian, D. Holten, J. S. Lindsey, *J. Org. Chem.* **2002**, *67*, 7329–7342.
- [432] M. Natali, S. Campagna, F. Scandola, *Chem. Soc. Rev.* **2014**, *43*, 4005–4018.
- [433] J. S. High, L. G. C. Rego, E. Jakubikova, *J. Phys. Chem. A* **2016**, *120*, 8075–8084.
- [434] W. A. Maza, C. M. Vetromile, C. Kim, X. Xu, X. P. Zhang, R. W. Larsen, *J. Phys. Chem. A* **2013**, *117*, 11308–11315.
- [435] E. M. Finnigan, R. Rein, N. Solladié, K. Dahms, D. C. G. Götz, G. Bringmann, M. O. Senge, *Tetrahedron* **2011**, *67*, 1126–1134.
- [436] N. Zarrabi, B. J. Bayard, S. Seetharaman, N. Holzer, P. Karr, S. Ciuti, A. Barbon, M. D. Valentin, A. van der Est, F. D'Souza, P. K. Poddutoori, *Phys. Chem. Chem. Phys.* **2021**, *23*, 960–970.
- [437] V. S.-Y. Lin, M. J. Therien, *Chem. Eur. J.* **1995**, *1*, 645–651.
- [438] C. Muthiah, H. L. Kee, J. R. Diers, D. Fan, M. Ptaszek, D. F. Bocian, D. Holten, J. S. Lindsey, *Photochem. Photobiol.* **2008**, *84*, 786–801.
- [439] M. Taniguchi, D. Ra, C. Kirmaier, E. Hindin, J. K. Schwartz, J. R. Diers, R. S. Knox, D. F. Bocian, J. S. Lindsey, D. Holten, *J. Am. Chem. Soc.* **2003**, *125*, 13461–13470.
- [440] H. L. Kee, J. R. Diers, M. Ptaszek, C. Muthiah, D. Fan, J. S. Lindsey, D. F. Bocian, D. Holten, *Photochem. Photobiol.* **2009**, *85*, 909–920.
- [441] M. Taniguchi, J. S. Lindsey, D. F. Bocian, D. Holten, *J. Photochem. Photobiol. C Photochem. Rev.* **2021**, 100401.
- [442] N. C. M. Magdaong, M. Taniguchi, J. R. Diers, D. M. Niedzwiedzki, C. Kirmaier, J. S. Lindsey, D. F. Bocian, D. Holten, *J. Phys. Chem. A* **2020**, *124*, 7776–7794.
- [443] M. O. Senge, I. Bischoff, N. Y. Nelson, K. M. Smith, *J. Porphyrins Phthalocyanines* **2012**.
- [444] J. P. Maher, in *Chemistry of Elements Second Edition* (Eds.: N.N. Greenwood, A. Earnshaw), Butterworth-Heinemann, Oxford, **1997**, pp. 216–267.
- [445] A. W. Apblett, in *Encyclopedia of Inorganic and Bioinorganic Chemistry*, John Wiley & Sons, Ltd, **2012**.
- [446] K. Klotz*, W. Weistenhöfer*, F. Neff, A. Hartwig, C. van Thriel, H. Drexler, *Dtsch. Ärztebl. Int.* **2017**, *114*, 653–659.
- [447] I. O. Igbokwe, E. Igwenagu, N. A. Igbokwe, *Interdiscip. Toxicol.* **2019**, *12*, 45–70.
- [448] C. C. Willhite, N. A. Karyakina, R. A. Yokel, N. Yenugadhati, T. M. Wisniewski, I. M. F. Arnold, F. Momoli, D. Krewski, *Crit. Rev. Toxicol.* **2014**, *44 Suppl 4*, 1–80.
- [449] H. Fischer, M. Schubert, *Ber. Dtsch. Chem. Ges.* **1924**, *57*, 610–617.

- [450] A. Al-Sheikh Ali, J. Cipot-Wechsler, T. S. Cameron, A. Thompson, *J. Org. Chem.* **2009**, *74*, 2866–2869.
- [451] T. E. Wood, A. Thompson, *Chem. Rev.* **2007**, *107*, 1831–1861.
- [452] T. E. Wood, Md. I. Uddin, A. Thompson, in *Handbook of Porphyrin Science, With Applications to Chemistry, Physics, Materials Science, Engineering, Biology and Medicine* (Eds.: K. M. Kadish, K. M. Smith, R. Guilard), World Scientific Publishing Company, Vol. 8, USA, **2010**, pp. 235–291.
- [453] G. P. Arsenault, E. Bullock, S. F. MacDonald, *J. Am. Chem. Soc.* **1960**, *82*, 4384–4389.
- [454] S. Datta, D. A. Lightner, *Monatsh. Für Chem.* **2008**, *139*, 1113–1117.
- [455] H. Falk, *The Chemistry of Linear Oligopyrroles and Bile Pigments*, Springer Verlag, Wien, Austria, **1989**.
- [456] S. Goeb, R. Ziessel, *Tetrahedron Lett.* **2008**, *49*, 2569–2574.
- [457] P. A. Jacobi, J. Guo, *Tetrahedron Lett.* **1995**, *36*, 2717–2720.
- [458] T. D. Lash, S. Chen, *Tetrahedron* **2005**, *61*, 11577–11600.
- [459] N. Boens, B. Verbelen, W. Dehaen, *Eur. J. Org. Chem.* **2015**, *2015*, 6577–6595.
- [460] A. Loudet, K. Burgess, *Chem. Rev.* **2007**, *107*, 4891–4932.
- [461] J. R. Stork, V. S. Thoi, S. M. Cohen, *Inorg. Chem.* **2007**, *46*, 11213–11223.
- [462] W. Wan, M. S. Silva, C. D. McMillen, S. E. Creager, R. C. Smith, *J. Am. Chem. Soc.* **2019**, *141*, 8703–8707.
- [463] C. G. Gianopoulos, K. Kirschbaum, M. R. Mason, *Organometallics* **2014**, *33*, 4503–4511.
- [464] C. G. Gianopoulos, N. Kumar, Y. Zhao, L. Jia, K. Kirschbaum, M. R. Mason, *Dalton Trans.* **2016**, *45*, 13787–13797.
- [465] M. Saikawa, M. Daicho, T. Nakamura, J. Uchida, M. Yamamura, Tatsuya. Nabeshima, *Chem. Commun. Camb.* **2016**, *52*, 4014–4017.
- [466] Y. Murakami, K. Sakata, K. Harada, Y. Matsuda, *Bull. Chem. Soc. Jpn.* **1974**, *47*, 3021–3024.
- [467] I. Toguchi, H. Ishikawa, Y. Morioka, Atsushi. Oda, *Organic Electroluminescent Components* **2000**, U.S. Pat US 6,759,144 B2.
- [468] M. A. Filatov, S. Karuthedath, P. M. Polestshuk, S. Callaghan, K. J. Flanagan, T. Wiesner, F. Laquai, M. O. Senge, *ChemPhotoChem* **2018**, *2*, 606–615.
- [469] M. A. Filatov, S. Karuthedath, P. M. Polestshuk, S. Callaghan, K. J. Flanagan, M. Telitchko, T. Wiesner, F. Laquai, M. O. Senge, *Phys. Chem. Chem. Phys.* **2018**, *20*, 8016–8031.
- [470] Z. Melissari, R. M. Williams, M. O. Senge, in *Applications of Porphyrinoids as Functional Materials* (Eds.: H. Lang, T. Ruffer), Royal Society of Chemistry, Germany, **2021**, pp. 252–291.
- [471] R. W. Wagner, J. S. Lindsey, *Pure Appl. Chem.* **1996**, *68*, 1373–1380.
- [472] C. Brückner, Y. Zhang, S. J. Rettig, D. Dolphin, *Inorg. Chim. Acta* **1997**, *263*, 279–286.
- [473] V. S. Thoi, J. R. Stork, D. Magde, S. M. Cohen, *Inorg. Chem.* **2006**, *45*, 10688–10697.
- [474] A. Ryan, A. Gehrold, R. Perusitti, M. Pinteá, M. Fazekas, O. B. Locos, F. Blaikie, M. O. Senge, *Eur. J. Org. Chem.* **2011**, *2011*, 5817–5844.
- [475] S. G. Telfer, J. D. Wuest, *Chem. Commun.* **2007**, 3166–3168.
- [476] J. Chen, T. Fan, Z. Xie, Q. Zeng, P. Xue, T. Zheng, Y. Chen, X. Luo, H. Zhang, *Biomaterials* **2020**, *237*, 119827.

- [477] M. Kasha, H. R. Rawls, M. A. El-Bayoumi, *Pure Appl. Chem.* **1965**, *11*, 371–392.
- [478] B. Bosnich, *Acc. Chem. Res.* **1969**, *2*, 266–273.
- [479] D. Veldman, S. M. A. Chopin, S. C. J. Meskers, M. M. Groeneveld, R. M. Williams, R. A. J. Janssen, *J. Phys. Chem. A* **2008**, *112*, 5846–5857.
- [480] B. Ventura, G. Marconi, M. Bröring, R. Krüger, L. Flamigni, *New J. Chem.* **2009**, *33*, 428–438.
- [481] J. E. Fergusson, C. A. Ramsay, *J. Chem. Soc.* **1965**, 5222–5225.
- [482] E. Xochitiotzi-Flores, A. Jiménez-Sánchez, H. García-Ortega, N. Sánchez-Puig, M. Romero-Ávila, R. Santillan, N. Farfán, *New J. Chem.* **2016**, *40*, 4500–4512.
- [483] J. M. Sutton, E. Rogerson, C. J. Wilson, A. E. Sparke, S. J. Archibald, R. W. Boyle, *Chem. Commun.* **2004**, 1328–1329.
- [484] Z. Gao, Y. Hao, M. Zheng, Y. Chen, *RSC Adv.* **2017**, *7*, 7604–7609.
- [485] R. W. Redmond, J. N. Gamlin, *Photochem. Photobiol.* **1999**, *70*, 391–475.
- [486] M. C. DeRosa, R. J. Crutchley, *Coord. Chem. Rev.* **2002**, *233–234*, 351–371.
- [487] E. Boix-Garriga, B. Rodríguez-Amigo, O. Planas, S. Nonell, in *Singlet Oxygen: Applications in Biosciences and Nanosciences* (Eds.: S. Nonell, C. Flors), Royal Society of Chemistry, Vol. 1, Cambridge, UK, **2016**, pp. 23–46.
- [488] S. Paul, P. Kundu, P. Kondaiah, A. R. Chakravarty, *Inorg. Chem.* **2021**, *60*, 16178–16193.
- [489] A. M. Potocny, R. S. Riley, R. K. O’Sullivan, E. S. Day, J. Rosenthal, *Inorg. Chem.* **2018**, *57*, 10608–10615.
- [490] R. Lincoln, L. Kohler, S. Monro, H. Yin, M. Stephenson, R. Zong, A. Chouai, C. Dorsey, R. Hennigar, R. P. Thummel, S. A. McFarland, *J. Am. Chem. Soc.* **2013**, *135*, 17161–17175.
- [491] Y. Jenkins, A. E. Friedman, N. J. Turro, J. K. Barton, *Biochemistry* **1992**, *31*, 10809–10816.
- [492] B. M. Zeglis, V. C. Pierre, J. K. Barton, *Chem. Commun.* **2007**, 4565–4579.
- [493] M. R. Gill, J. A. Thomas, *Chem. Soc. Rev.* **2012**, *41*, 3179–3192.
- [494] C. Mari, V. Pierroz, R. Rubbiani, M. Patra, J. Hess, B. Spingler, L. Oehninger, J. Schur, I. Ott, L. Salassa, S. Ferrari, G. Gasser, *Chem. Eur. J.* **2014**, *20*, 14421–14436.
- [495] C. V. Kumar, J. K. Barton, N. J. Turro, *J. Am. Chem. Soc.* **1985**, *107*, 5518–5523.
- [496] J. K. Barton, A. Danishefsky, J. Goldberg, *J. Am. Chem. Soc.* **1984**, *106*, 2172–2176.
- [497] J. K. Barton, J. J. Dannenberg, A. L. Raphael, *J. Am. Chem. Soc.* **1982**, *104*, 4967–4969.
- [498] S. I. Pascu, P. A. Waghorn, T. Conry, B. Lin, C. James, J. M. Zayed, in *Advances in Inorganic Chemistry* (Eds.: R. van Eldik, C.D. Hubbard), Academic Press, Oxford, UK, **2009**, pp. 131–178.
- [499] V. Ciaffaglione, P. A. Waghorn, R. M. Exner, F. Cortezon-Tamarit, S. P. Godfrey, S. Sarpaki, H. Quilter, R. Dondi, H. Ge, G. Kociok-Kohn, S. W. Botchway, I. M. Eggleston, J. R. Dilworth, S. I. Pascu, *Bioconjug. Chem.* **2021**, *32*, 1374–1392.
- [500] *WaveMetrics, Inc, IgorPro, Version 7.0.8.1, 1988-2018, Lake Oswego, Oregon, USA.*

- [501] *OriginPro 8.5*, OriginLab Corporation, Northampton, MA, USA.
- [502] F. Menges, *Spectragryph-Optical Spectroscopy Software, Version 1.2.13*, 2016-2019, [Http://Www.Effemm2.de/Spectragryph/](http://www.Effemm2.de/Spectragryph/).
- [503] Bruker, *APEX3 V2017.3-0*, Bruker AXS Inc., Madison, Wisconsin, (USA), 2017.
- [504] G. M. Sheldrick, *Acta Crystallogr.* **2015**, *A71*, 3–8.
- [505] O. V. Dolomanov, L. J. Bourhis, R. J. Gildea, J. A. K. Howard, H. Puschmann, *J. Appl. Crystallogr.* **2009**, *42*, 339–341.
- [506] G. M. Sheldrick, *SADABS*, University of Göttingen, Göttingen (Germany), 2016.
- [507] L. Krause, R. Herbst-Irmer, G. M. Sheldrick, D. Stalke, *J. Appl. Crystallogr.* **2015**, *48*, 3–10.
- [508] G. M. Sheldrick, *Acta Crystallogr.* **2015**, *C71*, 3–8.
- [509] A. L. Spek, *Acta Crystallogr.* **2020**, *E76*, 1–11.
- [510] A. L. Spek, *Acta Crystallogr.* **2009**, *D65*, 148–155.
- [511] A. L. Spek, *Acta Crystallogr.* **2015**, *C71*, 9–18.
- [512] D. Magde, J. H. Brannon, T. L. Cremers, J. Olmsted, *J. Phys. Chem.* **1979**, *83*, 696–699.
- [513] A. M. Brouwer, *Pure Appl. Chem.* **2011**, *83*, 2213–2228.
- [514] P. G. Seybold, M. Gouterman, *J. Mol. Spectrosc.* **1969**, *31*, 1–13.
- [515] G. A. Crosby, J. N. Demas, *J. Phys. Chem.* **1971**, *75*, 991–1024.
- [516] F. Wilkinson, W. P. Helman, A. B. Ross, *J. Phys. Chem. Ref. Data* **1993**, *22*, 113–262.
- [517] P. Wang, F. Qin, Z. Zhang, W. Cao, *Opt. Express* **2015**, *23*, 22991.
- [518] Gaussian 16, Revision C.01, M. J. Frisch, G. W. Trucks, H. B. Schlegel, G. E. Scuseria, M. A. Robb, J. R. Cheeseman, G. Scalmani, V. Barone, G. A. Petersson, H. Nakatsuji, X. Li, M. Caricato, A. V. Marenich, J. Bloino, B. G. Janesko, R. Gomperts, B. Mennucci, H. P. Hratchian, J. V. Ortiz, A. F. Izmaylov, J. L. Sonnenberg, D. Williams-Young, F. Ding, F. Lipparini, F. Egidi, J. Goings, B. Peng, A. Petrone, T. Henderson, D. Ranasinghe, V. G. Zakrzewski, J. Gao, N. Rega, G. Zheng, W. Liang, M. Hada, M. Ehara, K. Toyota, R. Fukuda, J. Hasegawa, M. Ishida, T. Nakajima, Y. Honda, O. Kitao, H. Nakai, T. Vreven, K. Throssell, J. A. Montgomery, Jr., J. E. Peralta, F. Ogliaro, M. J. Bearpark, J. J. Heyd, E. N. Brothers, K. N. Kudin, V. N. Staroverov, T. A. Keith, R. Kobayashi, J. Normand, K. Raghavachari, A. P. Rendell, J. C. Burant, S. S. Iyengar, J. Tomasi, M. Cossi, J. M. Millam, M. Klene, C. Adamo, R. Cammi, J. W. Ochterski, R. L. Martin, K. Morokuma, O. Farkas, J. B. Foresman, and D. J. Fox, *Gaussian, Inc., Wallingford CT*, 2019.
- [519] M. D. Hanwell, D. E. Curtis, D. C. Lonie, T. Vandermeersch, E. Zurek, G. R. Hutchison, *J. Chem. Informatics*, 2012, *4*, Version 1.2.0.
- [520] A. R. Allouche, *J. Comput. Chem.* 2011, *32*, 174–182, Version 2.5.0.
- [521] A. A. Ryan, M. O. Senge, *Eur. J. Org. Chem.* **2013**, 2013, 3700–3711.
- [522] H. Sugimoto, M. Muto, T. Tanaka, A. Osuka, *Eur. J. Org. Chem.* **2011**, 71–77.
- [523] S. Sengupta, U. K. Pandey, *Org. Biomol. Chem.* **2018**, *16*, 2033–2038.

Appendix

Chapter 2

X-Ray crystal structure¹³

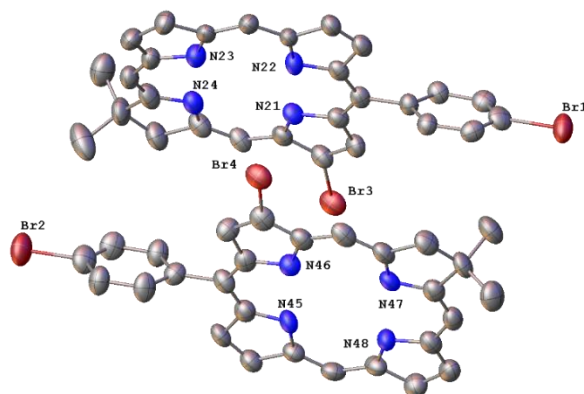


Figure A 1. View of the asymmetric unit of **FB1**, with heteroatoms labelled and displacement shown at 50% probability with hydrogen atoms invisible. Br3 and Br4 are only 3% occupied.

¹³ Crystal structures were determined by Dr. Brendan Twamley, TCD.

Absorption and fluorescence emission spectra

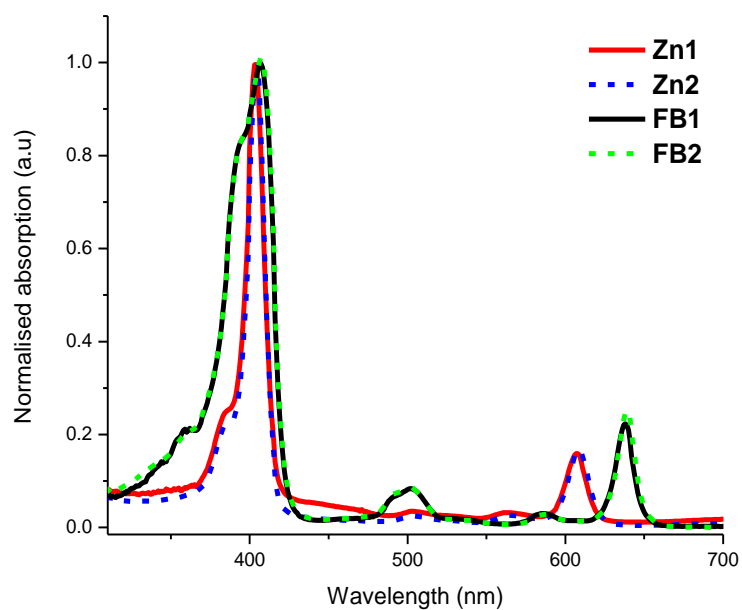


Figure A 2. Normalised UV-Visible absorption spectra of the chlorins in dichloromethane (**Zn1** red, **Zn2** dashed blue, **FB1** black, **FB2** dashed green).

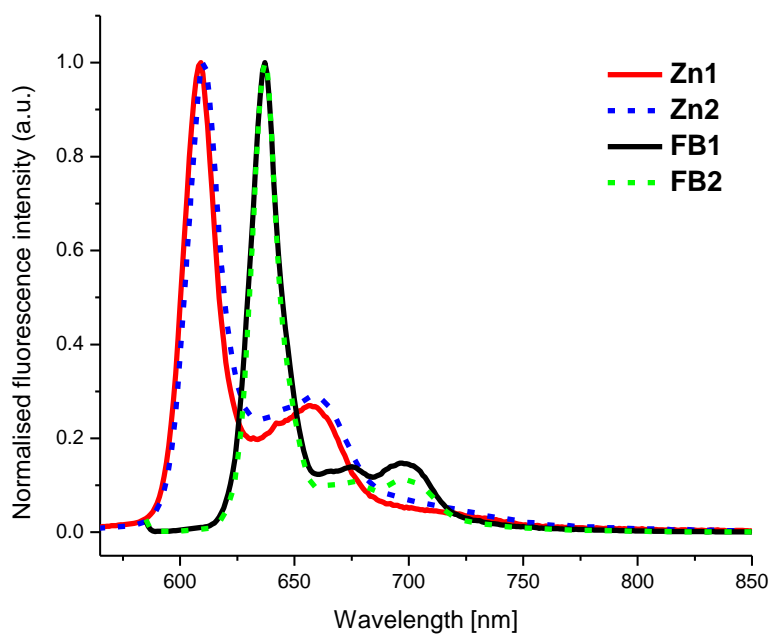


Figure A 3. Normalised fluorescence emission spectra of the chlorins in methanol (**Zn1** red, **Zn2** dashed blue, **FB1** black, **FB2** dashed green).

Fluorescence decays

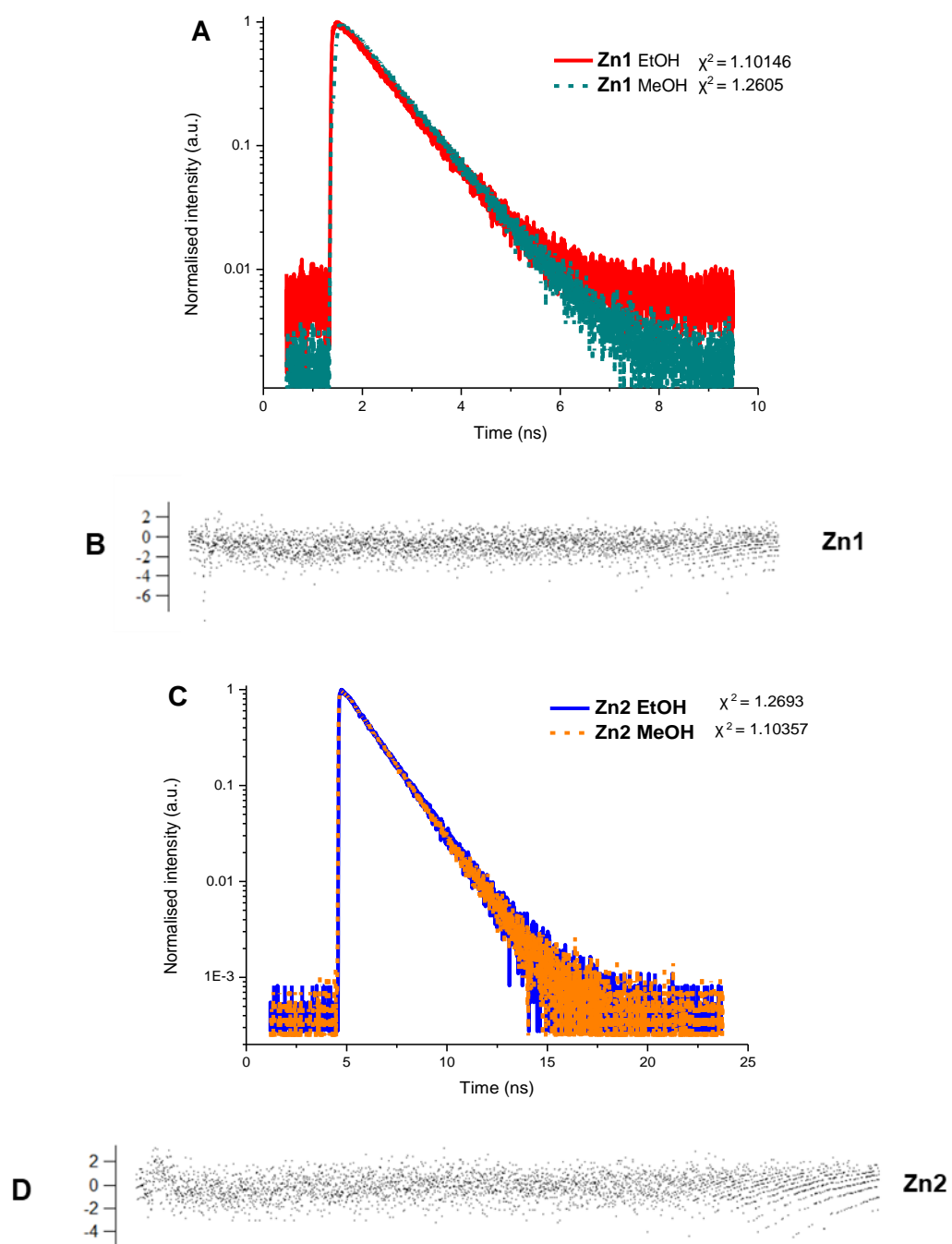


Figure A 4. Fluorescence lifetime decay profiles of **Zn1** (A) and **Zn2** (C) and representative residuals of **Zn1** in ethanol (B) and **Zn2** in methanol (D); red line: **Zn1** in ethanol; dark cyan dashed line: **Zn1** in methanol; blue line: **Zn2** in ethanol, orange dashed line: **Zn2** in methanol); $\lambda_{\text{exc}} = 400 \text{ nm}$; $\lambda_{\text{det}} = 610 \text{ nm}$.

Triplet-triplet transient absorption spectra (TA)

Transient absorption spectroscopy at **ambient** conditions (ethanol/methanol)

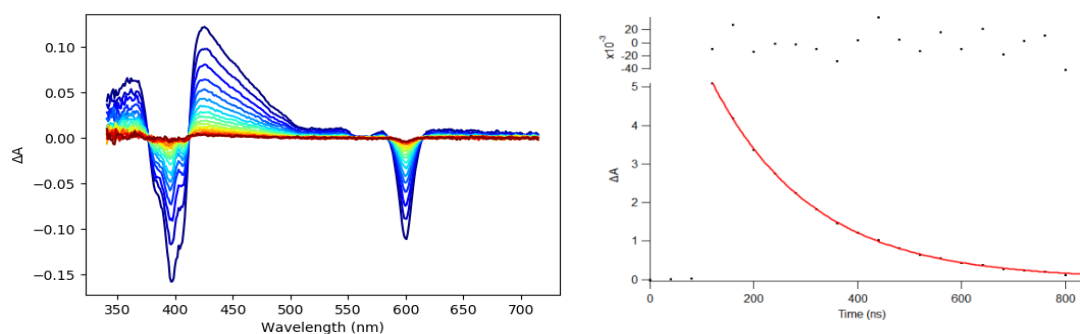


Figure A 5. TA spectra of **Zn1** (left) and time trace fitting with monoexponential decay function for the range from 426 to 545 nm (right) in MeOH at ambient conditions; $\lambda_{\text{exc}} = 604$ m; incremental time: 40 ns; $\tau_{\text{T}} = 190 \pm 5$ ns.

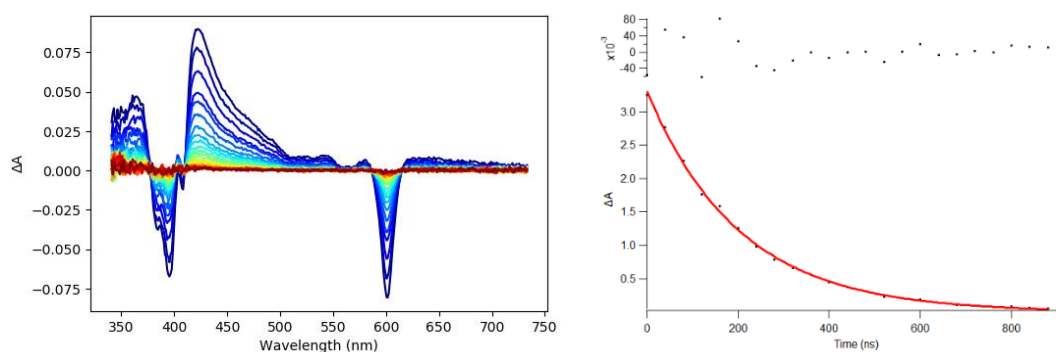


Figure A 6. TA spectra of **Zn2** (left) and time trace fitting with monoexponential decay function for the range from 421 to 520 nm (right) in MeOH at ambient conditions; $\lambda_{\text{exc}} = 604$ m; incremental time: 40 ns; $\tau_{\text{T}} = 210 \pm 11$ ns.

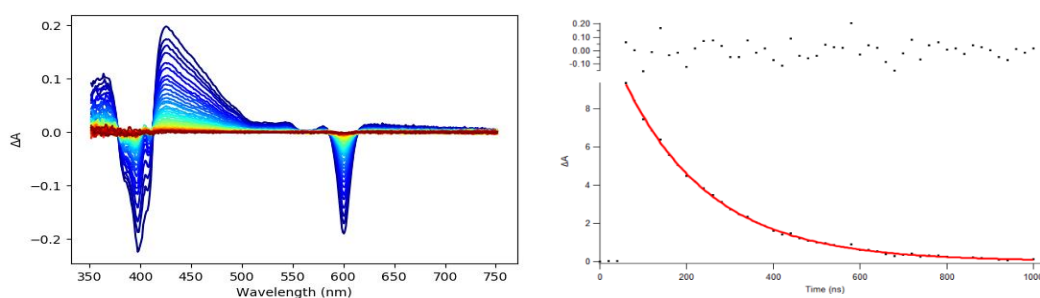


Figure A 7. TA spectra of **Zn1** (left) and time trace fitting with monoexponential decay function for the range from 425 to 519 nm (right) in EtOH at ambient conditions; $\lambda_{\text{exc}} = 604$ nm; incremental time: 20 ns; $\tau_{\text{T}} = 190$ ns \pm 10 ns.

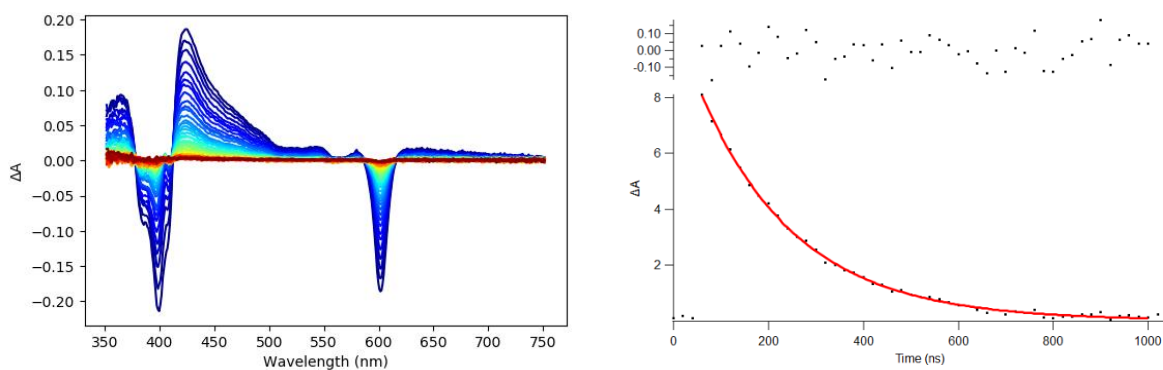


Figure A 8. TA spectra of **Zn2** (left) and time trace fitting with monoexponential decay function for the range from 423 to 527 nm (right) in EtOH at ambient conditions; $\lambda_{\text{exc}} = 604$ nm; incremental time: 20 ns; $\tau_{\text{T}} = 205 \text{ ns} \pm 11 \text{ ns}$.

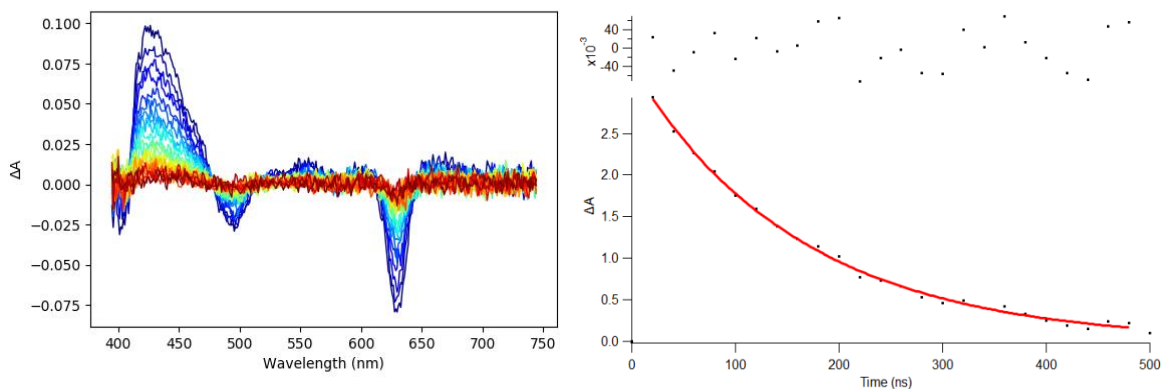


Figure A 9. TA spectra of **FB1** (left) and time trace fitting with monoexponential decay function for the range from 424 to 475 nm (right) in MeOH at ambient conditions; $\lambda_{\text{exc}} = 637$ nm; incremental time: 20 ns; $\tau_{\text{T}} = 160 \pm 11 \text{ ns}$.

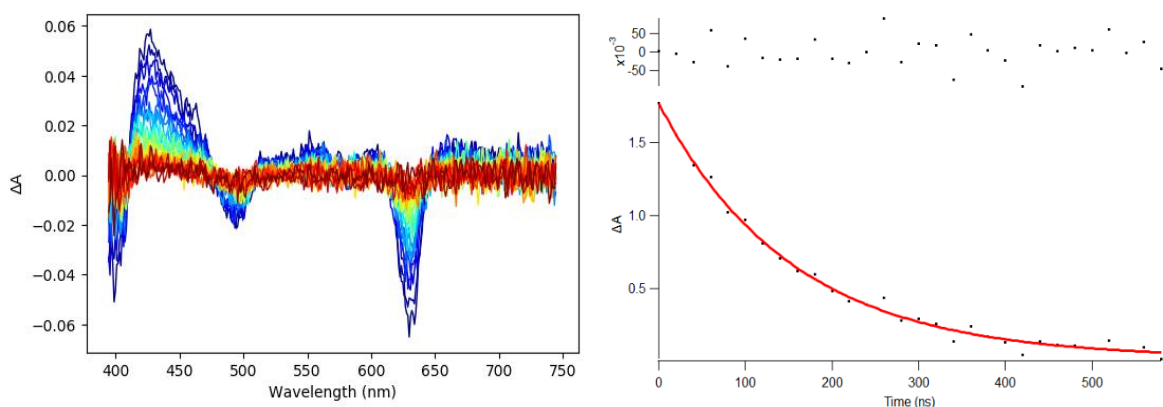


Figure A 10. TA spectra of **FB2** (right) and time trace fitting with monoexponential decay function for the range from 425 to 473 nm (right) in MeOH at ambient conditions; $\lambda_{\text{exc}} = 637$ nm; incremental time: 20 ns; $\tau_{\text{T}} = 150 \pm 10 \text{ ns}$.

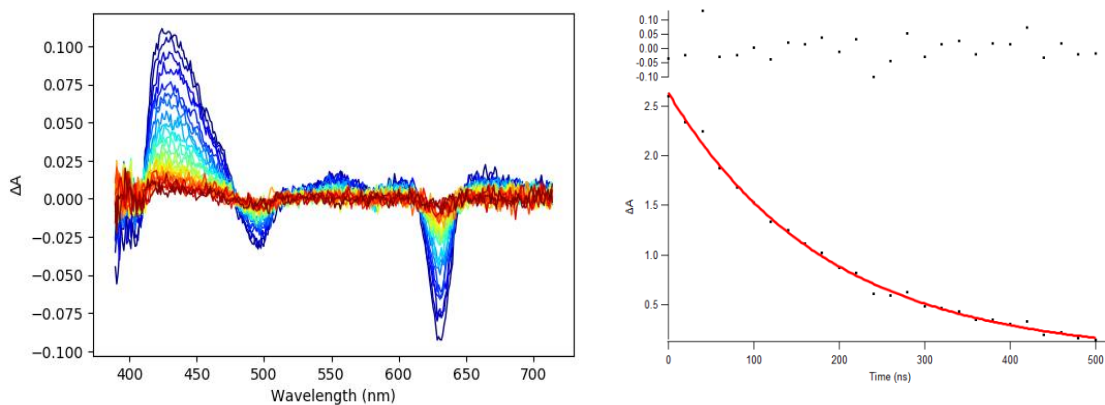


Figure A 11. TA spectra of **FB1** (left) and time trace fitting with monoexponential decay function for the range from 430 to 474 nm (right) in EtOH at ambient conditions;

$\lambda_{\text{exc}} = 635 \text{ nm}$; incremental time: 20 ns; $\tau_{\text{T}} = 170 \text{ ns} \pm 14 \text{ ns}$.

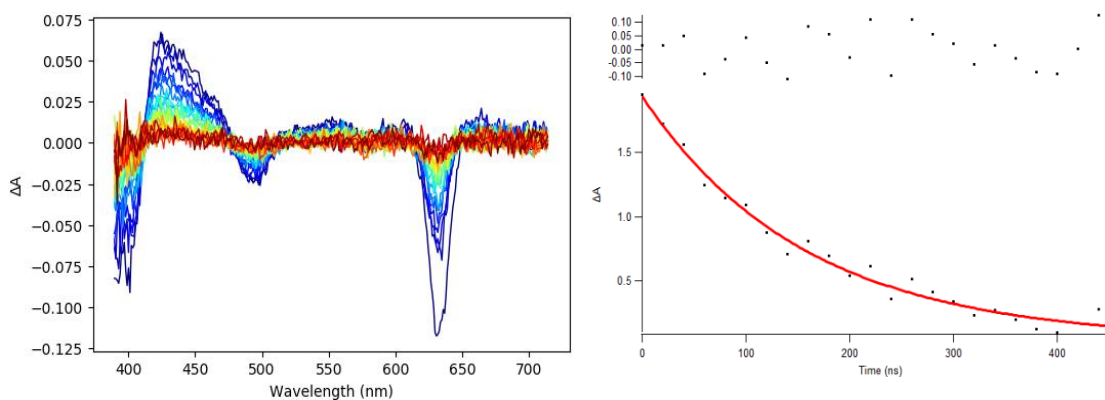


Figure A 12. TA spectra of **FB2** (left) and time trace fitting with monoexponential decay function for the range from 424 to 473 nm (right) in EtOH at ambient conditions;

$\lambda_{\text{exc}} = 635 \text{ nm}$; incremental time: 20 ns; $\tau_{\text{T}} = 160 \text{ ns} \pm 11 \text{ ns}$.

Transient absorption spectra in **oxygen free conditions** (ethanol/methanol)

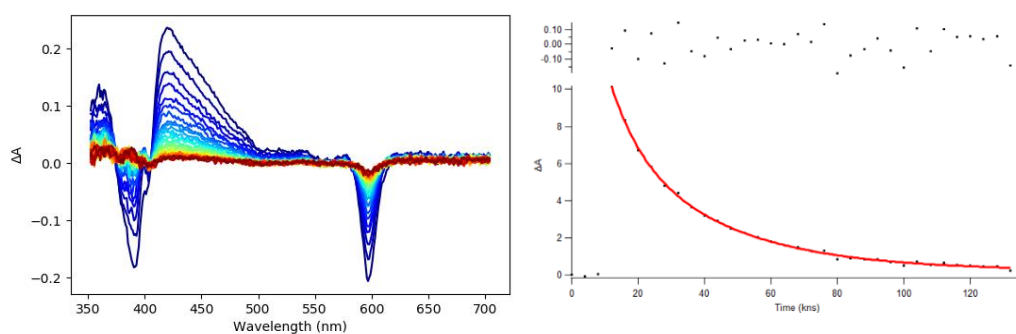


Figure A 13. TA spectra of **Zn1** (left) and time trace fitting with biexponential decay function for the range from 420 to 526 nm (right) in MeOH in oxygen free conditions; $\lambda_{exc} = 604$ nm; incremental time: 4000; $\tau_T = 32 \pm 6 \mu s$ (76 %) and $9 \pm 3 \mu s$ (24 %).

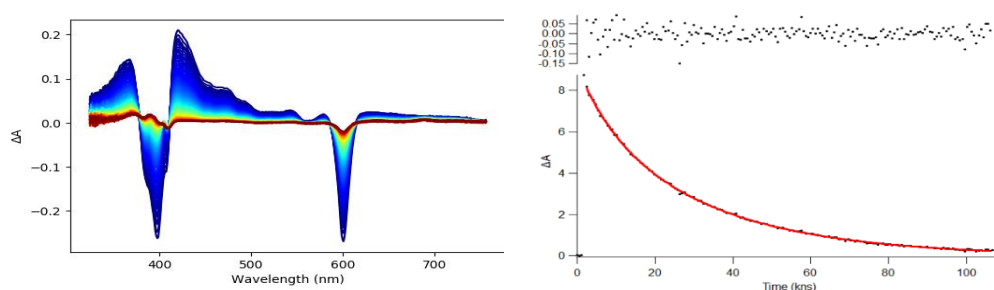


Figure A 14. TA spectra of **Zn2** (left) and time trace fitting with biexponential decay function for the range from 421 to 559 nm (right) in MeOH in oxygen free conditions; $\lambda_{exc} = 604$ nm; incremental time: 600; $\tau_T = 32 \pm 2 \mu s$ (92 %) and $9 \pm 2 \mu s$ (8%).

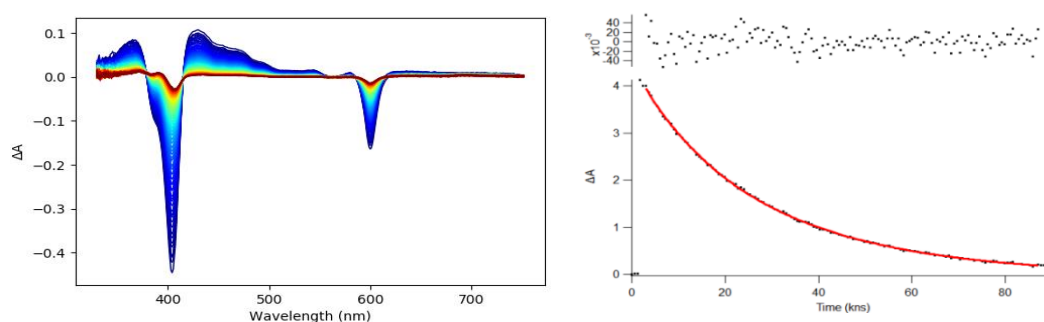


Figure A 15. TA spectra of **Zn1** (left) and time trace fitting with biexponential decay function for the range from 430 to 524 nm (right) in EtOH in oxygen free conditions; $\lambda_{exc} = 604$ nm; incremental time: 600; $\tau_T = 34 \pm 2 \mu s$ (84 %) and $15 \pm 2 \mu s$ (16%).

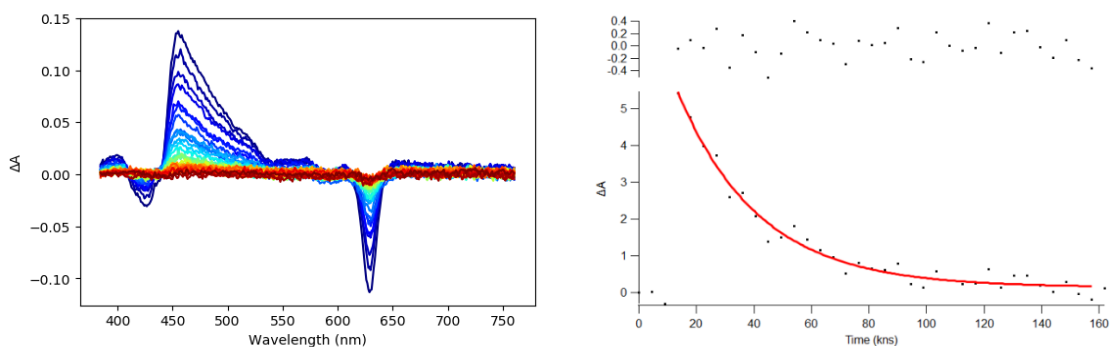


Figure A 16. TA spectra of **Zn2** (left) and time trace fitting with monoexponential decay function for the range from 455 to 553 nm (right) in EtOH in oxygen free conditions; $\lambda_{exc} = 604$ nm; incremental time: 4500 ns; $\tau_T = 29 \pm 4$ μ s.

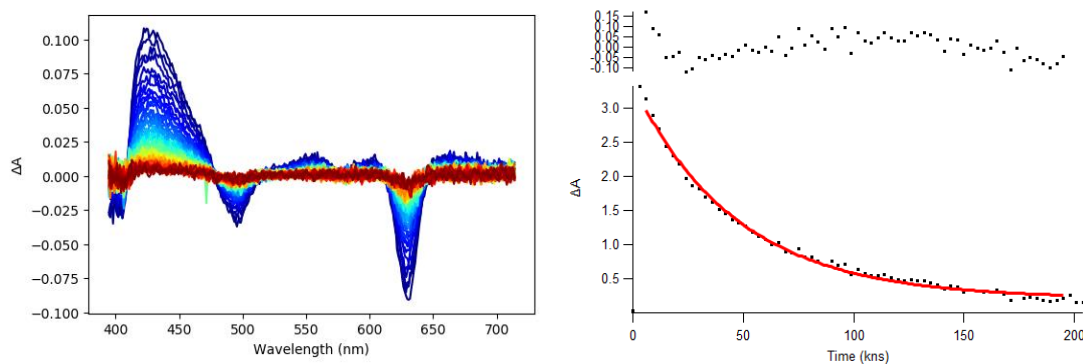


Figure A 17. TA spectra of **FB1** (left) and time trace fitting with monoexponential decay function for the range from 424 to 474 nm (right) in MeOH in oxygen free conditions; $\lambda_{exc} = 637$ nm; incremental time: 3000 ns; $\tau_T = 47 \pm 2$ μ s.

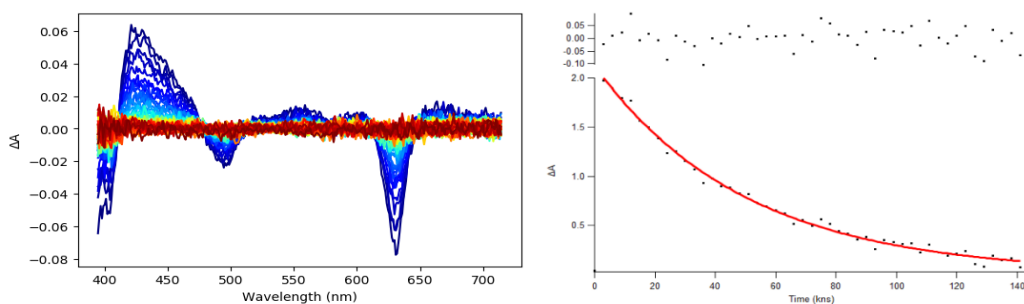


Figure A 18. TA spectra of **FB2** (left) and time trace fitting with monoexponential decay function for the range from 422 to 475 nm (right) in MeOH in oxygen free conditions; $\lambda_{exc} = 637$ nm; incremental time: 3000 ns; $\tau_T = 50 \pm 4$ μ s.

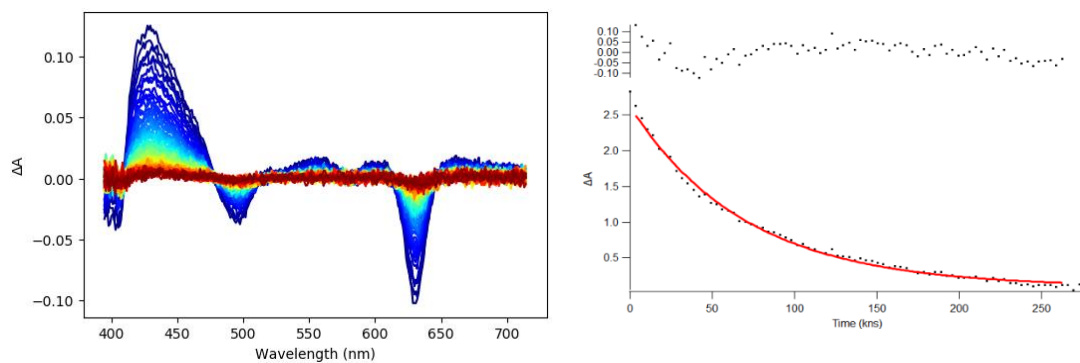


Figure A 19. TA spectra of **FB1** (left) and time trace fitting with monoexponential decay function for the range from 427 to 474 nm (right) in EtOH in oxygen free conditions; $\lambda_{exc} = 635$ nm; incremental time: 3500 ns; $\tau_T = 70 \pm 3$ μ s.

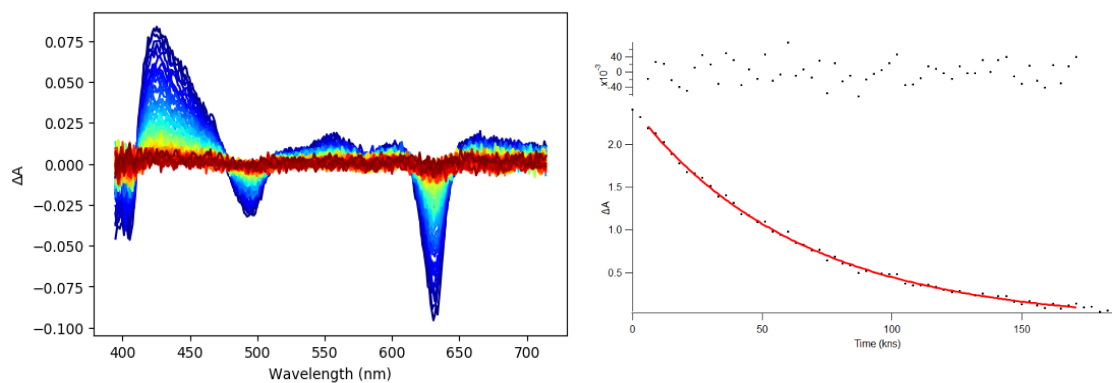


Figure A 20. TA spectra of **FB2** (left) and time trace fitting with monoexponential decay function for the range from 422 to 466 nm (right) in EtOH in oxygen free conditions; $\lambda_{exc} = 635$ nm; incremental time: 3000 ns; $\tau_T = 64 \pm 3$ μ s.

Singlet oxygen emission spectra

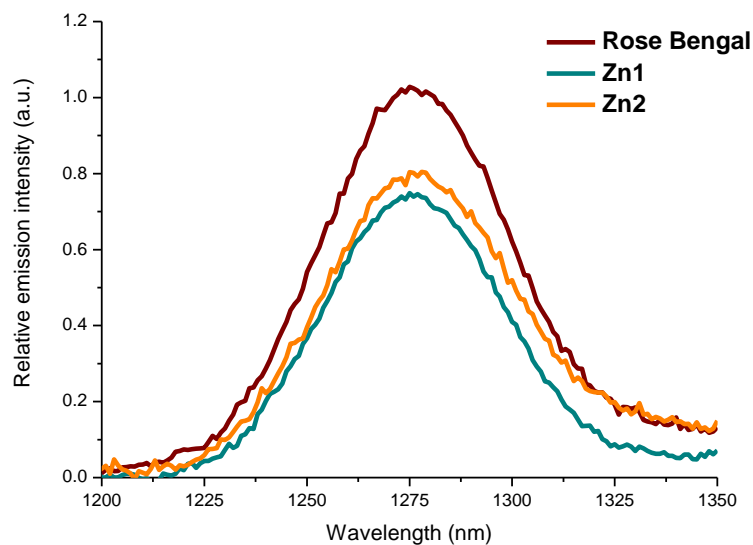


Figure A 21. Singlet oxygen emission spectra of **Zn1**, **Zn2** and Rose Bengal in EtOH, $\lambda_{\text{exc}} = 558 \text{ nm}$; 15 s integration time; $\Phi_{\Delta} \text{Zn1} = 0.88$; $\Phi_{\Delta} \text{Zn2} = 0.77$.

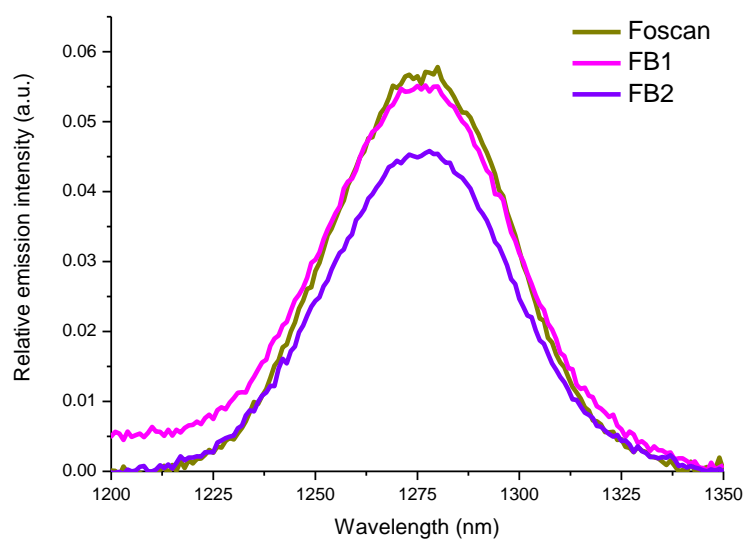


Figure A 22. Singlet oxygen emission spectra of **FB1**, **FB2** and Foscan in MeOH, $\lambda_{\text{exc}} = 500 \text{ nm}$; 15 s integration time; $\Phi_{\Delta} \text{FB1} = 0.45$; $\Phi_{\Delta} \text{FB2} = 0.41$.

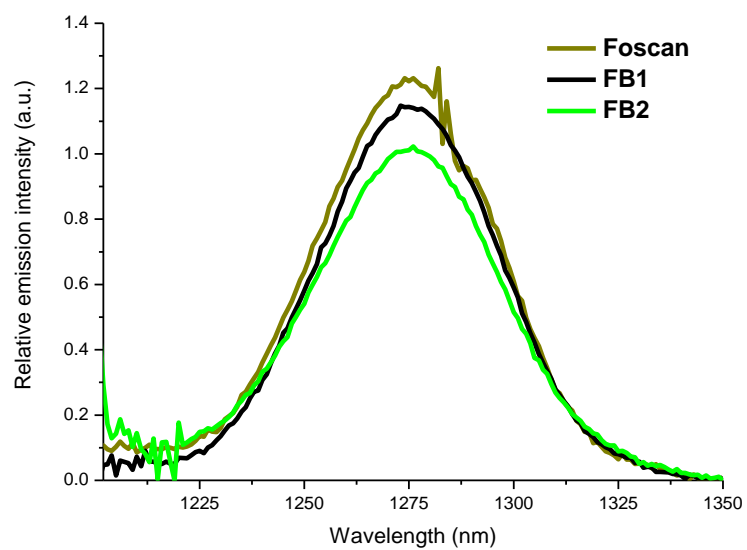


Figure A 23. Singlet oxygen emission spectra of **FB1**, **FB2** and Foscan in EtOH, $\lambda_{\text{exc}} = 500$ nm; 15 s integration time; Φ_{Δ} **FB1** = 0.63; Φ_{Δ} **FB2** = 0.61.

Chapter 3

Absorption and fluorescence emission spectra

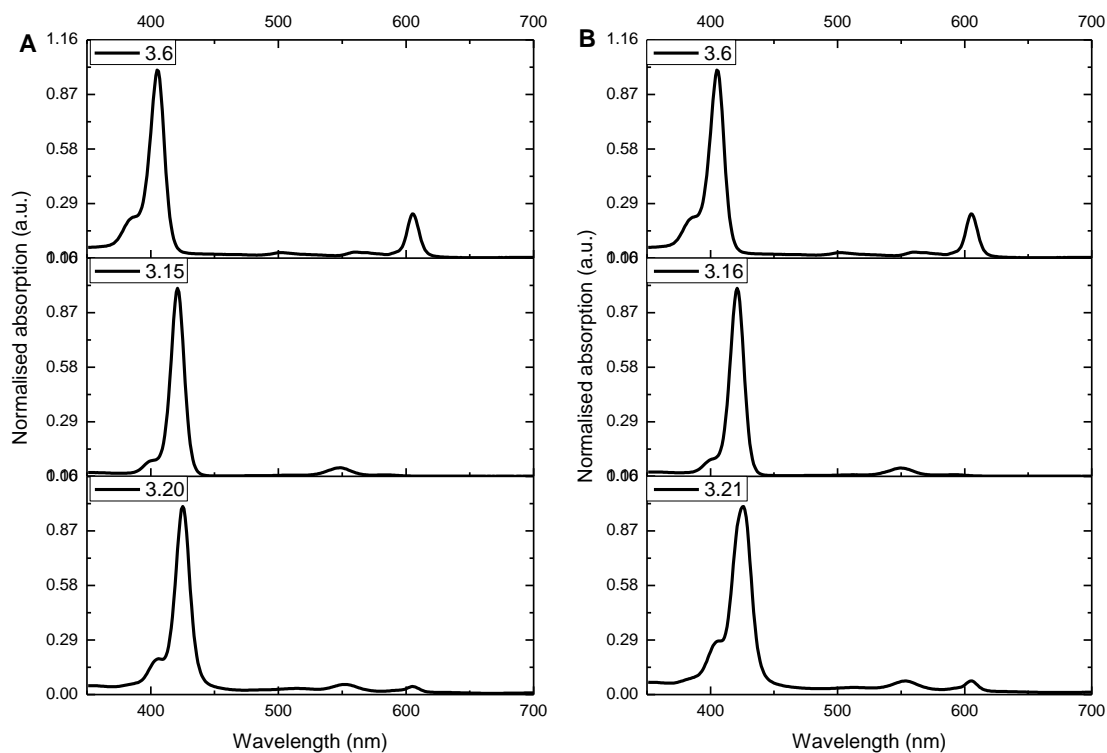


Figure A 24. Normalised absorption spectra of the benchmark chlorin **3.6** and porphyrins **3.15** (A) and **3.16** (B) with the respective dyads **3.20** (A) and **3.21** (B) in toluene.

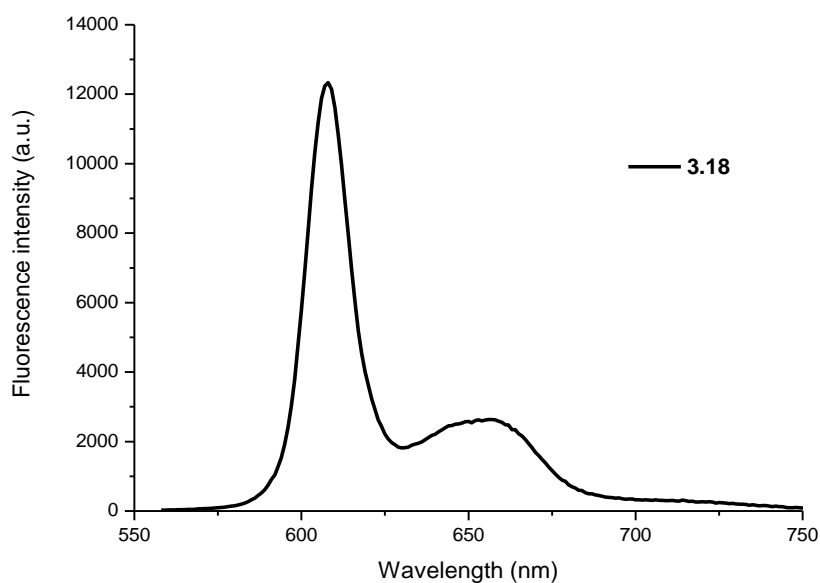


Figure A 25. Fluorescence emission spectrum of **62.1** in methanol ($\lambda_{\text{exc}} = 552$ nm).

Fluorescence decays

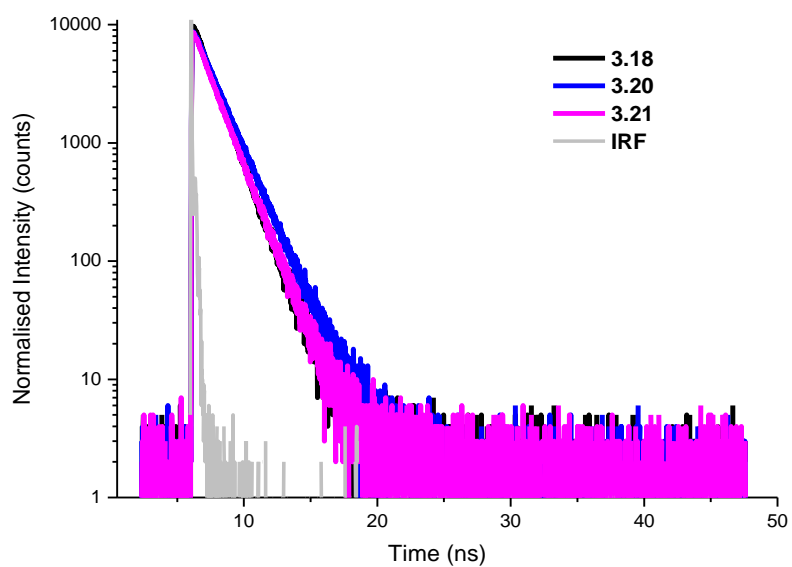


Figure A 26. Fluorescence lifetime decays of dyads in toluene; $\lambda_{\text{exc}} = 425 \text{ nm}$; $\lambda_{\text{det}} = 610 \text{ nm}$.

Triplet-triplet transient absorption spectra at ambient conditions

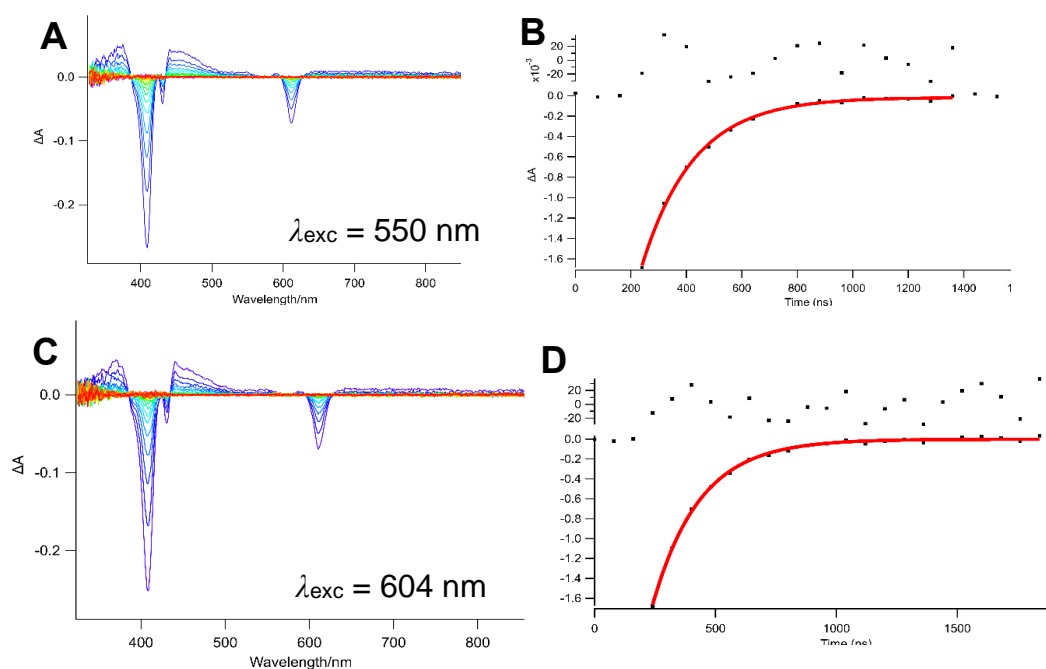


Figure A 27. TA spectra of **3.18** (left) and time trace fitting with monoexponential decay function (right) in ethanol; $\lambda_{exc} = 550$ nm; $\tau_T = 190 \pm 12$ ns (**A and B**); $\lambda_{exc} = 604$ nm; $\tau_T = 190 \pm 12$ ns (**C and D**); 80 ns t_{inc} .

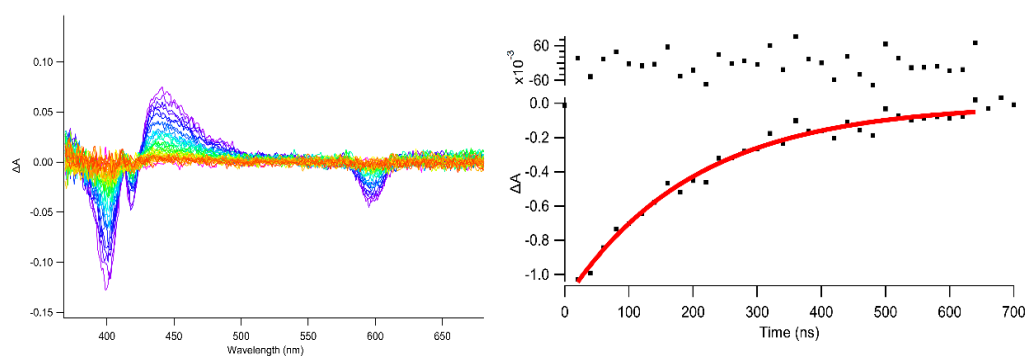


Figure A 28. TA spectra of **3.18** (left) and time trace fitting with monoexponential decay function (right) in methanol; $\lambda_{exc} = 604$ nm; $\tau_T = 200 \pm 30$ ns; 20 ns t_{inc} .

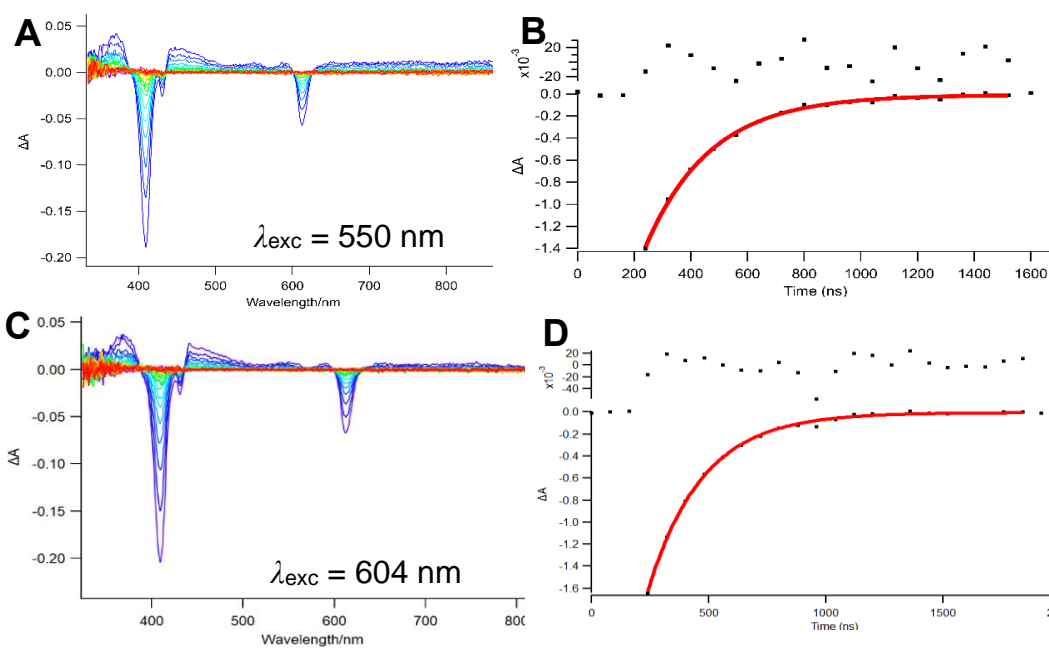


Figure A 29. TA spectra of **3.18** (left) and time trace fitting with monoexponential decay function (right) in toluene; λ_{exc} = 550 nm; τ_T = 230 ± 13 ns (**A** and **B**); λ_{exc} = 604 nm; τ_T = 230 ± 9 ns (**C** and **D**); 80 ns t_{inc}.

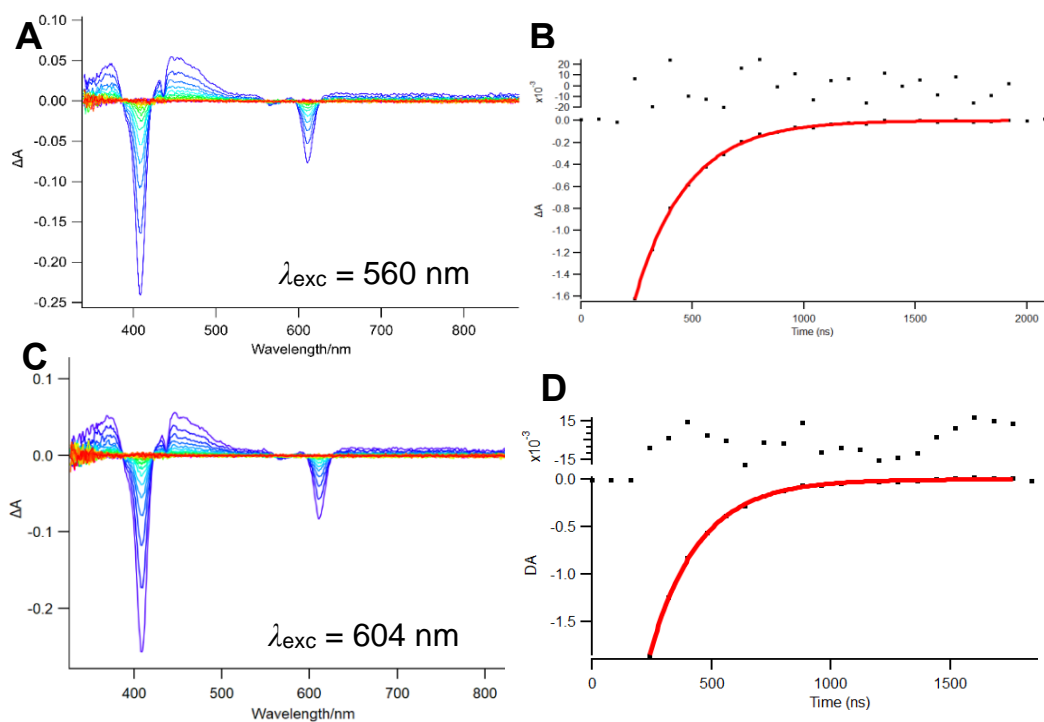


Figure A 30. TA spectra of **3.20** (left) and time trace fitting with monoexponential decay function (right) in ethanol; λ_{exc} = 560 nm; τ_T = 210 ± 7 ns (**A** and **B**); λ_{exc} = 604 nm; τ_T = 200 ± 5 ns (**C** and **D**); 80 ns t_{inc}.

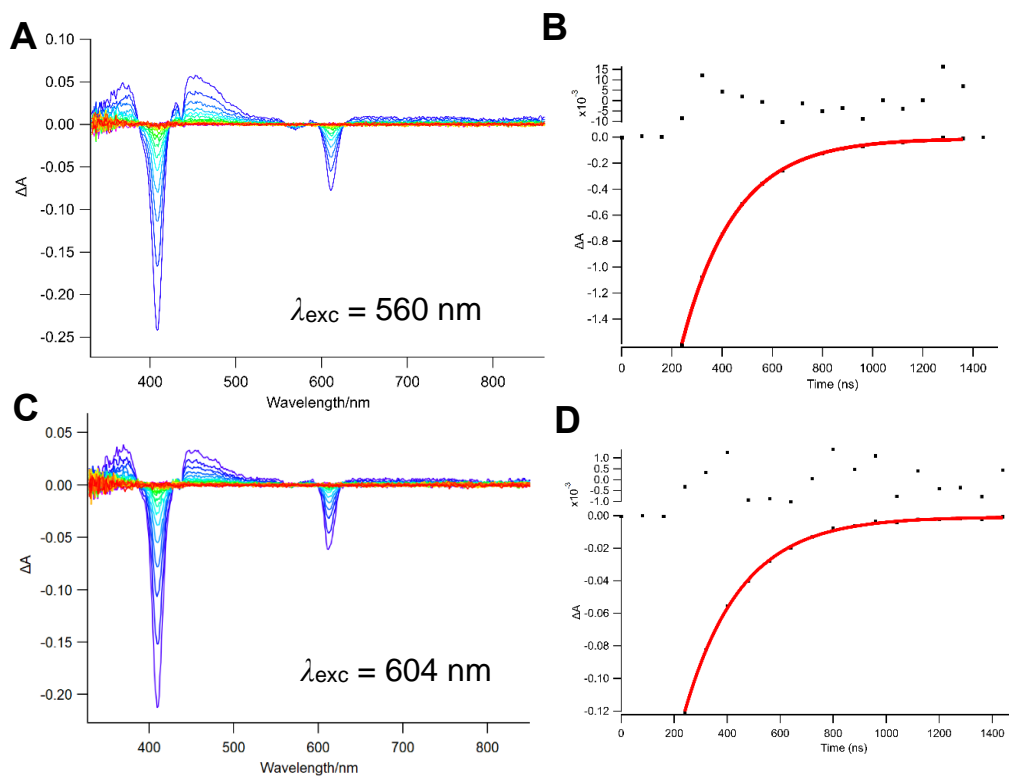


Figure A 31. TA spectra of **3.20** (left) and time trace fitting with monoexponential decay function (right) in toluene; $\lambda_{exc} = 560$ nm; $\tau_T = 210 \pm 5$ ns (**A and B**); $\lambda_{exc} = 604$ nm; $\tau_T = 230 \pm 7$ ns (**C and D**); 80 ns t_{inc} .

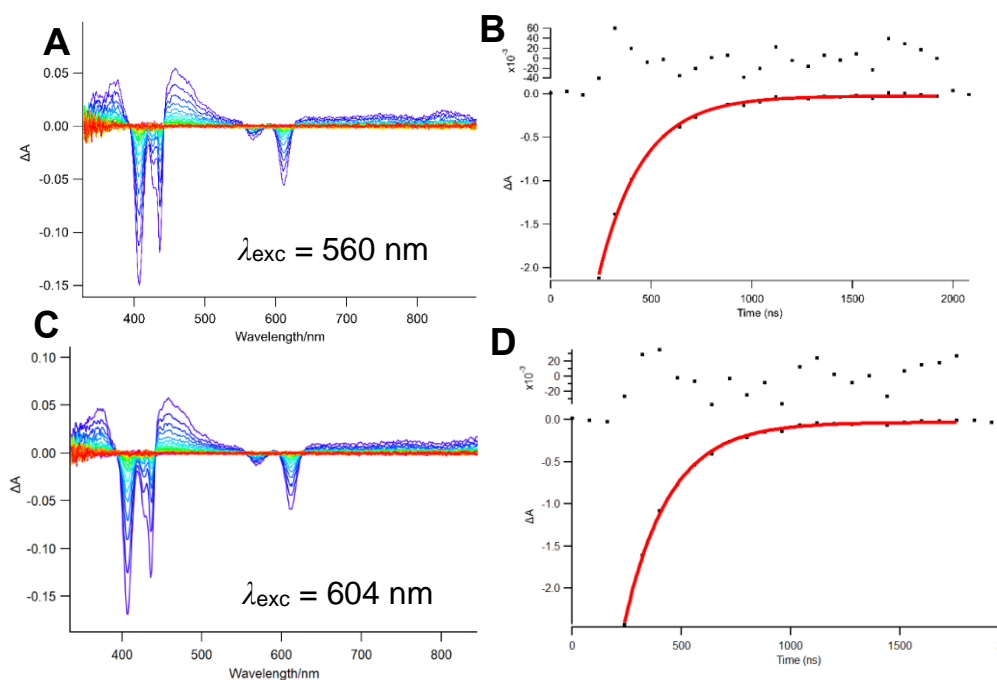


Figure A 32. TA spectra of **3.21** (left) and time trace fitting with monoexponential decay function (right) in ethanol; $\lambda_{exc} = 560$ nm; $\tau_T = 220 \pm 10$ ns (**A and B**); $\lambda_{exc} = 604$ nm; $\tau_T = 210 \pm 8$ ns (**C and D**); 80 ns t_{inc} .

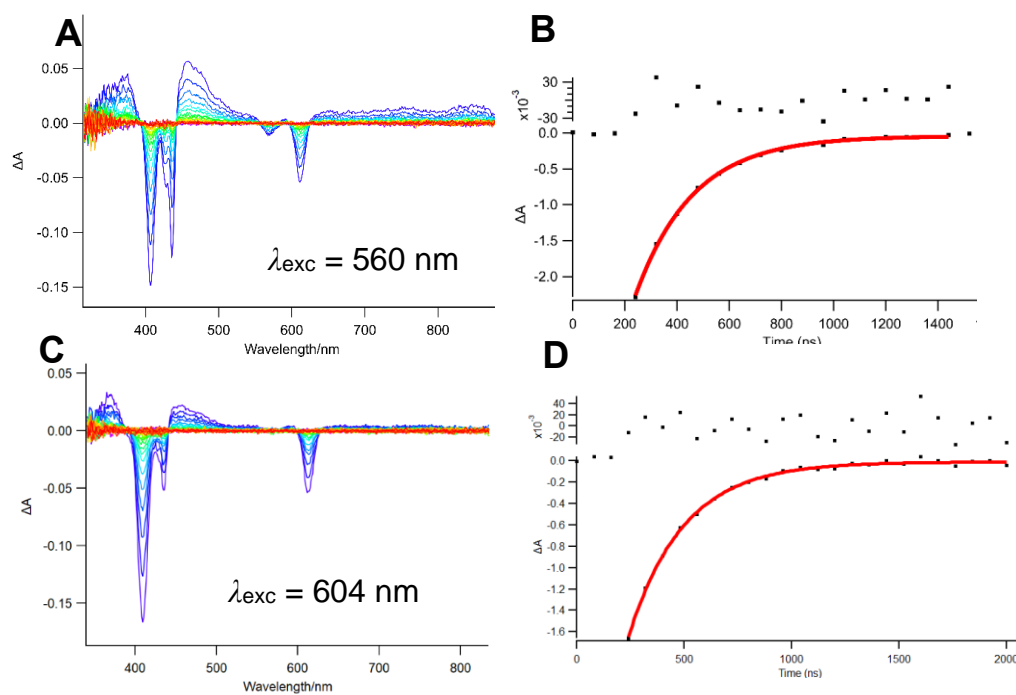


Figure A 33. TA spectra of **3.21** (left) and time trace fitting with monoexponential decay function (right) in toluene; $\lambda_{exc} = 560$ nm; $\tau_T = 220 \pm 9$ ns (**A** and **B**); $\lambda_{exc} = 604$ nm; $\tau_T = 260 \pm 13$ ns (**C** and **D**); 80 ns t_{inc} .

Singlet oxygen emission spectra

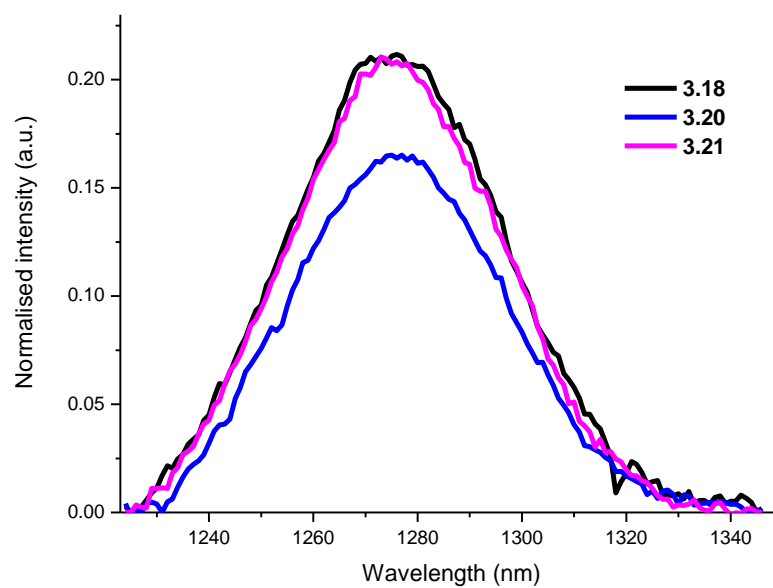


Figure A 34. Singlet oxygen emission spectra of dyads in toluene, $\lambda_{\text{exc}} = 550 \text{ nm}$; 10 s integration time.

Chapter 4

X-Ray crystal structures¹⁴

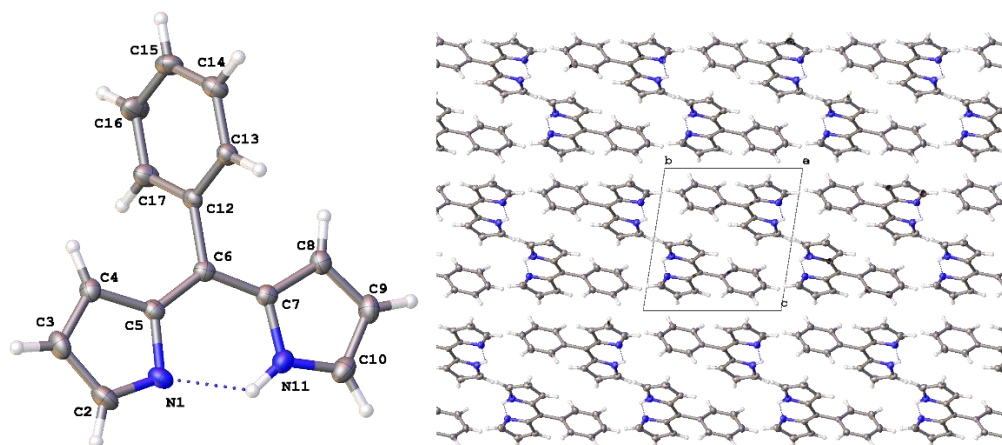


Figure A 35. Molecular structure (left) and packing diagram viewed normal to the a-axis (right) with hydrogen bonding indicated by dotted lines of **DIPY1** (thermal ellipsoid plot), shown with atomic displacement at 50% probability.

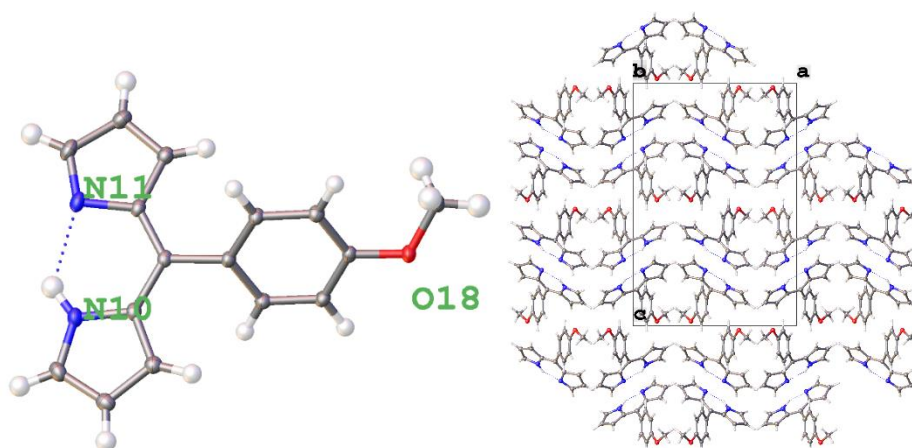


Figure A 36. Molecular structure (left) and packing diagram viewed normal to the b-axis (right) with hydrogen bonding indicated by dotted lines of **DIPY6** (thermal ellipsoid plot), shown with atomic displacement at 50% probability.¹⁵

¹⁴ Crystal structures were determined by Dr. Brendan Twamley, TCD unless stated otherwise.

¹⁵ Crystal structure **DIPY6** was determined by Dr. Christopher J. Kingsbury, TCD.

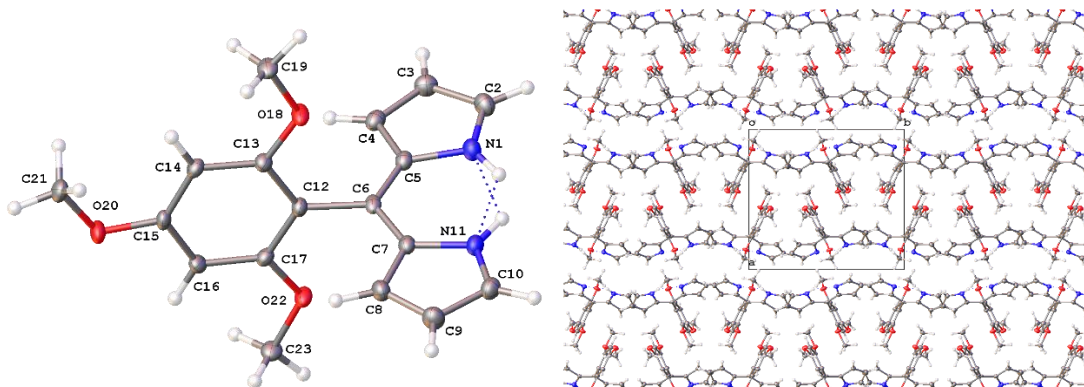


Figure A 37. Molecular structure (left) and packing diagram of one moiety viewed normal to the *c*-axis (right) of **DIPY7** (thermal ellipsoid plot), shown with atomic displacement at 50% probability.

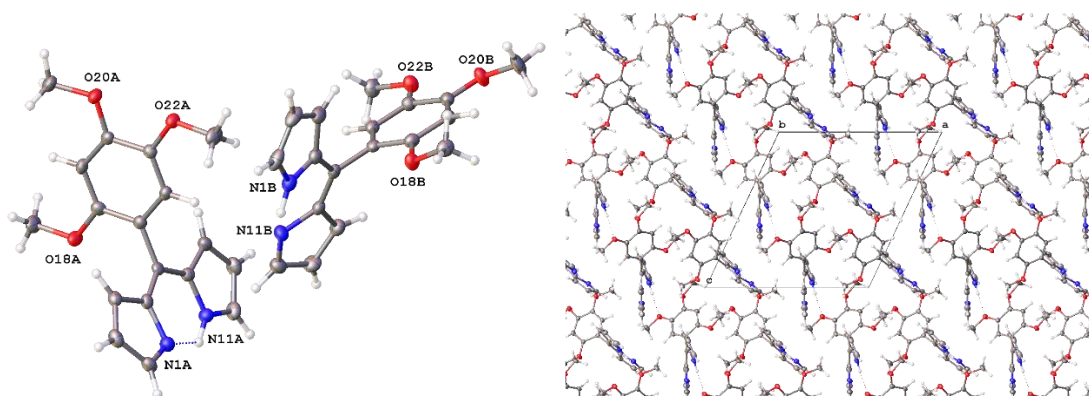


Figure A 38. Molecular structure showing both independent molecules in the asymmetric unit (left) and packing diagram viewed normal to the *b*-axis (right) of **DIPY8** (thermal ellipsoid plot), shown with atomic displacement at 50% probability.

Triplet-triplet transient absorption spectra (TA)

Transient absorption spectroscopy at **ambient** conditions (ethanol/toluene/DCM)

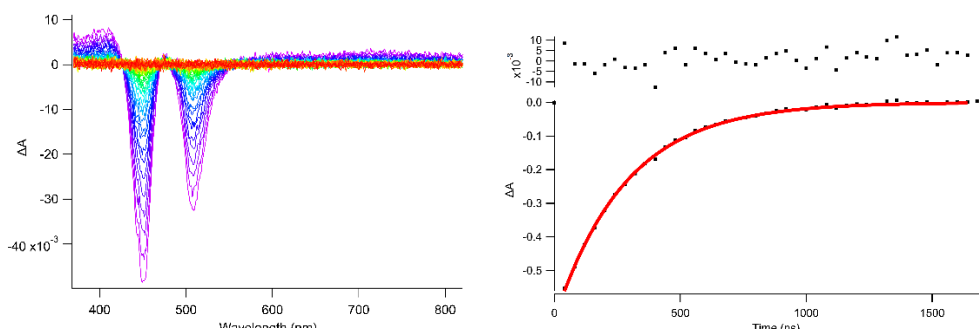


Figure A 39. TA spectra of $A\ell(DIPY)_31$ (left) and time trace fitting with monoexponential decay function (right) in toluene at ambient conditions; 40 ns t_{inc} ; $\lambda_{exc} = 450$ nm; $\tau_T = 280 \pm 5$ ns.

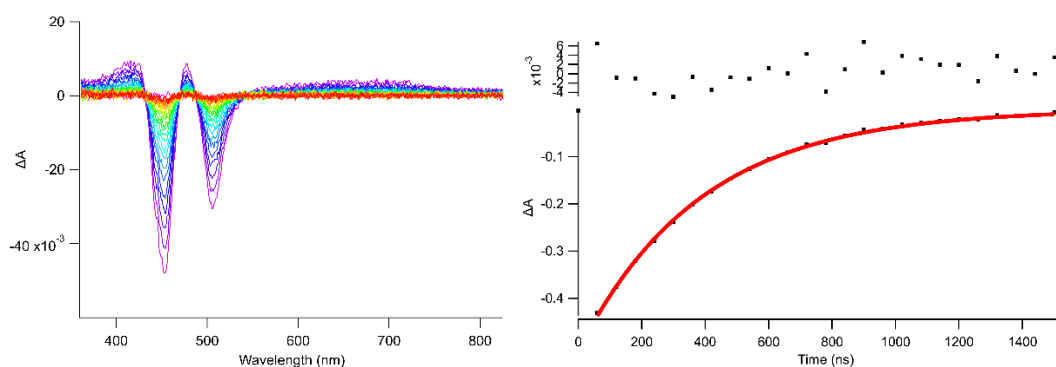


Figure A 40. TA spectra of $A\ell(DIPY)_32$ (left) and time trace fitting with monoexponential decay function (right) in toluene at ambient conditions; 60 ns t_{inc} ; $\lambda_{exc} = 450$ nm; $\tau_T = 380 \pm 6$ ns.

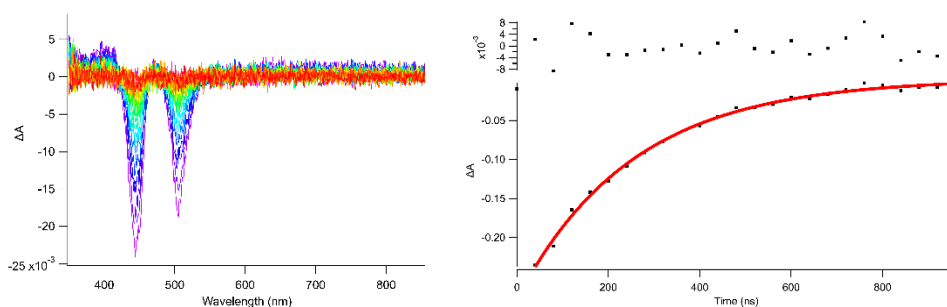


Figure A 41. TA spectra of $A\ell(DIPY)_33$ (left) and time trace fitting with monoexponential decay function (right) in ethanol at ambient conditions; 40 ns t_{inc} ; $\lambda_{exc} = 450$ nm; $\tau_T = 250 \pm 17$ ns.

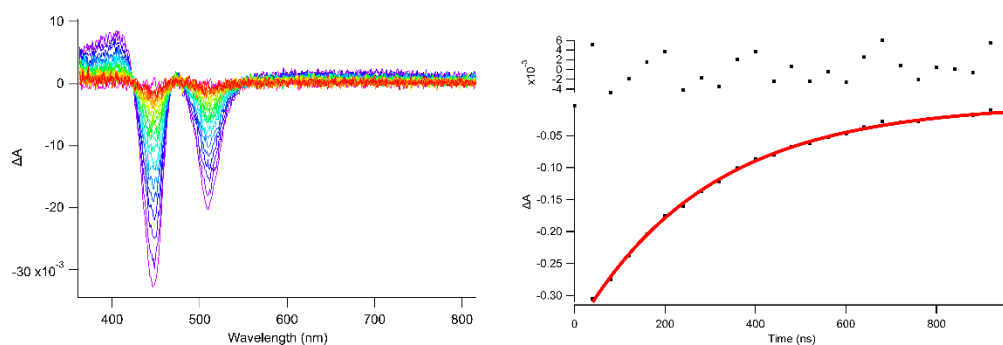


Figure A 42. TA spectra of $\text{Al}(\text{DIPY})_3$ (left) and time trace fitting with monoexponential decay function (right) in toluene at ambient conditions; 40 ns t_{inc} ; $\lambda_{\text{exc}} = 450$ nm; $\tau_{\text{T}} = 290 \pm 6$ ns.

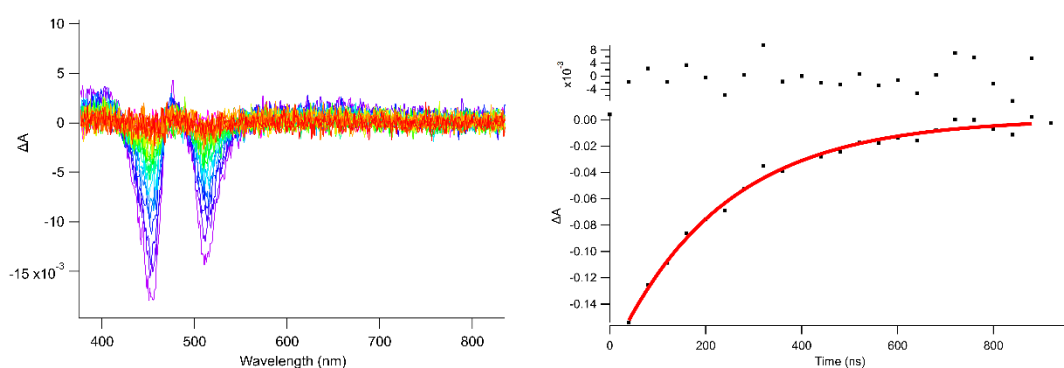


Figure A 43. TA spectra of $\text{Al}(\text{DIPY})_3$ (left) and time trace fitting with monoexponential decay function (right) in ethanol at ambient conditions; 40 ns t_{inc} ; $\lambda_{\text{exc}} = 450$ nm; $\tau_{\text{T}} = 230 \pm 26$ ns.

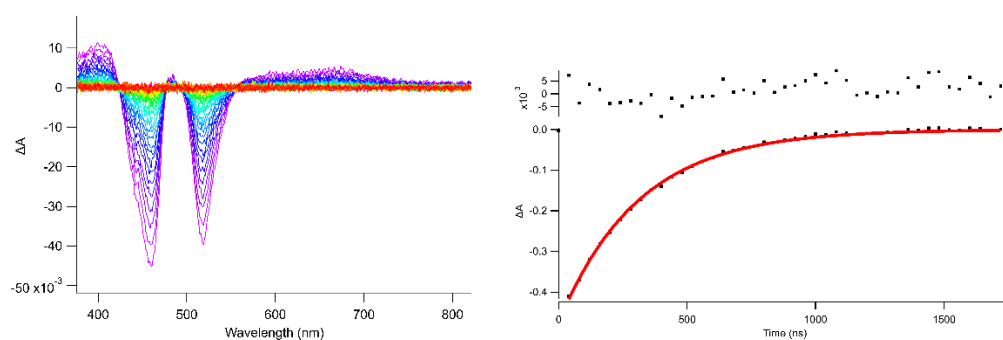


Figure A 44. TA spectra of $\text{Al}(\text{DIPY})_3$ (left) and time trace fitting with monoexponential decay function (right) in toluene at ambient conditions; 40 ns t_{inc} ; $\lambda_{\text{exc}} = 450$ nm; $\tau_{\text{T}} = 310 \pm 6$ ns.

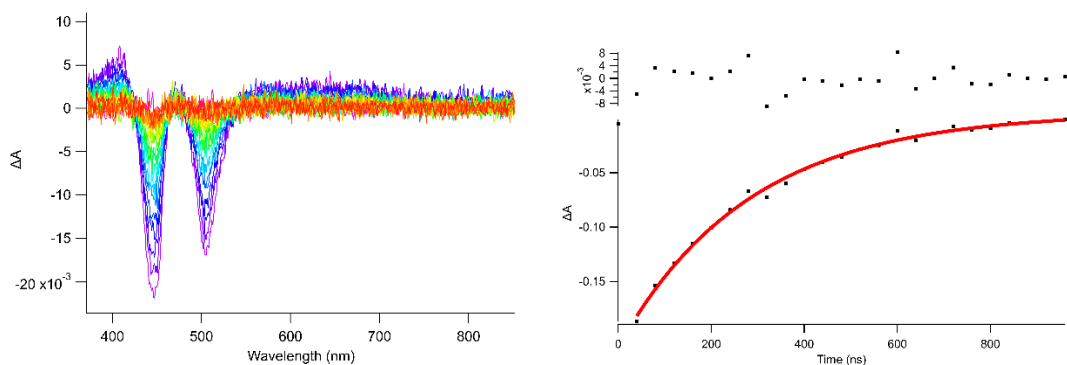


Figure A 45. TA spectra of $A\lambda(\text{DIPY})_35$ (left) and time trace fitting with monoexponential decay function (right) in ethanol at ambient conditions; 40 ns t_{inc} ; $\lambda_{\text{exc}} = 450$ nm; $\tau_T = 280 \pm 25$ ns.

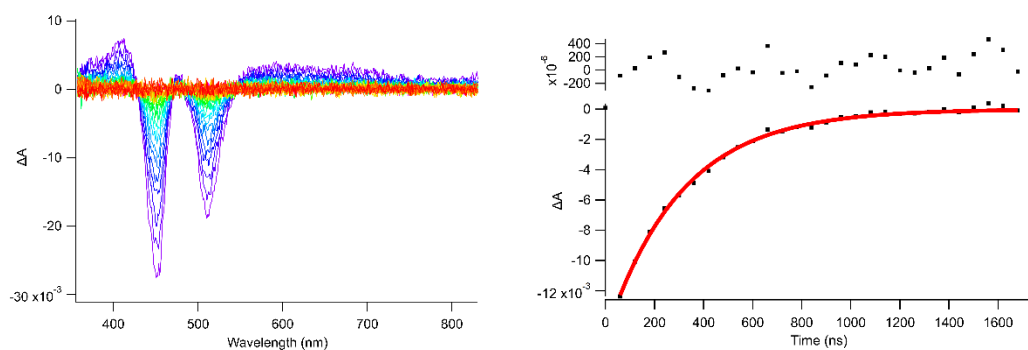


Figure A 46. TA spectra of $A\lambda(\text{DIPY})_35$ (left) and time trace fitting with monoexponential decay function (right) in toluene at ambient conditions; 60 ns t_{inc} ; $\lambda_{\text{exc}} = 450$ nm; $\tau_T = 300 \pm 12$ ns.

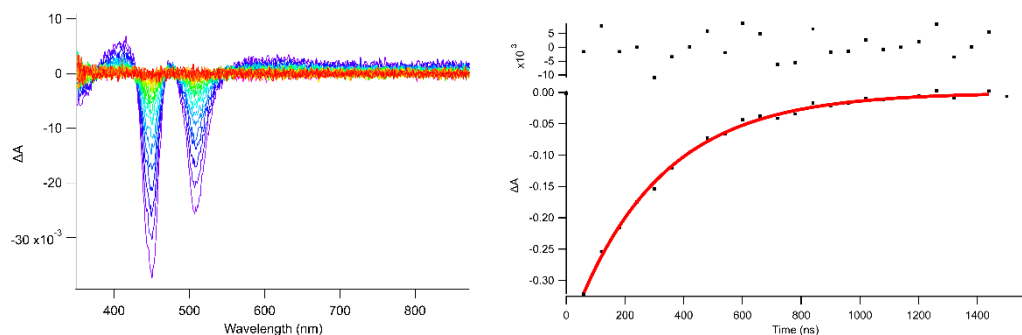


Figure A 47. TA spectra of $A\lambda(\text{DIPY})_36$ (left) and time trace fitting with monoexponential decay function (right) in toluene at ambient conditions; 60 ns t_{inc} ; $\lambda_{\text{exc}} = 450$ nm; $\tau_T = 300 \pm 11$ ns.

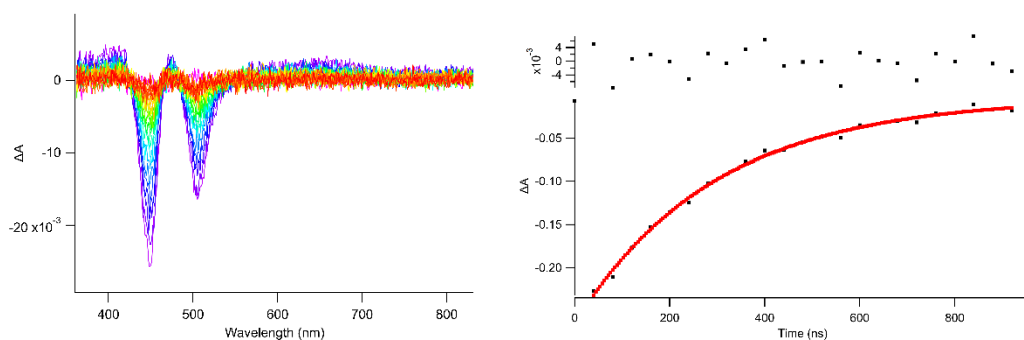


Figure A 48. TA spectra of **A₂(DIPY)₃8** (left) and time trace fitting with monoexponential decay function (right) in ethanol at ambient conditions; 40 ns t_{inc} ; λ_{exc} = 450 nm; $\tau_T = 300 \pm 25$ ns.

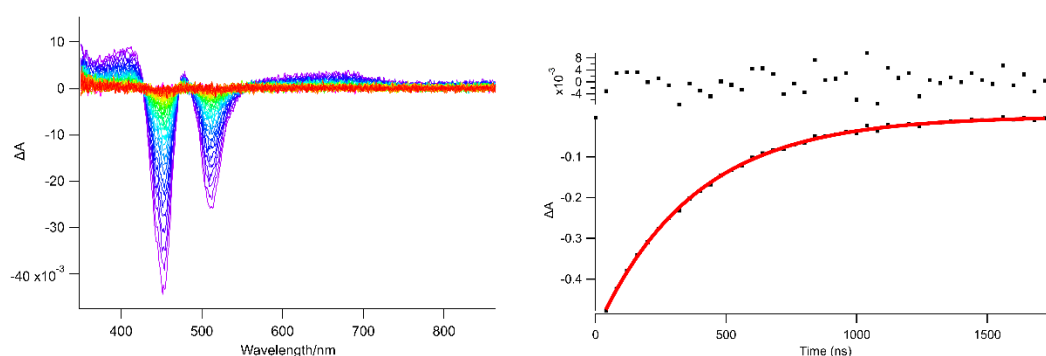


Figure A 49. TA spectra of **A₂(DIPY)₃8** (left) and time trace fitting with monoexponential decay function (right) in toluene at ambient conditions; 40 ns t_{inc} ; λ_{exc} = 450 nm; $\tau_T = 370 \pm 5$ ns.

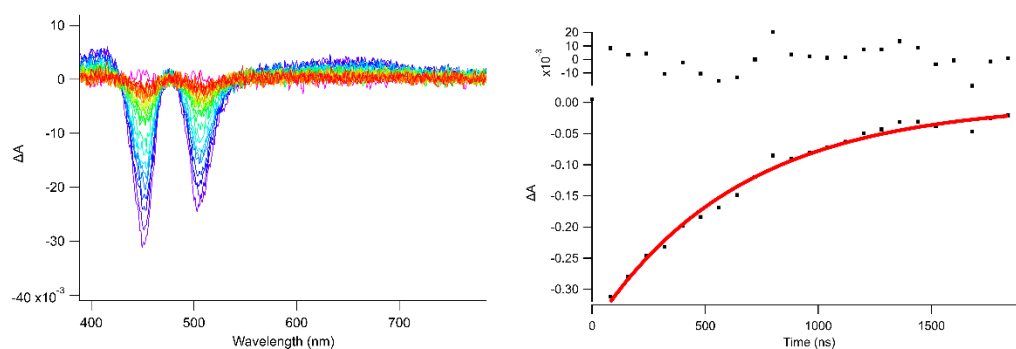


Figure A 50. TA spectra of **A₂(DIPY)₃8** (left) and time trace fitting with monoexponential decay function (right) in DCM at ambient conditions; 80 ns t_{inc} ; λ_{exc} = 450 nm; $\tau_T = 650 \pm 40$ ns.

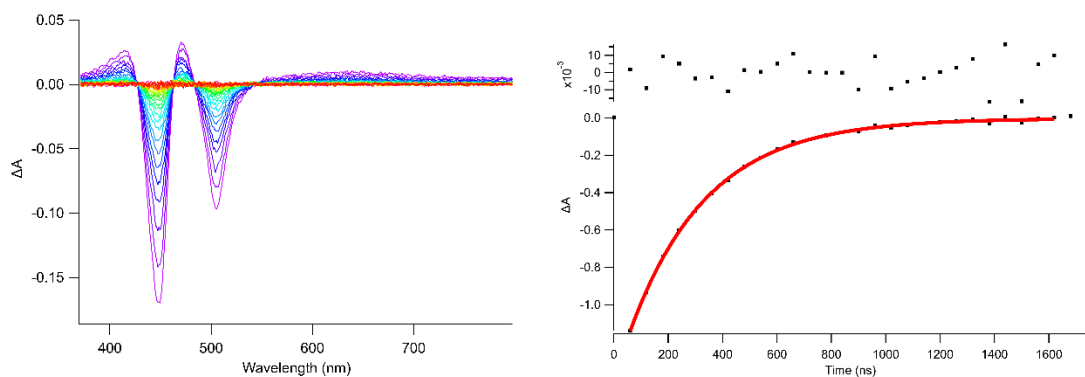


Figure A 51. TA spectra of $A\lambda(DIPY)_39$ (left) and time trace fitting with monoexponential decay function (right) in ethanol at ambient conditions; 60 ns t_{inc} ; $\lambda_{exc} = 450$ nm; $\tau_T = 280 \pm 8$ ns.

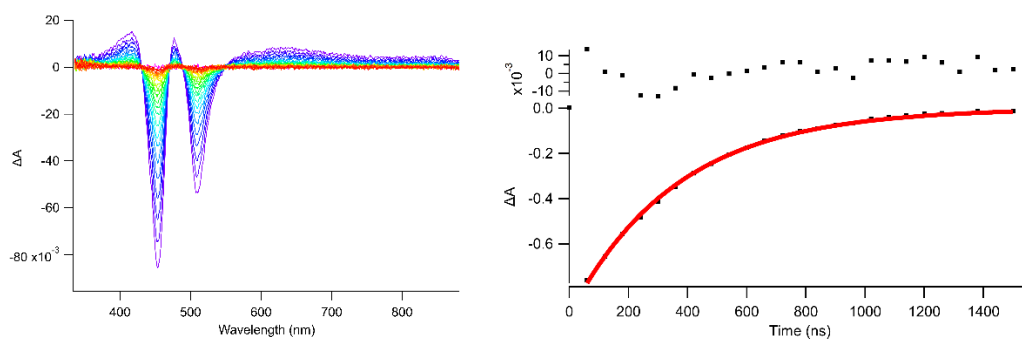


Figure A 52. TA spectra of $A\lambda(DIPY)_39$ (left) and time trace fitting with monoexponential decay function (right) in toluene at ambient conditions; 60 ns t_{inc} ; $\lambda_{exc} = 450$ nm; $\tau_T = 360 \pm 7$ ns.

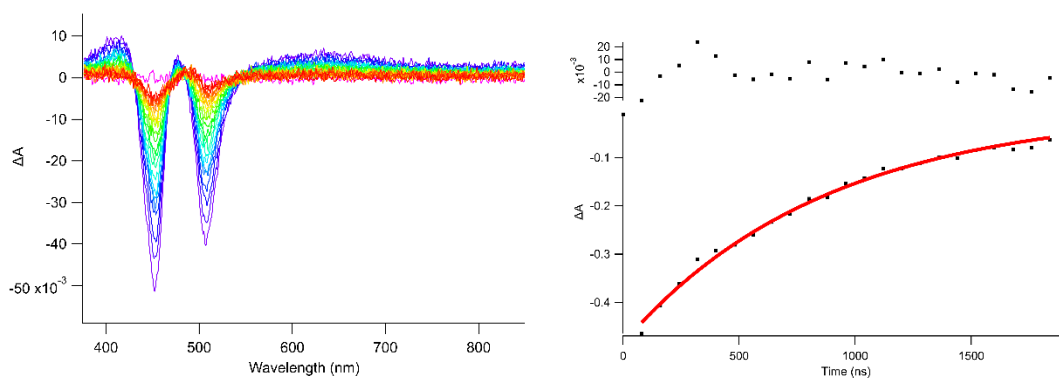


Figure A 53. TA spectra of $A\lambda(DIPY)_39$ (left) and time trace fitting with monoexponential decay function (right) in DCM at ambient conditions; 60 ns t_{inc} ; $\lambda_{exc} = 450$ nm; $\tau_T = 870 \pm 39$ ns.

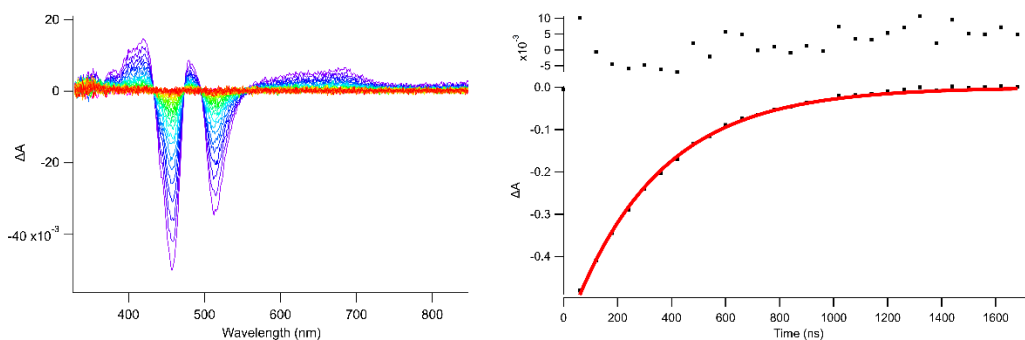


Figure A 54. TA spectra of $A\ell(DIPY)_310$ (left) and time trace fitting with monoexponential decay function (right) in toluene at ambient conditions; 60 ns t_{inc} ; $\lambda_{exc} = 450$ nm; $\tau_T = 330 \pm 9$ ns.

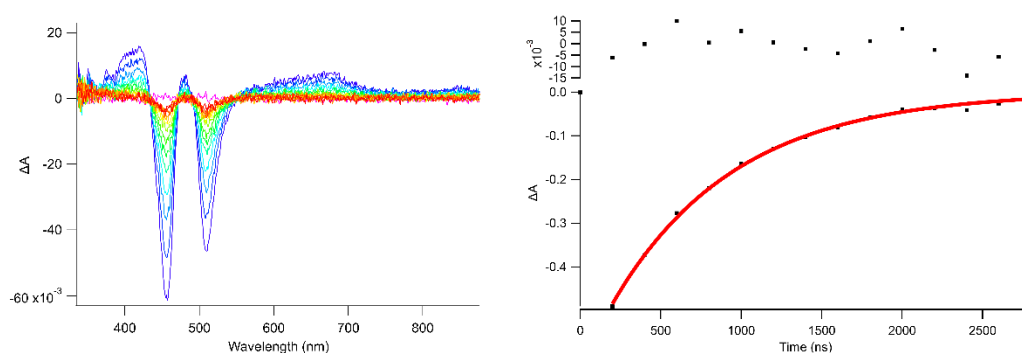


Figure A 55. TA spectra of $A\ell(DIPY)_310$ (left) and time trace fitting with monoexponential decay function (right) in DCM at ambient conditions; 200 ns t_{inc} ; $\lambda_{exc} = 450$ nm; $\tau_T = 760 \pm 34$ ns.

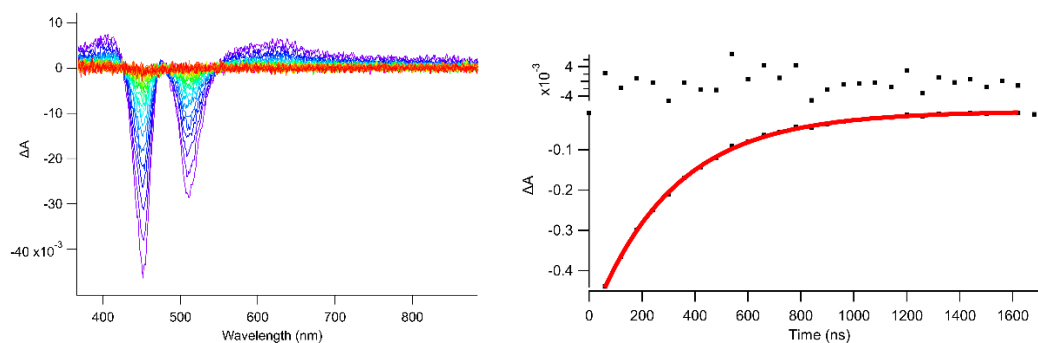


Figure A 56. TA spectra of $A\ell(DIPY)_311$ (left) and time trace fitting with monoexponential decay function (right) in toluene at ambient conditions; 60 ns t_{inc} ; $\lambda_{exc} = 450$ nm; $\tau_T = 320 \pm 7$ ns.

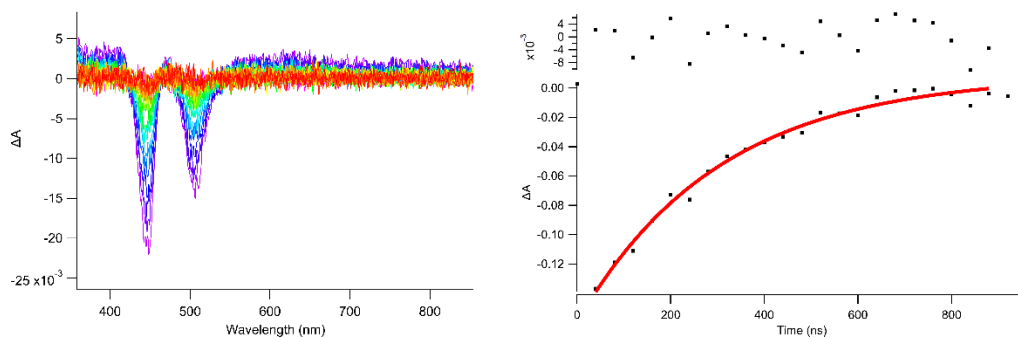


Figure A 57. TA spectra of **Aλ(DIPY)₃12** (left) and time trace fitting with monoexponential decay function (right) in ethanol at ambient conditions; 40 ns t_{inc} ; λ_{exc} = 450 nm; $\tau_T = 300 \pm 50$ ns.

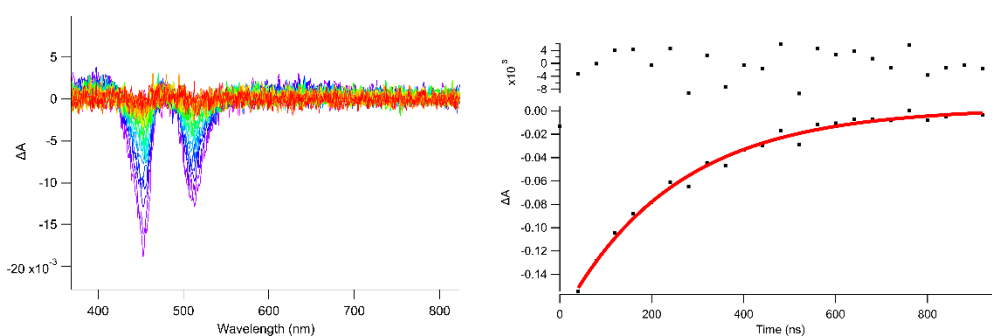


Figure A 58. TA spectra of **Aλ(DIPY)₃13** (left) and time trace fitting with monoexponential decay function (right) in ethanol at ambient conditions; 40 ns t_{inc} ; λ_{exc} = 450 nm; $\tau_T = 250 \pm 30$ ns.

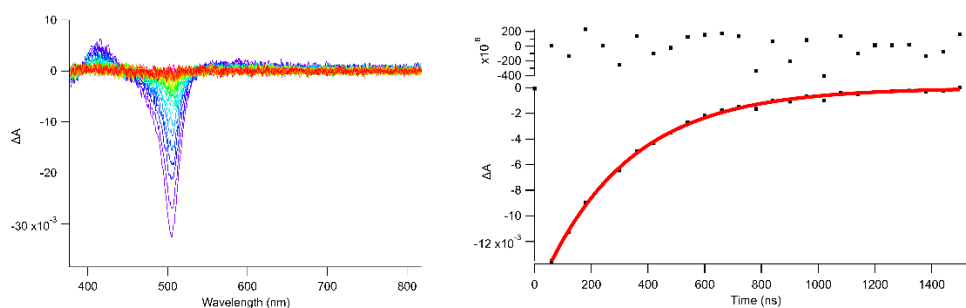


Figure A 59. TA spectra of **Aλ(DIPY)₃15** (left) and time trace fitting with monoexponential decay function (right) in toluene at ambient conditions; 60 ns t_{inc} ; λ_{exc} = 450 nm; $\tau_T = 310 \pm 9$ ns.

Transient absorption spectra in **oxygen free conditions** (ethanol/toluene)

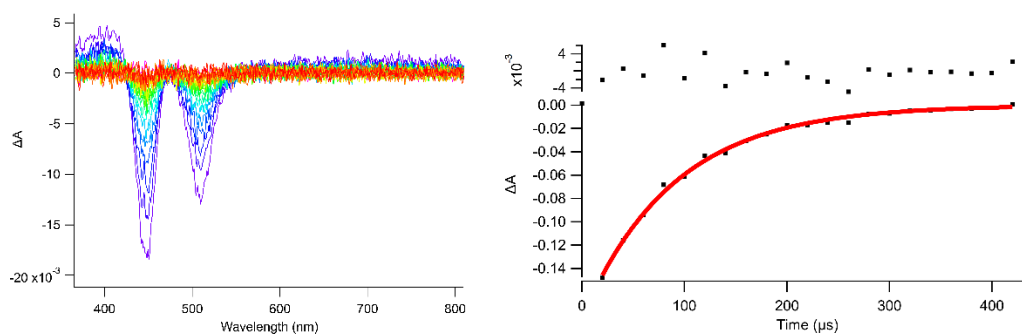


Figure A 60. TA spectra of **Al(DIPY)₃1** (left) and time trace fitting with monoexponential decay function (right) in toluene in oxygen free conditions; 20 μs t_{inc} ; $\lambda_{exc} = 450 \text{ nm}$; $\tau_T = 89 \pm 4 \text{ μs}$.

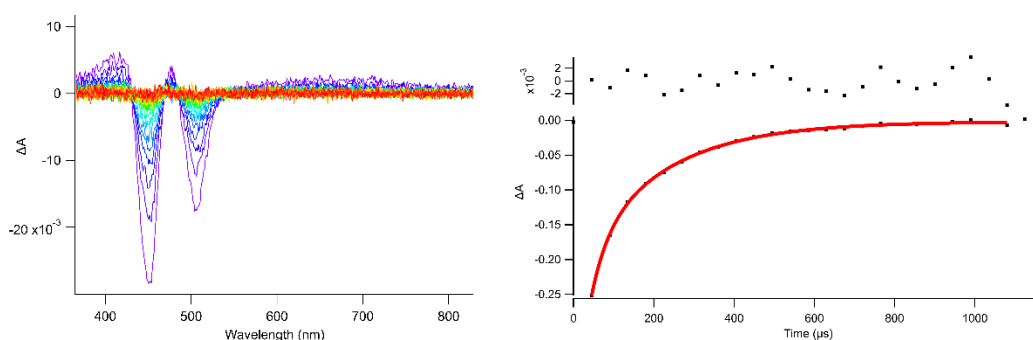


Figure A 61. TA spectra of **Al(DIPY)₃2** (left) and time trace fitting with bi-exponential decay function (right) in toluene in oxygen free conditions; 45 μs t_{inc} ; $\lambda_{exc} = 450 \text{ nm}$; $\tau_{T1} = 202 \pm 22 \text{ μs}$, $\tau_{T2} = 39 \pm 11 \text{ μs}$.

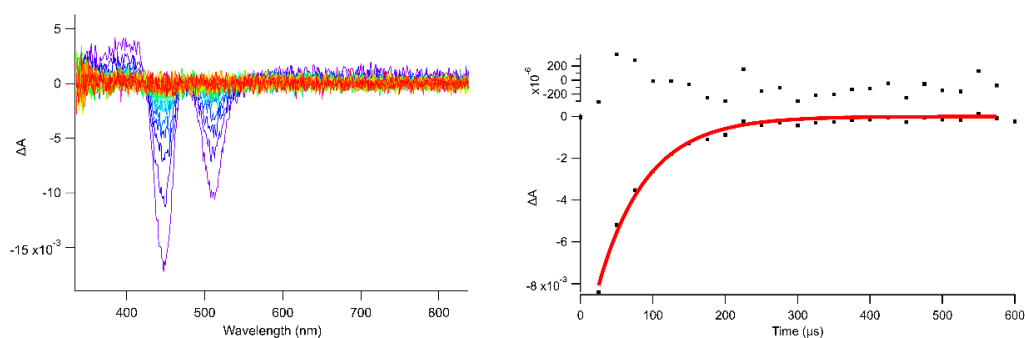


Figure A 62. TA spectra of **Al(DIPY)₃3** (left) and time trace fitting with monoexponential decay function (right) in toluene in oxygen free conditions; 25 μs t_{inc} ; $\lambda_{exc} = 450 \text{ nm}$; $\tau_T = 66 \pm 5 \text{ μs}$.

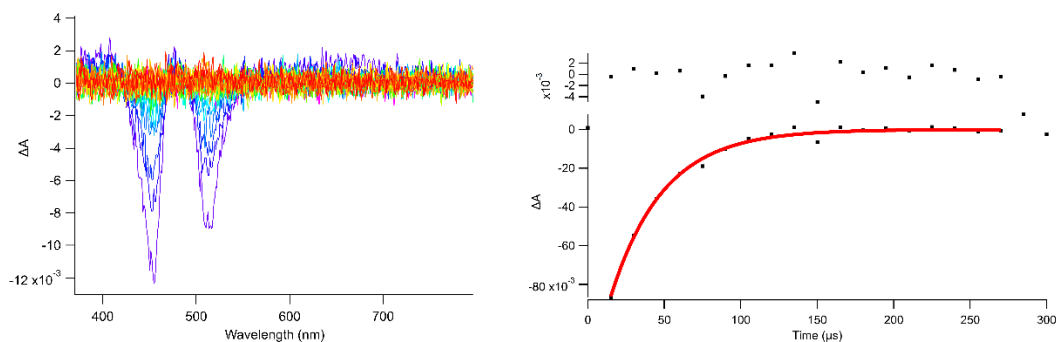


Figure A 63. TA spectra of $A\lambda(\text{DIPY})_34$ (left) and time trace fitting with monoexponential decay function (right) in ethanol in oxygen free conditions; $15 \mu\text{s } t_{\text{inc}}$;
 $\lambda_{\text{exc}} = 450 \text{ nm}; \tau_{\text{T}} = 34 \pm 3 \mu\text{s}$.

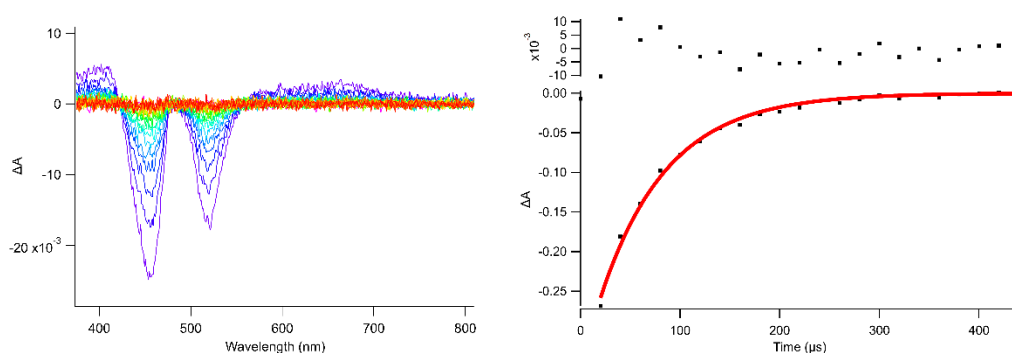


Figure A 64. TA spectra of $A\lambda(\text{DIPY})_34$ (left) and time trace fitting with monoexponential decay function (right) in toluene in oxygen free conditions; $20 \mu\text{s } t_{\text{inc}}$;
 $\lambda_{\text{exc}} = 450 \text{ nm}; \tau_{\text{T}} = 67 \pm 4 \mu\text{s}$.

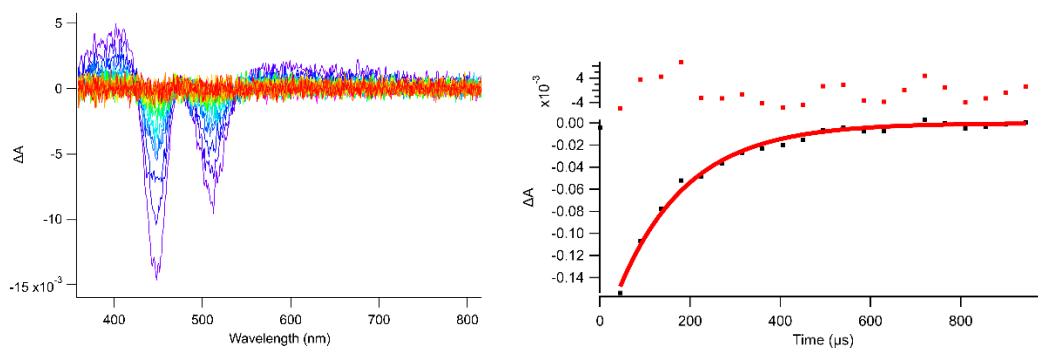


Figure A 65. TA spectra of $A\lambda(\text{DIPY})_35$ (left) and time trace fitting with monoexponential decay function (right) in toluene in oxygen free conditions; $45 \mu\text{s } t_{\text{inc}}$;
 $\lambda_{\text{exc}} = 450 \text{ nm}; \tau_{\text{T}} = 150 \pm 12 \mu\text{s}$.

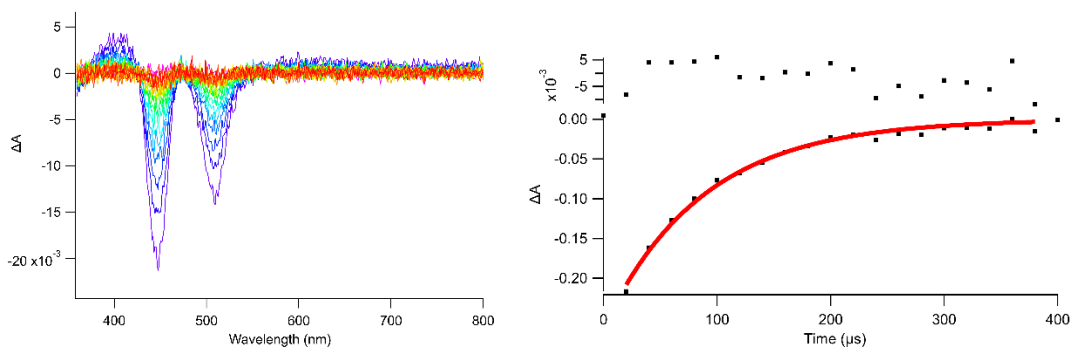


Figure A 66. TA spectra of $\text{Al}(\text{DIPY})_3\mathbf{6}$ (left) and time trace fitting with monoexponential decay function (right) in toluene in oxygen free conditions; $20 \mu\text{s } t_{\text{inc}}$; $\lambda_{\text{exc}} = 450 \text{ nm}$; $\tau_{\text{T}} = 86 \pm 6 \mu\text{s}$.

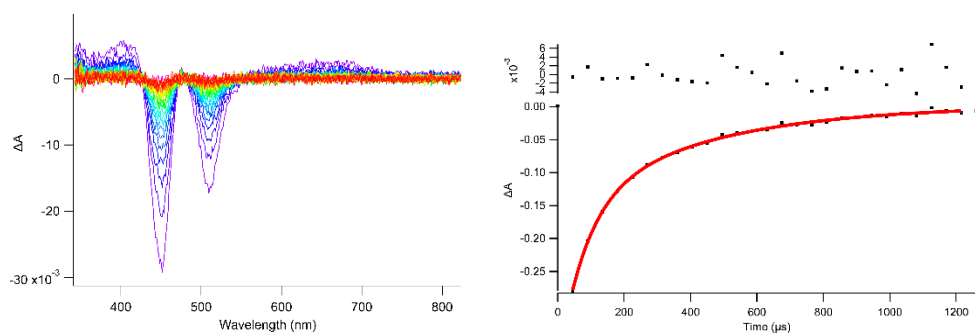


Figure A 67. TA spectra of $\text{Al}(\text{DIPY})_3\mathbf{8}$ (left) and time trace fitting with monoexponential decay function (right) in toluene in oxygen free conditions; $45 \mu\text{s } t_{\text{inc}}$; $\lambda_{\text{exc}} = 450 \text{ nm}$; $\tau_{\text{T}} = 190 \pm 20 \mu\text{s}$.

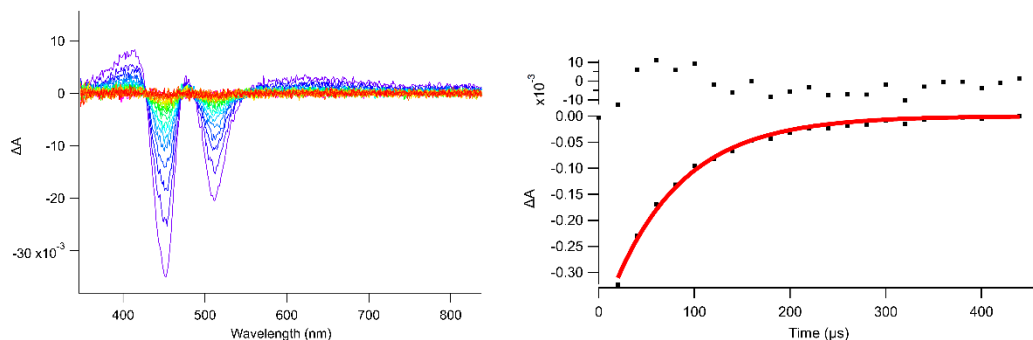


Figure A 68. TA spectra of $\text{Al}(\text{DIPY})_3\mathbf{9}$ (left) and time trace fitting with monoexponential decay function (right) in toluene in oxygen free conditions; $20 \mu\text{s } t_{\text{inc}}$; $\lambda_{\text{exc}} = 450 \text{ nm}$; $\tau_{\text{T}} = 74 \pm 4 \mu\text{s}$.

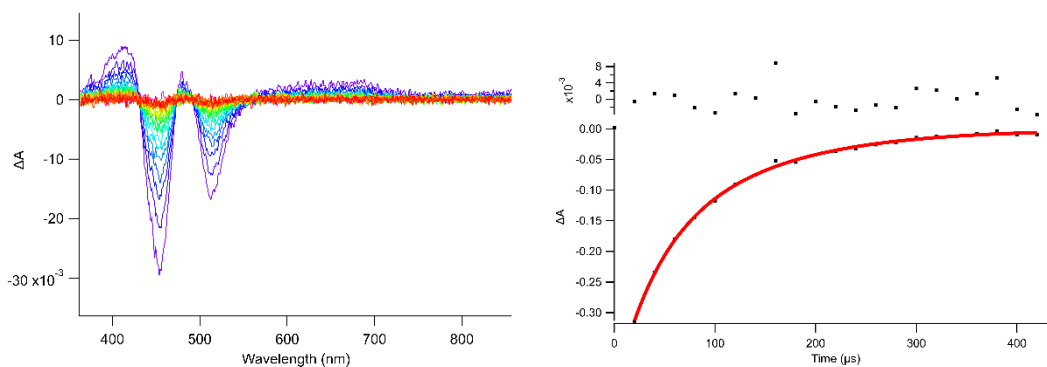


Figure A 69. TA spectra of **Al(DIPY)₃10** (left) and time trace fitting with monoexponential decay function (right) in toluene in oxygen free conditions; 20 μs t_{inc} ;
 $\lambda_{exc} = 450 \text{ nm}$; $\tau_T = 86 \pm 5 \text{ μs}$.

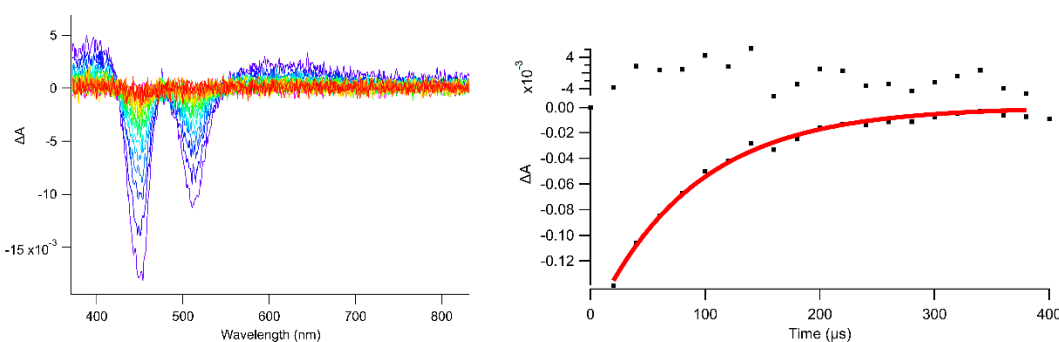


Figure A 70. TA spectra of **Al(DIPY)₃11** (left) and time trace fitting with monoexponential decay function (right) in toluene in oxygen free conditions; 20 μs t_{inc} ;
 $\lambda_{exc} = 450 \text{ nm}$; $\tau_T = 88 \pm 6 \text{ μs}$.

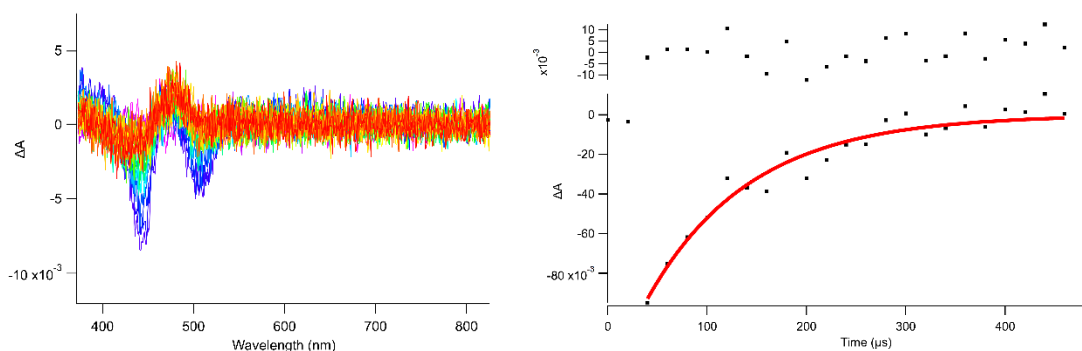


Figure A 71. TA spectra of **Al(DIPY)₃12** (left) and time trace fitting with monoexponential decay function (right) in ethanol in oxygen free conditions; 20 μs t_{inc} ;
 $\lambda_{exc} = 450 \text{ nm}$; $\tau_T = 100 \pm 16 \text{ μs}$.

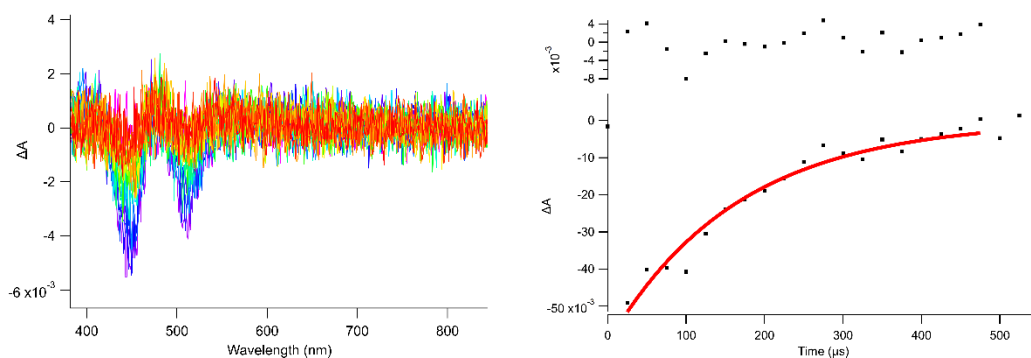


Figure A 72. TA spectra of **Aℓ(DIPY)₃13** (left) and time trace fitting with monoexponential decay function (right) in ethanol in oxygen free conditions; 25 μs t_{inc} ; $\lambda_{exc} = 450 \text{ nm}$; $\tau_T = 170 \pm 20 \text{ } \mu\text{s}$.

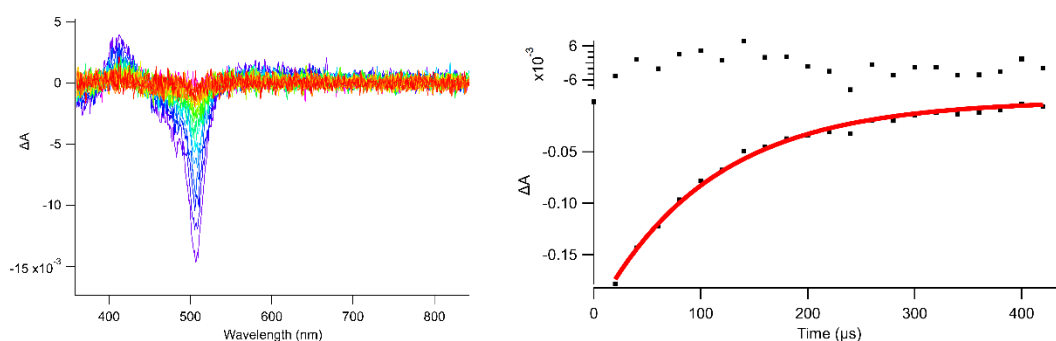


Figure A 73. TA spectra of **Aℓ(DIPY)₃15** (left) and time trace fitting with monoexponential decay function (right) in toluene in oxygen free conditions; 20 μs t_{inc} ; $\lambda_{exc} = 450 \text{ nm}$; $\tau_T = 110 \pm 6 \text{ } \mu\text{s}$.

Singlet oxygen emission spectra

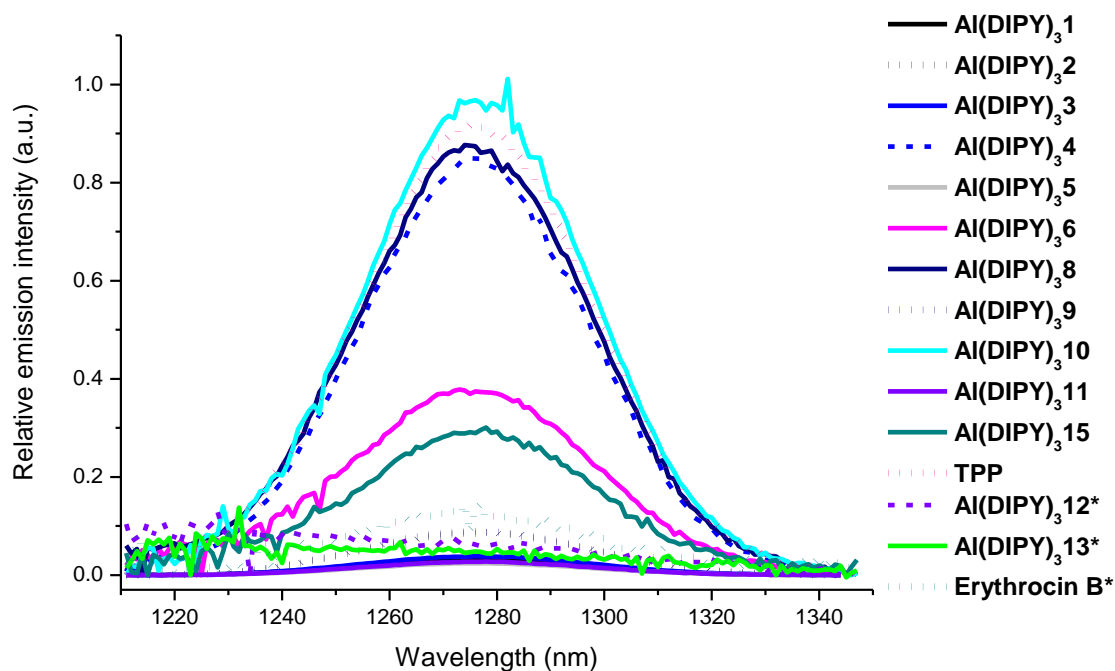


Figure A 74. Singlet oxygen emission spectra of $Al(DIPY)_3$ complexes after excitation at 508 nm in toluene (H_2TPP as reference compound) and ethanol (*, erythrocin B as reference compound).

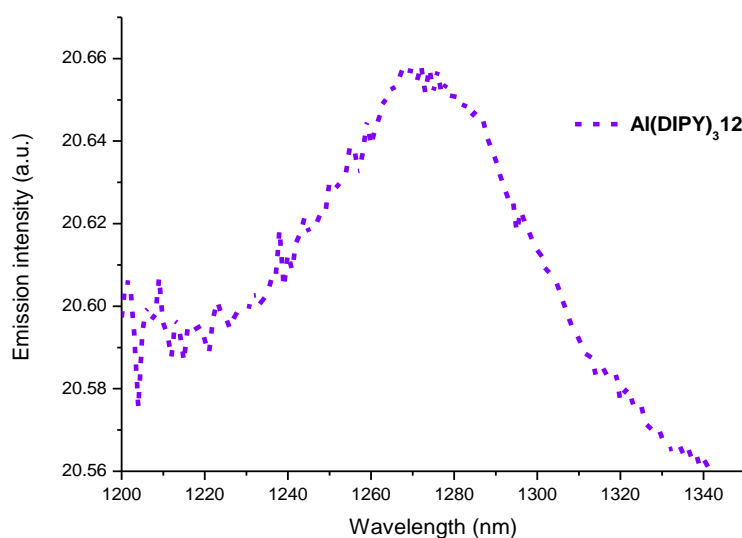


Figure A 75. Singlet oxygen emission spectra of $Al(DIPY)_3 12$ after excitation at 500 nm in THF (ratio of singlet oxygen quantum yield of $Al(DIPY)_3 12$ in THF and reference compound erythrocin B in ethanol was calculated = 0.65)